Acta Physica Hungarica

VOLUME 60, NUMBERS 1–2, 1986

Akadémiai Kiadó, Budapest

ACTA PHYS. HUNG. APAHAQ 60 (1–2) 1–134 (1986) HU ISSN 0231–4428

ACTA PHYSICA HUNGARICA

A JOURNAL OF THE HUNGARIAN ACADEMY OF SCIENCES

EDITED BY
I. KOVÁCS

Acta Physica publishes original papers on subjects in physics. Papers are accepted in English, French, German and Russian.

Acta Physica is published in two yearly volumes (4 issues each) by

AKADÉMIAI KIADÓ
Publishing House of the Hungarian Academy of Sciences
H-1054 Budapest, Alkotmány u. 21

Subscription information

Orders should be addressed to

KULTURA Foreign Trading Company
1389 Budapest P.O. Box 149

or to its representatives abroad.

Acta Physica is indexed in Current Contents, in Physics Abstracts and in Current Papers in Physics.

ACTA PHYSICA HUNGARICA

VOLUME 60

AKADÉMIAI KIADÓ, BUDAPEST

1986

CONTENTS

Volume 60

CONTENTS

Manuscript received by Akadémiai Kiadó: 17 May 1985
Manuscript received by the Printers: 12 June 1985
Date of publication: 30 April 1986

PRINTED IN HUNGARY

Akadémiai Kiadó és Nyomda, Budapest

Acta Physica Hungarica 60 (1—2), pp. 3—17 (1986)

THE LEVEL STRUCTURE OF ^{140}Ce

A. M. HASSAN

Reactor and Neutron Physics Department, Nuclear Research Centre, Atomic Energy Authority (Abu-Zaabal), Cairo, Egypt

S. ABDEL-MALAK, M. A. ABOU-LEILA, A. SROOR and H. A. ISMAIL

Nuclear Physics Laboratory, Ein Shams University, Faculties of Education and Girls Heliopolis, Cairo, Egypt

(Received in revised form 13 December 1983)

The reinvestigation of the level structure of ^{140}Ce fed from the β-decay of ^{140}La (T= 40.2 h) has been carried out by means of singles and gamma–gamma coincidence measurements using Ge(Li), hyperpure Ge and NaI (Tl) detectors.

More than 52 gamma-ray transitions could be identified, thirteen of them of energies at 20.7, 167.89, 411.9, 468.60, 668.85, 700.29, 721.09, 976.69, 995.7, 1009.80, 1061.88, 1150.18 and 1214.90 keV have been observed and fitted in the level scheme for the first time.

The energy levels of the nucleus under investigation have been discussed and the experimental results obtained are compared with the previous work.

1. Introduction

The decay of ^{140}La to levels in ^{140}Ce is of particular interest, since the daughter nucleus has a magic number of neutrons ($N = 82$) and its energy levels can have features typical of single closed shell nucleus, i.e. a large energy gap between the ground and the first excited state.

A considerable number of investigations [1–6] have been carried out to study the level structure of ^{140}Ce fed from β-decay of ^{140}La ($T_{1/2} = 40.2$ h).

However several discrepancies have been reported concerning the energy levels and gamma transitions in ^{140}Ce nucleus.

For instance Baer et al [1] proposed two energy levels at 3123.0 and 3389.6 keV which could not be confirmed by Karlsson et al [2], Baer et al [3], Kalinnikov et al [4], Ardisson et al [5] and Kaur et al [6]. In the mean time Karlsson et al [2] proposed the three new energy levels at 2325.0, 3216.1 and 3322.0 keV which were not confirmed by Baer et al [3], Kalinnikov et al [4], Ardisson et al [5] and Kaur et al [6]. Also Kalinnikov et al [4] proposed three new energy levels at 2533.0, 3016.1 and 3498.0 keV not observed by others [5, 6].

Also Ardisson et al [5] proposed two new energy levels at 2495.0 and 3473 keV not observed by Kaur et al [6]. Moreover, Kaur et al [6] proposed an energy level at 3000.7 keV.

Therefore, it has been thought that a reinvestigation of the gamma-ray transitions in ^{140}Ce nucleus using a large volume of Ge(Li) detector and a hyper pure Ge detector together with a fast–slow coincidence circuit may yield information which may help in solving some of these discrepancies.

2. Experimental procedure

Since natural lanthanum contains the stable isotopes ^{138}La and ^{139}La with abundances of 0.089% and 99.911%, respectively, so the source of ^{140}La was simply produced by irradiating the 1.7 mg lanthanum oxide in the Egyptian Research Reactor–1 (ET-RR-1).

In the present study the gamma transitions associated with the decay of ^{140}La into ^{140}Ce have been investigated using the 76.1 cm^3 Ge(Li) detector (Coaxial Type) and a spectroscopy amplifier in conjunction with the 4096 channels pulse height analyzer.

A hyper pure Ge detector LEPS, (planar type), 10 mm active diameter and 7 mm active depth, provided with a preamplifier, spectroscopy amplifier and 4096 pulse height analyser has been used to investigate the low energy gamma transitions ($E_\gamma < 350$ keV). The resolution of the hyper pure Ge is 511 eV for 122 keV and 204 eV for 5.9 keV.

The gamma–gamma coincidence measurements have been carried out using a Ge(Li)–NaI(Tl) spectrometer provided with a fast–slow coincidence circuit. The resolving time of the fast–slow coincidence circuit was 16.2 ns, while that of the slow coincidence circuit was 1.38 μs.

The gamma-singles spectra have been measured once every life-time to make sure that the gamma transitions obtained belong only to the ^{140}Ce nucleus.

The relative gamma-ray intensities have been estimated using the efficiency curves of the Ge(Li) and the hyper pure Ge detectors [7], measured under the same conditions of this experiment. The evaluation procedure was carried out manually.

Using the Ge(Li)–NaI(Tl) coincidence spectrometer [7] three runs have been performed where the NaI(Tl) detector is used to select gamma transitions of energies at 328.8, 486.9, 1596.6 keV, respectively, for gating purposes. But due to the fact that the resolution of the NaI(Tl) detector is about 9% at 1333 keV the other neighbouring gamma transitions were included in the 328.8 keV gate mentioned above.

3. Results and discussion

A) Gamma-ray singles spectrum

The gamma-ray singles spectrum obtained using the Ge(Li) spectrometer is shown in Figs 1a and b.

Fig. 2 presents the gamma-ray singles spectra for $E_\gamma < 350$ keV obtained by using the hyper pure Ge spectrometer. From these two figures, about 13 gamma-ray transitions could be noticed for the first time. These transitions have the energies at 20.7, 167.89, 411.90, 468.60, 668.85, 700.29, 721.09, 976.69, 995.70, 1009.80, 1061.88, 1150.18 and 1214.90 keV.

There is no evidence for the presence of the gamma rays at 42.0, 798.0, 936.0, 1045.0, 1303.0, 1404.9, 1521.8, 1903.0, 3123.0 and 3319.7 keV which have been mentioned in references [1–6]. The relative intensities of the gamma-ray transitions obtained have been estimated taking into consideration the intensity of gamma-ray transition at 1596.6 keV as 100%.

The energies and relative intensities [7] of the well resolved 52 gamma-ray transitions are presented in Table I together with the previous data for the sake of comparison.

B) Gamma–gamma coincidence spectra

(i) When the NaI(Tl) detector was used to gate (1550 keV $< E_\gamma <$ 1650 keV), the gamma transitions identified for the first time in the present singles spectra at 411.9, 468.6, 668.85, 700.29, 1009.8, 1061.88, 1150.18 and 1214.9 keV have been followed by the cascades at 411.9–486.93–1596.6 keV, 468.6–950.98–1596.6 keV, 668.85–950.98–1596.6 keV, 700.29–919.54–1596.6 keV, 1150.18–751.65–1596.6 keV, 1214.9–307.04–1596.6 keV, respectively, as shown in Table II and Fig. 3.

The following gamma-ray transitions have been seen also by this gate: (307.04 [1, 2, 3, 4, 6]), 438.14 [4, 6], 618.14 [1–4, 6] and 1419.93 [4] keV which were observed in the previous work as mentioned above.

(ii) When the NaI(Tl) detector in the Ge(Li)–NaI(Tl) coincidence spectrometer was used to select the ($450 < E_\gamma < 525$) gating gamma-ray transitions, the two new gamma-ray transitions at 411.9 and 700.29 keV have been followed by the cascades at 411.9–486.93 keV and 700.29–432.61–486.93 keV, respectively, as presented in Table III and illustrated in Fig. 4. Using this gate the gamma-ray transitions at 438.24 [4, 6] and 1414.93 keV [4] have been observed as well.

(iii) When the NaI(Tl) detector was used to select the $300 < E_\gamma < 360$ keV gating gamma-ray transitions, the new gamma-ray transitions at 976.69, 1061.86, 1214.9 keV have been followed by the cascades at 976.69–328.82 keV, 1061.88–328.82 keV and 1214.9–307.04 keV, respectively, as shown in Table IV and Fig. 5.

The gamma-ray transition at 618.14 [1–4, 6] keV has been also observed in the same gate.

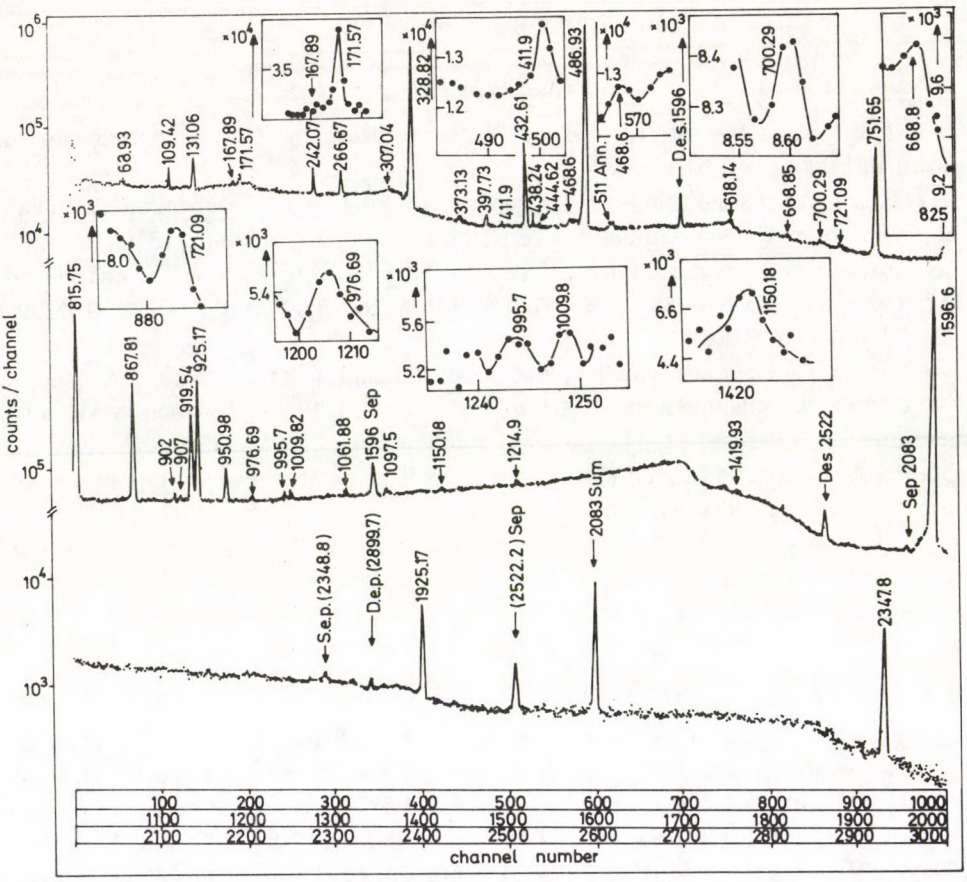

Fig. 1a. The gamma-ray singles spectrum associated with the decay of ^{140}La to ^{140}Ce obtained using a 76.1 cm^3 Ge(Li) spectrometer

C) Level structure of ^{140}Ce

The gamma-ray transitions identified in the present gamma-ray singles and gamma–gamma coincidence spectra could be used to reconstruct the level structure of ^{140}Ce and the suggested level scheme is illustrated in Fig. 6.

From this level structure one can conclude the following:

1) Thirteen gamma-ray transitions of energies at 20.7, 167.89, 411.9, 468.6, 668.85, 700.29, 721.09, 976.69, 995.7, 1009.80, 1061.88, 1150.18 and 1214.9 keV have been identified for the first time in the singles and/or gamma–gamma coincidence spectra and were fitted in the suggested level structure as shown in Fig. 6.

Although some of the new gamma-ray transitions (which showed a somewhat weak indication) were submerged in the Compton edges in the singles spectrum, yet

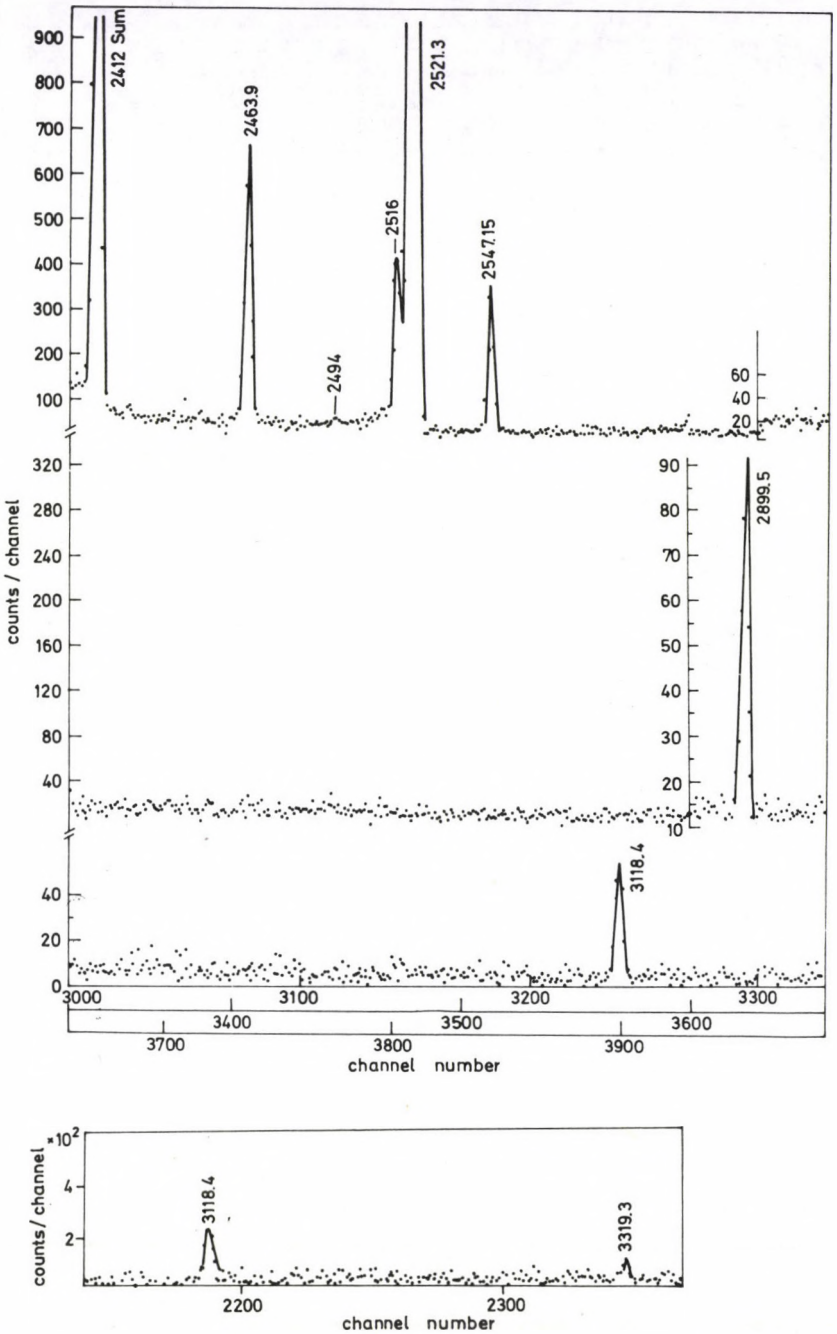

Fig. 1b. The gamma-ray singles spectrum associated with the decay of ^{140}La to ^{140}Ce obtained using a 76.1 cm^3 Ge(Li) spectrometer

Table I

Energies and relative intensities of gamma-ray transition in ^{140}Ce following the decay of ^{140}La

Present work		R. Kaur et al [6]		Ardisson et al [5]		Kalinnikov et al [4]		Assignments
E_γ [keV]	I_γ	E_γ [keV]	I_γ	E_γ [keV]	I_γ	E_γ [keV]	I_γ	
20.7[a)]	0.011 ± 0.001	–	–	–	–	–	–	2515.71 – 2495.0
24.6	0.156 ± 0.006	24.5	–	–	–	–	–	2107.7 – 2083.1
62.13	0.01 ± 0.001	64.135	–	64	0.04	64.13	20.04	2411.9 – 2349.7
68.93	0.07 ± 0.002	68.916	0.070 ± 0.016	69.1	0.1	68.9	0.064	2480.8 – 2411.9
109.42	0.119 ± 0.006	109.418	0.17 ± 0.01	109.4	0.22	109.4	0.21	2521.3 – 2411.9
131.06	0.52 ± 0.020	130.97	0.44 ± 0.01	131	0.61	131.122	0.5	2480.8 – 2349.7
167.89[b)]	–	–	–	–	–	–	–	2515.7 – 2347.8
171.57	0.147 ± 0.006	173.4	0.12 ± 0.01	173.5	0.2	173.5	0.13	2521.3 – 2349.7
242.07	0.544 ± 0.028	242.06	0.45 ± 0.01	242	0.47	241.9	0.41	2349.7 – 2107.7
266.67	0.504 ± 0.027	266.6	0.52 ± 0.01	266	0.59	266.5	0.49	2349.7 – 2083.1
307.04	0.055 ± 0.002	307.1	0.022 ± 0.006	–	–	306.9	0.035	1903.2 – 1596.1
328.82	22.6 ± 1.10	328.78	21.5 ± 0.36	328.8	19.9	328.7	19.4	2411.9 – 2083.1
373.13	0.058 ± 0.002	373.13	–	–	–	–	–	2480.8 – 2107.7
397.73	0.126 ± 0.006	397.73	0.078 ± 0.003	398	0.04	397	1.1	2480.8 – 2083.1
411.9	0.054 ± 0.002	–	–	–	–	–	–	2495.0 – 2083.1
432.61	2.99 ± 0.050	432.66	3.05 ± 0.03	432.6	3.0	432	2.85	2515.7 – 2083.1
438.24	0.036 ± 0.001	438	0.005 ± 0.003	–	–	438.5	0.021	2521.3 – 2083.1
444.62	0.005 ± 0.002	445	0.005 ± 0.003	–	–	446	0.025	2347.8 – 1903.2
468.6	0.004 ± 0.002	–	–	–	–	–	–	3016.1 – 2547.1
486.93	49.9 ± 2.40	486.9	46.55 ± 0.88	487.1	49	487	45	2083.1 – 1596.1
618.14	0.114 ± 0.004	618.2	0.049 ± 0.006	–	–	618.2	0.045	2521.3 – 1903.2
668.85	0.038 ± 0.001	–	–	–	–	–	–	3216.0 – 2547.1
700.29	0.014 ± 0.001	–	–	–	–	–	–	3216.0 – 2515.7
721.09[a)]	0.03 ± 0.001	–	–	–	–	–	–	3216.0 – 2495.0
751.65	4.75 ± 0.230	751	4.45 ± 0.05	752	4.25	751.8	4.4	2347.8 – 1596.1
–	–	–	–	798	0.18	–	–	–
815.75	28.11 ± 1.40	815.7	24.0 ± 0.40	815	22.4	815.8	23.5	2411.9 – 1596.1
867.81	6.14 ± 0.30	867.8	5.69 ± 0.06	867.9	5.6	867.9	5.6	2463.9 – 1596.1
902.0*[)]	0.3 ± 0.012	–	–	902	0.24	–	–	–
907.0*[)]	0.32 ± 0.012	–	–	907	0.28	906.4	0.06	–
919.54	3.03 ± 0.14	919.4	2.83 ± 0.04	919	3.08	919.6	2.64	2515.7 – 1596.1

925.17	7.35 ±0.36	925.14	7.26 ±0.08	925.2	7.84	925.2	7.1	2521.3 – 1596.1
–	–	–	–	–	–	936.9	0.06	–
950.98	0.583 ± 0.02	950.95	0.553 ± 0.007	951	0.44	951.4	0.55	2547.1 – 1596.1
976.69	0.044 ± 0.001	–	–	–	–	–	–	3498.0 – 2521.3
995.7	0.020 ± 0.001	–	–	–	–	–	–	2898.9 – 1903.2
1009.80	0.0142 ± 0.001	–	–	–	–	–	–	3473.8 – 2463.9
–	–	1045	0.024 ± 0.004	–	–	–	–	–
1061.88	0.045 ± 0.001	–	–	–	–	–	–	2473.8 – 2411.9
–	–	–	–	–	–	1088	0.003	–
1097.5	0.033 ± 0.001	1097	0.024 ± 0.005	–	–	–	–	3000.7 – 1903.2
1150.18	0.023 ± 0.001	–	–	–	–	–	–	2498.0 – 2347.8
1214.9	0.076 ± 0.002	–	–	–	–	–	–	3118.4 – 1903.5
–	–	1303.3	0.046 ± 0.005	–	–	–	–	–
–	–	1404.9	0.066 ± 0.009	–	–	–	–	–
1414.9[b]	–	–	–	1416	0.2	1415	0.006	3498.0 – 2083.1
1419.93	0.082 ± 0.002	–	–	–	–	1419.5	–	3016.1 – 1596.1
–	–	–	–	1521.8	0.15	–	–	–
1596.6	100	1596.9	100	1596	100	1596.4	100	1596.1 – 0
–	–	–	–	1877	0.015	–	–	–
–	–	1909	0.002 ± 0.002	–	–	1903.13	0.006	–
1925.17*)	–	1924*)	0.014 ± 0.003	–	–	–	–	–
2083	3.03 ±0.14	2082.9	0.045 ± 0.003	–	–	–	–	–
2347.8	1.14 ±0.05	2347.8	0.89 ±0.01	2348.4	–	2348.1	–	2347.8 – 0
2463.9	0.2 ±0.01	2464.0	0.012 ± 0.001	2464.4	–	2465.3	–	2463.9 – 0
2494	–	–	–	2494	–	–	–	–
2521.3	3.82 ±0.18	2521.36	3.58 ±0.05	2521.8	–	2521.7	–	2521.34 – 0
–	–	–	–	–	–	2533.4	–	–
2547.15	0.118 ± 0.006	2547.19	0.105 ± 0.002	2547.9	0.191	2547.5	0.11	2547.1 – 0
2899.5	0.0633 ± 0.002	2899.5	0.07 ±0.001	2898.9	0.073	2899.7	0.065	2899.5 – 0
3118.4	0.023 ± 0.001	3118.4	0.027 ± 0.001	3119.1	0.023	3119	0.027	3118.4 – 0
3319.3	0.05 ±0.001	3319.3	0.004 ± 0.003	3319.1	0.0447	3319.6	0.0047	3319.3 – 0

[a] Singles only
[b] Coincidence only
*) Not fitted in the decay scheme

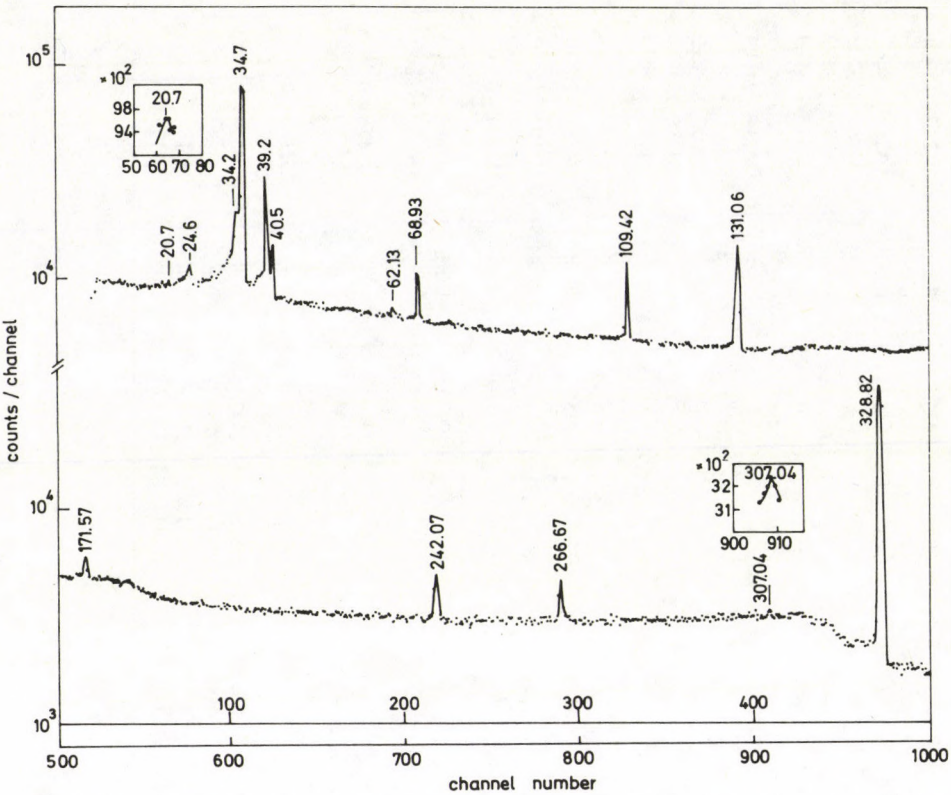

Fig. 2. The gamma-ray singles spectrum ($E_\gamma < 350$ keV) using the hyper pure Ge spectrometer

Table II

Results of γ–γ coincidence studies using Ge(Li)–NaI(Tl) spectrometer (Gate width 1550–1650 keV)

E_γ in gate	Observed γ-transitions in coincidence with E_γ in gate				
1596	109.42	131.06	167.89	171.57	266.67
	307.04	328.82	397.73	411.9	432.61
	438.24	444.62	468.6	486.93	618.14
	668.85	700.29	751.65	815.75	867.81
	919.54	925.17	950.98	995.7	1009.80
	1061.88	1097.5	1150.18	1214.9	1419.93

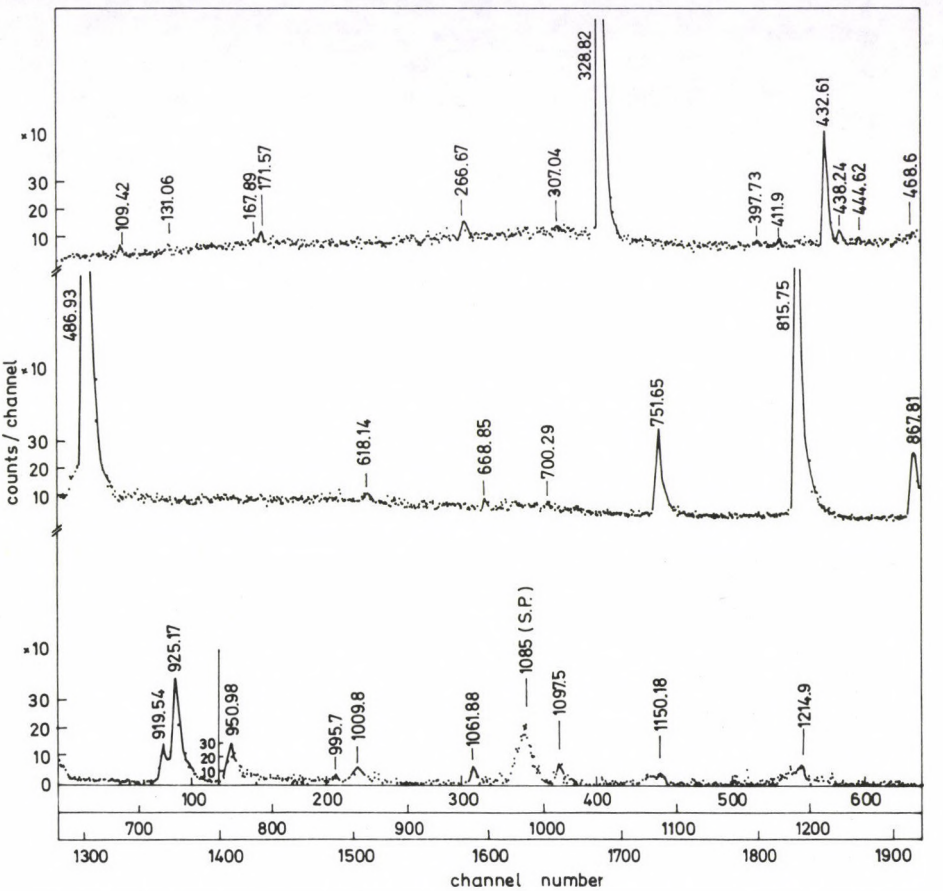

Fig. 3. The γ–γ coincidence spectrum obtained using Ge(Li)—NaI(Tl) spectrometer: γ-transition in gate is 1596.6 keV

Table III

Results of γ–γ coincidence studies using Ge(Li)–NaI(Tl) spectrometer. (Gate width 450–525 keV)

E_γ in gate	Observed gamma transition in coincidence with E_γ in gate				
486.93	62.13	68.93	109.42	131.06	171.57
	266.67	328.82	397.73	411.9	432.61
	438.24	700.29	1414.9		

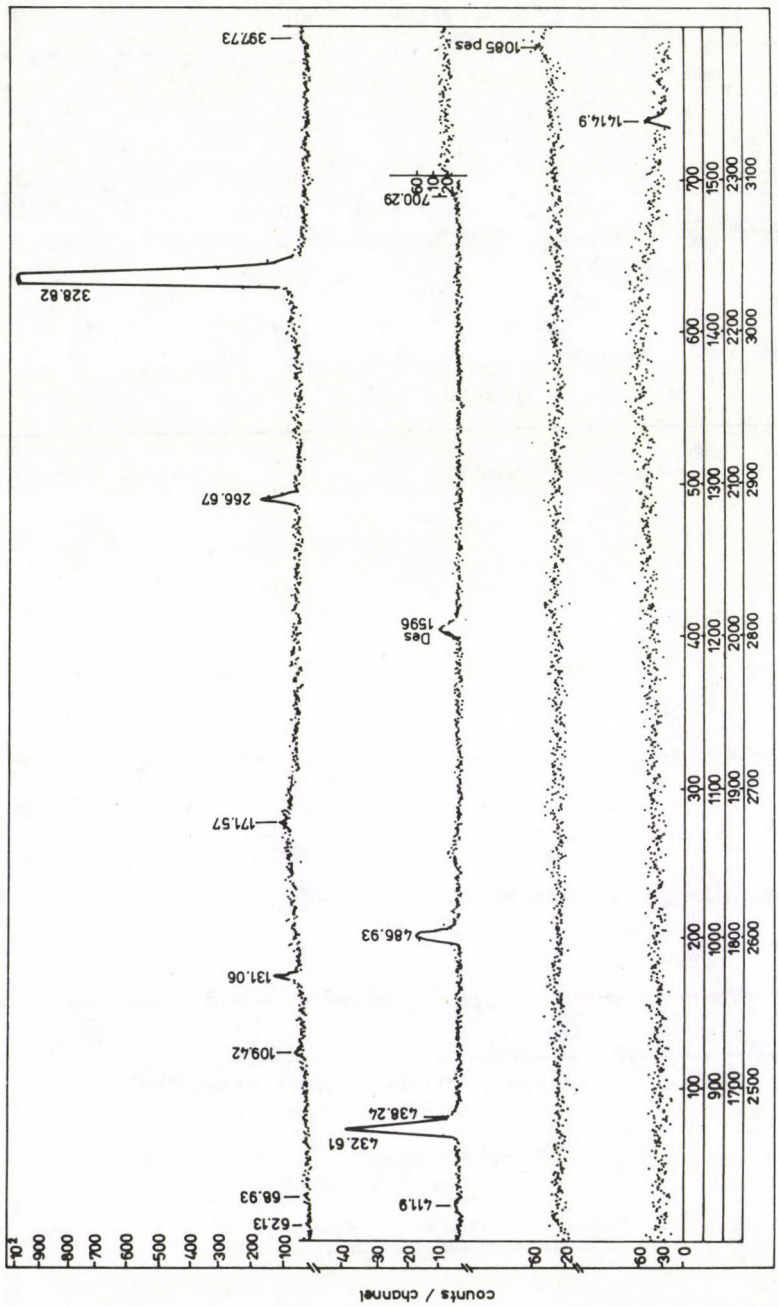

Fig. 4. The γ–γ coincidence spectrum obtained using Ge(Li)—NaI(Tl) spectrometer: γ-transition in gate is 486.93 keV

Table IV

Results of γ–γ coincidence studies using Ge(Li) NaI(Tl) spectrometer. (Gate width 300–360 keV)

E_γ in gate	Observed gamma transitions in coincidence with E_γ in gate				
307.04	444.62	618.14	995.7	1097.5	1214.9
328.8	68.93	109.42	486.93	976.69	1061.88

they were clearly confirmed in the coincidence runs to fit and confirm different energy levels. Some comments follow on these new gamma-ray transitions observed in the present work.

— The 20.7 keV transition was observed in the (HPGe) singles spectrum, see Fig. 2.
— The 167.89 keV transition was observed only in coincidence gate of 1596 keV, as shown in Fig. 3.
— The 373.13 keV transition was previously observed by Kaur et al [6] and it is only confirmed in the present singles spectrum, Fig. 1a.
— The 411.9 keV transition is identified in the singles spectrum, Fig. 1a, and confirmed as well in the 1596, 486.93 keV coincidence gates.
— The 468.6 keV transition submerged in the Compton edge and accordingly it was not clear in the singles spectrum, but it is confirmed in the 1596 keV coincidence gate as shown in Fig. 3.
— The 668.85 keV transitions was clearly observed in the 1596 keV coincidence gate as shown in Fig. 3.
— The 700 29 keV transition could be observed in the singles spectrum shown in Fig. 1a and confirmed due to its observation in the coincidence gates of 486.93 and 1596.6 keV shown in Figs 4 and 3, respectively.
— The 721.09 keV transition was observed in the singles spectrum shown in Fig. 1a and could be fitted in the decay scheme according to energy considerations to fit between the 3216.0 and 2495.0 keV levels.
— The 976.69 keV transition was clear in the singles spectrum in Fig. 1a and it was confirmed clearly in the coincidence measurements in the 328.8 keV coincidence gate as shown in Fig. 5.
— The 995.7 keV transition is confirmed due to its presence in the 1596 keV and 307.04 keV coincidence gates as shown in Figs 3 and 5.
— The 1009.8 keV transition could be confirmed without doubt in the 1596 keV coincidence gate shown in Fig. 3.
— The 1061.88 keV transition is observed in the singles spectrum in Fig. 1a and confirmed in the coincidence gates of 1596 and 328.8 keV shown in Figs 3 and 5.
— The 1150.18 keV transition was clear in both singles spectrum (Fig. 1a) and in coincidence measurements at gate of 1596 keV shown in Fig. 3.

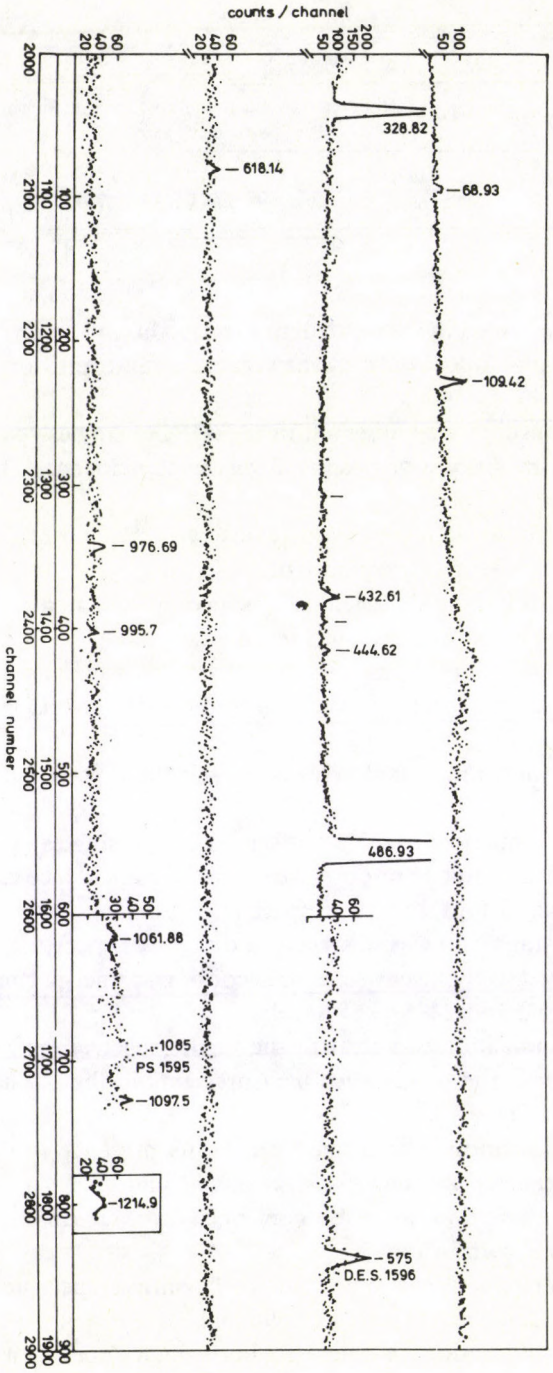

Fig. 5. The γ–γ coincidence spectrum obtained using Ge(Li)—NaI(Tl) spectrometer: γ-transitions in gate are 307.4 and 328.82 keV

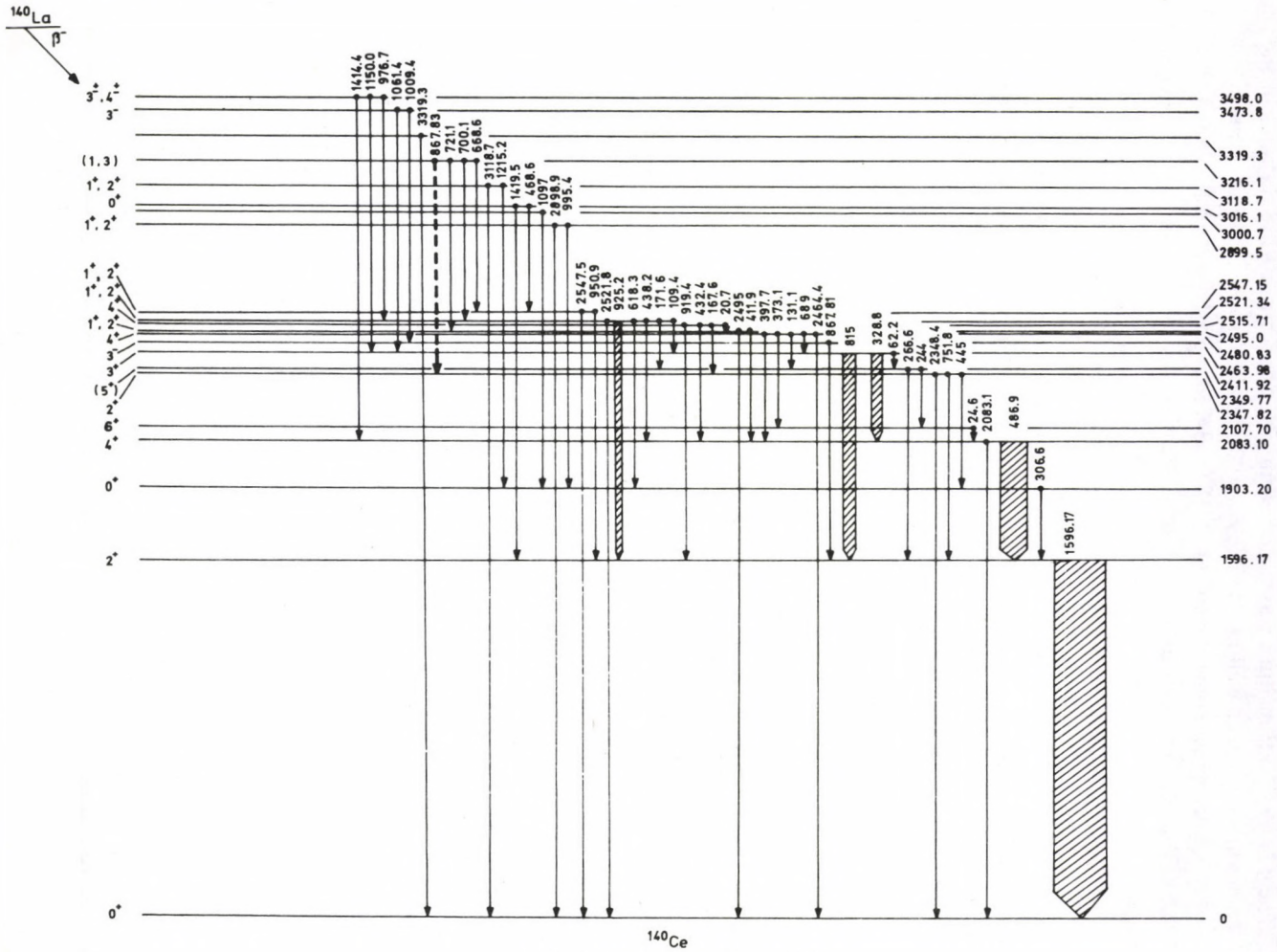

Fig. 6. The level structure of ^{140}Ce

— The 1214.9 keV transition was observed in singles spectrum (Fig. 1a) and in the coincidence gates as well at 1596 keV and 307.04 keV shown in Figs 3 and 5.

2) Concerning some levels at 3418.0, 3473.8, 3261.1, 3016.1, 3000.7 and 2494.0 keV it was essential to give a brief discussion:

i) The 3498.0 keV level:

It is proposed by Kalinnikov et al [4] as depopulated by 1414.9 and 1088 keV gamma-ray transitions. However, the 1414.9 keV transition could not be observed by others [6] but it is confirmed in the present coincidence measurements. In addition, the present study has revealed other depopulating gamma-ray transitions at 976.69 and 1150.18 keV in both the singles and gamma–gamma coincidence spectra.

ii) The 3473.8 keV level:

This energy level is proposed by Ardisson et al [5] but was discarded by Kaur et al [6]. In the present work, its presence is confirmed by the observation of the new depopulating gamma-ray transitions at 1061.88 and 1009.82 keV in both the singles and gamma–gamma coincidence spectra.

iii) The 3216.1 keV level:

It is proposed by Karlsson et al [2] as being depopulated by the gamma-ray transition at 867.81 keV. Later, Baer et al [3] took into consideration the 2463.98 keV level proposed by Hasen and Nathan [8], and assigned the 867.81 keV γ-ray as the transition depopulating the 2463.98 level to the 1596.1 keV level. This position and this level were confirmed later [4, 5, 6]. The 867.81 keV γ-ray transition is confirmed also in the present work to depopulate the 2463.98 level. Yet its presence as depopulating the 3216.1 keV level could not be ruled out as the 3216.1 keV level was confirmed due to the observation of the new gamma transitions depopulating it at 668.85, 700.2, and 721.0 keV in the singles spectrum and the observation of 668.85 and 700.2 keV transitions in the coincidence measurements.

iv) The 3016.1 keV level:

It is proposed by Kalinnikov et al [5] as depopulated by the 1419.93 keV gamma-ray transition, however, this line could not be observed by others [5, 6], but was observed in this work in both the singles and coincidence spectra. In the meantime this level could be depopulated by the new gamma-ray transition at 468.6 keV which was observed in the singles and the gamma–gamma coincidence spectra.

v) The 3000.7 keV level:

This energy level is proposed by Kaur et al [6] to fit the previously [8] proposed gamma-ray transitions at 1404.9 and 1097.2 keV. Although, in the present work the 1404.9 keV gamma-ray transition was not observed, however, the 3000.7 keV level is confirmed by the presence of the 1097.2 keV gamma-ray transition in both singles and coincidence measurements.

vi) The 2494.0 keV level:

This energy level is proposed by Ardisson et al [5] depopulated by the gamma-ray transition at 2494.0 keV but Kaur et al [6] did not include this level in their investigation. The present data shows the presence of the 2494.0 keV transition and, in addition, suggests the depopulation by the new gamma transition at 411.9 keV which could be identified in the singles spectrum and is confirmed by the coincidence measurements. Also, this level is populated by the new gamma-ray transitions at 20.7 and 721.09 keV observed in the present singles spectra.

The energy levels at 3123.0 and 3389.6 keV proposed by Baer et al [1], 2325.0 and 3322.0 keV by Karlsson et al [2] and 2533.0 keV by Kalinnikov et al [4] could not be confirmed in the present work, since there was no experimental evidence of the gamma-ray transitions populating and/or depopulating these energy levels.

References

1. H. W. Baer, J. J. Reidy and M. L. Wiedenbeck, Nucl. Phys., *86*, 332, 1966.
2. S. E. Karlsson, B. Svahn, H. Pettersson and G. Malmsten, Nucl. Phys., *A100*, 113, 1967.
3. H. W. Baer, J. J. Reidy and M. L. Wiedenbeck, Nucl. Phys., *A133*, 33, 1968.
4. V. G. Kalinnikov, Kh. L. Ravn, H. G. Honsen and N. A. Lebedev, Bull Acad. Sci. USSR, Phys. Ser., *34*, 815, 1971.
5. G. Ardisson and C. Marrol, Rev. Roum Phys., *16*, 1045, 1971.
6. R. Kaur, A. K. Shorma, S. S. Sooch and P. N. Trehan, J. of the Phys. Soc. of Japan, Vol. *49*, No. 6, December 1980.
7. A. T. Sroor, Ph. D. Thesis, to be presented to the Faculty of Girls, Ain Shams University.
8. R. J. Gehrke, U. S. AEC Report ANCR-1088, 392, 1972.

Acta Physica Hungarica 60 (1—2), pp. 19—30 (1986)

SOME TEMPERATURE DEPENDENT PROPERTIES OF POTASSIUM DIHYDROGEN PHOSPHATE

H. I. FARAG, M. S. ELMANHARAWY

Physics Unit, National Cancer Institute, Cairo University, Cairo, Egypt

and

A. ABDEL-KADER

Physics Department, Faculty of Science, Menoufia University, Menoufia, Egypt

(Received in revised form 3 January 1984)

Single crystals of potassium dihydrogen phosphate (KDP) have been grown at room temperature from saturated aqueous solutions. The thermal behaviour has been studied by differential thermal analysis and confirmed by X-ray diffraction and infrared spectroscopy. When heated to 613 K, KDP loses its water content and a transition takes place from the tetragonal ortho-phase to the monoclinic meta-phase. The resistivity of KDP crystals has been found to decrease exponentially with temperature over the temperature range of 293 K to 383 K above which it attains a constant value independent of further temperature rises up to 478 K. A value of 0.588 eV has been estimated for the activation energy of rotation of the phosphate group which controls conduction over the temperature dependent region of the resistivity curve. Glow curves of gamma-ray irradiated single crystals subsume peaks similar to those detected for the polycrystalline powder. Energy depths varying from 0.20 eV to 0.46 eV have been calculated for the various trapping states created by gamma irradiation. Effects of increasing gamma dose have been studied and found to cause an increase in number and intensity of the glow peaks. Slight shifts in peak temperatures to lower values are also noted at high gamma doses and attributed to the combined effect of dose rate and interactions between trapping centres.

Introduction

Potassium dihydrogen phosphate (KDP) belongs to a group of materials which are hydrogen bonded ferroelectrics. The hydrogen atoms play the main role in the ferroelectric properties of the material which appear at its ferroelectric phase transition [1–3]. Ferroelectric crystals have been classified into two groups: the order–disorder group and the displacive one. In the first group, phase transition is associated with the ordering of ions but in the second group it is associated with the displacement of a whole sublattice of ions of one type relative to another sublattice. KDP belongs to the order–disorder class of ferroelectrics including crystals with hydrogen bonds in which the motion of protons is related to the ferroelectric properties of the material [4].

Numerous publications exist on KDP characteristics but we were unable to trace any report so far on the thermoluminescence of the material. Structural studies, for example, were reported as early as 1947 [5] but the most important work in this

domain is that of Bacon and Pease [6] which showed KDP to have tetragonal crystal structure at room temperature with a space group $I\bar{4}2d$; i.e. in the paraelectric phase. Positions of the potassium and phosphorus atoms are fixed by symmetry but the sixteen oxygen atoms in the unit cell exist in a set of general positions. Neutron diffraction studies were later made to determine the precise positions of the hydrogen and oxygen atoms and to investigate the origin of ferroelectricity [6, 7].

Several models have been also proposed to explain the mechanism of phase transition in KDP-type materials. The model of Imry and his coworkers appears to be widely accepted and shows these hydrogen bonded crystals to exhibit both a low temperature ferroelectric phase transition and a high temperature one [8]. The latter phase transition has been the subject of further investigations related to its detection in dielectric measurements, infrared reflection studies and differential thermal analysis [9–12].

Electrical condution has been reported in both pure and doped single crystals of KDP-type materials with the objective to explain the mechanism of phase transition as well as the observed conduction. These studies are of significance related to the application of KDP-type materials either as electro-optical polarizers or harmonic generators in several optical devices. The optical properties of these materials have been the subject of several discussions and disputes because of several uncertainties and ambiguities in the reported data as well as in their interpretation [13–16].

In the present paper, some temperature-dependent properties of carefully prepared KDP single crystals are reported. The thermal behaviour of the material has been investigated by differential thermal analysis and checked by X-ray diffraction and infrared spectroscopy. Electrical conductivity has been also studied. Most important of all is the thermoluminescence analysis for gamma ray irradiated single crystals which to our knowledge has not been previously reported.

Experimental

(i) Material and X-ray analysis

Single crystals were grown using a Hopkin and Williams potassium dihydrogen phosphate as the starting material for crystallization; the reagent used being of the purest grade available. Crystal growth took place at room temperature by a twice recrystallization process from saturated aqueous solutions. Crystals of reasonable dimensions were cleaved and polished while others were ground in an agate mortar and the polycrystalline powder was stored in a desiccator ready for use when needed. The structure of these crystals was identified in a Shimadzu X-ray diffractometer using the Cu K_α radiation of 1.5418×10^{-10} m. The data were then compared with the index cards of the American Society for Testing Materials. The X-ray diffraction pattern showed sharp lines indicating a high degree of crystallinity. At room temperature,

KDP was found to have a tetragonal structure. The lattice constants a and b have been estimated as 7.447×10^{-10} m while the parameter c has a value of 6.974×10^{-10} m; the lattice constants being evaluated by means of the equation applicable to this type of structure [17]. The volume of the unit cell is thus equal to $386.763 \times (10^{-10}\ \text{m})^3$ while that of one molecule is $96.656 \times (10^{-10}\ \text{m})^3$; the latter being deduced from the molecular weight of KDP (136.09 g); its density (2338 kg/m^3) and Avogadro's number. Accordingly, the unit cell comprises four KDP molecules. Estimated values of the lattice constants, the unit cell volume and the number of molecules per unit cell have been found to agree closely with reported values [4–6]. This is a fairly good evidence that the preparation technique adopted in this work for growing KDP single crystals from saturated aqueous solutions is satisfactory and reliable.

(ii) Measurements

The thermal behaviour of KDP was studied in the Shimadzu differential thermal analyzer. Samples were contained in platinum crucibles during measurements and variations in their specific heat with rising temperature were traced relative to aluminium oxide which served as a reference. Infrared spectroscopy was made on KDP samples before and after their subjection to differential thermal analysis. Transmittance was measured in the wavenumber range of 20000 m^{-1} to 4×10^5 m^{-1} in the IR 4220 Beckman spectrophotometer using the well known KBr disc technique.

Electrical measurements were performed at different temperatures on KDP single crystals of various dimensions. The two rectangular opposite faces (001) of the crystal were painted with silver paste before it was mounted in the cell used for holding it during measurements. A block diagram of the circuit used for measuring I–V characteristics is shown in Fig. 1 which includes the cell oven system used for heating the sample to any desired temperature. A potential difference of 0–800 V was applied across the crystal from a stabilized d.c. power supply and was measured by a vacuum tube voltmeter. The current flowing through the crystal was measured by a Kiethley 610C solid state electrometer. The decade resistor introduced into the circuit served to protect the electrometer against sudden changes in current. Measurements made above room temperature were carried out with the cell sample system placed in an oven; the temperature of sample being measured by an iron-constantan thermocouple connected to a pyrometer.

Glow curves were measured in an apparatus of a layout similar to that previously described [18]. The gammatron S80 cobalt unit was used for irradiation of sample while being held in vacuum at liquid nitrogen temperature. Single crystals and polycrystalline powders were separately given gamma ray doses varying from 10^2 Gy to 10^4 Gy. They were then heated in dark at a slow rate of 0.25 K/s and only glow curves with the best linear heating rates were selected for analysis. For each given gamma ray dose, three curves were recorded; the reproducibility of measurements was

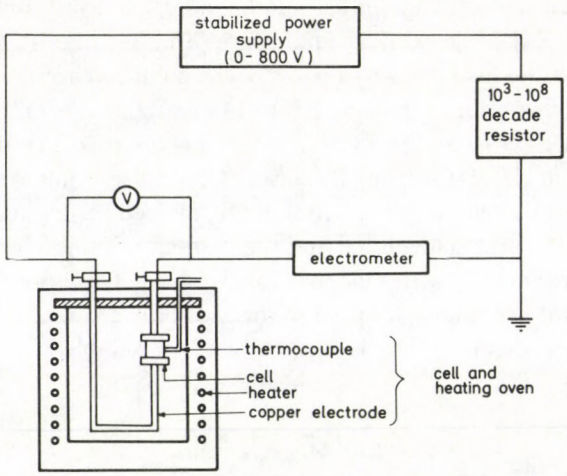

Fig. 1. Circuit diagram for d.c. two-terminal methods for measuring I–V characteristics and temperature-dependence of resistivity

found to be fairly satisfactory. For example, in a group of three glow curves measured for a single crystal dosed with 100 Gy, identical peaks were within 3 K of each other while the glow intensities of these peaks only varied by less than 6% between the most and the least intense ones.

Results and discussion

Differential thermal analysis patterns for KDP are shown in Fig. 2 for two different heating rates. For the lower rate of 5 K/min, two endothermic peaks are evident at 513 K and 548 K which shift to higher temperatures when the heating rate increases to 10 K/min; the estimated shift being 10 K for each peak. The sample starts to decompose around 478 K and 483 K for the lower and higher heating rates, respectively. Both curves return to their base lines at about 608 K and 618 K indicating complete decomposition of samples. As the Shimadzu differential thermal analyzer used in the present work was not equipped with a thermogravimetric analyzer, the estimation of the weight loss of sample resulting from decomposition was only possible by accurate weighing before and after heating. For the two heating rates employed, the estimated weight losses of samples correspond to the following reaction:

$$KH_2PO_4 \xrightarrow{\text{heat}} KPO_3 + H_2O\,,$$

i.e. loss of water and a transformation of the original orthophosphate to a meta-phosphate as an end product. The two endothermic peaks in Fig. 2 have been identified

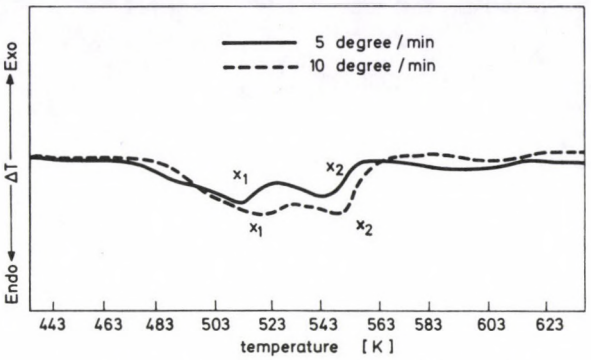

Fig. 2. Differential thermal analysis patterns for KDP

as due to the formation of the pyrophosphate as an intermediate product (Peak X_1) which in turn transforms on further heating to the metaphosphate (Peak X_2). The full decomposition process which describes the thermal behaviour of KDP can be thus written as:

$$2KH_2 \xrightarrow{\text{heat}} K_2H_2P_2O_7 + H_2O \xrightarrow{\text{heat}} 2KPO_3 + 2H_2O\,.$$

The proposed decomposition process was confirmed by X-ray diffraction for the end product of the reaction. The pattern obtained elucidated the formation of KPO_3 which was found to have a monoclinic crystal structure with an angle B of 101° and lattice constants a_0, b_0 and c_0 of 13.998×10^{-10} m, 4.544×10^{-10} m and 10.309×10^{-10} m, respectively. The number of KPO_3 molecules in the unit cell turned out to be eight.

Further confirmation of the proposed decomposition was obtained from optical measurements on samples in the infrared range. The identical bands appearing in Fig. 3 for powder and single crystal samples after being heated in the DTA equipment to about 673 K at the rate of 5 K/min indicated that both sample types were subjected to complete decomposition with a transition from the tetragonal KH_2PO_4 to the monoclinic KPO_3. The similarity between the infrared bands in the spectra of the end products of the heating process and those appearing in the spectrum of a standard KPO_3 sample supported the proposed thermal behaviour.

Electrical measurements were made on cleaved and polished KDP single crystals of reasonable dimensions ($3.040 \times 2.225 \times 1.435$ mm^3). The current passing through the crystal was measured along its c axis as a function of the applied potential difference, the resulting I–V characteristic curves were always ohmic in form. At room temperature, the value of 7.3×10^5 ohm · cm was estimated for the resistivity of KDP; the corresponding value of its conductivity being 1.37×10^{-6} ohm^{-1} cm^{-1}. Figure 4 is a representative example of the type of temperature dependence of resistivity curves

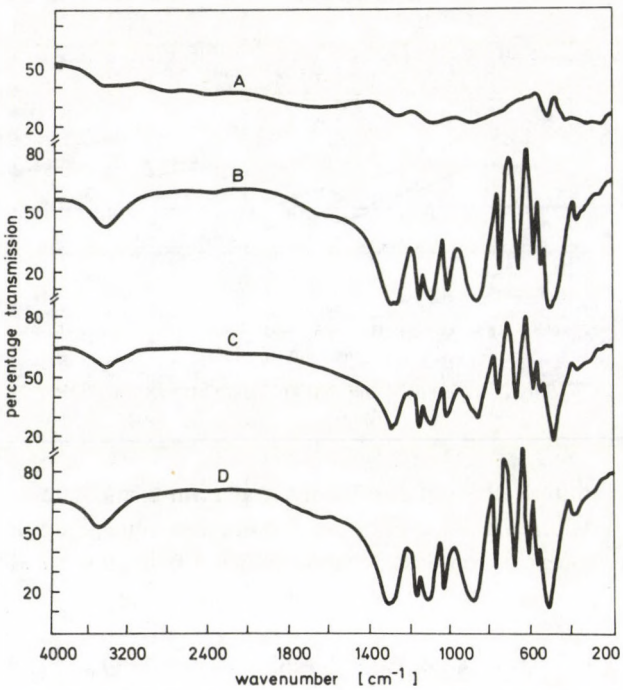

Fig. 3a. Infrared spectra: (A) for KDP polycrystalline sample before heating; (B) for KDP polycrystalline sample after heating to 673 K; (C) for KDP single crystal after heating to 673 K; and (D) for a standard KPO_3 sample

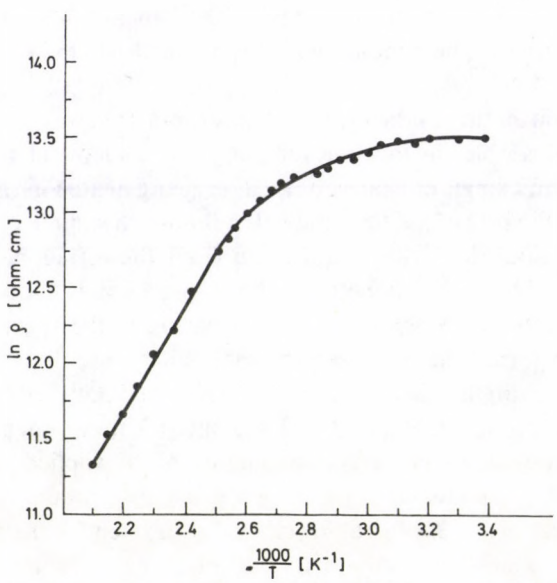

Fig. 4. Temperature dependence of resistivity curve for KDP

obtained for KDP single crystals over the temperature range of 293 K to 478 K. The upper temperature limit was set by the instabilities of current measurements due to the beginning of sample decomposition. The resistivity temperature relationship can be easily divided into two distinct regions. Over the range of 293 K to 383 K, the material showed a slight decrease of resistivity with increase of temperature, i.e. it was slightly dependent on temperature. The second region, which extends over a temperature range of 383 K to 478 K, showed a marked decrease in resistivity with rising temperature; a behaviour which resembles that of semiconductors and insulators. Harris and Vella [19] reported a knee in the KDP conductivity temperature curve at 383 K which is consistent with our results in this paper but they ascribed the knee to sample decomposition. Their view of knee attribution contradicts our differential thermal results which showed that KDP started to decompose around 478 K. The knee appearing in our resistivity curve at 383 K cannot be ascribed to sample decomposition.

It is also of interest to indicate that the plot of $\ln \rho$ against $1/T$ over the temperature range of 293 K to 478 K (Fig. 4) consists of two linear parts which follow the elementary equation of ionic conductors [20]

$$\rho = \rho_0 \exp(E/2kT),$$

where ρ is the resistivity at absolute temperature T, ρ_0 is a constant, k is the Boltzmann's constant and E is the activation energy for conduction process. Application of this equation yielded two activation energies of 0.588 eV and 0.104 eV over the temperature ranges of 383 K to 478 K and 293 K to 383 K, respectively. The value of 0.588 eV is approximately consistent with the activation energies obtained by different workers on pure KDP between 0.52 eV–0.58 eV [21–25], while the value 0.104 eV is close to the reported value of the activation energy for proton migration in KDP [26]. One should stress the conduction mechanism in KDP which remains still unresolved and not fully understood despite the intensive work published on this subject so far [21–25]. In some cases, conduction has been attributed totally to proton migration in the hydrogen bond network while in some other cases it has been explained partly in terms of proton migration and partly in terms of defects as in ionic solids. Blinc et al [11] suggested that the rotation of phosphate groups rather than proton jumps was responsible for conduction in KDP, though the implications of this suggestion in terms of crystal structure were not worked out. Because of these disputes, one should refer to the nuclear magnetic resonance work of Blinc et al [27, 28] on KDP single crystals. They have found two types of frequencies, one due to phosphate rotation which was found to be temperature-dependent, and the other due to proton jumps, which was temperature independent. As we have obtained two distinct parts in the conductivity temperature curve of KDP, one between 293 to 383 K which is temperature-independent and the other between 383–478 K which is temperature-dependent; it seems reasonable to explain the conductivity behaviour of our KDP crystals as being controlled by the rotation of phosphate groups with an activation

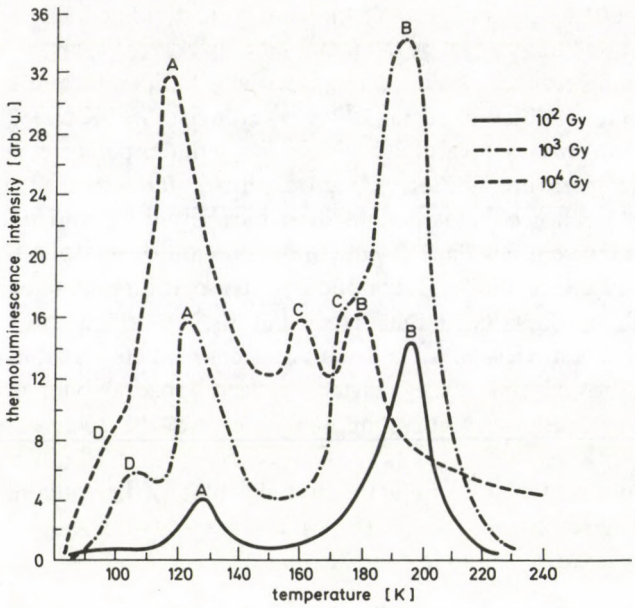

Fig. 5. Thermal glow curves for gamma-ray irradiated polycrystalline KDP powder

energy of 0.588 eV over the temperature range of 383 K to 478 K, whereas at lower temperatures (293–383 K) proton jumps with an activation energy of 0.104 eV are responsible for the observed conduction.

When KDP samples were irradiated at 77 K by gamma doses of 10^2 Gy to 10^4 Gy and then heated in the dark, a strong bluish thermal glow was emitted which could be seen with the naked eye. Figure 5 shows glow curves recorded for the gamma ray irradiated polycrystalline powder. The curve recorded after dosage to 100 Gy subsumes two separate glow peaks (A) and (B) with their glow maxima situated at 128 K and 197 K, respectively. When the dose increases to 10^3 Gy, shoulders (C) and (D) appear around 175 K and 107 K on the low temperature sides of peaks (B) and (A). For a gamma dose of 10^4 Gy, shoulder (C) develops into a well-defined peak with its glow maximum intensity located at 160 K. Appearance of shoulders at doses exceeding 10^2 Gy seems to result from new groups of traps due to crystal defects created by gamma radiation. The number of these traps increases with increasing radiation dose. At lower doses, this number is sufficiently small and the detection of the associated glow is not practically feasible. This accounts also for the observed dependence of the glow intensity on the gamma dose; an increase in dose causes a corresponding increase in glow intensity. Some slight shifts of peak temperature to lower values are noted with the increase of gamma dose. This behaviour could be either a dose rate effect or a combination of this effect and interactions occurring between various trapping states.

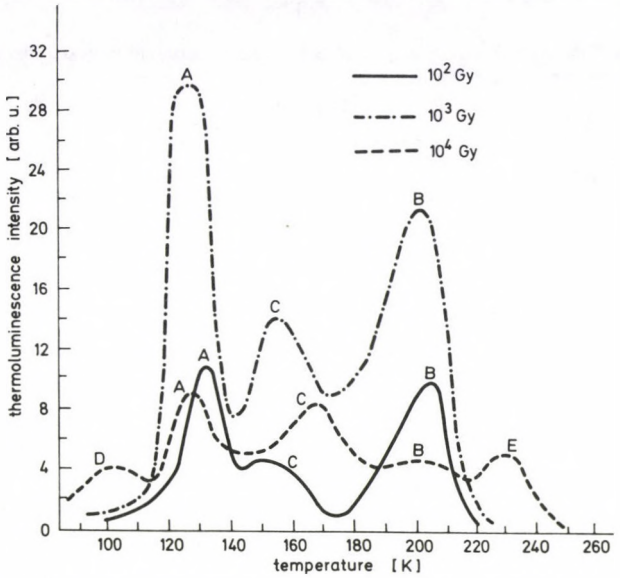

Fig. 6. Thermal glow curves for gamma-ray irradiated KDP single crystal

This view is supported by similar shifts observed in other gamma irradiated materials which were attributed to similar reasons [29].

An illustrative example of the type of glow curves detected for KDP single crystals after dosage with gamma radiation is shown in Fig. 6. The various peak temperatures have been collected in Table I together with those of the polycrystalline powder for comparison. For a gamma dose of 100 Gy, it is obvious that the major glow peaks (A) and (B) detected for powder samples are present for single crystals; the peak temperatures for the two sample types agree within 5 K which is of the order of the experimental statistical error. The relative glow intensities vary, however, rather widely between them due to the different sample masses used in both cases. For a gamma dose of 10^3 Gy, peak (D) appearing at 107 K for the polycrystalline powder is not observed for the single crystal. It is only detectable at 104 K together with a new peak (E) at 230 K at gamma ray doses of 10^4 Gy; the origin of the 230 K peak is difficult to explain at present.

The observed effects of gamma radiation in KDP can be discussed in terms of two main phenomena which operate in the material at the same time during irradiation. Gamma radiation creates trapping centres, the number of which increases with the increase of dose. In addition, it also acts as an exciting source for the material raising electrons from the filled band of the crystal which are later trapped by states created by radiation damage or by uncontrollable impurities present originally in the host material. When released on heating, trapped electrons will recombine with holes

Table I

Glow peak temperatures and trap depths for KDP irradiated with gamma rays

Gamma dose [Gy]	Type of sample / Glow peak	Polycrystalline powder					Single crystal				
		A	B	C	D	D	A	B	C	D	E
10^2	T[K]	128	197	–	–	–	130	202	153	–	–
	E [eV]	0.26	0.39	–	–	–	0.26	0.41	0.31	–	–
10^3	T[K]	124	195	175	107	–	126	200	153	–	–
	E [eV]	0.25	0.39	0.35	0.21	–	0.25	0.40	0.31	–	–
10^4	T[K]	118	178	160	101	–	126	200	168	104	230
	E [eV]	0.24	0.36	0.32	0.20	–	0.25	0.40	0.34	0.21	0.46

left in the filled band to give the bluish thermal glow. Increase in the glow intensity observed with increase in dose from 10^2 Gy to 10^3 Gy results from an increased number of excited electrons leading to an increased recombination probability. The decrease in intensities of all glow peaks noted at 10^4 Gy is caused by a new group of traps with an energy depth of 0.46 eV created by radiation at such high dose levels. These new traps participate in the trapping process reducing the number of electrons originally available for other trap levels.

Because of the interference between various glow peaks, it is not easy to deduce accurately the type of recombination involved in the glow process of KDP from the shape of the experimental glow curve. However, if one excludes the slight dose rate dependent shifts previously noted with increasing dose, the peak temperature can be considered to a good approximation as fairly constant over a wide range of total gamma ray doses. This is a reasonably good evidence that a monomolecular recombination process is mainly involved in the glow process [30]. In this case, the escape frequency factors can be calculated either by the initial rise method of Garlick and Gibson [31] or by that of Grossweiner [32]. Escape frequency factors of the order of 10^{11} s^{-1} have been estimated for the main glow peaks (A) and (B). Since the heating rate employed in this work is sufficiently slow (0.25 K/s), the trap depth E can be estimated by Urbach's empirical formula: $E(\text{eV}) = T_m/500$ which is applicable in this case; T_m(K) being the peak temperature [33]. Trap depths for the various glow peaks have been estimated by this formula and listed in Table I.

Experimental values of trap depths and escape frequency factors can be used to calculate theoretical glow curves in situations where the glow kinetics are monomolecular and retrapping is absent. The approximation used for such calculations has been given in detail elsewhere [34]. Its validity has been tested and found to give good agreement between experimental and calculated curves. When this approximation is used together with the experimental values of trap depths and escape frequency factors estimated for KDP single crystals dosed with 10^3 Gy, the theoretical glow curve shown

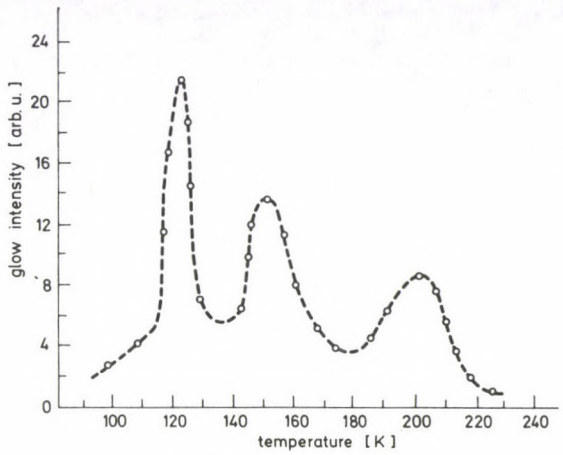

Fig. 7. Glow curves for KDP single crystal dosed to 10^3 grays: solid line represent experimental curve; circles represent theoretically calculated points

in Fig. 7 is obtained; the experimental curve for the same sample has been included for comparison. The excellent agreement existing between both curves supports our previous assumption that monomolecular kinetics are mainly involved in the flow process of KDP.

References

1. W. G. Cady, Piezoelectricity, McGraw–Hill Inc., New York, 1946.
2. F. Jena and G. Shirance, Ferroelectric Crystals, Pergamon Press, Oxford, 1962.
3. E. Nakumura, T. Mitsui and J. Furuishi, J. Phys. Soc. Japan, *18*, 1477, 1963.
4. R. J. Mayer and J. L. Bjorkstam, J. Phys. Chem. Solids, *23*, 619, 1962.
5. A. R. Ubbelohde and I. Woodward, Proc. Roy. Soc., *A188*, 358, 1947.
6. G. E. Bacon and R. S. Pease, Proc. Roy. Soc., *A220*, 397, 1953; Proc. Roy. Soc., *A230*, 359, 1955.
7. R. J. Nelmes, N. S. J. Kennedy and E. Baharie, Ferroelectrics (G. B.), 21, 439, 1978; Ferroelectrics (G. B.), *24*, 237, 1980; J. Phys. Chem., *13*, 4841, 1980.
8. Y. Imry, I. Pelah and E. Wiener, J. Chem. Phys., *43*, 2332, 1965.
9. J. Grunberg, S. Levin, I. Pelah and E. Wiener, Solid State Commun., *5*, 863, 1967.
10. J. Grunberg, S. Levin, I. Pelah and Gerlich, Phys. Stat. Solidi, *B49*, 857, 1972.
11. R. Blinc, V. Dimic, D. Kolar, G. Lahajnar, J. Stepisnik, S. Zumer, N. Vene and D. Hadzi, J. Chem. Phys., *49*, 4996, 1968.
12. E. Rapopert, J. Chem. Phys., *53*, 311, 1970.
13. G. Baldini, M. Cottini and E. Grilli, Solid State Commun., *11*, 1257, 1972.
14. S. Saito, K. Wada and R. Onaka J. Phys. Soc. Japan, *37*, 711, 1974.
15. B. N. Grib, I. I. Kondilenko, P. A. Korotkov, A. I. Pisanski and Yu. P. Tsyashchenko, Opt. Spectrosc., *38*, 415, 1975.
16. R. Abe, J. Phys. Soc. Japan, *47*, 1177, 1979.
17. E. F. Kaelble, Handbook of X-rays for Diffraction, Emission, Absorption and Microscopy, McGraw–Hill Inc., New York, 1967.

18. M. S. Elmanharawy, Rev. Roum. Phys., *14*, 1245, 1969.
19. L. B. Harris and G. J. Vella, J. Chem. Phys., *58*, 4550, 1973.
20. A. F. Loffe, Physics of Semiconductors, infosearch Ltd., London, 1960.
21. V. H. Schmidt and E. A. Uehling, Phys. Rev., *126*, 447, 1962.
22. A. I. Al–Adl, A. Abdel–Kader, M. S. Elmanharawy and H. I. Farag, Proceedings of the Fifth Conference on Solid State Physics, Assiut University, Egypt, February, 1982.
23. M. O'Keefe and C. T. Perrino, J. Phys. Chem. Solids, *28*, 211, 1967.
24. E. Murphy, J. Appl. Phys., *35*, 2609, 1964.
25. J. M. Pollock and M. Sharan, J. Chem. Phys., *51*, 3604, 1969.
26. M. Sharon and A. K. Kalia, J. Solid State Chem., *21*, 171, 1977.
27. R. Blinc, J. Stepisnik and S. Zumer, J. Chem. Phys., *54*, 187, 1971.
28. R. Blinc and J. Pirs, J. Chem. Phys., *54*, 1535, 1971.
29. L. F. Heckelsberg and F. Daniels, J. Phys. Chem., *61*, 414, 1957.
30. L. I. Grossweiner and M. S. Matheson, J. Chem. Phys., *22*, 1514, 1954.
31. G. F. J. Garlick and A. F. Gibson, Proc. Phys. Soc., *60*, 574, 1948.
32. L. I. Grossweiner, J. Appl. Phys., *24*, 1306, 1953.
33. F. Urbach, Cornell Symposium on Preparation and Characteristics of Solid State Luminescent Materials, Wiley, New York, 1948.
34. M. S. Elmanharawy, Proc. Math. Phys. Soc. Egypt, *49*, 139, 1980.

Acta Physica Hungarica 60 (1—2), pp. 31—37 (1986)

CHARACTERISTIC SOLUTION OF A WEAK WAVE PROBLEM IN GASEOUS FLOWS AT VERY HIGH TEMPERATURE

R. P. UPADHYAY, A. S. RAI and RISHI RAM

School of Applied Sciences, Institute of Technology, B. H. U.
Varanasi 221005, India

(Received 19 January 1984)

The propagation of a weak discontinuity has been studied along the characteristic path by using the characteristics of the governing quasi-linear hyperbolic system as reference coordinate system. The characteristic solution for the time-dependent amplitude of a weak wave has been obtained and the critical time for the breakdown of characteristic solution has been determined. It is shown that all compressive waves will grow and terminate into shock waves, while all expansion waves will decay out.

1. Introduction

The non-linear weak waves have been extensively studied during the last decade. The most interesting part of this study is that it is a subclass of non-linear waves which admit analytic solutions. The propagation of such waves has been studied by many researchers. Whitham [1] and Jeffrey [2] provided a theoretical foundation for the study of non-linear wave propagation. Murray [3] studied perturbation effects on the decay of weak waves generated by the non-linear first order wave equation. Becker [4], Becker and Schmitt [5] studied the problem of growth and decay of a weak wave in relaxing gases and obtained the critical time for the shock formation. Rarity [6] studied the problem of breakdown of characteristic solutions of flows with vibrational relaxation. Ram [7], Rai, Gaur and Ram [8] studied the behaviour of weak waves under radiative heat flux effects. By using the method of characteristics, Ram [9] studied the effects of radiative heat flux on the global and local behaviour of weak waves.

The propagation of a weak wave in gas flows with very high temperature becomes an interesting problem when the thermal radiation stresses play an important role in the determination of the flow field, while the radiative heat flux is not a dominant factor in the determination of the flow properties. Most of the authors have studied radiative heat flux effects on the growth of weak discontinuities and very little work has been reported for the effects of radiation stresses as the dominant factor of a thermal radiation. The purpose of the present communication is to investigate the effect of

radiative pressure and radiation energy density on the amplitude of a weak discontinuity during the propagation. Pai [10] has suggested that when the mean free path of radiation is very small, the radiative heat transfer term can be neglected except in the boundary layer region. We aim to obtain the characteristic solution of a weak wave problem in gas flows at such a high temperature and low pressure that the radiation pressure number R_p is not negligible, but the profiles structured by radiant heat transfer can be assumed to be embedded in the discontinuity itself.

2. Wave propagation

The basic equations for axi-symmetric gas flows at very high temperature [10] can be written in the following forms:

$$\frac{\partial u}{\partial t}+u\frac{\partial u}{\partial x}+\left(\frac{1+4R_p}{\rho}\right)\frac{\partial p}{\partial x}-\frac{4pR_p}{\rho^2}\frac{\partial \rho}{\partial x}=0, \tag{1}$$

$$\frac{\partial p}{\partial t}+u\frac{\partial p}{\partial x}+p\left\{\frac{\nu+16(\nu-1)R_p}{1+12(\nu-1)R_p}\right\}\frac{\partial u}{\partial x}+\left\{\frac{\nu+16(\nu-1)R_p}{1+12(\nu-1)R_p}\right\}\frac{\delta pu}{x}=0, \tag{1}$$

$$\frac{\partial \rho}{\partial t}+u\frac{\partial \rho}{\partial x}+\rho\frac{\partial u}{\partial x}+\frac{\delta \rho u}{x}=0, \tag{3}$$

where p, ρ, u and ν have their usual meaning in gas-dynamics. Here δ is a parameter of symmetry and takes the values 0, 1 and 2 for planar, cylindrical and spherical symmetry. The radiation pressure p_R and the radiation energy density E_R are related by the following relation,

$$E_R=3p_R=a_RT^4, \qquad R_p=\frac{p_R}{p},$$

where a_R is the Stefan–Boltzmann constant, T is the absolute temperature and R_p is the radiation pressure number.

The above system of equations (1)–(3) is hyperbolic in nature and represents a wave motion. It can be put in matrix form

$$\frac{\partial \bar{U}}{\partial t}+\bar{A}\frac{\partial \bar{U}}{\partial x}+\bar{B}=0, \tag{4}$$

where $\bar{U}$, $\bar{B}$ are column matrices and $\bar{A}$ is a square matrix of order (3×3) given by

$$\bar{U}=\begin{bmatrix} u \\ p \\ \rho \end{bmatrix}, \qquad \bar{A}=\begin{bmatrix} u & (1+4R_p)/\rho & -4pR_p/\rho^2 \\ Q_p & u & 0 \\ \rho & 0 & u \end{bmatrix}$$

and

$$\bar{B}=\begin{bmatrix} 0 \\ \delta Qpu/x \\ \delta\rho u/x \end{bmatrix}, \qquad Q=\frac{\nu+16(\nu-1)R_p}{1+12(\nu-1)R_p}.$$

A function $\bar{U}(x, t)$ satisfying (4) everywhere except at a characteristic curve $S(t)$, where $\bar{U}$ is continuous but $\bar{U}_t$ and $\bar{U}_x$ may suffer from finite jumps, is said to be a weak wave or a weak discontinuity. The equations of characteristics for the system (4) are given by

$$\frac{dx}{dt}=\mathrm{u}\pm C_R \qquad \text{and} \qquad \frac{dx}{dt}=u, \tag{5}$$

where plus and minus sign respectively represent the positive and negative direction of the propagation and C_R is given by

$$C_R^2=\frac{p}{\rho}\left\{\frac{\nu+20(\nu-1)R_p+16(\nu-1)R_p^2}{1+12(\nu-1)R_p}\right\}.$$

3. Time dependence of wave amplitude

The system (4) is hyperbolic in nature and so we can introduce the characteristic coordinates as our reference frame. Now we introduce two characteristic coordinates α and ψ as follows:

(i) ψ is a particle tag so that ψ is constant along a particle path $\frac{dx}{dt}=u$ in the (x, t) plane. If the characteristic wave front traverses a particle at time t^*, this particle and its path will be labelled by $\psi=t^*$.

(ii) α is a wave tag so that α is constant along an outgoing characteristic $\frac{dx}{dt}=u+C_R$ in the (x, t) plane. If an outgoing wave is generated at time t', it will be labelled by $\alpha=t'$.

In this way we observe that for each pair of values (α, ψ) there is a corresponding pair (x, t) in the (x, t) plane such that:

$$\frac{\partial x}{\partial\alpha}=u\frac{\partial t}{\partial\alpha}, \tag{6}$$

$$\frac{\partial x}{\partial\psi}=(u+C_R)\frac{\partial t}{\partial\psi}. \tag{7}$$

In consequence of this transformation we have

$$\frac{\partial \bar{U}}{\partial t} = \frac{\frac{\partial \bar{U}}{\partial \psi}\frac{\partial x}{\partial \alpha} - \frac{\partial \bar{U}}{\partial \alpha}\frac{\partial x}{\partial \psi}}{J}, \tag{8}$$

$$\frac{\partial \bar{U}}{\partial x} = \frac{\frac{\partial \bar{U}}{\partial \alpha}\frac{\partial t}{\partial \psi} - \frac{\partial \bar{U}}{\partial \psi}\frac{\partial t}{\partial \alpha}}{J}, \tag{9}$$

where

$$J = \frac{\partial(x,t)}{\partial(\alpha,\psi)} = -C_R \frac{\partial t}{\partial \alpha}\frac{\partial t}{\partial \psi}$$

is the Jacobian of transformation and it plays an important role as a deciding factor in the shock formation. Since doubling or overlapping of fluid particles is prohibited by physical considerations, $\frac{\partial t}{\partial \psi} \neq 0$. Consequently $J=0$, iff $\frac{\partial t}{\partial \alpha}=0$, when two adjoining characteristics merge into a shock wave. Hence $J=0$ will provide us a condition for the steepening of the wave front to form a shock wave. Transforming (1)–(3) into the characteristic coordinate system (α, ψ), we get

$$\rho C_R \frac{\partial u}{\partial \alpha}\frac{\partial t}{\partial \psi} + (1+4R_p)\left(\frac{\partial p}{\partial \psi}\frac{\partial t}{\partial \alpha} - \frac{\partial p}{\partial \alpha}\frac{\partial t}{\partial \psi}\right) + \frac{4pR_p}{\rho}\left\{\frac{\partial \rho}{\partial \alpha}\frac{\partial t}{\partial \psi} - \frac{\partial \rho}{\partial \psi}\frac{\partial t}{\partial \alpha}\right\} = 0, \tag{10}$$

$$C_R \frac{\partial p}{\partial \alpha}\frac{\partial t}{\partial \psi} - Qp\frac{\partial u}{\partial \alpha}\frac{\partial t}{\partial \psi} + Qp\frac{\partial u}{\partial \psi}\frac{\partial t}{\partial \alpha} + \frac{\delta Qp\, uC_R \frac{\partial t}{\partial \alpha}\frac{\partial t}{\partial \psi}}{x(\alpha,\psi)} = 0, \tag{11}$$

$$C_R \frac{\partial \rho}{\partial \alpha}\frac{\partial t}{\partial \psi} - \rho\frac{\partial u}{\partial \alpha}\frac{\partial t}{\partial \psi} + \rho\frac{\partial u}{\partial \psi}\frac{\partial t}{\partial \alpha} + \frac{\delta \rho u\, C_R \frac{\partial t}{\partial \alpha}\frac{\partial t}{\partial \psi}}{x(\alpha,\psi)} = 0. \tag{12}$$

The Eqs (6), (7), (10), (11) and (12) provide us five equations for five unknowns u, p, ρ, x and t. From (10), (11) and (12) we get

$$(1+4R_p)\frac{\partial p}{\partial \psi} + \rho C_R \frac{\partial u}{\partial \psi} = -(1+4R_p)\frac{\delta Q\, pu \frac{\partial t}{\partial \psi}}{x(\alpha,\psi)}. \tag{13}$$

The boundary conditions at the wave front are

$$[p]=0, \quad [\rho]=0, \quad [u]=0, \quad [T]=0, \quad t=\psi \quad \text{at} \quad \alpha=0. \tag{14}$$

Since the flow ahead of the wave is uniform and at rest, the second set of boundary conditions is

$$\frac{\partial p}{\partial \psi}=0,\quad \frac{\partial \rho}{\partial \psi}=0,\quad \frac{\partial u}{\partial \psi}=0,\quad \frac{\partial T}{\partial \psi}=0,\quad \frac{\partial t}{\partial \psi}=1 \quad \text{at} \quad \alpha=0. \tag{15}$$

The Eq. (11) yields

$$C_{R_0}\frac{\partial p}{\partial \alpha}=Q_0 p_0 \frac{\partial u}{\partial \alpha} \qquad \text{at} \qquad \alpha=0. \tag{16}$$

An evaluation of (6) and (7) at the wave front yields:

$$\frac{\partial x}{\partial \alpha}=0,\quad \frac{\partial x}{\partial \psi}=C_{R_0} \quad \text{at} \quad \alpha=0, \tag{17}$$

where '0' represents the value of a flow parameter evaluated just ahead of the wave front. Differentiating (13), (16) and (17) with respect to α and with respect to ψ and then evaluating at the wave front $\alpha=0$, we get

$$\frac{\partial^2 u}{\partial \alpha \partial \psi}=\frac{C_{R_0}K_1\delta}{\psi}a(t), \tag{18}$$

where

$$a(t)=\left[\frac{\partial u}{\partial x}\right]=-\frac{\partial u}{\partial \alpha}\Big/ C_R\frac{\partial t}{\partial \alpha} \tag{19}$$

is the amplitude of the wave and K_1 is a non-dimensional constant given by

$$K_1=\frac{(1+4R_p)_0 Q_0 p_0}{(1+4R_p)_0 Q_0 p_0+C_{R_0}^2\rho_0}. \tag{20}$$

In order to discuss the behaviour of the wave we differentiate (20) with respect to ψ and make use of (18) and (19) to get

$$\frac{da}{d\psi}+\left(\frac{K_1\delta}{\psi}\right)a+\left(\frac{Q+1}{2}\right)a^2=0. \tag{21}$$

This is the fundamental differential equation which governs the growth and decay behaviour of a weak wave.

4. Global behaviour of the solution

The characteristic solution of (21) is given by

$$a(\psi)=\left\{\frac{K_2}{1+K_1\delta}\psi+\frac{1}{a(0)}\right\} \quad \text{on} \quad \alpha=0 \quad t=\psi, \tag{22}$$

Table I

Effect of R_p on critical time t_c

Values of R_p	Value of t_c at $\delta=0$	Value of t_c at $\delta=1$	Value of t_c at $\delta=2$
0.00	0.8333	1.2500	1.5000
0.05	0.8378	1.2800	1.7292
0.10	0.8409	1.3090	1.7790
0.15	0.8431	1.3310	1.8197
0.20	0.8449	1.3490	1.8530
0.25	0.8461	1.3650	1.8857
0.30	0.8472	1.3760	1.9053
0.35	0.8481	1.3881	1.9281
0.40	0.8488	1.3978	1.9467
0.45	0.8494	1.4063	1.9632
0.50	0.8500	1.4139	1.9778

The Table shows the effect of radiation pressure number R_p on the critical time t_c. The increasing values of R_p increase the value of t_c. Thus it may be concluded that the radiation pressure number has a stabilizing effect in the sense that it delays the shock formation. It is apparent from Eq. (23) that the critical time t_c increases with δ. This implies that the curvature has also stabilizing effect in the sense that it resists or delays the shock formation. Thus we conclude that all compressive waves will ultimately terminate into shock waves after a finite critical time t_c.

where

$$K_2 = \frac{Q+1}{2}.$$

It follows from (22) that if $a(0)>0$, $a(\psi)$ decreases monotonically with ψ and tends to zero as $t\to\infty$. It implies that an expansion wave, for which $a(0)>0$, will decay out and will be damped ultimately. If $a(0)<0$, then there exists a finite critical time t_c given by

$$t_c = \frac{1+K_1\delta}{|a(0)|K_2}, \tag{23}$$

such that

$$\lim_{t\to t_c} a(t) = \infty .$$

This implies that within a finite time t_c the amplitude $a(t)$ becomes exceedingly large and consequently there occurs a breakdown of the wave at $t=t_c$ and a shock type discontinuity appears. Now to investigate the effects of the radiation pressure and radiation energy density we have Table I.

References

1. G. B. Whitham, Linear and Non-linear Waves, Wiley Interscience, New York, 1974.
2. A. Jeffrey, and T. Tanuitt, Non-linear Wave Propagation, Academic Press, New York, 1964.
3. J. D. Murray, Siam J. On Appl. Maths., 273, 1970.
4. E. Becker, J. Aerospace, *74*, 736, 1070.
5. E. Becker and H. Schmitt, Ing. Arch., *36*, 335, 1968.
6. B. S. H. Rarity, J. Fluid Mech., *27*, 49, 1967.
7. R. Ram and S. Srinivasan, ZAMM, *57*, 191, 1977.
8. A. Rai, M. Gaur and R. Ram, Acta Phys. Hung., *45*, 9, 1978.
9. R. Ram, Appl. Sci. Research, *34*, 93, 1978.
10. S. I. Pai, Jour. Math. Phys. Sci., *3*, 361, 1969.

Acta Physica Hungarica 60 (1—2), pp. 39—41 (1986)

AN EXACT SOLUTION IN A SCALAR-TENSOR THEORY OF GRAVITATION

D. R. K. REDDY, V. U. M. RAO and P. INNAIAH*

Department of Applied Mathematics, Andhra University
Waltair, India

(Received 8 March 1984)

Vacuum field equations for the conformally flat spherically symmetric static space-time are obtained in a scalar-tensor theory of gravitation proposed by Dunn. It is shown that the most general conformally flat spherically symmetric static vacuum solution in this theory represents only purely flat space-time.

1. Introduction

Recently Dunn [1] has constructed a scalar-tensor theory of gravitation using a non-Riemannian geometry in which both the metric tensor and the scalar function have unambiguous geometric interpretation. The scalar is introduced by defining a linear connection with non-vanishing torsion. It is pointed out that the field equations of the theory and the Lagrangian from which they are derived are identical with those given by Dicke [2] in an alternate formulation of the Brans–Dicke [3] theory. By using a static spherically symmetric solution to the field equations Dunn [1] has also found that, with a proper choice of parameter, this theory agrees with the three crucial tests of general relativity. In the regions of space-time with zero charge and zero mass densities, the field equations of the scalar-tensor theory formulated by Dunn are

$$\begin{aligned} R_{ij}-\frac{1}{2}Rg_{ij}&=6K^2\lambda^{-2}\left(\lambda_{,i}\lambda_{,j}-\frac{1}{2}g_{ij}\lambda_{,s}\lambda^{,s}\right),\\ \partial[\lambda_{,j}(-g)^{1/2}g^{js}]/\partial x^s-(\lambda_{,s}\lambda_{,i}/\lambda)g^{si}(-g)^{1/2}&=0, \end{aligned} \tag{1}$$

where R_{ij} is the Ricci tensor, R the curvature scalar of the metric g_{ij}, λ is the scalar field and K a constant. If either $K=0$ or $\lambda=$ constant, the connection of the space-time is metric preserving and torsion free, i.e. we have a Riemannian geometry.

Singh [4] has investigated cylindrically symmetric solutions of the field equations of this theory for the Einstein–Rosen metric while Reddy [5] has discussed plane symmetric solutions in this theory.

* Gandhi Institute of Technology and Management, Waltair, India.

In the present paper we obtain the most general conformally flat spherically symmetric static solution of the field equations of the scalar-tensor theory proposed by Dunn [1]. It is observed that the static conformally flat solution, in this theory, is simply the empty flat space-time. There has been much recent interest in conformally flat space-times (Reddy [6, 7], Banerjee and Santos [8] and Stewart [9]).

2. Metric and field equations

Recently Banerjee and Santos [8] have written the most general static conformally flat spherically symmetric metric in isotropic coordinates as

$$ds^2 = e^2\alpha[-(ar^2+b)^2dt + dr^2 + r^2d\theta^2 + r^2\sin^2\theta d\varphi^2], \tag{2}$$

where α is a function of r alone and a and b are constants.

Considering the general static spherically symmetric conformally flat line element (2) and assuming λ as a function of r only, the field equations (1) can be written as

$$3\alpha'^2 + \frac{4\alpha'}{r} + \frac{4a(1+r\alpha')}{ar^2+b} + 3K^2\varphi'^2 = 0, \tag{3}$$

$$2\alpha'' + \alpha'^2 + \frac{2\alpha'}{r} + \frac{4a(1+r\alpha')}{ar^2+b} - 3K^2\varphi'^2 = 0, \tag{4}$$

$$2\alpha'' + \alpha'^2 + \frac{4\alpha'}{r} - 3K^2\varphi'^2 = 0, \tag{5}$$

$$\varphi'' + \varphi'\left(2\alpha' + \frac{2}{r} + \frac{2ar}{ar^2+b}\right) = 0, \tag{6}$$

where we have put $\lambda = e^{\varphi}$, φ being a scalar function.

3. Solutions of the field equations

We, now, discuss the static solution of the field equations (3) to (6). The question of over determinacy in solving the field equations in this case is settled by satisfaction of all the field equations by actual substitution of the solution derived.

It can be easily verified that when the scalar field $\lambda = e^{\varphi} =$ constant the field equations (3) to (6) yield a solution which describes an empty flat space-time of Einstein's theory.

When λ is not a constant, but is a function of r only, Eqs (4) to (6) reduce to

$$e^{2\alpha}r^2(ar^2+b)\varphi' \sim C_1 \tag{7}$$

$$e^{2\alpha}(b-ar^2)^2 = C_2, \qquad C_2 \neq 0, \tag{8}$$

which, in turn, yield the solution

$$e^{2\alpha}=\frac{C_2}{(b-ar^2)^2}, \qquad C_2\neq 0,$$
$$\lambda=e^{\varphi}=C_3\exp\left[(C_1/C_2)\left(ar-\frac{b}{r}+\frac{2u}{r}\log\frac{1+u}{1-u}\right)\right], \tag{9}$$

where we have put $u=\sqrt{abr}$ and C_i's are constants of integration.

Using solution (9) in (3) we have

$$12ab(ar^2+b)^2r^4+3K(C_1/C_2)^2(b-ar^2)^6=0. \tag{10}$$

This is true only if either $a=0$ or $b=0$ with $C_1=0$, which implies that the flat space-time is the only possible solution of the field equations. Thus unlike in Brans–Dicke scalar-tensor theory (Banerjee and Santos, Reddy) the only spherically symmetric static conformally flat vacuum solution in this theory is simply the empty flat space-time of Einstein's theory.

4. Conclusion

Here we have shown that the most general conformally flat spherically symmetric static vacuum solution, in the scalar-tensor theory proposed by Dunn, is simply the empty flat space-time of Einstein's theory. It is observed that the situation in this theory is quite different from that in Brans–Dicke scalar-tensor theory. It may also be noted in this context that Einstein's vacuum equations have no conformally flat solution space-times other than the trivial one of the Minkowski metric.

Acknowledgement

One of the authors (V. U. M. Rao) is grateful to the Council of Scientific and Industrial Research, India, for providing a Research Associateship.

References

1. K. A. Dunn, J. Math. Phys., *15*, 389, 1974.
2. R. H. Dicke, Phys. Rev., *125*, 2163, 1962.
3. C. Brans and R. H. Dicke, Phys. Rev., *124*, 925, 1961.
4. T. Singh, J. Math. Phys., *16*, 2517, 1975.
5. D. R. K. Reddy, Aust. J. Phys., *30*, 109, 1977.
6. D. R. K. Reddy, J. Math. Phys., *20*, 23, 1979.
7. D. R. K. Reddy, J. Math. Phys., *20*, 1313, 1979.
8. A. Banerjee and N. O. Santos, J. Math. Phys., *22* 1075, 1981.
9. B. W. Stewart, J. Phys. A Math. Gen., *15* 2519, 1982.

Acta Physica Hungarica 60 (1—2), pp. 43—49 (1986)

ANALYSIS OF THE IV-TH POSITIVE SYSTEM OF THE $^{13}C^{16}O$ MOLECULE

J. DOMIN

Atomic and Molecular Physics Laboratory, Pedagogical College
Rzeszów, Poland

(Received 17 May 1984)

Twenty eight bands of the fourth positive system have been photographed in the ultraviolet region between 210 and 270 nm, in the spectrum of the $^{13}C^{16}O$ molecule. Rovibrational structure of these bands was analysed and molecular constants were calculated for the $A^1\Pi$ state. Detailed assignments of the observed perturbations in $A^1\Pi$ state are given.

Introduction

Of all molecular states, the ground electronic state of $^{12}C^{16}O$ molecule is studied extensively [1, 2, 3]. The rovibrational structure of the other singlet states is also sufficiently known [4—10].

The ground state of the $^{13}C^{16}O$ molecule was investigated with very high accuracy [11—15]. The data on the upper electronic states are rather limited in this isotopic molecule. The rotational structure of the $A^1\Pi$ state is known from the research of the Ångström bands [16, 17] for low vibrational levels (to $v=6$).

The analysis of the fourth positive system of the CO molecule makes it possible to investigate the $A^1\Pi$ state. As yet, only one successful attempt has been made (McCulloh and Glockler [18]) to examine this system in the $^{13}C^{16}O$ molecule. These authors published the wave numbers of 35 heads occurring in the 200–256 nm region, on the basis of the photographs with a reciprocal linear dispersion of about 0.56 nm/mm. Their analysis is limited to the vibrational numbering of bands and to the estimation of the vibrational constants for a ground state.

The mere selection of bands for Deslandres table contained so many gaps that a correct vibrational numbering was difficult.

Now, 28 bands situated in the 210–270 nm region have been chosen to obtain a more complete elaboration of the electronic state $A^1\Pi$ in the $^{13}C^{16}O$ molecule. These bands represent the vibrational levels from $v''=12$ to $v''=22$ in the ground state, but in the upper electronic state they represent the levels from $v'=3$ to $v'=11$. Observation of a greater number of vibrational levels in the $A^1\Pi$ state allowed to determine a set of molecular constants for this state. Moreover, numerous rotational perturbations were identified in this state.

Experimental details

Emission bands of the fourth positive system were excited in a water-cooled Geissler's tube filled with $^{13}C^{16}O$ gas having 95% of ^{13}C. The spectrum was photographed with a PGS-2 grating spectrograph (VEB C. Zeiss, Jena) in X^{th}, XI^{th} and XII^{th} orders (a reciprocal linear dispersion of about 0.04 nm/mm) on ORWO UV-1 type plates. Overlapping orders were separated by a standard monochromator for this type of spectrograph.

Thorium lines excited in a water-cooled hollow-cathode lamp were used as standards [19]. Measurements of the lines were performed using Abbé-type comparator. The accuracy of wave numbers for sufficiently separated lines is about 0.05–0.1 cm^{-1} and for lines with worse conditions of measurements it is about 0.2–0.3 cm^{-1}.

Analysis of the system

In this work 28 bands have been taken for a detailed examination of the rovibrational structure of the $A^1\Pi$ state. Owing to our proper choice bands with unblended structure have been obtained, with a larger representation of the vibrational levels in both electronic states.

The band of the fourth positive system ($A^1\Pi \rightarrow X^1\Pi$) transition contains P, Q and R branch. At the beginning combination relations ([20], p. 177) were used for rotational assignments of quantum number J in each branch. After that the whole rotational structure of the system was tested by the Jenkins and McKellar formulae ([20], p. 188). This verification is especially effective when the Jenkins and McKellar method is based on all three branches simultaneously. In addition, it also allowed to make a choice of several band pairs satisfying the same relations. In cases of rotational perturbations, the application of this method gives good results, when we use formulae yielding the quantities for a ground state which is unperturbed.

Some obvious combination relations for lower vibrational levels of the $A^1\Pi$ state were also applied. As these relations connect the fourth positive system with the Ångström system, we could assure that both systems are interpreted in accordance with each other.

After gaining a correct rotational structure of the system, the molecular constants were calculated for both electronic states. However, the perturbations occurring in the $A^1\Pi$ state have an effect on the values of constants belonging to this state. This especially concerns higher rotational constants, that is in our case the constants D_v. For that reason our purpose here was to receive band origins and rotational constants B_v. Therefore we have taken into account the rotational lines with $J \leq 20$. The values of measured wave numbers for the IV-th positive band system are not published here, but they are available from the author.

Table I

Band origins of the IV-th positive system for the $^{13}C^{16}O$ molecule [cm^{-1}]

v′ \ v″	12	13	14	15	16	17	18	19	20	21	22
3	45507.96										
4	46856.92	45060.46	43288.20								
5		46377.09	44604.79	42856.91							
6			45891.30*	44143.38*	42420.04*	40720.69*					
7				45391.76**	43668.14	41968.88	40294.12**				
8					44887.44	43188.32	41513.30	39862.29	38235.18		
9							42697.79	41046.77	39419.82		
10								42199.53*	40572.56*	38969.50*	
11										40090.04*	38510.95*

* — values for perturbed bands in the origin.
** — values for blended bands.

Determination of molecular constants

Having completed the rotational analysis we could perform the calculation of molecular constants. Band origins σ_0, the magnitudes B_v, ΔB and ΔG for both electronic states and then the Dunham coefficients Y_{lj} were calculated.

Band origins were obtained by extrapolation of Q branches and also by interpolation between P and R branches [20]. The listed values in Table I are mean values received from both methods.

The determination of spectroscopic constants of $A^1\Pi$ state presents certain difficulties because of the perturbations occurring there. The data involving perturbed levels (i.e. $v' = 6$, 8, 10 and 11) were eliminated in our calculations. This elimination was made in calculations of constants B'_v and of first vibrational quanta ΔG. The centrifugal contributions were neglected in the evaluation of rotational constants. The rotational constants B'_v were determined on the basis of the averaged combination differences [20] received from all bands associated with a particular vibrational level. These averaged combination differences were fitted to the least squares routine. The values obtained for constants B'_v are shown in Table II. Finally, the set of rotational constants

Table II

Rotational constants B_v for unperturbed vibrational levels of the $A^1\Pi$ state

v	B_v [cm^{-1}]	Number of equations*
3	1.46515(64)	15
4	1.44398 (46)	16
5	1.42064(97)	15
7	1.37743 (76)	16
9	1.33143 (57)	15

* Number of equations fitted to least squares routine

including the values of B'_v for lower vibrational levels [10, 16] and also values of ΔB was the basis for calculations of Dunham coefficients Y_{01} and Y_{11}. These coefficients for upper electronic state were computed with the help of a least squares method (Table V).

Vibrational constants Y_{10} were found on the basis of the vibrational quanta, obtained by a Jenkins and McKellar method taking into account the suitable pairs of bands (Table III). The set of vibrational quanta also includes the values obtained in our laboratory for lower vibrational levels [10, 16]. Values of coefficients Y_{10} obtained by least squares routine are listed in Table V.

Table III

Vibrational quanta and values of ΔB for $A^1\Pi$ state

v_1	v_2	$G(v_1)-G(v_2)$	$B_{v_1}-B_{v_2}$	Number of equations*
4	3	1350.034 (19)	−0.02179 (12)	16
5	4	1316.638 (24)	−0.02196 (16)	15
7	5	2534.726 (25)	−0.04460 (14)	15
9	7	2403.786 (22)	−0.04489 (16)	15

* Number of equations fitted to least squares routine

It should be noted that the analysis of the system allowed to receive also a set of Dunham coefficients for the ground state. These coefficients are in good agreement with those published by other investigators [11—15], but they are not included here.

Observed perturbations

In the $A^1\Pi$ state of the $^{13}C^{16}O$ molecule several perturbations can be observed just like in the natural molecule. These perturbations can be attributed to interactions between the $A^1\Pi$ state and other near lying states. Interactions among the components of different types of electronic states always give a typical run of lines in the branches

Table IV

Observed perturbations of the $A^1\Pi$ state in the $^{13}C^{16}O$ molecule

$A^1\Pi$ (v)	Maximum perturbation (J)	Perturbing term (Triplet components)	
6	≤1	$\Omega=3$,	$v=12$ ($d^3\Delta$)
8	15; 16	$\Omega=3$	$v=15$ ($d^3\Delta$)
	19; 20	$\Omega=2$	
	23; 24	$\Omega=1$	
10	7; 8	F_1	$v=23$ ($a'^3\Sigma^+$)
	9; 10	F_2	
	12; 13	F_3	
10	14; 15	F_1	$v=15$ ($e^3\Sigma^-$)
	17; 18	F_2	
	20; 21	F_3	
11	4; 5	$\Omega=2$	$v=19$ ($d^3\Delta$)
	9; 10	$\Omega=1$	

Table V

Dunham coefficients Y_{ij} for the $A^1\Pi$ state in the $^{13}C^{16}O$ molecule

Y_{ij}	After Schmid and Gerö (a)*	After Simmons et al [24]*	After Rytel (b)*	Present results
Y_{10}	–	1484.396	1484.573 (66)	1484.94 (49)
Y_{20}	–	−18.5447	−16.899 (26)	−17.054 (85)
Y_{30}	–	0.71576	0.0136 (28)	0.03165 (10)
Y_{01}	1.5405	1.5405	1.54384 (57)	1.5451 (13)
Y_{11}	−0.02083	−0.02173	−0.02097	−0.02245 (21)

(a) — R. Schmid, L. Gerö, Z. Phys., *101*, 343, 1936.
* — Values recalculated from data on the natural molecule.
(b) — M. Rytel, Acta Phys. Polon. *A38*, 299, 1970.

which is a matter of holding the selection rules. A useful and detailed description of perturbation phenomena for different types of electronic states was given by Kovács [21, 22]. On the basis of these considerations and also data [8] available on localisations of the perturbing states we can identify types of interacting states. We could not observe here all perturbations occurring in the $A^1\Pi$ state because the rotational lines with higher J were neglected in our measurements. Detailed statements of the observed perturbations are summarized in Table IV.

Especially complicated but solvable was the rotational structure of the vibrational level $v'=10$, because levels $v=15$ of $e^3\Sigma^-$ and $v=23$ of $a'^3\Sigma^+$ converge there. Besides, a detailed analysis of displacements of the lines allowed to establish the rotational assignments.

It should be noted that perturbations attributed to $d^3\Delta$ state have a specific run. As mentioned before [23, 24], the $d^3\Delta$ state has properties of intermediate coupling between Hund's cases (a) and (b). If the perturbing state $d^3\Delta$ is in case (a) (lower J) then a perturbation selection rule $\Delta\Omega=0$ becomes valid, whereas for $d^3\Delta$ state in case (b) (higher J) the selection rules $\Delta N=0, \pm 1$ are valid. Therefore in the limits of case (a) only the $F_3(\Omega=1)$ component of triplet $d^3\Delta$ would perturb the $A^1\Pi$ state, while in the limits of case (b) all three triplet components could perturb the $A^1\Pi$ state. The first of these effects can be observed in vibrational level $v'=6$, whereas the second one in the level $v'=8$ of the $A^1\Pi$ state in the $^{13}C^{16}O$ molecule.

Acknowledgments

The author wishes to express his appreciation to Prof. M. Rytel for inspiration and guidance in completing this work.

This work was supported in part by the N. Copernicus Astronomical Center, Polish Academy of Sciences.

References

1. P. H. Krupenie, Not. Bur. Stand. U.S. NSRDS-5 1966.
2. S. E. Schwartz and B. A. Thursch, J. Mol. Spectrosc., *32*, 343, 1969.
3. J. T. Yardley, J. Mol. Spectrosc., *35*, 314, 1970.
4. L. Gerő, Z. Phys., *99*, 52, 1936.
5. L. Gerő, Z. Phys., *100*, 374, 1936.
6. R. Schmid and L. Gerő, Z. Phys., *101*, 343, 1936.
7. R. Kepa and M. Rytel, Acta Phys. Polon., *A37*, 585, 1970.
8. S. G. Tilford and J. D. Simmons, J. Phys. Chem. Ref. Data, Vol. 1, No. 1, 1972.
9. R. Kepa, M. Knot–Wisniewska and M. Rytel, Acta Phys. Polon., *A48*, 819, 1975.
10. R. Kepa, Acta Phys. Hung., *45*, 133, 1978.
11. J. W. C. Johns, A. R. W. Mc–Kellar and D. Weitz, J. Mol. Spectrosc., *51*, 539, 1974.
12. A. H. M. Ross, R. S. Eng and H. Kildal, Opt. Comm., *12*, 433, 1974.
13. T. R. Tood, C. M. Clayton, W. B. Telfair, T. K. McCubbin and Ir. J. Pliva, J. Mol. Spectrosc., *62*, 201, 1976.
14. Da–Wun Chen, K. Narahari Rao and Robin S. McDowell, Canad. J. Phys., *61*, 71, 1976.
15. R. M. Dale, M. Herman, J. W. C. Johns, A. R. W. McKellar, S. Nagler and I. K. M. Strathy, Canad. J. Phys., *57*, 677, 1979.
16. M. Rytel, Acta Phys. Polon., *A37*, 539, 1970.
17. J. Janjic, J. Danielak, R. Kepa and M. Rytel, Acta Phys. Polon., *A41*, 757, 1972.
18. K. E. McCulloh and G. Glockler, Phys. Rev., *89*, 145, 1953.
19. A. Giacchetti, J. Opt. Soc. Am., *60*, 474, 1970.
20. G. Herzberg, Spectra of Diatomic Molecules, Van Nostrand, Princeton, 1950.
21. I. Kovács, Rotational Structure in the Spectra of Diatomic Molecules, Akadémiai Kiadó, Budapest and Adam Hilger Ltd. London, 1969.
22. I. Kovács, Canad. J. Phys., *36*, 309, 1958.
23. P. K. Carrol, J. Chem. Phys., *36*, 2861, 1962.
24. J. D. Simmons, A. M. Bass and S. G. Tilford, Astrophys. J., *155*, 345, 1969.

Acta Physica Hungarica 60 (1—2), pp. 51—55 (1986)

ELECTRON PARAMAGNETIC RESONANCE OF Mn^{2+} IN $Ce_2\ Zn_3\ (NO_3)_{12}.24H_2O$ SINGLE CRYSTALS

V. P. SETH, V. K. JAIN and R. S. BANSAL

Physics Department, M. D. University, Rohtak Haryana, India

(Received 22 May 1984)

Electron paramagnetic resonance of Mn^{2+} in $Ce_2\ Zn_3\ (NO_3)_{12}.24H_2O$ single crystals has been studied in X-band at 290 and 90K. Mn^{2+} substitutes for Zn^{2+} sites. The spin-Hamiltonian parameters are evaluated.

1. Introduction

The hydrated double nitrates with the general formula $M_2^{111}\ M_3^{11}\ (NO_3)_{12}.24H_2O$, where M^{111} is a trivalent cation (Bi or an ion of the 4f group) and M^{11} is a divalent cation (Zn, Mg or an ion of the 3d group), form an interesting isomorphous series of salts for electron paramagnetic resonance (EPR) studies of S-state ions (Mn^{2+}). The trivalent lanthanide ions are generally paramagnetic, their spin-lattice relaxation times at sufficiently high temperature are much shorter than those of the S-tate ions. Because of this behaviour the magnetic interaction between the paramagnetic ions and the S-state ions are averaged to zero with the consequence that magnetic resonance absorption by the S-state ion can be observed without extensive broadening. In this paper we report the EPR of Mn^{2+} doped into $Ce_2Zn_3(NO_3)_{12}.2H_2O$(CZN) single crystals at 290K and at 90K.

2. Crystal sturcture

The crystal structure of $Ce_2\ Mg_3\ (NO_3)_{12}.24H_2O$ has been determined by Zalkin et al [1]. The other hydrated double nitrates are expected to have a similar structure. The unit cell of double nitrates is rhombohedral with space group $R\bar{3}$. The unit cell contains one divalent ion in Y-site (site I) and two in X-site (site II) with point symmetries C_{3i} and C_3, respectively. The trivalent ion is found at a site of C_{3i} point symmetry and the rest of the atoms are in position of general type of the space group.

3. Experimental details

Singel crystals of hydrated double nitrates doped with Mn^{2+} were grown by slow evaporation of aqueous solution of $Ce(NO_3)_3 . 6H_2O$ and $Zn(NO_3)_2 . 6H_2O$ mixed in stoichiometric ratios. The Mn^{2+} were introduced into the host lattice by adding a small amount (0.1 % by weight) of manganese nitrate. The EPR measurements were performed on a JEOL JES-FE 3X homodyne spectrometer, operating at ~ 9.45 GHz, equipped with TE_{011}-cylindrical cavity and 100 kHz field modulation. The resonance line of DPPH with $g = 2.0036$ is used as a reference line for magnetic field strength. The crystals were mounted on quartz rods. The angular variation studies were done using JES-UCR-2X sample angular rotating device. The liquid nitrogen temperature measurements were made by using ES-UCD-2X insertion type dewar.

4. Results and discussion

Angular variation studies of Mn^{2+} spectra reveal the presence of two inequivalent Mn^{2+} centres [2–5] of unequal intensity. The spectrum having low intensity is due to Mn^{2+} substituting the divalent Zn^{2+} at site I while the spectrum having large intensity is due to Mn^{2+} substituting for Zn^{2+} at site II (Fig. 1). The Mn^{2+} centre occupying the site II is more intense because there are twice as many X sites as Y

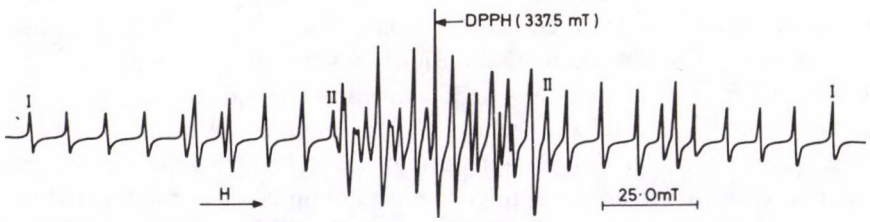

Fig. 1. EPR spectrum of Mn^{2+} in $Ce_2 Zn_3 (NO_3)_{12} . 24H_2O$ single crystals at 290K. The positions of extreme hyperfine lines of Mn^{2+} complexes for two sites are designated by I and II, respectively

sites. The principal axes of the spectra were located by searching the directions of extrema in the spread of the spectrum. It was found that the principal z axes of two Mn^{2+} complexes are along the trigonal axis (c axis) and x axis is perpendicular to the trigonal axis. The spectra of Mn^{2+} showing large zero field splitting (site I) were measured for various angles of the magnetic field relative to the c axis. Fig. 2 shows the angular variation of the allowed fine structure transitions ($\Delta M = \pm 1$) in the zx plane for site I. The angular variation of the spectrum in the plane perpendicular to the c axis shows $\pi/3$ rotation symmetry, however, the change in the position of fine structure transitions is very small and this variation is within the experimental error.

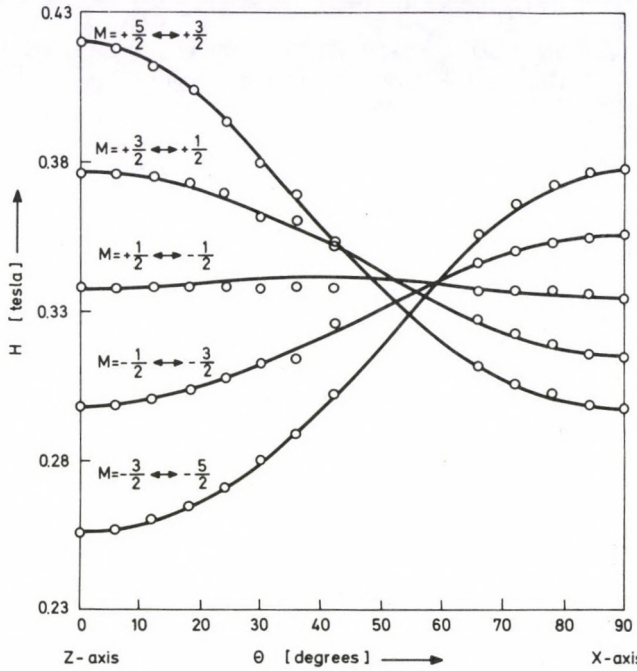

Fig. 2. Angular dependence of allowed fine structure transitions ($\Delta M = \pm 1$) of Mn^{2+} for site I in the zx plane at 290K

Experiments were also performed at 90K in order to observe the effect of paramagnetic Ce^{3+} ions on Mn^{2+} spectra. It is observed that Ce^{3+} ions behave as diamagnetic ions at 90K. Experiments at 4.2K were not possible.

The EPR spectrum of Mn^{2+} for both sites can be explained by the spin-Hamiltonian of the form [6]

$$\mathcal{H} = \beta g_{\parallel} H_z S_z + \beta g_{\perp}(H_x S_x + H_y S_y) + D\left(S_z^2 - \frac{35}{12}\right) -$$

$$- \frac{7}{36}(a-F)\left(S_z^4 - \frac{95}{14}S_x^2 + \frac{81}{16}\right) + AI_z S_z + B(S_x I_x + S_y I_y) +$$

$$+ (a\sqrt{2}/36)\left\{S_z\left\{S_+^3 \exp(-3i\varphi) + S^3 \exp(3i\varphi)\right\} +\right.$$

$$\left. + \left\{S_+^3 \exp(-3i\varphi) + S_-^3 \exp(3i\varphi)\right\} S_z\right],$$

where the z axis is parallel to the trigonal symmetry axis of the crystal. The symbols have their usual meaning and $S = I = \frac{5}{2}$ for Mn^{2+}.

Table I

Spin-Hamiltonian parameters for Mn^{2+} in $Ce_2\ Zn_3\ (NO_3)_{12}.24H_2O$ single crystals at 290K and 90K. All crystal fields and h.f. parameters are in units of $10^{-4}\ cm^{-1}$

Spin-Hamiltonian parameters	Site I		Site II	
	290K	90K	290K	90K
D	-188.6 ± 1.0	-210.3 ± 3.1	14.7 ± 2.5	-59.1 ± 0.8
$a-F$	8.8 ± 1.0	7.5 ± 0.8	7.0 ± 0.4	8.7 ± 1.1
$g_{\|\|}$	2.0010 ± 0.0020	2.0026 ± 0.0018	2.0021 ± 0.0008	2.0024 ± 0.0010
$g_{\perp}$	2.0044 ± 0.0010	2.0034 ± 0.0019	2.0023 ± 0.0015	2.0028 ± 0.0010
A	-90.5 ± 0.5	-90.8 ± 1.0	-89.9 ± 1.0	-89.4 ± 1.0
B	-89.0 ± 0.5	-90.1 ± 1.0	-88.7 ± 1.0	-88.3 ± 1.0

Using the above spin-Hamiltonian, the Mn^{2+} EPR spectra were analysed and the best fit parameters thus obtained are given in Table I for both sites at 290K and 90K. The signs of the parameters are only relative. As usual the value of A has been taken [7, 8] to be negative. The magnitude of the splitting of the hyperfine sextets appearing at high fields and at low fields when the magnetic field is parallel to the z axis suggests [9] a sign to the axial parameter D. The observed value of A indicates that Mn^{2+} at both sites are surrounded by six water molecules as the covalency parameter determined from the curve (hyperfine parameter vs covalency) given by Simanek and Muller [10] indicates the characteristic covalency of Mn^{2+}–$6H_2O$ complex. The line width of Mn^{2+} in CZN is of the order of 1.1 mT. In hydrated crystals, an appreciable degree of line broadening of the order of 1.0 mT can originate due to local magnetic fields of proton nuclear moments in the water molecules [11].

From Table I it is clear that the value of zero-field splitting parameter D is very different for the two sites and is sensitive to temperature. The relative insensitivity of the parameter D of site I to temperature given in Table I has also been noted [12] for Ni^{2+} in $La_2\ Mg_3\ (NO_3)_{12}.24H_2O$ (LMN) and $La_2\ Zn_3\ (NO_3)_{12}.24H_2O$ (LZN). The magnitude of D increases with decrease in temperature. An increase in the value of D at low temperature can probably be explained as due to thermal contraction and vibrational mechanism of the lattice [13, 14]. The different values of D for Mn^{2+} at two sites indicate that the two sites differ greatly in the static crystal field seen by the ions. The crystal field is presumed to be due to an octahedron of water molecules oriented with (111) axis along the trigonal axis of the crystal, and it appears that the octahedron is nearly perfect for site II and has appreciable trigonal distortion for the site I. The large difference in the D value is also observed for Ni^{2+} doped LMN, LZN single crystals [12] and for Mn^{2+} in $Nd_2Mg_2(NO_3)_{12}.24H_2O$ [15]. In the theoretical analysis of the ground state splitting of the S-state ion it is generally recognised that more than one mechanism is needed to account for the magnitude of the parameter D.

Acknowledgement

This work was supported by UGC, New Delhi.

References

1. A. Zalkin, J. D. Forrester and D. H. Templeton, J. Chem. Phys., *29*, 2881, 1963.
2. V. K. Jain, Z. Naturf., *33a*, 1389, 1978.
3. V. K. Jain, Phys. Stat. Sol., (b) *105*, 723, 1981.
4. D. Van Ormondt and T. Thalhammer, Phys. Letters, *14*, 169, 1965;
   B. M. Brandt, D. Van Ormondt and T. Thalhammer, Phys. Letters, *19*, 549, 1966.
5. H. A. Buckmaster, J. C. Dering and D. J. I. Fry, J. Phys. C *1*, 599, 1968.
6. S. Geschwind, Phys. Rev., *121*, 363, 1961.
7. R. E. Watson and A. J. Freeman, Phys. Rev., *123*, 2027, 1961.
8. R. J. Richardson, S. Lee and T. J. Menne, Phys. Rev., *B2*, 2295, 1970.
9. W. Low, Paramagnetic Resonance in Solids (Solid State Physics. Suppl. 2), Academic Press, New York, 1960.
10. E. Simanek and K. A. Müller, J. Phys. Chem. Solids, *31*, 1027, 1970.
11. A. Abragam and B. Bleaney, Electron Paramagnetic Resonance of Transition Ions, Clarendon Press, Oxford, 217.
12. R. T. Dixon and J. W. Culvahouse, Phys. Rev., *133*, 2279, 1971.
13. W. M. Walsh, Phys. Rev., *114*, 1473, 1959.
14. I. N. Geifman and M. D. Glinchuk, Soviet Phys. Solid State, *13*, 872, 1971.
15. V. K. Jain, Acta Phys. Polon., *A55*, 29, 1979.

Acta Physica Hungarica 60 (1—2), pp. 57—65 (1986)

A REISSNER–NORDSTRÖM INTERIOR SOLUTION

L. K. PATEL and BHARAT M. PANDYA

Department of Mathematics, Gujarat University
Ahmedabad, 380 009 India

(Received 30 May 1984)

An interior solution of the Einstein–Maxwell equations for a charged static sphere is obtained. The physical 3-space $t=$constant of the solution is spheroidal. The solution is interpreted as a charged analogue of Vaidya–Tikekar solution. The details of the solution are also discussed.

1. Introduction

Many research workers have devoted considerable attention to the problem of finding interior solutions of the Einstein–Maxwell equations corresponding to a static charged sphere. The sphere of uniform density has been discussed by Kyle and Martin [1] and Mehra and Bohra [2]. The sphere of charged dust has been investigated by Bonner and Wickramasuriya [3], Raychaudhuri [4] and Tikekar [5]. The other cases of interior solutions for a charged fluid sphere have been discussed by Efinger [6], Wilson [7], Kramer and Neugebauer [8], Bekenstein [9], Krori and Barua [10], Bailyn [11] and Whitman and Burch [12]. In all the above mentioned solutions the space-times are not conformally flat. Chang [13] has obtained some conformal flat interior solutions of Einstein–Maxwell equations for a charged static sphere.

In all these cases except Tikekar [5], the physical 3-space $t=$constant is spherical. The aim of the present investigation is to obtain an interior solution for a charged perfect fluid sphere with the following properties:

(i) The space-time describing the solution is not conformally flat.

(ii) The associated physical 3-space $t=$constant is spheroidal.

Vaidya and Tikekar [14] have discussed the space-times, with physical 3-space spheroidal, in great detail. They have shown that the line-element describing such space-times can be expressed in the form

$$ds^2=e^{\nu}\,dt^2-\left(1-\frac{kr^2}{R^2}\right)\left(1-\frac{r^2}{R^2}\right)^{-1}dr^2-r^2(d\theta^2+\sin^2\theta\,d\varphi^2), \tag{1}$$

where ν is an arbitrary function of r. Here R and k are constants and $k<1$. The line-element (1) is regular at all points where $r^2<R^2$. We name the coordinates as $x^1=r$, $x^2=\theta$, $x^3=\varphi$ and $x^4=t$ when $k=0$, the physical 3-space $t=$constant in (1) becomes spherical.

2. Einstein–Maxwell equations

We shall develop Einstein–Maxwell field equations for a static spherically symmetric distribution of matter in the form of a charged perfect fluid with the metric (1) as the space-time metric associated with the distribution. For a charged perfect fluid the energy momentum tensor is

$$T_k^i=(\not{p}+\rho)v^iv_k-\not{p}\delta_k^i-F^{i\lambda}F_{k\lambda}+\frac{1}{4}\delta_k^iF_{mn}F^{mn}. \tag{2}$$

Here $\not{p}$, ρ and v^i denote respectively the fluid pressure, matter density and the unit time like four velocity field of the fluid. F_{ik} are the components of the electromagnetic field tensor satisfying Maxwell's equations

$$F_{ik,j}+F_{kj,i}+F_{ji,k}=0, \tag{3a}$$

$$\partial/\partial x^j(F^{ij}\sqrt{-9})=4\pi\sqrt{-9}J^i. \tag{3b}$$

The four-current vector J^i and the charge density σ are related by

$$J^i=\sigma v^i. \tag{4}$$

Since the field is static, we have

$$v^i=(0,0,0,e^{-\nu/2}). \tag{5}$$

Since there is only a radial electric field, the only non-vanishing component of F_{ik} is F_{14}. The Maxwell equations (3a) and (3b) lead us to write

$$F_{14}=\frac{-e^{\nu/2}}{r^2}\left[\frac{1-\frac{kr^2}{R^2}}{1-\frac{r^2}{R^2}}\right]^{1/2}\int_0^r 4\pi\sigma\left[\frac{1-\frac{kr^2}{R^2}}{1-\frac{r^2}{R^2}}\right]^{1/2}dr. \tag{6}$$

We write

$$-F_{41}F^{41}=E^2(r), \tag{7}$$

where $E(r)$ can be interpreted as the field intensity. The results (6) and (7) imply

$$4\pi\sigma=\frac{1}{r^2}\left[\frac{d}{dr}(r^2E)\right]\left(1-\frac{r^2}{R^2}\right)^{\frac{1}{2}}\left(1-\frac{kr^2}{R^2}\right)^{-\frac{1}{2}} \tag{8}$$

Subsequently,

$$Q(r)=4\pi\int_0^r\left(1-\frac{kr^2}{R^2}\right)^{1/2}\left(1-\frac{r^2}{R^2}\right)^{-1/2}\sigma r^2\,dr \tag{9}$$

represents the total charge contained within the sphere of radius 'r'.

The Einstein–Maxwell equations give

$$-8\pi p + E^2 = \left[\frac{1-k}{R^2} - \frac{\nu'}{r}\left(1-\frac{r^2}{R^2}\right)\right]\left(1-\frac{kr^2}{R^2}\right)^{-1}, \tag{10}$$

$$-8\pi p - E^2 = -\left[\frac{\nu''}{2} + \frac{\nu'^2}{4} + \frac{\nu'}{2r}\right]\left(1-\frac{r^2}{R^2}\right)\left(1-\frac{kr^2}{R^2}\right)^{-1} + \frac{(1-k)r}{R^2}\left[\frac{\nu'}{2} + \frac{1}{r}\right]\left(1-\frac{kr^2}{R^2}\right)^{-2}, \tag{11}$$

$$8\pi\rho + E^2 = \frac{3(1-k)}{R^2}\left(1-\frac{k}{3}\cdot\frac{r^2}{R^2}\right)\left(1-\frac{kr^2}{R^2}\right)^{-2}. \tag{12}$$

Here and in what follows an overhead dash denotes the differentiation with respect to r.

3. Solution of field equations

We have three equations (10), (11) and (12) and four variables ρ, p, ν and E^2. Hence we have only one free variable. In this Section we specify E^2 and solve these three equations for the remaining three functions. Let us assume,

$$E^2 = \frac{\alpha^2 r^2}{R^4\left(1-\frac{kr^2}{R^2}\right)^2}, \tag{13}$$

where α is a constant.

Equating the values of p from (10) and (11) and using (13) we get the differential equations

$$(1-k+kz^2)\frac{d^2F}{dz^2} - kz\frac{dF}{dz} - [k(1-k)+2\alpha^2]F = 0, \tag{14}$$

where $z^2 = 1-\frac{r^2}{R^2}$ and $F = e^{\nu/2}$.

To solve the linear differential equation (14), we change the independent variable z to u defined as follows:

$$u^2 = \frac{k}{k-1}z \qquad \text{if} \quad k<0,$$

and

$$u^2 = \frac{k}{1-k}z \qquad \text{if} \quad 0<k<1.$$

The Eq. (14) reduces to the convenient form

$$(1-u^2)\frac{d^2F}{du^2}+u\frac{dF}{du}+\left(1-k+\frac{2\alpha^2}{K}\right)F=0. \tag{15}$$

The points $u=\pm 1$ are regular singular points and all other points are regular points for Eq. (15). If we seek a series solution of this equation in the form $F=\Sigma A_k u^k$, we get the following recurrence relation for the coefficients A_k

$$(n+2)(n+1)A_{n+2}=\left[n^2-2n+k-1-\frac{2\alpha^2}{k}\right]A_n.$$

If the parameters k and α are related in such a way that the equation

$$\left(n^2-2n+k-1-\frac{2\alpha^2}{k}\right)=0$$

admits integral values of n as solutions, either of the two sets $(A_0, A_2, A_4, \ldots)$, $(A_1, A_3, A_5, \ldots)$ contains a finite number of elements and the corresponding terms in the solution-series constitute a finite polynomial. It can be verified that if k is to be in the range $k<1$, the simplest value of k is $-1-\sqrt{1+2\alpha^2}$, which corresponds to $n=3$. A little computation yields the following closed-form solution of Eq. (14)

$$F=e^{\nu/2}=Az\left[1-\frac{2k}{3(k-1)}\cdot z^2\right]+B\left[1-\frac{k}{k-1}\cdot z^2\right]^{3/2}, \tag{16}$$

where A and B are undetermined constants of integration. The closed-form solutions of (14) have also been obtained for

$$k=\frac{-7}{2}\left(1+\sqrt{1-\frac{8\alpha^2}{49}}\right) \quad \text{etc.}$$

but are not reported here.

The matter density and pressure are found to be

$$8\pi\rho=\frac{(k^2-10k+6)+(4k-k^2)z^2}{2R^2(1-k+kz^2)^2} \tag{17}$$

$$\left\{8\pi p-\frac{k(k+2)(1-z^2)}{2R^2(1-k+kz^2)^2}\right\}R^2(1-k+kz^2)\left[Az\left\{1-\frac{2k}{3(k-1)}z^2\right\}+\right.$$

$$\left.+B\left\{1-\frac{k}{k-1}z^2\right\}^{3/2}\right]=Az\left\{k-3+\frac{2k(7-k)}{3(k-1)}z^2\right\}+$$

$$+B\left(1-\frac{k}{k-1}z^2\right)^{1/2}\left[k-1+\frac{k(7-k)}{(k-1)}z^2\right]. \tag{18}$$

Using the results (8) and (13) we obtain the charge density σ as

$$4\pi\sigma = \frac{\alpha}{R^2}(1-z^2)^{\frac{1}{2}}(3-5k-5kz^2)(1-k+kz^2)^{-\frac{5}{2}}, \tag{19}$$

where $\alpha^2 = k(k+2)$. It is not difficult to see that the matter density ρ and the charge density σ are positive for all z. Here it should be noted that the range for k is $k \leq -2$.

We consider a situation where in the spherical charged perfect fluid distribution extends to a finite radius $a < R$. The interior metric (1) with e^{ν} given by (16) should then match with the external Reissner–Nordström metric

$$ds^2 = \left(1 - \frac{2m}{r} + \frac{q^2}{r^2}\right)dt^2 - \left(1 - \frac{2m}{r} + \frac{q^2}{r^2}\right)^{-1} dr^2 - r^2(d\theta^2 + \sin^2\theta\, d\varphi^2), \tag{20}$$

across the boundary $r = a$. Here m and q respectively denote the total mass and the total charge of the sphere. The relations (9) and $Q(a) = q$ give us

$$q^2 = \frac{\alpha^2 a^6}{R^4\left(1 - \frac{ka^2}{R^2}\right)^2} = \frac{k(k+2)a^6}{2R^4\left(1 - \frac{ka^2}{R^2}\right)^2}. \tag{21}$$

The appropriate boundary conditions

$$e^{\nu(a)} = \left(1 - \frac{a^2}{R^2}\right)\left(1 - \frac{ka^2}{R^2}\right)^{-1} = 1 - \frac{2m}{a} + \frac{q^2}{a^2}$$

and $p(r=a) = 0$ determine the constants m, A and B as

$$\frac{2m}{a}\left(1 - \frac{ka^2}{R^2}\right)^2 = \frac{a^2}{R^2}\left[(1-k)\left(1 - \frac{ka^2}{R^2}\right) + \frac{k(k+2)a^2}{2R^2}\right], \tag{22}$$

$$-6B\left[(1-k)\left(1 - \frac{ka2}{R^2}\right)\right]\left(1 - \frac{a^2}{R^2}\right)^{-\frac{1}{2}}$$

$$= 2k(7-k)\frac{a^2}{R^2} - (k^2+2k+9) + \frac{k(k+2)a^2}{2R^2\left(1 - \frac{ka^2}{R^2}\right)}\left[3 - k - 2k\frac{a^2}{R^2}\right], \tag{23}$$

$$\frac{A\left(1 - \frac{a^2}{R^2}\right)^{\frac{1}{2}}}{3(1-k)}\left(3 - k - 2k\frac{a^2}{R^2}\right) = \frac{\left(1 - \frac{a^2}{R^2}\right)^{\frac{1}{2}}}{\left(1 - \frac{ka^2}{R^2}\right)^{\frac{1}{2}}} - B\left(\frac{1 - \frac{ka^2}{R^2}}{1-k}\right)^{\frac{3}{2}}. \tag{24}$$

Thus the final form of the metric of our solution is

$$ds^2 = \left[Az\left\{1-\frac{2k}{3(k-1)}z^2\right\}+B\left(1-\frac{k}{k-1}z^2\right)^{\frac{3}{2}}\right]^2 dt^2 - \left[\frac{1-\frac{kr^2}{R^2}}{1-\frac{r^2}{R^2}}\right] dr^2 - r^2(d\vartheta^2+\sin^2\vartheta d\varphi^2), \tag{25}$$

where the constants A and B are given by the equations (23) and (24). When $\alpha=0$, the electromagnetic field disappears and we get the solution discussed by Vaidya and Tikekar [14] in connection with the exact relativistic model for a superdense star.

4. Details of the solution

The expression (17) for matter density implies that at $r=0$

$$8\pi\rho_0 = 3(1-k)/R^2. \tag{26}$$

As $k<-2$, the central density ρ_0 is positive. At the origin, we see that the intensity E also vanishes. It can be verified that ρ' is negative. So that as r increases, the density decreases from the maximum value ρ_0 at the centre. On the boundary $r=a$ it attains the value

$$8\pi\rho_a = \left[3(1-k)+\frac{ka^2}{2R^2}(k-4)\right]\left(1-\frac{ka^2}{R^2}\right)^{-2} \tag{27}$$

we find that the ratio ρ_a to ρ_0 is given by

$$\lambda = \rho_a/\rho_0 = \left[1+\frac{k(k-4)}{6(1-k)}\frac{a^2}{R^2}\right]\left(1-\frac{ka^2}{R^2}\right)^{-2}. \tag{28}$$

We have verified that $\lambda<1$. The equation (28) determines a^2/R^2 in terms of k and λ as

$$a^2/R^2 = \frac{[k-4+12\lambda(1-k)-\sqrt{(k-4)^2+24\lambda(1-k)(2-5k)}]}{12\lambda k(1-k)}. \tag{29}$$

Substituting $r=0$ in (18) we get the central pressure p_0. It is given by

$$8\pi p_0 = \frac{A(k^2+2k+9)(1-k)^{1/2}+3B(5k+1)}{R^2[A(k-3)(1-k)^{1/2}-3B]}. \tag{30}$$

As noted earlier, our solution is a charged analogue of the Vaidya–Tikekar solution. The uncharged solution is interpreted as an exact relativistic model for a superdense star. Therefore, we are tempted to say that our solution represents a model for a charged superdense star.

Table I

Masses and equilibrium radii of charged superdense-star models corresponding to $K=-3$ and $\rho_a=2\times10^{14}$ gm cm^{-3}

No.	λ	a/R	m/a	R	a	m	$m/M_\odot$	A	B	A/B	q
1	0.90000	0.14590	0.04032	53.53730	7.81135	0.31496	0.21353	1.62313	1.01464	1.59972	0.19144
2	0.85000	0.18296	0.06153	52.02890	9.51917	0.58574	0.39711	1.55456	1.02187	1.52129	0.35465
3	0.80000	0.21660	0.08353	50.47540	10.93320	0.91320	0.61912	1.48199	1.02893	1.44033	0.55073
4	0.75000	0.24868	0.10637	48.87260	12.15380	1.29283	0.87649	1.40490	1.03570	1.35648	0.77650
5	0.70000	0.28025	0.13015	47.21540	13.23200	1.72220	1.16759	1.32263	1.04201	1.26930	1.03008
6	0.65000	0.31204	0.15497	45.49790	14.19710	2.20015	1.49163	1.23438	1.04765	1.17823	1.31028
7	0.60000	0.34469	0.18094	43.71300	15.06760	2.72633	1.84836	1.13915	1.05230	1.08253	1.61643
8	0.55000	0.37884	0.20820	41.85200	15.85530	3.30105	2.23800	1.03565	1.05549	0.98121	1.94818
9	0.50000	0.41518	0.23692	39.90430	16.56740	3.92515	2.66112	0.92223	1.05656	0.87286	2.30543
10	0.45000	0.45456	0.26732	37.85660	17.20810	4.59998	3.11863	0.79662	1.05447	0.75547	2.68831
11	0.40000	0.49811	0.29965	35.69150	17.77840	5.32738	3.61178	0.65576	1.04760	0.62596	3.09714
12	0.35000	0.54743	0.33429	33.38640	18.27670	6.10968	4.14216	0.49519	1.03319	0.47928	3.53237
13	0.30000	0.60491	0.37169	30.90980	18.69770	6.94973	4.71168	0.30821	1.00626	0.30630	3.99543
14	0.25000	0.67449	0.41251	28.21660	19.03170	7.85080	5.32257	0.08408	0.95681	0.08788	4.48412
15	0.20000	0.76320	0.45773	25.23770	19.26140	8.81644	5.97725	−0.19611	0.86097	−0.22778	5.00132
16	0.15000	0.88560	0.50887	21.85650	19.35610	9.84874	6.67779	−0.57016	0.63837	−0.89316	5.54528

The mass m recorded in the table is measured in km. The corresponding value in gm is $M=mc^2/G$. $1M_\odot=1.475$ km.

In order to have some information about the model, we shall now take up a numerical study of various parameters occurring in our solution. Using the scheme outlined above, we take the matter density on the boundary $r=a$ of the star as $\rho_a=2\times10^{14}$ gm.cm^{-3}. Again we choose different values for the ratio $\lambda=\rho_a/\rho_0$ and for each chosen value of λ and the assumed value of ρ_a we compute ρ_0. If we assign a particular value to the constant α, then $k=-1-\sqrt{1+2\alpha^2}$ gives us k. We take $1+2\alpha^2=4$ so that $k=-3$. Equation (26) then gives us R. The Eq. (29) then gives us an estimate of a, the radius of the star. The Eqs (21) and (22) are then used to determine the charge q and the mass m respectively. The mass m given by Eq. (22) will be in km. The mass M of the star in gm is obtained by $M=mc^2/G$. The constants A and B can be calculated from the Eqs (23) and (24). The results of the calculations for various values of λ are given in the Table I.

Table II

Masses and equilibrium radii of uncharged superdense-star models corresponding to $K=-3$ and $\rho_a=2\times10^{14}$ gm cm^{-3}

No.	λ	R	a	m	$m/M_\odot$
1	0.90000	53.53730	7.91347	0.32452	0.22002
2	0.85000	52.02890	9.64711	0.60131	0.40767
3	0.80000	50.47540	11.08450	0.93398	0.63321
4	0.75000	48.87260	12.32740	1.31718	0.89300
5	0.70000	47.21540	13.42720	1.74777	1.18493
6	0.65000	45.49790	14.41420	2.22385	1.50769
7	0.60000	43.71300	15.30700	2.74433	1.86056
8	0.55000	41.85200	16.11780	3.30874	2.24321
9	0.50000	39.90430	16.85430	3.91708	2.65565
10	0.45000	37.85660	17.52120	4.56977	3.09815
11	0.40000	35.69150	18.12010	5.26762	3.57127
12	0.35000	33.38640	18.65020	6.01177	4.07578
13	0.30000	30.90980	19.10770	6.80372	4.61269
14	0.25000	28.21660	19.48450	7.64522	5.18320
15	0.20000	25.23770	19.76650	8.53808	5.78853
16	0.15000	21.85650	19.92890	9.48364	6.42959

The mass m recorded in the table is measured in km.
The corresponding value in gm is $M=mc^2/G$. $1M_\odot=1.475$ km

From the Table it is clear that a/R, m/a and q are decreasing functions of λ. A is an increasing function of λ. From the Table it is clear that the radius a of the star is of the order of a few kilometres. We have given values of a, R, m and $m/M_\odot$ corresponding to the uncharged case for various values of λ the Table II. Comparing these two Tables, it is clear that the radius a of the charged star is always smaller than that of the uncharged star. In both cases, m is a decreasing function of λ. But the rate of decrease of m of Table I is higher than that of m of Table II. We have verified that when $\lambda\leq0.1170$,

the expression

$$1-\frac{2m}{a}+\frac{q^2}{a^2}$$

becomes negative. Therefore, we must take $\lambda > 0.1170$.

Here it should be noted that the physical requirements $\not{p} \geq 0$, $\rho > 0$ and $\rho - 3\not{p} \geq 0$ impose more restrictions on λ. In particular $\rho_0 > 0$, $\not{p}_0 \geq 0$ and $\rho_0 - 3p_0 \geq 0$ imply that $\lambda \geq 0.3310$. Therefore, we can go as far as the first twelve values of λ in the Table I. For this range of λ, the maximum radius is 18.2767 and the maximum mass is 4.14216 $M_\odot$. We have verified that m/q is approximately constant. Therefore, the graph of m against q is approximately a straight line. Though the numerical calculations have been carried out for the exact solution corresponding to $\alpha = \sqrt{3/2}$, the method is quite general and can be used for any real value of α.

We have thus formulated a physically viable model of charged superdense star which permits densities of the order 2×10^{14} gm cm^{-3} and radii of the order of a few kilometres. From the Table I it is clear that the introduction of charge gives us smaller values of a than those of the uncharged case. This is a noteworthy feature of our model.

Acknowledgements

The authors are highly indebted to Professor P. C. Vaidya for many helpful discussions. They also wish to thank the authorities of the Rollwala Computer Centre, Gujarat University, for providing the facilities to perform the numerical calculations.

References

1. C. F. Kyle and A. W. Martin, Nuovo Cim., *50*, 583, 1967.
2. A. L. Mehra and M. Bohra, Gen. Rel. Grav., *11*, 333, 1979.
3. W. B. Bonnor and S. B. P. Wickramasuriya, Mon. Not. R. Astron. Soc., *170*, 643, 1975.
4. A. K. Raychaudhuri, Ann. Inst. Henri Poincaré, *A22*, 229, 1975.
5. R. Tikekar, A Class of Static Charged Dust Spheres in General Relativity (preprint).
6. H. J. Efinger, Z. Phys., *188*, 31, 1965.
7. S. J. Wilson, Canad. J. Phys., *47*, 2401, 1967.
8. D. Kramer and G. Neugebauer, Ann. Phys. (Leipzig), *27*, 129. 1973.
9. J. D. Bekenstein, Phys. Rev., *D4*, 2185, 1971.
10. K. D. Krori and J. Barua, J. Phys. A Math., *8*, 508, 1975.
11. M. Bailyn., Phys. Rev., *D8*, 1036, 1973.
12. P. G. Whitman and R. C. Burch, Phys. Rev., *D24*, 2049, 1981.
13. Z. S. Chang, Gen. Rel. Grav., *15*, 293, 1983.
14. P. C. Vaidya and R. Tikekar, J. Astrophys Astr., *3*, 325, 1982.

Acta Physica Hungarica 60 (1—2), pp. 67—73 (1986)

ROTATIONAL-VIBRATIONAL PERTURBATION FACTOR FOR RARE-EARTH NUCLEI

T. BAYOMY, A. HILAL, M. EL ZAIKI and N. EL DEBAWI

Department of Physics, Faculty of Science, University of Zagazig
Zagazig, Egypt

(Received 12 June 1984)

In the framework of explaining the rotational-vibrational perturbation to the pure rotational spectrum of the even–even nuclei of rare-earth metals, a new numerical value has been calculated for a previously estimated [4] adjusting factor. Precise calculations have shown that this factor is, unfortunately, by no means constant. Moreover, the deformation parameter has been computed for those nuclei. The graphical representation of both the adjusting factor, b, and the reciprocal of the deformation parameter, β^{-1}, against the mass number, A, has been discussed. It has been found that b varies with A in a similar manner as β^{-1}.

1. Introduction

The formulation of a real unified nuclear model still constitutes a true challenge in building a complete and clear picture of the nuclear structure. Such a searched nuclear model has necessarily to thoroughly explain any nuclear spectroscopic data, whether for closed shell rigid spherical nuclei or for deformed nonrigid axially symmetric ones.

Eliot [1] has presented one of the earliest attempts to relate the successful features of the shell model to those of the collective model. However, this work may be considered to be only a simplification of the mathematical steps given in the more general treatment of the cluster model, in which it was concluded that the adiabatic condition used to differentiate between rotations, vibrations and single particle excitations is too restrictive.

Other trials [2–4] have been made in this direction with the aim to find a nuclear model capable of describing different nuclear phenomena. In his work, Sheline [4] for example, investigated the effect of nuclear vibrations in such a unified model. Considering an even–even nucleus, one must be aware of some certain established facts [5] such as the ratio of about 2.2 for the energy of the second excited state to the first excited one, the E2 character of the transition to the first 2^+ state and the increasing number of observations of multiplets (2^+, 4^+) and (0^+, 2^+, and 4^+) for the second excited state. These features supply, namely, an evidence that these states are vibrations.

Further, being aware of the fact that vibrational energy level spacings are not small compared with the single particle spacings, it has been suggested that the vibrations cannot follow the single particle motion adiabatically as the rotation motion does. In spite of the fact that emphasis has been placed on investigating vibrations from spherical to deformed even–even nuclei, yet is has been found that the nature of both γ and β vibrations from spherical to deformed nuclei gives a qualitative evidence of the single particle states in these deformed nuclei.

An additional benefit of calculating the γ and β vibrations in deformed nuclei is to offer a theoretical implication for the type of collective model to supply some information about the rotation-vibration interaction in such nuclei.

Because of the unavailability of experimental nuclear data, Sheline has chosen the Pu^{238} nucleus that has both a well-established ground state rotational band as well as established γ and β vibrational bands. In his publication, Sheline concluded that in order to reproduce the established experimental values of γ and β vibrational bands, the previously formulated equation [6] has to be extended by an additional term in $I^2(I+1)^2$. As a result of his calculations, he was obliged to multiply the suggested term into an "adjusting factor b". Calculations on the heads of γ and β vibrational bands of the nucleus Pu^{238} have produced a numerical value of 2.12 for the factor b. It has been then assumed that this value remains constant for all nuclei of the periodic table.

Meanwhile, many authors [7–9] have dealt with investigations concerning even-even nuclei. In order to reproduce the level energies of the ground-state bands, Mariscotti has proposed a variable-moment-of-inertia, in which the energy of a certain level with an angular momentum I was considered to consist of a potential energy term containing the ground state moment of inertia J_0 together with a rotational energy term containing the moment of inertia of this level under test. Level energies as well as moments of inertia for 88 cases have been tabulated.

Our present paper starts with an attempt to apply the "adjusting factor b" to different nuclei in the light of these recently added nuclear experimental and theoretical data concerning even–even nuclei. Further, it is of interest to examine the nature of variation of the deformation parameter β with the mass number A of the rare-earth elements.

2. Theoretical basis of calculations

The rotational spectrum of a low energy excited even–even nucleus has been approximated by [6]

$$E=\frac{1}{2}\varepsilon I(I+1), \tag{1}$$

where I is a quantum number characterizing the rotation of an axially symmetric deformed nucleus. The energy term ε is equal to $\frac{\hbar}{J_0}$, with J_0 the moment of inertia perpendicular to the nuclear symmetry axis.

However, this pure rotational spectrum is perturbed through the γ and the β vibrations. This fact has been corrected for by means of the addition of a rotational–vibrational interaction term that may be formulated as [10]

$$\begin{aligned} \Delta E_t &= \Delta E_\beta + \Delta E_\gamma \\ &= -\frac{3}{2}\left(\frac{1}{\hbar\omega_\beta}\right)^2 \varepsilon^3 I^2(I+1)^2 - \frac{1}{2}\left(\frac{1}{\hbar\omega_\gamma}\right)\varepsilon^3 I^2(I+1)^2 \\ &= -2\left(\frac{1}{\hbar\omega_{\text{vib}}}\right)^2 \varepsilon^3 I^2(I+1)^2 . \end{aligned} \tag{2}$$

In order to correct for such a rotational–vibrational interaction, Sheline proposed the addition of a term $I^2(I+1)^2$ to Eq. (1), so we have

$$E = \frac{1}{2}\varepsilon\, I(I+1) - BI^2(I+1)^2 . \tag{3}$$

Now, relating the rotation–vibration interaction energies as expressed in Eq. (2) with the proposed term of Eq. (3) one obtains

$$\hbar\omega_\beta = \left[\frac{3/2\varepsilon^3}{B - \frac{\varepsilon^3}{2}\Big/(\hbar\omega_\gamma)^2}\right]^{1/2} . \tag{4}$$

Let us rewrite this formula as

$$B = \frac{\varepsilon^3}{2}\left[\frac{1}{(\hbar\omega_\gamma)^2} + \frac{3}{(\hbar\omega_\beta)^2}\right]. \tag{5}$$

Calculations undertaken for Pu^{238} have shown that [4] if Eq. (3) is to agree with the formula (4), then constant B has to be multiplied by an adjusting factor, $b = 2.12$.

In order to test this factor for various rare-earths, it is convenient to write Eq. (3) in the following form

$$X = bB = \frac{\varepsilon^3}{2}\left[\frac{1}{(\hbar\omega_\gamma)^2} + \frac{3}{(\hbar\omega_\beta)^2}\right]. \tag{6}$$

On the other hand, let us introduce shortly the headlines necessary for calculating the deformation parameter β. The reduced transition probability of the pure electric quadrupole transition may be expressed in terms of the half-life time $t_{1/2}$ as follows

$$B(E2) = \frac{\ln 2}{1.23 \times 10^{-2} E^5 (1+\alpha_T) t_{1/2}} . \tag{7}$$

α_T refers here to the total internal conversion coefficient and is determined for our calculations by means of an interpolation procedure available in the literature [12].

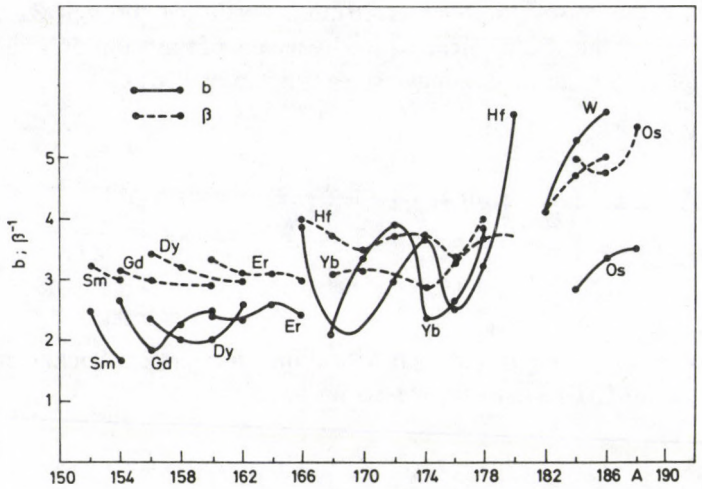

Fig. 1. Relation between the adjusting factor b and the mass number A. Variation of the reciprocal of the deformation factor, β^{-1} with the mass number (dotted line)

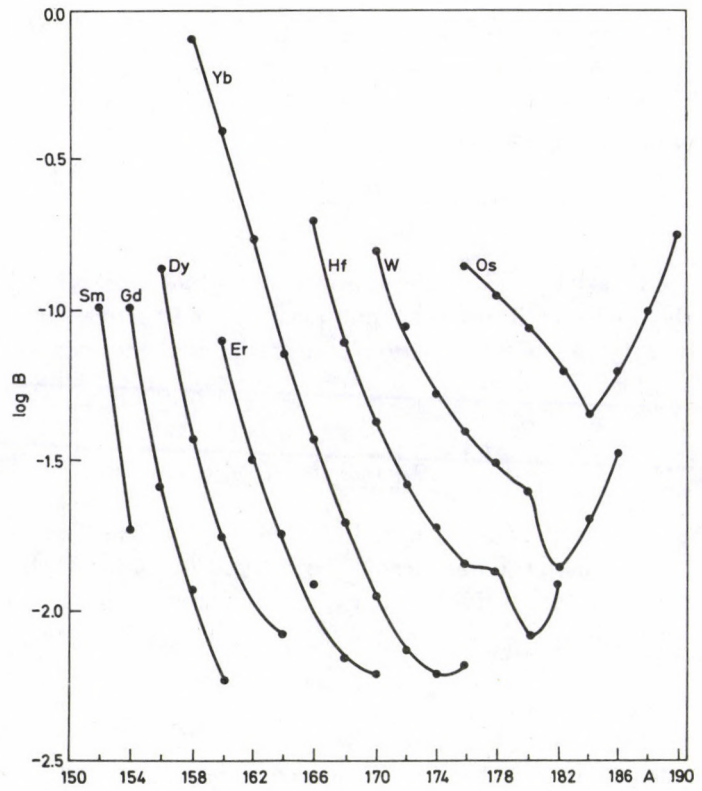

Fig. 2. Relation between the rotational-vibrational interaction term B and the mass number A

Table I

Some rotational constants for the ground state bands for the rare-earth nuclei together with the corresponding γ and β vibrational energies (all energies are given in keV)

Nucl.	2^+	4^+	6^+	2^+ γ-vib.	0^+ β-vib.	ε	$B \times 10^2$	$X = Bb \times \times 10^2$	$b = \frac{X}{B}$	$\beta \times 10^2$	β^{-1}
Nd^{150}	130	381	721	1062	677	44	13.3	31.7	2.39	28.1	3.56
Sm^{152}	122	366	707	1086	685	41	10.2	25.2	2.47	30.7	3.26
Sm^{154}	82	267	547	1440	1100	27	1.9	3.1	1.64	33.3	3.00
Gd^{154}	123	371	718	996	681	41	10.0	26.7	2.67	31.8	3.15
Gd^{156}	89	288	585	1154	1050	30	2.6	4.6	1.80	33.4	2.99
Gd^{158}	80	261	539	1187	1196	27	1.2	2.6	2.24	33.9	2.95
Gd^{160}	75	249	514	989	1381	25	0.8	2.1	2.51	34.5	2.9.
Dy^{156}	138	405	771	891	675	47	13.7	39.3	2.87	29.0	3.45
Dy^{158}	99	317	638	946	991	33	3.7	7.5	2.00	31.2	3.20
Dy^{160}	87	284	581	966	1275	29	1.8	3.6	2.02	33.5	2.99
Dy^{162}	89	266	549	888	1400	27	1.8	2.7	2.56	33.7	3.00
Dy^{164}	73	242	501	762	—	25	0.8	—	—	33.7	3.00
Er^{160}	126	390	765	854	894	42	7.9	19.5	2.45	29.8	3.36
Er^{162}	102	330	667	901	1087	34	3.2	7.6	2.37	32.5	3.08
Er^{164}	92	299	614	860	1246	31	1.8	4.7	2.60	31.9	3.13
Er^{166}	81	265	545	786	1460	27	1.2	3.0	2.41	33.5	2.99
Er^{168}	80	264	549	821	1217	27	0.7	3.3	4.84	33.4	3.00
Er^{170}	79	206	541	932	889	26	0.6	4.5	7.25	33.1	3.02
Yb^{158}	358	835	1404	—	—	120	79.6	—	—	19.4	5.15
Yb^{160}	243	638	1147	—	—	82	39.6	—	—	22.1	4.53
Yb^{162}	166	487	923	—	—	56	16.9	—	—	26.9	3.72
Yb^{164}	124	386	760	864	—	42	7.4	—	—	30.9	3.23
Yb^{166}	102	331	668	932	—	34	3.7	—	—	30.8	3.25
Yb^{168}	88	287	585	984	1156	29	2.0	4.2	2.13	32.0	3.12
Yb^{170}	84	277	573	1146	1072	28	1.1	3.8	3.37	31.8	3.14
Yb^{172}	79	260	540	1466	1043	26	0.8	2.9	3.91	32.2	3.11
Yb^{174}	76	253	536	1634	1489	26	0.6	1.6	2.34	34.2	2.93
Yb^{176}	82	272	565	1261	—	27	0.6	—	—	29.8	3.36
Hf^{166}	159	470	897	852	695	54	15.0	58.4	3.90	24.9	4.16
Hf^{168}	124	386	757	874	940	42	7.5	17.1	2.24	26.6	3.76
Hf^{170}	101	322	643	987	880	34	4.3	9.6	2.26	28.8	3.47
Hf^{172}	95	309	628	1075	871	32	2.6	7.9	3.02	26.5	3.76
Hf^{174}	91	298	608	1227	828	31	1.9	7.1	3.74	26.6	3.76
Hf^{176}	88	290	597	1341	1150	30	1.4	3.7	2.55	29.8	3.37
Hf^{178}	93	307	632	1175	1198	31	1.3	4.3	3.18	27.3	3.66
Hf^{180}	93	309	641	1200							
Hf^{180}	93	309	641	1200	1107	31	0.8	4.8	5.79	26.6	3.76
Hf^{182}	98	322	666	—	—	33	1.2	—	—	—	—
W^{170}	156	462	874	—	—	53	15.2	—	—	—	—
W^{172}	123	377	727	—	—	42	9.2	—	—	—	—
W^{174}	112	355	704	—	—	38	5.4	—	—	—	—
W^{176}	109	349	699	—	—	37	4.4	—	—	—	—
W^{178}	106	343	695	—	—	36	3.1	—	—	—	—
W^{180}	104	338	688	—	—	35	2.5	—	—	25.8	3.88
W^{182}	100	329	681	1221	1136	33	1.4	5.6	4.13	24.4	4.18
W^{184}	111	364	748	903	1002	37	2.0	10.9	5.32	23.4	4.28
W^{186}	123	397	809	738	882	41	4.4	19.8	5.83	21.8	4.58
Os^{176}	135	395	742	—	—	46	14.3	—	—	—	—

Table I (cont.)

Nucl.	2^+	4^+	6^+	2^+ γ-vib.	0^+ β-vib.á	ε	$B\times 10^2$	$X=Bb\times$ $\times 10^2$	$b=\frac{X}{B}$	$\beta\times 10^2$	β^{-1}
Os^{178}	132	398	761	—	—	45	11.3	—	—	—	—
Os^{180}	132	408	794	—	—	45	8.8	—	—	—	—
Os^{182}	127	400	793	891	—	43	6.6	—	—	23.2	4.3
Os^{184}	120	384	774	943	1042	40	4.4	12.7	2.87	19.9	5.02
Os^{186}	137	434	869	768	1061	46	6.3	21.4	3.39	20.7	4.83
Os^{188}	155	478	940	633	1086	52	10.1	35.8	3.54	18.0	5.54
Os^{190}	187	548	1050	558	912	63	18.1	—	—	18.4	5.44

This reduced transition probability is related to the intrinsic quadrupole moment, Q_0 through the formula [10]

$$B(E2)_{I+2\to 2}=\frac{15}{32\pi}e^2Q_0^2\frac{(I+i)(I+2)}{(2I+3)(I+5)}. \tag{8}$$

From this value of Q_0, the deformation parameter, β, is obtained as [11]

$$\beta\cong\frac{\sqrt{5\pi}Q_0}{3ZR_0^2}=90.91\frac{Q_0}{Z}A^{-\frac{2}{3}}. \tag{9}$$

3. Results and discussion

Using the available experimental data [12] concerning the 2^+, 4^+ and 6^+ states of the ground state rotational band of the even–even nuclei of the rare-earths, we applied Eq. (3) to calculate the value of the constant B necessary to reproduce the established γ or β vibration. These values are given in column 8 of Table I. In column 9 we show the corresponding values of the variable $X=bB$ as given by Eq. (6) and in column 10 we tabulate the numerical values of the adjusting factor b that has been earlier assumed constant for all nuclei.

It is apparent, however, that the factor b varies widely from one isotope to another. It is of course of special interest to study the nature with which b varies with the nuclear constants. It has been found here suitable to give a graphical representation of b against the mass number A. Such a plot is given by the continuous line of Fig. 1. Unfortunately, it is by no means possible to find a rule for this trend of variation. However, this representation will give some information regarding the variation with A of the nuclear deformation parameter as will be seen below.

The values of the deformation parameter as calculated from Eq. (9) are given in column 11 beside their reciprocals β^{-1} in column 12. The values of β^{-1} are represented by dotted lines in Fig. 1. As a rule, one can say that β^{-1} changes with the mass number A in a similar manner to that of b, that is to say, β^{-1} increases with b. The only deviation

from this rule until now is the case of 0*s*. However, this deviation may be understood in the light of the behaviour of those isotopes regarding the rotational-vibrational interaction term B as shown in Fig. 2. One notices, namely, that the increase of B for osmium continues to a larger extent than for the other isotopes.

Acknowledgement

We are indebted to Prof. Z. Awwad for enlightening discussions as well as for thoroughly reading the manuscript.

References

1. J. P. Eliott, Proc. Roy. Soc. (London), *A245*, 128, 562, 1958.
2. G. Scharf-Goldhaber and J. Weneser, Phys. Rev., *98*, 212, 1955; see also M. Nagasaki and T. Tamura, Prog. Theoret, Phys., (Kyoto) *12*, 248, 1954.
3. A. Bohr, Dan. Matt. Phys. Medd. *26*, No. 14, 1952.
4. R. K. Sheline, Rev. Mod. Phys., *32*, 1–24, 1960.
5. A. S. Davidov and C. F. Philippov, Nucl. Phys., **8**, 237, 1958; *10*, 645, 1959.
6. K. Adler, A. Bohr, T. Huus, B. Mottelson and A. Winther, Rev. Mod. Phys., *28*, 432, 1956.
7 M. A. J. Mariscotti, G. Scharf-Goldhaber and B. Buck, Phys. Rev., *178*, 1864, 1968.
8. D. Ward, R. M. Diamond and F. S. Stephan, Nuc. Phys., *A117*, 309, 1968.
9. R. F. Casten, H. G. Borner, J. H. Pinston and W. F. Davidson, Nucl, Phys., *A309*, 206, 1978.
10. A. Bohr and B. Mottelson, Dan. Matt. Fys. Medd., *27*, 16, 1953.
11. N. P. Heydenburg and G. M. Temmer, Annual Review of Nuclear Science Vol, *6*, 77, 1956.
12. Table of Isotopes, Seventh Edition, Ed. by C. M. Lederer and V. S. Shirley, John Wiley and Sons, Inc., New York–Chichester–Brisbane–Toronto, 1978.

Acta Physica Hungarica 60 (1—2), pp. 75—94 (1986)

NEW MODEL OF THE METAGALAXY

A. MÉSZÁROS*

Central Research Institute for Physics
1525 Budapest, Hungary

(Received in revised form 12 July 1984)

The known physical laws do not exclude the existence of anticollapsing bodies in nature (anticollapse is a gravitational collapse with time reversal). In the paper it is shown that the metagalaxy, i.e. the observed part of the universe, may in first approximation be the interior of a giant anticollapsing body having a boundary beyond the particle horizon. This is the "anticollapse model" of the metagalaxy. The advantage of this model follows from the fact that some anisotropies in the metagalaxy, e.g. the cosine-anisotropy of the intensity of cosmic background radiation, the cosine-anisotropy of the Hubble parameter at a given distance, the gradient of the mean matter density, etc. are already considered in first approximation. The theoretical considerations about anticollapse show and the present-day cosmological observations support the opinion that the anticollapse model of the metagalaxy is better than the usual Friedmann model.

Introduction

At present the widely accepted basic assumption of cosmology is the cosmological principle — this being the assumption that the complete physical universe is isotropic and homogeneous on a sufficiently large scale. However, we must admit that the main argument for this assumption is only the human wish for beauty and simplicity. Homogeneity and isotropy can be verified by observations only in the region that we observe, i.e. in the metagalaxy. But the metagalaxy, as it follows from present-day observations, is not the whole universe, and thus the observational verification of homogeneity and isotropy in the whole universe is not possible. (To-day it is practically certain that there was a big bang in our past. Thus our past light cone cannot be extended to past infinity and it is in principle limited by the instant of the big bang. It is said that the directly observable part of the universe is limited by the particle horizon. The difference between the parts of the universe that are observable in practice and in principle is, at least for our purposes, not essential. Therefore in this paper "the metagalaxy" and "the part of the universe closed by the particle horizon" are used as corresponding notions. We would mention that throughout the paper we assume the non-existence of particles moving on space-like curves.)

It is useful to define the cosmological principle in two steps which, together, give the full principle. First one supposes that the metagalaxy is homogeneous and isotropic

* Present address: Department of Astronomy and Astrophysics, Charles University Svédská 8, 15.000 Prague-5, ČSSR

on a sufficiently large scale, and second that these properties may be extrapolated and are valid in the complete universe. The second step is a bold extrapolation. First, symmetry properties of the metagalaxy that are not precisely verified by observations are extrapolated. Second, this extrapolation cannot be confirmed by direct observations (this is the main counter-argument). Third, we know from the history of astronomy that it is dangerous to think about an observed part of the universe as if it were the whole universe. (In the 16th and 17th century some astronomers, e.g. Kepler, thought that for all practical purposes the Solar system was the whole universe; in the 19th century, astronomers thought that our Galaxy was the whole universe; to-day one usually thinks that the metagalaxy and the parts of the universe where the symmetry properties of the metagalaxy are valid is the whole universe.) Fourth, it is clear that the human mind can study only a limited part of the complete universe, and therefore it is never correct to speak about the properties of the whole universe, see Fock [1]. We may conclude that the second step of the cosmological principle is not satisfactory. Of course, this does not mean that the second step is completely wrong. It is highly non-physical to suppose that the properties of the metagalaxy are fulfilled in it and nowhere else. The situation is as follows. One may extrapolate the symmetry properties of the metagalaxy to some regions beyond the particle horizon, too, but it is not necessary that these properties be valid in the whole universe. Therefore in what follows we shall strictly distinguish between the notions "complete physical universe" (for brevity "universe") and "the metagalaxy together with the regions of the universe, where the properties of the metagalaxy are valid" (for brevity "M-galaxy"). It is almost certain that the M-galaxy and metagalaxy are not identical or, equivalently, that the edge of the M-galaxy (if it exists, of course) is not identical to the particle horizon. The M-galaxy and the universe may be — but need not be — identical. They are identical if both steps of the cosmological principle are accepted. In this case the universe-M-galaxy is described in first approximation by a Friedmann model, and in second approximation the existence of the objects in the metagalaxy follows from the perturbations on the Friedmann background. If the M-galaxy and universe are not identical, i.e. the M-galaxy has an edge and an exterior, then the first step of cosmological principle may still be accepted. In this case the interior of the M-galaxy (and thus the metagalaxy too, if the edge of M-galaxy is completely beyond the particle horizon) is described in first approximation by a Friedmann metric. Indeed, if this description holds, then the question of the existence of the edge of M-galaxy has minimal physical meaning. In any case one has to consider that in fact the usual Friedmann model in cosmology is a model of the metagalaxy and not of the universe.

Of course, all this is not new. For example de Sitter ([2], p. 708) speaks about a "tremendous extrapolation, which is a very dangerous operation", in the discussion of extrapolation of the properties of the metagalaxy to the universe. Caution may be found in later works too. For example, Rees [3] speaks carefully: "... the observable part of the universe can be described by a Robertson–Walker metric with a precision of $\lesssim 1$ part in 10^3", and put the question: "could we be in an 'island' embedded in

Minkowski space?" This question is practically the same as the following one: Has the M-galaxy an edge? (We have seen that this is equivalent to the question: Is not the M-galaxy identical to the universe?)

Let us assume for the moment that the M-galaxy having an edge is an island in Minkowski space. This island may have various forms, and the interior may be described by various metric tensors, too. Requiring the maximum possible simplicity we specify the M-galaxy. We suppose that the M-galaxy is in first approximation a spherically symmetric body which must be anticollapsing and which has a spherical surface. Thus we have restricted ourselves to an M-galaxy inside of which the metric tensor in first approximation is not so complicated but may already differ from the Friedmann metric. The anticollapse is necessary to explain the big bang and the Hubble expansion of the metagalaxy. As it follows from Birkhoff's theorem there is a Schwarzschild vacuum beyond the M-galaxy. (We suppose that there is a vacuum in the exterior of the M-galaxy.) The surface of the M-galaxy may be — but need not be — completely beyond the particle horizon. Obviously, the surface of the M-galaxy must actually be a layer in space where the properties of the M-galaxy are broken down.

The assumption that the metagalaxy is in first approximation the interior of the anticollapsing spherical M-galaxy that is not identical to the universe, serves as a basis for a new model of the metagalaxy, the "anticollapse model". The scheme of the model is given by Fig. 1. This model of the metagalaxy differs from the usual Friedmann model in two aspects: first, that one considers some anisotropies of matter density, the Hubble parameter and others in the metagalaxy already in the first approximation (this says that the first step of the cosmological principle is already rejected); second, that the model proclaims the edge of M-galaxy and thus the non-identity of the M-galaxy and the universe. This model needs a detailed study, a comparison with the usual Friedmann model and, of course, must explain the present-day cosmological

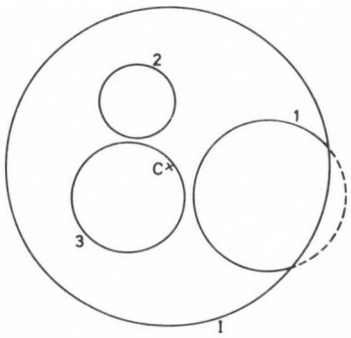

Fig. 1 Scheme of the anticollapse model of the metagalaxy (one space dimension is omitted). Circle I is the expanding surface of the M-galaxy that is actually a layer where the properties of the M-galaxy are broken down. Circles 1.2 and 3 correspond to the possible particle horizon at present; in case 1 part of the surface of the M-galaxy is observable; in case 2 the surface and the centre of the M-galaxy is beyond the particle horizon; in case 3 the centre C is already in the inside of the metagalaxy

observations. In addition to this, if we want to change the Friedmann model of the metagalaxy into the anticollapse one, then it is natural to require that the anticollapse model be a more convenient means of explaining the cosmological observations than the usual Friedmann one.

This paper deals with the anticollapse model of the metagalaxy. We study the simplest anticollapse described by the well-known Tolman solution (see Appendix). Indeed, one may study various anticollapses (for example one may consider various non-spherical, rotating, etc. anticollapses, too), but for our purposes it is sufficient to restrict ourselves to the simplest model in which the metric tensor is different from the Friedmann metric tensor.

We proceed here as follows. In Sections 1, 2 and 3 we study the theory of anticollapse. In Sections 4 and 5 some observational data are compared with the results of Sections 1, 2 and 3. Finally, the conclusions of the paper are summarized. In the Appendix the well-known Tolman solution is provided.

We assume for our present purposes that Einstein's General Theory of Relativity with vanishing cosmological constant describes gravitation. The sign convention $+$, $-$, $-$, $-$ and the system $c=G=1$ are used.

1. General considerations on anticollapse

In this Section we study the general features of anticollapse which are described by the Tolman solution — for details, see Appendix — having the form:

$$ds^2=dT^2-A(R,T)\cdot dR^2-r^2(R,T)\cdot dU^2; \qquad dU^2=d\theta^2+\sin^2\theta\cdot d\varphi^2,$$

$$\theta\in[0,\pi]; \quad \varphi\in[0,2\pi]; \quad R\in[0,R_0];$$

$$A(R,T)=\frac{\left(\frac{\partial r(R,T)}{\partial R}\right)^2}{1+g(R)}\equiv\frac{r'^2}{1+g}; \qquad \left(\frac{\partial r(R,T)}{\partial T}\right)^2\equiv\dot{r}^2=g(R)+\frac{F(R)}{r(R,T)};$$

$$r(R,T)=\frac{F(R)}{2g(R)}\cdot(ch-1); \qquad T_0(R)+T=\frac{F(R)}{2g(R)^{3/2}}\cdot(sh\eta-\eta);$$

$$0<R_0<\infty; \quad \eta\in[0,\infty]; \quad g(R)=sh^2R;$$

or

$$r(R,T)=\left(\frac{9}{4}\cdot F(R)\right)^{1/3}\cdot(T_0(R)+T)^{2/3}; \qquad R_0=1; \quad F(R)=2mR^3;$$

$$g(R)=0; \quad T\in[-T_0R),\infty];$$

or

$$r(R, T)=\frac{F(R)}{-2g(R)}\cdot(1-\cos\eta);\qquad T_0(R)+T=\frac{F(R)}{2(-g(R))^{3/2}}\cdot(\eta-\sin\eta);$$

$$0<R_0\leq\frac{\pi}{2};\quad \eta\in[0,2\pi];\quad g(R)=-\sin^2 R;$$

$$8\pi\cdot\mu(R, T)=\frac{F'(R)}{r(R, T)^2\cdot r'};\qquad T_0'(R)\geq 0;\quad F'(R)>0;\quad r'(R, T)>0;$$

$$\lim_{R\to 0}\frac{F(R)}{g(R)}=0;\qquad F(R_0)=2m. \tag{1.1}$$

In this solution R, θ, φ are the comoving coordinates; T is the proper time; $\mu(R, T)$ the density; m the mass of the body; $T_0(R)$, $F(R)$ are some functions with defined properties; $'\equiv\frac{\partial}{\partial R}$ and $\dot{}\equiv\frac{\partial}{\partial T}$.

The main puzzle of anticollapse is the time instant $T=-T_0(R)$. We cannot yet describe the singularity $\mu=\infty$ by present-day physical laws, and we know nothing about the case of its break-off. Thus we cannot explain the beginning of the anticollapse. We may imagine it roughly as an explosion whose cause is unknown. About a spherically symmetric explosion one may assume that the explosion begins at the centre of a spherical body. Thus the singularity is first broken in the centre. From this one may suppose too that in the layers of smaller R the singularity is broken off before (more precisely not later than) the layers of larger R. Thus one may suppose the validity of $T_0'(R)<0$, i.e. one may have without loss of generality

$$T_0(R)=\text{const.}\equiv 0. \tag{1.2}$$

Obviously, the rough consideration leading to this restriction is not satisfactory from every point of view, i.e. condition (1.2) need not be valid by all means. Nevertheless, we shall use it. Thus we have a uniform density near the singularity, and the density is always uniform in the case $g(R)=0$. As we know, in the case of uniform density the Tolman metric is identical to the Friedmann metric (see Appendix).

There are practically infinitely various cases of anticollapse. The solutions $g(R)\neq 0$ give an infinite number of anticollapses because R_0 may be chosen variously, and the various values of R_0 give essentially differing solutions. For example, in the case $g(R)=-\sin^2 R$ there is an essential difference between the cases $0<R_0\ll\frac{\pi}{2}$ and $0<R_0\lesssim\frac{\pi}{2}$. The maximum radius is clearly

$$r\left(R_0,\frac{\pi\cdot m}{\sin^3 R_0}\right)=\frac{2m}{\sin^2 R_0}\equiv r_{\max}. \tag{1.3}$$

Thus if $0 < R_0 \ll \frac{\pi}{2}$ holds we have $r_{max} \gg 2m$, but if $0 < R_0 \lesssim \frac{\pi}{2}$ holds we have $r_{max} \gtrsim 2m$, where $2m$ is the gravitational radius. Similarly, the case $g(R) = sh^2 R$ has different properties for $0 < shR_0 \ll 1$, for $0 < shR_0 \lesssim 1$ and for $shR_0 > 1$. For the period $T \to \infty$ the radial velocities are given by

$$\dot{r} \cong shR \,. \tag{1.4}$$

From the physical point of view it is reasonable to suppose that for $T \to \infty$ the anticollapsing body is practically only a set of different fragments immersed in a vacuum and moving with constant velocities; these fragments apparently arose by an explosion at a point. Thus for $T \to \infty$ the radial velocities of fragments near to the boundary are non-relativistic for $0 < shR_0 \ll 1$ and are relativistic for the other cases. Because for the usual astronomical bodies the non-relativistic velocities are characteristic, it seems that we may require the condition

$$shR_0 \ll 1 \tag{1.5}$$

for $g(R) = sh^2 R$. Of course, this condition need not by all means be fulfilled.

The existence of $g(R) = 0$ may be exluded because this is only one case among the infinite number of anticollapses. However, this case is very important, because anticollapses $g(R) \neq 0$ (R_0 very small) may be identified with $g(R) = 0$ (except for the parts $r \sim r_{max}$ or $r \to \infty$). This says that an anticollapsing body with uniform density may be excluded, because this is only one case among the infinite number of cases. But for small values of time the density is still nearly uniform, and if R_0 is very small, too, then the nearly uniform density is fulfilled over a long time.

Summarizing the results of this Section one may claim that the features of anticollapse are practically the same as those of collapse (except, of course, for the time reversal). Nevertheless, one has two essential differences: a) Restriction (1.2) seems to be allowed for anticollapse; b) The case $g(R) = sh^2 R$ is physically reasonable here; condition (1.5) may be required for it.

2. How to distinguish the interior of a Friedmann universe from the interior of an anticollapsing body

The question posed in the Section's title is studied here since this is of essential importance in the anticollapse model of the metagalaxy.

Suppose that there is an observer in the interior of an anticollapsing body. The observer's coordinates are $[\bar{T}, \bar{R}, \theta, \varphi]$ ($\bar{T}$ is determined by $\bar{\eta}$) $0 \leq \bar{R} < R_0$. From which observations can he proclaim that he is in the interior of an anticollapsing body and not in a Friedmann universe?

If the surface, and thus the exterior, of the anticollapsing body is observable, then it is obvious that the observed neighbourhood is the interior of the anticollapsing body.

But the surface is not observable for small $\bar{R}$, $\bar{T}$. In order to explain this we need the following consideration: The nearest point of the surface is clearly R_0, θ, φ. (Of course, if $\bar{R}=0$ is chosen then any point of the surface may be chosen.) It is enough to study the direction to this point. Hence $dU=0$ follows and the null curves are given by

$$\pm dT=\sqrt{A(R, T)}\cdot dR\,. \tag{2.1}$$

After integration we obtain (for the sake of completeness we also consider the case $g(R)=0$)

$$\begin{aligned} &\text{const}\pm T^{1/3}=\frac{F(R)^{1/3}}{12^{1/3}} \qquad \text{for} \quad g(R)=0\,; \\ &\text{const}\pm\eta=\int\frac{\frac{\partial}{\partial R}\left(\left|\frac{F(R)}{g(R)}\right|\right)dR}{\sqrt{1+g(R)}\cdot\frac{F(R)}{|g(R)|^{3/2}}}\equiv G(R) \qquad \text{for} \quad g(R)\neq 0\,. \end{aligned} \tag{2.2}$$

Clearly $G(R)'>0$ holds. We must use the $-$, sign because this describes the null particle coming to the observer. We require that the particle be coming to the point $[\bar{R}, \theta, \varphi]$ at time $\bar{T}$. Hence

$$\begin{aligned} &\bar{T}^{1/3}-T^{1/3}=\frac{1}{12^{1/3}}(F(R)^{1/3}-F(\bar{R})^{1/3}), \qquad \text{for} \quad g(R)=0\,; \\ &\text{or} \\ &\bar{\eta}-\eta=G(R)-G(\bar{R}) \qquad \text{for} \quad g(R)\neq 0\,. \end{aligned} \tag{2.3}$$

If the condition

$$\begin{aligned} &\bar{T}^{1/3}<12^{-1/3}\cdot(F(R_0)-F(\bar{R})) \qquad \text{for} \quad g(R)=0\,; \\ &\text{or} \\ &\bar{\eta}<G(R_0)-G(\bar{R}) \qquad \text{for} \quad g(R)\neq 0 \end{aligned} \tag{2.4}$$

holds, then the point $(\bar{R}_0, \theta, \varphi]$ of the surface (and thus the full surface and the exterior) is not observable. From (2.4) it is obvious that for small $\bar{T}$, $\bar{R}$ the surface is not observable. Note that $G(R)=R$ holds in the case of uniform density, and in this special case the particle horizon at time $\bar{T}$ is given by the circle of radius $\bar{\eta}$ (see Fig.2).

Suppose now that the surface of the anticollapsing body is not observable. Then the centre $R=0$ of the body may be — but need not be — beyond the particle horizon. Because the density is a function of R, i.e. there is a gradient in the matter density and one may detect this gradient, it is reasonable to claim the observed neighbourhood as the interior of an anticollapsing body from the observation of matter density. (A Friedmann universe interior needs a uniform density.) Because physically it is reasonable to suppose that the density is a monotonous function of R, the observer in $[\bar{R}, \theta, \varphi]$ (except for the special case $\bar{R}=0$) must detect a "cosine anisotropy" of the

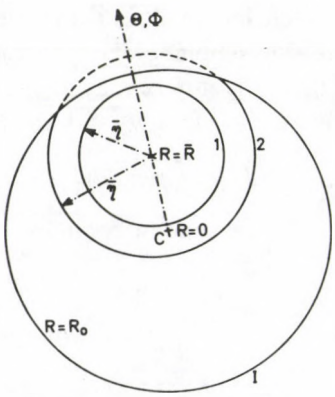

Fig. 2. Observable part of the interior of an anticollapsing body with uniform density (one space dimension is omitted). Circles 1 and 2 determine the possible particle horizons. In case 1 condition (2.4) is fulfilled; in case 2 it is not

density at a given distance R_A — this distance is much smaller than the distance of the centre. One has

$$\mu(R, T)=\mu(\bar{R}, T)+\Delta\mu\cdot\cos\alpha; \qquad R_A=\text{const}\ll\bar{R}; \tag{2.5}$$

where α is the angle between the direction of the centre and of the observed direction (see Fig. 3).

Note that other parameters can depend on R, too. For example, the "Hubble parameter"

$$H(R, T)\equiv\frac{\dot{r}(R, T)}{r(R, T)}\sim\frac{F(R)}{|g(R)|^{3/2}} \tag{2.6}$$

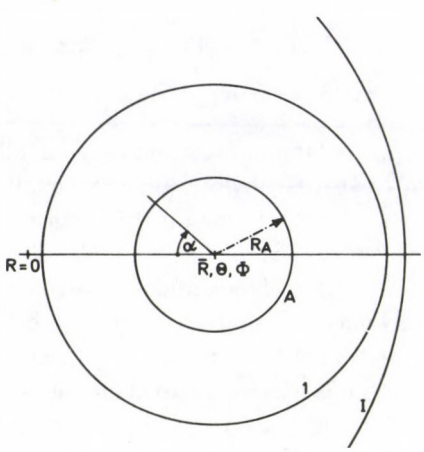

Fig. 3. Cosine anisotropy of density at a given distance (one space dimension is omitted). Circle I determines the surface, 1 the particle horizon. On the circle A, whose radius is R_A, one has $\mu=\mu(\bar{R})+\Delta R\cdot\cos\alpha$. In the Figure the circles are not in proportion. In fact, the condition $R_A<<R$ is fulfilled

for non-uniform density depends on R, and therefore may have a "cosine anisotropy" at a given distance similarly to density. It is interesting that the "deceleration parameter" $-\ddot{r}\cdot r/\dot{r}$ does not depend on R.

If the observer does not observe any surface $R=R_0$ and there are roughly uniform density, Hubble parameter, etc., then the situation is highly complicated. In this case the observer must utilize the observations of matter density, Hubble parameter, etc. because there is no other possibility. This case may occur for very small $\bar{T}$ and $\bar{R}$.

We can summarize that the observer can distinguish by observations the interior of an anticollapsing body from the Friedmann universe (except for small $\bar{R}$, $\bar{T}$).

3. Matching of the Tolman interior and Schwarzschild exterior

In this Section we study the connection between the Tolman interior and Schwarzschild exterior. For our immediate purposes we take the function $g(R)$ (for the case $g(R)=0$ the function $F(R)$) arbitrarily and therefore we have freedom of choice of the comoving coordinate R (see Appendix).

The exterior of an anticollapsing body is given by the Schwarzschild metric

$$ds^2=\left(1-\frac{2m}{v}\right)dt^2\pm 2\sqrt{\frac{2m}{v}}\,dv\,dt-dv^2-v^2dU^2, \tag{3.1}$$

where v is the radial coordinate, t the time. The metric is defined for the values $v_0<v<\infty$, where v_0 is the radius of the surface at a given time t. The form (3.1) is not time-symmetric, and the surface $v=2m$ may be considered as a one-way membrane (only if $v_0<2m$, of course). There are two possible cases of metric (3.1): "+", the future directed non-space-like curves cross $v=2m$ from inside to outside; "−", from outside to inside, see e.g. Hawking and Ellis ([4], p. 151).

The radius of an anticollapsing body increases and at a given instant (determined by time T) "the surface exceeds the gravitational radius from inside to outside". The objects of the surface may be considered as free-falling objects in the Schwarzschild metric. We have already mentioned that for the "−", case of (3.1) any objects move to inside crossing $v=2m$. From this it seems that one necessarily has to consider the "+", case in the Schwarzschild metric. We shall show here that this is not so, and the more natural case "−", may be taken too for the exterior of an anticollapsing body. (If "+", were necessary, then the existence of anticollapsing bodies would be questionable. Observations of our neighbourhood suggest that the "+", is highly non-probable. In addition, with $g(R)<0$ one would obtain an incomprehensible result. For the anticollapse period one would suppose "+", but for the collapse period "−".)

Given the Schwarzschild exterior

$$ds^2=\left(1-\frac{2m}{v}\right)dt^2-2\sqrt{\frac{2m}{v}}\,dv\cdot dt-dv^2-v^2dU^2 \tag{3.2}$$

and the Tolman interior

$$ds^2 = dT^2 - A(R, T) \cdot dR^2 - r^2(R, T) \cdot dU^2 \tag{3.3}$$

of an anticollapsing body, where the functions $A(R, T)$, $r(R, T)$ are given by (1.1). The matching on the surface $R = R_0$ requires that the components of the metric tensor and their first derivatives together with some combinations of the second derivatives be continuous on this surface in a conveniently chosen coordinate system. For the second derivatives the continuity can be reformulated to continuity $T^{ij} \cdot n_j$, where n^i is the normal vector to the surface, and this is automatically fulfilled for zero pressure; see Lichnerowicz [5]. To fulfil the requirements for the components of the metric tensor and their first derivatives we write down metric (3.2) in the coordinates R, T, θ, φ. (Obviously, the coordinates θ, φ of the exterior are identical to those of the interior.) Then the coordinates $R > R_0$ will determine the exterior, $R < R_0$ the interior. The matching is ensured if (3.2) has the same form as (3.3) in a layer $R \in [R_0, R_0 + \Delta R]$, where ΔR is infinitesimally small. In the layer $R \in [R_0, R_0 + \Delta R]$ we search for a coordinate transformation

$$v \equiv v(R, T); \qquad t \equiv t(T, R). \tag{3.4}$$

The function $v(R, T)$ is immediately determined because $r^2(R, T) \cdot dU^2 = v^2(R, T) \cdot dU^2$ holds in $R \in [R_0, R_0 + \Delta R]$ for $r(R, T) = \pm v(R, T)$. Because r and v are taken to be non-negative, one has $v(R, T) = r(R, T)$. We have to search for $t(R, T)$. One has in the layer $R \in [R_0, R_0 + \Delta R]$

$$\begin{aligned} ds^2 = \left(1 - \frac{2m}{r}\right) \cdot (t' dR + \dot{t} dT)^2 - 2\sqrt{\frac{2m}{r}} \cdot (t' dR + \dot{t} dT) \cdot (r' dR + \dot{r} dT) - \\ - (r' dR + \dot{r} dT)^2 - r^2 dU^2, \end{aligned} \tag{3.5}$$

where the dependence on R and T of functions $r(R, T)$, $t(R, T)$ is not written down, and $' \equiv \frac{\partial}{\partial R}$; $\dot{} \equiv \frac{\partial}{\partial T}$. Hence it follows that the equations

$$\left(1 - \frac{2m}{r}\right) \cdot t'^2 - 2\sqrt{\frac{2m}{r}}\, t' r' - r'^2 = -A\,; \tag{3.6}$$

$$\left(1 - \frac{2m}{r}\right) \cdot \dot{t}^2 - 2\sqrt{\frac{2m}{r}}\, \dot{t} \cdot \dot{r} - \dot{r}^2 = 1\,, \tag{3.7}$$

$$\left(1 - \frac{2m}{r}\right) t' \dot{t} - \sqrt{\frac{2m}{r}} (t' \dot{r} + \dot{t} r') - r' \dot{r} = 0 \tag{3.8}$$

must be fulfilled in the layer $R \in [R_0, R_0 + \Delta R]$. Equivalent forms of equations (3.6)–(3.8) are:

$$t' = \frac{r' \sqrt{\frac{2m}{r}} \pm \sqrt{X}}{1 - \frac{2m}{r}}; \qquad X = r'^2 - A\left(1 - \frac{2m}{r}\right); \tag{3.9}$$

$$\dot{t} = \frac{\dot{r} \sqrt{\frac{2m}{r}} \pm \sqrt{Y}}{1 - \frac{2m}{r}}; \qquad Y = \dot{r}^2 + 1 - \frac{2m}{r}; \tag{3.10}$$

$$t'\dot{t} - \left(\dot{r} + \sqrt{\frac{2m}{r}}\,\dot{t}\right) \cdot \left(r' + \sqrt{\frac{2m}{r}}\,t'\right) = 0. \tag{3.11}$$

Equations (3.9), (3.10) are capable of determining t, and therefore (3.11) must follow from (3.9), (3.10). Substituting t' and $\dot{t}$ into (3.11) one has after some calculation

$$\sqrt{XY} = \dot{r} \cdot r', \tag{3.12}$$

and hence

$$r'^2 - A\dot{r}^2 - A\left(1 - \frac{2m}{r}\right) = 0. \tag{3.13}$$

Because

$$A = r'^2 \cdot (1+g)^{-1}, \qquad \dot{r}^2 = g + \frac{F}{r} \tag{3.14}$$

hold, one has

$$F(R) = 2m. \tag{3.15}$$

This condition is clearly fulfilled for $R = R_0$. But it must be fulfilled in the layer $R \in [R_0, R_0 + \Delta R]$, that is, $F'(R_0) = 0$ is required, too. Using the transformation $\bar{R} \equiv \bar{R}(R)$, one may easily have $F'(\bar{R}_0) = 0$, and therefore without loss of generality the condition

$$\left.\frac{dF(R)}{dR}\right|_{R=R_0} = 0 \tag{3.16}$$

holds, and thus equations (3. 8) and (3. 11) are not considered in what follows. To solve (3.9), (3.10) we use the Taylor expansion

$$t(R, T) = t_0(R_0, T) + t_1(R_0, T) \cdot \Delta R + \frac{1}{2} t_2(R_0, T) \cdot \Delta R^2 + \ldots; \tag{3.17}$$

$$r(R, T) = r_0(R_0, T) + r_1(R_0, T) \cdot \Delta R + \frac{1}{2} r_2(R_0, T) \cdot \Delta R^2 + \ldots; \tag{3.18}$$

$$A(R, T) = A_0(R_0, T) + A_1(R_0, T) \cdot \Delta R + \ldots; \tag{3.19}$$

and we search for the functions t_0, t_1, t_2. Substituting into (3. 9) and (3. 10) one obtains

$$t_1 + t_2 \cdot \Delta R = \left. \frac{r' \cdot \sqrt{\frac{2m}{r}} \pm \sqrt{X}}{1 - \frac{2m}{r}} \right|_{R=R_0} + \left(\left. \frac{r' \cdot \sqrt{\frac{2m}{r}} \pm \sqrt{X}}{1 - \frac{2m}{r}} \right)' \right|_{R=R_0} \cdot \Delta R ; \quad (3.20)$$

$$\dot{t}_0 + \dot{t}_1 \cdot \Delta R = \left. \frac{\dot{r} \cdot \sqrt{\frac{2m}{r}} \pm \sqrt{Y}}{1 - \frac{2m}{r}} \right|_{R=R_0} + \left(\left. \frac{\dot{r} \cdot \sqrt{\frac{2m}{r}} \pm \sqrt{Y}}{1 - \frac{2m}{r}} \right)' \right|_{R=R_0} \cdot \Delta R ; \quad (3.21)$$

i.e. functions t_0, t_1, t_2 are immediately determined. Of course, there is a solution only if

$$\left(\left. \frac{r' \cdot \sqrt{\frac{2m}{r}} \pm \sqrt{X}}{1 - \frac{2m}{r}} \right)' \right|_{R=R_0} = \left(\left. \frac{\dot{r} \cdot \sqrt{\frac{2m}{r}} \pm \sqrt{Y}}{1 - \frac{2m}{r}} \right)' \right|_{R=R_0} \quad (3.22)$$

holds. Because $(\dot{r} \cdot f(r))' = (r' \cdot f(r))\cdot$ is fulfilled, it must be

$$\left(\left. \frac{\sqrt{X}}{1 - \frac{2m}{r}} \right)' \right|_{R=R_0} = \left(\left. \frac{\sqrt{Y}}{1 - \frac{2m}{r}} \right)' \right|_{R=R_0} . \quad (3. 23)$$

Using the relation $X = \dot{r}^2 \cdot r'^2 \cdot (1+g)^{-1}$ (which holds for $R = R_0$ only, but may be substituted immediately into (3.23)), $\ddot{r} = -\frac{F(R)}{2r^2}$ and (3.14), condition (3.23) may be verified after a longer calculation. We found the function $t(R, T)$ in the layer $R \in [R_0, R_0 + \Delta R]$. We obtained two cases. (Note that there are two other cases, which are meaningless. One may take in (3. 9) $\pm$, but in (3. 10) $\mp$. These choices, instead of leading to (3. 12) lead to the relation $-\sqrt{XY} = \dot{r} \cdot r'$, which cannot be fulfilled because $\sqrt{XY}$ and $\dot{r} \cdot r'$ are both positive.) The function $t_0(R_0, T)$ has the form

$$t_0(R_0, T) = \frac{\sqrt{\left(g(R_0) + \frac{2m}{r(R_0, T)} \right) \cdot \frac{2m}{r(R_0, T)}} \pm \sqrt{1 + g(R_0)}}{1 - \frac{2m}{r(R_0, T)}} \cdot dT = \int W(T) \cdot dT . \quad (3.24)$$

$W(T) > 0$ holds for "+", and $r(R_0, T) > 2m$. In other cases $W(T) < 0$, and in this situation the times t and T have opposite sense. Therefore, the "+", is more acceptable from the physical point of view.

Summarizing we may say that there is a good matching of the metrics (3. 2), (3. 3). Of course, in practice the surface of an anticollapsing body is only a layer in which the nearly Tolman metric changes into the nearly Schwarzschild metric. Thus the matching is more complicated than in this Section. In addition, shortly after the break-off of the singularity the condition of the zero pressure is not fulfilled everywhere in the interior (the pressure must be zero on the surface only), and thus the Tolman metric cannot be used for the interior. The matching is complicated by this fact, too. (Note that not only the matching, but the whole behaviour of anticollapse is complicated shortly after the break-off of the singularity. In this paper we assume that near to the singularity the anticollapse—at least in the central regions—may be described by the ultrarelativistic case $p = \frac{\mu}{3}$, see Appendix.)

4. On the existence of anticollapsing bodies in the metagalaxy

In this Section we investigate the occurrence of anticollapse in the metagalaxy.

Unfortunately, it is highly unlikely that one can directly observe an anticollapse. This is obvious from the following fact: the characteristic time of an anticollapse is $\sim 2m$. This time is very small (for example $\sim 10^{-5}$ s for the stellar masses; $\sim 10^4$ s for the masses of galaxies in the usual system). Thus an anticollapse must be a rapid and fully unexpected phenomenon—"a black hole explodes"—, therefore direct observational evidence is questionable. The situation is more hopeful with $g(R) > 0$; this may be observed in the period $T \to \infty$. It is natural to assume about an anticollapsing body that there are perturbations of matter distribution and emission—absorption, respectively, on the edge. Thus an anticollapsing body at $T \to \infty$ is only roughly spherical and is in practice constituted from a set of different fragments, which apparently arose from a point. The radial velocities of these fragments are constant (see Section 1 and mainly (1.4)). Systems with these properties are known (e.g. stellar associations), but it is not certain that these systems arose by virtue of an anticollapse. This is only one among the numerous possibilities. Further study is still necessary.

Summarizing the considerations of the Section one may say: "The existence of an anticollapse in the metagalaxy must not be excluded even though its existence has not been confirmed by observations."

5. Can the metagalaxy be an interior of a giant anticollapsing body?

In this Section we study the main question of this paper. We have seen that theoretical considerations do not exclude the possibility that the M-galaxy is an anticollapsing body not identical to the universe. We shall study the cosmological observations. Let us assume that the metagalaxy is the interior of the giant M-galaxy

having an edge. We shall consider the cosmological data and shall study that they would give arguments for or against our assumption. At the end of the Section these arguments are summarized.

It seems that no edge (i.e. a layer where the number of extragalactic objects rapidly diminishes) of the M-galaxy can be observed from the Earth to-day. Thus the boundary of the M-galaxy must be completely beyond the particle horizon if the anticollapse model is accepted. Note that the regions of the metagalaxy near to the particle horizon are not well enough known, therefore we cannot exclude the possibility that some part of the edge of the M-galaxy is observable. From this point of view the work of Fliche, Souriau and Triay [6] is remarkable. Nevertheless, we cannot yet claim the detection of the boundary of the M-galaxy and, therefore, we suppose the edge to be beyond the particle horizon in the anticollapse model. In any case, if the M-galaxy is an anticollapsing body, then it is not old (i.e. the Hubble time is much smaller than $2m$ of the anticollapsing body) and we are far away from its boundary (see (2. 4)). Of course, these facts do not allege that our neighbourhood, e.g. the supergalaxy, is near or practically in the centre of the M-galaxy. Not knowing the value $2m$ of the M-galaxy we can say nothing on this question. Not detecting the edge of the M-galaxy the second possibility, i.e. that there is no edge, may be realized, too. Thus, we have no pro or counter-argument yet.

The observational evidence of the homogeneity of the mean matter density in the metagalaxy from the counting of extragalactic objects is not satisfactorily accurate. For example, de Vaucoulers [7] claimed that up to scales of hundreds of Mpc the mean matter density seems to decrease with the size of the averaging volume. This may determine density gradients on the scales of ~ 0.1 Huble radius. Of the earlier papers, that of Shapley [8] is noteworthy, where the large-scale irregularities are investigated. In fact, the question of the large-scale homogeneity of matter density was already studied by Hubble, and is still being studied; see Peebles ([9], §2), Rees [3]. We are in the situation that the present cosmological observations do not confirm—but do not exclude—a gradient of matter density on the scale of the Hubble radius. Indeed, the works of de Vaucoulers [7] and Fliche, Souriau and Triay [6] are remarkable but, in fact, we have no good argument for our assumption. Nor, of course, for our counter-argument.

The Hubble parameter shows a cosine anisotropy at distances of $70 \sim 120$ Mpc; Rubin et al [10]. This is not unexpected in the anticollapse model. The explanation for this anisotropy by the sun's peculiar motion, i.e. that the Hubble parameter is homogeneous—and the observed anisotropy is caused by the sun's motion, needs a peculiar motion in direction $\alpha = (2 \pm 1.3)\text{h}$; $\delta = (53 + 11)^\circ$ with velocity (600 ± 125) km/s. This explanation seems to be plausible but is not satisfactory from every point of view, as we shall see.

Similarly to the Hubble parameter, the temperature of the cosmic background radiation (CBR) may depend on R in the anticollapse model, and therefore the intensity of it coming to Earth may show a cosine anisotropy. As the observations suggest, the

intensity of CBR is highly but not fully isotropic. Cosine anisotropy has been detected; Smoot, Gorenstein and Muller [11], Fabbri et al. [12], Boughn, Cheng and Wilkinson [13]. If the radiation is isotropic, one needs a sun's peculiar motion in direction $\alpha = (11 \pm 0.6)$h; $\delta = (6 \pm 10)°$ with the value (390 ± 60) km/s. (This value is taken from the paper of Smoot, Gorenstein and Muller [11]). This required peculiar motion is not possible if the mentioned anisotropy of the Hubble parameter is explained by the peculiar motion, too. Thus either the anisotropy of the Hubble parameter, or of the intensity of the CBR, or of both must be an actual anisotropy. (Obviously we assume that the measurements are correct.) It seems to be certain that there is a peculiar motion of the sun in direction $\alpha = 21.2$h; $\delta = 48°$ with velocity (300 ± 50) km/s determined by the rotation of the Milky Way galaxy. It seems that the sun's peculiar motion relative to nearby galaxies hardly differs from this value; see the work of Smoot, Gorenstein and Muller [11]. (In our rough considerations uncertainties of ~ 50–10 km/s in the value, and ~ 20–$30°$ in the direction of peculiar motion are allowed.) Taking into account this fact it seems that there is a net $\sim 0.2\%$ cosine anisotropy of the CBR in the direction $\alpha \sim 10$h; $\delta \sim -20°$ intrinsic to the CBR. On the other hand, an essential part—maybe the total—of the anisotropy of the Hubble parameter may be caused by the sun's peculiar motion. Nevertheless, one cannot reject a net anisotropy of the Hubble parameter in a direction that differs from the direction of the anisotropy of the CBR by more than 90° (the value 180° cannot be excluded). These facts present a challenge to Friedmann models of the metagalaxy but the anticollapse model explains them easily. If the direction of the cosine anisotropy of the CBR implies the direction to or from the centre of the M-galaxy, then the cosine anisotropy of the Hubble parameter in this direction—or opposite to this direction—is not unexpected in the anticollapse model. Thus the detected cosine anisotropies of the Hubble parameter and the CBR would seem to be arguments in favour of our assumption. Indeed, we must make an admission that from these observations we cannot obtain extensive consequences, because the interpretation of data is not unequivocal. In addition, one cannot exclude the possibility that the net anisotropy of the CBR is caused by local effects of irregular distribution of mass in clusters of galaxies (see Peebles [14]).

The quadrupole anisotropy of CBR, see Boughn, Cheng and Wilkinson [13], Fabbri et al. [12], probably needs a non-Friedmann model of the metagalaxy; see Fabbri and Melchiorri [15]. These anisotropies need irregularities of the order of 10^{-3} extending over the particle horizon in the usual Friedmann model; (Fabbri and Melchiorri [15]). On the other hand, it has been shown by Grishchuk and Zeldovich [16], see Rees [3], p.297) too, that the expected fluctuations on the scale of the Hubble radius are $\lesssim 10^{-4}$. Because in the anticollapse model of the metagalaxy some irregularities beyond the particle horizon arise already in the first approximation, in this model the situation is not so bad. It seems that we have a good argument for our assumption. Nevertheless, some caution is necessary. Similarly to the cosine anisotropy, there may be other explanations too; Peebles [14], Ceccarelli et al. [17]. In

any case, it is not yet certain that the Friedmann model must be rejected. (The suggestion of this rejection may be found in the paper of Fabbri and Melchiorri [15].)

The other cosmological observations, i.e. the detection of the X-ray background, the investigation of intergalactic matter and of non-luminous objects in clusters of galaxies, etc. are not sufficiently precise for our purposes (for a survey see Rees [3]). Thus we have no other pro or counter argument.

Summarizing the observational data it seems that there are more arguments for the anticollapse model of the metagalaxy than against in. Nevertheless, present-day cosmological observations do not allow us to decide between the two models. In any case, the usual Friedmann model need not necessarily be rejected yet.

Conclusion

The usual model of the metagalaxy explains the existence of the astronomical bodies by perturbations on the Friedmann background. In other words, in first approximation the metagalaxy is described by a Friedmann metric, and in second approximation one considers the perturbations on this background. In the last few years some observations, which are mentioned in Section 5, challenge this model. For example, the paper of Fabbri and Melchiorri [15] calls for a non-Friedmannian model.

In this paper we proposed a new model of the metagalaxy, the anticollapse model. This supposes that already in the first approximation the metric of the metagalaxy is a Tolman metric, and in the second approximation one has to consider the perturbations on this background. This model implies the edge of the M-galaxy, too. (The M-galaxy is the part of the universe where the properties of the metagalaxy are still fulfilled.)

In the paper we have studied anticollapse on the whole. It was shown that anticollapsing bodies may have some interesting features, nevertheless they do not differ essentially from the usual astronomical bodies. Roughly speaking, one may imagine the anticollapse as an explosion. The existence of an anticollapse in the metagalaxy is not excluded by theoretical arguments or by observations. It is shown too that the anticollapse model of the metagalaxy seems to be better than the usual Friedmann one. Nevertheless the Friedmann model cannot be rejected by present-day cosmological observations. The cosmological observations must be more precise before we decide between the two models.

If the M-galaxy were actually an anticollapsing body having an edge beyond the particle horizon then, of course, some new problems would arise. In this case one would have to study the question of second approximation (this question was not dealt with in this paper); the influence of the boundary of the M-galaxy in the interior; the features of the edge; the size of the M-galaxy; the direction and centre of the M-galaxy; the age of the M-galaxy compared with its gravitational radius; the properties of the exterior; etc. A satisfactory anticollapse model of the M-galaxy would have to answer these

questions, too. We have not studied them here because present-day observations are not satisfactorily precise (for example the gravitational radius of the M-galaxy can hardly be determined), or are not essential (for example the question of the actual properties of the M-galaxy's exterior seems to be purely academic).

Throughout the paper we have assumed that: If the metagalaxy is not an interior of a Friedmann universe, then it is an interior of an anticollapsing body described by the Tolman solution. Indeed, one may consider more general cases of anticollapse, e.g. the non-spherical anticollapse, the anticollapse of a rotating body, etc. but our simplest case was sufficient.

Acknowledgement

I would like to thank Dr. B. Lukács and Dr. Á. Sebestyén for illuminating discussions.

Appendix

Here we summarize the well-known Tolman solution. It may be found, for example, in the book of Landau and Lifshitz ([18], §103).

The interior of a spherical body with changing radius is known in a special case. We consider the energy momentum tensor as

$$T^{ij} = (p+\mu)\cdot u^i u^j - g^{ij}\cdot p\,; \tag{A.1}$$

where p is the pressure, μ is the density and u^i is the four-velocity. If we take $p=0$ and $u^i \equiv [1, 0, 0, 0]$, then the metric tensor of the interior of a spherical body is known, and is given by the Tolman metric:

$$ds^2 = d\,T^2 - A(R, T)\cdot dR^2 - r^2(R, T)\cdot dU^2\,; \qquad dU^2 \equiv d\theta^2 + \sin^2\theta\cdot d\varphi^2\,; \tag{A.2}$$

$$\theta \in [0, \pi]\,; \qquad \varphi \in [0, 2\pi]\,; \qquad 0 \le R \le R_0 < \infty\,; \tag{A.3}$$

The coordinates R, θ, φ are the comoving coordinates. The surface of the body is given by the relation $R = R_0$. T is the proper time. We have

$$A(R, T) = \frac{\left(\dfrac{\partial r(R, T)}{\partial R}\right)^2}{1+g(R)}\,; \qquad g(R) > -1\,; \qquad \left(\frac{\partial r(R, T)}{\partial T}\right)^2 = g(R) + \frac{F(R)}{r(R, T)}\,; \tag{A.4}$$

where $g(R)$, $F(R)$ are arbitrary functions. There are three possibilities of the function $r(R, T)$;

if

$$g(R) > 0, \qquad \text{then} \quad r(R, T) = \frac{F(R)}{2g(R)}\cdot(\operatorname{ch}\eta - 1)\,;$$

$$T_0(R) \pm T = \frac{F(R)}{2g(R)^{\frac{3}{2}}}\cdot(\operatorname{sh}\eta - \eta)\,; \qquad \eta \in [0, \infty)\,; \tag{A.5}$$

$$\text{if} \qquad g(R)=0, \qquad \text{then} \quad r(R,T)=\frac{9}{4}(F(R))^{\frac{1}{3}}\cdot(T_0(R)\pm T)^{\frac{2}{3}}; \tag{A.6}$$

$$T\in(-\infty, T_0(R)] \quad \text{for} \quad "-"; \qquad T\in[-T_0(R), \infty) \quad \text{for} \quad "+";$$

$$\text{if} \qquad -1<g(R)<0, \qquad \text{then} \quad r(R,T)=\frac{F(R)}{-2g(R)}\cdot(1-\cos\eta); \tag{A.7}$$

$$T_0(R)\pm T=\frac{F(R)}{2(-g(R))^{\frac{3}{2}}}\cdot(\eta-\sin\eta);\ \eta\in[0,\pi] \text{ for } "-";\quad \eta\in[0,2\pi] \text{ for } "+";$$

$$8\pi\cdot\mu(R,T)=\frac{\dfrac{dF(R)}{dR}}{r(R,T)^2\cdot\dfrac{\partial r(R,T)}{\partial R}}. \tag{A.8}$$

The functions $F(R)$, $g(R)$, $T_0(R)$ are arbitrary functions fulfilling some conditions only, which are mentioned in this Appendix. For example, one has

$$F(R)\geq 0; \qquad \lim_{R\to 0}\frac{F(R)}{g(R)}=0 \quad \text{for} \quad g(R)\neq 0 \tag{A.9}$$

and

$$F(0)=0 \text{ for } g(R)=0; \quad F(R_0)=2m;$$

where m is the mass of the body and thus $2m$ is the gravitational radius. Note that for $\eta\to 0$ the cases are identical to the case $g(R)=0$. Thus near to the singularity $\mu=\infty$ all cases are identical.

The solutions with + sense of time give the anticollapse; the solutions with − sense of time the collapse. Present known physical laws allow the existence of anticollapse, too. We would mention that in (A.7) the definition of η is not satisfactorily obvious. One may suppose that a collapse in the case $g(R)<0$ begins from the maximum size of the body, but in the case of anticollapse there is a full anticollapse–collapse period. This expectation is confirmed by the values of η. Nevertheless, one cannot exclude other cases by the known physical laws. For example, there may be reiterating anticollapse–collapse periods, too. Note that $g(R)>0$ in the case of collapse seems not to be physically reasonable because it needs a non-probable initial condition—a systematic spherical motion to the centre at $T=-\infty$.

The condition $\dfrac{dT_0(R)}{dR}\geq 0$ is fulfilled in the case of collapse because $T_0(R_2)\geq T_0(R_1)$ holds for any $R_0\geq R_2\geq R_1\geq 0$. Similarly, $-T_0(R_2)\leq -T_0(R_1)$ holds in the case of anticollapse for any $R_0\geq R_2\geq R_1\geq 0$. From this it follows that in any case the following condition is fulfilled:

$$\frac{dT_0(R)}{dR}\geq 0. \tag{A.10}$$

In the Tolman solution the coordinate R is not yet fixed. We may introduce a new $\bar{R}$ coordinate by the transformation $\bar{R} \equiv \bar{R}(R)$. Therefore, without loss of generality, we use in the whole paper (except for Section 3)

$$g(R) = -\sin^2 R \quad \text{for} \quad g(R) < 0; \quad 0 < R_0 \leq \frac{\pi}{2}; \tag{A.11}$$

$$g(R) = sh^2 R \quad \text{for} \quad g(R) > 0; \tag{A.12}$$

$$F(R) = 2m \cdot R^3; \quad R_0 = 1 \quad \text{for} \quad g(R) = 0. \tag{A.13}$$

Indeed, there may be some cases of the Tolman solution when these choices are not allowed. For example, if $g(R)$ has several local maxima and minima, then these choices are not possible. We do not consider these possibilities.

The positive value of density needs $\dfrac{dF(R)}{dR} \Big/ \dfrac{\partial r(R, T)}{\partial R} > 0$. One usually requires $\dfrac{dF(R)}{dR} > 0$ and $\dfrac{\partial r(R, T)}{\partial R} >$ too, and therefore in this paper we require them too.

We consider still the special case of uniform density. It is obvious that the density is uniform if and only if (see (A.8) and (A.9) for the integration constant)

$$F(R) = A(T) \cdot r^3(R, T) \tag{A.14}$$

holds, where $A(T)$ is a suitable function. We see that in the case of $g(R) = 0$ the requirement of uniform density is identical to the requirement of $T_0(R) = \text{const}$.

This constant may be taken to be zero. For $g(R) \neq 0$ one has $r(R, T) \sim F(R)/g(R)$, that is, $g(R) = C(T) \cdot F(R)^{\frac{2}{3}}$, where $C(T)$ is a function. Nevertheless, this function cannot depend on T, and therefore in the case of uniform density the condition

$$F(R) = 2m \cdot \left(\frac{g(R)}{g(R_0)} \right)^{\frac{3}{2}} \tag{A.15}$$

holds. The metric tensor is the well-known Friedmann metric:

$$\begin{gathered} ds^2 = dT^2 - a(R, T)^2 \cdot (dR^2 + f(R)^2 \cdot dU^2); \qquad a(R, T) = \frac{r(R, T)}{f(R)}; \\ f(R) = |g(R)| \quad \text{for} \quad g(R) \neq 0; \quad f(R) = R \quad \text{for} \quad g(R) = 0. \end{gathered} \tag{A.16}$$

We would remark that near to the singularity the pressure certainly cannot be zero. Nevertheless, considering the ultrarelativistic case $p = \dfrac{\mu}{3}$, one may confirm that the general feature of collapse or anticollapse remains unchanged in the presence of the pressure too; see Lifshitz and Khalatnikov [19].

References

1. V. Fock, Contemporary Physics—Trieste Symp. 1968, Ed. A. Salam, Vol. 1., 511, IAEA, 1969.
2. W. de Sitter, Nature, *128*, 706, 1931.
3. M. J. Rees, Quantum Gravity 2, A Second Oxford Symp., Ed. C. J. Isham, R. Penrose, D. W. Sciama, Clarendon Press, Oxford, 1981, p. 273.
4. S. W. Hawking and G. F. R. Ellis, The Large Scale Structure of Space-Time, Cambridge Univ. Press, 1973.
5. A. Lichnerowicz, Théories relativités de la gravitation et de l' electromagnétisme, Masson, Paris, 1955.
6. H. H. Fliche, J. M. Souriau, R. Triay, Astron, Astrophys. (Germany), *108*, 256, 1982.
7. G. de Vaucoulers, Science, *167*, 1203, 1970.
8. H. Shapley, Proc. Nat. Acad. Sciences, *24*, 282, 1938.
9. P. J. E. Peebles, The Large-Scale Structure of the Universe, Princeton Univ. Press, New York, 1980.
10. V. C. Rubin, W. K. Ford, N. Thonnard, M. S. Roberts and J. A. Graham, Astron. J., *81*, 687, 1976.
11. G. F. Smoot, M. V. Gorenstein and R. A. Muller, Phys. Rev. Lett., *39*, 898, 1977.
12. R. Fabbri, I. Guidi, F. Melchiorri and V. Natale, Phys. Rev. Lett., *44*, 1563, 1980.
13. S. P. Boughn, E. S. Cheng and D. T. Wilkinson, Ap. J. Lett., *243*, L 113, 1981.
14. P. J. E. Peebles, Ap. J. Lett., *243*, L 119, 1981.
15. R. Fabbri and F. Melchiorri, Gen. Rel. Grav., *13*, 201, 1981.
16. L. P. Grishchuk and Y. B. Zel'dovich, Sov. Astr., *22*, 125, 1978.
17. C. Caccarelli, G. Dall'Oglio, B. Melchiorri, F. Melchiorri and L. Pietranera, Ap. J., *260*, 484, 1982.
18. L. D. Landau and E. M. Lifshitz, Tyeoriya polya, Nauka, Moscow, 1973.
19. E. M. Lifshitz and I. M. Khalatnikov, Zh. E. T. F., *30*, 149, 1960.

Acta Physica Hungarica 60 (1—2), pp. 95—105 (1986)

STUDIES ON THE DECAY OF ^{187}W

A. M. HASSAN

Reactor and Neutron Physics Department, Nuclear Research Centre, Atomic Energy Authority (Abu-Zaabal) Cairo, Egypt

S. ABDEL-MALAK, M. A. ABOU-LEILA, A. EL-SHERSHABY and H. A. ISMAIL

Nuclear Physics Laboratory, Ein Shams University, Faculties of Education and Girls Heliopolis, Cairo, Egypt

(Received in revised form 20 July 1984)

The gamma-ray spectrum due to the decay of ^{187}W (23.9 h) to ^{187}Re has been investigated using Ge(Li), hyper pure Ge and the Ge (Li) – NaI (Tl) gamma–gamma coincidence spectrometers.

More than 60 gamma-ray lines could be indentified and fitted in a proposed level structure of ^{187}Re. The gamma-ray lines at 65.4, 103.8, 115.5, 147.3, 154.4, 178.8, 191.1, 201.8, 261.0, 262.7, 345.7 and 641.1 keV have been observed for the first time. The energy levels as well as the gamma-ray transitions used to reconstruct the level structure of this nucleus have been discussed.

1. Introduction

There are considerable discrepancies in the level structure of ^{187}Re due to the decay of ^{187}W (23.9 h), proposed by different authors [1 – 17]. For instance the energy level at 529 keV proposed by Maack Bisgard et al [2] and observed by Langhoff [4] was not confirmed by other more recent investigations, the same argument applies to the energy level at 582 keV suggested by Bisgard et al [5]. Also, Michaelis [3] and Bashandy [6] proposed two new levels at 760 and 911 keV, which were not confirmed by other investigations. Brenner and Meyer [16], in their studies on the decay of ^{187}W, added about forty weak gamma-ray transitions to the level structure of ^{187}Re, some of these new gamma-ray lines have been used to propose the new levels at 816.6, 826.8, 844.7, 960.2, 1190.4, 1220.8 and 1230.1 keV. The most recent studies by S. Yamada et al [17] on the low lying energy levels in ^{187}Re show that more than forty one gamma-ray transitions could be observed, seven of them were observed for the first time. Three new levels at 1000.93, 969.28 and 933.54 keV were added to the level structure and need confirmation.

Accordingly, it has been decided to reinvestigate this nucleus using a large volume Ge(Li) detector and a hyper pure Ge detector together with the fast-slow coincidence circuit, which may give some more information about the ^{187}Re level structure and find some reasonable solutions for these discrepancies.

2. Experimental procedure

A 1.35 mg of natural ^{186}W has been irradiated in one of the vertical channels of the Egyptian Research Reactor at AEA-Inchass. The gamma-ray transitions associated with the decay of ^{187}W into ^{187}Re have been investigated using the coaxial Ge(Li) detector of active volume 76.7 cm^3 coupled with a FET-preamplifier, spectroscopy amplifier and 4096 pulse-height analyzer. The resolution of the Ge(Li) detector was 2.2 keV at the 1333 keV gamma line of ^{60}Co. The gamma-ray transitions in the low energy region ($E_\gamma < 280$ keV) have been measured using a hyper pure Ge detector (planar type, 10 mm active diameter and 7 mm active depth). The resolution of the hyper pure Ge was 511 eV for 122 keV photons and 204 eV for 5.9 keV photons.

The gamma–gamma coincidence measurements have been carried out using a Ge (Li) — NaI (Tl) spectrometer provided with a fast-slow coincidence circuit which was explained in details in [18]. The NaI(Tl) used has an energy resolution of 9% at the 662 keV gamma ray transition of ^{137}Cs. The time resolution of the fast-slow coincidence circuit was about 16.2 μs, while that of the slow coincidence circuit was about 1.38 μs.

The singles spectra have been measured once every day for a period of 7 days to make sure that the gamma-ray transitions under investigation (including the new transitions) belong only to the ^{187}Re.

The relative gamma-ray intensities have been estimated using the efficiency curves of the Ge(Li) and the hyper pure Ge detectors measured under the same conditions of this experiment [18].

Using the Ge(Li)–NaI(Tl) gamma–gamma coincidence spectrometer, three runs were performed where the NaI(Tl) detector was used for gating purposes to select the gamma-ray transitions in the energy regions of (40–120), (100–180) and (580–650) keV. Due to the poor resolution of the NaI(Tl) detector used, other neighbouring gamma-ray transitions were included in each of the above mentioned energy ranges.

3. Results and discussion

A. *Gamma ray singles spectra*

The gamma-ray single spectrum obtained using the hyper pure Ge spectrometer for $E_\gamma < 280$ keV and the gamma-ray transition at 641.1 keV taken by the Ge(Li) spectrometer are shown in Fig. 1.

From the singles spectra studied more than 60 gamma-ray lines have been identified, eight of them at 65.4, 103.8, 115.5, 154.4, 178.8, 261.0, 262.7 and 641.1 keV have been observed for the first time. Also another four new gamma-ray transitions at 147.3, 191.1, 201.3 and 345.7 keV were observed in the coincidence spectra only.

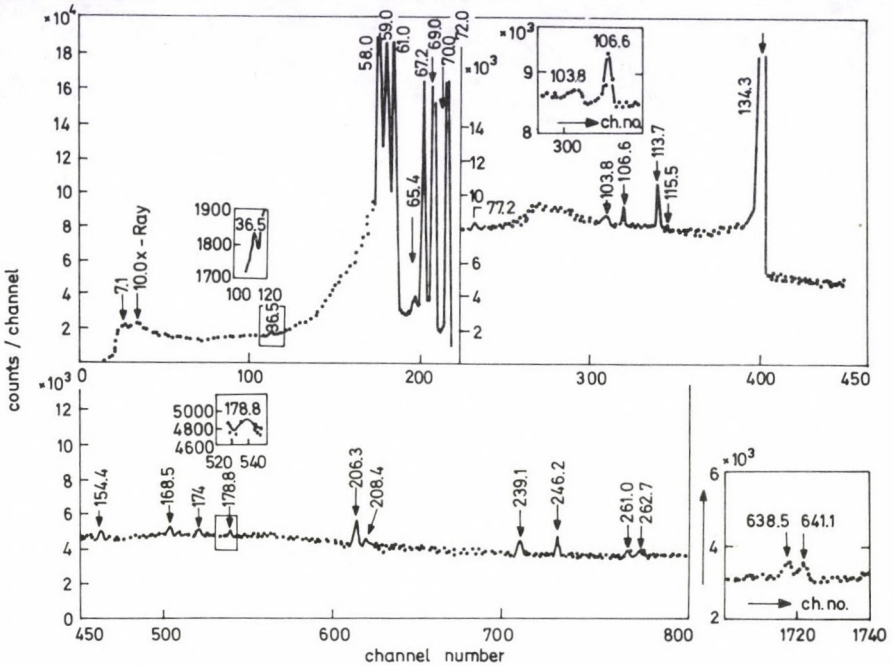

Fig. 1. A portion of the gamma-ray singles spectra ($E_\gamma < 280$ keV) using the hyper pure Ge spectrometer. The gamma-ray transition at 641.1 keV taken by the Ge(Li) spectrometer is shown

The gamma ray lines at 16.6, 29.23, 40.9, 93.0, 100.0, 123.0, 138.5, 165.6, 275.0, 347.0, 375.9, 564.0, 578.0, 767.0, 844.0 and 1086.0 keV which were reported by Brener et al [16] could not be observed in the present work. Also the gamma-ray lines at (96.0, 529.0), (301.0, 760.0, 777.0, 626) (106, 911) and 448.0 keV reported in [2, 4], [3], [6], [5], respectively and the gamma lines at 141.22, 727.22, 794.8, 835.55, 933.8, 958.78 and 1000.82 keV reported by Yamada et al [17] were not clear in our spectra.

The gamma-ray lines observed in the present work are presented in Table I together with the recent data [13, 16, 17] for the sake of comparison. The relative intensities of the gamma-ray lines below 250.0 keV obtained by the pure Ge detector were calculated taking the intensity of the gamma-ray line at 246.0 keV as 100%, which was normalized later to the intensity value of the gamma-ray line at 479.5 keV. The relative intensities of the gamma-ray lines which have the energy values higher than 250.0 keV obtained by the Ge(Li) detector have been calculated taking into consideration the intensity of the gamma-ray line at 479.5 keV as 100%.

Table I

Energies and relative intensities of gamma-ray transitions in ^{147}Re following the decay of ^{187}W

Present work		Yamada et al [17]		Brenner et al [16]		Krane et al [13]		Assignment from level — to level
E_γ [keV]	I_γ	E_γ [keV]	I_γ	E_γ [keV]	I_γ	E_γ [keV]	I_γ	
7.1	0.3 +0.013	7.49	9.71	7.1	–	–	–	625.5 – 618.4
–	–	–	–	16.61	0.027	–	–	–
–	–	–	–	29.23	0.016	–	–	618 – 589
36.5*	0.05 +0.0016	36.24	0.1	36.38	0.099	–	–	625.5 – 589, 618.4 – 582
–	–	–	–	40.92	0.008	–	–	–
43.8[a]		–	–	43.66	0.008	–	–	816.6 – 772.8
65.4	0.76 ±0.03	–	–	–	–	–	–	647.4 – 582
70.2[a]		–	–	–	–	–	–	582 – 511.8
72	47.2 ±2.19	72.02	39.61	72.46	50.99	–	–	206.3 – 134.3
77.2	0.04 ±0.001	77.23	0.15	77.34	0.031	–	–	589 – 511.8
–	–	–	–	93.22	0.027	–	–	–
103.8	0.037 ±0.001	–	–	–	–	–	–	685.8 – 582
106*	0.11 ±0.005	106.6	0.15	106.59	0.114	107	–	618.4 – 511.8, 879.5 – 772.8
113.7	0.26 ±0.01	113.77	0.3	113.75	0.35	114	–	625.5 – 511.8
115.5	0.019 ±0.001	–	–	–	–	–	–	960.2 – 844.7
–	–	–	–	123.79	0.012	–	–	–
134.3	40.74 ± 1.89	134.25	33.53	134.22	40.31	134	–	134.3 – 0
–	–	–	–	138.5	0.019	–	–	–
–	–	141.22	0.03	–	–	–	–	827.19 – 685.8
147.3[a]	–	–	–	–	–	–	–	772.8 – 625.5
154.4	0.058 ±0.002	–	–	–	–	–	–	772.8 – 618.4
–	–	–	–	165.67	0.004	–	–	302.8 – 134.3
168.5	0.05 ±0.0016	168.15	0.01	169.5	0.012	–	–	302.8 – 134.3
174	0.07 ±0.002	–	–	174.04	0.002	–	–	685.8 – 511.8
178.8	0.05 ±0.0018	–	–	–	–	–	–	864.6 – 685.8
191.1[a]	–	–	–	–	–	–	–	816.6 – 625.5
198.2[a]	–	–	–	198.34	0.008	–	–	816.6 – 618.4
201.3[a]	–	–	–	–	–	–	–	826.8 – 625.5
206.3	0.61 ±0.025	206.18	0.53	206.29	0.65	206	–	206.3 – 0
208.4	0.006 ±0.001	–	–	208.28	0.003	–	–	826.8 – 618.4
239.1	0.35 ±0.015	238.82	0.76	239.03	0.395	239	–	864.6 – 625.5

246.2	0.54 ±0.023	246.33	0.44	246.18	0.54	246	–	864.6 – 618.4
261	0.04 ±0.001	–	–	–	–	–	–	772.8 – 511.8
262.7	0.04 ±0.001	–	–	–	–	–	–	844.7 – 582
–	–	–	–	275.61	0.008	–	–	864 – 589
345.7[a]	–	–	–	–	–	–	–	1190.4 – 844.7
–	–	–	–	352,86	0.007	–	–	865 – 512
–	–	–	–	374.31	0.012	–	–	–
–	–	–	–	375.93	0.015	–	–	–
454.7	0.12 ±0.005	454.85	0.17	454.92	0.134	454	–	589 – 134.3
479.5	100	479.56	100	479.53	100	479	–	685.8 – 206.3
484.1[a]	–	–	–	484.15	0.079	–	–	618.4 – 134.3
491.2[a]	–	–	–	492.8	0.118	–	–	625.5 – 134.3
511.8	2.63 ±0.111	511.7	3.49	511.76	2.95	511	–	511.8 – 0
551.5	21.2 ±0.93	551.57	23.89	551.55	23.28	552	–	685.8 – 134.3
–	–	562.01	0.01	564.62	0.055	–	–	1190 – 626
573.4	0.015 ±0.001	–	–	573.71	0.002	–	–	1220.8 – 647.4
576.7	0.03 ±0.001	575.83	0.01	576.31	0.03	–	–	879.5 – 302.8
–	–	–	–	578.72	0.004	–	–	–
582	0.2 ±0.008	–	–	–	–	–	–	582 – 0
589	0.49 ±0.002	589.12	0.61	589.09	0.55	589	–	589 – 0
611.7[a]	0.005	612.9	0.01	612.92	0.009	–	–	1230.1 – 618.4
618.4	30.5 ±1.34	618.35	29.92	618.37	28.73	618	–	618.4 – 0
625.5	4.43 ±0.194	625.49	5.1	625.52	4.98	625	–	625.5 – 0
638.5*	0.13 ±0.005	638.65	0.08	638.65*	0.014	–	–	772.8 – 134.3, 844.7 – 20.63
641.1	0.13 ±0.005	–	–	–	–	–	–	1230.1 – 589
647.4	0.03 ±0.001	–	–	647.3	0.003	–	–	647.4 – 0
682.3[a]	–	682.26	0.03	682.34	0.031	–	–	816.6 – 134.3
685.8	114.25 ±5.01	685.8	133.48	685.81	124.9	686	–	685.8 – 0
692.5[a]	–	693.19	0.07	693.06	0.006	–	–	826.8 – 134.3
–	–	727.22	0.17	–	–	–	–	933.54 – 206.2
730.3[a]	–	–	–	730.32	0.079	–	–	864.6 – 134.3
745.2	1.24 ±0.054	745.29	1.46	745.2	1.363	746	–	879.5 – 134.3
–	–	–	–	767.37	0.007	–	–	–
772.8	17.71 ±0.78	772.85	20.81	772.87	18.87	773	–	772.8 – 0
–	–	794.8	0.11	–	–	–	–	1000.93 – 206.2
816.6	0.04 ±0.001	816.49	0.05	816.56	0.045	–	–	816.6 – 0
825.9	0.009 ±0.001	–	–	825.96	0.001	–	–	960.2 – 134.3

Table I (cont.)

Present work		Yamada et al [17]		Brenner et al [16]		Krane et al [13]		Assignment From level — to level
E_γ [keV]	I_γ	E_γ [keV]	I_γ	E_γ [keV]	I_γ	E_γ [keV]	I_γ	
826.8	0.007 ± 0.001	–	–	826.65	0.001	–	–	826.8 – 0
–	–	835.55	0.04	–	–	–	–	969.28 – 134.3
–	–	–	–	844.7	0.001	–	–	845 – 0
864.6	1.45 ± 0.065	864.52	1.76	864.55	1.537	865	–	864.6 – 0
879.5	0.59 ± 0.025	879.46	0.72	879.43	0.648	880	–	879.5 – 0
–	–	933.8	0.06	–	–	–	–	933.6 – 0
960.2	0.006 ± 0.001	–	–	960.17	0.006	–	–	960.2 – 0
–	–	968.78	0.19	–	–	–	–	969.28 – 0
–	–	1000.82	0.02	–	–	–	–	1000.8 – 0
1056.1	0.012 ± 0.001	1051.36	0.02	1056.24	0.001	–	–	1190.4 – 134.3
–	–	–	–	1086.6	0.004	–	–	1221 – 134
1095.8	0.014 ± 0.001	1096	0.01	1095.9	0.0003	–	–	1230.1 – 134.3
1190.4	0.006 ± 0.001	1187.85	0.01	1190.38	0.0009	–	–	1190.4 – 0
1220.8	0.006 ± 0.001	–	–	1220.8	0.0007	–	–	1220.8 – 0
1230.1	0.006 ± 0.001	1230.33	0.01	1230.1	0.005	–	–	1230.1 – 0

[a] Coin only.

* Two positions in the decay scheme.

B. *Gamma–gamma coincidence spectra*

Using the gamma–gamma fast-slow coincidence spectrometer, three gates were selected in order to confirm and/or identify the new gamma transitions mentioned above.

(i) When the NaI(Tl) detector was used to gate (40 keV $< E_\gamma <$ 120 keV), the gamma-ray transitions at energies of 65.4, 103.8, 147.3, 154.4, 178.8, 191.1, 201.3, 261.0, 262.7 and 641.1 keV were identified and confirmed for the first time in the present singles and/or coincidence spectra as illustrated in Fig. 2.

Also, by using this gate the gamma-ray lines at 198.2, 208.4, 611.7 and 638.5 keV mentioned in [16] and the 582.0 keV of [5] have been confirmed.

(ii) The second gate was in the range of 100 up to 180 keV. In this gate the (103.8, 147.3, 154.4, 178.8, 191.1, 201.3, 261.0 and 262.7 keV) were confirmed. The coincidence spectrum is presented in Fig. 3. The energies at 43.8, 106.6, 168.5, 174, 198.3, 208.4, 454.7, 484.1, 491.2, 567.7, 582, 611.7, 638.5, 682.3, 692.5, 730.3 and 825.9 keV of [5, 15, 16] are also confirmed.

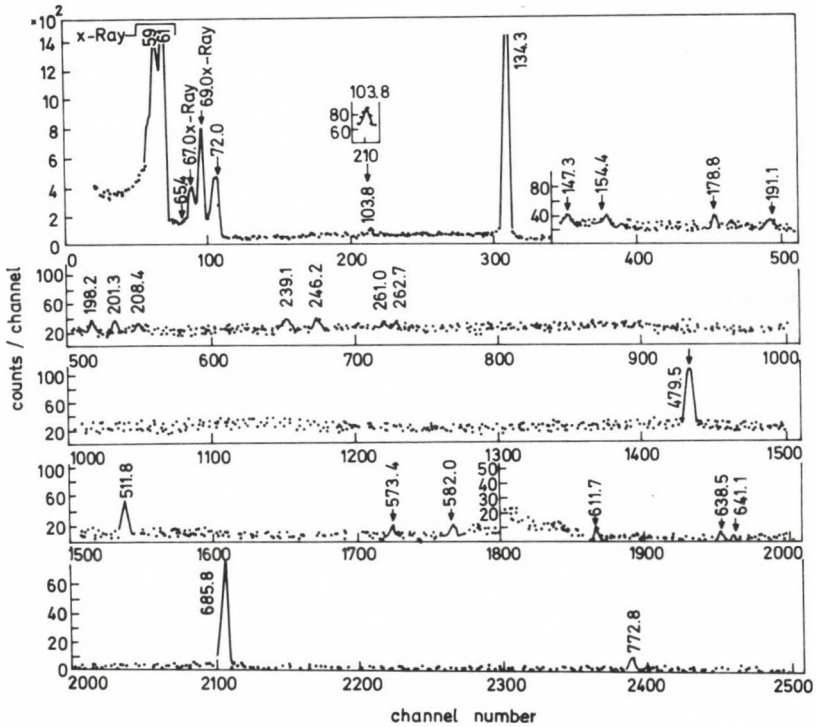

Fig. 2. The gamma–gamma coincidence spectrum obtained using the Ge(Li)–NaI(Tl) spectrometer (the gate width at 40–120 keV)

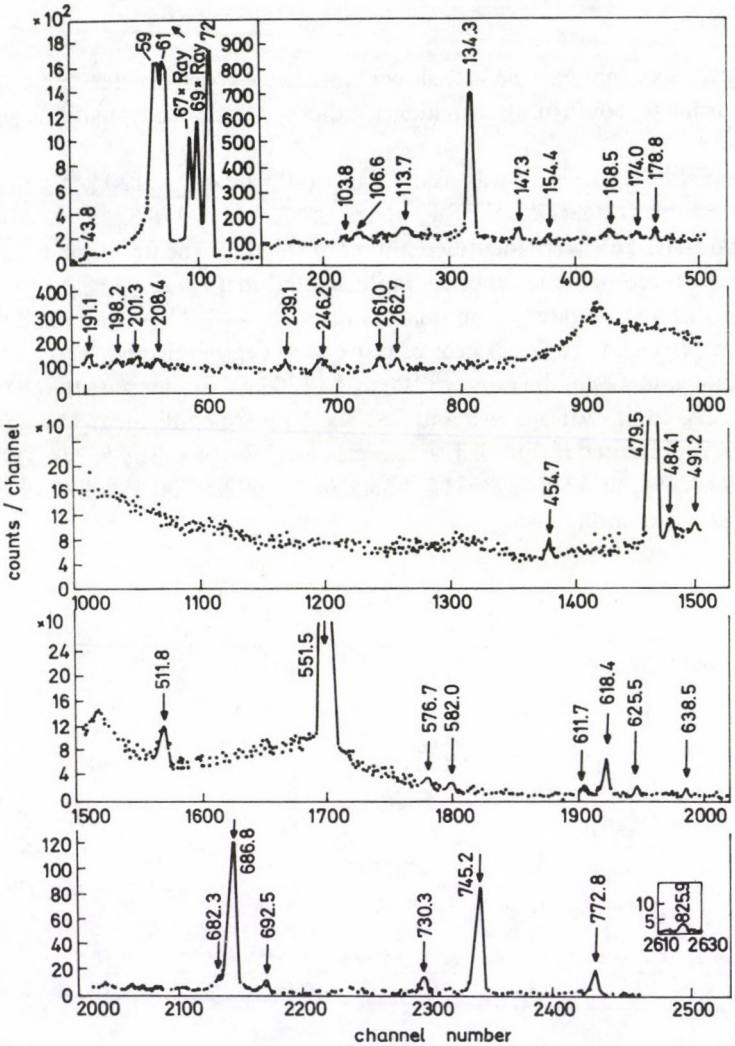

Fig. 3. The gamma–gamma coincidence spectrum obtained using Ge(Li)–NaI(Tl) spectrometer, the gate width at 100–180 keV

(iii) In the third gate, the energy range was ($580 < E < 650$ keV), two other new gamma transitions at energies 115.5 and 345.7 keV were observed to be in coincidence with $E_\gamma = 638.5$ keV as shown in Fig. 4.

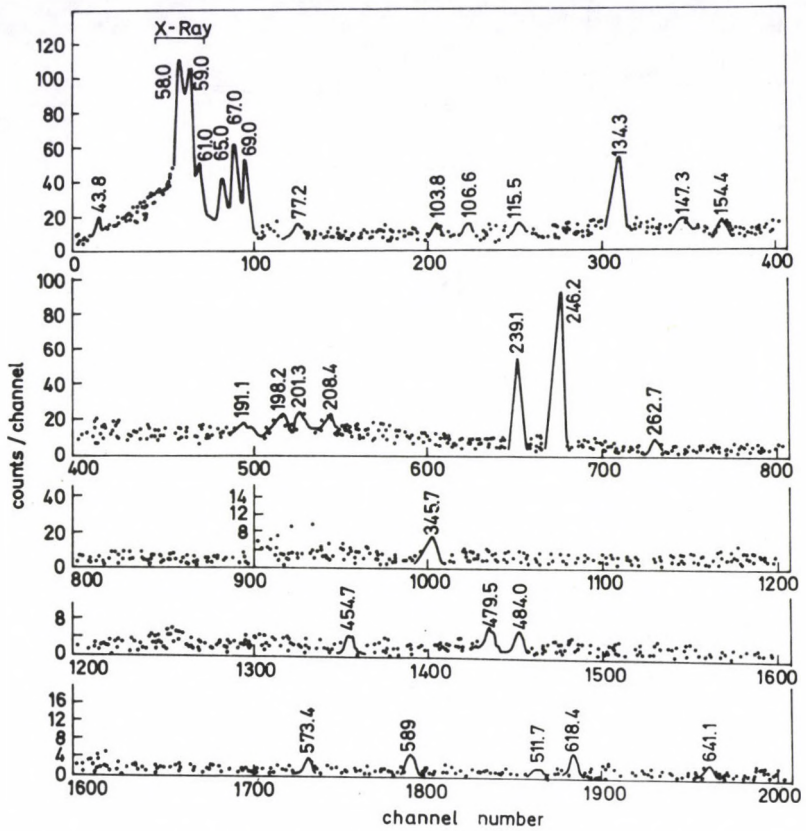

Fig. 4. The gamma–gamma coincidence spectrum obtained using Ge(Li)–NaI(Tl) spectrometer, the gate width at 580–650 keV

4. Level structure of ^{187}Re

The gamma-ray transitions identified and confirmed in the present investigation are fitted in a proposed level structure of ^{187}Re as shown in Fig. 5. Several remarks could be pointed out:

(i) Twelve gamma-ray transitions at energies of 65.4, 103.8, 115.5, 147.3, 154.4, 178.8, 191.1, 201.8, 261.0, 262.7, 345.7 and 641.1 keV have been identified for the first time in the singles and/or coincidence spectra.

(ii) The level at 529.0 keV proposed by [2, 4] and 911.0 suggested by [3, 6] as well as the energy levels at 933.54, 969.28 and 1000.93 keV proposed by [17] were not included in the present proposed level scheme due to the absence of the populating and/or depopulating transitions in the present singles and/or coincidence results.

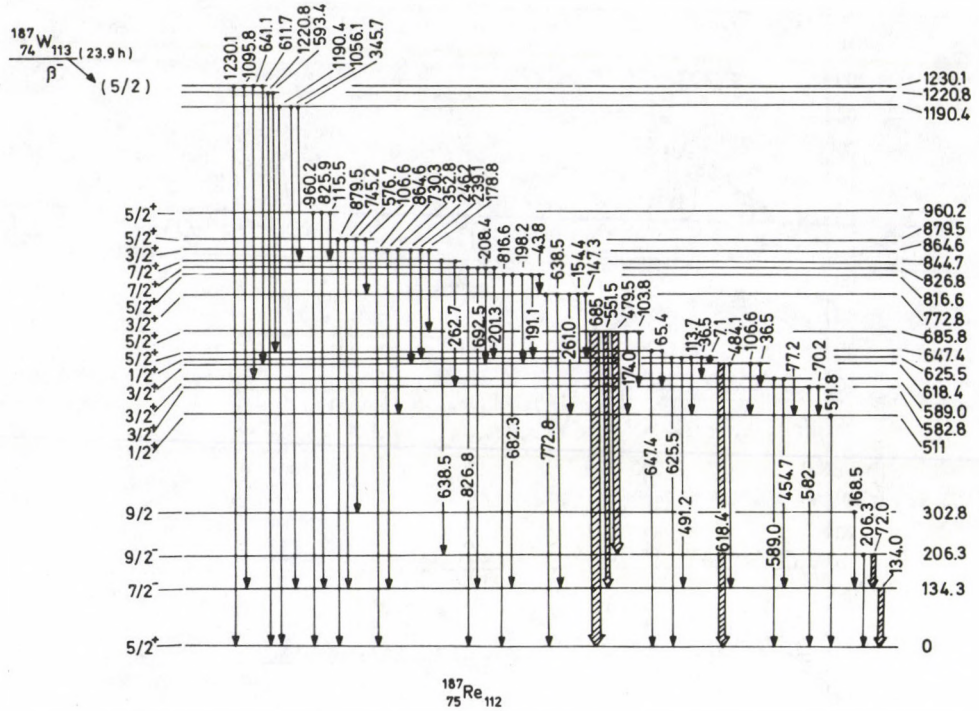

Fig. 5. The level structure of ^{187}Re

(iii) In addition, the present work confirms the 582.0 keV level proposed only by [5]. The 647.2 keV level observed by [15, 16] and the 816.6, 826.8, 844.7, 960.2, 1190.4 and 1230.1 keV levels proposed by [16] were also confirmed due to the presence of the gamma-ray transitions populating or depopulating these levels in the singles and/or coincidence spectra.

References

1. C. J. Gallagher, Jr., W. F. Edwards and G. Manning, Nucl. Phys, *19*, 18, 1960.
2. K. Maack Bisgard, K. Olesen and P. Ostergard, Nucl. Phys., *33*, 126, 1962.
3. W. Michaelis, Nucl. Phys., *48*, 422, 1963.
4. H. Langhoff, Phys. Rev., *135*, No. IB, 1964.
5. K. Maack Bisgard, L. J. Nielsen, E. Stabbel and P. Stergard, Nucl. Phys., *71*, 192, 1965.
6. E. Bashandy, M. G. Mousa and M. Migahed, Physica, *31*, 1125, 1965.
7. L. Funke, H. Grober, K. H. Kaun, H. Sodan and L. Werner, Nucl. Phys., *74*, 154, 1965.
8. J. J. Reidy and M. L. Wiedenbeck, Nucl. Phys., *79*, 193, 1966.
9. M. T. Lu and W. P. Al. Ford, Phys. Rev., *C3*, 1943, 1971.
10. K. M. Bisgard and E. Veje, Nucl. Phys., *A 103*, 545, 1967.

11. H. Langhoff, Phys. Rev., *159*, 1032, 1967.
12. W. Andjertscheff, F. Dubbers, K.-D. Schilling and F. Stary, Nucl. Phys., *A 137*, 693, 1969.
13. K. S. Krane and W. A. Steyert, Phys. Rev., *C7*, No. 4, 1973.
14. R. A. Meyer, J. C. Hill and D. S. Brenner, Bull. Amer. Phys. Soc. *19*, No. 4, 578, JH5, 1974.
15. Nuclear Data Sheets, for *A*-187, 1975.
16. D. S. Brenner and R. A. Meyer, Phys. Rev., *C 13*, 1288, 1976.
17. S. Yamada, S. Psud, Y. Miyatake and T. Hayashi, Nucl. Phys., *A 332*, 317, 330, 1979.
18. A. El-Shershaby, Ph. D. Thesis to be presented to Phys. Dep., Faculty of Girls, Ain Shams University, Cairo, 1983.

Acta Physica Hungarica 60 (1—2), pp. 107—112 (1986)

THE ELECTRICAL CONDUCTIVITY AND PYROELECTRICAL PROPERTIES OF FERRIC ACETYLACETONE SINGLE CRYSTAL

N. M. MOLOKHIA

Physics Department, Faculty of Education, Alexandria University
Alexandria, Egypt

(Received in revised form 14 August 1984)

The dielectric constant, the electrical conductivity and the pyroelectric behaviour of ferric acetylacetone $Fe(ac.ac)_3$ single crystal have been measured as a function of temperature from 20 to 140 °C. The measurements along the *b*-axis show a peak value in the dielectric constant at 82 °C, while no peaks were recorded along the other axes. This anomaly is described as due to a phase transition. On repeating these measurements at high frequency (100 kHz), no abnormality was obtained. The electrical conductivity measurements show a discontinuity around the transition temperature at 82 °C. The spontaneous polarization of the crystal was measured along the *b*-axis at different temperatures. The curve shows a rapid decrease in the crystal polarization between 60 and 100 °C.

Introduction

The ferroelectric-like behaviour of the acetylacetone compounds has drawn some attention due to the abnormality in the dielectric constant vs temperature curves. The acetylacetone is a substance that does the duty of two structure isomer each being capable of changing rapidly into the other when the equilibrium is disturbed, e.g. by addition of certain reagents. It forms organometallic complexes with many elements of different valencies. The dielectric properties of Na(ac.ac.) have been studied by many authors [1, 2]. They show that the compound underwent partial chemical transformation at certain temperature. Molokhia and Tawfik [3] studied the dielectric behaviour of K(ac.ac.). Two peaks were recorded in the dielectric constant os temperature curve at 10 and 21 °C. On studying Li(ac.ac), no abnormality was found in the dielectric constant [4]. It was concluded that the ferroelectric-like behaviour exhibited by the acetylacetone compounds with alkali metals, is due to molecular structure and is highly dependent on the ionic radii of the alkali metal. The dielectric behaviour of ferric acetylacetone $Fe(ac.ac.)_3$ polycrystals has been also studied [5]. A peak value was obtained in both dielectric constant and loss tangent at 85 °C. It has been explained as a transition temperature due to an internal structure reorientation at which the ferric acetylacetone changed from ketonic to enolic complex. In the present work, the ferroelectric acetylacetone was used in a form of single crystal. The dielectric

constant was measured as a function of temperature and frequency. Also the electrical conductivity and the pyroelectrical properties were studied at different temperatures in order to examine the semiconduction behaviour of $Fe(ac.ac.)_3$.

Experimental techniques

a) *Crystal preparation*

The ferric acetylacetone was prepared by adding ferric hydroxide to the equivalent amount of acetylacetone in alcohol. The single crystal was obtained by following the method of Louis et al [6]. The crystals obtained were lightly red and nearly transparent. Typical crystal dimensions are $0.3 \times 0.4 \times 0.7$ cm^3. Single crystal samples were electroded on opposing flat faces with silver paste. The electrical connections consisted of a thin copper wire attached with the same silver paste. The crystal orientation was determined by an X-ray diffractometer (Phillips PH23).

b) *Measurements*

The dielectric constant of the samples was measured by using the techniques developed by Glass [7]. In this method, the crystal is considered as a dielectric medium in between a parallel plate capacitor. The capacitance is linearly related to the dielectric constant perpendicular to the two opposing electroded faces. A circuit of an operational amplifier was used in which the gain is directly proportional to the capacitance of the sample. A Keithly model 616 electrometer operational amplifier was used. Another electrometer of the same type was used as a unity gain amplifier to isolate the circuit from the oscillator. A modified radio frequency oscillator was used giving signals up to 200 kHz with an accuracy of $\pm 1\%$.

Measurements of volume conductivity were carried out using a two probe method, placing a known voltage across the crystal and measuring the current with a nanoammeter (Phillips PM 2435).

The pyroelectric measurements were carried out using a charge integration technique adopted by Lipscomb et al [8]. An operational amplifier is used as a current integrator. The temperature of the sample is changed causing a change in the sample polarization P_s. The charge that flows to the plates of the capacitor is integrated and the output of the operational amplifier is proportional to the change in polarization of the sample. The pyroelectric coefficient is the rate of change of polarization with respect to the temperature and is perpendicular to the electrodes.

Results and discussion

a) *Dielectric constant*

The dieleetric constant of ferric acetylacetone was measured as a function of temperature along the three axes of the crystal. Fig. 1 shows the effect of temperature on the dielectric constant at a frequency of 1 kHz. The measurements along the *b*-axis show a peak value in the dielectric constant at 82 °C. No anomalous behaviour was recorded along the *a*- or *c*-axis. The position of the peak was found to be shifted two degrees (82 °C) when measuring the dielectric constant while the temperature is decreasing. As shown from Fig. 1, the dielectric constant increased from 25 at room temperature to 415 at the same rate. After the temperature reaches 110 °C, the dielectric constant increased rapidly up to the melting point of the crystal (180 °C).

This behaviour along the *b*-axis is inconsistent with the work done on the polycrystal ferric acetylacetone [5], in which a pronounced peak in the dielectric constant was recorded at 86 °C, giving an indication that a certain transformation might be developed in this compound. The existence of such anomalous behaviour along the *b*-axis only suggests that the transformation is mainly due to crystal structure variation.

The anomaly in the dielectric constant along the *b*-axis has been also studied at different frequencies. Fig. 2 illustrates this behaviour at 1, 50 and 100 kHz. As shown in the Figure, the dielectric constant at the peak value decreased with increasing frequency. At 100 kHz, no abnormality in the dielectric constant was obtained. The acetylacetone is polar in nature, it has a very active hydrogen atom in the CH_2 group which tends to be replaced by the iron atom to form the ferric acetylacetone. The total polarization of this compound in the single crystal form may be composed of electronic, ionic and space charge polarizations. The space charge polarization is only

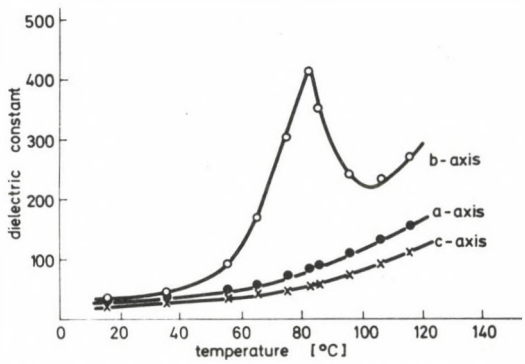

Fig. 1. Effect of temperature variation on the dielectric constant of $Fe(ac.ac.)_3$ single crystal along the different axes at 1 kHz

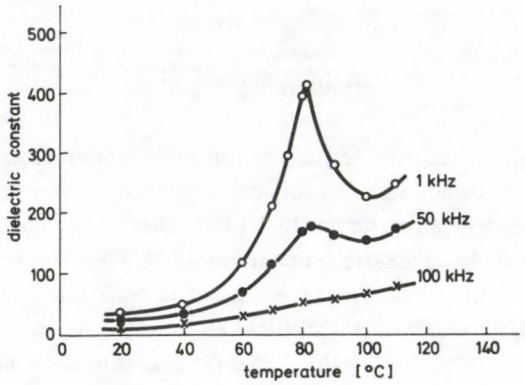

Fig. 2. Variation of dielectric constant with temperature along the *b*-axis for the $Fe(ac.ac)_3$ single crystal at different frequencies

active at low frequencies, while at high frequencies, the electronic and ionic polarization are predominant. Since the dielectric constant is directly proportional to the space charge polarization, it is expected that on increasing the frequency, the dielectric constant decreases as shown in Fig. 2.

b) *Electrical conductivity*

The electrical conductivity (σ) of ferric acetylacetone single crystal was measured as a function of temperature. Fig. 3 shows the logarithm of conductivities against the reciprocal of the absolute temperature along the three axes of the single crystal. The curves illustrate an increase in the electrical conductivity with temperature along the different axes. The measurements along the *b*-axis show a discontinuity around the transition temperature (82 °C). On calculating the activation energy from the slope of the straight parts of these curves, it was found to be 0.92, 0.86 and 1.16 eV for the *a*, *b* and *c*-axes, respectively. The existence of such activation energy in the crystal may be due to some imperfections in the crystal structure resulting from the space charge polarization.

c) *Pyroelectric properties*

The abnormality appearing in the dielectric constant on changing the sample temperature is usually accompanied by the onset of a spontaneous polarization (P_s) of the crystal. Fig. 4 illustrates the change in spontaneous polarization (ΔP_s) vs temperature along the *b*-axis. As shown in the Figure ΔP_s rapidly decreases between 60 and 100 °C passing through the transition temperature. On cooling the sample, the

curve was reproducible with a slight difference in the value of ΔP_s. A trial has been made to reverse the direction of the spontaneous polarization by poling the crystal under a field of 1000 V/cm. No change was observed in the direction of ΔP_s, although some change was recorded in the magnitude of ΔP_s. The onset of spontaneous polarization below the transition temperature in this material suggests that the ferric acetylacetone is of ferroelectric behaviour.

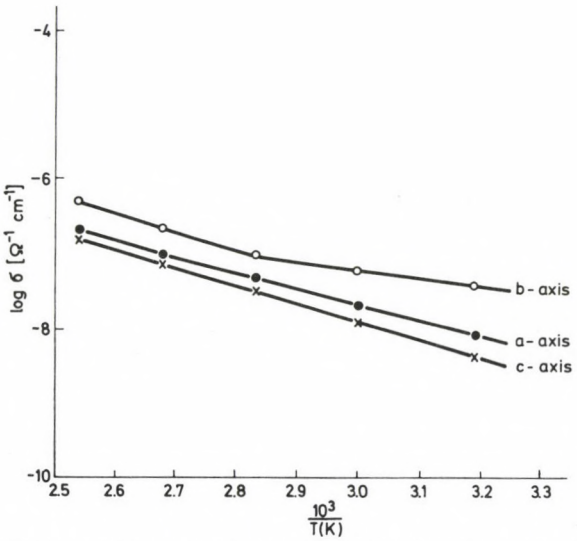

Fig. 3. Electrical conductivity of Fe(ac.ac.)$_3$ single crystal as function of temperature along the three axes

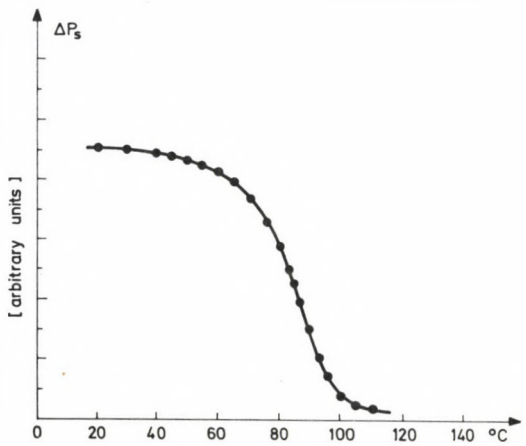

Fig. 4. The temperature dependence of the spontaneous polarization along the *b*-axis of the *b*-axis of the Fe(ac.ac.)$_3$ single crystal

In conclusion, the ferric acetylacetone single crystal undergoes a phase change from a nonpolar to a polar state at 82 °C. The dielectric anomaly along the *b*-axis and the discontinuity in the electrical conductivity together with the pyroelectric effect that accompanies the transition resemble those of a first order ferroelectric transition.

Acknowledgement

The author would like to thank Dr. J. Mason at Sheffield University, England for useful discussions and for his interest in this work.

References

1. R. Kamel and M. Hilal, Mol. Cryst. Liq. Cryst., *31*, 9, 1975.
2. A. Tawfik and N. Molokhia, Acta Phys. Polon., *A56*, 155, 1975.
3. N. Molokhia and A. Tawfik, Egypt. J. Phys. Solids, *1*, 97, 1980.
4. N. Molokhia and M. El Shahat, J. Chem. Tech. Biotech., *31*, 56, 1981.
5. N. Molokhia, M. El Shahat and E. El Sawi, Ferroelectrics, *31*, 23, 1981.
6. Louis, Hatch and Sutherland, J. Org. Chem., *13*, 249, 1948.
7. A. M. Glass, J. Appl. Phys., *40*, 4699, 1969.
8. J. F. Lipscomb, A. F. Garito and T. S. Wei, Ferroelectrics, *23*, 161, 1980.

Acta Physica Hungarica 60 (1—2), pp. 113—126 (1986)

FRANCK–CONDON FACTORS, *r*-CENTROIDS AND ELECTRONIC TRANSITION MOMENT VARIATION WITH INTERNUCLEAR DISTANCE OF $B^1\Sigma - X^1\Sigma$ BAND SYSTEM OF BeO USING RKR POTENTIAL

N. R. TAWDE

4. Manisha Hous. Society, Aurangabad (Deccan), India

and

V. G. TULASIGERI

Department of Physics, Karnatak University, Dharwad, India

(Received 30 August 1984)

The applicability of RKR — the true potential in comparison to that of Morse potential, has been tested for the transition ($B^1\Sigma - X^1\Sigma$) of BeO band system through various tests. The expression $R_e(r)$, the electronic transition moment variation with internuclear distance r, using the Franck — Condon (FC) factors and r-centroids ($\bar{r}_{v'v''}$) of the true potential has been derived and evaluated for both linear and quadratic fitting. This has further been used to calculate the smoothed Condon factor $P_{v'v''}$ and the ratio $\beta(=I/\nu^4/P_{v'v''})$ representing its comparison with experimental band strengths (I/ν^4). Through the comparative study of such values, viz. $p'^s_{v'v''}$'s, β's and vibrational temperatures deduced both under constancy of R_e and the variation of R_e with r, the efficacy of true potential in relation to that of Morse potential has been discussed.

1. Introduction

In recent years, much interest is being focussed on the theoretical aspects [1–14] of the BeO ($B^1\Sigma - X^1\Sigma$) band system. The study of this diatomic molecule is of considerable significance because of its astrophysical importance like other related oxides of alkaline earths [15–19]. As the bands of the BeO molecule can be easily produced in the laboratory, any difficulties encountered in getting spectral information of such molecules directly from astral sources could be overcome by investigating them in laboratory sources.

In this regard, experiments were conducted to excite the bands of BeO molecule in laboratory sources. They were then subjected to measurement for peak intensities [16, 20]and integrated intensities [21]. These experimental values of relative intensities of the vibrational bands of BeO molecule, in conjunction with their theoretically computed vibrational transition probabilities not only lead to the estimation of the temperature of the source, but also to the study of the variation of electronic transition moment R_e with internuclear distance r, i.e. the $R_e(r)$ variation.

Such a study of $R_e(r)$ variation has been made for the band system $B^1\Sigma - X^1\Sigma$ of BeO molecule by Sreedhar Murthy [21]. He has derived $R_e(r)$ variation by using his own data of integrated intensities and employing the r-centroid ($\bar{r}_{v'v''}$) method of Nicholls and Jarmain [22]. On the other hand, one of the authors, Tulasigeri [23], using the integrated intensities of Sreedhar Murthy has evaluated $R_e(\bar{r}_{v'v''})$ for the same band system by adopting the method of regression of Cunio and Jansson [25] for both linear and quadratic fitting.

The validity of the expression derived for $R_e(\bar{r}_{v'v''})$ vitally depends upon the reliability of the integrated intensity values and the accuracy of the vibrational wave functions which, in turn, are used to calculate the theoretical vibrational transition probabilities. In the present band system under study, although Sreedhar Murthy has used accurate data of band intensities — the integrated intensities — the Franck–Condon (FC) factors used by him are those obtained by employing the potential energy function of Morse [27]. However, these latter data of FC factors on the basis of Morse potential function in the theoretical computations suffer from the limitation that this potential generally holds in the region of relatively lower vibrational quantum numbers only. The applicability of the Morse potential function, on considerations of Sharma [28], has been examined by an application of various tests. These tests have led us to the conclusion that the Morse potential energy curves do not run the course as given by the Rydberg–Klein–Rees [29–31] (RKR) potential, an expression considered to be conforming to experimental data and hence realistic.

The situation as presented above called for the application of RKR potential to the BeO band system and this study has been undertaken in the present investigation. The FC factors thus computed by the application of RKR potential have been used to derive $R_e(r)$, the electronic transition moment variation expression and with it to obtain an estimate of the temperature of the source. The results thus obtained are presented in the following Section.

2. Construction of potential energy curves and their comparative study

2.1. Construction of the curves

In the manner similar to that shown by Tawde and Tulasigeri [32, 33], the values of turning points r_{min} and r_{max} have been calculated with RKR and Morse potential energy functions for the vibrational levels $v = 0$ to $v = 10$ of the two electronic states $B^1\Sigma$ and $X^1\Sigma$ of BeO band system. These turning point values are recorded in Table I.

With the use of the data of Table I, the potential energy curves have been constructed and represented to scale in Fig. 1. The molecular constants used for calculating the turning point values and other calculations involved in the present investigation are taken from Herzberg [34] and they are reproduced in Table II.

Table I

Eigenvalues and turning points of the potential energy curves of $B'\Sigma$ and $X'\Sigma$ of BeO molecule

v	Energy value E [cm^{-1}]	RKR (Authors)		Morse (Authors)	
		r_{min} [nm]	r_{max} [nm]	r_{min} [nm]	r_{max} [nm]
0	741	0.1271_9	0.1397_8	0.1271_9	0.1397_7
	684	0.1300_7	0.1431_7	0.1300_2	0.1431_2
1	2204	0.1233_7	0.1453_1	0.1233_1	0.1452_5
	2039	0.1259_7	0.1487_6	0.1258_8	0.1486_6
2	3644	0.1208_7	0.1493_6	0.1208_4	0.1493_6
	3379	0.1233_6	0.1529_2	0.1232_0	0.1527_6
3	5061	0.1189_8	0.1529_6	0.1189_4	0.1529_2
	4703	0.1213_4	0.1564_9	0.1211_3	0.1562_7
4	6453	0.1174_3	0.1562_3	0.1173_7	0.1561_7
	6012	0.1196_8	0.1597_3	0.1194_0	0.1594_5
5	7812	0.1160_9	0.1593_0	0.1160_3	0.1592_3
	7305	0.1182_6	0.1627_5	0.1179_2	0.1624_1
6	9168	0.1149_2	0.1622_3	0.1148_5	0.1621_6
	8583	0.1170_1	0.1656_2	0.1166_0	0.1652_1
7	10.489	0.1138_8	0.1650_6	0.1138_0	0.1649_9
	9845	0.1158_9	0.1683_7	0.1154_2	0.1679_0
8	11.788	0.1129_3	0.1678_5	0.1128_5	0.1677_5
	11.092	0.1148_7	0.1710_3	0.1143_5	0.1705_1
9	13.062	0.1120_6	0.1705_5	0.1119_8	0.1704_7
	12.324	0.1139_5	0.1736_3	0.1133_6	0.1730_4
10	14.313	0.1112_6	0.1732_2	0.1111_8	0.1731_5
	13.540	0.1131_0	0.1761_7	0.1124_5	0.1755_2

Note. Upper number in each vibrational state corresponds to $X'\Sigma$ state and lower number to $B'\Sigma$ state.

Table II

Molecular constants of BeO ($B'\Sigma - X'\Sigma$) band system

State	ω_e [cm^{-1}]	$\omega_e x_e$ [cm^{-1}]	r_e [nm]	B_e [cm^{-1}]
$X'\Sigma$	1487.323	11.8297	0.13308	1.6510
$B'\Sigma$	1370.817	7.7455	0.13622	1.5758

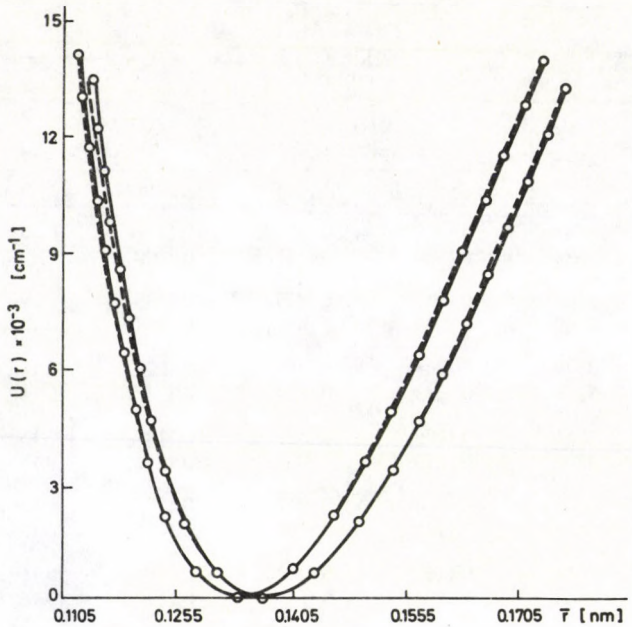

Fig. 1. Potential energy curves
○○○○ — RKR potential
– – – – — Morse potential

2.2. Comparative study of the curves

There are two criteria, viz. α_e test and B_v test employed earlier by Tawde and Tulasigeri, which have been applied here to test the relative merit of Morse potential with respect to RKR potential as explained below.

The evaluation of theoretical α_e values has been done by using the Pekeris [35] expression for Morse potential and that of B_v values by the theoretical expression of Jarmain [36] on the computed normalised vibrational wave functions of both Morse and RKR potentials. These calculated values of α_e and B_v are then compared with the observed α_e and B_v data on the system under study. Of these, the two sets of comparative values are drawn up in columns 2 and 3 of Table III. The deviation of the observed set of values from the calculated ones is also worked out and shown in column 4 of the same Table. The study of the relative magnitudes of these deviations with respect to the two electronic states of the molecular system reveals that the deviation in the upper state is greater than in the lower state. Since the theoretical α_e expression is based on Morse potential, the test leads to the conclusion that one would expect Morse potential energy curves to diverge more in the upper electronic state than in the lower one. This is generally confirmed by the comparison of the data on r_{min} and r_{max}, the

Table III

Results of α_e test

Electronic state	α_e (calculated) [cm^{-1}]	α_e (observed) [cm^{-1}]	Deviation [cm^{-1}]
$X'\Sigma$	18.4×10^{-3}	19.0×10^{-3}	0.6×10^{-3}
$B'\Sigma$	13.2×10^{-3}	15.4×10^{-3}	2.2×10^{-3}

centre position and the halfwidths entered in Table I, corresponding to the two states and it is also verifiable from the plot of the two $U(r)$ curves, RKR and Morse (Fig. 1).

Taking now the B_v test for the study of the comparative merits of the two potential energy curves, the computed normalised vibrational wavefunctions have been employed for calculating the rotational constant B_v by using the following relation of Jarmain

$$B_v = \frac{h}{8\pi^2 c\mu} \int_0^\infty \left\{\frac{\psi_v(r)}{r}\right\}^2 dr . \tag{1}$$

The B_v values thus calculated have been recorded in columns 3 and 4 of Table IV. The experimental values of the quantity available from the work of Lagerqvist and Westoo [37], are entered in column 5 of the same Table IV, for comparison. It is apparent from the comparison that in the upper state the Morse potential theoretical values of B_v deviate appreciably from the experimental ones; whereas in the case of RKR potential, the situation is almost in contrast to this, showing appreciable agreement of the theoretical B_v values with the observed ones, both in the ground and upper states. It is

Table IV

B_v test for wave functions

State	v	B_v (derived) RKR (Authors)	B_v (derived) Morse (Authors)	B_v (observed)
$X'\Sigma$	0	1.640	1.642	1.641_5
	1	1.625	1.623	1.622_3
	2	1.605	1.605	1.603_5
	3	1.587	1.583	1.584_6
	4	1.566	1.616	1.565_6
	5	1.555	1.642	1.546_5
$B'\Sigma$	0	1.566	1.569	1.568_4
	1	1.552	1.556	1.552_9
	2	1.534	1.543	1.537_1
	3	1.523	1.529	1.521_6

only in the ground sate ($X'\Sigma$) that the Morse potential holds good for a relatively greater region, i.e. up to $v'' \simeq 3$ but in the upper state as concluded above, it gives a deviation that increases steadily from as low a value as $v' \simeq 1$.

The findings as above from B_v test are generally in agreement with the results of the α_e test and in point of their comparison with the turning points r_{min} and r_{max}. The conclusion is, therefore, inevitable that the RKR potential is of much greater validity than the Morse potential in the theoretical interpretation of the phenomenon, if reliance is to be placed on the available data of experimental observations.

3. Computation of Franck–Condon factors and *r*-centroids

The FC factors and *r*-centroids have been computed by using the normalised wavefunctions based on RKR potential in a manner similar to the earlier investigations of the present authors [32, 33 and 42]. The values thus obtained are recorded in columns 2 and 4 of Table V. Similar data based on Morse potential required for

Table V

Franck–Condon factors and *r*-centroids of the $B'\Sigma - X'\Sigma$ band system of BeO

Band	FC-factors ($q_{v'v''}$)		*r*-centroids ($\bar{r}_{v'v''}$) [nm]	
	RKR (Authors)	Morse (Sreedhar Murthy)	RKR (Authors)	Morse (Sreedhar Murthy)
(0, 0)	0.888	0.893	0.1353	0.1352
(0, 1)	0.105	0.103	0.1490	0.1492
(0, 2)	0.003	0.004	0.1696	0.1642
(1, 0)	0.101	0.100	0.1224	0.1222
(1, 1)	0.697	0.712	0.1364	0.1363
(1, 2)	0.179	0.178	0.1507	0.1508
(1, 3)	0.010	0.010	0.1665	0.1662
(2, 1)	0.178	0.166	0.1235	0.1227
(2, 2)	0.556	0.577	0.1377	0.1375
(2, 3)	0.252	0.233	0.1515	0.1524
(2, 4)	0.020	0.017	0.1682	0.1685
(3, 2)	0.212	0.207	0.1237	0.1232
(3,3)	0.446	0.478	0.1390	0.1388
(3, 4)	0.296	0.273	0.1533	0.1541
(3, 5)	0.025	0.023	0.1714	0.170

comparative study are available from the work of Sreedhar Murthy [21]. The same is reproduced in columns 3 and 5 of Table V, side by side with the corresponding values under RKR potential.

4. Derivation of electronic transition moment variation with internuclear distance

There are two methods available for the derivation of $R_e(r)$, the relation expressing the variation of electronic transition moment R_e, with internuclear distance r. The methods are: (4.1) — Rescaling Procedure and (4.2) — the Regression Procedure. Both these methods are outlined in the following paragraphs with their application to the band system under study.

4.1. The Rescaling Procedure

The start is made through the semi-empirical method of Nicholls and Jarmain which makes use of the r-centroid concept defined by the equation —

$$\bar{r}_{v'v''} = \frac{\int \psi_{v'} r \psi_{v''}\, dr}{\int \psi_{v'} \psi_{v''}\, dr} \tag{2}$$

whose accuracy depends upon the validity of the equation below

$$\int \psi_{v'} r^n \psi_{v''}\, dr = (\bar{r}_{v'v''})^n \int \psi_{v'} \psi_{v''}\, dr\,. \tag{3}$$

The above equation (3) has the limitation that it is valid only for a small part of the range of integration, i.e. for small values of index n. With this limitation, using the r-centroid concept, the expansion involving integrated intensity I of a band emerges as

$$\left(\frac{I}{q_{v'v''}\nu^4}\right)^{1/2} = (KN_{v'})^{1/2}\, R_e(\bar{r}_{v'v''})\,, \tag{4}$$

where K = constant, $N_{v'}$ = population in the initial vibrational level, ν = frequency of the vibrational band, R_e = electronic transition moment, $\bar{r}_{v'v''}$ = r-centroid, $q_{v'v''}$ = Franck–Condon factor.

Here, as $N_{v'}$ is a constant for a particular progression, the Eq. (4) above shows that

$$R_e(\bar{r}_{v'v''}) \alpha \left(\frac{I}{q_{v'v''}\nu^4}\right)^{1/2} \tag{5}$$

using the values of I/ν^4, $q_{v'v''}$ and $\bar{r}_{v'v''}$ graphical plot is made of $(I/q_{v'v''}\,\nu^4)^{1/2}$ against $\bar{r}_{v'v''}$ which corresponds to each v' level, $N_{v'}$ being constant for the same. Many such curves for each v' level are plotted. They thus represent curves for each v'' progression, but do not correspond to the same scale. In order to bring them to the same scale, the method of Turner and Nicholls has been adopted. By this method, the rescaled values needed for bringing all the curves to the same scale were calculated and with these, the final curve was obtained by fitting by means of least square technique. This procedure enabled the $R_e(r)$ relation to be derived. The values of integrated intensities required for

the derivation were those of Sreedhar Murthy, whereas the FC factors and $\bar{r}_{v'v''}$ values are the data under RKR potential computed in the course of the present investigation and the values of wavelengths being those adpted from the work of Shimauchi [38] and of Becart and Mahieu [39]. The resulting relation for $R_e(r)$ is

$$R_e(r) = K(1 - 0.9856r). \tag{6}$$

4.2. The Regression Procedure

In the method method outlined above certain limitations are involved. These are in respect of the rescaling of the quantity $(I/q_{v'v''}\nu^4)^{1/2}$ wherein some of the points corresponding to the quantity are left out of consideration, as they do not fall in the common range. Because of this situation, the points actually reckoned are reduced in number. Thus only a few points would be effective in the determination of $R_e(r)$ variation. Consequently, an error in a single point leads to a larger percentage error

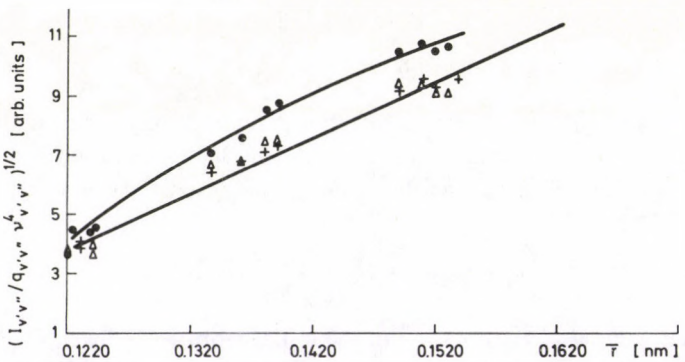

Fig. 2. Rescaled $(I_{v',v''}/q_{v',v''}\nu^4_{v',v''})^{1/2}$ against $\bar{\gamma}_{v',v''}$ for the BeO $(B'\Sigma - X'\Sigma)$ transition
●●●● — RKR (parabola) regression procedure
△ △ △ △ — RKR } (linear) Turner & Nicholls procedure
+ + + + — Morse }

than when one takes into account all the measured intensity values. It is, therefore, imperative that all the measured intensities are used to get a better value of $R_e(r)$. This is possible to achieve through the method of regression due to Cunio and Jansson. Here, by the application of this method, using only the RKR data, the relation $R_e(r)$ has been derived. As usual, the scaling factors have been determined afvaluation of the matrix elements and these are used to obtain the rescaled values. With these values, employing both linear and quadratic fittings, $R_e(R)$ relations have been arrived at. The resulting

linear and quadratic expressions for these relations are respectively

$$R_e(r) = K(1 - 0.9854r), \tag{7}$$

$$R_e(r) = K(1 - 1.285\,r + 0.334\,r^2). \tag{8}$$

The graphical representation of Eq. (8) along with linear fittings under both RKR (Eq. (6)) and Morse (Sreedhar Murthy [21] data), is given in Fig. 2. In the graph, the linear fitting of regression method has not been shown as this method is primarily intended only for quadratic fitting. However, the Eq. (7) enables comparison to be made with the earlier Eq. (6).

5. Relative smoothed Condon factors

For deriving smoothed Condon factors $P_{v'v''}$ on RKR potential, the linear equation (6) and the quadratic relation (8) have been used. The resulting $P_{v'v''}$ values are tabulated in columns 3 and 5 of Table VI. In order to compare these $P_{v'v''}$ values with the experimental band strengths (I/ν^4), the ratios $\beta(=I/\nu^4/P_{v'v''})$ have been calculated for each of the bands of the system and are recorded in succeeding columns 6 and 8 of the Table. The $P_{v'v''}$'s and β's under Morse potential needed for comparison, are those of Sreedhar Murthy [21]. These are reproduced in columns 4 and 7, respectively, of the

Table VI

Comparison of I/ν^4 values with smoothed Condon factors $P_{v'v''}$

Band	I/ν^4	$P_{v'v''}$ (Nicholls & Jarmain)		$P_{v'v''}$ (Regression) RKR	Ratio $\beta=(I/\nu^4/P_{v'v''})$ (Nicholls & Jarmain)		Ratio $\beta=(I/\nu^4/P_{v'v''})$ (Regression) RKR
		RKR (Authors)	Morse (Sreedhar Murthy)		RKR (Authors)	Morse (Sreedhar Murthy)	
(0, 0)	1	1	1	1	1	1	1
(0, 1)	0.24	0.22	0.23	0.22	1.09	1.04	1.09
(0, 2)	0.009	0.014	0.015	0.010	0.64	0.60	0.90
(1, 0)	1	1	1	1	1	1	1
(1, 1)	20.76	19.22	19.77	23.00	1.08	1.05	0.90
(1, 2)	10.45	9.80	9.84	10.90	1.06	1.07	0.96
(1, 3)	0.49	0.96	0.97	0.98	0.51	0.51	0.50
(2, 1)	1	1	1	1	1	1	1
(2, 2)	11.81	8.45	9.87	9.74	1.40	1.20	1.21
(2, 3)	8.11	7.30	7.88	7.76	1.11	1.03	1.05
(2, 4)	0.44	1.03	0.97	0.64	0.43	0.45	0.69
(3, 2)	1	1	1	1	1	1	1
(3, 3)	7.80	5.99	6.69	6.86	1.30	1.17	1.14
(3, 4)	7.59	7.59	7.53	7.87	1.00	1.01	0.96
(3, 5)	0.80	1.17	0.98	0.95	0.68	0.82	0.84

same Table. All such values for the ratio β both under the method of Nicholls and Jarmain and under regression procedure are normalised on the basis of unity for the first band in each v'' progression of the system.

From Table VI it is clear that when comparison is made between RKR and Morse data for values of ratio β, smoothening by $R_e(r)$ relation of quadratic fitting has improved the β values, tending them more towards unity than the same effected by using the method of Turner and Nicholls. But as far as the methods of evaluating $R_e(r)$ variation are concerned, the regression method is the better of the two, as can be seen from a comparison of values under column 8 with those under columns 6 and 7 of Table VI. This conclusion certainly leads us to claim the superiority of regression method over the method of Turner and Nicholls. However, here, any conclusion regarding the suitability of one potential over the other may not be in order.

6. Vibrational temperature

Using the available data of integrated intensity measures of bands of the system as also the FC factors and $P_{v'v''}$ values on the basis of RKR potential, the theoretical estimates of temperature of excitation under constancy of R_e and under its variation with r, have been made by an application of a method treated in Herzberg [34]. The exact formula for intensity in emission is

$$\log_e \sum_{v''} \left(\frac{I_{em}^{nm}}{v^4} \right) = C_1 - \frac{G'(v')hc}{kT}, \tag{9}$$

where C_1 = a constant, $G(v)$ = vibrational quanta, k = Boltzmann constant, c = velocity of light, h = Planck's constant, T = absolute temperature, v = frequency of the band, I_{em} = intensity in emission.

This has been made use of in determining the effective vibrational temperature of the source. In the case of temperature determination under variation of R_e with r, Eq. (6) has been used. The values thus obtained are entered in columns 2 and 3 of Table VII. For comparing these temperature values under RKR potential with those under Morse potential, the latter data from the work of Sreedhar Murthy [21], both with constancy of R_e as well as its variation with r, have been used. The same are reproduced in columns 2 and 3 of the Table VII next to RKR temperature values.

It is seen from Table VII that our present derivation of temperature values under RKR potential shows almost the same trend as Sreedhar Murthy's results with Morse potential. The trend is that the temperature derived with R_e as constant changes to a lower value with R_e taken as a variable with r. Sreedhar Murthy has concluded from his own results and from the earlier ones of Lagerqvist [40], Coheur and Coheur [41] and Tawde and Hussain [20] that there is optimum temperature of the order of 4000 K for the system of BeO. Since the results of temperature derived from our present investigation on BeO are of the same order of magnitude, particularly under R_e as

Table VII

Derived vibrational temperatures

Potential	with R_e – constant T	with $R_e(r)$ – variable T
RKR (Authors)	4882 K	4027 K
Morse (Sreedhar Murthy)	4840 K	4000 K

variable with r, they can be said to support the conclusion of Sreedhar Murthy. From these observations it follows that for the theoretical temperature estimate, one has to take into account the variation of R_e with r in the case of the present system of BeO. At the same time, no conclusion regarding the suitability of one potential over the other can be drawn, as the temperature estimates made either under constant R_e or variable R_e, come out almost to be the same for both RKR and Morse potential.

7. Discussion

From the deviations noticed between r_{min} and r_{max} of RKR and Morse potentials, as also the deviations between experimental and calculated α_e values and of B_v values in Tables I, III and IV, respectively, one can conclude that the ground state ($X'\Sigma$) of the present BeO band system under investigation can reasonably be represented by Morse potential, whereas the upper state ($B'\Sigma$) of the same band system cannot be so represented, as the deviation of the Morse potential curves from those of RKR is appreciable even for low vibrational quantum numbers (see Fig. 1). Of the two potentials RKR and Morse, the former is the realistic one in the sense that it is built on experimental data. Hence the FC factors evaluated by using the RKR potential would be realistic, since in the evaluation of the factors, both the ground and upper states are involved. The deviations of Morse potential from RKR which have been found to result by applying the various tests will necessarily make the results derived from it erroneous. This conclusion supports the earlier findings of Tulasigeri [23] and of Tawde and Tulasigeri [32, 33, 42]. Regarding the suitability of RKR potential for the present band system, it is obvious that as far as the evaluation of FC factors is concerned, the RKR potential is better suited than Morse.

Now as regards the $R_e(r)$ relation obtained here, mention should be made of the self-absorption effect. According to Linton and Nicholls [43], the experimental measures of intensities are required to be corrected for self-absorption especially in the case of high temperature source, as neglect of this effect would lead to erroneous expression for $R_e(r)$. In the present study of the band system of BeO ($B'\Sigma - X'\Sigma$), the

intensity values are those of Sreedhar Murthy which have not been corrected for self-absorption. Leaving this aspect apart, however, and keeping in view only the objective of relative efficacy of RKR and Morse potentials, taking or not taking into account the self-absorption effect, does not result in any change in the $R_e(r)$ relation as the deviation of it is independent of this effect. Now looking at the derived $R_e(r)$ expressions, one could find that they are more or less the same for both the potentials. This lends support to our earlier conclusion and holds good in so far as the study presented here of the two potentials and of the band system is concerned. Further it supports the point made out above regarding the better suitability of RKR potential than Morse.

In the evaluation of the FC factors, one has to take into account the vibration-rotation interaction. If one neglects this, it will certainly affect the FC factors, but not significantly as evident from the results of Drake, Tyte and Nicholls [44]. These authors have applied the vibration-rotation interaction correction to the case of the present BeO band system and have come to the conclusion that this interaction does not cause any significant change in the values of FC factors. Again, this finding lends further support to the case made out above regarding the preference for RKR potential over Morse's.

The next point that now remains to be examined is the role of $R_e(r)$ derivations on the theoretically computed vibrational temperatures. From the results of derived vibrational temperatures recorded in Table VII, it is seen that the values as obtained here under RKR potential almost coincide in magnitude with Sreedhar Murthy's Morse potential values, either with $R_e(r)$ as constant or with $R_e(r)$ as variable. Yet in spite of this agreement, when we consider the comparative closeness of approach of the two temperatures, viz. one with $R_e(r)$ as variable and the other $R_e(r)$ as constant to the true temperature of the source emitting the bands, it is found that the one with the inclusion of $R_e(r)$ as variable, under both RKR and Morse potentials, tends towards the true temperature. As against this the temperatures derived under the constancy of R_e are far above the true temperature. The conclusion is in conformity with the expectation that the $R_e(r)$ variation has to be taken into account in obtaining the measures of vibrational temperature values.

The general outcome of all this evidence from temperature results is that one cannot say with certainty that the RKR potential is better suited than the Morse potential, whereas actually it should have yielded better results than the Morse potential. This point needs close scrutiny — this is made in the discussion that follows.

A glance at the results of $R_e(r)$ relations and vibrational temperatures reveals that both these potentials yield almost the same results. However, in this context, a word about the very method involved in the derivation of $R_e(r)$ relation and the vibrational temperature will be in order. In the derivation of $R_e(r)$ relation, the usual rescaling method of Turner and Nicholls and the method of regression due to Cunio and Jansson, are used. Of these two methods, it is the latter one, i.e. the method of regression that has yielded a truer expression for $R_e(r)$ than the method of Turner and Nicholls.

This is verifiable from the values of the ratio $\beta\left(=\frac{I/\nu^4}{P_{v'v''}}\right)$ of Table VI. The β-values calculated by using the rescaling procedure of Turner and Nicholls for both RKR and Morse potentials are almost the same. Although there is an improvement of $R_e(r)$ relation by the method of regression, a point favouring RKR potential, this alone is not enough to draw a definite conclusion regarding the relative merits of the two potentials.

From the standpoint of experimental study made of the present band system, it is evident that the overlapping of the bands being very small, much better accuracy is expected in the resultant intensity measures of bands. It is evident therefore that the $R_e(r)$ equation derived for this system of BeO with the use of results under RKR potential is more accurate than the corresponding $R_e(r)$ derived under Morse potential. But so far as the temperature results are concerned, nothing definite can be said about the preference for one potential over the other, as there is no significant difference between the two sets of temperature values corresponding to these potentials, as can be seen from Table VII.

References

1. S. N. Thakur and R. B. Singh, J. Sci. Res. Banaras Hindu (India), *18*, 253, 1967.
2. M.Yoshimine, J. Phys. Soc. Japan, *25*, 1100, 1968.
3. H. F. Schaefer III, J. Chem. Phys., *55*, 176, 1971.
4. H. R. Liszt and W. H. Smith, JQSRT, *11*, 1043, 1971.
5. S. V. O'Neil, P. K. Pearson and H. F. Schaefer, Chem. Phys. Lett., *10*, 404, 1971.
6. B. Rai and S. N. Rai, Indian J. Pure Appl. Phys., *10*, 401, 1972.
7. P. K. Pearson, S. V. O'Neil and H. F. Schaefer, J. Chem. Phys., *56*, 3938, 1972.
8. G. A. Capelle, S. E. Johnson and N. P. Broida, J. Chem. Phys., *56*, 6264, 1972.
9. N. Sreedhar Murthy and U. D. Prahllad, J. Phys. B. Atom. Molec. Phys., *11*, 825, 1978.
10. C. W. Bauschlicher Jr. and D. R. Yarkony, J. Chem. Phys., *72*, 1138, 1980.
11. C. W. Bauschlicher Jr., B. H. Lengsfield and D. R. Yarkony, J. Chem. Phys., *73*, 5702, 1980.
12. Y. Yoshioka and K. D. Jordan, J. Chem. Phys., *73*, 5889, 1980.
13. Y. Yoshioka and K. D. Jordan, Chem. Phys., *56*, 303, 1981.
14. C. W. Bauschlicher Jr., P. S. Bagus, D. R. Yarkony and B. H. Lengsfield, J. Chem. Phys., *74*, 3965, 1981.
15. D. N. Davis, Ap. J., *106*, 28, 1947.
16. R. C. Johnson and E. G. Dunstan, Phil. Mag., *16*, 472, 1933.
17. R. S. Richardson, Ap. J., *73*, 216, 1931.
18. P. Swings, J. Opt. Soc. Am., *41*, 153, 1951.
19. Mckeller, Pub. Dom. Astrophys. Obs., *7*, 361, 1948.
20. N. R. Tawde and A. G. Hussain, Bom. Univ. Jour., *17*, 12, 1949.
21. N. Sreedhar Murthy. Thesis, Karnatak Univ., Dharwad, 1958.
22. R. W. Nicholls and W. R. Jarmain, Proc. Phys. Soc., *69A*, 253, 1956.
23. V. G. Tulasigeri, Thesis, Karnatak Univ., Dharwad, 1972.
24. R. G. Turner and R. W. Nicholls, Can. J. Phys., *32*, 475, 1954.
25. B. E. Cunio and R. E. Jansson, JQSRT, *8*, 1963, 1968.
26. R. N. Zare, E. O. Larsson and B. A. Berg, J. Mol. Spectry, *15*, 117, 1965.
27. P. M. Morse, Phys. Rev., *34*, 57, 1929.
28. A. Sharma, JQSRT, *7*, 283 and 289, 1967.
29. R. Rydberg, Z. Phys., *73*, 376, 1931.
30. O. Klein, Z. Phys., *76*, 226, 1932.

31. A. L. G. Rees, Proc. Phys. Soc., *A59*, 998, 1947.
32. N. R. Tawde and V. G. Tulasigeri, J. Phys. B, Atom. Molec. Phys., *5*, 1681, 1972.
33. N. R. Tawde and V. G. Tulasigeri, Acta Phys. Hung., *38*, 299, 1975.
34. G. Herzberg, Molecular Spectra and Molecular Structure, I, 2nd Ed., D. Van Nostrand Company, Inc. New York, 1950.
35. C. L. Pekeris, Phys. Rev., *45*, 98, 1934.
36. W. R. Jarmain, Can. J. Phys., *38*, 217, 1960; *41*, 414, 1963.
37. A. Lagerqvist and R. Westoo, Ark. f. Mat. Astr. Phys., Bd *32A*, No. 5, 1945.
38. M. Shimauchi, Science of Light, *7*, 101, 1958.
39. M. Becart and J. M. Mahieu, Comp. Rend., *256*, 5533, 1963.
40. A. Lagerqvist, Dissertation, Stockholm, p. 27, 1948.
41. F. P. Coheur and P. M. Coheur, Phys. Rev., *69*, 240, 1946.
42. N. R. Tawde and V. G. Tulasigeri, Acta Phys. Hung., *50*, 103, 1981.
43. C. Linton and R. W. Nicholls, JQSRT, *9*, 1, 1969.
44. G. W. F. Drake, D. C. Tyte and R. W. Nicholls, JQSRT, *7*, 639, 1967.

Acta Physica Hungarica 60 (1—2), pp. 127—134 (1986)

MKN OSCILLATOR MODEL, FRANCK–CONDON FACTORS AND *r*-CENTROIDS FOR $A^2\Pi - X^2\Sigma$ TRANSITION OF BO MOLECULE

B. S. NAVATI and V. M. KORWAR

Department of Physics, Karnatak University
Dharwad-580 003, India

(Received in revised form 2 October 1984)

Efficacy of the recently proposed MKN oscillator model has been tested by taking a number of electronic states of diatomic molecules. For comparison, the Morse function is also processed. The authors' approximation method and Langer's approximation method are used to find wave functions. FC factors and *r*-centroids are reported for the observed bands of $A^2\Pi - X^2\Sigma$ transition of the BO molecule.

1. Introduction

Recently, we [1] have proposed a new approximation method for solving the Schrödinger wave equation for the vibrating diatomic molecule whose potential energy varies in accordance with the recently proposed MKN oscillator model (Morse–Korwar–Navati oscillator model). In the same paper the applicability of the MKN model and the validity of approximation method to determine the wave functions have been tested, taking a number of electronic states of diatomic molecules.

In the present paper, we have tried to explore the possibility of applying the MKN model to the $X^2\Sigma$, $A^2\Sigma$ states of AlO; $X^1\Sigma$, $A^1\Sigma$ states of BaO; $X^2\Sigma$, $A^2\Pi$ states of BO and $X^2\Pi$, $B^2\Sigma$ states of the SiCl molecule. The new approximation method has been put to test by applying it to the $A^2\Pi \rightarrow X^2\Sigma$ transition of BO molecule. We have also evaluated the eigenfunctions by yet another method known as Langer's [2] approximation method, with a view to comparing the performance of the two methods. Franck–Condon factors (FC factors) and *r*-centroids obtained by using the wave functions, computed by both the methods and their comparison with realistic RKR and RKRV results decide the relative merits of the methods.

2. MKN potential energy function

The one dimensional vibrational time independent Schrödinger wave equation is written as

$$\frac{d^2\psi^v}{dr^2} + \frac{2\mu}{\hbar^2}[E_v - U(r)]\psi^v = 0\,. \tag{1}$$

Quantities in the equation carry their usual meaning. $U(r)$ in the above equation is the five parameter MKN oscillator model, having the following form

$$U(r)=D_e[1-\exp\{-\alpha(r)(r-r_e)\}]^2, \tag{2.1}$$

where

$$\alpha(r)=\alpha\exp\left[b\left\{\left(\frac{r_e}{r}\right)^2-1\right\}+a\left\{\frac{r_e}{r}-1\right\}\right]. \tag{2.2}$$

Explicit expressions which determine the parameters of the oscillator model are given in our paper [1]. The MKN function reduces to the simple Morse function [3] when parameters a and b in Eq. (2.2) are zero.

A more significant test of the MKN function and Morse function lies in the comparison of $U(r_{\min})$ and $U(r_{\max})$ values of particular vibrational states computed on these models with the observed vibrational energies of these states. $r_{\max}$, $r_{\min}$ values required for this purpose are computed by the well known realistic RKR procedure. The results of these computations are reported in the Tables Ia, Ib, Ic and Id. The data employed in the present calculations are taken from Mummigatti et al [4] for $X^2\Sigma$ AlO, $A^2\Sigma$ AlO, $X^2\Sigma$ BO, $A^2\Pi$ BO states. Constants reported in Robert [5] are used for $X^1\Sigma$ and $A^1\Sigma$ states of BaO. For the constants of $X^2\Pi_r$ and $B^2\Sigma$ states of SiCl, values of Bredohl et al [6] have been taken.

3. Wave functions, FC factors and r-centroids

3.1 Authors' method

A new approximation method to obtain vibration eigenfunctions suitable for the MKN oscillator model has been described in detail by Navati and Korwar [1], however, the final expression for un-normalized wave function of vibrational quantum number v at $r=r_j$, under the suggested approximation is given below:

$$\Phi^v(r=r_j)=\Phi^v_{1j}(r=r_j)=\exp\left(\frac{-Z_j}{2}\right)Z_j^{1/2(K-2v-1)}\left/\begin{matrix}K-2v-1\\(Z_j)\\K-v-1\end{matrix}\right., \tag{3.1}$$

where

$$Z_j=K\exp\{-\alpha_j(r_j-r_e)\}\,; \qquad K=\frac{W_e}{W_eX_e}, \tag{3.2}$$

$$\left/\begin{matrix}K-2v-1\\(Z_j)\\K-v-1\end{matrix}\right. =(-1)^v\sum_{l=0}^{v}(-1)^l\binom{v}{l}\frac{\Gamma(K-v)}{\Gamma(K-v-l)}Z_j^{v-l}. \tag{3.3}$$

Table Ia

Vibrational energies in Joules/molecule

U(obs)	Present work		v	Present work		U(obs)
	$U(r_{min})$	$U(r_{max})$		$U(r_{min})$	$U(r_{max})$	
	$X^2\Sigma$ AlO			$A^2\Sigma$ AlO		
$*(10^{-23})$	$*(10^{-23})$	$*(10^{-23})$		$*(10^{-23})$	$*(10^{-23})$	$*(10^{-23})$
968.69	977.72	961.61	0	869.75	855.73	862.01
	977.56	961.73		857.10	866.10	
2885.31	2903.34	2873.50	1	2589.01	2566.15	2575.51
	2902.44	2874.02		2520.54	2616.03	
4774.26	4801.53	4758.57	2	4290.86	4265.18	4274.99
	4799.49	4759.56		4139.87	4366.17	
6635.52	6674.70	6615.30	3	5976.00	5951.84	5960.46
	6671.21	6616.77		5721.52	6110.33	
8469.11	8523.84	8443.44	4	7643.46	7626.38	7631.90
	8518.62	8445.37		7267.79	7846.22	
10275.01	10350.27	10242.61	5	9293.57	9288.30	9289.33
	10343.13	10244.97		8781.11	9571.71	
12053.25	12154.92	12012.83	6	10922.97	10938.99	10932.75
	12145.52	12015.58		10260.12	11287.14	
13803.80	13938.58	13754.08	7	12539.19	12574.69	12562.14
	13926.74	13757.16		11713.01	12987.77	
15526.67	15702.51	15466.24	8	14133.15	14199.10	14177.52
	15688.72	15469.60		13133.35	14676.87	
17221.86	17447.43	17149.42	9	15709.34	15810.92	15778.87
	17430.16	17153.01		14524.34	16352.52	
18889.38	19174.50	18803.62	10	17265.31	17410.07	17366.21
	19154.23	18807.37		15886.53	18014.28	

* The quantity in the bracket at the top of each column indicates the factor by which entries in the respective columns are to be multiplied to get U in Joules/molecule.

Upper values correspond to MKN potential and lower values are due to Morse potential.

Table Ib

Vibrational energies in Joules/molecule

U(obs)	Present work		v	Present work		U(obs)
	$U(r_{min})$	$U(r_{max})$		$U(r_{min})$	$U(r_{max})$	
	$X^1\Sigma$ BaO			$A^1\Sigma$ BaO		
$*(10^{-23})$	$*(10^{-23})$	$*(10^{-23})$		$*(10^{-23})$	$*(10^{-23})$	$*(10^{-23})$
663.95	663.84	664.03	0	495.21	495.33	495.27
	663.22	664.57		498.38	492.63	
1985.73	1985.83	1985.64	1	1481.14	1480.78	1480.93
	1982.42	1988.22		1498.52	1467.72	
3299.35	3299.76	3299.07	2	2460.96	2459.50	2460.08
	3292.20	3304.34		2499.61	2432.81	
4604.81	4605.98	4604.11	3	3434.96	3431.31	3432.72
	4593.16	4612.45		3500.66	3388.99	
5902.12	5904.51	5900.77	4	4403.37	4396.12	4398.84
	5885.47	5912.43		4501.21	4336.82	
7191.27	7195.26	7189.12	5	5366.11	5354.09	5358.56
	7169.12	7204.31		5500.75	5276.82	
8472.27	8478.46	8469.08	6	6323.44	6305.08	6311.56
	8444.27	8487.90		6499.24	6209.17	
9745.11	9754.22	9740.60	7	7275.49	7249.06	7258.14
	9711.53	9763.15		7496.57	7134.30	
11009.79	11022.56	11003.70	8	8222.27	8186.13	8198.21
	10970.51	11030.02		8492.55	8051.65	
12266.31	12283.59	12258.39	9	9164.09	9116.14	9131.78
	12221.49	12288.51		9487.34	8962.03	
13514.68	13537.21	13504.72	10	10100.91	10039.19	10058.82
	13464.42	13538.66		10480.75	9865.36	

* The quantity in the bracket at the top of each column indicates the factor by which entries in the respective columns are to be multiplied to get U in Joules/molecule.

Upper values correspond to MKN potential and lower values are due to Morse potential.

Table Ic

Vibrational energies in Joules/molecule

U(obs)	Present work		v	Present work		U(obs)
	$U(r_{min})$	$U(r_{max})$		$U(r_{min})$	$U(r_{max})$	
	$X^2\Sigma$ BO			$A^2\Pi$ BO		
*(10^{-23})	*(10^{-23})	*(10^{-23})		*(10^{-23})	*(10^{-23})	*(10^{-23})
1866.19	1868.73	1864.18	0	1250.10	1243.02	1246.05
	1862.55	1869.09		1233.30	1255.83	
5563.41	5568.65	5559.98	1	3711.33	3701.25	3704.92
	5534.52	5582.95		3618.77	3759.44	
9213.73	9222.81	9208.59	2	6124.22	6117.81	6119.47
	9146.70	9254.15		5918.96	6230.18	
12817.14	12831.95	12809.70	3	8488.55	8492.17	8489.73
	12702.60	12879.95		8142.17	8660.94	
16373.66	16396.52	16363.27	4	10803.91	10824.16	10815.67
	16204.11	16459.11		10293.04	11048.42	
19883.28	19917.71	19868.88	5	13070.04	13113.56	13097.32
	19653.70	19990.50		12374.92	13390.60	
23346.00	23395.75	23326.72	6	15285.46	15360.64	15334.66
	23052.17	23473.83		14389.35	15686.63	
26761.83	26831.32	26736.75	7	17435.45	17564.92	17527.69
	26400.97	26908.70		16339.32	17935.28	
30130.75	30238.99	30098.84	8	19565.52	19726.32	19676.42
	29701.26	30294.75		18226.46	20136.03	
33452.78	33577.73	33413.12	9	21630.15	21844.51	21780.84
	32954.13	33631.90		20053.06	22288.29	
36727.91	36889.99	36679.49	10	23644.40	23919.42	23840.95
	36160.89	36919.92		21820.56	24391.83	

* The quantity in the bracket at the top of each column indicates the factor by which entries in the respective columns are to be multiplied to get U in Joules/molecule.

Upper values correspond to MKN potential and lower values are due to Morse potential.

Table Id

Vibrational energies in Joules/molecule

U(obs)	Present work		v	Present work		U(obs)
	$U(r_{min})$	$U(r_{max})$		$U(r_{min})$	$U(r_{max})$	
	$X^2\Pi$ SiCl			$A^2\Sigma$ SiCl		
*(10^{-23})	*(10^{-23})	*(10^{-23})		*(10^{-23})	*(10^{-23})	*(10^{-23})
530.54	530.39	530.66	0	699.56	699.65	699.61
	525.80	534.51		707.12	693.56	
1585.18	1584.85	1586.49	1	2088.37	2086.34	2087.20
	1559.79	1603.88		2130.20	2057.65	
2631.26	2630.38	2631.93	2	3464.19	3456.02	3459.28
	2574.94	2669.14		3557.80	3398.73	
3668.78	3666.88	3670.13	3	4828.01	4808.34	4815.84
	3573.20	3728.44		4987.76	4717.64	
4697.69	4694.29	4700.07	4	6180.48	6143.25	6156.89
	4555.63	4780.85		6419.10	6021.39	
5718.04	5712.55	5721.74	5	7522.71	7460.45	7482.42
	5522.94	5825.76		7851.91	7304.80	
6729.82	6721.39	6735.26	6	8854.84	8760.19	8792.43
	6475.45	6862.87		9285.59	8571.28	
7733.02	7721.09	7740.47	7	10178.17	10042.16	10086.93
	7413.89	7891.73		10720.91	9820.29	
8727.66	8711.30	8737.51	8	11620.95	11429.15	11490.04
	8338.32	8912.24		12298.08	11172.14	
9713.72	9692.02	9726.35	9	12800.19	12553.25	12629.39
	9249.11	9924.19		13596.51	12268.39	
10691.20	10663.39	10706.90	10	14100.34	13782.37	13877.34
	10146.66	10927.34		15037.71	13467.94	

* The quantity in the bracket at the top of each column indicates the factor by which entries in the respective columns are to be multiplied to get U in Joules/molecule.

Upper values correspond to MKN potential and lower values are due to Morse potential.

Table II

$A^2\Pi - X^2\Sigma$ transition of the BO molecule

Band $v'-v''$	Franck–Condon factors $q_{v'v''}$				r-centroids, $\bar{r}_{v'v''} \times 10^{10}$			
	RKR	MKN Present work		RKRV	RKR	MKN Present work		RKRV
		Authors' approximation	Langer			Authors' approximation	Langer	
0–0	0.036	0.035	0.036	0.036	1.276	1.276	1.275	1.274
0–1	0.133	0.132	0.136	0.133	1.302	1.303	1.302	1.303
0–2	0.228	0.228	0.235	0.226	1.330	1.329	1.329	1.331
0–3	0.245	0.238	0.259	–	1.358	1.357	1.357	–
0–4	0.185	0.189	0.201	0.183	1.387	1.385	1.385	1.385
0–5	0.104	0.113	0.119	–	1.416	1.412	1.414	–
1–0	0.101	0.101	0.105	0.107	1.258	1.258	1.258	1.256
1–1	0.187	0.194	0.200	0.188	1.284	1.283	1.283	1.282
1–2	0.099	0.103	0.108	0.096	1.310	1.309	1.309	1.311
1–3	0.016	0.016	0.003	–	1.325	1.325	1.329	–
1–4	0.059	0.058	0.052	–	1.369	1.368	1.368	–
1–5	0.158	0.156	0.161	–	1.397	1.400	1.406	–
2–0	0.155	0.151	0.166	0.164	1.241	1.241	1.239	1.237
2–1	0.111	0.120	0.121	0.108	1.265	1.265	1.265	1.265
2–3	0.104	0.085	0.092	0.088	1.321	1.319	1.320	1.321
2–4	0.128	0.106	0.116	0.101	1.347	1.346	1.346	1.345

Here α_j is the value of $\alpha(r)$ determined by Eq. (2.2) at $r = r_j$. The un-normalized wave functions have been evaluated at intervals of 0.001 nm of r, the internuclear distance. Normalized wave functions ψ^v are then calculated using the expression for Φ^v and the normalizing factor determined by applying the normalization condition.

3.2 Langer's method

Langer's approximation method suggested by Langer [2] to find ψ^v has been recently reviewed and applied by Patil et al [7]. Using the potential function as in Eq. (2.1) the Schrödinger wave equation (1) for vibrating BO molecule has been solved by this approximation method.

Vibration wave functions, computed using both the methods, for $v'' = 0, 1, 2, 3, 4, 5$ of $X^2\Sigma$ and $v' = 0, 1, 2$ of $A^2\Pi$ state of BO have been employed to calculate the FC factors $q_{v'v''}$ and r-centroids $\bar{r}_{v'v''}$ for the $A^2\Pi - X^2\Sigma$ transition of the BO molecule. The results obtained are recorded in Table II. For comparison RKR values of Liszt et al [8] and RKRV values of Mummigatti et al [9] are also entered in the same Table up to three decimal places.

4. Conclusion

Critical examination of Tables Ia to Id reveals that the MKN function, being more flexible, predicts the $U(r_{min})$ and $U(r_{max})$ values fairly well, whereas the simple Morse function results deviate from the observed values to the greater extent, thus proving its validity only at low quantum numbers. Percentage deviation of the factor $[U(\text{MKN}) - U(\text{obs})]$ throughout the range of r values varies from

0.30% to 1.5% in $X^2\Sigma$ AlO, 0.01% to 0.90% in $A^2\Sigma$ AlO,
0.004% to 0.17% in $X^1\Sigma$ BaO, 0.01% to 0.42% in $A^1\Sigma$ BaO,
0.06% to 0.44% in $X^2\Sigma$ BO, 0.014% to 0.82% in $A^2\Pi$ BO,
0.02% to 0.26% in $X^2\Pi$ SiCl, 0.01% to 1.61% in $B^2\Sigma$ SiCl.

The Tables of data clearly indicate the superiority of the MKN function over the simple Morse function whose flexibility is limited. To decide the relative merit of the two approximation methods RKR and RKRV FC factors are compared with FC factors obtained by using wave functions of both the approximation methods. FC factors computed with the use of wave functions obtained by the authors' method compare better with RKR and RKRV results than do the results based on Langer's approximation method. Therefore, we assert that the authors' method yields better results than does Langer's. Another point in favour of the authors' method is that it is very simple and yields results comparable with RKR results.

As expected, r-centroids computed using both the methods agree with RKR results very closely. This is due to the fact that r-centroids are not so sensitive as FC factors are to the potentials and to the approximation methods. In conclusion, we add that for $A^2\Pi - X^2\Sigma$ transition of BO the authors' approximation method is more reliable than Langer's method.

References

1. B. S. Navati and V. M. Korwar, Pramana, *20*, 457, 1983; *23*, 833, 1984.
2. R. E. Langer, Phys. Rev., *75*, 1573, 1949.
3. P. M. Morse, Phys. Rev., *34*, 57, 1929.
4. V. M. Mummigatti, Astrophysically Significant Molecules, Ph. D. Thesis, Karnatak University, Dharwad, 1982.
5. Robert W. Field, J. Chem. Phys., *60*, 2400, 1974.
6. H. Bredohl, Ph. Demoulin, Y. Houbrechts and F. Melen J. Phys. B. At. Mol. Phys., *14*, 1771, 1981.
7. D. C. Patil and V. M. Korwar, Acta Phys. Hung., *43*, 203, 1977.
8. H. S. Liszt and W. M. Hayden Smith, JQSRT, *11*, 1043, 1971.
9. V. M. Mummigatti and B. G. Jyoti, Curr. Sci., *46*, 412, 1977.

Acta Biochimica et Biophysica

Academiae Scientiarum Hungaricae

Editors:
F. B. Straub
and J. Tigyi

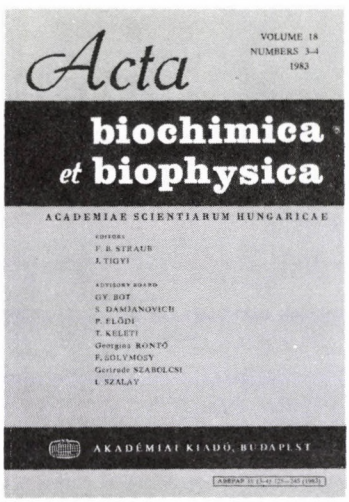

The journal publishes original papers on biochemistry and biophysics. Its main topics are: proteins (structure and synthesis), enzymes, nucleic acids, regulatory and transport processes, bioenergetics, excitation, muscular contraction, radiobiology, biocybernetics, functional structure and ultrastructure. Book reviews are also presented.

Founded 1965
Papers in English
Publication: one volume of four issues annually
Price per volume: $44.00; DM 99,—
Size: 17 × 25 cm
ISSN 0001–5253

Order form
to be returned to
KULTURA
Hungarian Foreign Trading Company
P.O. Box 149, H-1389 Budapest, Hungary

☐ Please enter my/our subscription for
ACTA BIOCHIMICA ET BIOPHYSICA for one year

☐ Please enter my/our standing order for
ACTA BIOCHIMICA ET BIOPHYSICA starting with

Name: _____

Address: _____

Date and signature: _____

Contents of Volume 17. Numbers 3–4

1828

Akadémiai Kiadó

Publishing House
of the Hungarian Academy of Sciences
Budapest

Invitation for papers

Manuscripts should be sent to
M. Sajgó
University of Agriculture
2103 Gödöllő, Hungary (biochemistry)
A. Niedetzky
P.O. Box 99
7643 Pécs
Hungary (biophysics)

NOTES TO CONTRIBUTORS

I. PAPERS will be considered for publication in Acta Physica Hungarica only if they have not previously been published or submitted for publication elsewhere. They may be written in English, French, German or Russian.

Papers should be submitted to

Prof. I. Kovács, Editor
Department of Atomic Physics, Technical University
1521 Budapest, Budafoki út 8, Hungary

Papers may be either articles with abstracts or short communications. Both should be as concise as possible, articles in general not exceeding 25 typed pages, short communications 8 typed pages.

II. MANUSCRIPTS

1. Papers should be submitted in three copies.
2. The text of papers must be of high stylistic standard, requiring minor corrections only.
3. Manuscripts should be typed in double spacing on good quality paper, with generous margins.
4. The name of the author(s) and of the institutes where the work was carried out should appear on the first page of the manuscript.
5. Particular care should be taken with mathematical expressions. The following should be clearly distinguished, e.g. by underlining in different colours: special founts (italics, script, bold type, Greek, Gothic, etc.); capital and small letters; subscripts and superscripts, e.g. x^2, x_3; small *l* and l; zero and capital O; in expressions written by hand: *e* and *l*, *n* and *u*, *v* and v, etc.

A List of Symbols on a separate sheet should be attached to each paper.

6. References should be numbered serially and listed at the end of the paper in the following form: J. Ise and W. D. Fretter, Phys. Rev., *76,* 933, 1949.

For books, please give the initials and family name of the author(s), title, name of publisher, place and year of publication, e.g.: J. C. Slater, Quantum Theory of Atomic Structures, I. McGraw-Hill Book Company, Inc., New York, 1960.

References should be given in the text in the following forms: Heisenberg [5] or [5].

7. Captions to illustrations should be listed on a separate sheet, not inserted in the text.
8. In papers submitted to Acta Physica all measures should be expressed in SI units.

III. ILLUSTRATIONS AND TABLES

1. Each paper should be accompanied by three sets of illustrations, one of which must be ready for the blockmaker. The other sets attached to the copies of the manuscript may be rough drawings in pencil or photocopies.
2. Illustrations must not be inserted in the text.
3. All illustrations should be identified in blue pencil by the author's name, abbreviated title of the paper and figure number.
4. Tables should be typed on separate pages and have captions describing their content. Clear wording of column heads is advisable. Tables should be numbered in Roman numerals (I, II, III, etc.).

IV. RETURN OF MATERIAL

Owing to high postage costs, the Editorial Office cannot undertake to return *all* material not accepted for any reason for publication. Of papers to be revised (for not being in conformity with the above Notes or other reasons) only *one* copy will be returned. Material rejected for lack of space or on account of the Referees' opinion will not be returned to authors outside Europe.

Periodicals of the Hungarian Academy of Sciences are obtainable at the following addresses:

AUSTRALIA
C.B.D. LIBRARY AND SUBSCRIPTION SERVICE
Box 4886, G.P.O., *Sydney N.S.W. 2001*
COSMOS BOOKSHOP, 145 Ackland Street
St. Kilda (Melbourne), Victoria 3182

AUSTRIA
GLOBUS, Höchstädtplatz 3, *1206 Wien XX*

BELGIUM
OFFICE INTERNATIONAL DE LIBRAIRIE
30 Avenue Marnix, *1050 Bruxelles*
LIBRAIRIE DU MONDE ENTIER
162 rue du Midi, *1000 Bruxelles*

BULGARIA
HEMUS, Bulvar Ruszki 6, *Sofia*

CANADA
PANNONIA BOOKS, P.O. Box 1017
Postal Station "B", *Toronto, Ontario M5T 2T8*

CHINA
CNPICOR, Periodical Department, P.O. Box 50
Peking

CZECHOSLOVAKIA
MAĎARSKÁ KULTURA, Národní třida 22
115 66 Praha
PNS DOVOZ TISKU, Vinohradská 46, *Praha 2*
PNS DOVOZ TLAČE, *Bratislava 2*

DENMARK
EJNAR MUNKSGAARD, Norregade 6
1165 Copenhagen K

FEDERAL REPUBLIC OF GERMANY
KUNST UND WISSEN ERICH BIEBER
Postfach 46, *7000 Stuttgart 1*

FINLAND
AKATEEMINEN KIRJAKAUPPA, P.O. Box 128 *SF- 00101 Helsinki 10*

FRANCE
DAWSON-FRANCE S. A., B. P. 40, *91121 Palaiseau*
EUROPÉRIODIQUES S. A., 31 Avenue de Versailles, *78170 La Celle St. Cloud*
OFFICE INTERNATIONAL DE DOCUMENTATION ET LIBRAIRIE, 48 rue Gay-Lussac
75240 Paris Cedex 05

GERMAN DEMOCRATIC REPUBLIC
HAUS DER UNGARISCHEN KULTUR
Karl Liebknecht-Straße 9, *DDR-102 Berlin*
DEUTSCHE POST ZEITUNGSVERTRIEBSAMT Straße der Pariser Kommüne 3–4, *DDR-104 Berlin*

GREAT BRITAIN
BLACKWELL'S PERIODICALS DIVISION
Hythe Bridge Street, *Oxford OX1 2ET*
BUMPUS, HALDANE AND MAXWELL LTD.
Cowper Works, *Olney, Bucks MK46 4BN*
COLLET'S HOLDINGS LTD., Denington Estate *Wellingborough, Northants NN8 2QT*
WM. DAWSON AND SONS LTD., Cannon House *Folkstone, Kent CT19 5EE*
H. K. LEWIS AND CO., 136 Gower Street
London WC1E 6BS

GREECE
KOSTARAKIS BROTHERS INTERNATIONAL BOOKSELLERS, 2 Hippokratous Street, *Athens-143*

HOLLAND
MEULENHOFF-BRUNA B. V., Beulingstraat 2,
Amsterdam
MARTINUS NIJHOFF B.V.
Lange Voorhout 9–11, *Den Haag*
SWETS SUBSCRIPTION SERVICE
347b Heereweg, *Lisse*

INDIA
ALLIED PUBLISHING PRIVATE LTD., 13/14
Asaf Ali Road, *New Delhi 110001*
150 B-6 Mount Road, *Madras 600002*
INTERNATIONAL BOOK HOUSE PVT. LTD.
Madame Cama Road, *Bombay 400039*
THE STATE TRADING CORPORATION OF INDIA LTD., Books Import Division, Chandralok 36 Janpath, *New Delhi 110001*

ITALY
INTERSCIENTIA, Via Mazzé 28, *10149 Torino*
LIBRERIA COMMISSIONARIA SANSONI, Via Lamarmora 45, *50121 Firenze*
SANTO VANASIA, Via M. Macchi 58
20124 Milano
D. E. A., Via Lima 28, *00198 Roma*

JAPAN
KINOKUNIYA BOOK-STORE CO. LTD.
17-7 Shinjuku 3 chome, Shinjuku-ku, *Tokyo 160-91*
MARUZEN COMPANY LTD., Book Department, P.O. Box 5050 Tokyo International, *Tokyo 100-31*
NAUKA LTD. IMPORT DEPARTMENT
2-30-19 Minami Ikebukuro, Toshima-ku, *Tokyo 171*

KOREA
CHULPANMUL, *Phenjan*

NORWAY
TANUM-TIDSKRIFT-SENTRALEN A.S., Karl Johansgatan 41–43, *1000 Oslo*

POLAND
WĘGIERSKI INSTYTUT KULTURY, Marszalkowska 80, *00-517 Warszawa*
CKP-I W, ul. Towarowa 28, *00-958 Warszawa*

ROUMANIA
D. E. P., *Bucuresti*
ILEXIM, Calea Grivitei 64–66, *Bucuresti*

SOVIET UNION
SOJUZPECHAT — IMPORT, *Moscow*
and the post offices in each town
MEZHDUNARODNAYA KNIGA, *Moscow G-200*

SPAIN
DIAZ DE SANTOS, Lagasca 95, *Madrid 6*

SWEDEN
GUMPERTS UNIVERSITETSBOKHANDEL AB
Box 346, *401 25 Göteborg 1*

SWITZERLAND
KARGER LIBRI AG, Petersgraben 31, *4011 Basel*

USA
EBSCO SUBSCRIPTION SERVICES
P.O. Box 1943, *Birmingham, Alabama 35201*
F. W. FAXON COMPANY, INC.
15 Southwest Park, *Westwood Mass. 02090*
READ-MORE PUBLICATIONS, INC.
140 Cedar Street, *New York, N. Y. 10006*

YUGOSLAVIA
JUGOSLOVENSKA KNJIGA, Terazije 27, *Beograd*
FORUM, Vojvode Mišića 1, *21000 Novi Sad*

Index: 26.022

Acta Physica Hungarica

VOLUME 60, NUMBERS 3–4, 1986

Akadémiai Kiadó, Budapest

ACTA PHYS HUNG. APAHAQ 60 (3–4) 135–346 (1986) HU ISSN 0231-4428

ACTA PHYSICA HUNGARICA

A JOURNAL OF THE HUNGARIAN ACADEMY OF SCIENCES

EDITED BY
I. KOVÁCS

Acta Physica publishes original papers on subjects in physics. Papers are accepted in English, French, German and Russian.

Acta Physica is published in two yearly volumes (4 issues each) by

AKADÉMIAI KIADÓ
Publishing House of the Hungarian Academy of Sciences
H-1054 Budapest, Alkotmány u. 21

Subscription information

Orders should be addressed to

KULTURA Foreign Trading Company
1389 Budapest P.O. Box 149

or to its representatives abroad.

Acta Physica is indexed in Current Contents, in Physics Abstracts and in Current Papers in Physics.

CENTRE FOR INTERNATIONAL WORKSHOPS IN THEORETICAL PHYSICS

The extensive international network of the theoretical physics research community has gained additional support when, in 1983, the new workshop centre of the Hungarian Academy of Sciences was inaugurated. Yielding to the increasing desire of theoreticians for an institutional framework for such meetings, the International Workshop for Theoretical Physics is now available for organizing activities in the currently developing "offspring" of theoretical physics.

This new international forum is supervised and sponsored by the Hungarian Academy of Sciences, and by its Central Research Institute for Physics, its purpose is to foster the exchange of information between researchers in Hungary and their counterparts abroad. The scientific activities are coordinated by the Scientific Council of the organization, headed by three co-chairmen one of whom acts as the executive chairman. Proposals for international workshops in theoretical physics can be made by any domestic research group, and these are presented to the Scientific Council.

The requisite infrastructure for workshop activities has been made available at the Central Research Institute of Physics whose director general, along with the head of the Department of Mathematical and Physical Sciences of the Academy has overall responsibility for the Workshop.

The new organization has evoked vigorous interest in the physics community. In the opening year (1983), three meetings were organized dealing with: collision of relativistic heavy ions, cometary models, and quantum-chromodynamics on a lattice, with a total of 42 foreign participants from various countries. The following year, the number of workshops under the auspices of the IWTP had grown to 6. Three of these were devoted to solids and statistical physics, the others related to tests of quantum chromodynamics, cosmology and neurophysics. The number of foreign participants totalled 51 from more than thirteen countries. Activities on a similar scale have countinued in 1985. Workshop titles include: few body systems, general relativity, chaotic phenomena, phase transitions, hadron structure, and microcomputing.

Up till now, the International Workshop has done more than justify the expectations: it has proved that leading experts from home and abroad are happy to take part. Not only these workshops have helped international activities in theoretical physics but they have also contributed to the recognition of physics research in Hungary as well as abroad. It has been suggested that the International Workshop should continue its activities adhering to what is now a proven course. The existence of this international forum challenges us, however, to think about future possibilities of action. New ideas concerning the extension of forms of cooperation would be welcomed.

With any enquiry please contact one of the three co-chairmen:

T. SIKLÓS (Executive Chairman)
Central Research Institute for Physics, Budapest
tel.: 699-499

K. NAGY
Roland Eötvös University, Budapest
tel.: 187-924

Z. PERJÉS
Central Research Institute for Physics, Budapest
tel.: 699-499

CONTENTS

FLUIDS, PLASMAS AND ELECTRIC DISCHARGES

CONDENSED MATTER

INTERDISCIPLINARY

Manuscript received by Akadémiai Kiadó: 17 May 1985
Manuscript received by the Printers: 12 June 1985
Date of publication: 5 November 1986

PRINTED IN HUNGARY

Akadémiai Kiadó és Nyomda, Budapest

Acta Physica Hungarica 60 (3—4), pp. 137—143 (1986)

EFFECTIVE CHARGE OF Kr AND Cu IONS AROUND 4 MeV PER NUCLEON*

M. I. W. LABOR**

Department of Physics, Polytechnic of the South Bank
London, SE1 OAA, England

(Received 12 July 1984)

The effective charges of Kr and Cu ions around 4 MeV per nucleon have been calculated from their experimental energy loss values in aluminium, nickel and gold. The effective charge results have been fitted to a universal curve whose expression assumes the Thomas–Fermi model of the atom. The final expression has been compared with other analytical expressions obtained for ions with energy between 1 and 10 MeV per nucleon.

1. Introduction

Heavy ions, as nuclear projectiles, play an increasingly prominent role in nuclear studies and their charge variation as they penetrate through matter has become important.

Heavy ions ($Z > 2$) cannot be regarded as charge invariant over a wide range of energy; as they are continually subject to charge–exchange processes. This effect is a function of the path traversed by the ions and is analogous to optical electronic transitions in atoms.

The effective charge, Z_{eff}, of an ion is defined as $Z_{\text{eff}} = \gamma Z$, where Z is the nuclear charge and γ a parameter with values given by $0 < \gamma < 1$.

The amount of published information on the theory of charge-exchange process is very limited and there is perhaps no comprehensive treatment of this effect which might furnish absolute values for γ.

An experimental method to determine γ is to find the ratio of the experimental stopping powers for the ion and for a reference ion of known charge (usually proton) at the same velocity in the same material, through the formula

$$\gamma_{\text{ion}}^2 = \frac{Z_p^2 \gamma_p^2 (dE/dx)_{\text{ion}}}{Z_{\text{ion}}^2 (dE/dx)_p} . \tag{1}$$

* Part of a Ph. D. Thesis

** Permanent address: Physics Department, Fourah Bay College, University of Sierra Leone, Sierra Leone

Proton is used as reference ion since its effective charge and stopping powers are well known.

Northcliffe [1] has obtained an empirical curve for the deviation of the effective charge and has represented the parameter γ_{ion} by the expression

$$\gamma_{ion}^2 = 1 - 1.85 \exp(-2V_r), \tag{2}$$

where V_r is the ratio of the ion velocity in the material to the orbital velocity of the electron in the ion. For ions with $Z_{ion} < 10$ the expression is valid for $V_r = 1.35\, E/Z_{ion}$. As the ion captures more electrons, the expression given for V_r above becomes inappropriate. Heckman [2] and Rosenblatt [3] have considered the velocity of the ion relative to the Thomas–Fermi velocity of the captured electron in the ion. They have shown that

$$V_r = \frac{137\beta}{Z_{ion}^{2/3}}$$

is a more suitable expression.

Booth et al [4] have obtained a universal curve for the charge variation of heavy ions with energy between 1 and 10 MeV per nucleon, by fitting their oxygen and chlorine results to an expression of the form

$$\gamma_{ion}^2 = \varepsilon Z_{ion}^{4/3},$$

where ε is the energy of the ion in MeV per nucleon. They observed that previous calculations for $\gamma_{ion}(Z_{ion} < 20)$ are within 5% of their predicted universal curve.

This paper is a direct result from work done on the determination of the stopping powers of aluminium, nickel and gold for Cu and Kr ions with energy around 4 MeV per nucleon, and presents results aimed at testing the validity of the universal curve for ions with $20 < Z_{ion} < 40$.

The stopping power measurements used in this work are tabulated and comparison made with those semi-empirically obtained by Northcliffe and Schilling [5]. The universal curve generated in this work is also compared with that generated by Booth et al [4].

2. Stopping power data

In this Section, the stopping power measurements for Kr and Cu ions around 4 MeV per nucleon in Al, Ni and Au, used in calculating the γ_{ion} are tabulated (Table I). These results are part of a Ph.D. thesis [6] submitted by the author to the University of Manchester, England. The work was carried out using the Manchester University Linear Accelerator. A direct comparison between our experimental dE/dx results and those semi-empirical calculations obtained by Northcliffe and Schilling [5] shows a discrepancy between 3% and 20%. Efken et al [7] have also found a 10%–30%

Table I

Measured stopping powers for Cu ions
dE/dx [MeV/mgcm^{-2}]

Energy [MeV/A]	Aluminium	Nickel	Gold
3.00	30.62	21.85	13.66
3.20	30.22	21.60	13.58
3.40	29.81	21.35	13.50
3.60	29.41	21.11	13.42
3.80	29.00	20.86	13.34
4.00	28.59	20.61	13.26
4.20	28.19	20.37	13.18

deviation between their helium-4 dE/dx results and those obtained by Northcliffe and Schilling [5]. Ward et al [8] have also noticed a 4–15% discrepancy for oxygen–16. No experimental results for Kr and Cu ions in Al, Ni and Au were available for comparison. But from the above discussion, it is obvious that our discrepancy with Northcliffe and Schilling [5] agrees with other observed discrepancies. Figure 1 shows the dE/dx curves obtained for Cu and Kr ions in Al, Ni and Au.

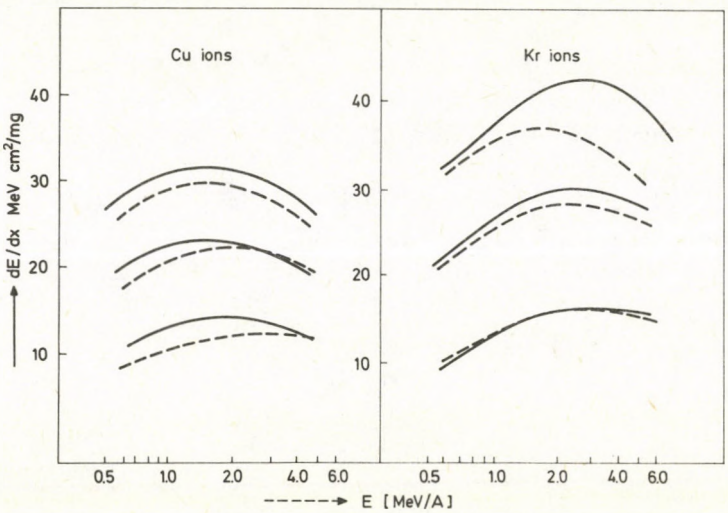

Fig. 1. Stopping power curves for Cu and Kr ions ——— This work – – – – Northcliffe and Schilling

3. Effective charge analysis

The effective charge parameter, γ, in Eq. (1) is that of the proton at the same velocity at which the $(dE/dx)_p$ and $(dE/dx)_{ion}$ are obtained. γ_p was extracted from the measurements of Hall, and a curve interpolating his measurements has an analytical form

$$\gamma_p^2 = [1 - \exp(-150\varepsilon)] \exp[-0.835 \exp(-14.5\varepsilon)] . \tag{3}$$

The energy loss of protons in Al and Au was obtained from the experimental results of Anderson [9] who has achieved an accuracy of 0.3% in his measurements. The dE/dx values for protons in Ni used, were those obtained semiempirically by Williamson [10] since his proton dE/dx values, for most metals, are in reasonably good agreement with Anderson's [9].

The expression for γ_{ion} used in the analysis assumes the Thomas–Fermi model of the atom, and is given by

$$\gamma_{ion}^2 = 1 - \exp(-Ax + Bx^2 - Cx^3) , \tag{4}$$

where A, B and C are constants and X is a function of ion energy (in MeV/A), and Z_{ion} of the form

$$f(x) = f(\varepsilon Z_{ion}^{4/3}) .$$

Equations (3) and (4) together with the dE/dx ion values listed in Tables I and II were substituted in Eq. (1) to form a subroutine in the fitting programme. The values of the constants, with their errors from the best fits are shown in Tables III and IV.

Similar calculations have been performed with the dE/dx data generated empirically by Northcliffe and Schilling [5]. The values of the constants obtained for Cu ions were 22.2 ± 0.2, 266.0 ± 18.5 and 1599.6 ± 360.4 for A, B and C, respectively, for aluminium, 22.4 ± 0.2, 287.4 ± 18.2 and 1776.8 ± 353.6 for gold and in the case of nickel the values were 22.3 ± 0.2, 274.8 ± 18.3 and 1644.2 ± 356.7. Those obtained for Kr ions were 22.6 ± 0.2, 316.0 ± 24.8 and 2058.7 ± 644.7 for aluminium, 22.5 ± 0.2, 298.0 ± 24.6 and 1466.2 ± 637.9 for gold; and 23.1 ± 0.2, 366.1 ± 24.7 and 3015.4 ± 641.7 for nickel.

Table II

Measured stopping powers for Kr ions
dE/dx [MeV/mgcm^{-2}]

Energy [MeV/A]	Aluminium	Nickel	Gold
3.00	43.71	31.03	17.37
3.20	43.30	30.79	17.28
3.40	42.89	30.56	17.19
3.60	42.48	30.33	17.10
3.80	42.07	30.09	17.01
4.00	41.66	29.86	16.92
4.20	41.25	29.63	16.83

Table III

Values of A, B and C for Cu ions

	Elements		
	Aluminium	Gold	Nickel
A	23.5 ± 0.5	25.7 ± 0.8	25.0 ± 0.8
B	201.0 ± 36.9	403.7 ± 35.0	398.2 ± 31.6
C	1033.3 ± 622.6	3342.6 ± 466.3	3230.5 ± 512.0

Table IV

Values of A, B and C for Kr ions

	Elements		
	Aluminium	Gold	Nickel
A	27.5 ± 2.9	28.6 ± 6.1	23.0 ± 0.5
B	361.4 ± 190.2	601.5 ± 402.9	231.7 ± 43.7
C	3564.4 ± 3163.5	6589.8 ± 6642.6	900.9 ± 986.0

The constants A and B from our data are in fairly good agreement with those from Northcliffe and Schilling [5]. Despite the constant C is poorly determined, it does not affect the value of γ_{ion} significantly. Any disagreement in the values of the constants with Northcliffe and Schilling [5] could be attributed to the discrepancy in the dE/dx_{ion} data.

4. Discussion and conclusions

The error in the effective charge parameter γ_{ion} mainly depends on any systematic error in determining experimentally the stopping powers of Al, Ni and Au for Cu and Kr ions. These have an error of 2.5%, and may be regarded as a true representative for the final error in the effective charge curves shown in Fig. 2.

The effective charge parameter as defined in Eq. (1) is expected to be valid only in the region of electronic stopping power, and it was therefore necessary to consider any nuclear stopping power contribution. Estimates of the nuclear dE/dx, using the theory of Lindhard et al [11], were found to be about 2% and were therefore neglected.

Since the effective charge is expected to be independent of the stopping material, a universal curve, similar to Booth et al [4], was generated and is shown in Fig. 3. The values of the constants obtained for the universal curve, together with those from Booth et al [4] are shown in Table V.

The constants A and B are in excellent agreement with Booth et al [4]. While there appears to be a discrepancy in the value of C, it should be borne in mind that the energy range covered by Booth et al [4] is considerably greater than that of the present work.

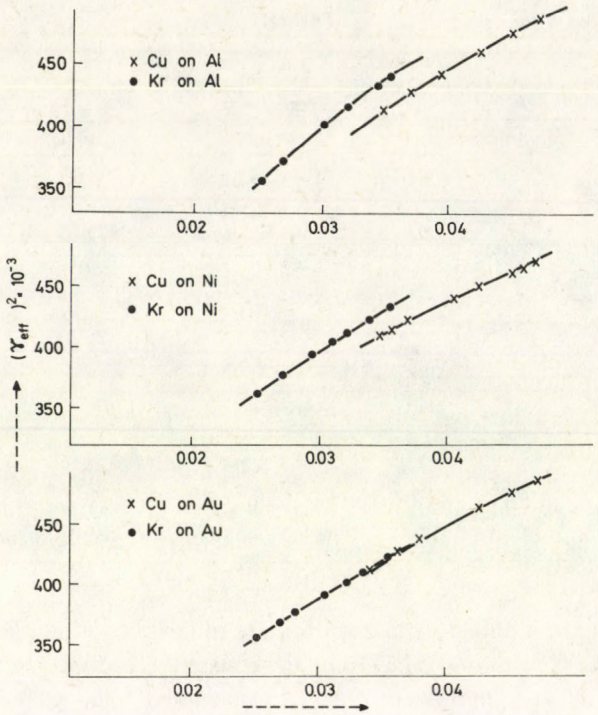

Fig. 2. Effective charge curves for Cu and Kr ions

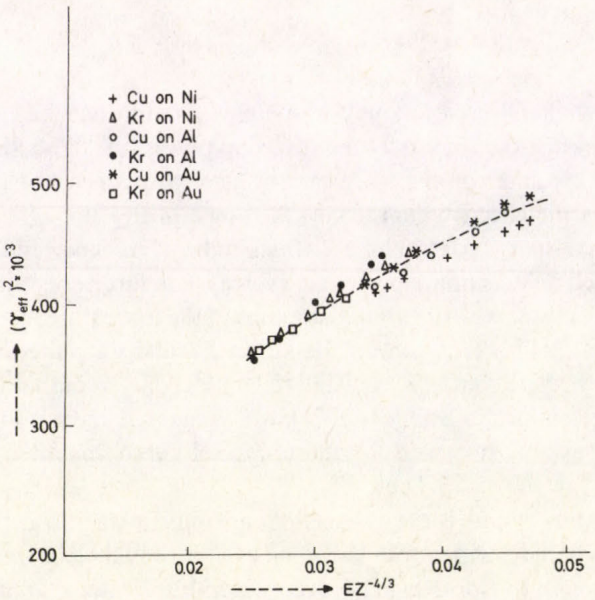

Fig. 3. Universal effective charge curve – – – – Best fit

Table V

Values of universal curve's constants

Constant	This work*	Booth et al
A	25.6	24.7
B	366	247.6
C	3110	1311.0

* Errors shown in Table III

The results of the present work, and the foregoing discussions strongly suggest that the effective charge Z_{eff}, of an ion can be expressed as

$$Z_{\text{eff}} = \gamma_{\text{ion}} Z_{\text{ion}} ,$$

where

$$\gamma_{\text{ion}}^2 = 1 - \exp(-Ax + Bx^2 - Cx^3)$$

and $x = \varepsilon Z^{-4/3}$ and may be valid for $20 < Z_{\text{ion}} < 40$ at an ion energy between 1 and 10 MeV per nucleon.

The agreement between our work and those of Booth et al [4] and Northcliffe and Schilling [5] suggests further that it would be most valuable to extract γ_{ion} at higher energy ranges for wider range of Z_{ion}. This would directly test the extent of the accuracy of the expression for the universal curve.

Acknowledgements

The author wishes to express gratitude to both the academic and technical staff of Schuster Laboratory, Manchester University, for all assistance rendered. Special thanks go to Professor Marx, Hungary, for editing the manuscript.

References

1. L. C. Northcliffe, Phys. Rev., *120*, 1744, 1960.
2. H. H. Heckman and B. L. Perkins, Phys. Rev., *79*, 504, 1960.
3. S. Rosenblatt and P. G. Roll, Rev. Sci. Inst., *31*, 5, 578, 1960.
4. W. Booth and I. S. Grant, Nucl. Phys. *63*, 3, 481, 1965.
5. L. C. Northcliffe and R. F. Schilling, Nuclear Data Tables, *7A*, 233, 1970.
6. M. Labor, Ph.D Thesis, Manchester University, 1976.
7. D. Efker and D. Hahn, Hahn-Meitner-Institut für Kernforschung, Berlin, Germany.
8. D. Ward, Canadian Journal of Physics, *50*, 2302, 1972.
9. H. H. Anderson, C. C. Hanke, H. Sørensen and P. Vajda, Phys. Rev., *153*, 2, 338, 1967.
10. C. Williamson, Tables of Ranges and Stopping Powers of Chemical Elements for Charged Particles of Energy 0.05 to 500 MeV. Oak Ridge National Laboratory, Oak Ridge, USA, 1966.
11. J. Lindhard, M. Scharff and H. E. Schiott, Mat. Fys. Medd. Dan Vid. Selsk *33*, 14, 1963.

Acta Physica Hungarica 60 (3—4), pp. 145—160 (1986)

THE NATURE OF A QUANTUM STATE

J. G. GILSON

Department of Applied Mathematics
Queen Mary College, London E1 4NS

(Received in revised form 7 August 1984)

The Schrödinger equation type of description for fundamental processes is analysed, in terms of an alternative theory which describes the fluid behaviour of a polarized vacuum in a hyperspace. It is shown that Schrödinger quantum states can always be generated from an impulsive production of mass dipoles by processes which are classically explicable. A set of natural reference frames are introduced in relation to which it is shown that the Schrödinger structure assumes a very simple form in terms of local rotations. A fundamental vector potential that is involved in the underlying electromagnetic fluid movement is examined and Hamilton–Lagrange aspects of the polarized flow paths are discussed.

1. Introduction

Orthodox quantum theory is surprisingly unhelpful in explaining the 'physical nature' of a quantum state. In fact, the 'orthodoxy' is that there is no reason why quantum theory should be 'self explanatory', when all that is required from a theory is that it should have a mathematical form from which physically confirmable answers can be obtained to 'philosophically allowable' input questions. In this author's view, that position represents an abandonment of the search for an 'understanding' of natural phenomena and merely covers up a weakness in the way in which quantum theory is presented as being a description of nature. Much turns, of course, on what is a 'philosophically allowable question'. This author will here be concerned with asking the 'unallowable' type of question. 'What is a quantum state' is possibly the prototype of a large class of such questions. It will be shown, in this article, that quite clear answers can be given to some of these 'non allowable" questions. Thus showing that quantum mechanics is not what some authorities would have us believe it is. To see the quantum theory from an alternative point of view we need an alternative formulation of that theory at least, and possibly a generalization of it, so that its character can be assessed in a broader context. This author has developed an alternative formalism which can be shown to contain the Schrödinger system as a subspace process [1, 2, 3, 4]. We shall use this alternative theory to show that important aspects of the local structure of quantum systems, barely uncovered and certainly not explained by the orthodox theory, can be fully explained in terms of familiar 'classical' ideas and processes. However, the author does take a great liberty in constructing this alternative theory in that he uses 'negative' mass as an intrinsic part of the structure. The reason for this rather dramatic departure

from the norm is a fundamental proposition that the 'quantum state' is a state of 'mass polarization' of the vacuum and this at the 'low energy' region of quantum theory. That this postulated negative mass is not directly and obviously noticeable, is explained by the assumption that it occurs as part of a 'polarization' process and so locally and usually positive and negative mass 'monopoles' cancel to produce zero 'rest mass'. However, these mass monopoles, being frequently in different 'kinematic' states, can make an overall non-zero contribution to the local quantum energy. To set up the alternative theory for a system composed of one particle moving in three dimensions under the influence of a prescribed external potential $V(\mathbf{x})$, we need a six dimensional Euclidean configuration space E_6. The E_6 geometry will be used as a framework for the usual position vector $\mathbf{x} \equiv (x^1, x^2, x^3)$ and for an additional three vector $\mathbf{y} \equiv (y^1, y^2, y^3)$, composed of the analytic continuations of the $x^i, (i = 1, 2, 3)$ into the complex planes, $z^i = x^i + \sqrt{-1}\, y^i$. There are many two dimensional subspaces of E_6 but we single out here $E_2^i (i = 1, 2, 3)$, where E_2^i is the space of the two coordinate variables (x^i, y^i), because these three subspaces provide us with a rather simple projective basis for the full E_6 theory. The full E_6 theory [Gilson 1983] which contains the three dimensional Schrödinger equation case becomes quite complicated and consequently to some extent obscures the simple nature of the underlying physical activities that are involved. It is thus best for our present purpose to work in one of the two dimensional subspaces, E_2^1, say, of E_6. This is equivalent to working with the one dimensional Schrödinger equation. We lose very little by confining our attention to the E_2^1 subspace as it turns out that the two dimensional subspaces, $E_2^i, (i = 1, 2, 3)$ provide especially simple projective background frames in which all the structure can be clearly displayed in detail.

Consequently these frames can be used to adequately describe all the 'essential' physics of the theory. As our discussion will be confined to the variables (x^1, y^1) and corresponding velocity variables (u^1, v^1), we shall therefore drop the superscript '1' for the rest of this paper in favour of just (x, y) and (u, v). Work with related motivations or containing related material can be found in references [7] through to [23].

2. Generation of a state

We make the firm assumption that 'the quantum state' is a state of energization of the vacuum. Crudely, this means that a local condition of 'nothingness' can separate into positive and negative mass constituents of equal modular magnitude under some circumstances. If the monopolar components of this 'polarization' were to appear with velocities of equal magnitude and were not spatially displaced, there would still be 'nothing' locally. However, it will be assumed that, in most cases of interest, the positive and negative mass monopoles separate spatially to produce 'dipoles' and also appear with differing speeds and directions of motion. Thus, in such terms, a kinematical and dynamical state of matter can be visualized as coming into being from the vacuum. In the following pages, a mathematically detailed version will be given showing how these

assumptions imply that an 'energized vacuum' will have all the special characteristics of a 'quantum state'. Having accepted that polarized mass is to be the basic constituent of the theory, we further assume that it occurs in fluid form and occupies extended regions of space. It thus can flow and consequently we need a velocity field,

$$\boldsymbol{\beta} = u(x, y, t)\mathbf{e} + v(x, y, t)\mathbf{e}' , \tag{2.1}$$

to describe its motion in the E_2^1 subspace with changing time. $\mathbf{e}$ and $\mathbf{e}'$ are a pair of unit orthogonal base vectors in E_2^1. We make another assumption about the projection of the flow in the E_2^1 subspace. This is that positive mass is only free to move in the $\pm e$ directions, while the negative mass motion is confined to the $\pm\mathbf{e}'$ directions. The $\pm\mathbf{e}$ directions are to be identified with the x degree of freedom of ordinary 'physical' Euclidean 3-space. The $\pm\mathbf{e}'$ directions correspond to the y degree of freedom associated with the analytic continuation of x. From orthodox quantum theory it is well known that quantum states often change discontinuously. This can happen spontaneously or it can be induced by interaction with some other system. In particular, the electron moving under the influence of an electromagnetic field can absorb or emit a 'photon' and so change from one specific quantum state to another entirely different quantum state. Clearly, in this case, the electromagnetic field is supplying an 'impulse' to the initial quantum state in the form of the 'photon' and this causes the 'jump'. This particular type of quantum 'jump' phenomena is often regarded as one of the main characteristic features of the quantum systems which distinguish them from 'classical' systems. Hence, the following proposition is worth considering. 'All quantum states can be formed by the application of impulses'. It has long been known that fluid systems having a motion that has been generated from rest by impulses can sometimes be very conveniently described by a velocity potential (Miln–Thomson, [5], page 84). It will be shown here that we can also make use of a connection between quantum 'jumps' and a fluid velocity potential. Suppose that the fluid motion given by the field $\boldsymbol{\beta}(x, y, t)$ of (2.1) is generated from rest by a force field $\mathbf{F}_0$ acting uniformly over a finite but small time interval τ_0. As the momentum associated with $\boldsymbol{\beta}$ is,

$$\mathbf{p} = m_0(u\mathbf{e} - v\mathbf{e}') , \tag{2.2}$$

according to our proposition that positive mass m_0, say, is carried by the u flow and negative mass $(-m_0)$ is carried by the v flow, it follows that

$$\mathbf{F}_0\tau_0 = m_0(u\mathbf{e} - v\mathbf{e}') = \mathbf{p} . \tag{2.3}$$

If we now assert that the force field $\mathbf{F}_0$ involved in the impulsive production of the state of flow $\boldsymbol{\beta}$ from rest can be derived from a potential W then,

$$u\mathbf{e} - v\mathbf{e}' = -\nabla\alpha_1 , \quad \text{say} , \tag{2.4}$$

where

$$\alpha_1 = \tau_0 W/m_0 \tag{2.5}$$

is the velocity potential for the monopolar relative velocity field $u\mathbf{e}-v\mathbf{e}'$ which will be denoted by $\bar{\boldsymbol{\beta}}$. So far, we could have been talking about the generation from the vacuum of a 'single' dipole. Certainly not necessarily a 'point' dipole, but rather some sort of 'single' but distributed object with the velocity field $\boldsymbol{\beta}(x, y, t)$. We wish now to bring 'probabilities' or state 'densities' into the structure and to do this we consider an 'assembly' of dipoles generated by the impulsive field $\mathbf{F}_0$. We shall assume that the assembly of induced dipoles is composed of a large number of mass dipoles distributed over some region of E_2^1. Suppose the distribution of a total of N dipoles, say, is given by the density function $\rho(x, y, t)$ when generated from the vacuum at time t. If the definite impulsive force field $\mathbf{F}_0$ is responsible for each member of the assembly of dipoles then clearly $\mathbf{F}_0$ does not uniquely determine where any individual dipole will appear in E_2^1, when the production takes place at time t. That is to say, when $\mathbf{F}_0$ generates 'one' dipole, it can appear at any one of the, $x\mathbf{e}+y\mathbf{e}'$, vector positions with probability density $N^{-1}\rho(x, y, t)$. It is convenient to introduce a small comparison volume v_0 and a dimensionless function $\rho^{(0)}$ which are related by $\rho^{(0)}=\rho(x, y, t)v_0$.

Then $\rho^{(0)}(x, y, t)$ is a number of dipoles within the comparison volume v_0 which would give the actual density ρ. Thus for one dipole we can introduce the missing information (Brillouin, [6]) with regard to the appearance of one dipole within the comparison volume v_0 at (x, y) upon impulsive production at time t. This missing information will be denoted by,

$$s_0=-\kappa \ln \rho^{(0)}(x, y, t)\,,$$

where κ is Boltzmann's constant, and so entropy units are being used in defining s_0. Also, it should be noted that the entropy $s_0=-\kappa \ln \rho^{(0)}$ can be positive or negative according to whether $\rho^{(0)}$ is less than or greater than unity. Thus at some positions s_0 can represent 'missing' information while at other positions it can represent 'information'. To proceed further, we have to attribute another physical characteristic to the mass dipoles. We shall, in fact, call them 'composite' mass dipoles and assume that the positive–negative mass separation involved in their production also involves a 'charge' separation or an electric polarization. Thus we shall assume that, when one monopole of one electronic rest mass m_0 is generated, it carries with it one electronic charge $-|e|$ and, when an opposite monopole of rest mass $-m_0$ is generated, it carries with it one positronic charge $|e|$. The magnitude of a set of 'primary' monopolar separations will be taken to be l_0, where $\tau_0 c=l_0$, c being the speed of light and τ_0 being the time involved in the production of the state introduced earlier. Thus the impulsive production of a state with the velocity field, $\boldsymbol{\beta}=u\mathbf{e}+v\mathbf{e}'$, for the N dipole assembly simultaneously involves the production of a current density,

$$\mathbf{j}=-|e|\rho(u\mathbf{e}-v\mathbf{e}')\,. \tag{2.6}$$

It is now possible to make a remarkable connection between the electrodynamics and the statistics of the vacuum system by using Maxwell's equation,

$$\nabla_A \mathbf{B}_0=\mu_0\mathbf{j}\,, \tag{2.7}$$

where we are assuming that **j** is the 'total' current in E_2^1 associated with a magnetic induction vector $\mathbf{B}_0$ which will be considered to be an 'intrinsic' magnetic field associated with the 'primary' dipoles. Thus if each 'primary' dipole has a magnetic moment of one Bohr magneton, $l_0|e|c\mathbf{e}_A\mathbf{e}'$, chosen as indicated by the vector product to point in a direction $\mathbf{k}=\mathbf{e}_A\mathbf{e}'$, orthogonal to the E_2^1 subspace, then the primary magnetic induction vector $\mathbf{B}_0$ will be given by

$$\mathbf{B}_0 = 1_0|e|c\rho\mathbf{k}\,. \tag{2.8}$$

The unit vector **k**, having been chosen in E_6, also serves to introduce a three space E_3^1 containing E_2^1 and also vector products formed from 2-vectors in E_2^1. As we have taken $l_0|e|c$ to be one Bohr magneton, l_0 will have the value, $l_0=\hbar/2m_0c$, and consequently the state production impulsive time τ_0 will have the value, $\tau_0=l_0/c=\hbar/2m_0c^2$.

Thus $\mathbf{B}_0$ is the primary magnetic induction vector generated simultaneously with the appearance of the velocity field $\boldsymbol{\beta}$ and the 'electric' dipole moment, $-|e|l_0\mathbf{k}$ per dipole. (2.7) and (2.8) lead to the connection, mentioned earlier, between the electrodynamics and the statistics for this system which can be expressed by the relations,

$$u=-cl_0\frac{\partial \ln}{\partial y}\rho^{(0)} \tag{2.9}$$

and

$$v=-cl_0\frac{\partial \ln}{\partial x}\rho^{(0)}\,, \tag{2.10}$$

giving the velocity components in terms of the distribution function $\rho^{(0)}$. These imply that

$$\frac{\partial u}{\partial x}=\frac{\partial v}{\partial y}\,. \tag{2.11}$$

However, from (2.4), we also have,

$$\nabla_A\bar{\boldsymbol{\beta}}=0\,, \tag{2.12}$$

where

$$\bar{\boldsymbol{\beta}}=u\mathbf{e}-v\mathbf{e}' \tag{2.13}$$

is the relative monopolar velocity in E_2^1. From (2.4), it also follows that

$$\frac{\partial u}{\partial y}=-\frac{\partial v}{\partial x}\,. \tag{2.14}$$

(2.11) and (2.14) are the well known Cauchy–Riemann equations which indicate that u and v can be combined together in the form, $u+\sqrt{-1}v$, to produce an analytic function $f(x+\sqrt{-1}y)$, of the complex variable $z=x+\sqrt{-1}y$. Further, from (2.9) and (2.10) it can be seen that $cl_0\ln\rho^{(0)}$ can be taken to be the stream function for the relative

monopolar velocity field, $\bar{\boldsymbol{\beta}}$, given by (2.3). The story so far can be summarized in the form of the following theorem and two corollaries about the existence and significance of special state functions.

"Theorem"

The 'input' disorder associated with the production of a quantum state is equal to $\kappa\alpha_2$, where

$$\alpha_2 = cl_0 \ln \rho^{(0)} \tag{2.15}$$

is the stream function for the local relative monopolar motion and is also one member of a pair of conjugate functions (α_1, α_2) in the sense of the theory of functions of a complex variable. The other member of the pair, α_2, is the velocity potential for the induced relative monopolar motion.

'Corollary 1'

The theorem implies the existence of a 'complex' potential,

$$\alpha(z, t) = \alpha_1(x, y, t) + \sqrt{-1}\,\alpha_2(x, y, t), \tag{2.16}$$

at the time of production t, for the relative monopolar flow,

$$\bar{\boldsymbol{\beta}} = u\mathbf{e} - v\mathbf{e}' = \mathbf{p}/m_0 \tag{2.17}$$

or as indicated by (2.17) for, what is the same thing p/m_0, the projection of the local momentum into E_2^1 divided by m_0.

'Corollary 2'

By means of the conformal transformation,

$$\psi(z, t) = \exp(\alpha(z, t)/2icl_0) \tag{2.18}$$

at time t, we can infer the existence of an analytic function $\psi(z, t)$ of the complex variable z which can be shown to be the 'wave function' for the system.

In Section 5, it will be shown that a third corollary could be appended to the previous two. This to the effect that $m_0\alpha_1(x, y, t)$ is equal to minus the classical Lagrangian action $\int_{t_0\,(\text{path})}^{t} L(t')dt'$, taken along a path between times t_0 and t, apart from a possible additive constant, and that α_2 is the change in disorder or entropy taken along the same path between the same times and also apart from a possible additive

constant. It follows that for this system there is a general connection between Lagrangian action and entropy, essentially expressed by the 'theorem' stated earlier. It is interesting that Miln-Thomson ([5], page 147) remarks on the usefulness of a function of form rather like (2.18) in connection with some types of fluid motion but presumably with no thoughts of quantum-theory in mind! Clearly the $\sqrt{-1}$ in (2.18) plays a critical role in the formalism. The particular conformal transformation (2.18) is that one which 'completely' linearizes the differential statement of this theory in the form of the analytically continued Schrödinger equation for $\psi(z, t)$.

3. Natural reference frames

We have so far considered the polarized vacuum system from the point of view of a preassigned Euclidean frame of reference E_2^1 with the given configuration coordinates (x, y). If there is an external potential $V(x, y)$ involved, the frame E_2^1 would usually be chosen, if possible, as that one in which the source or sources of the external field are 'rigidly' fixed at given positions within it. Certainly, such a frame would be a first choice and would be expected to give the simplest view of the system. Normally one would also prefer the reference frame E_2^1 to be a non-rotating 'inertial' frame. Quantum systems are usually, or at least initially, discussed in such frames of reference, where basically the external potential determines the frame. Thus we are motivated to consider how these 'unavoidable' frame based viewpoints might be colouring our ideas about how the 'vacuum' might be expected to behave and, we also seek to determine how the mathematical description of the vacuum should be formulated so as to disentangle mathematical 'irrelevancies' such as geometrical 'rigidity'. It turns out that there is a simple solution to this particular difficulty in the case of the polarized vacuum system. This solution arises because of a fundamental characteristic of the quantum process. As is well known from orthodox quantum theory, changes of energy or 'packets' of energy often occur in the form, $\Delta E = hf$, where h is Planck's constant and f is a frequency. Almost invariably nowadays, we find the same relation written in the form $\Delta E = \hbar\omega$, where $\hbar = h/2\pi$ and ω is an 'angular' frequency. The practical reason for the more common usage of $\hbar$ and ω rather than h and f is the fact that the former quantities occur more frequently in formulae when they are expressed most simply. The author believes that this is actually a consequence of 'angular' velocities being 'fundamental' to quantum mechanics while not being measures of any rotation rates in ordinary configuration Euclidean three space but rather a measure of local rotation rates in the hyperspaces $E_3^i (i = 1, 2, 3)$ of the present theory of the vacuum. It is well known that in fluid theory the vorticity $\boldsymbol{\zeta} = \frac{1}{2} \nabla_A \boldsymbol{\beta}$ can be regarded as a field of local rotation rates. There is the well known suggestion that, if a small element of a fluid in motion with velocity field $\boldsymbol{\beta}$ were to be frozen suddenly, it would then be found to be rotating with an

angular velocity $\tilde{\boldsymbol{\Omega}} = \frac{1}{2} \nabla_A \boldsymbol{\beta}$ (Miln-Thomson, [5] page 45). Use will be made of these ideas in a moment. However, it is possible to imagine a more 'intrinsic' type of local rotational motion in which a field of local rotation rates is given but which is not necessarily derivable by taking the curl of some velocity field. For example, suppose that rotation rates were associated with each member of our field of primary induced dipoles in an 'intrinsic' way to give an angular velocity field $\boldsymbol{\Omega}$ according to the formula,

$$\boldsymbol{\Omega} = \Omega_0 \rho^{(0)}(x, y, t)\mathbf{k}\,, \tag{3.1}$$

where Ω_0 is a 'fundamental' angular velocity.

We can use the length l_0, introduced earlier, to define such a fundamental angular velocity by means of the formula, $\Omega_0 = \tau_0^{-1}$, $l_0 = c\tau_0$. τ_0 is the 'impulse time' used earlier. The $\rho^{(0)}$ in (3.1) was defined in the abstract frame E_2^1 and so we shall interpret Ω_0 as being an 'intrinsic' angular velocity field associated with the density of dipole states in E_2^1 and representing a local rotation rate 'relative' to the abstract frame E_2^1. We know from orthodox quantum theory that energies are associated with 'rotation' rates and we also know from relativity that mass is associated with energy according to Einstein's formula. Thus we can express the relation between a local energy change per dipole, $2m_0c^2 = m_0c^2 - (-m_0c^2)$, and the angular velocity $\boldsymbol{\Omega}$ consequent upon the production of the primary dipolar field by the impulse as,

$$c\rho^{(0)}\mathbf{k} = 1_0\boldsymbol{\Omega}\,. \tag{3.2}$$

However, the primary rest mass distribution 'vector' $m_0c^2\rho^{(0)}k$, from (3.2) has been defined via $\rho^{(0)}$ which itself was defined relative to the abstract Euclidean frame E_2^1 and so, as a 'physical' distribution of rest mass, its pedigree is suspect for the 'frame difficulty' reasons discussed earlier. On the other hand, once the quantum state has been generated, there is at our disposal the velocity field, $\boldsymbol{\beta} = u\mathbf{e} + v\mathbf{e}'$, and its local angular velocity, $\tilde{\boldsymbol{\Omega}} = \frac{1}{2} \nabla_A \boldsymbol{\beta}$. Thus, if the velocity field $\boldsymbol{\beta}$ represents a single extended but possibly rather 'wobbly' entity, surely the rest mass distribution for such an extended system should be measured 'locally' in whatever frame is attached to the 'particle' locally and is moving and rotating with it. This can be regarded as a generalization of the idea that the rest energy of a 'point' particle is a form of potential energy moving with the particles rest frame to the case of the extended fluid system which does not necessarily have a single unique rest frame. If it is accepted that 'distributed' rest mass 'should' be measured 'relative' to the 'natural frames that is to say, relative to the local frames determined by the angular velocity field $\tilde{\boldsymbol{\Omega}} = \frac{1}{2} \nabla_A \boldsymbol{\beta}$ and we are prepared to neglect the relativistic effects associated with high velocities, it is then possible to regard the 'so defined' relative rest mass distribution as giving a good approximation to the rest mass in E_3^1 also. Thus, we shall define the 'physical' or 'relative' restmass distribution, $m_0c^2\rho_T^{(0)}$, for our extended fluid system, by measuring

the 'intrinsic' rotation rate 'relative' to the 'natural' frames determined by $\tilde{\mathbf{\Omega}}$. Hence

$$m_0 c^2 \rho_T^{(0)} \mathbf{k} = \frac{\hbar}{2}(\mathbf{\Omega}_0 - \tilde{\mathbf{\Omega}}). \tag{3.3}$$

This being, in fact, an energy 'vector' associated with the intrinsic rotation rates measured relative to the induced assembly of 'natural frames' which are 'locally' rotating with the velocity field of the polarized vacuum. It follows that in changing from the abstract frame E_3^1 definition for the local rest mass distribution to the 'natural' frame definition, $\rho^{(0)}$ becomes $\rho_T^{(0)}$ according to the formula,

$$m_0 \rho_T^{(0)} = m_0 \left(\rho^{(0)} - \frac{l_0}{2c} \left(\frac{\partial v}{\partial x} - \frac{\partial u}{\partial y} \right) \right), \tag{3.4}$$

from (3.1) and (3.3).

Let us now consider an approximate classical energy E_c per dipole which includes the rest mass distribution $m_0 c^2 \rho^{(0)}$,

$$E_c = m_0 c^2 \rho^{(0)} + K + V_1. \tag{3.5}$$

Besides containing the abstract frame rest mass $m_0 c^2 \rho^{(0)}$, this is composed of the monopolar kinetic energy, $K = \frac{1}{2} m_0 (u^2 - v^2)$, and the external potential energy $V_1(x, y)$. It is now natural to define a 'non-rest' energy for the extended system as,

$$\begin{aligned} E_Q &= E_c - m_0 c^2 \rho_T^{(0)} \\ &= K + V + m_0 c l_0 \frac{\partial v}{\partial x} = K + V + V_Q, \end{aligned} \tag{3.6}$$

by (3.4), (3.5) and the Cauchy–Riemann equation (2.14). E_Q is obviously the real part of the local quantum energy, $i\hbar\, \partial \ln \psi / \partial t$, or alternatively,

$$E_Q = \frac{\partial \alpha_1}{\partial t},$$

by Corollary 1, to the theorem of Section 2.

$$V_Q = m_0 c l_0 \mathbf{\Omega} \cdot \mathbf{k} \tag{3.7}$$

is the additional potential experienced by a quantum particle over and above the prescribed external potential $V(x, y)$ in E_2^1. It is clear from this way of deriving V_Q that it arises directly from the choice of the abstract frame E_2^1, to look at the energy of the field, rather than using the 'natural frames'. Apparently, a quantum particle 'sees' its own rest energy from the natural frames, whilst the external observer of the system looking at non-rest energy, is constrained to use the abstract frame. There is no difficulty in showing, on the basis of the structure examined in this article, that the wave function, $\Psi(z, t)$ identified earlier (2.18), satisfies the analytically continued Schrödinger

equation,

$$i\hbar\frac{\partial\Psi(z,t)}{\partial t}=-\frac{\hbar}{2m_0}\frac{\partial^2\psi(z,t)}{\partial z^2}+V(z)\psi(z,t) \tag{3.8}$$

and that on the subspace $y=0$, this reduces to the usual one dimensional Schrödinger equation for $\psi(x,t)$. All that is required to arrive at equation (3.8) for ψ is the natural assumption that, once the primary dipoles are impulsively induced, they flow in a conserved manner, apart from the influence of a source term $\Gamma=\rho V_2/m_0cl_0$, arising from the external field,

$$\frac{\partial\rho}{\partial t}=-\nabla\cdot(\rho\boldsymbol{\beta}^{(c)})+\Gamma, \tag{3.9}$$

where $\boldsymbol{\beta}^{(c)}=\frac{1}{2}\boldsymbol{\beta}$ is the dipolar centroidal velocity field (Gilson [1]–[4]). The three dimensional Schrödinger equation 'case' only differs from the work discussed so far in 'complexity' in that it involves the three complex configuration variables z^i $(i=1,2,3)$ and therefore to formulate the theory in terms of 'real' velocity fields the six dimensional Euclidean space E_6 is required. In the next Section, we shall look closer at some more physical pictures of the vacuum process that are contained in this 'alternative' to Schrödinger quantum theory.

4. The vector potential A

Let us return to the question of the 'impulsive' production of a quantum state from rest. With the impulsive generating force field $\mathbf{F}_0$, (2.3), we can associate an 'electrical' vector potential $\mathbf{A}$ according to the formula,

$$-2|e|\mathbf{A}=\tau_0\bar{\mathbf{F}}_0=\mathbf{I}_0. \tag{4.1}$$

$\bar{\mathbf{F}}_0=F_{01}\mathbf{e}-F_{02}\mathbf{e}$ is used in (4.1) rather than $\mathbf{F}_0=F_{01}\mathbf{e}+F_{02}\mathbf{e}'$ so that $\mathbf{A}$ relates to the velocity field $\boldsymbol{\beta}$ rather than to the relative monopolar velocity field $\bar{\boldsymbol{\beta}}$. Thus we define $\mathbf{A}$ so that an electrical impulse associated with the charge 'change', $-2|e|$, is the same as the mechanical impulse $\mathbf{I}_0$ associated with the time change τ_0. The vector potential $\mathbf{A}$ is generated simultaneously with the velocity field $\boldsymbol{\beta}$. We use $\mathbf{A}$ to define a 'secondary' magnetic induction vector $\tilde{\mathbf{B}}$, say, according to the formula,

$$\tilde{\mathbf{B}}=\nabla_A\mathbf{A}=-\nabla_A\frac{\tau_0}{|e|}\mathbf{F}_0. \tag{4.2}$$

Using (2.3), this becomes,

$$\tilde{\mathbf{B}}=-\frac{m_0}{|e|}\tilde{\boldsymbol{\Omega}}. \tag{4.3}$$

Thus with the definition (4.1) for **A**, we can account for a secondary magnetic induction vector $\tilde{\mathbf{B}}$ derivable from the vorticity of the velocity field $\boldsymbol{\beta}$ and related to $\tilde{\boldsymbol{\Omega}}$ in the same way as magnetic induction in the cyclotron is related to angular velocity. Thus $|\tilde{\boldsymbol{\Omega}}|$ is the Larmor frequency associated with the secondary magnetic induction $\tilde{\mathbf{B}}$. Using $\tilde{\mathbf{B}}$ and **A**, the local quantum energy E_Q (3.6) can be expressed in the compact form,

$$(E_Q - V_1)\rho = \mathbf{j}\cdot\mathbf{A} - \mathbf{B}_0\cdot\tilde{\mathbf{B}}/\mu_0 = -\nabla\cdot\mathbf{P}, \quad \text{say.} \tag{4.4}$$

j is given by (2.6) and $\mathbf{B}_0$ by (2.8). (4.4) shows up clearly the 'complete' electromagnetic nature of E_Q in which even the kinetic energy, $\frac{1}{2}m_0(u^2-v^2)=\mathbf{j}\cdot\mathbf{A}$, is included as an interaction term between **j** and **A**. The term $\frac{1}{\mu_0}(\mathbf{B}_0\cdot\tilde{\mathbf{B}})$ is clearly an interaction between the primary and secondary magnetic induction effects. In (4.4), the 'secondary' polarization vector **P** has been introduced analogously with the Maxwell form $\sigma = -\nabla\cdot\mathbf{P}$. It is not difficult to confirm that **P** has the form,

$$\mathbf{P} = -\lambda|e|\boldsymbol{\beta}^{(c)}\Lambda\mathbf{B}_0, \tag{4.5}$$

where λ is a 'vacuum' elasticity 'constant' with the value, $\lambda = m_0/\mu_0 e^2$. It is clear from (4.5) that **P** lies in the (x, y) plane and actually results from the polarizing effect of the Lorentz forces which arise from the dipolar centroidal velocity field $\boldsymbol{\beta}^{(c)} = \frac{1}{2}\boldsymbol{\beta}$ and the intrinsic magnetic induction vector $\mathbf{B}_0$. We finally remark that **A** can be put into the simple form,

$$\mathbf{A} = -\frac{m_0}{|e|}\boldsymbol{\beta}^{(c)}, \tag{4.6}$$

which shows its close relation with the dipolar centroidal velocity field $\boldsymbol{\beta}^{(c)}$.

5. Hamilton—Lagrange aspects

Let us consider the velocity potential α_1 given by Eq. (2.5) more closely. The total differential of α_1 for the E_2^1 subspace and the time coordinate is

$$d\alpha_1 = \frac{1}{m_0}E_Q\,dt - u\,dx + v\,dy, \tag{5.1}$$

by (2.4) and (3.6). Thus using (3.6), $d\alpha_1$ can be put into the form,

$$d\alpha_1 = \left(\frac{u^2-v^2}{2} + cl_0\frac{\partial v}{\partial x} + V_1/m_0 - \frac{u\,dx}{dt} + \frac{v\,dy}{dt}\right)dt. \tag{5.2}$$

Thus the total change in α_1 taken along some finite given path starting at time t_0 from position (x_0, y_0) and terminating at some later time t at position (x, y) for a path

specified by $\dot{x}=f$, $\dot{y}=g$ is,

$$\alpha_1(t)-\alpha_1(t_0)=\int_{t_0(\text{path})}^{t}\left(\frac{u^2-v^2}{2}+cl_0\frac{\partial v}{\partial x}+V_1/m_0-uf+vg\right)dt'. \tag{5.3}$$

In fact, any path of 'reasonable' behaviour can be used to evaluate the integral (5.3) between the 'events' (x_0, y_0, t_0) and (x, y, t) provided α_1 is single valued and the two events lie on the path. This follows from the condition,

$$\oint_C d\alpha_1=0, \tag{5.4}$$

for any closed contour C in the three-space $\mathbf{R}\equiv(x, y, t)$ containing the two events $\mathbf{R}$ and $\mathbf{R}_0$ as 'extreme' events in 'time'. This can be seen from (5.1) because

$$\frac{d\alpha_1}{ds}=\frac{d\mathbf{R}}{ds}\cdot\nabla_{\mathbf{R}}\alpha_1, \tag{5.5}$$

where $\nabla_{\mathbf{R}}$ is the three space gradient and where s is any suitable parameter on the closed contour C. Thus Stoke's theorem can be used to evaluate the contour integral (5.4) and the value zero is obtained. We can make some use of this freedom to choose a path between two 'events'. If we take the special 'classical like' path defined by,

$$\dot{x}=\boldsymbol{\beta}\cdot\mathbf{e}=u, \qquad \dot{y}=\boldsymbol{\beta}\cdot\mathbf{e}'=v, \tag{5.6}$$

and provided we choose initial and terminal events which actually lie on this path, then the integral (5.3) reduces to the form,

$$\alpha_1(t)-\alpha_1(t_0)=-\frac{1}{m_0}\int_{t_0}^{t}(K-V_T)\,dt' \tag{5.7}$$

$$=-\varphi/m_0, \quad \text{say.} \tag{5.8}$$

$$V_Q=m_0cl_0\frac{\partial v}{\partial x} \tag{5.9}$$

is the 'extra' quantum potential and

$$V_T=V_1+V_Q \tag{5.10}$$

is the total potential experienced by a particle under quantum conditions. (5.8) is, as one might expect, the usual formula for Hamilton's principal function φ. Thus apart from the additive constant $\alpha_1(t_0)$, Hamilton's principal function φ and the real part α_1 of the complex potential α only differ by the factor $-m_0$. This conclusion is the source of the third possible corollary to the theorem of Section 2 mentioned earlier. There is no

difficulty in showing that the Hamilton–Jacobi equation,

$$\frac{\partial \varphi}{\partial t} + H(q_1, q_2, p_1, p_2, t) = 0, \tag{5.11}$$

where $q_1 = x$ and $q_2 = y$, and also Hamilton's equations,

$$\dot{p}_i = -\frac{\partial H}{\partial q_i},$$

$$v_i = \frac{\partial H}{\partial p_i}, \qquad (i = 1, 2), \tag{5.12}$$

hold for this vacuum system. In fact, it is obvious that the H in (5.1) is the real part, E_Q, of the Schrödinger 'local' energy which is given by (3.6). Let us now consider the total differential of α_2, the imaginary part of the complex potential α in E_2^1. This is

$$d\alpha_2 = \frac{1}{m_0} E_2 \, dt - \frac{\partial \alpha_1}{\partial y} dx + \frac{\partial \alpha_1}{\partial x} dy. \tag{5.13}$$

We recall the expression (3.6) for E_Q, the real part of the local quantum energy,

$$E_Q = \frac{m_0}{2}(u^2 - v^2) + m_0 c l_0 \frac{\partial v}{\partial x} + V_1. \tag{5.14}$$

As E_Q is the real part of a complex function and u and v are the real and imaginary parts of another complex function, the local quantum momentum divided by m_0, inspection of (5.14) suggests that the imaginary part E_2 of the local quantum energy should be taken to be

$$E_2 = m_0 uv - m_0 c l_0 \frac{\partial u}{\partial x} + V_2, \tag{5.15}$$

where V_2 is the imaginary part of $V(x + iy)$. (5.15) is the correct form for E_2 as can be confirmed from orthodox quantum theory. If we substitute (5.15) into (5.18), we obtain,

$$d\alpha_2 = \left(uv - c l_0 \frac{\partial u}{\partial x} + V_2/m_0 - \frac{v \, dx}{dt} - \frac{u \, dy}{dt} \right) dt, \tag{5.16}$$

having used (2.4). We have the same freedom in choosing a path when integrating (5.16) between initial and terminal events as we had in the case of $d\alpha_1$ and for the same reasons. Suppose then that we choose initial and terminal events at times t_0 and t lying on a dipolar centroidal path. This is a path determined by the differential equations, $\dot{x} = u/2$, $\dot{y} = v/2$.

However, if the dipolar motion is such that the dipole state density ρ in E_2^1 is conserved apart from the external field source term Γ, we can assume that the continuity equation (3.9) holds. Integrating (5.16) along the the dipolar centroidal path,

we obtain,

$$\alpha_2(t)-\alpha_2(t_0)=\int_{t_0}^{t}\left(-cl_0\frac{\partial u}{\partial x}+\frac{V_2}{m_0}\right)dt'. \tag{5.17}$$

However, from the continuity equation (3.9), we can calculate the total rate of change of $\ln\rho$ 'following' the centroidal flow,

$$\left.\frac{d\ln\rho}{dt}\right|_{\beta^{(c)}}=\frac{\partial\ln\rho}{\partial t}+\boldsymbol{\beta}^{(c)}\cdot\nabla\ln\rho=-\frac{\partial u}{\partial x}+\frac{V_2}{m_0cl_0}, \tag{5.18}$$

where Γ is identified with $\rho V_2/m_0cl_0$ and the Cauchy–Riemann equation (2.16) has been used. (5.18) can be used in the integral (5.17) to give

$$\alpha_2(t)-\alpha_2(t_0)=cl_0\int_{t_0}^{t}\left.\frac{d\ln\rho}{dt}\right|_{\beta^{(c)}}dt'. \tag{5.19}$$

Thus, after integrating between t_0 and t (5.19) gives,

$$\alpha_2(t)-\alpha_2(t_0)=cl_0[\ln\rho(x,y,t)-\ln\rho(x_0,y_0,t_0)]. \tag{5.20}$$

This implies that

$$\alpha_2=cl_0\ln\rho(x,y,t)+\text{a constant} \tag{5.21}$$

and confirms the relation (2.15), $\alpha_2=cl_0\ln\rho^{(0)}(x,y,t)$, connecting the stream function α_2 with the dipole state distribution function $\rho^{(0)}(x,y,t)$. The work of this Section also confirms the general consistency of this formalism and its character as being conceptually and structurally part of 'classical' dynamical theory.

This article will be concluded by showing that in terms of local rotations in the hyperspace E_3^1 and relative to the natural frames discussed earlier, in Section 3, Schrödinger quantum theory can be put into a very simple and illuminating form.

6. Conclusions

In Section 5, we considered the changes in α_1 taken along the 'classical like' paths (5.6). Let us now consider changes in α_1 taken along the dipolar centroidal paths. In this case, we find,

$$\frac{1}{cl_0}\frac{d}{dt}(\alpha_1\mathbf{k})|_{\beta^{(c)}}=\tilde{\boldsymbol{\Omega}}+(V_1/m_0cl_0)\mathbf{k}. \tag{6.1}$$

The unit vector $\mathbf{k}=\mathbf{e}_4\mathbf{e}'$ of Section 2 has been introduced into the equation so that $\alpha_1 k$ can be treated as a vector quantity pointing in a direction perpendicular to the

hyperspace E_2^1. The quantity on the left hand side of (6.1) is an angular velocity calculated following the dipolar centroidal field $\boldsymbol{\beta}^{(c)}$. Let us denote this dipolar angular velocity by

$$\boldsymbol{\Omega}_c = \frac{1}{cl_0}\frac{d}{dt}(\alpha_1 \mathbf{k})_{\boldsymbol{\beta}^{(c)}}. \tag{6.2}$$

Equation (6.1) also contains another angular velocity $V_1 \mathbf{k}/m_0 cl_0$ which apparently is injected linearly into the flow by the action of the external field V_1. We shall denote this contribution to the rate of rotation of the dipoles by

$$\boldsymbol{\Omega}_{ex} = V_1 \mathbf{k}/m_0 cl_0. \tag{6.3}$$

Using these symbols, Eq. (6.1) assumes the simple form,

$$\boldsymbol{\Omega}_r = \boldsymbol{\Omega}_{ex}. \tag{6.4}$$

In terms of

$$\boldsymbol{\Omega}_r = \boldsymbol{\Omega}_c - \tilde{\boldsymbol{\Omega}},$$

the angular velocity following the dipolar centroidal flow relative to the 'natural frames'.

(6.4) is a vector form for the real part of a differential equation for the complex potential α and as such it expresses most of the physics that is expressed by the usual Schrödinger equation. In fact, the only part of the Schrödinger structure that (6.4) does not contain is the continuity condition (3.9) and even this can be put into a simple form very much like (6.4) but that will not be used in this article. Equation (6.4) is a notably simple statement about the field of mass dipoles which contains the 'essence' of Schrödinger quantum theory. It says that relative to the 'natural frames' the total local angular velocity of the dipolar centroidal fluid 'particles', as they move about, is simply determined by the imposed external 'electromagnetic' local angular velocity function $\boldsymbol{\Omega}_{ex}$. It appears that the external field 'clamps' all the total moving dipolar local rotation rates at a prescribed value relative to the natural frames, whilst all the interesting structure and movement of Schrödinger quantum systems show up in terms of the 'internal' local adjustments of velocity and density which must take place along the dipolar paths to maintain this constraint. The power of the alternative view of quantum mechanics developed in this paper to explain in detail local processes that are taking place behind the usual formulation of that theory is extensive. It is difficult to believe that there could be a simpler expression of quantum theory than equation (6.4). The alternative theory puts the quantum process into an entirely new light with regard to the philosophical question of 'what is a quantum state'. A summary of the answer that has emerged from the preceding work to this important question now follows.

The 'quantum state' is a positive-negative mass fluid, polarized condition of the vacuum, which can be energised into processes of dipolar creation, flow rotation and electrothermodynamical activity over hyperspaces which contain the usual Euclidean three dimensional configuration space. It is particularly interesting that all the

processes involved can be explained in 'classical' terms with local rotations of the dipolar fluid playing a central and significant part. Briefly, Schrödinger quantum theory can be translated into the science of tracking dipolar vortices in the vacuum through hyperspace.

References

1. J. G. Gilson, Acta Phys. Hung., *44*, 333, 1978.
2. J. G. Gilson, Ann. Inst. Henri Poincaré, *XXXII*, 4, 319, 1980.
3. J. G. Gilson, Annales de la Fondation Louis de Broglie, *6*, 1, 1981.
4. J. G. Gilson, Hadronic Journal, *5*, 1489, 1982.
5. L. M. Miln-Thomson, Theoretical Hydrodynamics, Macmillan and Co. Ltd., New York, 1949.
6. L. Brillouin, Science and Information Theory, Academic Press, New York, 1960.
7. S. N. Bagchi, Proc. I.A.C.S., *58*, 21, 1975.
8. A. Blaquiere, Journal of Optimization and Application, *32*, 4, 463, 1980.
9. D. Bohm and B. J. Hiley, Foundations of Physics, *5*, 1, 1975.
10. D. Bohm and J. P. Vigier, Phys. Rev., *96*, 208, 1954.
11. V. Buonomano, Il Nuovo Cimento, *57B*, 146, 1980.
12. G. Cavalleri, Phys. Rev., *D.23*, 363, 1981.
13. P. Claverie and S. Diner, International Journal of Quantum Chemistry, *XII*, Suppl. 1., 41, 1977.
14. L. de Broglie, La Thermodynamique de la Particle Isolée, Gauthier-Villars, Paris, 1964.
15. J. Fronteau and A. Tellez-Arenas, Il Nuovo Cimento, *36B*, N.1, 1976.
16. J. Fronteau, Hadronic Journal, *4*, 742, 1981.
17. P. F. Gonzales-Diaz, Il Nuovo Cimento, *64B*, N. 2. 347, 1981.
18. P. G. Harper, Communications to the Royal Society of Edinburgh (Physical Sciences), *18*, 241, 1980.
19. Max Jammer, The Philosophy of Quantum Mechanics, John Wiley and Sons, N. Y., 1974.
20. L. Jánossy, Foundations of Physics, *6*, 341, 1976.
21. F. London, Super Fluids, *1*, Dover Publications Inc. N. Y. 1960.
22. E. Madelung, Zs. f. Phys., *40*, 332, 1926.
23. T. Takabayasi, Progress of Theor. Phys., *9*, 187, 1953.

Acta Physica Hungarica 60 (3—4), pp. 161—172 (1986)

ELECTRON BOMBARDMENT TECHNIQUE FOR THE STUDY OF ELECTRICAL TRANSPORT PROPERTIES IN ORGANIC SEMICONDUCTORS

M. SALEH*

Department of Physics, University of Nairobi
Nairobi, Kenya

and

M. S. ZAFAR

Department of Physics, University of the Punjab
New Campus, Lahore, Pakistan

(Received in revised form 10 September 1984)

This paper describes in some detail the electron bombardment technique used for the study of electrical transport properties in organic semiconductors. A platelet specimen is fitted with electrodes on opposite sides and charge carriers are generated near the top electrode by a short bombarding pulse. Both light and electron pulses have been used for irradiating the crystal specimen and the particular advantages of electron beam excitation are discussed. A steady or pulsed applied field draws one type of carriers across the specimen and the transit time 'T' is determined by charge integration. This leads directly to the drift mobility. However, in the case of p–n junction solar cells, the samples were bombarded with electron beam under reverse-biased conditions and the lifetime of minority charge carriers was determined from the decay of the concentration of excess minority charge carriers. Lifetime of minority charge carriers in silicon solar cells was found to be ~ 25 μs, whereas in silicon specimens the lifetime of charge carriers was ~ 8 μs. Measurement of carrier lifetimes, drift mobilities and carrier yields in organic semiconductors with the electron bombardment technique provides valuable information regarding the generation and recombination mechanisms, and the evaluation of the perfection of organic semiconductors which are to be used later for the fabrication of a variety of devices. Details of a space charge avoidance technique are given.

1. Introduction

This paper describes in some detail the electron bombardment technique used for the study of electrical transport properties in organic semiconductors. Both light and electron pulses have been used for irradiating the crystal specimen and the particular advantages of electron beam excitation are discussed (see Section 2). Measurement of carrier lifetimes, drift mobilities and carrier yields in organic semiconductors with the electron bombardment technique provides valuable information regarding the generation and recombination mechanisms, and the

* Present address: Physics Department, Bahauddin Zakariya University, Multan, Pakistan

evaluation of the perfection of organic semiconductors [1–14]. Lifetime of charge carriers $\sim\mu s$ have been measured in organic semiconductors by using the electron bombardment technique (see Sections 1.1, 1.4 and 3). However, this order of magnitude of lifetime of charge carriers in organic semiconductors could not be obtained by using the conventional optical method (see Sections 1.4 and 2).

1.1 Basis of experiment

Figure 1 shows a schematic arrangement for the measurement of transit time of holes in a crystal specimen. A platelet like specimen is fitted with electrodes on opposite sides and charge carriers are generated near the top electrode by a short pulse of electrons of energy between 10 and 50 keV. A steady or pulsed applied field draws one

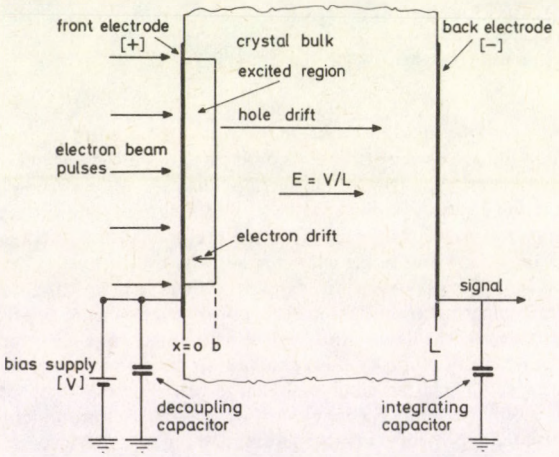

Fig. 1. Schematic arrangement for the measurement of transit time of holes in a crystal specimen

type of carriers across the specimen and the transit time '*T*' is determined by charge integration. This leads directly to the drift mobility. The temperature of the specimen could be increased or decreased if needed (see Section 3, Fig. 4). However, in the case of *p–n* junction solar cells, the samples were bombarded with electron beam under reverse-biased conditions and the lifetime of minority charge carriers was determined from the decay of the concentration of excess minority charge carriers, that is, the time taken for the excess current to decay to 33 per cent of the peak value was recorded (see Sections 1.4 and 3). The bombarding electron pulses may be envisaged as generating electron–hole pairs in the region penetrated, and the subsequent drift of these carriers as inducing charges on the electrodes. A bias field is essential not only to produce the drift, but also to prevent immediate recombination.

1.2 Preparation of specimens

Platelet like ⟨111⟩-oriented silicon specimens cleaved from the crystal boule (intrinsic carrier concentration $\sim 10^{10}$ atoms cm^{-3}, at room temperature) with a diamond wheel had surfaces of 5 mm × 5 mm, and thickness varying between 0.5 − 1.2 mm. Surfaces of the specimen were smoothed by lapping with 600 mesh Carborundum (SiC) and double distilled water and subsequently etched in a mixture of acetic acid (CH_3COOH), nitric acid (HNO_3) and hydrofluoric acid (HF) in the ratio 8 : 2 : 1, for ten seconds and then finally washed with deionized water.

Specimens were prepared for electron bombardment by evaporating circular metal electrodes, onto each face in turn. The silicon wafers were placed in the vacuum system (pressure $\leq 1333 \cdot 10^{-4}$ Pa (10^{-6} torr)) for about half an hour prior to evaporation in order to ensure fresh surface by sublimation. Aluminium was then flash evaporated from a 3-strand tungsten helix covered by a radiation shield with a hole 4 mm in diameter, and at a distance of about 125 mm, from the silicon wafer placed on a brass mask. Silicon wafers were then heated at 425 °C in the vacuum system for half an hour and then allowed to cool down naturally to room temperature in order to ensure good ohmic contacts. However, for preparing *p–n* junction solar cells, *n*-type ⟨111⟩-oriented silicon wafers (impurity concentration $\sim 10^{16}$ atoms cm^{-3} of phosphorous at room temperature) with surfaces of 5 mm × 5 mm, and thickness varying between 0.2 − 0.5 mm, were employed. Aluminium was slowly evaporated onto one side of the *n*-type wafer which was then heated in the vacuum system (pressure $\leq 1333 \cdot 10^{-4}$ Pa (10^{-6} torr)) for 12 hours and subsequently allowed to cool down gradually to attain room temperature in about 5 hours to form the *p*-type region (p^+) into the *n*-type wafer which also acted as an ohmic contact for the *p*-type region. For the ohmic contact on the opposite face of the *n*-type wafer, aluminium electrode was fitted as explained above in the case of silicon specimens.

1.3. Space charge avoidance

The field in which the carriers drift is modified by the charge of the carriers themselves, but provided this field is much less than that on the electrodes due to its geometrical capacitance and the applied voltage, the drifting carriers will not significantly disturb the uniformity of the field. This condition may be expressed [15], as

$$Ne \ll C_s V,$$

where N is the excess number of carriers of one sign present, e is the electronic charge, C_s is the capacitance of the crystal specimen and V is the potential difference applied across the crystal. Experimentally, a violation of the above condition may be recognised by an apparent dependence of mobility on the bias voltage and the dose rate [16]. The internal field may further be perturbed if appreciable densities of trapped

carriers are permitted to accumulate, leading again to an apparent field dependent mobility. However, it has to be noted that in high-resistivity materials, such as anthracene, the density of free carriers at all practicable temperatures is very small and such carriers play no role in drift mobility measurements [2, 4]. Moreover, precautions such as those discussed in Section 3 are essential to avoid space charge effects. The induced conductivity transient may thus be treated analytically in terms of the drift of a sheet of charge across a parallel plate capacitor in which the field is uniform. In particular, it is well known from elementary electrostatics that when a charge Q moves a distance δx towards one of the plate, a charge $\delta q = \frac{Q \cdot \delta x}{L}$ (where L is the plate separation) is transferred around the external circuit from one conducting plate to the other.

When a sheet of free carriers is created by a short bombarding pulse near the bombarded electrode, the induced signals observed, while carriers of one sign are drawn across the bulk of the material and towards the far electrode, are as sketched in Fig. 2.

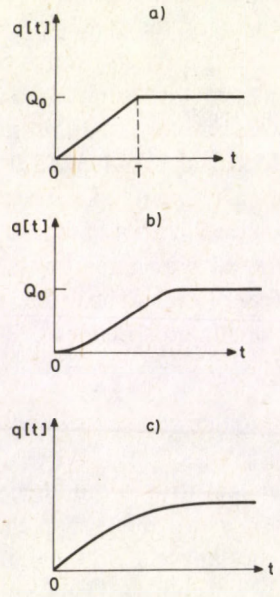

Fig. 2(a) Ideal charge profile, showing well-defined ramp
(b) Practical charge profile, showing broadening of the drifting sheet caused by finite pulse length, penetration depth, diffusion, and mild trapping
(c) Typical distortion of (a) caused by trapping of carriers in the crystal bulk

Three cases can easily be distinguished:

(i) The depth of penetration (b) is very much smaller than the specimen thickness; the length of the excitation pulse T_b is considerably smaller than the time taken by the

sheet of carriers to reach the far electrode; no carriers are lost en route; all the carriers reach the far electrode at the same time, T, after the pulse, i.e., ignoring any spread due to diffusion, (see Fig. 2(a)). The mobility of the carriers can then be calculated from $\mu = \frac{L^2}{TV}$.

(ii) If the depth of penetration and the length of the excitation pulse are finite, the charge induced on the far electrode will also have a component arising from the flow of carriers to the front (bombarded) electrode. Moreover, the arrival of carriers at the rear surface will no longer appear to be instantaneous, but will extend over a finite time. The uncertainty will in practice be further increased owing to the broadening of the drifting sheet caused by diffusion, non-uniform excitation density in the excited region, the imperfect shape of the exciting pulse, trapping and release of carriers by shallow trap levels (imperfections) and a certain amount of bimolecular recombination in the region of excitation, as it is seen in Fig. 2(b).

(iii) Severe or deep trapping reduces the number of carriers moving in the sheet, and the simple charge ramp in Fig. 2(a) becomes unobservable. In less severe cases trapping in the bulk (see Fig. 2(c)) may also be possible. Delany [17] was able to correct his charge-transit curves in anthracene using the simple analysis of Hecht [18].

1.4. Nature of specimen electrodes

The nature of specimen electrodes is of importance but it depends to a large extent on the solid under investigation. The type of drift mobility experiment described here relies on a well defined pulse of generated carriers and any effect which tends appreciably to broaden the sheet of carriers must be avoided (see Section 1.3). This applies particularly to the injection of excess charge from the electrode during and after the transit of the generated (primary) carriers. In an extreme case, such as a CdS crystal or film with an injecting top electrode, the turnover at T in the integrated electron signal will be completely absent [19]. Therefore, ideally, the top electrode should be blocking to the charge carrier under investigation and extracting to that of the opposite sign.

Artificial blocking electrodes have been used in drift mobility work, but the problem is that they normally tend also to impede the extraction of the opposite type of generated carrier. This is likely to produce disturbing polarisation effects and space charge avoidance techniques (see Sections 1.3 and 3) are essential. Spear and Mort [20] have used 0.5 μm Pyrex films as a blocking top electrode on CdS crystals. The incident electron beam penetrated this electrode with negligible loss of energy. There is, however, some uncertainty in this arrangement as to the actual potential which develops across the crystal. Therefore, it is better to avoid the use of artificial blocking layers and, if possible, to find a metallic electrode giving minimum injection. For example, aluminium electrodes, sufficiently thin to transmit the bombarding electrons

without undue absorption, were applied to both surfaces of the anthrancene crystal by evaporation in vacuum [21]. Field and temperature dependence of carrier yield in crystalline anthracene under electron bombardment by Saleh [4, 5] showed that in the best anthracene crystals, the electron and hole charge–carrier trappings at 323 K were completely absent and the carrier yields were equal, i.e., equal numbers of electrons and holes were produced by the electron bombardment at the rate of about 580 – 600 eV per pair. The values for the drift mobilities normal to the basal plane, viz., $\mu_h = 0.92 \pm 0.02\ \mathrm{cm^2\ s^{-1}\ V^{-1}}$ and $\mu_e = 0.38 \pm 0.02\ \mathrm{cm^2\ s^{-1}\ V^{-1}}$ and their temperature coefficients agreed well with other published values [2–5, 7–10].

The above observations also indicate that the use of the electron bombardment technique can lead to the evaluation of the perfection of organic semiconductors. Moreover, measurement of lifetime of minority charge carriers in organic semiconductors with the electron bombardment technique can determine the crucial parameters like current gain of bipolar transistors, photovoltaic response of solar cells and so on. In view of this, determination of lifetime may be considered as one of the most crucial parameters in the characterization of semiconductor materials which are to be used later for the fabrication of a variety of devices.

Lifetime can be defined in general as the average time for which a free-charge carrier exists in a given semiconductor before it gets lost by recombination. It may be realized that the value of lifetime in a semiconductor is determined by the actual mechanism involved in the recombination of the free carriers.

Lifetime of the minority charge carriers was measured in silicon solar cells by using the electron bombardment technique (see Sections 1.1, 1.3 and 3), and found to be $\sim 25\ \mu s$. However, in silicon specimens, lifetime of charge carriers was found to be $\sim 8\ \mu s$ by this technique. This order of magnitude of lifetime could not, however, be obtained by using the conventional optical method. The low value of lifetime of charge carriers in the case of electron bombarded silicon is attributed to the introduction of recombination centres by high-energy electron irradiation [22]. However, the influence of electron bombardment on the lifetime of semiconductors is important because many types of semiconductor devices are intended for operation in nuclear reactor or space environments.

2. Advantages of electron beam excitation over optical excitation

Both light and electron pulses have been used for irradiating the organic semiconductors (see for instance [1–7, 19, 21, 23]). The main advantages of electron beam excitation over optical excitation are as follows:

(i) Electron beam excitation largely overcomes the problem of absorption in the top electrode which may be a serious one when optical excitation is used in the 'sandwich' cell configuration. A thin evaporated metal electrode may easily absorb

almost all the incident light intensity, particularly in the ultraviolet, while it would practically be transparent to a 10 keV electron beam [1–4, 11, 21].

(ii) There is ample intensity, even with ns pulses, for the generation of a sufficient number of carriers. The design and construction of a suitable high voltage electron gun with magnetic focusing is a relatively easy matter [1–4, 11, 21].

(iii) The depth of the generation region below the top surface of the crystal specimen can be varied within wide limits by means of the accelerating potential V_b applied to the electron gun. Ehrenberg and King [24] have investigated experimentally the penetration depths of electrons in polystyrene by measuring the extent of the luminosity on the basis of its density and similarly estimates for the case of anthracene and other organic semiconductors may be made from their data [1, 17, 20].

The main disadvantage for irradiating the solids with electron pulses lies in the fact that the experiment has to be carried out in vacuum, $1333 \cdot 10^{-2}$ Pa (10^{-4} torr) or better. If the solid under investigation is mounted in the same system, its vapour pressure has to be sufficiently low in the temperature range of interest. However, in the rare gas solids such as solid Ar, Kr and Xe vapour pressures of several ten thousand Pa (several hundred torr) occur near the triple point. But this problem can be overcome by growing and investigating the specimen in a small chamber isolated from the main vacuum system [25].

3. The bombarding apparatus

Figure 3 shows the schematic diagram of the bombarding apparatus employed for the measurement of lifetime of charge carriers and drift mobility in a crystal specimen. The central feature was the demountable bombarding tube, evacuated to a pressure of about $1333 \cdot 10^{-4}$ Pa (10^{-6} torr). The E.H.T. supply consisted of an 8 kV, 8 kHz oscillator followed by a 12-stage Cockroft–Walton voltage multiplier. The output voltage was continuously variable between -5 kV and -100 kV nominally, and was stabilized by feedback.

The electron gun was a directly heated tetrode, in which the earthed specimen chamber constitutes the anode. The apex of the filament (hair-pin shape) was placed within a few mm of the gun modulator aperture. The exact positioning of the filament, which was possible under operating condition, was usually made such that the electron gun had a cut-off voltage of about 16 V. The filament current was derived from a 6 V accumulator via a power transistor in emitter follower configuration. The bias of the modulator could be varied between -36 and 0 V, with respect to the filament. The separation between the grid and the first anode was about 1 mm. The first anode was maintained at a constant $+300$ V with respect to the filament.

The bistable beam pulse generator [21] produced pulses of total height 16 V and full-width-half-height duration 90 ns. For beam current measurement, the pulser was triggered at 10 kHz., by a free-running multivibrator; for bombardment experiments, at

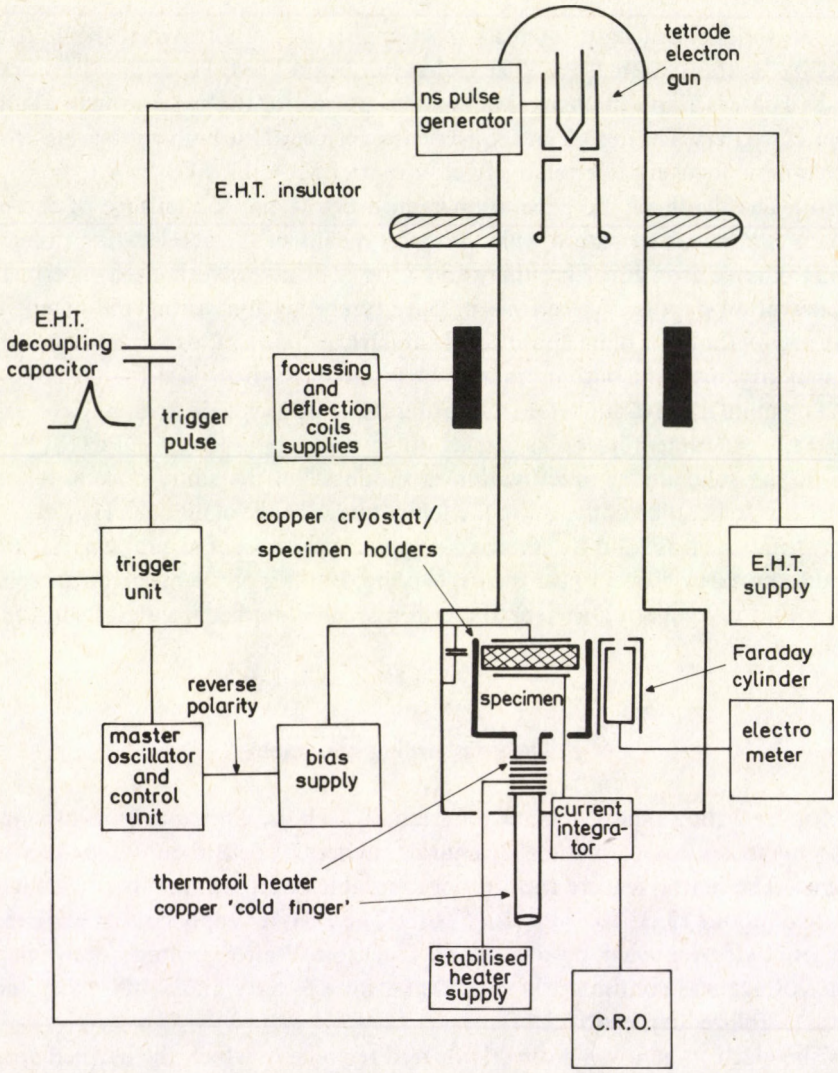

Fig. 3. Schematic diagram of the apparatus employed

rates between 0 and 0.28 Hz, by means of the 'dekatron' circuit described by Saleh [21]. The latter supplied trigger pulses for the electron beam and oscilloscope, as well as initiating a reversal of polarity of the specimen bias between successive pulses to minimize space charge accumulation.

The d.c. supplies for the focusing coil and the deflection coils were current-stabilised. Both the Faraday cylinder and the specimen holder in Fig. 4 were coated with a fluorescent deposit to enable the beam position to be observed, and were situated off the axis of the tube so as to avoid any background current from negative ions.

The crystal specimen was sandwiched between the platinum foil and a small brass disc by means of a phosphor bronze spring with P.T.F.E. insulating bush cemented to it with Durofix. The type of mounting employed in the bombarding apparatus is shown in Fig. 4.

Signal detection and measurement was performed by direct connection of the back (unbombarded) electrode of the specimen to the input of the current integrator or

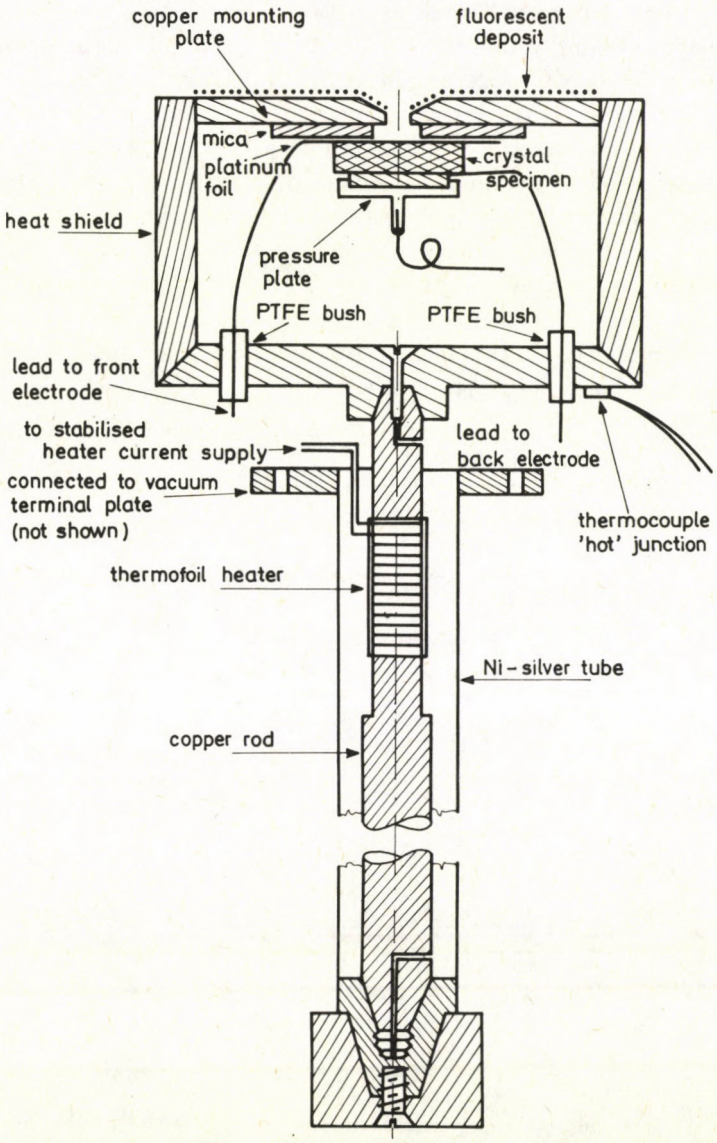

Fig. 4. Specimen mounting with cryostat tube assembly

charge-sensitive amplifier [21]. The time constant of the integrator was about 25 ms, and the sensitivity 8×10^{10} VC^{-1}. This allowed measuring induced charge transients as small as 10^{-13} C per pulse using an 85 MHz oscilloscope (Tektronix type 581 with 86 preamplifier). The bombarding dose was measured by deflecting the beam, pulsed at a high repetition rate, into a screened Faraday cage and integrating the current; the sensitivity of this arrangement was 2×10^{-16} C per pulse.

The high sensitivity of the measuring system allowed the use of such low bombarding doses that both thermal damage and space-charge effects were mostly negligible (a typical bombarding pulse contained 1.5×10^7 electrons per cm^2).

The temperature of the specimen, if needed, (Fig. 4) could be reduced to 272, 195 or 85 K by immersing the copper 'cold finger' in ice, solid CO_2 or liquid nitrogen respectively, while the 'Minco thermofoil' heater, which was cemented to the copper cold finger, was used to obtain intermediate or elevated temperatures [21]. The temperature of the specimen can be measured using a chromel-alumel thermocouple connected to a Pye 'Research' potentiometer via chromel and alumel vacuum-tight lead-throughs to an accuracy of ± 0.5 K.

The time sequence used in the experimental arrangement shown in Fig. 3 to observe induced signals at the back (unbombarded) electrode in an essentially unpolarised specimen, is illustrated in Fig. 5.

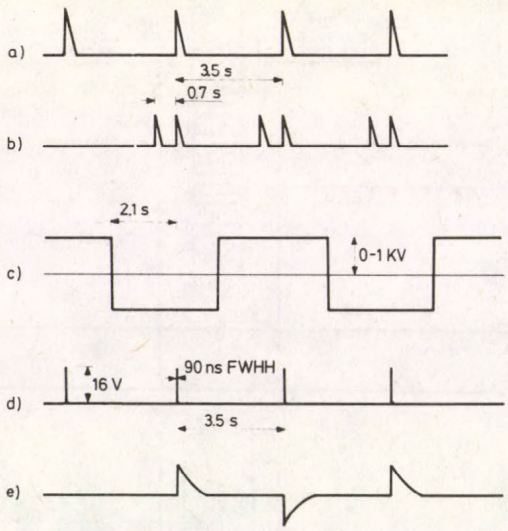

Fig. 5. Switching scheme to neutralise space charge
(a) Beam trigger pulses
(b) C.R.O. trigger pulses
(c) Bias field pulses
(d) Beam current pulses
(e) Observed signals (polarity inverted by integrator)

(a) represents the output of the master trigger unit in the form of short pulses, 3.5 s apart to trigger the ns beam pulse generator.

(b) represents the pulses applied to the oscilloscope time base unit. An extra pulse preceding the beam trigger pulse by about 0.7 s is used to provide base lines for the display.

(c) shows the specimen bias field pulses obtained by the reversing action of two Hg-wetted relays in series at the output of 1 kV stabilised power supply; a continuously variable voltage was obtained from a potentiometer provided with a 50 Hz filter.

The beam pulses (d) occur approximately 2.1 s after each bias reversal, by which time the bias has attained a steady value.

(e) shows the observed signals (not to scale).

4. Conclusions

It may be stated that the electron bombardment technique is superior to the conventional optical method and the measurement of lifetime of charge carriers in organic semiconductors with this technique can lead to the evaluation of the perfection of semiconductor materials which are to be used later for the fabrication of a variety of devices.

Acknowledgement

One of us (M. Saleh) wishes to thank Dr. J. Hirsch of Birkbeck College, University of London, London, U.K., for helpful discussions.

References

1. W. E. Spear, Proc. Phys. Soc., *B70*, 669, 1957; *B70*, 1139, 1957; *76*, 826, 1960.
2. J. L. Delany and J. Hirsch, J. Chem. Phys., *48*, 4717, 1968.
3. B. Sansal and M. Schott, Solid State Commun., *8*, 1499, 1970.
4. M. Saleh, J. Phys. C: Solid State Phys., *9*, 4165, 1976.
5. M. Saleh, Jap. J. of Appl. Phys., *17*, No. 6, 1031, 1978.
6. M. Saleh and M. S. Zafar, Acta Phys. Hung., *45*, 233, 1978.
7. R. G. Kepler, Phys. Rev., *119*, 1226, 1960.
8. R. G. Kepler, Organic Semiconductors, p. 1. The Macmillan Co., New York, 1962.
9. C. Bogus, Z. Phys., *207*, 181, 1967.
10. H. Bauser, Naturwissenschaften, *54*, 505, 1967.
11. M. Saleh, Physica Status Solidi, *A78*, K 137-K 140, 1983.
12. D. C. Hoestry and G. M. Letson, J. Chem. Phys. Solids, *24*, 1609, 1963.
13. V. S. Gerasimenko, Yu. N. Ivaschenko, M. A. Iovu, M. S. Iovu, A. V. Mironos, V. L. Smirnov, M. R. Chernii and S. D. Shutov, J. Phys. Colloq. (France), *42*, No. C-4, pt. 2, 963, 1981.
14. A. Schmillen and W. Falter, Z. Phys., *218*, 401, 1969.
15. A. Rose, R. C. A. Rev., *12*, 362, 1951.
16. L. M. Schwartz and W. G. Horning, J. Phys. Chem. Solids, *26*, 1821, 1965.
17. J. L. Delany, Ph. D. Thesis, University of London, 1967.

18. K. Hecht, Z. Physik, *77*, 235, 1932.
19. G. W. Bradberry and W. E. Spear, Brit. J. Appl. Phys., *15*, 1127, 1964.
20. W. E. Spear and J. Mort, Proc. Phys. Soc., *81*, 130, 1963.
21. M. Saleh, Ph. D. Thesis, University of London, 1972.
22. G. K. Wertheim, Phys. Rev., *105*, 1730, 1957.
23. M. Saleh, Physica Scripta (Sweden), *19*, 54, 1979; *21*, 220, 1980.
24. W. Ehrenberg and D. E. N. King, Proc. Phys. Soc., *81*, 751, 1963.
25. L. S. Miller, S. Howe and W. E. Spear, Phys. Rev., *166*, 871, 1968.

Acta Physica Hungarica 60 (3—4), pp. 173—175 (1986)

GUPTA–BLEULER QUANTISATION OF THE FREE MASSLESS SPIN 2 FIELD

A. MÉSZÁROS*

Central Research Institute for Physics
H-1525 Budapest 114, Hungary

(Received in revised form 13 September 1984)

Using eight pseudoparticles the precise procedure of Gupta–Bleuler quantisation is given for the free massless spin 2 field.

As far as it is known, the precise procedure of Gupta–Bleuler quantisation for the free massless spin 2 field has not been given yet. Indeed, already Gupta formulated the procedure a long time ago [1], but he used ad hoc nine pseudoparticles. This is in fact an incomprehensible choice. The potential of the spin 2 field is a symmetric $U^{ij}=U^{ji}$ tensor, and therefore there should obviously be two physical and eight unphysical polarisations. This preciseness has an essential importance in quantum gravity, because in the case of self-interacting gauge fields these pseudoparticles determine the behaviour of ghost particles [2], [3].

This paper gives the precise procedure of quantisation. Of course, the questions that are identical to the case of spin 1 field—opposite sign of commutators, indefinite metric, etc. (for details see, e.g., [4])—are not considered here.

In the Lorentz gauge the equations of the free massless spin 2 field are given by [5]

$$\Box U^{ij}=0; \qquad 2U^{ij}{}_{,j}=U'^{i}; \qquad U^{i}_{i}\equiv U, \tag{1}$$

where an index after a comma denotes partial derivatives, $\Box\equiv\partial^i\partial_i$ and the Latin indices take the values 0, 1, 2, 3. The indices are moved by the

$$\eta^{ij}=\eta_{ij}\equiv\mathrm{diag}\,(1,\ -1,\ -1,\ -1)$$

Minkowskian metric tensor of flat space-time. We have still the following gauge freedom:

$$\tilde{U}^{ij}=U^{ij}+V^{(i,j)}; \qquad \Box V^{i}=0, \tag{2}$$

* Address: Department of Astronomy and Astrophysics, Charles University, Prague 5, Svédská 8, ČSSR.

where ( ) denotes symmetrisation without the factor $\frac{1}{2}$ and V^i are C^3 functions of x^i coordinates. In momentum space we have

$$U^{ij}=(2\pi)^{-\frac{3}{2}}\int\frac{d\mathbf{k}}{\sqrt{2k_0}}(\bar{U}^{ij}(\mathbf{k})e^{ik_nx^n}+\overset{+}{U}{}^{ij}(\mathbf{k})e^{-ik_nx^n}), \tag{3}$$

where $k^i\equiv[k^0,\mathbf{k}]$ is the wave vector.

In order to introduce the eight pseudopolarisations we shall use the orthonormal e, f, n, m vectors. They fulfil the following relations (see [4]):

$$m^im^j-e^ie^j-f^if^j-n^in^j=\eta^{ij};\qquad e^ie_i=f^if_i=n^in_i=-m^im_i=-1;$$

$$e^if_i=e^in_i=e^im_i=f^in_i=f^im_i=n^im_i=0;\qquad k^ik_i=(k^0)^2-|\mathbf{k}|^2=0;$$

$$k^i=k^0(n^i+m^i);\qquad e^i\equiv[0,\mathbf{e}];\qquad f^i\equiv[0,\mathbf{f}];\qquad n^i\equiv\left[0,\frac{\mathbf{k}}{|\mathbf{k}|}\right];$$

$$m^i\equiv[1,0,0,0]. \tag{4}$$

One may write:

$$\sqrt{2}\overset{\pm}{U}{}^{ij}(\mathbf{k})=\overset{\pm}{a}(\mathbf{k})(e^ie^j-f^if^j)+\overset{\pm}{b}(\mathbf{k})e^{(ifj)}+\overset{\pm}{c}(\mathbf{k})e^{(ini)}+\overset{\pm}{d}(\mathbf{k})e^{imj)}+$$
$$+\overset{\pm}{g}(\mathbf{k})f^{(inj)}+\overset{\pm}{h}(\mathbf{k})f^{(imj)}+\overset{\pm}{p}(\mathbf{k})(m^im^j+n^in^j)+\overset{\pm}{r}(\mathbf{k})m^{(inj)}+$$
$$+\frac{\overset{\pm}{u}(\mathbf{k})+\overset{\pm}{v}(\mathbf{k})}{\sqrt{2}}(m^im^j-n^in^j)+\frac{\overset{\pm}{u}(\mathbf{k})-\overset{\pm}{v}(\mathbf{k})}{\sqrt{2}}(e^ie^j+f^if^j). \tag{5}$$

One has the conditions

$$(2\bar{U}^{ij}(\mathbf{k})k_j-k^i\bar{U}(\mathbf{k}))|\phi\rangle=0;\qquad\langle\phi|(2\overset{+}{U}{}^{ij}(\mathbf{k})k_j-k^i\overset{+}{U}(\mathbf{k}))=0, \tag{6}$$

where $|\phi\rangle$ is the state vector of Fock space. Hence

$$(\bar{d}(\mathbf{k})-\bar{c}(\mathbf{k}))|\phi\rangle=(\bar{h}(\mathbf{k})-\bar{g}(\mathbf{k}))|\phi\rangle=(\bar{p}(\mathbf{k})-\bar{r}(\mathbf{k}))|\phi\rangle=$$
$$=(\bar{u}(\mathbf{k})-\bar{v}(\mathbf{k}))|\phi\rangle=0 \tag{7}$$

and

$$\sqrt{2}\bar{U}^{ij}(\mathbf{k})|\phi\rangle=(\bar{a}(\mathbf{k})(e^ie^j-f^if^j)+\bar{b}(\mathbf{k})e^{(ifj)}+\frac{\bar{c}(\mathbf{k})}{k^0}e^{(ikj)}+$$
$$+\frac{g(\mathbf{k})}{k^0}f^{(ikj)}+\frac{\bar{p}(\mathbf{k})}{(k^0)^2}k^ik^j+\frac{u(\mathbf{k})}{\sqrt{2}k^0}((m^i-n^i)k^j+k^i(m^j-n^j)))|\phi\rangle \tag{8}$$

follows (similar relations hold for conjugates, too). Denoting

$$\sqrt{2}k_0\overset{\pm}{V}(\mathbf{k})=\overset{\pm}{c}(\mathbf{k})e^i+\overset{\pm}{g}(\mathbf{k})f^i+\overset{\pm}{p}(\mathbf{k})(m^i+n^i)+\frac{\overset{\pm}{u}(\mathbf{k})}{\sqrt{2}}(m^i-n^i) \tag{9}$$

one immediately sees that only the polarisations given by operators $\overset{\pm}{a}(\mathbf{k})$, $\overset{\pm}{b}(\mathbf{k})$ have physical meaning; compare with (2). The commutators are the following:

$$[\bar{a}(\mathbf{k}), \overset{+}{a}(\mathbf{q})] = [\bar{b}(\mathbf{k}), \overset{+}{b}(\mathbf{q})] = [\bar{c}(\mathbf{k}), \overset{+}{c}(\mathbf{q})] = -[\bar{d}(\mathbf{k}), \overset{+}{d}(\mathbf{q})] =$$
$$= [\bar{g}(\mathbf{k}), \overset{+}{g}(\mathbf{q})] = -[\bar{h}(\mathbf{k}), \overset{+}{h}(\mathbf{q})] = [\bar{p}(\mathbf{k}), \overset{+}{p}(\mathbf{q})] = -[\bar{r}(\mathbf{k}), \overset{+}{r}(\mathbf{q})] =$$
$$= [\bar{u}(\mathbf{k}), \overset{+}{u}(\mathbf{q})] = -[\bar{v}(\mathbf{k}), \overset{+}{v}(\mathbf{q})] = \delta(\mathbf{k}-\mathbf{q}). \tag{10}$$

A long but straightforward calculation leads to the relation:

$$2[\bar{U}^{ij}(\mathbf{k}), \overset{+}{U}{}^{pr}(\mathbf{q})] = \delta(\mathbf{k}-\mathbf{q})\,(\eta^{ip}\eta^{jr} + \eta^{ir}\eta^{jp} - \eta^{ij}\eta^{pr}). \tag{11}$$

In order to write down the dynamical invariants we proceed as follows. As Lagrangian one may use

$$L = \frac{1}{2} : U^{ij,k} U_{ij,k} : - \frac{z}{2} : U^{,i} U_{,i} :, \tag{12}$$

where z is an arbitrary real number; $z \neq \frac{1}{4}$. For any z one obtains $\Box U^{ij} = 0$. In standard way from (12) one obtains the four-momentum:

$$P^i = \int d\mathbf{k} \cdot k^i (\overset{+}{U}{}^{jm}(\mathbf{k}) \bar{U}_{jm}(\mathbf{k}) - z \overset{+}{U}(\mathbf{k}) \bar{U}(\mathbf{k})) \tag{13}$$

and hence

$$\langle \phi \mid P^i \mid \phi \rangle = \langle \phi \mid \int d\mathbf{k} \cdot k^i (\overset{+}{a}(\mathbf{k}) \bar{a}(\mathbf{k}) + \overset{+}{b}(\mathbf{k}) \bar{b}(\mathbf{k}) + 2(1-2z) \overset{+}{v}(\mathbf{k}) \bar{v}(\mathbf{k})) \mid \phi \rangle. \tag{14}$$

Thus obviously $z = \frac{1}{2}$ is the right choice in (12).

Acknowledgement

Thanks are due to Dr. Á. Sebestyén for valuable remarks.

References

1. S. N. Gupta, Proc. Phys. Soc., *65*, 161, 1952.
2. N. N. Bogolyubov, D. V. Shirkov, Kvantoviye polya, Nauka, Moscow, 1980.
3. M. J. Duff, in Quantum Gravity, An Oxford Symp., ed. by C. J. Isham, R. Penrose and D. W. Sciama, Clarendon Press, Oxford, 1975.
4. N. N. Bogolyubov, D. V. Shirkov, Vvedyenyiye v tyeoriyu kvantovanikh poley, Nauka, Moscow, 1973.
5. W. E. Thirring, Annals of Phys., *16*, 96, 1961.

Acta Physica Hungarica 60 (3—4), pp. 177—186 (1986)

ABSOLUTE ELECTRONIC TRANSITION MOMENT VARIATION IN NOγ ($A^2\Sigma^+ - X^2\Pi_{1/2}$) SYSTEM

V. G. TULASIGERI and V. M. KORWAR

Department of Physics, Karnatak University
Dharwad 580003, India

(Received 18 September 1984)

Making use of relative electronic transition moment variation R_e with internuclear distance r, $R_e(r)$, absolute $R_e(r)$ values have been evaluated for each band of the NOγ system. Using these values, a linear and a quadratic relation for absolute $R_e(r)$ have been given for the entire band system. It has been found that there is constancy of R_e in the progression with $v'=0$, and in the progressions with $v'=1$, 2, it has been found to vary with 'r' and the variation is both linear and quadratic, respectively.

1. Introduction

The NOγ system ($A^2\Sigma^+ - X^2\Sigma_{1/2}$) has been the subject of vigorous investigation in recent times, especially with regard to its electronic transition moment variation with internuclear distance. Several workers in the field have studied the usual relative transition moment variation, $R_e(r)$ in this band system. Most of them have given linear equations for this variation; only Jain and Sahni [1] have given a quadratic equation. Very recently the present authors [2] have also given their own equations for $R_e(r)$ by using two different methods, namely, the usual methods of Nicholls and Jarmain [3] and Turner and Nicholls [4] and the method of regression [5]. The authors [2] give not only the linear relation for $R_e(r)$ but also a quadratic relation for it.

Absolute $R_e(r)$ is derived in a similar manner as relative $R_e(r)$ by the usual method of Nicholls and Jarmain [3], but with the difference that it is now derived using band intensities in definite units (photons/s). In the derivation of 'relative' $R_e(r)$, relative intensities are used. Only a few investigators [6–8] have dealt with this 'absolute' $R_e(r)$ in some detail. While Jeunehomme [8] using his own life-time determination of the $v'=0$ level, computed absolute R_e only for the (0, 0) band of NOγ system, Navati and Korwar [7] gave only a linear equation for absolute $R_e(r)$. Mohlmann et al [6] have derived both relative and absolute R_e values and compared by plotting them against $\bar{r}_{v',v''}$. They have concluded that R_e is independent of r. All these investigators [6–8] have only derived linear R_e. As mentioned in the paper [2] of the present authors the trend of variation was noticed to be nonlinear and an attempt to fit the points to a quadratic equation was made. This was for relative $R_e(r)$ variation. In pursuance of this to absolute $R_e(r)$ variation, in the present investigation we have studied absolute $R_e(r)$ in depth. We have employed two methods in this study.

2. Determination of absolute $R_e(r)$

The so-called oscillator strengths (f-values) of a band and the absolute $R_e(r)$, are connected by the relation

$$f_{v',v''} = (8\, mc\pi^2/3he^2) G' \nu_{v'v''} R^2(r_{v',v''}) q_{v',v''}\,, \tag{1}$$

where G' is the degeneracy of the upper state and all other parameters carry the usual meaning.

So, if one possessed f values, FC factors, wave numbers of bands, one can compute absolute $R_e(r)$ by Eq. (1) above. But, the determination of f values is not an easy task, while the other quantities required are easy to obtain. To evaluate oscillator strengths, one has necessarily to study bands in absorption, which, in general, is not as simple as the study in emission. This is clear from the scanty data available of f-values for the NOγ system—only four f values for $v''=0$, 1, 2 and 3 are available in the literature [9–12]. But, fortunately, there is an alternative way of computing absolute $R_e(r)$ even in the absence of f values. This is possible through the following relation connecting relative $R_e(r)$ and life-time (τ) values to f values and to the absolute $R_e(r)$ thereof.

$$f_{v',v''} = \left(\frac{mc}{8\pi^2 e^2}\right)\left(\frac{1}{\tau_{v'}}\right)\left(\frac{G'}{G''}\right)\frac{\nu_{v',v''} q_{v',v''} R^2(r_{v',v''})}{\sum\limits_{v''} \nu^3_{v',v''} q_{v',v''} R^2(r_{v',v''})}\,, \tag{2}$$

where G' is the degeneracy of the upper state, G'' is the degeneracy of the lower state and all other parameters carry the usual meaning. As can be seen from Eq. (2), even if one knows one τ value, say for the initial fixed level in a progression, one could compute f values for all the bands in that progression and hence, absolute R_e values for all the bands in the progression.

Many of the band spectroscopists [6, 13–15], have given values up to $v'=4$, starting from $v'=0$ for the NOγ system, hence for all the different v'' progressions with $v'=0$, 1, 2, 3 *and* 4 f values could be computed, as has been done by us in the present work. We have used 2 sets of τ values of Mohlmann et al [6] and of Smith et al [13] upto $v'=2$ only as absolute intensities in terms of photons/s for bands involving $v'=3$ and $v'=4$ are not available. Many of the earlier workers have assumed only one f value for the entire band system which is not correct as is clear from Eqs (1) or (2) above, which suggests one f value for each band. Hence, by using available intensities (photons/s) and the wavelengths as given by Mohlmann et al [6] for $v'=0$, 1 and 2 and by using Eq. (2), we have evaluated the f value for each band in the three progressions of the NOγ system.

Now, the relative $R_e(r)$ relations required in the determination of absolute $R_e(r)$ have been derived by us by two independent methods (i) procedure of Nicholls and Jarmain [3] (ii) the method of regression [5]. In the present work, RKR FC factors and r-centroids of Spindler et al [16] have been used. Molecular constants required for this

and other calculations in this paper are taken from Huber and Herzberg [17]. In the computation of absolute R_e values via f, while using relations (1) and (2), we have taken for $G'=1$ and $G''=2$ as given by Mulliken [18].

As mentioned earlier, while the earlier investigators [6–8] have derived only the linear $R_e(r)$ equation, we have attempted the quadratic $R_e(r)$ relation also. None of the previous workers except Tawde and Tulasigeri [19, 20], one of the present authors, have employed the method of regression [5], for deriving the $R_e(r)$ relation. The various 'relative' $R_e(r)$ relations under different methods are given in Table I.

Table I
Relative electronic transition moment variation $R_e(r)$

Type of fitting	RKR potential	
	Method of Nicholls and Jarmain	Method of regression
Linear fitting	$R_e(r)=K(1-0\cdot0132r)$	$R_e(r)=K(1+0\cdot4340r)$
Quadratic fitting	$R_e(r)=K(1-1\cdot7646r+0\cdot8169r^2)$	$R_e(r)=K(1-1\cdot9912r+0\cdot9103r^2)$

While computing absolute $R_e(r)$ values for different bands, we have used both linear and quadratic equations for relative $R_e(r)$ under both methods mentioned above. As there are two sets of τ values, two methods of obtaining relative $R_e(r)$ equations, which, in turn, are two in number, we will have eight sets of absolute R_e values which have been represented graphically in Figs 1 and 2 progressionwise.

Once the absolute R_e's have been evaluated, they could be represented by appropriate equations for the entire band system. This has been done by us in the present investigation. We have given both linear and quadratic representations to absolute R_e data. These are given in Table II.

These equations have been made use of in evaluating individual absolute $R_e(r)$ values. If the equations derived (or fitted) are correct, the absolute R_e values obtained from them should turn out to be the same (or very nearly so) as the ones used to derive the equations (see Figs 1 and 2). In other words, this ensures self-consistency of the equations. Further, the derived equations could be used to predict R_e values of the bands of a given system for which r-centroids data are available. This has been done for all the three progressions by representing them graphically in Fig. 3. Graphical representations for both methods (method of Nicholls and Jarmain [3] and method of regression [5]) have been shown in Fig. 3.

A graphical representation of all the above absolute R_e values alongside the experimental R_e values evaluated by using experimental oscillator strengths of Farmer et al [12] and of Weber et al [9] is shown in Figs 1, 2 and 3.

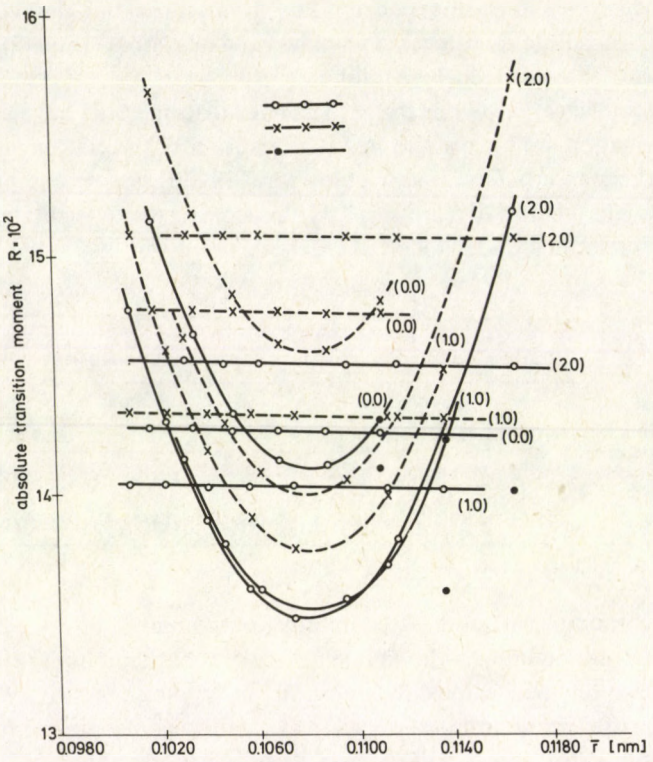

Fig. 1. Absolute transition moment R versus $\bar{r}_{v',v''}$ centroid for the $A^2\Sigma^+ - X^2\Pi_{1/2}$ transition in NO using RKR Franck–Condon factors [16] by the method of Nicholls and Jarmain [3] employing relative $R_e(r)$ equation (Table I). Experimental band intensities [6]
Solid curves: Mohlmann's τ values; dashed curves: Smith's τ values
● ——— absolute experimental transition moments [9, 12]
Note: ——— graphs drawn correct up to the fourth place of decimal

3. Results and discussion

Mohlmann et al [6] have concluded that R_e is constant for the entire band system. We, in our present work, have found a similar result only with the use of our linear relations for $R_e(r)$. So, we can say that when one fits the data to linear equations only, one observes no variation in R_e with r for the NOγ systems but, as we fitted the data to quadratic equation also, we could observe that R_e is not a constant, but it varies with r for the NOγ system. The present finding that R_e is not a constant, finds support from the work of Marr [21] who concluded that it is not correct to assume that R_e is independent of r.

The quadratic equations obtained by us for $R_e(r)$ of the NOγ system show an interesting trend of R_e. As one observes closely the results of absolute values of R_e, one

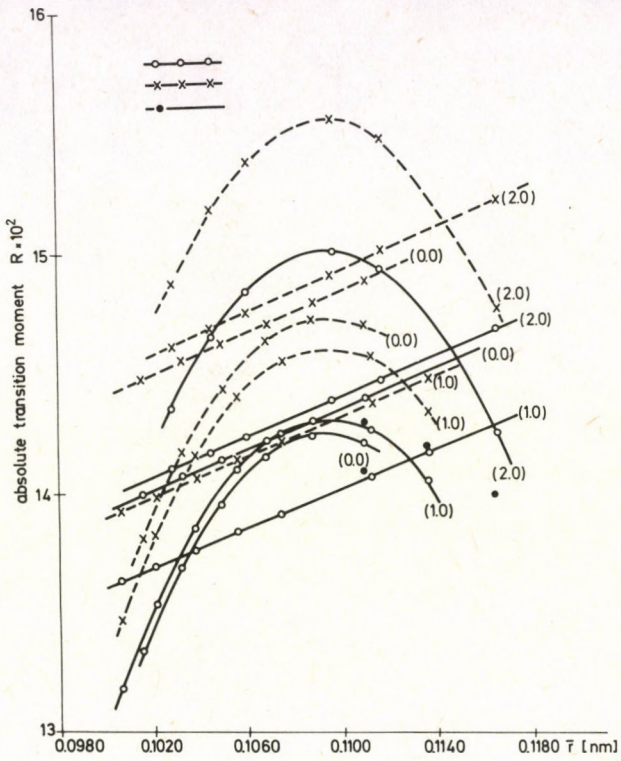

Fig. 2. Absolute transition moment R versus $\bar{r}_{v',v''}$ centroid for the $A^2\Sigma^+ - X^2\Pi_{1/2}$ transition in NO using RKR Franck–Condon factors [16] by the method of regression [5] employing relative $R_e(r)$ equations (Table I). Experimental band intensities [6]

Solid curves: Mohlmann's τ values

dashed curves: Smith's τ values

● ——— absolute experimental transition moments [9, 12]

Note: ——— graphs drawn correct up to the fourth place of decimal

finds that there is a particular trend of R_e in a particular progression; for instance in the $v'=0$, v'' progression, the linear term in the R_e equations (any of the equations under any method) predominates over the quadratic term, whereas in the $v'=1$, v'' progression, there is almost linear variation as before but there is a slight quadratic trend as well; for $v'=2$, v'' progression, the quadratic term in the equation predominates over the linear term. We may say that it has been possible for us to observe such different trends in different progressions only because of our in-depth study of the problem of variation of electronic transition moment. This aspect of the problem has been missed by the earlier investigators.

Another interesting feature found by us with regard to the quadratic variations of R_e is that the graphs (Figs 1, 2 and 3) depicting these variations in the case of the two methods show opposite curvatures.

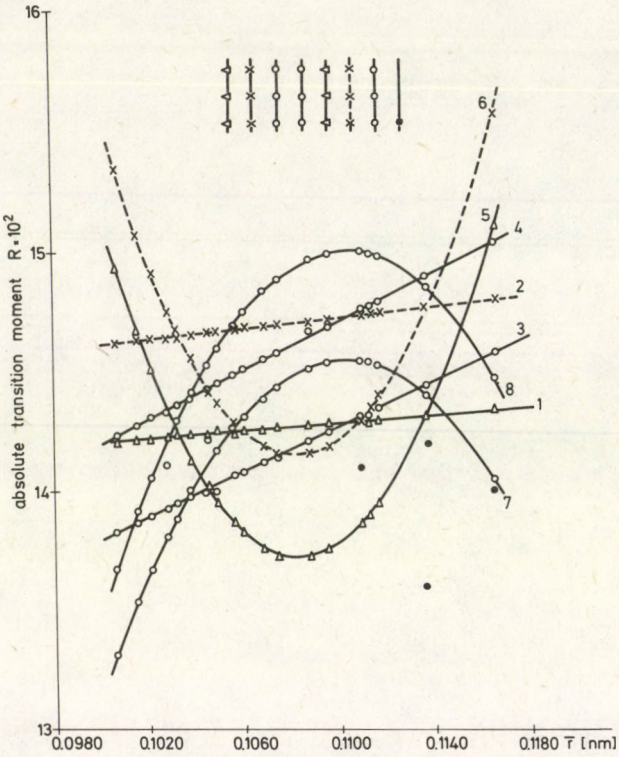

Fig. 3. Absolute transition moment R versus $\bar{r}_{v',v''}$ centroid for the $A^2\Sigma^+ - X^2\Pi_{1/2}$ transition in NO using RKR Franck–Condon factors [16] by the method of Nicholls and Jarmain [3] and the method of regression [5] employing experimental $R_e(r)$ equation (Table II). Experimental band intensities [6].
Curve 1: linear equation, Mohlmann's τ values, method of Nicholls and Jarmain [3]
Curve 2: linear equation, Smith's τ values, method of regression [5]
Curve 3: linear equation, Mohlmann's values, method of regression [5]
Curve 4: linear equation, Smith's τ values, method of regression [5]
Curve 5: quadratic equation, Mohlmann's τ values, method of Nicholls and Jarmain [3]
Curve 6: quadratic equation, Smith's τ values, method of Nicholls and Jarmain [3]
Curve 7: quadratic equation, Mohlmann's τ values, method of regression [5]
Curve 8: quadratic equation, Smith's values, method of regression [5]
● ——— absolute experimental transition moments [9, 12]
Note: ——— graphs drawn correct up to the fourth place of decimal

In fact, our present work can be extended further to include more and more bands. Even when one has not the complete data on f values, one could predict them by a semi-emphirical computation and extend the work of $R_e(r)$. Work in this direction is in progress and will form the subject of yet another paper by us.

Now a word about oscillator strength data. Earlier investigators [22, 23] assumed an effective electronic oscillator strength for the whole NOγ system. But doubts about this assumption were cast by Hebert and Nicholls [24] and also by Nicholls and Stewart [25]. Marr [21] concluded that such an assumption of a single

Table II

Absolute electronic transition moment variation $R_e(r)$

Type of fitting	RKR potential			
	Method of Nicholls and Jarmain		Method of regression	
	Mohlmann τ values	Smith τ values	Mohlmann τ values	Smith τ values
Linear fitting	$R_e(r)=(0.1337+0.0084r)$ $[R_e(r)=K(1+0.0625r)]$	$R_e(r)=(0.1346+0.0115r)$ $[R_e(r)=K(1+0.0855r)]$	$R_e(r)=0.0906+0.0474r)$ $[R_e(r)=K(1+0.5227r)]$	$R_e(r)=(0.0906+0.0514r)$ $[R_e(r)=K(1+0.5669r)]$
Quadratic fitting	$R_e(r)=(2.5675-4.4905r+$ $+2.0744r^2)$ $[R_e(r)=K(1-1.7490r+$ $+0.8079r^2)]$	$R_e(r)=(2.5886-4.5245r+$ $+2.0913r^2)$ $[R_e(r)=K(1-1.7476r+$ $+0.8079r^2)]$	$R_e(r)=(-1.4699+2.9306r-$ $-1.3291r^2)$ $[R_e(r)=K(1-1.9937r+$ $+0.9042r^2)]$	$R_e(r)=(-1.5669+3.1139r-$ $-1.4119r^2)$ $[R_e(r)=K(1-1.9873r+$ $+0.9011r^2)]$

Bracketed [ ] relations are the same as the others but for the constant outside the bracket. All the above equations are in the range $1.006 \leqq r \leqq 1.164$

Table III

Comparison of experimental oscillator strength f (upper number) and the absolute R_e (lower number) with the computed ones

Band	Farmer et al	Pery-Thorne et al	Bethke	Weber et al	Present authors							
					Method of Nicholls and Jarmain				Method of regression			
					Mohlmann τ_s'		Smith τ_s'		Mohlmann τ_s'		Smith τ_s'	
					Linear	Quadratic	Linear	Quadratic	Linear	Quadratic	Linear	Quadratic
(0,0)	4.01 ± 0.2	3.64 ± 0.05	3.99 ± 0.4	4.1 ± 0.8	4.09	4.12	4.38	4.41	4.18	4.07	4.47	4.36
	0.141	0.134	0.141	0.143	0.143	0.143	0.147	0.146	0.144	0.142	0.149	0.147
(1,0)	8.09 ± 0.4	–	7.88 ± 0.8	8.8 ± 1.8	8.61	8.85	8.98	9.22	8.81	8.66	9.19	9.03
	0.136		0.134	0.142	0.140	0.142	0.143	0.145	0.142	0.141	0.145	0.144
(2,0)	7.00 ± 0.4	–	6.73 ± 0.7	8.1	8.70	9.48	9.34	10.17	8.90	8.39	9.55	9.00
	0.130		0.128	(6.7 ± 1.4)*	0.145	0.152	0.151	0.157	0.147	0.143	0.152	0.148
				0.140								
(3,0)	2.4 ± 0.4	–	3.60 ± 0.4	–	–	–	–	–	–	–	–	–
	0.106		0.129									

* Experimental value. The value of oscillator strength f is to be multiplied by 10^{-4}.

value of f for the entire system was wrong. In Table III we have listed experimental f values of Farmer et al [9] alongside the theoretical f values computed by us by two methods. Also in the same Table are given absolute R_e values calculated by taking experimental and theoretically computed f values in the present work.

When one glances at this Table III and the Figs 1, 2 and 3, the following points of comparison arise:

(1) Our present calculations of f values compare more favourably with the corresponding experimental values of Weber et al [9] than of any other experimental investigator mentioned in Table III. Here we have preferred positive correction factor for experimental f of Weber et al [9] for comparison.

(2) In Fig. 1, with the method of Nicholls and Jarmain [3] the variation of R_e is found to be zero whereas in Figs 2 and 3, with the above method and with the method of regression [5] R_e increases linearly with r with a slight slope.

(3) With the use of two different sets of τ values, in Figs 1, 2 and 3, it is found that there is a systematic shift of the curves both with linear and quadratic fittings.

(4) Of the two methods employed for determining f and R_e values theoretically, the results with the method of regression [5] under both linear and quadratic fitting with Mohlmann's lifetime τ values turn out to be nearer the corresponding experimental results of Weber et al [9].

(5) But confining our attention only to the method of Nicholls and Jarmain [3] we may observe that Mohlmann's τ values yield favourable results.

(6) In general, it is found that Smith's τ values do not yield results comparable with the experimental ones.

All these observations made above can also be seen from Figs 1, 2 and 3.

References

1. D. C. Jain and R. C. Sahni. Trans. Faraday. Soc., *64*, 3169, 1968.
2. V. G. Tulasigeri and V. M. Korwar, Ind. J. Pure and Appl. Phys., *23*, 61, 1985.
3. R. W. Nicholls and W. R. Jarmain, Proc. Phys. Soc., *A69*, 253, 1956.
4. R. G. Turner and R. W. Nicholls, Canad. J. Phys., *32*, 468, 475, 1954.
5. B. E. Cunio and R. E. W. Jansson, JQSRT., *8*, 1763, 1968.
6. G. R. Mohlmann, H. A. Vansprang, E. Bloemen and F. J. DeHeer, Chem. Phys., *32*, 239, 1987.
7. B. S. Navati and V. M. Korwar, Physica, *124C*, 421, 1984.
8. M. Jeunehomme, J. Chem. Phys., *45*, 4433, 1966.
9. D. Weber and S. S. Penner, J. Chem. Phys., *26*, 860, 1957.
10. G. W. Bethke, J. Chem. Phys., *31*, 662, 1959.
11. A. Pery–Thorne and F. P. Banfield, J. Phys. B, Atom. Molec. Phys., *3*, 1011, 1970.
12. A. J. D. Farmer, V. Hasson and R. W. Nicholls, JQSRT, *12*, 627, 1972.
13. A. J. Smith and F. H. Read, J. Phys. B, Atom. Molec. Phys., *11*, 3263, 1978.
14. T. Hikida, S. Yagi and Y. Mori, Chem. Phys., *52*, 399, 1980.
15. O. Benoist D'Azy, R. Lopez-Delgado and A. Tramer, Chem. Phys., *9*, 327, 1975.
16. R. J. Spindler, Jr., L. Isaacson and T. Wentink, Jr., JQSRT, *10*, 621, 1970.
17. K. P. Huber and G. Herzberg, Molecular Spectra and Molecular Structure IV Constants of Diatomic Molecules, Van Nostrand Reinhold Company, New York, 1979.

18. R. S. Mulliken, J. Chem. Phys., *7*, 14, 1939.
19. N. R. Tawde and V. G. Tulasigeri, Acta Phys. Hung., *38*, 299, 1975.
20. N. R. Tawde and V. G. Tulasigeri, Acta Phys. Hung., *50*, 103, 1981.
21. G. V. Marr, Proc. Phys. Soc., *83*, 293, 1964.
22. B. H. Armstrong, J. Sokoloff, R. W. Nicholls, D. H. Holland and R. E. Meyerott., JQSRT, *1*, 143, 1961.
23. R. W. Patch, W. L. Shackleford and S. S. Penner, JQSRT, *2*, 263, 1962.
24. G. R. Hebert and R. W. Nicholls, Proc. Phys. Soc., *78*, 1024, 1961.
25. R. W. Nicholls and A. L. Stewart, Atomic and Molecular Processes, Academic Press, New York, 1962.

Acta Physica Hungarica 60 (3—4), pp. 187—191 (1986)

ON THE GRADED LIE ALGEBRA SU(n/n)

NGUYEN AI VIET

Center for Theoretical Physics
Nghia do, Tu liem, Ha noi, VSR

(Received in revised form 27 September 1984)

The theory of the GLA (graded Lie algebra) SU(n/n) is considered. It turns out that this GLA can be embedded into the GLA SU($n/n+1$). As the theory of the GLA SU(m/n) ($m \neq n$) has been well studied [1–8], we have a complete framework for the GLA SU(m/n).

Recently, there have been many attempts to study the Grand Unification model of strong, weak and electromagnetic interactions in the context of the gauge theory of the supergroup SU(m/n) [1–8]. This formulation has many interesting properties: the reasonable bare Weinberg angle is predicted, Higgs mesons and usual vector mesons are arranged together into an irreducible representation, ...

The supergroup SU(m/n) is generated by the generators T_B^A ($A, B = 1, \ldots, m+n$) of the GLA SU(m/n) satisfying the commutation rule [7, 8]

$$[T_A^B, T_C^D]_{(AB,CD)} = \delta_A^D T_C^B - (AB, CD)\delta_C^B T_A^D, \tag{1}$$

where

$$(AB\ldots, CD\ldots) = (-1)[(A)+(B)+\ldots][(C)+(D)+\ldots]$$

$$(A), (B), \ldots = \begin{cases} 0 & \text{for even indices } i = 1, \ldots, m; \\ 1 & \text{for odd indices } m+\alpha,\ \alpha = 1, \ldots, n. \end{cases}$$

The fundamental representation of these generators are the "supertraceless" hermitic $(m+n)\times(m+n)$ matrices of the following form:

$$h = \begin{pmatrix} a & b \\ b^+ & d \end{pmatrix}; \qquad \operatorname{Str} h = \operatorname{tr} a - \operatorname{tr} d = 0. \tag{2}$$

These matrices span a graded vectorspace, which is the direct sum of two vectorspaces $\mathfrak{U}$ and $\mathfrak{V}$.

The elements $u \in \mathfrak{U}$

$$u = \begin{pmatrix} a & 0 \\ 0 & d \end{pmatrix} \tag{3}$$

form the Bose sector, and the elements $v \in \mathfrak{V}$

$$v = \begin{pmatrix} 0 & b \\ b^+ & 0 \end{pmatrix} \tag{4}$$

form the Fermi sector of the GLA.

In the original paper of Dao Vong Duc and Nguyen thi Hong [8], the representations of this GLA have been studied on the basis of the generalized Gell-Mann's matrices. Due to the results of that paper the lengthy and complicated calculations of GLAS reduce to be clear and simple. Many important theorems, relations and useful techniques in the theory of Lie algebras can be generalized directly into the theory of GLAS in this representation. The authors have constructed tensor representations, invariant forms, then used them to construct the gauge theory of unified interactions [9], to calculate the relations between the decay amplitudes [10] and to derive the selection rules for the baryon-number non-conserving decays of nucleons [11].

However, this scheme does not work in the case of balanced indices ($m=n$). Because of the factor $\frac{1}{m-n}$ many important formulas become meaningless, if we take $m=n$. To overcome this trouble we use the following representation:

Bose sector spanned by

$$G_a=\begin{pmatrix}\lambda_a^{(n)} & 0\\ 0 & 0\end{pmatrix}$$

$a=1,\ldots,n^2-1$, λ_a denote the usual Gell-Mann's matrices, $I^{(n)}$ is the $n\times n$ unit matrix

$$F_a=\begin{pmatrix}0 & 0\\ 0 & \lambda_a^{(n)}\end{pmatrix},$$

$$H=\begin{pmatrix}I^{(n)} & 0\\ 0 & I^{(n)}\end{pmatrix}. \tag{5}$$

Note that G_a generate the group $SU(n)_G$, F_a generate the group $SU(n)_F$ and H generates $U(1)_H$. So we have the reduction $SU(n/n)\supset SU(n)\times SU(n)\times U(1)$.

Fermi sector spanned by

$$S_i^\alpha=\frac{1}{2}T_i^{m+\alpha},$$

$$\bar{S}_\alpha^i=\frac{1}{2}T_{m+\alpha}^i=(S_i^\alpha)^+. \tag{6}$$

On this basis, the GLA $SU(n/n)$ has the following form:

$$[G_a, G_b]=\mathrm{i}f_{abc}G_c,$$

$$[F_a, F_b]=\mathrm{i}f_{abc}F_c,$$

$$[G_a, F_b]=0,$$

$$[G_a, S_i^\alpha]=\frac{1}{2}S_i^\beta(\lambda_a)_\beta^\alpha,$$

$$[F_a, S_i^\alpha] = -\frac{1}{2}(\lambda_a)_i^j S_j^\alpha,$$

$$\{S_i^\alpha, S_j^\beta\} = 0,$$

$$\{S_i^\alpha, \bar{S}_\beta^j\} = \frac{1}{4}\delta_\alpha^\beta(\lambda_a)_i^j F_a + \frac{1}{4}\delta_i^j(\lambda_a)_\beta^\alpha G_a,$$

$$[H, S_i^\alpha] = [H, G_a] = [H, F_a] = 0. \tag{7}$$

We see that H forms the center of the GLA SU(n/n) and is called central charge. So the supergroup SU(n/n) is reductive (i.e. it can be represented as the product of a simple group and an Abelian group), while the supergroup SU(m/n) ($m \neq n$) is simple. We do not discuss the case $m = n = 1$, because the supergroup SU(1/1) is nilpotent.

Now we try to embed the GLA SU(n/n) into the GLA SU($n/n+1$), then all the results of the theory of the GLA SU($n/n+1$), which is the special case of the well-considered theory of the GLA SU(m/n) ($m \neq n$) [1–8], can be applied automatically for the GLA SU(n/n).

Using the results of [8], the generators of the GLA SU($n/n+1$) can be represented as follows:

$$G_a = \begin{pmatrix} \lambda_a^{(n)} & 0 \\ 0 & 0 \end{pmatrix} \qquad a = 1, \ldots, n^2 - 1,$$

$$F_b = \begin{pmatrix} 0 & 0 \\ 0 & \lambda_b^{(n+1)} \end{pmatrix} \qquad b = 1, \ldots, (n+1)^2 - 1,$$

$$H = \begin{pmatrix} (n+1)I^{(n)} & 0 \\ 0 & nI^{(n+1)} \end{pmatrix};$$

$I^{(k)}$ denotes the $k \times k$ unit matrix,

$$(S_i^\alpha)_A^B = \delta_A^\alpha \delta_i^B,$$

$$(\bar{S}_\alpha^i)_A^B = \delta_A^i \delta_\alpha^B. \tag{8}$$

We choose a new basis involving the generators: G_a ($a = 1, \ldots, n^2 - 1$), F_b ($b = 1, \ldots, (n+1)^2 - 1$), S_i^α, $\bar{S}_\alpha^i$ ($i = 1, \ldots, n$; $\alpha = 1, \ldots, n+1$) and

$$H' = \frac{1}{n+1}(H + F_{(n+1)^2-1}) = \begin{vmatrix} I^{(n)} & 0 & 0 \\ 0 & I^{(n)} & 0 \\ 0 & 0 & 0 \end{vmatrix}. \tag{9}$$

On this basis our GLA has the following form:

$$[H', G_a] = [H', F_b] = [H', S_i^\alpha] = [H', \bar{S}_\alpha^i] = 0$$

when

$$a=1, \ldots, n^2-1,$$

$$b=1, \ldots, n^2-1,$$

$$\alpha=1, \ldots, n,$$

$$[H', S_i^{n+1}]=S_i^{n+1},$$

$$[H', S_{n+1}^i]=-\bar{S}_{n+1}^i,$$

$$[H', F_c]=\frac{1}{n+1} f^k_{(n+1)^2-1,c} F_k; \quad c=n^2, \ldots, (n+1)^2-1,$$

f is the structure constant of the usual Lie algebra SU$(n+1)$,

$$\{S_i^\alpha, \bar{S}_\beta^j\}=\frac{1}{4}\delta_\beta^\alpha(\lambda_a^{(n+1)}-\frac{2}{n(n+1)}\delta_{a,(n+1)^2-1})_i^j F_a+$$

$$+\frac{1}{4}\delta_i^j(\lambda_p^{(n)})_\beta^\alpha G_p-\frac{1}{2n}\delta_\alpha^\beta\delta_i^j H',$$

$$\{S_i^\alpha, S_j^\beta\}=0,$$

$$[G_a, G_b]=\mathrm{i}f_{abc}G_c,$$

$$[F_a, F_b]=\mathrm{i}f_{abc}F_c,$$

$$[G_a, S_i^\alpha]=\frac{1}{2}(\lambda_a)_\beta^\alpha S_i^\beta,$$

$$[F_a, S_i^\alpha]=-\frac{1}{2}(\lambda_a)_i^j S_j^\alpha, \tag{10}$$

The generators H', G_a, F_b $(a, b=1, \ldots, n^2-1)$, S_i^α, $\bar{S}_\alpha^i$ $(\alpha=1, \ldots, n)$ span the subGLA SU(n/n) of the GLA SU$(n/n+1)$. So we have embedded SU(n/n) into SU$(n/n+1)$.

In fact, the GLA SU(n/n) can be embedded into SU(n/m) $(m>n)$ when replacing H by

$$H'=\begin{vmatrix} I^{(n)} & 0 & 0 \\ 0 & I^{(n)} & 0 \\ 0 & 0 & 0^{(m-n)} \end{vmatrix} \tag{11}$$

With such a new choice of basis, the terms of $\frac{1}{m-n}$ type disappear from the commutation relations as well as in the special case of $m=n+1$ (see the Eq. (10)).

Because of the absence of $\frac{1}{m-n}$ terms, even when the SU(m/n) symmetry of the model is broken down to the SU(n/n) one, there is no difficulty as there used to be in the usual choice of basis. So we have a complete framework for the general SU(m/n) and we can use the results in [8] directly for SU(n/n).

Acknowledgement

Thanks are due to Prof. Dao Vong Duc for much help and for the basic idea of this study. I am also grateful to Dr. Nguyen thi Hong for many helpful conversations.

References

1. Y. Ne'eman, Phys. Lett., *81B*, 190, 1979.
2. D. B. Fairlie, J. Phys., *G5*, 155, 1979.
3. E. J. Squires, Phys. Lett., *82B*, 375, 1979.
4. P. N. Dondi and P. D. Jarvis, Phys. Lett., *84B*, 75, 1979.
5. J. G. Taylor, Phys. Rev. Lett., *43*, 824, 1979.
6. P. N. Dondi and P. D. Jarvis, Z. Phys., *C4*, 201, 1980.
7. J. G. Taylor and C. Pickup, J. Phys. *A13*, 1537, 1979.
8. Dao Vong Duc, Nguyen thi Hong, Annals de l'Institute Henri Poincaré, *36A*, 495, 1985.
9. Dao Vong Duc, Nguyen thi Hong, Higgs bosons and gauge vector mesons in SU m/n superunification (to be published).
10. Dao Vong Duc, Nguyen thi Hong, JINR preprint, P2–81–725, Dubna 1981.
11. Dao Vong Duc, Nguyen thi Hong, JINR preprint, P2–82–274, Dubna 1982.

Acta Physica Hungarica 60 (3—4), pp. 193—201 (1986)

THE PIEZOELECTRIC-STRAIN CONSTANTS OF $NaNO_2$ CRYSTAL

A. M. ELDIB and H. F. HASSAN

Department of Physics, Faculty of Science
Al-Azhar University, Nasr City, Cairo, Egypt

(Received in revised form 2 October 1984)

Using a semiempirical LCAO method supported with charge self-consistent procedure applied at Γ-point, the effective charges on Na, N and O atoms for the ferro-electric $NaNO_2$ crystal have been calculated at different temperatures. Assuming a point charge model, the calculated effective charges are used to study the temperature dependence of the spontaneous polarization (P_s) of the crystal and in turn to calculate the piezoelectric-strain constants. A good agreement between the values of the physical quantities calculated in this work and the measured ones is reported. The calculated effective charges are used also to calculate the Madelung potentials for Na, N and O atoms in $NaNO_2$ crystal.

1. Introduction

Various properties of $NaNO_2$ crystal have been extensively studied since the discovery of its ferroelectric property [1]. It was found that $NaNO_2$ undergoes a first order phase transition from ferroelectric, with space group C_{2v}^{20}, to sinusoidal antiferroelectric phase at the Curie point ($T_c \simeq 163$ °C), which is followed by a second order transition to the paraelectric phase, with space group D_{2h}^{25}, at the Neel temperature ($T_N \simeq 165$ °C) [2]. Detailed information about the temperature dependence of the lattice parameters of $NaNO_2$ is measured also by Kucharzyk et al [2]. The piezoelectric constants have been measured by Hamano et al [3], and recently calculated by Kam et al [4]. The band structure has been investigated by Kam et al [4]. and also by Eldib [5], who has shown that the bands, except the high and empty ones have poor dependence on the coordination sphere number. It has been also shown that the filled levels depend slightly on the wave number. The comparison of those results with those of zero approximation and of NO_2^- [6] indicates that the filled levels may belong to the states of the NO_2^- group. This conclusion is in agreement with the experimental results given before by Chisler et al [7]. In addition, the calculations given in this work are based on an iterative self-consistent charge procedure. The application of such procedure over the entire Brillouin zone is unpractical due to its high computational time.

Accordingly, one may suggest to iterate on one point in the Brillouin zone. However, choosing the Γ point for these calculations leads to a good agreement with the previous results.

In this work, the temperature dependence of the atomic effective charges and spontaneous polarization (P_s) of $NaNO_2$ crystal are calculated. Using the values of P_s calculated in this work at different temperatures with the lattice parameters at the corresponding temperatures measured by [2], the piezoelectric-strain constants of $NaNO_2$ are calculated.

2. Methods

i. Effective charges

To obtain the effective charges on ions of a system, the eigenvalues and the corresponding eigenfunctions must be determined first. For this purpose one has to solve the system of equations.

$$\sum_j \{H_{i,j}(k) - E_a(\mathbf{K}) S_{i,j}(\mathbf{K})\} C_{a,j}(\mathbf{K}) = 0\,, \tag{1}$$

where (a) denotes different eigenvalues, $\mathbf{K}$ is the wave vector, i, j denote different atomic orbitals, $H_{i,j}(\mathbf{K})$ and $S_{i,j}(\mathbf{K})$ are the Hamiltonian and overlap matrix elements, and $E_a(\mathbf{K})$ are the energies (eigenvalues) of the eigenvectors $C_{a,j}(\mathbf{K})$.

The overlap matrix elements are calculated using the equations

$$S_{i,j}(\mathbf{K}) = \sum_{\mathbf{R}^n} S_{i,j}(\mathbf{R}_n) \exp(i\mathbf{K} \cdot \mathbf{R}_n)\,, \tag{2}$$

$$S_{i,j}(\mathbf{R}_n) = \int \varphi_i^*(\mathbf{r}) \varphi_j(\mathbf{r} - \mathbf{R}_n - \mathbf{R}_{vv'})\, d\tau\,, \tag{3}$$

where $\varphi_i(\mathbf{r})$ is the atomic wave function, $\mathbf{R}_v$ and $R_{v'}$ are the coordinate vectors of atoms v and v' in the first primitive cell at which φ_i and φ_j exist, $\mathbf{R}_{vv'} = \mathbf{R}_v - \mathbf{R}_{v'}$, and $\mathbf{R}_n$ is the translation vector.

The orbits used in this work are $3s$ for Na atom and $2s$, $2p$ for N and O atoms. The atomic wave functions are assumed to be of Slater type. The overlap integrals are calculated using the well known procedure explained by Mulliken et al [8]. The Hamiltonian matrix element is given by

$$H_{i,j}(\mathbf{K}) = \sum_{\mathbf{R}^n} \tilde{H}_{i,j}(\mathbf{R}_n) \exp(i\mathbf{K} \cdot \mathbf{R}_n)\,, \tag{4}$$

where

$$\tilde{H}_{i,j}(R_n) = \int \varphi_i^*(r) H \varphi_j(r - R_n - R_{vv'}) d\tau\,. \tag{5}$$

Neglecting the three center type integrals, it can be seen that

$$\tilde{H}_{i,j}(R_n) = \int \varphi_i^*(r) \left\{ -\frac{1}{2} V^2 + V^v(r) + V^{v'}(r - R_n - R_{vv'}) \right\} \varphi_j(r - R_n - R_{vv'}) d\tau\,, \tag{6}$$

where $V^{\nu}(r)$ is the potential due to atom ν, at which $\varphi_i(\mathbf{r})$ exists and $V^{\nu'}(\mathbf{r}-\mathbf{R}_n-R_{\nu\nu'})$ is the potential due to atom ν' at which $\varphi_j(\mathbf{r}-\mathbf{R}_n-\mathbf{R}_{\nu\nu'})$ exists. Within the approximation given in Eq. (6) and by the analogy with the semiempirical theory in molecules, it is clear that

$$\tilde{H}_{i,j}(\mathbf{R}_n)=\text{function of } (S_{i,j}(\mathbf{R}_n)=F(S_{i,j}(\mathbf{R}_n))\,. \tag{7}$$

Keeping this concept in consideration and starting from the molecular semiempirical formula, for example, Cusach's formula [9]

$$H_{i,j}=(2-|S_{i,j}|)S_{i,j}(H_{ii}+H_{jj})/2 \tag{8}$$

one can get for crystals the following formula:

$$H_{ij}(\mathbf{K})=\sum_{\mathbf{R}^n}\{(2-|S_{ij}(\mathbf{R}_n)|)S_{ij}(\mathbf{R}_n)(H_{ii}(q)+H_{jj}(q))/2\}\exp(i\mathbf{K}\cdot\mathbf{R}_n)\,. \tag{9}$$

On substituting from Eq. (2) and (9) in (1), the eigenvalues $E_a(\mathbf{K})$ and the coefficients $C_{a,j}(\mathbf{K})$ can be calculated. Using these $C_{a,j}(K)$ and the overlap from Eq. (3) the effective charges (q) can be calculated by means of Mulliken population analysis given by the formula

$$q_{\nu}=Z_{\nu}-\sum_{a=1}^{n}\eta_a\{\sum_j|C_{a,j}|^2+\sum_i\sum_{j\neq i}C^*_{a,i}C_{a,j}S_{i,j}\}\,, \tag{10}$$

where Z_{ν} is the number of valence electrons considered from atom ν, n is the number of filled eigenfunctions, η_a is the number of electrons in orbit a.

Using a self-consistent iteration procedure, the diagonal matrix elements $H_{ii}(q)$ in Eq. (9) can be corrected using the values of q obtained from Eq. (10). The dependence of H_{ii} on q is assumed to be in the form of a power series

$$H_{ii}(q_{\nu})=\sum_m A_m q^m=A_0+A_1q_{\nu}+A_2q_{\nu}^2+\ldots \tag{11}$$

where A_m are atomic orbital constants to be determined using the spectroscopic parameters for ionization energy of neutral and non-neutral atoms [10].

So far, the effect of the charge on the Hamiltonian is considered only for the same site. However, the electrostatic Coulomb potential due to the charges at different lattice sites may also affect the Hamiltonian. The electrostatic potential is obtained by calculating the Madelung potential, μ, from the equation

$$\mu_{\nu}=-\left[\sum_{\mathbf{R}^n}\frac{q_{\nu}}{|\mathbf{R}_n|}\right]_{\mathbf{R}_n\neq 0}+\left[\sum_{\nu\neq\nu'}\frac{q_{\nu'}}{|\mathbf{R}_n+\mathbf{R}_{\nu\nu'}|}\right]. \tag{12}$$

This equation can be calculated numerically as explained by Ziman [11]. The numerical solution for $NaNO_2$ at room temperature, leads to three equations for Na, N

and O atoms as follows:

$$\begin{aligned} \mu_{Na} &= 8.25229\ q_{Na} + 0.15464\ q_N - 1.13094\ q_O\,, \\ \mu_N &= 0.15464\ q_{Na} - 8.25229\ q_N - 8.14885\ q_O\,, \\ \mu_O &= -0.56547\ q_{Na} - 4.07443\ q_N + 7.89875\ q_O\,. \end{aligned} \tag{13}$$

Substituting the values of charges during the iteration procedure, the Madelung potential for each ion can be calculated in each iteration. For example, at 20 °C, the self consistent values of the charges are

$$q_{Na} = 0.78892\,, \qquad q_N = -0.12086 \qquad \text{and} \qquad q_O = -0.33403\,.$$

The corresponding self-consistent values of Madelung potentials at the same temperature obtained from Eq. (13) are

$$\mu_{Na} = 6.8696\,, \qquad \mu_N = 1.8466 \qquad \text{and} \qquad \mu_O = -2.5922\,(\text{eV})\,.$$

It must be remarked here that the values of the Hamiltonian for iteration number $m+1$ can be obtained by adding the values of μ obtained from the iteration number m to the corresponding diagonal matrix elements of the Hamiltonian.

ii. Spontaneous polarization

According to the structural classification for ferroelectrics [12], sodium nitrite is a member of the twodimensional class, in which polarity reorientation involves atomic displacements in a plane containing the polar axis. In addition $NaNO_2$ is a molecular crystal. These allow for a calculation of spontaneous polarization in terms of the point charge model in which

$$P_s = 1.6 \times 10^{-19} \times V^{-1} \sum_a q_a r_a\,, \tag{14}$$

where V is the unit cell volume and r_a are the atomic coordinates.

iii. Piezoelectric-strain constants

In the absence of an external electric field, the change in the polarization, P_s, produced to the lowest order due to the strain $\hat{S}$ can be written as:

$$\Delta P_i = \sum_l e_{il} S_l \qquad (i = 1, 2, 3;\ l = 1, 2, \ldots, 6)\,, \tag{15}$$

where

$$\text{the strain } \hat{S} = \text{elongation/original length}, \tag{16}$$

e_{il} are the piezoelectric-stress constants which are related to the piezoelectric-strain constants d_{in} by the equation

$$e_{il} = \sum_n d_{in} C_{nl} \qquad (n = 1, 2, \ldots, 6)$$

or in the matrix form

$$[e] = [d]\,[c]\,. \tag{17}$$

and C_{nl} are the elastic-stiffness constants.

Multiplying Eq. (17) by $[c]^{-1}$, one obtains

$$[d] = [e]\,[c]^{-1}\,. \tag{18}$$

3. Results and discussion

i. Effective charges

In order to obtain the parameters we use the atomic coordinates given by Kay and Frazer [13] multiplied by the lattice constants obtained in [2] in the temperature range from 20–163 °C. It must be remarked here, that in this calculation the lattice expansion is the only source of the temperature dependence.

Using Eq. (10) and the self-consistent procedure, the effective charges on atoms have been obtained. The results are shown in Fig. 1. These results show that the charge of sodium atom is divided between nitrogen and the two oxygen atoms (about 42% for each oxygen and about 16% for nitrogen atom). However, the three are negatively charged.

It is shown also that the charges of Na and N depend on the temperature more than that of O atoms. This may denote that the Na–N bond be affected by temperature easier than the N–O bond.

ii. Spontaneous polarization (P_s)

Using Eq. (14) for the point charge model, P_s has been calculated. The temperature dependence of P_s in the range from 20→ ~ 163 °C is shown in Fig. 2, curve No. 5. The results show that P_s depends slightly on the temperature in the mentioned range. At 100 °C the value of P_s equals 8.648 μC cm^{-2}. A comparison of the calculated P_s due to this work, and the measured and calculated results by other authors is presented also in Fig. 2. It is seen that the results depend on the experimental technique or the method of calculation. The saturation value of P_s as measured by Sawada et al [14] is ~9 μC cm^{-2}, while the one measured by Buchheit et al [15] is 11.7 μC cm^{-2}. Using the free energy principle P_s has been calculated by Nomura [16]. The saturation

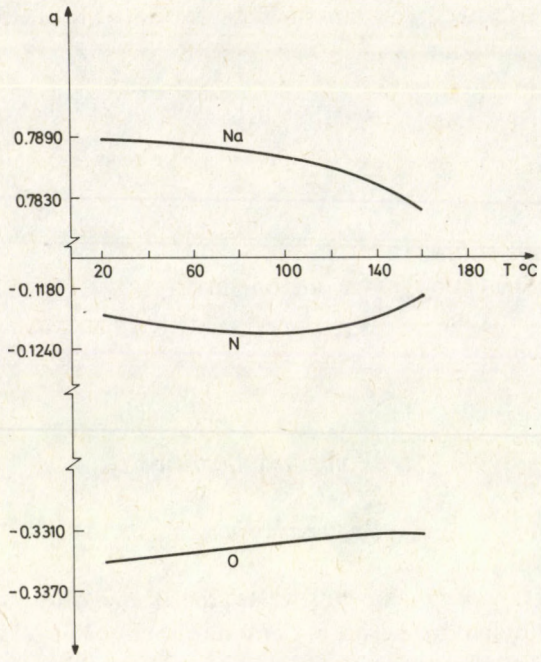

Fig. 1. Charges on Na, N and O atoms as obtained from Γ-point calculation in $NaNO_2$ crystal

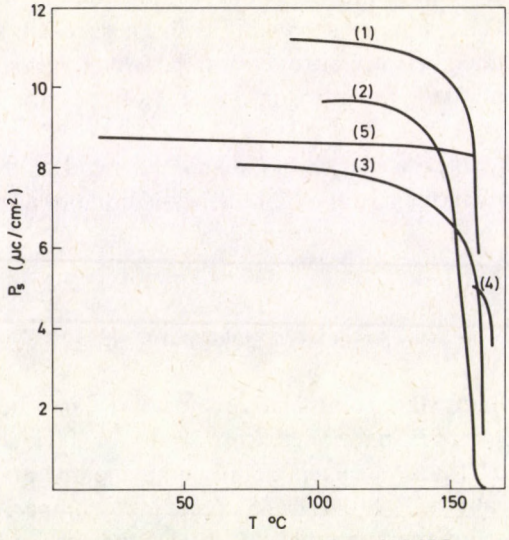

Fig. 2. Spontaneous polarization of $NaNO_2$

1. Measured by polarization reversal method [15]
2. Measured by pyroelectric current method [14]
3. Measured by hysteresis loop method [16]
4. Calculated [16]
5. This work

value of P_s is about 5.2 $\mu C\,cm^{-2}$, while the value measured by the same author is $\sim 8\ \mu C\,cm^{-2}$. It is clear from this comparison that the calculated value of P_s due to this work is in good agreement with the experimental values measured by Sawada et al [14], and Nomura [16].

iii. Piezoelectric-strain constants

Using Eq. (16) the strains at 120, 140 and 150 °C, relative to the dimensions at 100 °C, are calculated. The results are given in Table I. The values of P_s at 100, 120, 140 and 150 °C and the calculated corresponding strains, which are shown in Table I, are used to construct three equations for the three unknowns of the piezoelectric-stress

Table I

The strain S in the a, b and c directions at 120, 140 and 150°C relative to the dimensions at 100°C

Temperature	S_a	S_b	S_c
120	0.0032468	0.0017788	−0.000384
140	0.0074372	0.0041144	−0.001317
150	0.0104121	0.0056329	−0.002258

constants, $e_{2,l}$ (from crystal symmetry there is one component of P_s parallel to the b axis, thus e_{il} for $l > 3$ or $i \neq 2$ equals zero). A comparison of the results of the e_{il} values as calculated by Kam et al [4] and due to this work are given in Table II.

Table II

The piezoelectric-stress constants, in units of $10^{-2}\ C/m^2$

	$e_{2.1}$	$e_{2.2}$	$e_{2.3}$
Kam et al [4]	−7.599433	7.0566167	−8.51365
This work	−7.534210	4.2239200	−8.88896

Using the data for elastic-stiffness constants, C_{nl} given by Ota et al [17], the piezoelectric-strain constants are calculated. A comparison of the results due to this work, the values calculated by Kam [4] and the experimental results measured by Hamano et al [3] is shown in Table III.

Good agreement between the results of this work and those measured experimentally is reported.

Table III

Experimental and calculated values of the three piezoelectric-strain constants (units of 10^{-12} C/N)

	Measured [3]	Calculated [4]	This work
$d_{2,1}$	−2.833	−3.030	−2.7597
$d_{2,2}$	1.667	2.183	1.6087
$d_{2,3}$	−1.167	−1.176	−1.1960

4. Conclusion

It must be remarked here that the piezoelectric-strain constants are strongly affected by the value of the spontaneous polarization (P_s). Since P_s is a function of the effective charges on atoms, it is important, therefore, to use accurate values of charges when calculating P_s and in turn the piezo-electric strain constants. That is why a self-consistent procedure at Γ-point is used in this work to determine the values of the effective charges.

The good agreement obtained between the calculated values due to this work and the measured values for spontaneous polarization and the three piezoelectric constants leads to the conclusion that for such crystals, like $NaNO_2$, the Γ-point calculation is quite enough to give good information about the effective charges on atoms, spontaneous polarization as well as the piezoelectric constants.

Moreover, the semiempirical LCAO treatment supported by charge self-consistency and the suitable correction for the diagonal elements of the Hamiltonian as applied in this work, proves itself to be suitable for similar studies, however, without the complications of other methods.

References

1. S. Sawada, S. Nomura, S. Fujii and I. Yoshida, Phys. Rev. Lett., *1*, 320, 1958.
2. D. Kucharczyk, A. Pietrasko and K. Lukaszewicz, Phys. Stat. Sol., *A37*, 287, 1976.
3. K. Hamano, K. Negishi, M. Marutake and S. Nomura, Jpn. J. Appl. Phys., *2*, 83, 1962.
4. S. K. Kam and J. Henkel, Phys. Rev. (B), *17*, 1361, 1978.
5. A. M. Eldib, Egypt. J. Chem., *22*, 109, 1979.
6. F. Sultan, A. M. Eldib and H. F. Hassan, Egypt. J. Chem., 22, 165, 1979.
7. E. V. Chisler and M. S. Shure, Phys. Stat. Sol., *17*, 163, and 173, 1966.
8. R. S. Mulliken, C. A. Rieke, D. Orloff and H. Orloff, J. Chem. Phys., *17*, 1248, 1949.
9. L. C. Cusachs, J. Chem. Phys., *43*, S157, 1965.
10. C.E. Moore, Atomic Energy Levels, Vol. 1 and 2, U. S. National Bureau of Standards, Circ., No. 467, U. S. GPO., Washington D. C. 1949.
11. J. M. Ziman, Principles of the Theory of Solids, Cambridge University Press, London, 1972.

12. M. E. Lines and A. M. Glass, Principles and Applications of Ferroelectric and Related Materials, p. 179–181, Oxford, 1977.
13. M. I. Kay and B. C. Frazer, Acta Cryst., *14*, 56, 1961.
14. S. Sawada, S. Nomura and Y. Asao, J. Phys. Soc., Japan, *16*, 2207, 1961.
15. W. Buchheit and J. Petersson, Solid State Communication, *34*, 649, 1980.
16. S. Nomura, J. Phys. Soc. Japan, *16*, 2440, 1961.
17. K. Ota, Y. Ishibashi and Y. Takagi, J. Phys. Soc. Japan., *29*, 1545, 1970.

Acta Physica Hungarica 60 (3—4), pp. 203—211 (1986)

LOCAL-FIELD CORRECTIONS IN THE CALCULATION OF ELECTRONIC STOPPING POWER

I. NAGY, J. LÁSZLÓ and J. GIBER

Department of Atomic Physics, Institute of Physics, Technical University 1521 Budapest, Hungary

(Received 16 October 1984)

Energy losses of slow protons in a degenerate electron gas are calculated on the basis of the dielectric theory. The influence of various longitudinal dielectric functions is examined. It is shown that the correlations lead to the decrease of the energy losses in comparison to those stopping power calculations, where only the exchange effects are taken into account. The comparison of the results to the available experimental ones shows a very good agreement.

Introduction

It is easy to obtain the general formula for the stopping power from the classical equations of Maxwell. In this formula the longitudinal dielectric function plays an essential role. (The transversal dielectric function connected to the Cherenkov part can be neglected in the low bombarding velocity range under examination.) Thus the electronic stopping power depends on the accuracy of the longitudinal function both from the mathematical and physical point of view. The longitudinal dielectric function of an electron gas at absolute zero temperature can be defined as

$$\varepsilon_l = 1 + Q_0(1 - GQ_0)^{-1}, \tag{1}$$

where Q_0 is the well known Lindhard polarizability [1], G is the so-called local-field correction. All of these functions depend on frequency ω and wave vector $\mathbf{k}$. In the original paper of Lindhard $G=0$. This is valid if the one electron radius (the coupling constant) r_s is small ($r_s \ll 1$). In the velocity range of the bombarding proton, where $v \ll v_F$ (i.e. $\omega \ll 1$) the dependence of $G(k, \omega)$ on frequency can be neglected in the calculation of ε_l (v_F denotes the Fermi velocity). Therefore the available most exact $G(k)$ static function seems to be sufficient for the solution of the task. Numerical calculations for the G function were done by Tripathy and Mandal [2] and by Devreese et al [3] considering the exchange corrections. The dielectric function in [2] was presented by solving the equations of motion for the double-time retarded commutator of charge-density fluctuation operators. In [3] $G(k, \omega)$ was deduced to a sixfold integral obtained from the dynamical-exchange decoupling in the equation of motion for the Wigner distribution function, and from the variational treatment of the resulting integro-

differential equation. Their result [2, 3] is a universal function not depending on r_s. On the other hand $G(k)$ has a very sharp maximum at $k \cong 2k_F (G(k \cong 2k_F) \cong 2)$. (See curve 1 in Fig. 1) Sayasov [4] performed a calculation exceeding the Lindhard theory in

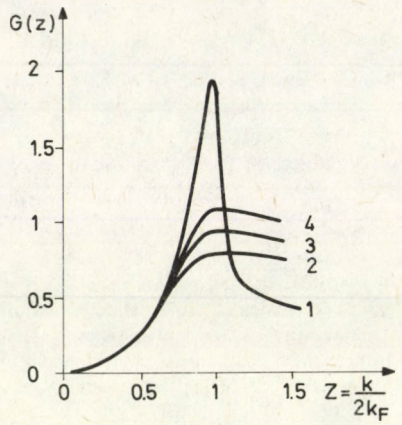

Fig. 1. Local-field correction functions vs the dimensionless parameter z. 1) after Tripathy and Mandal [2] and Devreese et al [3]. 2) after Lantto et al [5] for $r_s = 1$. 3) for $r_s = 3$. 4) for $r_s = 5$

relation to the stopping power applying this correction function. This G is not adequate for strongly correlated electron gases (e.g. for an electron gas of metallic density), because of the ingorance of the correlations. Lantto et al [5] took the correlations into account using the Fermi hypernetted-chain method for the description of the dielectric response with Jastrow variational many-body wave function for the electron fluid. The $G(k)$ function generated by them depends on r_s, and has no sharp maximum at $k \cong 2k_F (G(k \cong 2k_F) \cong 1)$. (See curves 2, 3 and 4 in Fig. 1 for $r_s = 1$, 3 and 5, respectively.) It is useful to note that the resulting G of Ichimaru and Utsumi [6] applying another theoretical physical method agrees to a high degree with that obtained by Lantto et al. The pronounced maximum in Devreese's $G(k)$ seems to be due to exchange contributions. On the other hand, the correlations are known to suppress the exchange effects. And this is deeply involved in the results of the stopping power.

Formalism

The formula determining the energy loss of a slow proton ($v \ll v_F$) according to [7] for example is

$$-dE/dx = 2e^2\pi^{-1} \int_0^1 y\,dy \int_0^\infty k\,dk\, |\varepsilon_l|^{-2} \operatorname{Im} \varepsilon_l , \qquad (2)$$

where y is the cosine of the angle between vectors **k** and **v**. Introducing the well known

notations according to Sayasov for example

$$z = k/2k_F \qquad \text{dimensionless variable},$$

$$\chi^2 = e^2/\pi\hbar v_F = v_0/\pi v_F = \alpha r_s/\pi \quad \text{density parameter}$$

(v_0 is the Bohr velocity, $v_0 = 2.18 \cdot 10^6$ m/s),

$$\alpha = (4/9\pi)^{1/3} \quad \text{scalar factor},$$

the following formula can be obtained from Eq. (2) considering Eq. (1) and after the integration by y

$$dE/dx = -4e^4 m_e^2 v (3\pi\hbar^3)^{-1} C(r_s), \tag{3}$$

where $C(r_s)$ to be analysed has the form

$$C(r_s) = \int_0^1 z^3 \{z^2 - \chi^2 f_1(z)\,[G(z) - 1]\}^{-2} dz. \tag{4}$$

$f_1(z)$ is z^2/χ^2 times the real part of the Lindhard polarizability. In the region under examination ($v \ll v_F$)

$$f_1(z) = 0.5 + 0.25(1/z - z) \ln |(z+1)/(z-1)|.$$

At the beginning of the following Section some approximative forms for $C(r_s)$ are shown, each being essentially valid in the $r_s \ll 1$ range. Then our results are summarized for $C(r_s)$ with the help of $G(k)$ functions considered the best by different authors.

Analysis of $C(r_s)$

If $G = 0$ and $f_1 = 1$ corresponding to the early Mott–Thomas–Fermi screening [8], then

$$C(r_s) = 0.5[\ln(1 + 1/\chi^2) - (1 + \chi^2)^{-1}] \tag{5}$$

can result. This is the function used by e.g. Arista and Brandt [9] as the modification of $C(r_s) \sim \ln(1/\chi^2)$ proposed by Fermi and Teller [10]. Using the collision theory of the stopping power calculation after Sigmund [11], the following formula can be originated from the well known $dE/dx = n v_F v m_e \sigma_{tr}$ relation after some transformation (n is the density of the electron gas, σ_{tr} is the transport cross section)

$$dE/dx = -4e^4 m_e^2 v (3\pi\hbar^3)^{-1} C'(r_s), \tag{6}$$

and

$$C'(r_s) = (\pi\chi^2)^{-2} \sum_{l=0}^{\infty} (l+1) \sin^2(\delta_l - \delta_{l+1}). \tag{7}$$

δ_l is the phase-shift of the electron scattering on the screened proton. As a screened potential Ferrell and Ritchie [12] used a Yukawa type potential, where the screening

was calculated in Thomas–Fermi approximation. $(V(x)=\frac{2}{x}\exp(-Kx)$ in atomic units, where $K=2(\chi^2)^{-1/2}/\pi)$. If the scattering is handled in first Born approximation with the above potential, then the following equation results for the sum in Eq. (7)

$$\sum_{l=0}^{\infty}(l+1)\sin^2(\delta_l-\delta_{l+1})=0.5(\pi\chi^2)^2[\ln(1+1/\chi^2)-(1+\chi^2)^{-1}]. \tag{8}$$

That means that $C'(r_s)$ is completely the same as in Eq. (5). On the other hand the exact assumption for the application of the Born approximation in the case of a Yukawa potential is

$$\pi\chi^2 2^{-1/2}[\ln(1+1/\chi^2)+2\,\mathrm{arctg}^2(\chi^2)^{-1/2}]^{1/2}\ll 1.$$

Therefore the Born approximation is adequate if $v_F \gg v_0$, which demands $\chi^2 \ll 1$, and so $r_s \ll 1$. If we do not restrict ourselves to the Born approximation when calculating the scattering, the phase shift factors have to be determined by some numerical methods. (See e.g. Calogero [13].) This can be more precise in itself, but the Yukawa potential includes the Thomas–Fermi approach. Therefore the complexity of the physical features of the electron gas must be included in the behaviour of the screened potential if the calculation is done due to the collision theory. Finally, we mention that the application of the ε_l function exceeding the Thomas–Fermi approximation, corresponding essentially to the Hartree–Fock approximation and fulfilling the compressibility rule leads to an unexpected result from the physical viewpoint at higher r_s values. In this case, it is easy to show that $f_1=(1-\chi^2)^{-1}$ (see e.g. formula 4.2 in [2]), and so from Eq. (4)

$$C(r_s)=0.5[\ln(1/\chi^2)^{+1}-1+\chi^2] \tag{9}$$

is obtained. The formal use of Eq. (9) results in a function that has a minimum at $r_s\cong 6(\chi^2=1)$. A modified Yukawa potential can be obtained with the above f_1, and thus $K'=K(1-\chi^2)^{-1}$ is the screening factor, which diverges to infinity if χ^2 converges to 1, i.e. $V(x)$ disappears. Thus the particle becomes free with no phase-shift. It is known that in the Hartree–Fock approximation $\chi^2=1$ is the stability limit of the electron gas in the jellium model. As χ^2 converges to 1 (but $\chi^2\neq 1$), the screening (K') is stronger, and so above $r_s\cong 5(\chi^2=0.83)$ the collision theory gives smaller values for $C(r_s)$ than the Lindhard–Winther calculation [14] in spite of the application of the exact phase-shift factors. We can now conclude that an analytical form of sufficient accuracy can be obtained only if $r_s\ll 1$. Here Eqs (5), (7) and (9) serve the same result corresponding to the Lindhard–Winther theory. (See curve 1 in Fig. 2, where $\chi^2\ll 1$).

The results of the numerical evaluation of Eq. (4) with the help of precise $G(k)$ functions are shown in Fig. 2. The result of the Lindhard–Winther theory is also drawn (curve 1). This is corresponding to $G=0$. If we use the G^D correction after Devreese et al, the $C(r_s)$ function has a minimum at $\chi^2=0.5$ in spite of the calculation of Sayasov [4]. (See curve 3.) As it was shown in the detailed numerical analysis, the sharp maximum of

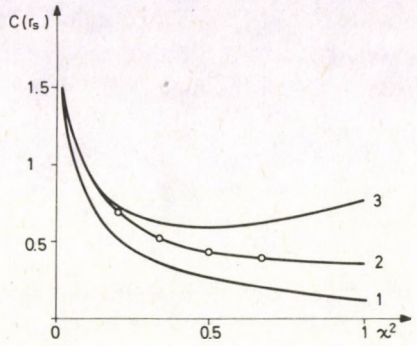

Fig. 2. $C(r_s)$ functions vs density parameter χ^2. 1) from Eq. (4) with $G=0$ after Lindhard and Winther [14]. 2) with $G=G^L$ after Lantto et al [5]. 3) with $G=G^D$ after Devreese et al [3]. 4) from Eq. (10) using the data of Pines and Nozieres [16] for $r_s=1$, 2, 3 and 4

G^D at $k\cong 2k_F$ (i.e. $z\cong 1$) influences the $C(r_s)$ functions resulting in 2 or 3 times higher values than the ones from the Lindhard theory. Curve 2 shows the $C(r_s)$ function obtained by the use of G^L after Lantto et al, where this local-field correction depends on the r_s values. This is a monotonically decreasing curve lying below the one of Sayasov. In the case of metallic densities ($\chi^2=0.5$) these data are 1.5 or 2 times higher than the Lindhard–Winther ones. At last we mention a parametrical analytical formula for $C(r_s)$, which allows a fast evaluation from the experimental point of view. If we use the Landau theory of Fermi liquids and the ε_l function given by Silin in the frame of this theory [15], we can have the following formula instead of Eq. (4) for the $v\ll v_F$ range

$$C(r_s)=(1+F_1^s/3)\,(1+F_0^s)^{-2}0.5[\,\ln(1+1\chi_x^2)-(1+\chi_x^2)^{-1}]\,, \tag{10}$$

where the modified density parameter is

$$\chi_x^2=\chi^2(1+F_0^s)^{-1}(1+F_1^s/3)^{-1}\,.$$

According to Pines and Nozieres [16] F_0^s and F_1^s can be determined from the effective mass formula

$$m_e^*/m_e=1+F_1^s/3\,,$$

and from the compressibility ratio

$$\kappa^0/\kappa=(1+F_0^s)\,(1+F_1^s/3)^{-1}\,,$$

where κ^0 and κ are the compressibilities of the free and correlated electron gas, respectively. These ratios can be simply counted in the knowledge of the correlation energies. The determination of the correlation energy values gives a somewhat more problematical task, as the dependence of the correlation energy on r_s is only approximatively known at higher r_s values [17, 18]. We evaluated Eq. (10) with the data

given by Pines and Nozieres (see also [19]) and we obtained the curve of Fig. 2 denoted by —○—. It can be seen that in the cases of electron gases of metallic density, the $C(r_s)$ function from Eq. (10) agrees well with the function determined from Eq. (4) with the help of G^L after Lantto et al.

Results

Supporting the choice of the $C(r_s)$ function, we compared our results to those of other theories and experiments. As it is stated by Andersen and Ziegler [20], the experimental results in the $v \ll v_F$ velocity range under examination are rather insufficient. Investigations under 10 keV bombarding energy were done by Nomura and Kiyono [21], Gott and Telkovskii [22], Arkhipov and Gott [23], and Wilcox [24]. It is worth mentioning that the determination of the so-called average velocity ($\bar{v}$) is quite different in the experiments of [21] and of [22 or 23]. Namely, the average velocity defined by Nomura and Kiyono is the double of that in [22] or [23]. Thus, if we suppose that the measurements are exact from every other viewpoint, the $C(r_s)$ value concluded from [22] or [23] has to be double of that from [21]. And really, the measurements give $C(r_s)=0.76$ for gold and silver targets. It is now proved that, considering the 10–15% experimental error of the measured data, the halves of the results of Gott and Telkovskii give the same as our calculation and the measurement of Nomura and Kiyono. Table I contains the theoretical results and the data of the above

Table I

Theoretical and experimental results for $C(r_s)$ values calculated and measured on gold target bombarded by slow protons. The origin of the results is detailed in the text

	Theory						Experiment	
	1)	2)	3)	4)	5)	6)	7)	8)
$C(r_s)$	0.45	0.45	0.61	0.26	0.448	0.39	0.49 ± 0.05	0.50

experiments for $C(r_s)$ calculated and measured on gold target ($r_s=3.01$, $\chi^2=0.5$). In the order of the columns, the following values are shown:

1) Present result calculated by Eq. (10) using the data of [16];
2) Present result calculated by Eq. (4) with G^L local-field correction after [18];
3) Present result calculated by Eq. (4) and that of Sayasov [4] with G^D local-field correction after [3];
4) Result from the Lindhard–Winther theory ($G=0$) [14];
5) Result from the Lindhard–Scharff–Schiott theory [25];

6) Result calculated by Eq. (7) after Echenique et al [26]. (The screened potential was calculated self-consistently by the density-functional formalism here);
7) Experimental result after [21];
8) Experimental result after [24].

A further important observation can be made from the analysis of the mechanical equation of motion. If we assume a priori the validity of the $m_p\ddot{x} = -k\dot{x}$ stopping formula, then the energy of the proton (with mass m_p, primary energy E_0 and primary velocity v_0) vs penetration depth x is the following

$$E(x) = 0.5 m_p v_0^2 (1 - x/x_M)^2 ,$$

where $x_M = m_p v_0/k$. If we use the notation $\Delta E = E_0 - E(\Delta x)$ for the total energy loss in the target (with thickness Δx), then

$$\Delta E/\Delta x = k v_0 (1 - \Delta x k/2 v_0 m_p) \tag{11}$$

is obtained for the "measurable" stopping power. If we want to characterize the dE/dx quantity with the primary velocity ambiguously, then $\Delta x/v_0$ has to be very small (regarding that $k/2m_p$ is constant). If this assumption cannot be valid, then $\Delta E/\Delta x \sim v_0^{1+s} (s > 0)$ will result when comparing two data (of small primary energy) according to Eq. (11). But $dE/dx \sim v_0^{1+s}$ is not a neccessary conclusion from this [27]! (For example in the case of a gold target with $\Delta x = 59$ nm [27] and $E_0 = 1$ and 2 keV, and $k = 7 \cdot 10^{-15}$ kgs^{-1}, then $dE/dx \sim E_0^{0.7}$ would be the formal result!)

Finally, let us examine the upper validity limit of the proton energy for Eq. (4) for "slow velocities" including a static G^L function. The measured data of Mertens and Krist [28] and Bauer et al [29] are the basis for this reason on gold and copper targets. The theoretical electronic stopping cross section values (S_e) are as follows

$$S_e^{Au} = 3.5 (E_0)^{1/2} ,$$

$$S_e^{Cu} = 2.6 (E_0)^{1/2} ,$$

where the $dE/dx = nS_e$ formula was used, where n is the electron density and dE/dx is obtained from Eq. (10). (E_0 should be substituted in keV, then the dimension of S_e is eVcm$^2 \cdot 10^{-15}$.) Table II contains the theoretical and experimental results for S_e (in the

Table II

Theoretical and experimental data for electronic stopping cross section of proton in gold and copper targets in units of eVcm$^2 \cdot 10^{-15}$ (E_0 is in keV)

Target	E_0	Present theory	Experiment
Au	30	19.2	22.9 [28]
	60	27.1	28.2 [28]
Cu	60	20.1	19.1 [29], 21.1 [28]

above units). The experimental error is about $\pm 5\%$. (The target thickness does not play a significant role at higher energies, see Eq. (11).) After a comparison it can be stated that our theoretical results are satisfying as far as some 10 keV. This surprisingly high limit must be due to the fact that the yv/v_F variable in the real and imaginary parts of the polarisability function changes the values of the corresponding functions slowly, and especially after the integration of Eq. (4) by y.

Conclusion

The possibilities of the description of the energy loss of a slow proton were examined in the frame of the dielectric theory. A local-field function including exchange and correlation corrections after Lantto et al was used for the determination of the longitudinal dielectric function. This calculation exceeds the original Lindhard–Winther theory. A parametric function was also deduced applying the Landau theory of Fermi liquids. From this latter equation using the data of Pines and Nozieres the same result could be obtained as from the previous formalism. The results in relation to the $C(r_s)$ function show good agreement with the compared experimental data. A good and a satisfactory agreement was found with the $C(r_s)$ value calculated from the Lindhard–Scharff–Schiott theory and from the density functional formalism used by Echenique et al, respectively.

References

1. J. Lindhard, K. Dan. Vidensk. Selsk. Mat. Fys. Medd., *28*, 8, 1954.
2. D. N. Tripathy and S. S. Mandal, Phys. Rev., *B16*, 231, 1977.
3. J. T. Devreese, F. Brosens and L. F. Lemmens, Phys. Rev. *B21*, 1349, 1980.
4. Yu. S. Sayasov, Z. Phys. A — Atoms and Nuclei, *313*, 9, 1983.
5. L. Lantto, P. Pietilainen and A. Kallio, Phys. Rev., *B26*, 5568, 1982.
6. S. Ichimaru and K. Utsumi, Phys. Rev., *B24*, 7385, 1981.
7. B. A. Trubnikov and Yu. H. Yavlinskii, Zh. Eksp. Teor. Fiz., *48*, 253, 1965.
8. N. W. Ashcroft and N. D. Mermin, Solid State Physics, pp. 341–342, Saunders College Philadelphia, 1981.
9. N. R. Arista and W. Brandt, J. Phys. C — Solid State Physics, *16*, L1217, 1983.
10. E. Fermi and E. Teller, Phys. Rev., *72*, 399, 1947.
11. P. Sigmund, Phys. Rev., *A26*, 2497, 1982.
12. T. L. Ferrell and R. M. Ritchie, Phys. Rev., *B16*, 115, 1977.
13. F. Calogero, Variable Phase Approach to Potential Scattering, p. 11, Academic Press, New York, London, 1967.
14. J. Lindhard and A. Winther, K. Dan. Vidensk. Selsk. Mat. Fys. Medd., *34*, 4, 1964.
15. V. P. Silin, Zh. Eksp. Teor. Fiz., *37*, 273, 1959.
16. D. Pines and Ph. Nozieres, The Theory of Quantum Liquids, Vol. 1, p. 332, Benjamin, New York, Amsterdam, 1966.
17. F. A. Stevens and M. A. Pokrant, Phys. Rev., *A8*, 990, 1973.
18. L. Lantto, Phys. Rev., *B22*, 1380, 1980.
19. T. M. Rice, Ann. Phys., *31*, 100, 1965.

20. H. H. Andersen and J. F. Ziegler, Hydrogen Stopping Powers and Ranges in all Elements, Pergamon, New York, Toronto, Oxford, Sydney, Frankfurt, Paris, 1977.
21. A. Nomura and S. Kiyono, J. Phys. D — Applied Physics, *8*, 1551, 1975.
22. Yu. V. Gott and V. G. Telkovskii, Radioteknika i Elektronika, *7*, 1956, 1962.
23. E. P. Arkhipov and Yu. V. Gott, Sov. Phys. JETP, *29*, 615, 1969.
24. H. A. Wilcox, Phys. Rev., *74*, 1743, 1948.
25. J. Lindhard, M. Scharff and E. M. Schiott, K. Dan. Vidensk. Selsk. Mat. Fys. Medd., *34*, 4, 1963.
26. P. M. Echenique, R. Nieminen and R. M. Ritchie, Solid State Comm., *37*, 779, 1981.
27. R. Blume, W. Eckstein and H. Verbeek, Nucl. Instrum. Meth., *194*, 67, 1982.
28. P. Mertens and Th. Krist, Nucl. Instrum. Meth., *194*, 57, 1982.
29. P. Bauer, F. Aumayer, D. Semrad and B. H. Scherzer, Nucl. Instrum. Meth. *229*, B1, N. 1., 1984.

Acta Physica Hungarica 60 (3—4), pp. 213—220 (1986)

MEASUREMENT OF THE TRANSMITTED AND REFLECTED CAPTURE GAMMA RAYS FOR HEAT RESISTANT CONCRETE SHIELD

A. S. MAKARIOUS, A. M. I. KANY* and A. EL-SAYED ABDO

Reactor and Neutron Physics Department, Nuclear Research Centre Atomic Energy Authority, Cairo, Egypt

(Received in revised form 16 October 1984)

The experimental measurements of the transmitted and the reflected (albedo) components of the capture secondary gamma rays, arising from interaction of reactor neutrons with heat resistant concrete shields have been carried out. This new type of concrete has been prepared from Egyptian ilmenite–limonite ores and has a density 3.44 gm/cm^3. The measurements were performed using a collimated beam of reactor neutrons emitted from one of the horizontal channels of the ET–RR–1 reactor.

A single stilbene crystal scintillator applying zero crossover technique for differentiation between gamma and neutron pulses has been utilized. The measured instrument spectra were transformed to energy spectra. From the measurements it is evident that the albedo capture gamma rays is very small in comparison with the total or the transmitted capture gamma rays.

1. Introduction

Reactor shielding is composed of elements with large and small atomic number in the form of heterogeneous compositions and homogeneous mixtures. To shield a stationary nuclear facility two requirements must be realized; minimum cost and small size. In addition to shield transport nuclear facility weight is to be minimized. As a result the hard component of the reactor shielding is generally close to the reactor core due to the high temperature arising in this region. As metal screens are placed close to the reactor core where high neutron fluxes are observed, and consequently intensive secondary gamma radiation is produced.

The principal components of the secondary gamma radiation of a nuclear facility shields are gamma radiation due to the radiative capture of thermal neutrons and gamma radiation due to the inelastic scattering of fast neutrons with the shielding materials. In some cases the secondary gamma radiation completely determines the radiation field behind the reactor shields.

* Department of Physics, Faculty of Science, Al-Azhar University, Cairo, Egypt

The knowledge of the secondary gamma radiation characteristics allows an optimal choice of thickness and alternation of layers from the point of view of both the minimum radiation heat generation and the minimum dose of mixed radiation behind the shield. The knowledge of the total capture secondary gamma rays requires the knowledge of the transmitted capture gamma rays and the reflected (albedo) capture gamma-rays. As the angular energy distribution of capture gamma-rays is more or less isotropic [1], it was found satisfactory to measure the capture gamma-rays at an angle (70° and 120° in our case) and for $\theta > 30°$ in order to avoid the contribution of primary gamma rays from the reactor core. The problem of generation and penetration of secondary gamma radiation in substances has been investigated mostly for simple geometries [2–7]. There are still many discrepancies between the experimental results and calculations of secondary gamma rays, therefore further measurements are very important for the theoreticians who may calculate this problem in future as a check for the computer code and the cross-section data sets which may be used.

In the present work both the transmitted and reflected (albedo) components of the total and capture secondary gamma rays for heat resistant concrete (ilmenite-limonite concrete) have been investigated.

2. Experimental details

A schematic diagram of the experimental layout was shown in Fig. 1. The transmitted and the reflected (albedo) components of capture gamma rays for heat resistant concrete have been investigated. The composition of the ilmenite–limonite concrete was shown in Table I. The decrease of the water content of concrete shield is accompanied by an increase in the neutron relaxation length, i.e. decrease in the shielding effectiveness specially for fast neutrons. The water content of hydrated portland cement decreases as the temperature is raised. The concrete is usually dehydrated completely when heated above 400 °C. However, if concrete is made with aggregates as shown in Table I, it may still retain 25 to 50% of its water content at this temperature, thus it is of great practical importance for fast neutrons attenuation especially for power reactors, where the temperature in the core is very high and may cause cracks in the biological shield if it is made from ordinary concrete. A cylindrical sample of ilmenite–limonite concrete with 15 cm diameter and 10 cm thick was placed in front of one of the horizontal channels of the ET–RR–1 reactor operated at full power (2 MW). The sample was placed normal to the reactor beam direction (i.e. $\theta_0 = 0°$) where θ_0 is the angle between the beam direction and the normal to the sample under investigation. The detector was placed at an angle of $\theta = 70°$ for the measurement of the transmitted secondary gamma rays, then at an angle of $\theta = 120°$ for the measurement of the reflected (albedo) secondary gamma rays, where θ is the angle between the detector and the normal to the sample. The primary gamma rays contribution at these angles is negligible. The sample and the detector centres were

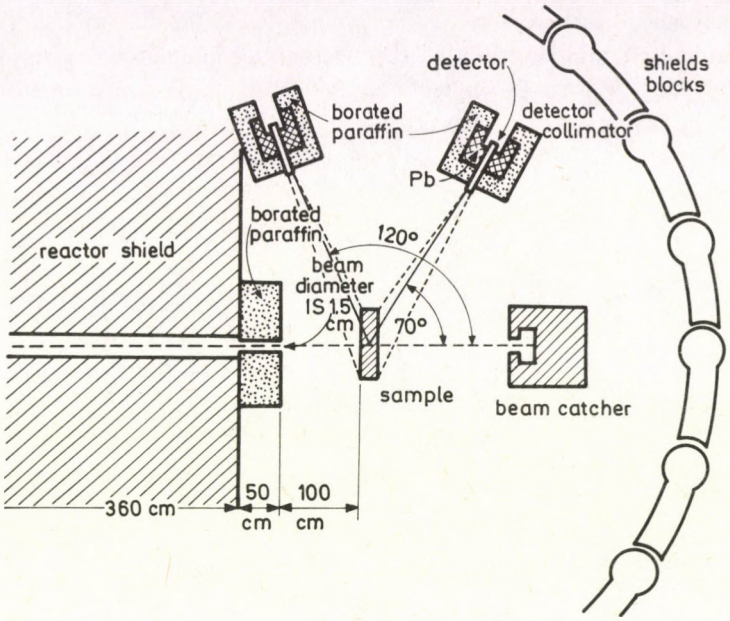

Fig. 1. The experimental configuration for both transmitted and reflected (albedo) secondary gamma rays

Table I

Ingredients of 1 m^3 of heat resistant concrete
(density = 3.44 gm/cm^3)

Material	Content	
	Aggregate density	Aggregate size
Ilmenite ore $FeO.TiO_2$	722 kg/m^3	40 – 60 mm
	482 kg/m^3	20 – 40 mm
	482 kg/m^3	10 – 20 mm
	241 kg/m^3	5 – 10 mm
	1927 kg/m^3	
Limonite ore $(Fe(OH)_6.Fe_2O_3)$	415 kg/m^3	
Portland cement	350 kg/m^3	
Water (after drying 28 days)	121 kg/m^3	

placed in the same horizontal plane with the beam centre. The sample was within the solid angle of the detector collimator. Two spectra were taken for each angle, one with a bare reactor beam and the other by placing a 0.4 mm thick cadmium sheet on the reactor channel (i.e. cadmium filtered beam). A background measurement was taken for each run.

Measurements were performed using a single crystal stilbene scintillator 40 mm diameter and 40 mm length coupled with a 56 AVP photomultiplier and a 1024

multichannel pulse height analyzer (type Omega–1). As the reactor beam is a mixed field of gamma rays and neutrons, so the discrimination against neutron pulses was achieved by using zero crossover technique of pulse shape discrimination. A block diagram of the zero crossover technique is shown in Fig. 2.

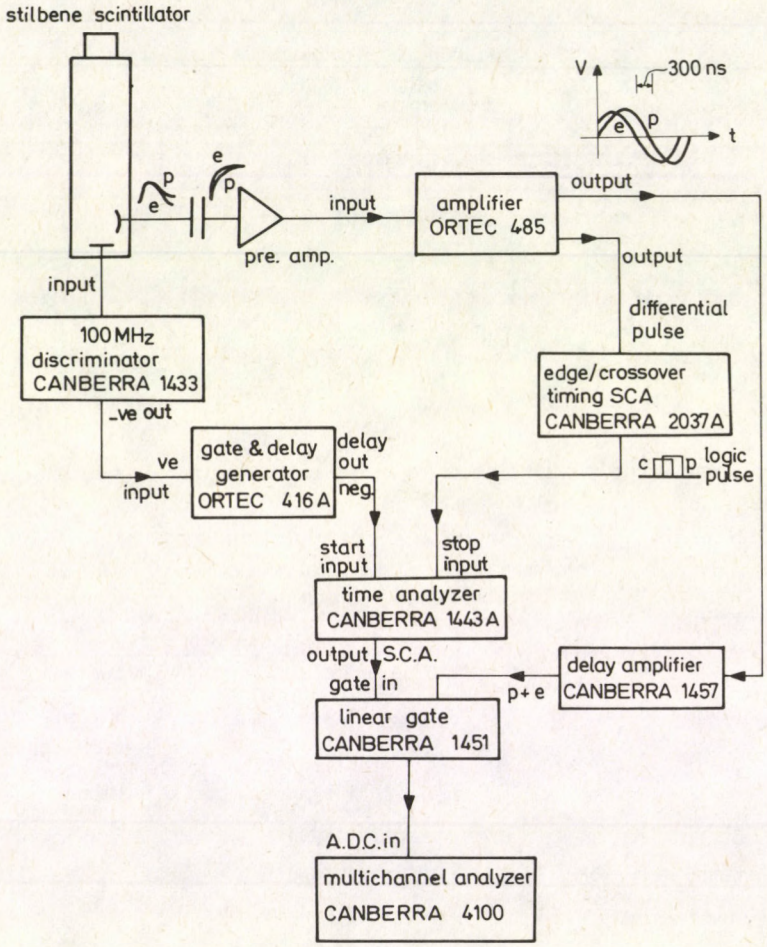

Fig. 2. Block diagram of the spectrometer assembly

The anode is operated near earth potential with the photocathode at 1900 V. With this high gain photomultiplier base the amplitude of the current pulse at the anode is not proportional to the amplitude of the scintillation pulse. Current pulses containing the same information as the scintillation pulse (i.e. linear signals) can be obtained from a suitably chosen dynode. The decoupling capacitor and resistor network at this dynode integrate the current pulse to produce a voltage step of rise time

determined by the scintillation decay times. The dynode voltage step is amplified and differentiated twice by means of resistor capacitor networks in the main amplifier to produce a bipolar voltage pulse which passes through zero at a time which depends only on the input pulse shape. The difference in zero crossing times between the anode current pulse (zero time reference marker), and the zero crossing of the doubly differentiated dynode voltage pulse for protons and electrons interacting with the scintillator is of the order of 350 ns. Time to pulse amplitude converters produce output signals of amplitude proportional to the time difference between its two input signals (designated start and stop) for time differences ≤ 1 μs. The start signal is derived from the anode current pulse and the stop signal from the edge cross over. The out pulses of the time to pulse amplitude converter are used to open the linear gate for the detected gamma rays. The signals from the linear amplifier are fed to the ADC of the multichannel pulse height analyzer for analysis. The details of the zero crossover technique for pulse shape discrimination are given elsewhere [8, 9]. A boron carbide filter of 1 cm thickness was placed in front of the detector collimator to prevent the occurrence of the 2.23 MeV capture gamma rays produced from the thermal neutrons capture by the hydrogen nuclei of the scintillator. A ZnS(Ag) scintillator of 3 cm diameter and 0.5 cm thick coupled with a photomultiplier type (∅ EY–16) was used as a monitor for the control of the reactor power variations. The spectrometer stability and energy scale were checked before each run. The energy width per channel was the same over the whole energy range for the chosen amplifier gain.

The radiative capture secondary gamma ray spectra were obtained by subtracting the gamma ray spectra measured with the cadmium filtered reactor beam from that with bare reactor beam. The instrumental gamma ray spectra were transformed to energy spectra [10].

3. Results and discussion

A display of the measured transmitted secondary gamma ray energy spectra for heat resistant concrete at an angle of $\theta = 70°$ for: (a) bare reactor beam, (b) cadmium filtered reactor beam is shown in Fig. 3. Also a display of the measured reflected (albedo) secondary gamma ray energy spectra for heat resistant concrete at an angle of $\theta = 120°$ for: (a) bare reactor beam, (b) cadmium filtered reactor beam, is shown in Fig. 4. In case of the reflected (albedo) secondary gamma ray measurements both the neutron beam and the detector face the same side of the concrete sample under investigation. Secondary gamma rays are generated as the result of the radiative capture of thermal neutrons and the inelastic scattering of fast neutrons. As the cadmium filter absorbs neutrons below 0.4 eV, so by subtracting the measured secondary gamma rays for a cadmium filtered reactor beam from that for a bare reactor beam the secondary gamma rays from the capture of thermal neutrons were obtained as in spectra (c) in Figs 3, 4. From those Figures it is evident that the secondary gamma

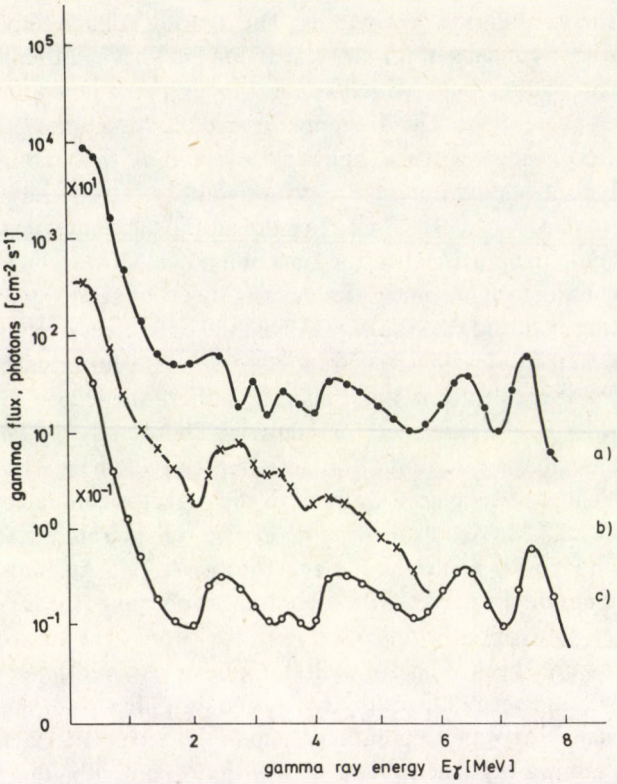

Fig. 3. The spectra of the transmitted secondary gamma rays from ilmenite–limonite concrete at an angle of $\theta = 70°$, for: (a) . . . bare reactor beam. (b) × × × cadmium filtered reactor beam. (c) ○–○–○ The difference of (a–b)

peaks coincide quite well with the gamma rays arising from the inelastic scattering and radiative capture of neutrons with concrete constituents. These relations show that the gamma rays energy 0.5 MeV gives the main contribution of secondary gamma rays for ilmenite-limonite concrete barriers. Also the rate of decrease of the secondary gamma flux with increasing the barrier thickness depends on gamma rays energy. This is due to the effects of build-up factor of gamma rays from the degradations of gamma rays of higher energies, and the different rates of removal or absorption of those gamma rays.

From the measurements it is evident that the albedo capture gamma rays are very small in comparison with the total or transmitted capture gamma rays. This may be attributed to the behaviour of the secondary gamma which tends to be peaked in the forward direction (transmitted secondary gamma rays). The reflected (albedo) secondary gamma rays are the result of the interaction of the incident neutrons with the first layers of the sample. As in this geometry the source and the detector were in the same side of the concrete barrier, so the generated secondary gamma rays from the deeper layers of the sample were absorbed during their long path back to the detector,

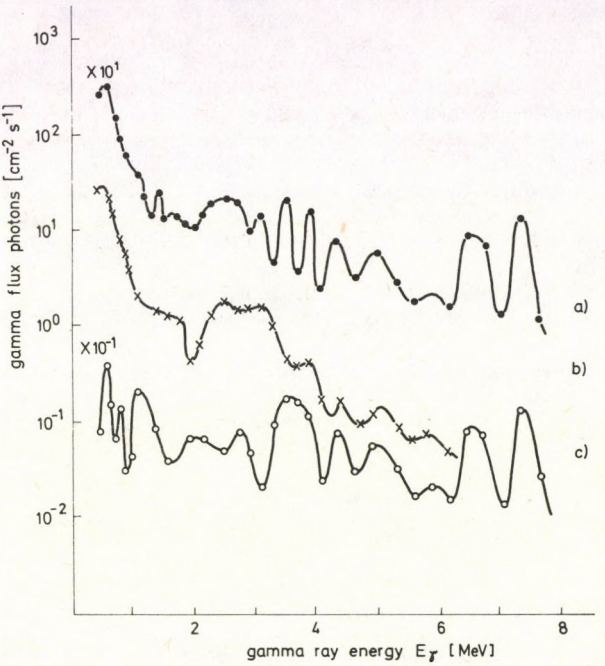

Fig. 4. The spectra of the reflected secondary gamma rays (albedo component) from ilmenite–limonite concrete at an angle of $\theta = 120°$, for: (a) . . . bare reactor beam. (b) × × × cadmium filtered reactor beam. (c) ○–○–○ The difference of (a–b)

while the transmitted secondary gamma rays are due to the interaction of neutrons with the whole sample thickness, especially the deeper layers which are the nearest to the detector, where most of the high energy neutrons were being thermalized and were strongly liable to undergo capture to produce secondary gamma rays.

From curves (c) of Figs 3, 4, it can be seen that the transmitted capture gamma rays intensity due to thermal neutrons is higher than the reflected capture gamma ray intensity which may be due to the following:

(a) In the albedo gamma measurements using the cadmium filtered reactor beam as in curve (b) of Fig. 4, the thermal reactor neutrons are captured in the cadmium yielding capture gamma rays which may undergo scattering in the first few layers of the used sample which then may reach the detector causing an increase of the reflected capture secondary gamma ray intensity. Consequently, the intensity of the reflected capture gamma rays due to thermal neutrons decrease as in curve (c) of Fig. 4.

(b) The effect of build-up factor of capture gamma rays may also cause the increase of the transmitted capture gamma rays due to reactor thermal neutrons as in curve (c) of Fig. 3.

(c) Also there is still a probability for thermal neutrons that can reach the stilbene crystal ($C_{14}H_{12}$) undergoing capture in hydrogen to yield a 2.23 MeV capture gamma ray which increases the transmitted capture gamma rays due to thermal neutrons.

References

1. A. S. Makarious, W. E. Ford III and K. R. Turnbull, ORNL/TM-5678, 1977.
2. H. Penkulm, Commission of the European Communities, Ispra (Italy). Joint Nuclear Research Centre. Translated by R. G. Mansfield from 1974 Reactor Meeting of the German Atomic Forum/KTG, Berlin, 4P. Dep. MTIS.
3. W. H. Scott, S. A. Dupree, D. E. Groce, D. L. Huffmen and E. A. Profio, Science Appl. INc. LaJolla, Calif. (U.S.A.) 1 Oct. 1972. Contract DASA 01–70–C–0053. 205p. (SAI–71–553–LJ; DNA–2994–F) NTIS.
4. I. V. Goryachev, Yu. I. Kolevatov and I. V. Kukhtevich, At. Energ. (U.S.S.R.); 31: No. 3, 209–14 (Sept. 1971), (in Russian).
5. Yu. A. Kazanski, V. I. Kukhtevich, E. S. Matusevich, B. I. Sinitsyn and S. G. Tsypin, Translation of Fizicheskye Issledovaniya Zaschity Reaktorov, Moscow, Atomizdat, 1966, 359P. (TT–68–50324; IPST–Cat. 5138) Dep. CFSTI.
6. A. T. Bakov and Yu. A. Kazanski, PP 156–63 of Voprosy, Fiziki Zaschity Reaktorov, Atomizdat, Moscow, 1966, 24P.. Dep. CFSTI.
D. I. Green, K. Preiss, S. P. Chilton and A. B. Chilton, (Illinois Univ., Urbana) Apr. 1969; Contract No. 0228–66–0311–72 P. (NRSS-9., USNRDL-TRC-69–1) CFSTI.
8. T. G. Miller, Nucl. Inst. and Meth., *63*, 121, 1968.
9. C. M. Cialella and J. A. Devanny., Nucl. Inst. and Meth., *60*, 269, 1968.
10. Yu. I. Kolevatov, Voprosy Dozimetri, Zaschity at IZ-Luchenie, Moscow, No. 10:131–7, 1969.

Acta Physica Hungarica 60 (3—4), pp. 221—226 (1986)

HYDROMAGNETIC RAYLEIGH PROBLEM IN A ROTATING FLUID

A. RAPTIS

University of Ioannina, Department of Mechanics
Ioannina, Greece

and

A. K. SINGH

Banaras Hindu University, Department of Mathematics
Varanasi–221005, India

(Received 18 October 1984)

An analysis of the MHD Rayleigh problem of a rotating fluid above a plate is carried out, when the magnetic Reynolds number of the flow is small and the magnetic field is fixed on the plate. An exact solution is obtained with the help of the Laplace transform technique. It is found that the effect of the magnetic field increases the primary flow and decreases the secondary flow.

1. Introduction

The classical Rayleigh problem for the flow due to the impulsive motion of an infinite plate is important in engineering. Rossow [1] and Chang and Yen [2] studied the hydromagnetic Rayleigh problem, whereas Soundalgekar and Pop [3] studied the same problem in the rotating frame of reference. Soundalgekar and Pop [3] studied the effect of magnetic field on the flow when the magnetic field is fixed relatively the system of reference.

The object of the present paper is to study the hydromagnetic Rayleigh problem, when the magnetic field is fixed on the moving plate and the magnetic Reynolds number of the flow is small. The solution of the problem is obtained with the help of the Laplace transform technique.

2. Mathematical analysis

The equation of continuity and the equation of motion along with the Maxwell's equations and Ohm's law for unsteady flow of viscous, incompressible and electrically conducting fluid are:

$$\nabla \cdot \mathbf{V} = 0, \tag{1}$$

$$\frac{\partial \mathbf{V}}{\partial t'} + (\mathbf{V} \cdot \nabla)\mathbf{V} + 2\Omega \bar{z}_0 \times \mathbf{V} = -\frac{1}{\rho} \nabla P + \nu \nabla^2 \mathbf{V} + \frac{1}{\rho} \mathbf{J} \times \mathbf{B}, \tag{2}$$

$$\nabla \times \mathbf{B} = \mu_e \mathbf{J}, \tag{3}$$

$$\nabla \times \mathbf{E} = -\frac{\partial \mathbf{B}}{\partial t'}, \tag{4}$$

$$\nabla \cdot \mathbf{B} = 0, \tag{5}$$

$$\mathbf{J} = \sigma(\mathbf{V} \times \mathbf{B} + \mathbf{E}), \tag{6}$$

where ρ, ν, σ, μ_e, $\mathbf{V}$, $\mathbf{J}$, $\mathbf{B}$, $\mathbf{E}$, P, $\mathbf{z}_0$ and Ω are respectively the density, the kinematic viscosity, the fluid conductivity, the magnetic permeability, the velocity vector, the current density, the magnetic field, the electric field, the pressure including the centrifugal term, the unit vector along the z'-axis and the constant angular velocity of the fluid about the z'-axis.

We consider the unsteady flow generated in a semi-infinitely extended fluid bounded by an infinite flat plate at $z' = 0$, subjected to a uniform magnetic field density B_0 which is perpendicular to the plate. Both the fluid and the plate are in a state of solid body rotation with the constant angular velocity Ω about z'-axis, which is perpendicular to the plate, and at time $t' = 0$ the plate is started impulsively with a uniform velocity U_0 (in the rotating frame of reference) at the direction of the x'-axis and the velocity field is of the form $\mathbf{V}(u, \upsilon, 0)$.

Since the plate is infinite in length all physical quantities will be functions of z' and t'. Then the equation of the conservation of electric change $\nabla \cdot \mathbf{J} = 0$ gives J_z = constant, where $\mathbf{J} \equiv (J_x, J_y, J_z)$. This constant is equal to zero ($J_z = 0$) when the plate is electrically non-conducting. Since the magnetic Reynolds number of the flow is small, the induced magnetic field can be neglected in comparison to the applied magnetic field. Hence we can take $\mathbf{B} \equiv (0, 0, B_0)$. Also we assume that the electric field is equal to zero.

Since the magnetic field is fixed on the moving plate it will be [4],

$$J_x = \sigma B_0 \upsilon', \qquad J_y = \sigma B_0 (u' - U_0).$$

By taking into account these assumptions Eq. (2) gives:

$$\frac{\partial u'}{\partial t'} - 2\Omega \upsilon' = \nu \frac{\partial^2 u'}{\partial z'^2} - \frac{\sigma B_0^2}{\rho}(u' - U_0), \tag{7}$$

$$\frac{\partial \upsilon'}{\partial t'} + 2\Omega u' = \nu \frac{\partial^2 u'}{\partial z'^2} - \frac{\sigma B_0^2}{\rho} \upsilon'. \tag{8}$$

The initial and boundary conditions are:

$$\text{For} \quad t' \leqq 0: \quad u' = 0, \qquad \upsilon' = 0 \qquad \text{for all} \quad z'.$$

$$\text{For} \quad t'>0: \begin{cases} u'=U_0, & v'=0 \quad \text{at} \quad z'=0, \\ u'\to 0, & v'\to 0 \quad \text{as} \quad z'\to\infty. \end{cases} \tag{9}$$

Introducing the dimensionless variables

$$z=\frac{z'U_0}{\nu}, \qquad t=\frac{t'U_0^2}{\nu}, \qquad (u, v)=(u', v')/U_0, \tag{10}$$

Eqs (7) and (8) become

$$\frac{\partial u}{\partial t}-2Kv=\frac{\partial^2 u}{\partial z^2}-M(u-1), \tag{11}$$

$$\frac{\partial v}{\partial t}+2Ku=\frac{\partial^2 v}{\partial z^2}-Mv, \tag{12}$$

where $M=\dfrac{\sigma B_0^2\nu}{\rho U_0^2}$ is the magnetic parameter and $K=\dfrac{\Omega\nu}{U_0^2}$ is the rotation parameter.

The initial and boundary conditions now become:

$$\text{For} \quad t\leqq 0: \quad u=0, \qquad v=0 \qquad \text{for all} \quad z.$$

$$\text{For} \quad t>0: \begin{cases} u=1, & v=0 \quad \text{at} \quad z=0, \\ u\to 0, & v\to 0 \quad \text{as} \quad z\to\infty. \end{cases} \tag{13}$$

It is quite complicated to solve Eq. (11) and (12) under the boundary conditions (13). So in order to simplify the mathematical part, we introduce a complex velocity defined by

$$q=u+iv, \tag{14}$$

which enables us to combine Eqs (11) and (12) into one equation as follows:

$$\frac{\partial q}{\partial t}+2Kiq=\frac{\partial^2 q}{\partial z^2}-M(q-1). \tag{15}$$

In view of (14), the conditions (13) reduce to:

$$\text{For} \quad t\leqq 0: \quad q=0 \qquad \text{for all} \quad z.$$

$$\text{For} \quad t>0: \begin{cases} q=1 & \text{at} \quad z=0, \\ q\to 0 & \text{as} \quad z\to\infty. \end{cases} \tag{16}$$

Applying Laplace transform, the solution of the Eq. (15), under the conditions (16), is given by

$$q=\frac{1}{2}\left(1-\frac{M}{m}\right)\left[e^{-z\sqrt{m}}\operatorname{erfc}\left(\frac{z}{2\sqrt{t}}-\sqrt{mt}\right)+e^{z\sqrt{m}}\operatorname{erfc}\left(\frac{z}{2\sqrt{t}}+\sqrt{mt}\right)\right]+$$

$$+\frac{M}{m}\left[1-e^{-mt}\operatorname{erf}\left(\frac{z}{2\sqrt{t}}\right)\right], \tag{17}$$

where $m=M+2iK$.

The non-dimensional components of shear-stress are given by

$$\tau_x + i\tau_y = -\left.\frac{\partial q}{\partial z}\right|_{z=0} = \frac{1}{\sqrt{\pi t}} e^{-mt} + \left(1 - \frac{M^2}{m}\right)\sqrt{m}\,\mathrm{erf}\,(\sqrt{mt}). \tag{18}$$

In Eqs (17) and (18) the complementary error function appears in the complex arguments and therefore to separate them into real and imaginary parts we use the following formula due to Abramowitz [5]

$$\mathrm{erf}\,(\alpha + ib) = \mathrm{erf}\,(\alpha) + \frac{e^{-\alpha^2}}{2\pi\alpha}[1 - \cos(2\alpha b) + i\sin(2\alpha b)] +$$

$$+ \frac{2e^{-\alpha^2}}{\pi}\sum_{\eta=1}^{\infty}\frac{e^{-\eta^2/4}}{\eta^2 + 4\alpha^2}[f_\eta(\alpha, b) + ig_\eta(\alpha, b)] + \varepsilon(\alpha, b), \tag{19}$$

where

$$f_\eta(\alpha, b) = 2\alpha - 2\alpha\cosh(\eta b)\cos(2\alpha b) + \eta\sinh(\eta b)\sin(2\alpha b),$$

$$g_\eta(\alpha, b) = 2\alpha\cosh(\eta b)\sin(2\alpha b) + \eta\sinh(\eta b)\cos(2\alpha b)$$

and

$$|\varepsilon(\alpha, b)| \simeq 10^{-16}|\mathrm{erf}\,(\alpha + ib)|.$$

3. Results and discussion

With the help of Eq. (19) we can take the expressions for the components of velocity and skin friction. For the sake of saving space these expressions are omitted.

In order to discuss the effects of the various parameters on the flow field near the plate, these equations are used for numerical calculations. The primary velocity profiles are plotted in Fig. 1 and the profiles due to secondary flow are shown in Fig. 2. It is seen from these Figures that the primary velocity increases with the magnetic parameter and decreases with the rotation parameter. The secondary velocity decreases when either the magnetic parameter M or the rotation parameter K increases.

The Table I shows the numerical values of the skin friction component τ_x and τ_y at the plate for different values of t, M and K. From this Table we conclude that the influence of the rotation parameter increases for both components of skin friction (τ_x and τ_y). Further, τ_x decreases and τ_y increases as the magnetic parameter M increases.

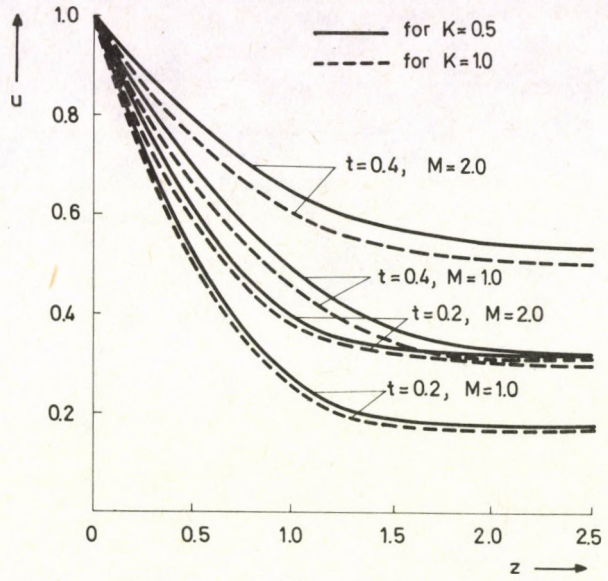

Fig. 1. Primary velocity profiles against z

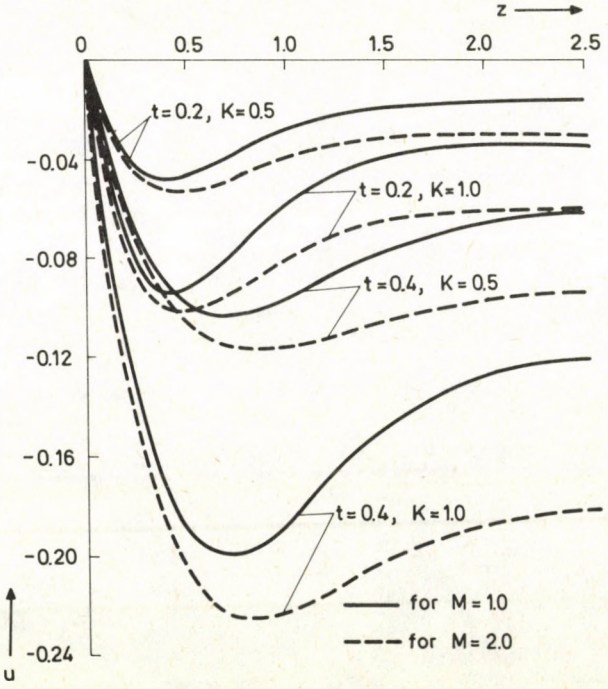

Fig. 2. Secondary velocity profiles against z

Table I

Numerical values of the skin-friction components

t	M	K	τ_x	τ_y
0.2	1.0	0.5	1.0420	0.2659
		1.0	1.0695	0.5296
	2.0	0.5	0.8553	0.2751
		1.0	0.8842	0.5480
0.4	1.0	0.5	0.6252	0.3874
		1.0	0.7051	0.7618
	2.0	0.5	0.4288	0.3989
		1.0	0.5108	0.7845

References

1. V. J. Rossow, NACA Report, No. 1958.
2. C. C. Chang and J. T. Yen, Phys. Fluids, *2*, 393, 1959.
3. V. M. Soundalgekar and I. Pop, Bull, Math. de la Soc. Math. de la R.S. de Roumanie, *14*, 375, 1970.
4. K. R. Cramer and S. I. Pai, Magnetofluid Dynamics for Engineers and Applied Physicists, McGraw-Hill Book Company, New York, 158, 1973.
5. B. M. Abramowitz and I. A. Stegun, Handbook of Mathematical Functions with Formulas, Graphs and Mathematical Tables, Washington, U.S. Gort, Printing Office, 1964.

Acta Physica Hungarica 60 (3—4), pp. 227—237 (1986)

HIGH RESOLUTION EMISSION SPECTRA OF THE 0–0, 0–1 AND 0–2 BANDS OF $E^1\Pi$–$A^1\Pi$ AND $B^1\Sigma^+$–$A^1\Pi$ TRANSITIONS IN $^{12}C^{18}O$ MOLECULE*

R. KĘPA

Atomic and Molecular Physics Laboratory
Pedagogical College, Rzeszów, Poland

(Received 30 November 1984)

In the emission spectrum of the $^{12}C^{18}O$ isotopic molecule the 0–0, 0–1 and 0–2 bands of two $E^1\Pi$–$A^1\Pi$ and $B^1\Sigma^+$–$A^1\Pi$ transitions have been photographed at high resolution. After a rotational analysis of bands the following molecular constants have been calculated: (1) the rotational constants B_0 and D_0 for the upper $E^1\Pi$ and $B^1\Sigma^+$ states and B_v, D_v for the $A^1\Pi$ state, (2) the reduced band origins c_{0v}, for both transitions, (3) the Λ-doubling constants for the $E^1\Pi$ state, (4) the distances between $v=0$ levels in the $E^1\Pi$, $C^1\Sigma^+$ and $A^1\Pi$ states. Some molecular constants have been derived from the combinational analysis of bands which belong to the $E^1\Pi$–$A^1\Pi$ and $B^1\Sigma^+$–$A^1\Pi$ and also $E^1\Pi$–$A^1\Pi$ and $C^1\Sigma^+$–$A^1\Pi$ transitions. Strong perturbation of the $A^1\Pi$ state by $e^3\Sigma^-$ nearby electronic state, observed in the 0–0 band of $B^1\Sigma^+$–$A^1\Pi$ system has also been analysed.

Introduction

Investigations of the electronic states in isotopic carbon monoxide molecules started in the sixties are systematically extended both to new isotopic molecules and new states. Up to now most explorations and the most precise data have been concerned with the ground state of this molecule. Explorations of this state have been performed so far in almost all molecules which have been produced in combination of the ^{12}C, ^{13}C and ^{14}C isotopes with ^{16}O, ^{17}O and ^{18}O one, excluding the $^{14}C^{17}O$ molecule [1–6].

Studies of the excited electronic states in isotopic molecules have not been performed so extensively as the ground state. Most investigations among excited states are concerned with the $A^1\Pi$ [7–14] and $B^1\Sigma^+$ states [10–15]. Less information is concerned with $C^1\Sigma^+$ [15–19] and still less with $E^1\Pi$ states [20–21]. Quite fragmentary studies are concerned with other singlet and triplet states [22–25]. But

* This work was financially supported by the Spectroscopy Committee of the Polish Academy of Sciences.

even studies of $E^1\Pi$, $B^1\Sigma^+$ and $A^1\Pi$ states in $^{12}C^{18}O$ molecule performed via analyses of the $E^1\Pi-A^1\Pi$ and $B^1\Sigma^+-A^1\Pi$ band systems are insufficient. The above analyses have been performed using the spectra obtained using the molecule insufficiently enriched in ^{18}O isotope. They were therefore insufficient for the registration of complete rotational structure of bands and even whole bands.

Therefore, in order to perform the complete rotational analysis and completion of the information about $E^1\Pi$, $B^1\Sigma^+$ and $A^1\Pi$ states in this molecule the bands of the $E^1\Pi-A^1\Pi$ and $B^1\Sigma^+-A^1\Pi$ systems in highly enriched $^{12}C^{18}O$ molecule were photographed and analysed.

Experimental details

The emission spectra of the $B^1\Sigma^+-A^1\Pi$ and $E^1\Pi-A^1\Pi$ systems were observed from a capillary Π-type Geissler discharge tube. The tube with one graphite electrode was filled with oxygen enriched with 90% ^{18}O isotope. Pressure in the lamp was 6 hPa. For obtaining the bands of the $B^1\Sigma^+-A^1\Pi$ i.e. Ångström system the lamp was supplied by an A.C. generator. The voltage and current were about 3 kV and 10 mA, respectively. The lamp for obtaining the $E^1\Pi-A^1\Pi$ bands was supplied by a 10 kV and 800 kHz A.C. generator. The spectra were photographed in the 5th, 6th and 7th orders by 2 meter plane-grating PGS-2 spectrograph. A reciprocal linear dispersion ranged from 0.06 to 0.09 nm/mm. The exposure times varied from 10–20 min for the Ångström bands to 6–9 h for the bands of $E^1\Pi-A^1\Pi$ system. For wavelength calibrating the Th standard lines [26] obtained from a few orders and spectral regions were used. The precision of the measurements is considered to be ~ 0.005 cm^{-1}, the absolute wavenumbers may be in error by 0.010–0.020 cm^{-1}, excluding the lines marked by asterisk. Tables I–VI present the wavenumbers of lines for both analysed systems.

Methods of calculations and results

A. Rotational constants

The rotational constants of all the analysed states were calculated by means of the $\Delta_2 F(J)$ rotational term differences. The values of these differences as one can see may be expressed by truncated power series:

$$\Delta_2 F_v(J) = \sum_{i=0}^{2} a_i \left(J + \frac{1}{2}\right)^{2i+1}, \tag{1}$$

where coefficients of these power series have the following relationships to rotational

Table I

0−0 band lines of the $E^1\Pi - A^1\Pi$ transition in $^{12}C^{18}O$ [cm^{-1}]

J	R_e	R_f	P_e	P_f
2	28 192.665*	28 191.117*	28 172.795*	28 172.394
3	197.323	196.944	171.145*	170.789
4	28 204.164	28 203.529*	170.552	169.966*
5	211.928	210.827	170.789	169.966
6	221.045	218.957	172.394	170.552
7	220.152*	227.967	164.081*	172.194
8	232.129	237.998	168.559	174.865
9	243.448	249.471 232.129*	172.394	178.837 161.178*
10	254.889	262.865* 245.755	176.379	184.807 167.673
11	266.829	259.362	180.861	193.339* 173.887
12	279.595	272.605	186.142	28 203.745 179.733
13	293.556	285.937	192.665	185.618
14	297.646*	299.580	189.395*	191.846
15	28 314.420*	28 313.720*	198.612	198.612
16	330.510	328.388	28 207.348	28 205.866*
17	346.619*	343.654*	216.032*	213.712
18	363.239*		225.120	222.255
19			234.841	231.176
20			245.090	241.262

Table II

0−1 band lines of the $E^1\Pi - A^1\Pi$ transition in $^{12}C^{18}O$ [cm^{-1}]

J	R_e	R_f	P_e	P_f
1	26 735.546	26 735.546		
2	740.724	740.724	26 722.099	26 722.099
3	746.718	746.529	720.523*	720.523
4	753.435	753.094	719.685*	719.685*
5	760.840	760.345	719.685*	719.490*
6	768.981	768.374	720.346*	720.020
7	777.822	777.061	721.739	721.308
8	787.451	786.476	723.875	723.288
9	797.792	796.621	726.741	725.988
10	26 808.867	26 807.512	730.345	729.478
11	820.692	819.243	734.708	733.766
12	833.280	829.512	739.831	736.648
13	846.755	26 843.703	745.861	26 743.377
14	861.861	857.479	753.435	749.759
15	26 873.970	871.926	26.758.157	756.823
16	889.871	887.124	766.597	764.570
17	26 906.153	26 903.199	775.477	773.257
18	923.115	920.051	784.948	
19	941.056*		795.139	
20	959.957*		26 806.097*	

Table III

0−2 band lines of the $E^1\Pi$–$A^1\Pi$ transition in $^{12}C^{18}O$ [cm^{-1}]

J	R_e	R_f	P_e	P_f
1	25 322.678	25 322.678		25 311.525
2	327.965*	327.965*	25 309.078*	*309224**
3	334.011	333.812	307.838*	307.838*
4	340.835	340.517	307.086*	307.086*
5	348.404*	347.984*	307.229*	307.086*
6	356.815	356.234	308.184	307.838*
7	365.950	365.297	309.848	309.522
8	375.881*	25 374.726	312.280	25 311.525
9	386.546	385.294	315.493	314.655
10	397.982*	396.534	319.485	318.463
11	25 410.228		25 408.500	324.236
12	423.222	421.226	329.786	328.304
13	436.991	434.693	336.071	334.353
14	451.510	448.883	343.178	341.160
15	466.862	463.876	351.046	348.739*
16	482.950	479.616	359.697	357.043
17	499.813	496.016*	369.147	366.176
18	25 517.479	25 513.355	379.361	376.064*
19	535.914	531.571*	390.343	386.853
20	555.115	550.366	25 402.152	398.188*
21	575.108		414.753*	

constants:

$$a_0 = 4B_v - 6D_v + \frac{27}{4}H_v,$$

$$a_1 = -8D_v + 34H_v, \qquad (2)$$

$$a_2 = 12H_v.$$

The rotational constants were calculated by least-squares procedure described in detail in an earlier paper [17]. Table VII lists the obtained results.

The differences between the rotational constants of both combining states were calculated using $f_Q(J)$, $f_{PR}(J)$ and $f_{\overline{PR}}(J)$ Kovács's functions [27]. Average values of these constants calculated in regular regions of respective branches of bands are as follows:

for the $E^1\Pi$–$A^1\Pi$ transition

$$B^E_{0(e)} - B^A_0 = \text{———}$$

$$B^E_{0(f)} - B^A_0 = (0.340 \pm 0.020)\ cm^{-1},$$

$$B^E_{0(e)} - B^A_1 = (0.36725 \pm 0.00033)\ cm^{-1},$$

Table IV

$0-0$ band lines of the $B^1\Sigma^+-A^1\Pi$ transition in $^{12}C^{18}O$ [cm^{-1}]

J	R		Q		P	
1	22 173.193		22 165.741			
2	178.376*		167.130		22 159.742	
3	184.188		169.233	22 134.348	158.223	
4	190.847		172.040	139.417	157.492	
5	198.478		175.575	145.727	157.653	22 139.914
6	22 207.362		179.915	153.227	159.130	145.380
7	218.350	22 206.251	185.140	161.834	162.685	150.611
8		217.921	191.371*	171.336		154.871
9		228.932	199.062	181.424		158.463
10		240.031	22 208.668	191.548		162.135*
11		251.624	220.632	22 201.325		166.356
12		263.993	234.817	210.788	150.611	171.336
13	263.993	277.547	250.994	220.305	163.876	177.462
14	281.198	293.025	268.813	230.132	173.715	185.560
15	297.488	22 311.438	288.099	240.411	182.610	196.530
16	22 313.066			251.243	190.847	22 210.281*
17	328.688			262.655	199.062	
18	344.631			274.697	22 207.636	
19	361.138			287.394	216.769	
20	378.249			22 300.746	226.520	
21	396.043			314.805	236.955	
22	22 414.667			329.712	248.186*	
23			342.864		260.701	255.778
24		22 452.846	360.538			271.728
25		473.919	377.932			285.473
26			397.249			22 300.143
27			22 423.640	22 404.951	22 307.016	320.683
28				428.386	324.965	
29				449.217	342.164	
30					360.128	

$$B^E_{0(f)} - B^A_1 = (0.35561 \pm 0.00057)\ \mathrm{cm}^{-1},$$

$$B^E_{0(e)} - B^A_2 = (0.38610 \pm 0.00001)\ \mathrm{cm}^{-1},$$

$$B^E_{0(f)} - B^A_2 = (0.37557 \pm 0.00012)\ \mathrm{cm}^{-1},$$

and for the $B^1\Sigma^+-A^1\Pi$ transition

$$B^B_0 - B^A_0 = (0.349 \pm 0.010)\ \mathrm{cm}^{-1},$$

$$B^B_0 - B^A_1 = (0.35189 \pm 0.00016)\ \mathrm{cm}^{-1},$$

$$B^B_0 - B^A_2 = (0.37065 \pm 0.00006)\ \mathrm{cm}^{-1}.$$

Table V

0−1 band lines of the $B^1\Sigma^+-A^1\Pi$ transition in $^{12}C^{18}O$ [cm^{-1}]

J	R		Q		P	
1	20 722.662		20 715.241		20 711.567	
2	727.778		716.645		709.212	
3	733.602		718.752		707.627	
4	740.117		721.573		706.727	
5	747.345		725.107*		706.544	
6	755.274		729.317		707.048	
7	763.906		734.242		708.273	
8	773.242		739.883		710.192	
9	783.289		746.227		712.818	
10	794.023		753.309		716.162*	
11	20 805.487		761.236		720.219	
12	817.698		772.133	767.687	725.009*	
13	830.744			778.044	730.651	
14	845.412	838.846		788.027	737.918	731.364
15	840.086	856.995		798.632	725.107	742.129
16		872.371		20 809.940		750.128
17		888.117		822.198		758.482
18		20 904.476		833.560		767.486
19		921.503		847.342		777.128
20		939.212		861.449		787.483
21		957.608		876.199		798.536*
22		976.712		891.633		20 810.254
23		996.499		20 907.764		822.699
24		21 016.980		924.599		835.866
25		038.191		942.153		849.745
26		060.160		960.457		864.381
27		084.155	20 980.796			881.064
28	21 105.597		998.603		20 895.205	
29	129.671		21 019.055		20 911.956	
30			040.129		929.394	
31			061.923		947.490	
32			084.430		966.305	
33			21 107.658			

B. Band origins

The reduced band origins, i.e. distances between combining vibronic levels were derived using $g_Q(J)$, $g_{PR}(J)$ and $g_{\overline{PR}}(J)$ Kovács's functions [27]. The results calculated by this method, details of which were already described previously [18, 21] are given in Table VIII.

Table VI

0–2 band lines of the $B^1\Sigma^+$–$A^1\Pi$ transition in $^{12}C^{18}O$ [cm^{-1}]

J	R	Q	P
1	19 309.742	19 302.335	19 298.606
2	314.948	303.821	296.384
3	320.878	306.044	294.899
4	327.573	309.014	294.160
5	335.017*	312.726	294.160
6	343.145*	317.196	294.899
7	352.036	322.484*	296.384
8	361.664	19 328.126	298.606
9	372.043	334.883*	19 301.571
10	383.156	342.316	305.285
11	395.009	350.484	309.742
12	19 407.617	359.381	314.948
13	420.962	369.036	320.878
14	435.050	379.440	327.573
15	449.886	390.569	335.010*
16	465.462*	19 402.450	343.187
17	481.797	415.076	352.139
18	498.850	428.453	361.843
19	19 516.672	442.580	372.301
20	535.246	457.461	383.519
21	554.603	473.094	395.522
22	574.775	489.497	19 408.340
23	595.862	19 506.673	422.072
24	19 618.488	524.653	437.369
25	19 635.894	543.483*	19 447.431
26		563.336	464.962
27		584.865	481.797
28			499.298
29			19 517.442*

Table VII

Rotational constants of the $E^1\Pi$, $B^1\Sigma^+$ and $A^1\Pi$ states in $^{12}C^{18}O$ molecule [cm^{-1}]

		Present results[a]	Present results[b]	After Kępa et al [20]
$E^1\Pi$	$B_{0(e)}$	1.87087(16)[c]	1.870803(84)	1.8697(9)
	$B_{0(f)}$	1.85939(24)	1.85974(18)	1.85933(33)
	$D_{0(e)} \cdot 10^6$	6.50(29)	6.079(66)	3.5(22)
	$D_{0(f)} \cdot 10^6$	4.86(47)	5.32(45)	5.4(9)
	$q_0 \cdot 10^3$[d]	11.48(29)	11.07(17)	10.4(10)
	$q_0^D \cdot 10^6$[d]	1.64(55)	0.76(46)	−1.9(14)

[a] The constants calculated from $\Delta_2 F(J)$ differences

[b] The constants calculated from Jenkins and McKellar method

[c] The uncertainties in parentheses are one standard deviation expressed in units of the last quoted digit of the coefficient

[d] The Λ-doubling parameters

Table VII (cont.)

		Present results	After Rytel [11]
$B^1\Sigma^+$	B_0	1.855597(69)	1.85533(12)
	$D_0 \cdot 10^6$	6.142(65)	6.11(12)

		Present results	After Rytel [11]	After Janjić et al [16]
$A^1\Pi$	B_0	1.5284(37)	–	–
	B_1	1.5040(10)	–	–
	B_2	1.48516(17)	1.48448(39)	1.48400(7)
	$D_0 \cdot 10^6$	–	–	–
	$D_1 \cdot 10^6$	5.6(15)	–	–
	$D_2 \cdot 10^6$	7.97(34)	7.2	–

[a] The values recalculated from the σ_{0v}-real band origins

Table VIII

Reduced band origins for the $E^1\Pi$–$A^1\Pi$ and $B^1\Sigma^+$–$A^1\Pi$ transitions in $^{12}C^{18}O$ molecule [cm^{-1}]

		Present results	After Kępa et al [20]
$E^1\Pi$–$A^1\Pi$	c_{00}	28178.01(10)	–
	c_{01}	26727.333(12)	26727.689(18)[a]
	c_{02}	25314.840(24)	–

		Present results	After Rytel [11]
$B^1\Sigma^+$–$A^1\Pi$	c_{00}	22163.504(10)	22163.54(5)[a]
	c_{01}	20713.0307(42)	20712.93(3)[a]
	c_{02}	19300.1051(60)	19300.15(3)[a]

[a] The values recalculated from the σ_{0v}-real band origins

C. Jenkins and McKellar method

Very useful for the calculations of the molecular constants and also for the rotational interpretation of bands was the method of combinations of the lines belonging to the $E^1\Pi$–$A^1\Pi$ system bands and respective bands of $B^1\Sigma^+$–$A^1\Pi$ and $C^1\Sigma^+$–$A^1\Pi$ [16] systems. Original formulas for this method were described by Jenkins and McKellar [28] and for our purpose should be a little modified as it was described

previously [21]. Results of these calculations by least-squares procedure are presented in Table IX. One can see that because in this method all effects connected with $A^1\Pi$ and other perturbing states were eliminated from the calculations, the calculated constants are of better accuracy. Therefore, from the differences of the rotational constants

Table IX

Constants for the $E^1\Pi$ state relative to $C^1\Sigma^+$ and $B^1\Sigma^+$ states calculated from Jenkins and McKellar method [cm^{-1}]

	Combination of the E–A and C–A transitions	Combination of the E–A and B–A transitions
$c^{EX}_{00(e)}$ [a]	1012.5418(80)	6014.6984(40)
$c^{EX}_{00(f)}$	1012.5618(46)	6014.708(10)
$B^E_{0(e)} - B^X_0$	0.019168(56)	0.015206(48)
$B^E_{0(f)} - B^X_0$	0.00846(12)	0.00414(16)
$D^E_{0(e)} - D^X_0$	$2.8(14) \cdot 10^{-7}$	$-6.3(12) \cdot 10^{-8}$
$D^E_{0(f)} - D^X_0$	$3.2(20) \cdot 10^{-7}$	$-8.2(44) \cdot 10^{-7}$

[a] X denotes $C^1\Sigma^+$ state for the values in the first column and $B^1\Sigma^+$ state for the second column, respectively

calculated by the Jenkins and McKellar method and from rotational constants of the $B^1\Sigma^+$ state, the constants B_0, D_0, q_0 and q_0^D were recalculated for the $E^1\Pi$ state. The results are listed in the second column of Table VII.

D. Partial analysis of perturbations of the $A^1\Pi$ state by $e^3\Sigma^-$

Of many observed perturbations in $A^1\Pi$ state the perturbation of the $v=0$ level by $v=1$ level in $e^3\Sigma^-$ is classified as the strongest and very extensive. The possibility of identification of a considerable number of the pairs of line and "extra line", observed in all three branches has given the opportunity for the analysis of the perturbing state. The $F_1(J)$ component of the $e^3\Sigma^-$ state perturbs the $Q(J)$ branch of the $B^1\Sigma^+$–$A^1\Pi$ transition and $F_2(J)$ and $F_3(J)$ components of the $e^3\Sigma^-$ state perturb the $P(J)$ and $R(J)$ branches.

The analysis and the calculations of constants are performed by the method of $f_x(J)$ and $g_x(J)$ functions described by Kovács [27]. For the calculations which are performed for the low rotational quantum number J, the following simplified formulas for the respective components of the $e^3\Sigma^-$ state were used [28]:

$$\begin{aligned} F_1(J) &= B_v J(J-1) - \lambda, \\ F_2(J) &= B_v J(J+1), \\ F_3(J) &= B_v (J+1)(J+2) - \lambda, \end{aligned} \tag{3}$$

where λ is the coefficient of the spin–spin interaction.

According to the simple relations which for the $^3\Sigma^- - ^1\Pi$ perturbations were described earlier [29] and by using the above calculated B_0^A and c_{00}^{BA} values the following constants of the $e^3\Sigma^-$ were computed:

$$B_1^e = 1.1962(6)\,\mathrm{cm}^{-1},$$

$$c_{01}^{Be} = 22128.206(42)\,\mathrm{cm}^{-1},$$

$$\lambda^e = 0.55\,\mathrm{cm}^{-1},$$

where c_{01}^{Be} is reduced band origin for the yet unobserved $B^1\Sigma^+ - e^3\Sigma^-$ transition.

Table X shows the present and earlier results computed by this method for the $^{12}C^{16}O$, $^{13}C^{16}O$ and $^{12}C^{18}O$ isotopic molecules.

Table X

Molecular constants of the $e^3\Sigma^-$ state derived from analysis of perturbations [cm^{-1}]

	$^{12}C^{18}O$	$^{13}C^{16}O$	$^{12}C^{16}O$
B_1^e	1.1962(6)[a] 1.1955(6)[b]	1.2032(5)[b]	1.2582(3)[b]
c_{01}^{Be}	22 128.206(42)[a]	22 125.51(36)[b]	22 113.34(1)[b]
λ^e	0.55[a]	1.05(8)[c] 0.94(19)[b]	0.84[d]

[a] Present results
[b] Rytel and Siwiec results [29]
[c] R. Kępa (unpublished)
[d] Herzberg et al results [30, 31]

References

1. K. P. Huber and G. Herzberg, Constants of Diatomic Molecules, Van Nostrand, New York, 1979.
2. A. H. M. Ross, R. S. Eng and H. Kildal, Opt. Commun., *12*, 433, 1974.
3. D. W. Chen, K. Narahari Rao and R. S. McDowell, J. Mol. Spectrosc., *61*, 71, 1976.
4. T. R. Todd, C. M. Clayton, W. B. Telfair, T. K. McCubbin and J. Pliva, J. Mol. Spectrosc., *62*, 201, 1976.
5. R. M. Dale, M. Herman, J. W. C. Johns, A. R. McKellar, S. Nagler and I. K. M. Strathy, Can. J. Phys., *57*, 677, 1979.
6. G. Guelachvili, J. Mol. Spectrosc., *75*, 251, 1979.
7. J. Domin, Acta Phys. Hung., *60*, 63, 1986.
8. A. C. Vikis, J. Chem. Phys., *69*, 697, 1978.
9. K. E. McCulloh and G. Glockler, Phys. Rev., *89*, 145, 1953.
10. M. Rytel, Acta Phys. Polon., *A37*, 559, 1970.
11. M. Rytel, Acta Phys. Polon., *A38*, 299, 1970.
12. Z. Malak, M. Rytel, J. D. Janjić and D. S. Pešić, Acta Phys. Hung., *55*, 85, 1984.
13. J. Domin, U. Domin, Z. Malak and M. Rytel, Acta Phys. Hung., *55*, 165, 1984.
14. J. Janjić, J. Danielak, R. Kępa and M. Rytel, Acta Phys. Polon., *A41*, 757, 1972.
15. S. G. Tilford and J. T. Vanderslice, J. Mol. Spectrosc., *26*, 419, 1968.

16. J. D. Janjić, Lj. U. Čonkić, D. S. Pešić, R. Kępa and M. Rytel, J. Mol. Spectrosc., *72*, 297, 1978.
17. R. Kępa, Acta Phys. Hung., *45*, 133, 1978.
18. R. Kępa, Acta Phys. Polon., *A62*, 467, 1982.
19. R. Kępa, to be published.
20. R. Kępa, M. Rytel and Z. Rzeszut, Acta Phys. Polon., *A54*, 355, 1978.
21. R. Kępa and Z. Rzeszut, Acta Phys. Hung., *50*, 237, 1981.
22. J. D. Simmons and S. G. Tilford, J. Chem. Phys., *45*, 2965, 1966.
23. J. D. Simmons and S. G. Tilford, J. Res. Nat. Bur. Stand. (U.S.), *75A*, 455, 1971.
24. T. Siwiec-Rytel, J. Mol. Spectrosc., *97*, 234, 1983.
25. T. Rytel and M. Rytel, Acta Phys. Hung., *55*, 69, 1984.
26. A. Giacchetti, J. Opt. Soc. Am., *60*, 474, 1970.
27. I. Kovács, Rotational Structure in the Spectra of Diatomic Molecules, Akadémiai Kiadó, Budapest and A. Hilger, London, 1969.
28. G. Herzberg, Spectra of Diatomic Molecules, Van Nostrand, Princeton, 1950.
29. M. Rytel and T. Siwiec, Acta Phys. Polon., *A44*, 67, 1973.
30. G. Herzberg and T. J. Hugo, Can. J. Phys., *33*, 757, 1955.
31. R. W. Field and H. Lefèbre-Brion, Acta Phys. Hung., *35*, 51, 1974.

Acta Physica Hungarica 60 (3—4), pp. 239—243 (1986)

EXTENSION OF THE CALLEN POSTULATE SYSTEM TO INCORPORATE THE NEGATIVE ABSOLUTE TEMPERATURE DOMAIN

K. MARTINÁS

Department for Low Temperature Physics
Roland Eötvös University, Budapest, Hungary

(Received 7 January 1985)

In this paper the necessary and sufficient additions are proposed to extend the validity of the postulate system proposed by Callen to thermodynamic systems with negative absolute temperatures.

1. Introduction

In 1956 Ramsey [1] showed that the experimental behaviour of certain systems under certain conditions corresponded to negative temperatures on the Kelvin scale. The possibility of negative absolute temperatures results in different difficulties in the different constructions of classical thermodynamics.

The negative absolute temperatures are impossible by the Planck–Poincaré statement of the second law.

The constructive thermodynamics, developed by Carathéodory [2] and Ehrenfest-Afanassjewa [3], Fényes [4], Gyarmati [5] and Kirschner [6, 7] can be made consistent with the negative Kelvin temperatures.

The axiomatic treatment of classical thermodynamics in the form proposed by Callen [8] is not applicable, as Callen's Postulate III says: "The entropy ... is a monotonically increasing function of the energy", i.e. the positivity of the temperature is postulated.

Our aim is to look for the necessary and sufficient alterations and additions to the postulate system proposed by Callen to extend its validity to thermodynamic systems with the possibility of equilibrium negative absolute temperature states.

In case of systems with positive absolute temperatures, the following postulate system yields the unique entropy function [9]:

Postulate I; There exist particular states (called equilibrium states) of simple systems that, macroscopically, are characterized completely by the internal energy U, the volume V, and the mole numbers $N_1, N_2, \ldots N_r$ of chemical components (extensive parameters).

Postulate II: There exists a function (called the entropy S) of the extensive parameters of any composite system, defined for all equilibrium states and having the

following property. The values assumed by the extensive parameters in the absence of an internal constraint are those that maximize the entropy over the manifold of constrained equilibrium states.

Postulate III: The entropy of a composite system is additive over the constituent subsystems. The entropy is continuous and differentiable and is a monotonically increasing function of the energy.

Postulate IV: The entropy of any system vanishes in the state for which

$$\frac{\partial U}{\partial S} = 0 ,$$

(that is, at the zero of temperature).

Postulate V:

$$\lim_{U/V \to \infty} \frac{\partial S}{\partial U} = 0 .$$

The Callen postulate system in the above form cannot be used in case of limited energy density systems, as Postulate V has no meaning; and Postulate III leads to contradictions in case of negative absolute temperature.

In the following the systems of limited energy density are called special thermodynamic systems, systems with unlimited energy density are called normal systems.

2. Special thermodynamic systems

Special systems are necessarily systems whose elements may assume only a finite number of discrete energy levels. Such systems can be realised only as parts of normal systems. To discuss the properties of special systems some definitions are needed.

3. Coextensive thermodynamic system

When the properties of a thermodynamic system may be divided into independent groups in such a way that the value of a property belonging to a certain group may be independent of the values of the properties belonging to the remaining groups, each independent group may be considered to define a distinct system. The manifold of these distinct systems is called coextensive thermodynamic system (CTS) [10].

Such a distinction between the subsystems of the total thermodynamic system is possible in the time interval smaller than the relaxation time between the subsystems, so the necessary condition of the existence of CTS is

$$\tau_i \gg \tau_s ,$$

where τ_i is the relaxation time between the subsystems, and τ_s is the relaxation time within a subsystem.

Nuclear-spin systems are examples of such division. The spin system in pure lithium fluoride is well isolated from the lattice system, as the ratio of spin–lattice to spin–spin relaxation times is large, the spin–lattice relaxation times are as large as 5 min at room temperature whereas the spin–spin relaxation time is less than 10^{-5} s [11]. Lasers and masers are examples of special systems, too, because of the limited number of discrete energy levels.

The introduction of coextensive thermodynamic systems gave the possibility to define the equilibrium state of the special systems in a time interval smaller than the relaxation time between the subsystems, when the interaction between the special system and the other subsystems of the total system is negligible. Because of the above restrictions the Callen postulates can be applied to the special systems in the following form:

Postulate I′: There exist particular states (called equilibrium states) of special systems that, macroscopically, are characterized completely by the internal energy U, the volume V, and the mole numbers $N_1, N_2, \ldots N_r$ of chemical components (extensive parameters).

Postulate II′: There exists a function (called the potential function P) of the extensive parameters of the special system, defined for all equilibrium states and having the following property. The values assumed by the extensive parameters in the absence of an internal constraint are those that maximize the potential function P over the manifold of constrained equilibrium states.

Postulate III′: The potential function P of a special system is additive over the constituent subsystems. P is continuous and differentiable function of the energy.

Postulate IV′: The entropy of any system vanishes in the state for which

$$\frac{\partial U}{\partial P} = 0 .$$

(that is at the zero of temperature).

Here we used the word ekaentropies instead of entropy as the postulate system in the above form does not define a unique entropy function, but a function family which contains the entropy, too.

The ekaentropies defined by the above postulate system can be written in the following form:

$$P = P(X_1, X_2, \ldots X_n) = \sum_i^n \Gamma_i X_i = \sum_i^{n-1} \int \Gamma_i \rho_i d^3 r = \int p d^3 r ,$$

where Γ_i is the i^{th} generalized intensive parameter. Because of the properties of equilibrium state, these generalised intensive parameters can be written as the

functions of entropic intensive parameters Y_i, $Y_i = \partial S/\partial X_i$,

$$\Gamma_i = \Gamma_i(Y_1, Y_2, \ldots Y_{n-1})$$

and

$$\det \Gamma_{ik} = \det - \frac{\partial \Gamma_i}{\partial Y_k} \geq 0$$

with the above notations the ekaentropies defined by the postulate system are as follows:

$$p = \sum_{ikl} \int\int \Gamma_{ik} s_{k1} \, d\rho_i \, d\rho_l + \sum_i \int \Gamma_{i0} \, d\rho_i + p_0 \,,$$

where the value of p_0 is fixed by Postulate IV, and

$$S_{ke} = \frac{\partial^2 S}{\partial \rho_i \, \partial \rho_k} \,.$$

The Callen postulate system in this form does not yield unique entropy function in case of special systems, as Γ_{ik} and Γ_{i0} are not defined.

Nevertheless, if we postulate the existence of the total equilibrium state of coextensive thermodynamic systems consisting of special systems and normal ones, then Postulate III yields that $\Gamma_{ik} = \rho_{ik}$, and it fixes the values of Γ_{i0}, too, [9] i.e. the possibility of the equilibrium between the normal systems and special ones ensures the unique entropy function of the special systems, if it is uniquely defined for normal systems.

The Postulate system in the following form defines unique entropy function.

4. The extended Callen postulate system

Postulate I:* The total equilibrium state of the coextensive thermodynamic systems is the equilibrium state of the composite system consisting of the subsystems of the coextensive thermodynamic systems.

Postulate I: There exist particular states (called equilibrium states) of simple systems that, macroscopically, are characterized completely by the internal energy U, the volume V, and the mole numbers $N_1, N_2, \ldots N_r$ of chemical components (extensive parameters).

Postulate II: There exists a function (called the entropy S) of the extensive parameters of any composite system, defined for all equilibrium states and having the following property. The values assumed by the extensive parameters in the absence of an internal constraint are those that maximize the entropy over the manifold of constrained equilibrium states.

Postulate III: The entropy of a composite system is additive over the constituent subsystems. The entropy is continuous and differentiable function of the extensive

parameters. In case of normal systems the entropy is a monotonically increasing function of the energy.

Postulate IV: The entropy of any system vanishes in the state for which

$$\frac{\partial U}{\partial S} = 0 .$$

Postulate V: In case of normal systems

$$\lim_{U/V \to \infty} \frac{\partial S}{\partial U} = 0 .$$

Acknowledgments

I thank Professor I. Kirschner and Dr. T. Geszti for valuable suggestions and helpful discussions.

References

1. N. F. Ramsey, Phys. Rev., *103*, 20, 1956.
2. C. Carathéodory, Math. Ann., *67*, 355, 1908.
3. T. Ehrenfest–Afanassjewa, Z. Phys., *33*, 933, 1925.
4. I. Fényes, Z. Phys. *134*, 95, 1952.
5. I. Gyarmati, Acta Chem. Hung., *80*, 147, 1962.
6. I. Kirschner, Acta Phys. Hung., *29*, 209, 1970.
7. I. Kirschner, Acta Phys. Hung., *30*, 61, 1971.
8. H. B. Callen, Thermodynamics, John Wiley, N. Y., 1960.
9. K. Martinás, Acta Phys. Hung., *50*, 121, 1981.
10. G. N. Hatsopoulos and J. H. Keenan, Principles of General Thermodynamics, John Wiley, N. Y., p. 375, 1965.
11. E. M. Purcell and R. V. Pound, Phys. Rev., *81*, 279, 1951.

Acta Physica Hungarica 60 (3—4), pp. 245—260 (1986)

THERMODYNAMICAL DERIVATION OF EQUATIONS OF MOTION FOR MULTICOMPONENT FLUIDS

B. NYÍRI

Institute of Physics, Technical University of Budapest
1521 Budapest, Hungary

(Received 10 January 1985)

In this work the thermodynamics of multicomponent fluids is treated, based on the mechanics of superposed continua. Balances of diffusion's momentum and energy are derived, and possible definitions and balances of internal energy are discussed. An entropy function is given, where the diffusion currents are the dynamic variables, thus the balances of the latter come from mechanical considerations. Constitutive equations of the components' pressure tensor and friction, and of heat conduction are derived, applying the local form of the Gyarmati Principle. The equivalence of Newton's Third Law and Onsager's Reciprocity Relations is shown for diffusion. The equations of motion lead to a system of telegraphist's equations, if viscosities are neglected. The results are compared with those of the "Wave Approach of Thermodynamics", and with the Theory of Dynamic Variables.

Introduction

It is an interesting problem of the non-equilibrium thermodynamics that the classical constitutive equations of diffusion give an infinite propagation velocity. Hence comes the question: what reasonable assumptions should be made—within the framework of the non-equilibrium thermodynamics—to get rid of this disturbing deficiency of the old theory.

The first systematic answer to this question was Gyarmati's "Wave Approach of Thermodynamics", introducing general inductivities through an extended entropy function, depending—beyond its classical variables—also on the current densities of transport processes [1, 2, 3, 4].

The systems to be described in this way are out of the local equilibrium. The general description of such systems can be carried out by the application of dynamic (or internal) variables, introduced more systematically by Verhás, who derived also balance equations for the dynamic variables [5, 6, 7].

Since in the "Wave Approach" the dynamic variables for diffusion are the current densities of the components, the existence of such balance equations involves the surprising fact that there must be a transport of currents, i.e. a "transport of transport".

It will be shown that both a finite propagation velocity, and the existence of the transport of currents (current of current) can be derived for diffusion, from a rather simple physical picture, by using the methods of classical theory.

In Section 1 we deal with the balance equations of masses, momenta and energies.

In Section 2 the entropy function and the entropy balance are discussed for the present case.

In Section 3 the constitutive equations are derived by the help of the local form of the Principle of Non-Equilibrium Thermodynamics, and the equivalence of Newton's third law and Onsager's reciprocity relations is discussed.

In Section 4 the equations of motion are presented. The analogue of the diffusion equations of the "Wave Approach" is derived as a special case, and semi-hyperbolic equations are obtained by linearisation.

In Section 5 the results are discussed and compared with the Wave Approach, and with the Theory of Dynamic Variables.

1. Balance equations

1.1 Balances of mass

The balance of the total mass reads [8, 9, 10]

$$\frac{\partial \rho}{\partial t} + \operatorname{div}(\rho \mathbf{v}) = 0, \tag{1.1}$$

where ρ is the density, and $\mathbf{v}$ is the velocity.

In a multicomponent, non-reacting system, the balance of a component's mass is [8, 9, 10]

$$\frac{\partial \rho_i}{\partial t} + \operatorname{div}(\rho_i \mathbf{v}_i) = 0, \qquad i = 1, 2, \ldots, n. \tag{1.2}$$

Here ρ_i stands for the mass density of the i-th component, and $\mathbf{v}_i$ is its velocity.

Since

$$\sum_{i=1}^{n} \rho_i = \rho \tag{1.3}$$

is valid, it follows that

$$\rho \mathbf{v} = \sum_i \rho_i \mathbf{v}_i. \tag{1.4}$$

Now, the diffusion velocities are defined [8, 9, 10] as

$$\mathbf{w}_i = \mathbf{v}_i - \mathbf{v}, \tag{1.5}$$

the diffusion currents as

$$\mathbf{J}_i = \rho_i \mathbf{w}_i, \tag{1.6}$$

the mass fractions as

$$c_i = \frac{\rho_i}{\rho} \tag{1.7}$$

and the specific diffusion currents as

$$\mathbf{j}_i = c_i \mathbf{w}_i \,. \tag{1.8}$$

Because of the above equations

$$\sum_i \mathbf{j}_i = 0 \tag{1.9}$$

does hold. Finally, the substantial mass balance of a component reads

$$\rho \frac{dc_i}{dt} + \operatorname{div} \mathbf{J}_i = 0 \,, \tag{1.10}$$

with the derivative taken in a baricentric frame.

1.2 Balances of momentum

Chauchy's equation of motion

$$\rho \frac{d\mathbf{v}}{dt} + \operatorname{Div} \boldsymbol{P}^c = \rho \mathbf{F} \tag{1.11}$$

is usually regarded as a momentum balance [8, 9]. Here the $\boldsymbol{P}^c$ pressure tensor is the negative of the Chauchy stress tensor, and $\mathbf{F}$ is the specific body force. We consider Chauchy's equation separately valid for each component continuum [8, 9, 11]

$$\rho_i \frac{d^{(i)}}{dt} \mathbf{v}_i + \operatorname{Div} \boldsymbol{P}_i = \rho_i \mathbf{F}_i^* + \rho_i \mathbf{F}_i \,. \tag{1.12}$$

The $\dfrac{d^{(i)}}{dt}$ time derivative is taken in a point travelling together with the component considered, i.e.

$$\frac{d^{(i)}}{dt} = \frac{d}{dt} + (\mathbf{w}_i \operatorname{grad}). \tag{1.13}$$

In (1.12) $\boldsymbol{P}_i$ is the pressure tensor of the i-th constituent, and the body force is split into an $\mathbf{F}_i$ external and an $\mathbf{F}_i^*$ internal part. Since $\rho_i \mathbf{F}_i^*$ are internal forces

$$\sum_i \rho_i \mathbf{F}_i^* = 0. \tag{1.14}$$

The consistency of (1.11) and (1.12) requires, according to Truesdell [11, 8], that

$$\boldsymbol{P} = \sum_i [\boldsymbol{P}_i + \rho_i(\mathbf{w}_i \circ \mathbf{w}_i)] \tag{1.15}$$

and

$$\rho \mathbf{F} = \sum_i \rho_i \mathbf{F}_i. \tag{1.16}$$

The symbol "$\circ$" stands for the diadic product of vectors.

For the sake of convenience, we define a $\boldsymbol{P}$ pressure tensor by

$$\boldsymbol{P} = \sum_i \boldsymbol{P}_i. \tag{1.17}$$

Let us transform (1.12) into a substantial balance with the help of the identities

$$\rho \frac{d}{dt}(c_i \mathbf{v}_i) = \rho_i \frac{d}{dt}\mathbf{v}_i + \mathbf{v}_i \rho \frac{dc_i}{dt},$$

$$\operatorname{Div}[\rho_i(\mathbf{v}_i \circ \mathbf{w}_i)] = \rho_i(\mathbf{w}_i \operatorname{grad})\mathbf{v}_i + \mathbf{v}_i \operatorname{div}(\rho_i \mathbf{w}_i).$$

Making use of (1.10) and (1.13) the substantial balance of a component's momentum reads

$$\rho \frac{d}{dt}(c_i \mathbf{v}_i) + \operatorname{Div}[\boldsymbol{P}_i + \rho_i(\mathbf{v}_i \circ \mathbf{w}_i)] = \rho_i \mathbf{F}_i^* + \rho_i \mathbf{F}_i. \tag{1.18}$$

This equation shows that the diffusion plays role in the transport of momentum.

According to (1.5) and (1.8) it is seen that the quantity $\mathbf{j}_i$ can be regarded as the specific momentum of diffusion. Introducing it into (1.18) we arrive at the balances of diffusion's momentum

$$\rho \frac{d}{dt}\mathbf{j}_i + \operatorname{Div}[\boldsymbol{P}_i + \rho_i(\mathbf{w}_i \circ \mathbf{w}_i)] =$$

$$= \rho_i \mathbf{F}_i^* + \rho_i \mathbf{F}_i - \rho_i \frac{d\mathbf{v}}{dt} - \rho(\mathbf{j}_i \operatorname{grad})\mathbf{v}. \tag{1.19}$$

The third term on the r.h.s. is a gravitational force due to the acceleration of the frame of reference, and the last term is also an inertial force arising from the inhomogeneity of the velocity field.

1.3 Energy balances

Since the balance equation of the total energy

$$\rho \frac{d\varepsilon}{dt} + \operatorname{div} \mathbf{J}_\varepsilon = 0 \tag{1.20}$$

[8] is rather formal, the specific energy ε is split into three parts

$$\varepsilon = \varepsilon_k + \varphi + u^*. \tag{1.21}$$

The sum of the kinetic energies of the components is denoted by ε_k, and φ is the specific potential energy. The remaining part, u^*, will be referred to as thermic energy.

Let us examine the

$$\varepsilon_k = \sum_i \frac{1}{2} c_i v_i^2 \tag{1.22}$$

total kinetic energy. Applying (1.5) and (1.9), it is seen that [8, 10]

$$\varepsilon_k = \frac{1}{2} v^2 + \sum_i \frac{1}{2} c_i w_i^2. \tag{1.23}$$

The first term is the usual expression of the translational kinetic energy ε_t, and the second is the kinetic energy ε_d of diffusion [8, 10]. Regarding the usual

$$\varepsilon = \varepsilon_t + \varphi + u \tag{1.24}$$

definition of the internal energy u [8, 10], it can be seen, that

$$u = u^* + \varepsilon_d. \tag{1.25}$$

For ε is the total energy, and so if the diffusion gives an ε_d contribution to it, then ε_d is necessarily included in the difference of ε and $(\varepsilon_t + \varphi)$. Thus the usual internal energy u, and the u^* suggested by De Groot and Mazur are equal if and only if no diffusion takes place [10]. The choice between these quantities depends possibly on the purpose of the description, i.e. to what details we are interested in the structure of motion, and so what kinds of motions are to be taken into account by their average only.

If we multiply (1.18) by $\mathbf{v}_i$, then after a short calculation, we get the balance of the i-th component's kinetic energy

$$\rho \frac{d}{dt} \varepsilon_{k,i} + \operatorname{div}\left[\boldsymbol{P}_i \mathbf{v}_i + \mathbf{w}_i \left(\frac{1}{2} \rho_i v_i^2 \right) \right] =$$

$$= \rho_i \mathbf{F}_i^* \mathbf{v}_i + \rho_i \mathbf{F}_i \mathbf{v}_i + \boldsymbol{P}_i : \operatorname{Grad} \mathbf{v}_i. \tag{1.26}$$

The colon denotes the internal product of tensors. Summing up the (1.26) balances, we get the balance of total kinetic energy.

$$\rho \frac{d\varepsilon_k}{dt} + \operatorname{div}\left\{ \boldsymbol{P}\mathbf{v} + \sum_i \left[\boldsymbol{P}_i \mathbf{w}_i + \rho_i (\mathbf{w}_i \circ \mathbf{w}_i) \mathbf{v}_i + \mathbf{w}_i \left(\frac{1}{2} \rho_i \mathbf{w}_i^2 \right) \right] \right\} =$$

$$= \rho \mathbf{F} \mathbf{v} + \boldsymbol{P} : \operatorname{Grad} \mathbf{v} + \sum_i \left[\rho_i \mathbf{F}_i^* \mathbf{w}_i + \rho_i (\mathbf{F}_i - \mathbf{F}) \mathbf{w}_i + \boldsymbol{P}_i : \operatorname{Grad} \mathbf{w}_i \right]. \tag{1.27}$$

This detailed equation clearly illustrates the physical structure of the kinetic energy current and source.

The balance of the translational energy reads [8]

$$\rho \frac{d\varepsilon_t}{dt} + \operatorname{div}\left[\boldsymbol{P}\mathbf{v} + \sum_i \rho_i (\mathbf{w}_i \circ \mathbf{w}_i)\mathbf{v} \right] =$$

$$= \rho \mathbf{F}\mathbf{v} + \boldsymbol{P} : \operatorname{Grad} \mathbf{v} + \sum_i \rho_i (\mathbf{w}_i \circ \mathbf{w}_i) : \operatorname{Grad} \mathbf{v}. \tag{1.28}$$

Subtracting this equation from (1.27), the balance of diffusional energy is obtained

$$\rho \frac{d\varepsilon_d}{dt} + \operatorname{div}\left\{ \sum_i \left[\boldsymbol{P}_i \mathbf{w}_i + \mathbf{w}_i \left(\frac{1}{2} \rho_i \mathbf{w}_i^2 \right) \right] \right\} =$$

$$= \sum_i [\rho_i \mathbf{F}_i^* \mathbf{w}_i + \rho_i \mathbf{F}_i^{\mathrm{exc}} \mathbf{w}_i + \boldsymbol{P}_i : \operatorname{Grad} \mathbf{w}_i - \rho_i (\mathbf{w}_i \circ \mathbf{w}_i) : \operatorname{Grad} \mathbf{v}]. \tag{1.29}$$

Here $\mathbf{F}_i^{\mathrm{exc}} = \mathbf{F}_i - \mathbf{F}$, it is the excess external force acting on the i-th component, which is zero only in the case of gravitation. The last terms of (1.28) and (1.29) describe an energy exchange between the average flow and diffusion. It is stressed that though ε_d appears as a part of internal energy, it is regarded an inherently reversible energy exchange. Its presence is caused by splitting the motion into translation and diffusion. We mention that (1.29) can be obtained also from (1.19), first constructing the balance of each component's diffusional energy, and then summing them up.

The next term to be discussed in (1.21) is the potential energy. Consistently with the view of superposed continua, we assume that each component has a potential energy φ_i, exactly [8]

$$\mathbf{F}_i = -\operatorname{grad} \varphi_i. \tag{1.30}$$

Let us restrict our examination to static field, so

$$\frac{\partial \varphi_i}{\partial t} = 0. \tag{1.31}$$

The total specific potential energy is

$$\varphi = \sum_i c_i \varphi_i, \tag{1.32}$$

thus

$$\rho \frac{d\varphi}{dt} = \sum_i \left[\varphi_i \rho \frac{dc_i}{dt} + \rho_i (\mathbf{v} \operatorname{grad}) \varphi_i \right].$$

After substituting from (1.10), a short calculation leads to the balance of potential energy

$$\rho \frac{d\varphi}{dt} + \operatorname{div}\left\{ \sum_i \rho_i \varphi_i \mathbf{w}_i \right\} = -\sum_i \rho_i \mathbf{F}_i^{\mathrm{exc}} \mathbf{w}_i - \rho \mathbf{F}\mathbf{v}. \tag{1.33}$$

Last, but not least, let us consider the thermic and the internal energy. With regard to the above energy balances, their balance equations in the present case read

$$\rho \frac{du^*}{dt} + \operatorname{div} \mathbf{J}_* = \sigma_{u^*}, \tag{1.34}$$

$$\rho \frac{du}{dt} + \operatorname{div} \mathbf{J}_q = \sigma_u, \tag{1.35}$$

with

$$\sigma_{u^*} = -\sum_i (\rho_i \mathbf{F}_i^* \mathbf{w}_i + \boldsymbol{P}_i : \operatorname{Grad} \mathbf{w}_i) - \boldsymbol{P} : \operatorname{Grad} \mathbf{v}, \tag{1.36}$$

$$\sigma_u = \sum_i \rho_i \mathbf{F}_i^{\mathrm{exc}} \mathbf{w}_i - \boldsymbol{P} : \operatorname{Grad} \mathbf{v} - \sum_i \rho_i (\mathbf{w}_i \circ \mathbf{w}_i) : \operatorname{Grad} \mathbf{v}, \tag{1.37}$$

$$\mathbf{J}_q = \mathbf{J}_* + \sum_i \left[\boldsymbol{P} \mathbf{w}_i + \mathbf{w}_i \left(\frac{1}{2} \rho_i w_i^2 \right) \right]. \tag{1.38}$$

Examining the last three equations it appears that, though σ_u and $\mathbf{J}_q$ are defined as heat source and heat current [8], the quantities σ_{u^*} and $\mathbf{J}_*$ stand much nearer to our physical picture of these. We have the firm conviction that u^* is also much more useful than u in the description of these processes. Nevertheless, the central role of the internal energy might be preserved, if its structure, or inner dynamism is taken into account somehow. This is what pushes the Theory of Dynamic Variables into prominence.

2. The entropy

2.1 The entropy function

The entropy of a multicomponent system usually depends on the internal energy, on the concentrations, on the mass density, and, if it is not in the state of local equilibrium, then—according to Verhás—also on some kind of ξ_i dynamic variables [5]

$$s = s(u, \rho, c_1, \ldots, c_n, \xi_1, \ldots, \xi_n). \tag{2.1}$$

In this work we suppose, that the entropy depends on the thermic energy, on the density, and on the concentrations so, as if the system would be in equilibrium

$$s = s(u^*, \rho, c_1, \ldots, c_n). \tag{2.2}_1$$

This hypothesis is consistent with (2.1), being a special case of that one. For (2.2) is equivalent to

$$s = s\left(u - \sum_i \frac{1}{2c_i} j_i^2, \rho, c_1, \ldots, c_n \right). \tag{2.2}_2$$

Comparing this with (2.1)

$$\xi_i = \mathbf{j}_i \tag{2.3}$$

is evident. By consequence, with hypothesis (2.2) we have specified the dynamic variables for a case of diffusion, and have given the dependence of the entropy on them.

Moreover, the balances of these dynamical variables are also at hand. They are the (1.19) momentum balances. Comparing (1.19) to the phenomenological balance given by Verhás [5]

$$\rho \frac{d}{dt} \xi_i + \operatorname{Div} \boldsymbol{J}_{\xi_i} = \boldsymbol{\sigma}_{\xi_i}, \tag{2.4}$$

it is seen that

$$\boldsymbol{J}_{\xi_i} = \boldsymbol{P}_i + \rho(\xi_i \circ \mathbf{w}_i),$$

$$\boldsymbol{\sigma}_{\xi_i} = \rho_i \left(\mathbf{F}_i^* + \mathbf{F}_i - \frac{dv}{dt} \right) - \rho(\xi_i \operatorname{grad}) \mathbf{v} \tag{2.5}$$

according to our hypothesis.

2.2 The entropy production

We shall need the σ entropy production for the derivation of the constitutive equations, so let us first calculate the substantial time derivative of the entropy (2.1). Using the corresponding balances it reads

$$\rho \frac{ds}{dt} = \frac{1}{T}(\sigma_u - \operatorname{div} \boldsymbol{J}_q) - \sum_i \frac{\partial s}{\partial c_i} \operatorname{div} \boldsymbol{J}_i -$$

$$- \rho^2 \frac{\partial s}{\partial \rho} \operatorname{div} \mathbf{v} - \sum_i \frac{\partial s}{\partial \xi_i} (\boldsymbol{\sigma}_{\xi_i} - \operatorname{Div} \boldsymbol{J}_{\xi_i}).$$

By a simple transformation and rearrengement we get the entropy balance [5]

$$\rho \frac{ds}{dt} + \operatorname{div} \left[\frac{1}{T} \mathbf{J}_q + \sum_i \left(\frac{\partial s}{\partial c_i} \mathbf{J}_i + \frac{\partial s}{\partial \xi_i} \boldsymbol{J}_{\xi_i} \right) \right] =$$

$$= \mathbf{J}_q \operatorname{grad} \frac{1}{T} + \frac{1}{T} \sigma_u - \rho^2 \frac{\partial s}{\partial \rho} \operatorname{div} \mathbf{v} +$$

$$+ \sum_i \left[\mathbf{J}_i \operatorname{grad} \frac{\partial s}{\partial c_i} + \boldsymbol{J}_{\xi_i} : \operatorname{Grad} \frac{\partial s}{\partial \xi_i} + \frac{\partial s}{\partial \xi_i} \boldsymbol{\sigma}_{\xi_i} \right]. \tag{2.6}$$

The expression in the divergence is the entropy current, and the r.h.s. is the entropy production. The derivatives of entropy (2.2) are the following [8, 10]

$$\left(\frac{\partial s}{\partial c_i}\right)_u = \left(\frac{\partial s}{\partial c_i}\right)_{u^*} + \left(\frac{\partial s}{\partial u^*}\right)_c \left(\frac{\partial u^*}{\partial c_i}\right)_u = \frac{1}{T}\left(\frac{1}{2} w_i^2 - \mu_i\right), \tag{2.7}$$

$$-\rho^2 \frac{\partial s}{\partial \rho} = \frac{\partial s}{\partial \rho^{-1}} = \frac{1}{T} p^e, \tag{2.8}$$

$$\frac{\partial s}{\partial \xi_i} = -\frac{1}{c_i T}\xi_i = -\frac{1}{T}\mathbf{w}_i. \tag{2.9}$$

Here the μ_i-s are the chemical potentials, p^e is the equilibrium pressure, and T is the absolute temperature. The entropy production, after substituting from (1.6), (1.37), (2.5), (2.3), reads

$$\sigma = \mathbf{J}_q \operatorname{grad}\frac{1}{T} + \frac{1}{T}\left[\sum_i \rho_i \mathbf{F}_i \mathbf{w}_i - \boldsymbol{P}\colon \operatorname{Grad}\mathbf{v} - \sum_i \rho_i (\mathbf{w}_i \circ \mathbf{w}_i)\colon \operatorname{Grad}\mathbf{v}\right] +$$

$$+ \frac{p^e}{T}\operatorname{div}\mathbf{v} + \sum_i \left\{\rho_i \mathbf{w}_i \operatorname{grad}\left(\frac{\mathbf{w}_i^2}{2T} - \frac{\mu_i}{T}\right) - \left[\boldsymbol{P}_i\colon \operatorname{Grad}\left(\frac{\mathbf{w}_i}{T}\right) + \rho_i(\mathbf{w}_i \circ \mathbf{w}_i)\colon \operatorname{Grad}\left(\frac{\mathbf{w}_i}{T}\right)\right] -$$

$$- \frac{\mathbf{w}_i}{T}\rho_i\left(\mathbf{F}_i^* + \mathbf{F}_i - \frac{d}{dt}\mathbf{v}\right) + \rho_i \frac{\mathbf{w}_i}{T}(\mathbf{w}_i \operatorname{grad})\mathbf{v}\right\}\Bigg\}. \tag{2.10}$$

Then, after a long but elementary calculation

$$\sigma = \left[\mathbf{J}_q - \sum_i \left(\mathbf{P}_i \mathbf{w}_i + \mathbf{w}_i \frac{\rho_i \mathbf{w}_i^2}{2}\right)\right] \operatorname{grad}\frac{1}{T} - \frac{1}{T}\boldsymbol{P}\colon \operatorname{Grad}\mathbf{v} + \frac{p^e}{T}\operatorname{div}\mathbf{v} +$$

$$+ \sum_i \left\{\rho_i \mathbf{w}_i \left[\operatorname{grad}\left(-\frac{\mu_i}{T}\right) - \frac{1}{T}F_i^*\right] - \frac{1}{T}\boldsymbol{P}_i\colon \operatorname{Grad}\mathbf{w}_i\right\}. \tag{2.11}$$

The current in the first bracket is the $\mathbf{J}_*$ current of thermic energy. To separate the isotropic part of stress, let p_i denote the third of the trace of $\boldsymbol{P}_i$, i.e.

$$p_i = \frac{1}{3}\sum_{\alpha=1}^{3}\{\boldsymbol{P}_i\}_{\alpha\alpha}$$

and let

$$p = \sum_i p_i.$$

If—for simplicity's sake—each $\boldsymbol{P}_i$ is assumed to be symmetric, and the symmetric and zero trace part of a tensor is denoted by s and 0 superscripts, then

$$\sigma = \mathbf{J}_* \operatorname{grad}\frac{1}{T} - \frac{1}{T}(p - p^e)\operatorname{div}\mathbf{v} - \frac{1}{T}\boldsymbol{P}^0\colon \operatorname{Grad}\mathbf{v}^{0s} -$$

$$-\sum_i \left\{ \frac{1}{T} \boldsymbol{P}_i^0 : \operatorname{Grad} \mathbf{w}_i^{0s} + \frac{p_i}{T} \operatorname{div} \mathbf{w}_i + \rho_i \mathbf{w}_i \left[\mathbf{F}_i^* + \operatorname{grad} \left(\frac{\mu_i}{T} \right) \right] \right\}. \tag{2.12}$$

This expression can already be used for calculations, yet it is more expedient to consider the $\mathbf{v}_i$ component velocities as variables, since they are independent, in contrary to the $\mathbf{w}_i$. So we apply (1.2), (1.3), (1.4), (1.5), and also

$$\mathbf{w}_i = \mathbf{v}_i - \sum_i c_k \mathbf{v}_k = \sum_k c_k (\mathbf{v}_i - \mathbf{v}_k)$$

and using the notation

$$\mathbf{Y}_i = \frac{1}{T} \rho_i \mathbf{F}_i^* + \rho_i \operatorname{grad} \left(\frac{\mu_i}{T} \right) - \frac{p^e}{T} \operatorname{grad} c_i, \tag{2.13}$$

the last term of (2.12) reads

$$\sum_{i,k} (\mathbf{v}_i - \mathbf{v}_k) c_k \mathbf{Y}_i = \sum_{i,k} \mathbf{v}_i (c_k \mathbf{Y}_i - c_i \mathbf{Y}_k) = \sum_i \mathbf{v}_i (\mathbf{Y}_i - c_i \sum_k \mathbf{Y}_k). \tag{2.14}$$

So, finally

$$\sigma = \mathbf{J}_* \operatorname{grad} \left(\frac{1}{T} \right) - \sum_i \left[\frac{1}{T} \boldsymbol{P}_i^0 : \operatorname{Grad} \mathbf{v}_i^{0s} + \frac{1}{T} (p_i - c_i p^e) \operatorname{div} \mathbf{v}_i + \right.$$

$$\left. + \mathbf{v}_i \left(\frac{1}{T} \rho_i F_i^* + \rho_i \operatorname{grad} \frac{\mu_i}{T} - c_i \sum_k \rho_k \operatorname{grad} \frac{\mu_k}{T} - \frac{p^e}{T} \operatorname{grad} c_i \right) \right] \tag{2.15}$$

is the form of σ we shall use from now on.

We have to emphasize that the p_i component pressures are not identical to the well-known partial pressures. The p_i component pressure is connected, per definitionem, to the transport of the momentum *of the* i-th component, while the partial pressure is connected to the transport of momentum *by the* (molecules of the) i-th component.

The expression (2.15) can be obtained in a much more straightforward way from the $(2.2)_1$ form of the entropy function—i.e. choosing u^* as independent variable, and so applying the corresponding (1.34) balance—,yet it is hoped that the above calculations give a better insight into the nature of the basic hypothesis. For example it shows that such a system is out of the local equilibrium, while the entropy function itself is the equilibrium one.

3. The constitutive equations

Here we are going to derive the constitutive equations, from the (2.15) form of the entropy production, with the help of the Variational Principle of Non-Equilibrium Thermodynamics. The local form of the Gyarmati Principle states [8]

$$\sigma - (\Phi + \Psi) = \max. \tag{3.1}$$

Here Φ and Ψ are positive definite, homogeneous quadratic functions—local dissipation potentials. The Ψ is a function of the α-type, and Φ is a function of the β or rate type variables [8].

We are going to vary with respect to the β-type variables only, that in this case are

$$\begin{aligned} \mathbf{X}_i^t &= \operatorname{Grad} \mathbf{v}_i^{0s}, \qquad & X_i^s &= \operatorname{div} \mathbf{v}, \\ \mathbf{X}_i^v &= \mathbf{v}_i, & \mathbf{X}_q^v &= \mathbf{J}_*. \end{aligned} \tag{3.2}$$

Thus, in the linear isotropic case [8, 10]

$$\Phi = \frac{1}{2} \sum_{i,k} \left(R_{ik}^t \mathbf{X}_i^t \cdot \mathbf{X}_k^t + R_{ik}^s X_i^s X_k^s + R_{ik}^v \mathbf{X}_i^v \mathbf{X}_k^v + 2R_{iq}^v \mathbf{X}_i^v \mathbf{X}_q^v + R_{qq}^v \mathbf{X}_q^{v2} \right). \tag{3.3}$$

Here, of course, $R_{ik} = R_{ki}$ and $R_{iq} = R_{qi}$. The Φ depending on the $\mathbf{v}_i$-s is not automatically Galilei invariant. For this invariance

$$\Phi(\mathbf{v}_1, \mathbf{v}_2, \ldots, \mathbf{v}_n) = \Phi(\mathbf{v}_1 + \mathbf{u}, \mathbf{v}_2 + \mathbf{u}, \ldots, \mathbf{v}_n + \mathbf{u}) \tag{3.4}$$

is necessary, with arbitrary, constant $\mathbf{u}$ vector. This requirement is satisfied only if

$$\sum_i R_{ik}^v = 0, \qquad \sum_i R_{iq}^v = 0. \tag{3.5}$$

For the extremum (3.1)

$$\delta[\sigma - (\Phi + \Psi)]_J = 0 \tag{3.6}$$

is necessary [8]. The variations of $\mathbf{v}_i$, $\mathbf{J}_*$ and of the derivatives of $\mathbf{v}_i$ are independent (locally) and arbitrary, and $\delta\Psi = 0$ automatically, thus (3.6) holds only if the

$$-\left(\frac{1}{T} \rho_i \mathbf{F}_i^* + \rho_i \operatorname{grad} \frac{\mu_i}{T} - c_i \sum_k \rho_k \operatorname{grad} \frac{\mu_k}{T} - \frac{p^e}{T} \operatorname{grad} c_i \right) =$$

$$= \sum_k R_{ik}^v \mathbf{v}_k + R_{iq}^v \mathbf{J}_*, \tag{3.7}$$

$$-\frac{1}{T} \boldsymbol{P}_i^0 = \sum_k R_{ik}^t \operatorname{Grad} \mathbf{v}_k^{0s}, \tag{3.8}$$

$$-\frac{1}{T} (p_i - c_i p^e) = \sum_k R_{ik}^s \operatorname{div} \mathbf{v}_k, \tag{3.9}$$

$$\operatorname{grad} \frac{1}{T} = R_{qq}^v \mathbf{J}_* + \sum_k R_{qk}^v \mathbf{v}_k \tag{3.10}$$

constitutive equations are valid.

To shed more light on the meaning of (3.7), we make use of (3.5) and write

$$-\left(\frac{1}{T}\rho_i \mathbf{F}_i^* + \rho_i \operatorname{grad}\frac{\mu_i}{T} - c_i \sum_k \rho_k \operatorname{grad}\frac{\mu_k}{T} - \frac{p^e}{T}\operatorname{grad} c_i\right) =$$

$$= \sum_k R_{ik}^v(\mathbf{v}_k - \mathbf{v}_i) + R_{iq}^v \mathbf{J}_*. \tag{3.11}$$

The velocity dependent terms on the r.h.s. describe the friction of the components on each other. Thus it is seen that the Onsager Reciprocity Relations for diffusion, together with the requirement of the Galilei invariance, are equivalent to Newton's third law (on action and reaction). The terms on the l.h.s. are also to be interpreted as forces, and—if necessary—they also can be split to parts, representing the pairwise antisymmetric interaction of the components. Such a splitting is that in (2.14), i.e. $(c_k \mathbf{Y}_i - c_i \mathbf{Y}_k)$. It is also seen that the role of the R_{ii}^v diagonal coefficients is secondary. The R_{ik}^v-s are usually called friction, drag, or diffusion coefficients. [9, 12, 13, 14, 20, 21, 22].

The Eqs (3.8) and (3.9) attribute viscosity and second or volume viscosity to each component in the mixture, and show that the momentum of one component can be transported by any of the others.

Equation (3.10) is the usual one for heat conduction in a multicomponent system.

4. The equations of motion

The equations (3.7), (3.8), (3.9) and (3.10), together with the corresponding (1.10), (1.18) and (1.34) balances, can be assumed to be a complete system of differential equations, describing the motion of a multicomponent, non-reacting fluid.

Inserting the pressure tensors and the internal forces from (3.8), (3.9) and (3.7) into the (1.18) balances, we get the equations of motion, which, by making use of (3.10) to substitute $\mathbf{J}_*$, read

$$\rho \frac{d}{dt}(c_i \mathbf{v}_i) = \operatorname{Div}\left\{-\rho_i(\mathbf{v}_i \circ \mathbf{w}_i) + \sum_k [R_{ik}^{t*} \operatorname{Grad} v_k^{Os} + (R_{ik}^{s*} \operatorname{div} v_k - c_i p^e)\boldsymbol{\delta}]\right\} +$$

$$+ \sum_k \left[\left(R_{ik}^{v*} + \frac{R_{iq}^{v*} R_{qk}^v}{R_{qq}^{v*}}\right)(\mathbf{v}_i - \mathbf{v}_k) - \frac{R_{iq}^{v*}}{R_{qq}^{v*}} \operatorname{grad}\left(\frac{1}{T}\right) -\right.$$

$$\left. - T\left(c_k \rho_i \operatorname{grad}\frac{\mu_i}{T} - c_i \rho_k \operatorname{grad}\frac{\mu_k}{T}\right)\right] + p^e \operatorname{grad} c_i + \rho_i \mathbf{F}_i, \tag{4.1}$$

where $R^* = TR$, and $\boldsymbol{\delta}$ is the unit tensor.

Let us examine (4.1) in some special cases. First, we consider an isotherm system, where no heat conduction occurs. Let us neglect the R_{iq}^v thermal diffusion coefficients, and assume the R_{ik}^{s*} and R_{ik}^{t*} viscosities and the R_{ik}^{v*} friction coefficients constant. In this

case

$$\rho_i \frac{\partial \mathbf{v}_i}{\partial t} + \rho_i(\mathbf{v}_i \text{ grad})\mathbf{v}_i = \sum_k \left[\frac{1}{2} R_{ik}^{t*} \Delta \mathbf{v}_k + \left(\frac{1}{6} R_{ik}^{t*} + R_{ik}^{s*} \right) \cdot \text{grad div } v_k + R_{ik}^{v*}(v_i - v_k) - \right.$$

$$\left. - (c_k \rho_i \text{ grad } \mu_i - c_i \rho_k \text{ grad } \mu_k) \right] - c_i \text{ grad } p^e + \rho_i F_i. \tag{4.2}$$

The analogy to the Navier–Stokes equation is clear, but beyond the usual terms there is a viscous coupling between the equations, and there are simple friction terms, too.

Neglecting the viscous effects in (4.2)

$$\rho_i \frac{d^{(i)}}{dt} v_i + \sum_k R_{ik}^{v*} \mathbf{v}_k = -(\rho_i \text{ grad } \mu_i - c_i \sum_k \rho_k \text{ grad } \mu_k) - c_i \text{ grad } p^e + \rho_i \mathbf{F}_i \tag{4.3}$$

is obtained. These equations are analogous to those in Gyarmati's Wave Approach [1]. To obtain equations explicitly for diffusion currents, it is better to use the (1.19) balance, that—after the same neglections—gives

$$\rho \frac{\mathrm{d}}{\mathrm{d}t} \mathbf{j}_i + \text{Div} \left[\frac{\rho}{c_i} (\mathbf{j}_i \circ \mathbf{j}_i) \right] + \sum_k R_{ik}^{v*} \frac{1}{c_k} \mathbf{j}_k = -\left(\rho_i \text{ grad } \mu_i - c_i \sum_k \rho_k \text{ grad } \mu_k \right) -$$

$$- c_i \text{ grad } p^e + \rho_i \mathbf{F}_i - \rho_i \frac{d}{dt} \mathbf{v} - \rho(\mathbf{j}_i \text{ grad}) \mathbf{v}. \tag{4.4}$$

Omitting the second order term on the l.h.s., we are looking at another analogue of the Wave Approach. The (4.4) system of equations considers the effects of the average motion too, thus it can be useful for immediate practical applications.

Let us return to Eq. (4.2). Its character is perhaps more accentuated in the linearised form. Let us assume that the $\mathbf{v}_i$ component velocities are small, that no external force occurs, and introduce the notation

$$-\alpha_{ik} = \rho_i \frac{\partial \mu_i}{\partial \rho_k} - c_i \sum_l \rho_l \frac{\partial \mu_l}{\partial \rho_k} + c_i \frac{\partial p^e}{\partial \rho_k}.$$

Considering the α_{ik}-s constant, and neglecting the second order terms of the derivatives of ρ_k and $\mathbf{v}_k$, then taking the divergence of both sides of (4.2), we apply the approximate of the (1.2) balance, i.e.

$$-\frac{1}{\rho_i} \frac{\partial \rho_i}{\partial t} = \text{div } \mathbf{v}_i.$$

In other words: restricting our examinations to small oscillations around an equilibrium state, we obtain

$$\frac{\partial^2 \rho_i}{\partial t^2} = \sum_k \left(b_{ik} \Delta \frac{\partial \rho_k}{\partial t} - d_{ik} \frac{\partial \rho_k}{\partial t} + a_{ik} \Delta \rho_k \right), \tag{4.5}$$

with

$$b_{ik}=\frac{1}{\rho_k}\left(\frac{2}{3}R_{ik}^{t*}+R_{ik}^{s*}\right),$$

$$d_{ik}=\frac{1}{\rho_k}R_{ik}^{v*}, \qquad a_{ik}=\frac{1}{\rho_k}\alpha_{ik}.$$

If the b_{ik}-s are zero, this is a system of telegraphist's equations describing damped diffusional waves.

5. Conclusions

We started off from considering a mixture to be a superposition of several continua or an N-body [8, 11, 15, 19]. By the use of correct balance equations—i.e. not neglecting the momentum and the kinetic energy of diffusion [8,10]—the consistent application of the Onsager–Gyarmati theory leads to new equations of diffusion and flow.

These equations, beyond the wave behaviour, show viscous effects even on the diffusion level of motion. The stress caused by the diffusion's momentum transport is also considered. The cross effects of the classical approach of diffusion proved to be arising from the friction of the components on one another. Thus, for diffusion, the equivalence of the Onsager Relations and Newton's third law is proven.

The classical diffusion equations come from the assumption

$$\rho_i\mathbf{F}_i^*+\rho_i\mathbf{F}_i=0. \tag{5.1}$$

This, using (3.7), reads

$$\sum_k R_{ik}^v\mathbf{w}_k+R_{iq}^v\mathbf{J}_*=c_i\left[\rho\,\mathrm{grad}\left(-\frac{\mu_i}{T}\right)+\sum_k\rho_k\,\mathrm{grad}\,\frac{\mu_k}{T}\right]+$$

$$+\frac{p^e}{T}\,\mathrm{grad}\,c_i+\rho_i\mathbf{F}_i. \tag{5.2}$$

The connection of this theory to the Wave Approach [1] can be also easily shown. When the diffusion currents are small, the entropy function (2.2) can be approximated by the first two terms of its Taylor series—according to its first argument—in the vicinity of u

$$s=s(u,\rho,c_k)-\frac{1}{T}\sum_i\frac{1}{2c_i}j_i^2. \tag{5.3}$$

This is the same entropy function used implicitly in the Wave Approach [1]

$$s=s_0(u,\rho,c_k)-\frac{1}{2}\sum_{i,k}m_{ik}\mathbf{J}_i\mathbf{J}_k, \tag{5.4}$$

if

$$\rho T m_{ik} = (\rho_i \rho_k)^{-1/2} \delta_{ik}. \tag{5.5}$$

Here δ_{ik} is the Kronecker delta.

In our case the inductivity matrix m_{ik} is diagonal, owing to two reasons. First, because we did not choose the variables at random. The mixing of the components by a linear transformation leads to a non-diagonal inductivity matrix. The second, and more essential cause of the diagonality is the assumption that $\rho_i \mathbf{v}_i$ is the momentum of a component, which is a very crude specialization of the general case.

The results can be obtained in several ways. One is the re-defining of the internal energy by changing u for u^*. An other way—which we followed, in the hope of deeper understanding—is the introduction of dynamic variables. It is not done in the widest generality, as done by Verhás [5, 16], but we have chosen the specific diffusion currents to be the dynamic variables, thus remaining consistent also with the idea of the entropy depending only on the thermic part of the energy.

In this way the balances of dynamic variables are gained, not from general considerations [5], but from the mechanical description of the mixture. The constitutive equations of the current $\boldsymbol{J}_{\xi_i}$ and source σ_{ξ_i} of the dynamic variables were obtained by the applied procedure—as suspected by Verhás [5]—and they read

$$\boldsymbol{J}_{\xi i} = \rho_i (\mathbf{w}_i \circ \mathbf{w}_i) - \sum_k [R_{ik}^{t*} \operatorname{Grad} \mathbf{v}_k^{os} + (R_{ik}^{s*} \operatorname{div} \mathbf{v}_k - c_i p^e)\boldsymbol{\delta}], \tag{5.6}$$

$$\boldsymbol{\sigma}_{\xi i} = \sum_k \left[R_{ik}^{v*} \mathbf{w}_k + R_{iq}^{v*} \mathbf{J}_* + T\left(c_k \rho_i \operatorname{grad} \frac{\mu}{T} - c_i \rho_k \operatorname{grad} \frac{\mu_k}{T}\right)\right] -$$

$$- p^e \operatorname{grad} c_i - \rho_i \left(\mathbf{F}_i - \frac{d\mathbf{v}}{dt}\right) + \rho_i (\mathbf{w}_i \operatorname{grad}) \mathbf{v}. \tag{5.7}$$

Though our results can be interpreted as a special case of the Theory of Dynamical Variables [5], our considerations find their firm base in the mechanics of continua and in the classical thermodynamics, standing somewhere between the general (and somewhat formal) theories [1, 5] and the direct physicochemical analysis of the matter. Thus, it is hoped, and expected not without any basis, that they can give the link between them, giving a tool even for the practical application of both.

References

1. I. Gyarmati, J. Non-Equilib. Thermodyn., *2*, 233, 1977.
2. C. Cattaneo, Atti del seminario matematico e fisico dell'Universita de Modena, *3*, 1948.
3. P. Vernotte, Comptes Rend., *246*, 3154, 1958.
4. Ph. M. Morse and H. Feshbach, Methods of Theoretical Physics, McGraw-Hill Book Comp. Inc., New York, Toronto, London, 1953.
5. J. Verhás, J. Non-Equilib. Thermodyn., *8*, 201, 1983.

6. H. Parkus, Coupled Fields in Mechanics, Lectures at the Technical University of Budapest in March and April, 1981.
7. H. E. Müser and J. Petersson, Fortschritte der Physik, *19*, 559, 1971.
8. I. Gyarmati, Non-Equilibrium Thermodynamics, Springer, Berlin, Heidelberg, New York, 1970.
9. C. Truesdell and R. Toupin, The Classical Field Theories, Handbuch der Physik, III/1. Springer, Berlin, Heidelberg, New York, 1960.
10. S. R. De Groot and P. Mazur, Non-Equilibrium Thermodynamics, North-Holland Publ. Co., Amsterdam, 1962.
11. C. Truesdell, Rend. Lincei, *22*, 33, 1957.
12. R. K. Ghai, H. Ertl and F. A. L. Dullien, A. I. Ch. E. Journal, *19*, 881, 1973.
13. O. Lamm, Acta Chem. Scand., *8*, 1120, 1954.
14. O. Lamm, J. Phys. Chem., *61*, 948, 1957.
15. R. M. Bowen and D. J. Garcia, Int. J. Engng. Sci., *8*, 63, 1970.
16. J. Verhás, Periodica Polytechnica, Ser. Mech. Engng., *21*, 49, 1977.
17. K. Hutter, Acta Mechanica, *27*, 1, 1977.
18. J. Bataille and J. Kestin, J. Non-Equilib. Thermodyn., *2*, 49, 1977.
19. I. Müller, Arch. Rat. Mech. Anal., *28*, 1, 1968.
20. T. Erdey-Grúz, Transport Processes in Aqueous Solutions, Akadémiai Kiadó, Budapest, 1971. (in Hungarian)
21. R. W. Laity, J. Phys. Chem., *63*, 80, 1959.
22. R. W. Laity, J. Phys. Chem., *30*, 682, 1959.

Acta Physica Hungarica 60 (3—4), pp. 261—277 (1986)

STUDIES ON THE DECAY OF ^{160}Tb

S. U. EL-KAMEESY, M. R. RADWAN, Z. MILIGY

Physics Department, Faculty of Science
Ain Shams University, Cairo, Egypt

and

A. Z. EL-BEHAY

Department of Radiation Physics and Protection
National Center for Radiation Research and Technology
Cairo, Egypt

(Received in revised form 24 January 1985)

The decay of ^{160}Tb (72.2 d) to ^{160}Dy has been studied using H. P. Ge and H. P. Ge–NaI(Tl) coincidence spectrometers. Angular correlation measurements have been made to estimate the spins and parities of some levels as well as the mixing ratios of their gamma transitions.

Forty gamma transitions have been observed having energies in the range from 86.79 to 1312.14 keV. Five of these transitions are found to be new and have energies 97.64, 110.13, 121.71, 189.72 and 202.78 keV. Our angular correlation measurements together with those from conversion electron studies permit the assignment of 3^-, 2^-, 3^+, 4^+ and 2^+ spins for the levels at 1386.44, 1264.73, 1049.09, 283.32 and 86.78 keV, respectively. Also the multipolarities of the 121.71 and 1102.62 keV transitions were found as M1 + E2 for the former and E1 + M2 for the latter. Their mixing ratios were estimated and compared with the corresponding values derived from internal conversion studies. The levels from this and previous work are compared with those calculated with the rotation–vibration model which is obtained by Faessler and Greiner.

1. Introduction

The decay scheme of ^{160}Tb is one of the most thoroughly investigated in the region of deformed nuclei. This nucleus has been studied early by Nathan [1] and Ofer [2]. Arns et al [3] were able to detect a new level at 1.2 MeV. Ewan et al [4] established the six levels with their J^π values as in Arns et al except the level at 1200 keV. In addition to these states two states of 1.2865 MeV (3^-) and 1.3582 MeV (2^-) were detected. Also an additional level at 1550 keV was reported by Michaelis [5].

A gamma–gamma angular correlation has been applied by Gupta et al [6] to determine the spin sequences and multipolarities of some transitions. The coincidence and directional correlation measurements coupled with the internal conversion and earlier γ-ray studies mentioned above have led to many spin and parity assignments to the levels of ^{160}Dy [7]. The gamma spectrum of ^{160}Tb was measured by Gunther et al [8] and the low lying negative parity states have been interpreted in this work as

members of two strongly mixed rotational bands. The coincidence studies of Ludington et al [9] employing to Ge(Li) detectors have led to a decay scheme which is essentially that given by previous investigators with the addition of levels at 1155.8, 1288.7 and 1535.2 keV. The level at 1155.8 keV has been identified as the 4^+ member of the gamma-vibrational band.

Although there is general agreement between the results of these authors, still there are some ambiguities noticed concerning few transitions, energy levels and spin–parity assignments. Accordingly, it was felt advisable to reinvestigate the energy level of ^{160}Dy through the study of single, coincidence and angular correlation with better techniques. It is hoped by such work to settle the previously reported discrepancies and to achieve a more reliable decay scheme. Another goal was to extend the comparison of the experimentally observed energy levels to those predicted with the rotation–vibration model of Faessler and Greiner [10].

2. Experimental procedure and results

A 2 mg of pure ^{159}Tb has been irradiated in the A.R.E. Reactor. The gamma-ray transitions associated with the decay of ^{160}Tb into ^{160}Dy have been investigated using a hyper pure Ge detector (coaxial type, 40.9 mm diameter and 39.5 mm length with total active volume 46.3 cc) coupled with an FET-preamplifier, spectroscopy amplifier and a 4096 multichannel analyzer with appropriate outputs to tellitype X–Y plotter or tape-recorder. The window to detector distance is 5 mm. The resolution of the detector was checked to be 2.5 keV for the 1.33 MeV line of ^{60}Co. All the used equipments were of ORTEC type.

The gamma–gamma coincidence measurements have been carried out using a H. P. Ge–NaI(Tl) spectrometer provided with a fast–slow coincidence circuit which has been explained in details in [11]. The time resolution of the fast–slow coincidence circuit was about 30 ns, while that of slow coincidence was about 1.1 μs.

The correlation data were collected using a directional correlation table with the H.P. Ge detector as the fixed detector and a 3-in by 3-in NaI(Tl) detector as the moving detector. The H.P. Ge detector has a photopeak–to–Compton ratio 54 : 1.

A. Gamma-ray single and coincidence spectra

Measurement of each spectrum has been performed by placing the source at 7 cm from the H.P. Ge detector. Since the gamma energies emitted from the decay of ^{160}Tb are extending up to about 1550 keV, the spectrum was measured to cover the whole energy range with reasonable resolution as shown in Fig. 1. In order to determine the energy per channel an ennergy calibration has been carried out using available standard sources together with a suitably calibrated pulser.

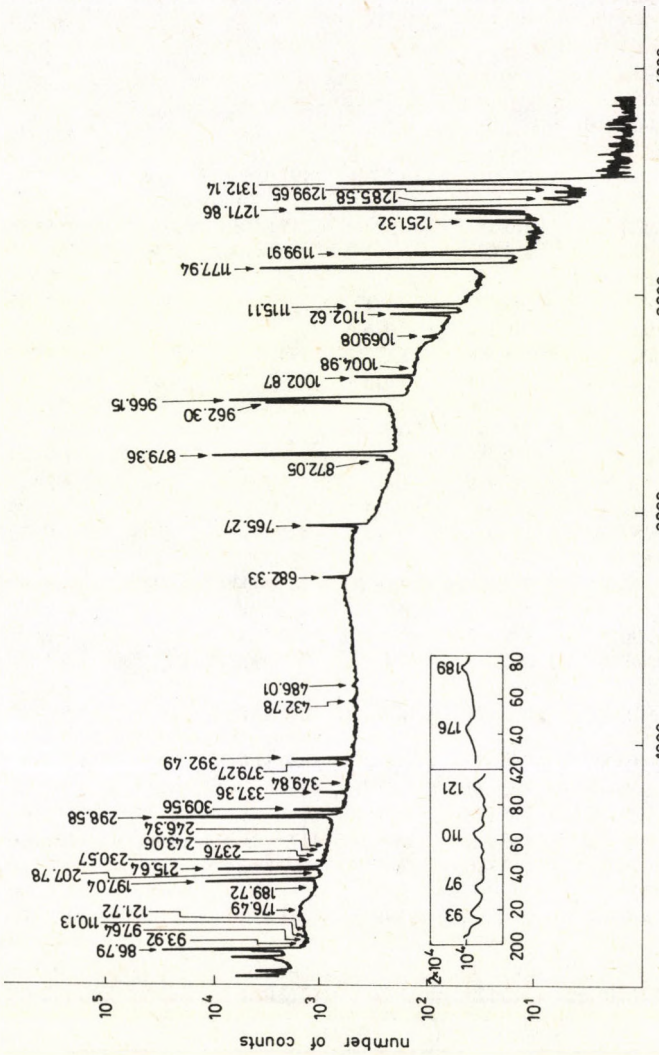

Fig. 1. Gamma-ray spectrum of ^{160}Tb obtained with an ORTEC Model (8200) H.P. Ge. detector

Table I

Energy and intensity values for transitions in ^{160}Dy following β-decay of ^{160}Tb

Present work		McAdams [13]		Keller [12]		Ludington [9]	
$E\gamma$	$I\gamma$	$E\gamma$	$I\gamma$	$E\gamma$	$I\gamma$	$E\gamma$	$I\gamma$
86.79 ± 0.08	13.400(2)	86.788	13	86.798	14.000	86.788	13.700
93.92 ± 0.03	0.066(20)	93.936	0.054			93.919	0.067
97.64 ± 0.04	0.021(3)						
110.13 ± 0.07	0.052(15)						
121.71 ± 0.09	0.061(17)						
176.49 ± 0.04	0.0041(10)					176.49	0.047
189.72 ± 0.06	0.033(4)						
197.04 ± 0.08	5.210(40)	197.036	5.22	197.036	5.16	197.035	5.22
202.78 ± 0.08	0.003(1)						
215.64 ± 0.05	4.0(1)	215.653	4	215.6418	3.91	215.646	3.93
230.57 ± 0.08	0.078(8)	230.602	0.082	230.6410	0.062	230.628	0.071
237.60 ± 0.09	0.011(3)	237.820	0.012			237.688	0.007
243.06 ± 0.05	0.021(4)	243.020	0.021			242.500	0.004
246.34 ± 0.09	0.027(4)	246.410	0.026			246.489	0.018
298.58 ± 0.03	27.0(8)	298.566	27	298.5790	27	298.582	27.100
309.56 ± 0.04	0.922(13)	309.573	0.918	309.5640	0.82	309.557	0.90
337.35 ± 0.05	0.36(7)	337.306	0.355	337.3470	0.34	237.324	0.33
349.84 ± 0.01	0.017(1)	349.690	0.018			349.940	0.014
379.27 ± 0.02	0.015(2)	379.250	0.017			379.449	0.014
392.49 ± 0.03	1.41(10)	392.489	1.4	392.4940	1.36	392.514	1.36
432.78 ± 0.01	0.022(6)	432.660	0.024			432.700	0.013
486.01 ± 0.05	0.087(10)	485.950	0.088	486.1650	0.096	486.075	0.08
682.33 ± 0.02	0.625(80)	682.329	0.617	682.2980	0.537	682.000	0.545
765.27 ± 0.04	2.11(20)	765.298	2.16	765.2600	1.93	766.000	2.03
872.05 ± 0.02	0.194(30)	872.030	0.207	872.1200	0.285	872.000	0.174
879.36 ± 0.02	30.000	879.367	30	879.3500	30	879.000	30
962.30 ± 0.06	9.66(20)	962.359	9.42	962.0000	10	962.000	10.2
966.15 ± 0.01	24.80(7)	966.165	24.8	966.1580	25.5	966.000	24.7
1002.87 ± 0.03	1.01(3)	1002.893	1.02	1002.8730	1.01	1003.00	0.98
1004.98 ± 0.04	0.10(2)					1005.00	0.10
1069.08 ± 0.09	0.112(20)	1069.073	0.104	1069.1130	0.113	1069.00	0.076
1102.62 ± 0.08	0.562(40)	1102.587	0.557	1102.6120	0.561	1103.00	0.5
1115.11 ± 0.01	1.52(14)	1115.117	1.48	1115.122	1.52	1115.000	1.5
1197.94 ± 0.04	15.2(6)	1177.952	15	1175.923	15.9	1178.000	14.8
1199.90 ± 0.07	2.47(20)	1199.886	2.37	1199.896	2.48	1200.000	2.24
1251.32 ± 0.06	0.097	1251.268	0.1	1251.340	0.096	1251.000	0.094
1271.86 ± 0.02	7.82(60)	1271.875	7.48	1271.873	7.81	1272.000	7.40
1285.58 ± 0.04	0.012(7)	1285.580	0.015			1286.100	0.011
1299.65 ± 0.06	0.004(1)	1299.310	0.006			1300.000	0.005
1312.14 ± 0.06	2.91(20)	1312.120	2.87	1312.000	3	1312.000	2.79

To determine the relative intensities of the gamma-transitions the trapezoid method was applied to estimate the area of each photopeak, then corrected for the detector efficiency and normalized to the electron intensities of Ewan et al [4]. Averages of the experimental and theoretical α_K-values were used along with the electron results of Ewan et al and Ludington et al [9].

Table I indicates that the best normalization procedure is to take the intensity in per cent per disintegration for the 879.36 keV transition as 30.0 which is used as normalization standard [9, 12].

The gamma–gamma coincidence data are shown in Table II. The real coincidences are represented in Figs 2a, 2b, 2c, 2d, 2e and 2f. The coincidence measurements with the same conditions (peak in gate and time) were repeated several times during a year.

Table II

H. P. Ge—NaI(Tl) coincidence results

Gate region	E [keV] in gate	E [keV] in coincidence
80–180	86.79, 93.92, 176.49	197.04, 215.64, 298.58, 879.36, 962.30, 1004.98, 1069.08, 1177.94, 1194.90, 1271.96, 1299.65, 1312.14
169–218	197.04, 215.64	86.79, 93.92, 121.71, 682.33, 765.27, 872.05, 962.30, 1002.87, 1004.98, 1102.62, 1115.11, 1251.32
262–313	298.58, 309.56	93.42, 176.49, 682.33, 765.27, 879.36, 962.30, 966.15
350–420	392.49	966.15, 879.36, 682.33, 176.49
826–921	872.05, 879.36	86.79, 189.72, 202.78, 230.57, 243.06, 298.58, 392.49, 432.78
920–1010	962.30, 966.15, 1002.87, 1004.98	86.79, 97.64, 110.13, 197.04, 215.64, 237.60, 298.58, 309.59, 337.60, 392.49, 349.84, 432.78, 486.01

The analysis of the observed gamma transitions and gamma–gamma coincidence has revealed 40 gamma transitions attributed to the decay of ^{160}Tb. All these transitions are observed in the single spectrum and are detected also in the gamma–gamma coincidence. Five new gamma transitions at 97.64, 110.13, 121.71, 189.72 and 202.78 keV are observed. Thirty three transitions are in excellent agreement with the previously reported data (McAdams [13]). The 1004.98 and 176.492 keV transitions are in agreement with the reported data of Ludington et al [9]. The gamma-ray transitions identified and confirmed in the present studies of the single and gamma–gamma coincidence spectra of the decay of ^{160}Tb are fitted in a proposed level structure of ^{160}Dy as shown in Fig. 3.

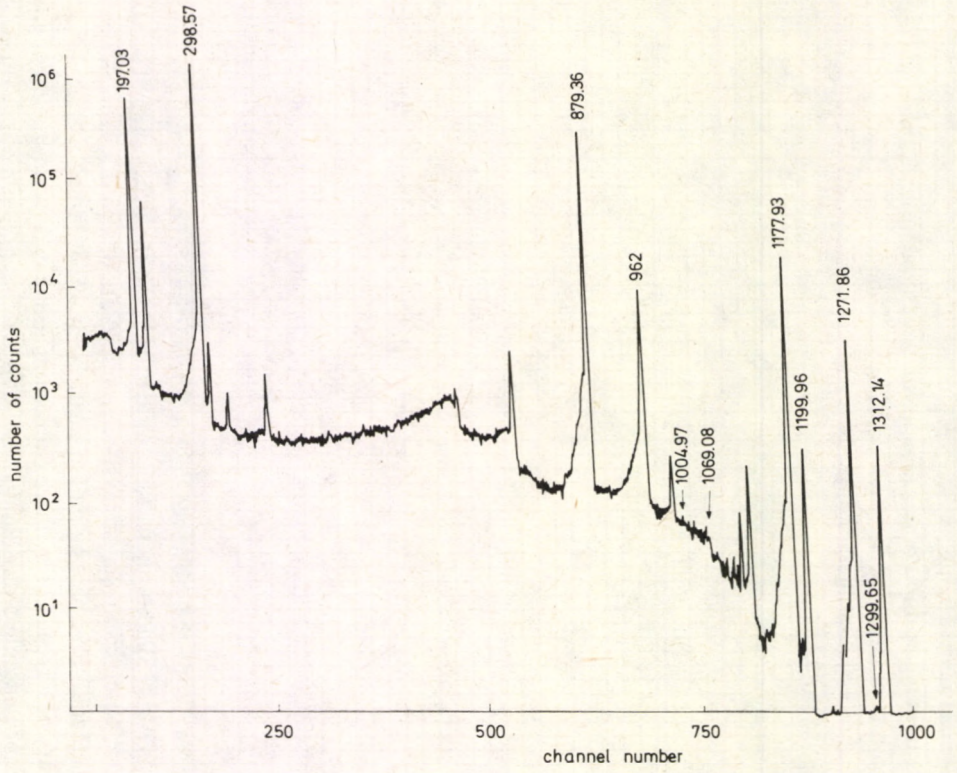

Fig. 2a. Coincidence spectra for gate (80–180 keV)

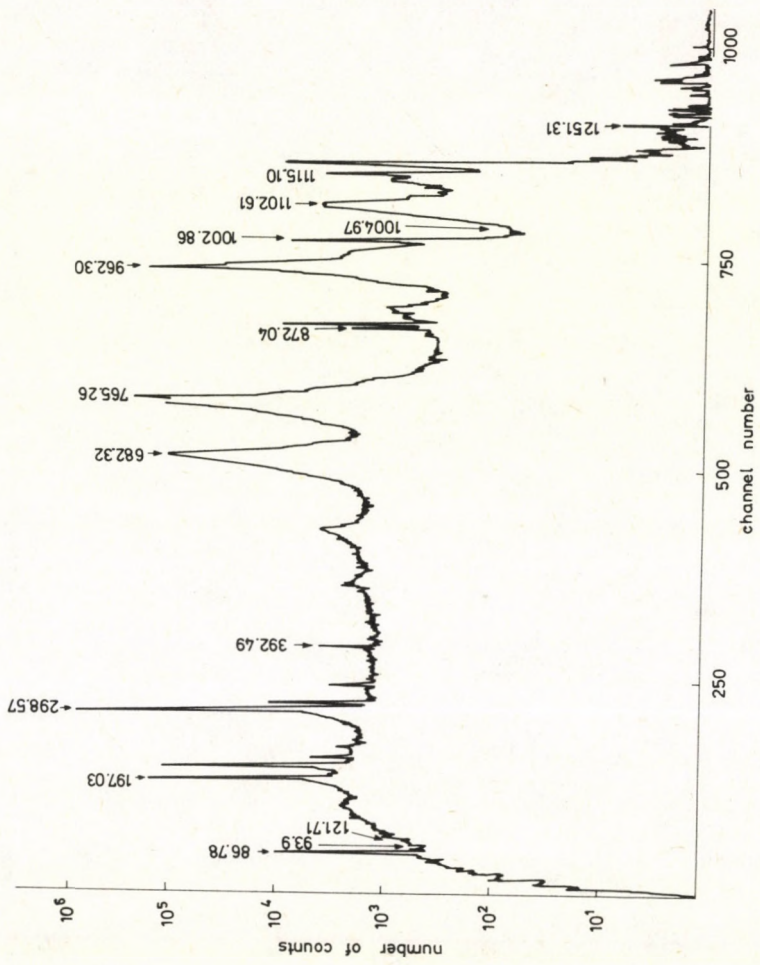

Fig. 2b. Coincidence spectra for gate (169–218 keV)

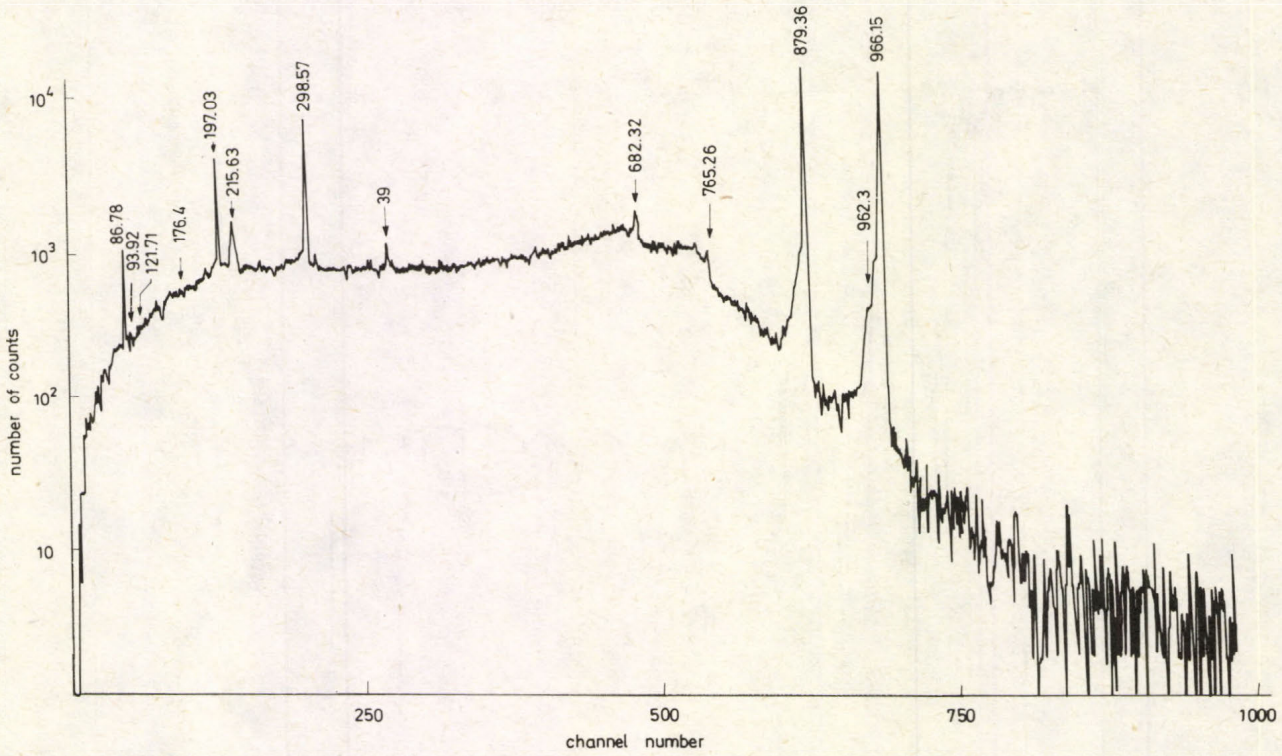

Fig. 2c. Coincidence spectra for gate (262–313 keV)

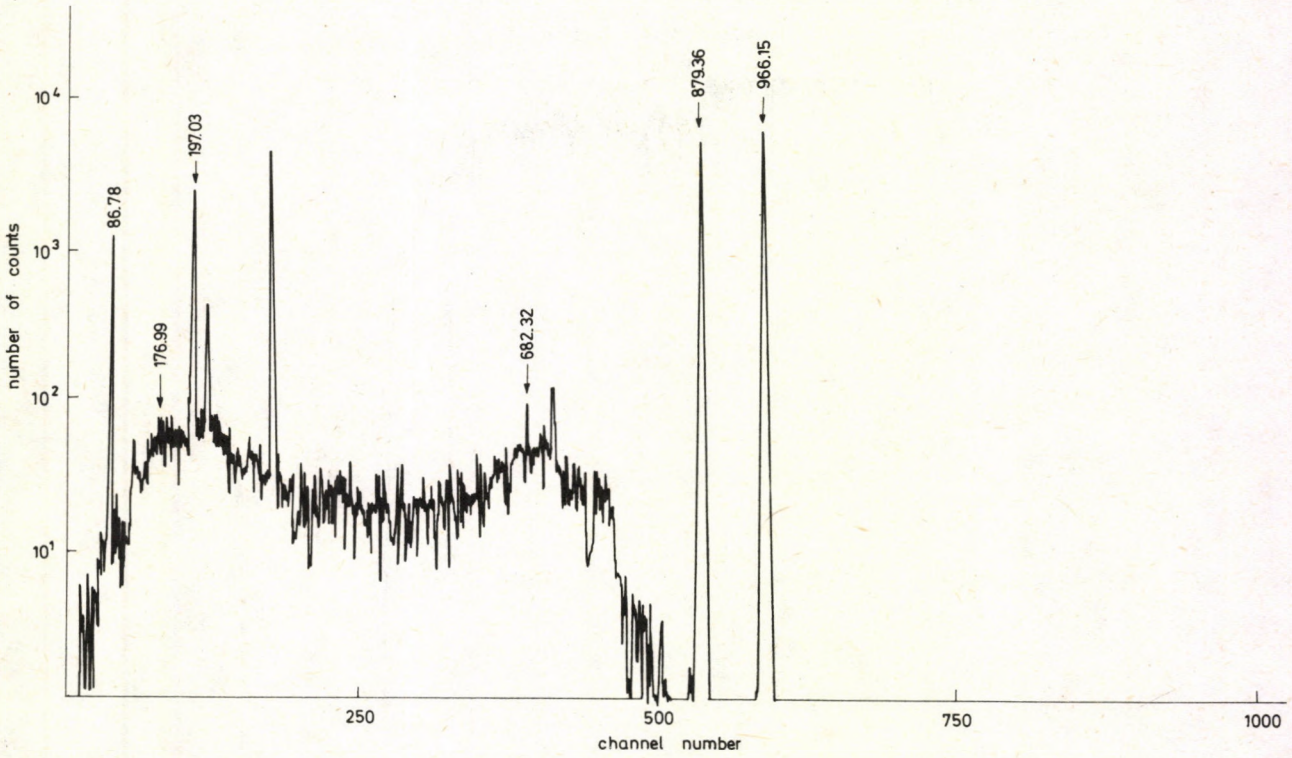

Fig. 2d. Coincidence spectra for gate (350–420 keV)

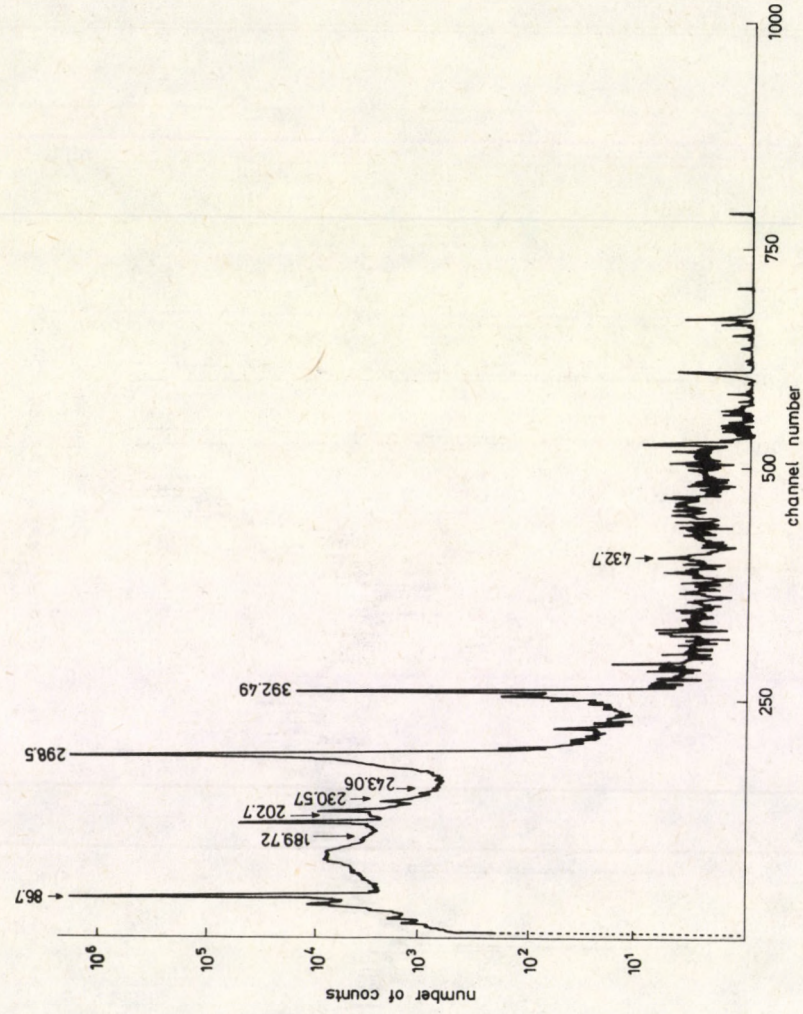

Fig. 2e. Coincidence spectra for gate (826–921keV)

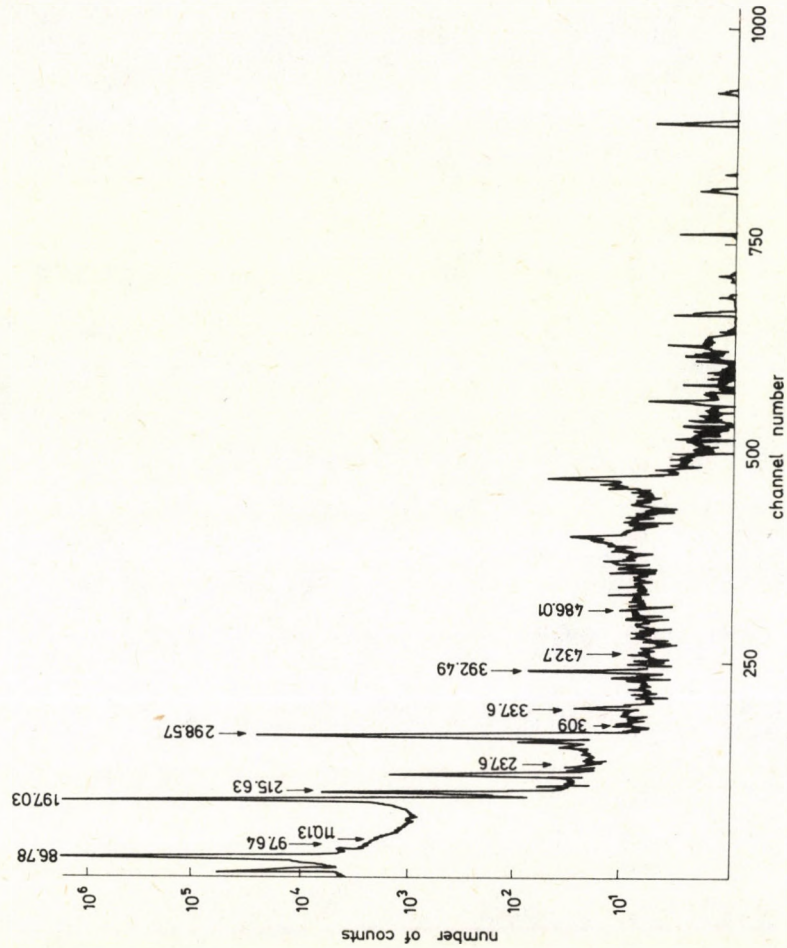

Fig. 2f. Coincidence spectra for gate (920–1010 keV)

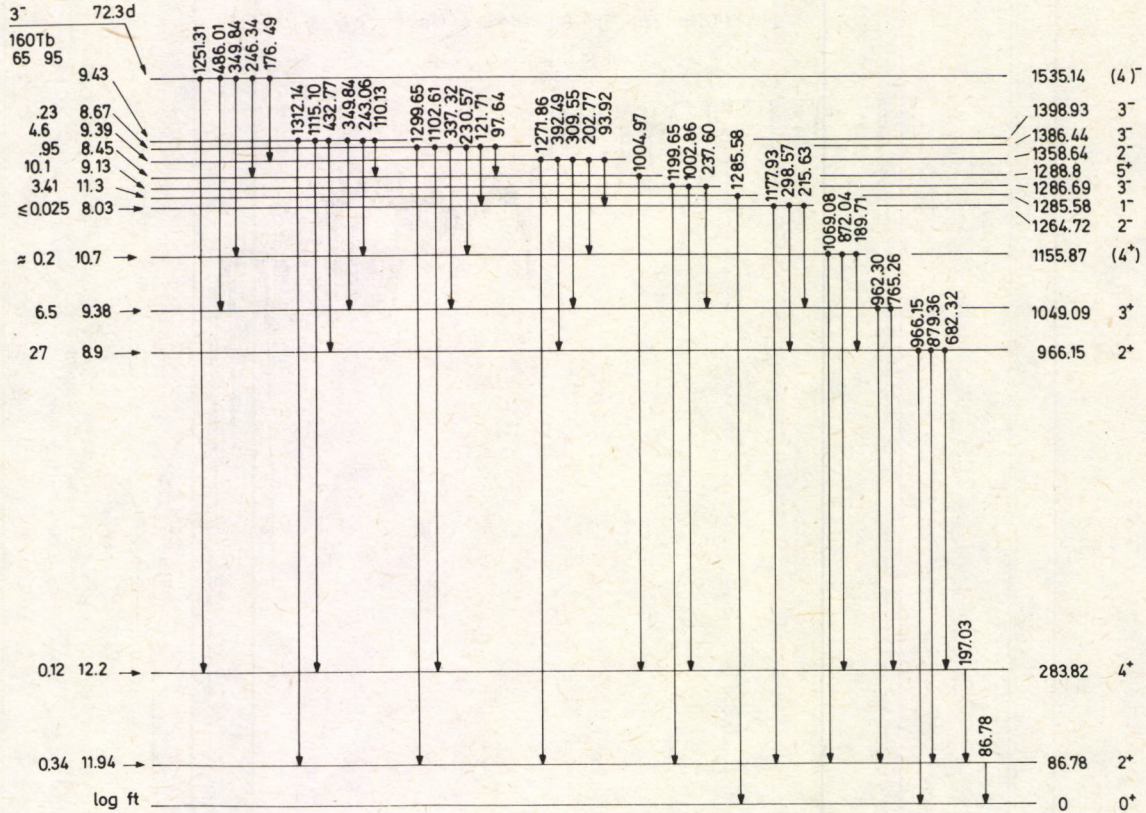

Fig. 3. Decay scheme of ^{160}Tb

B. Directional correlation data

The directional correlation of the γ-ray cascades (121.71–215.64) and (1102.62–197.04) were measured. The coincidence spectra were measured at angles of 90°, 120°, 150°and 180° subtended between the two detectors. The values of angular correlation coefficients are given in Table III together with the determined mixing ratios where the correlation function is given by $W(\theta)=1+A_{22}P_2(\cos\theta)+A_{44}P_4(\cos\theta)$. The results were corrected for finite solid angle of the detectors. The random coincidences were measured and subtracted. The data were analyzed by means of Arns–Wiedenbeck [14] plots and are shown in Figs 4 and 5.

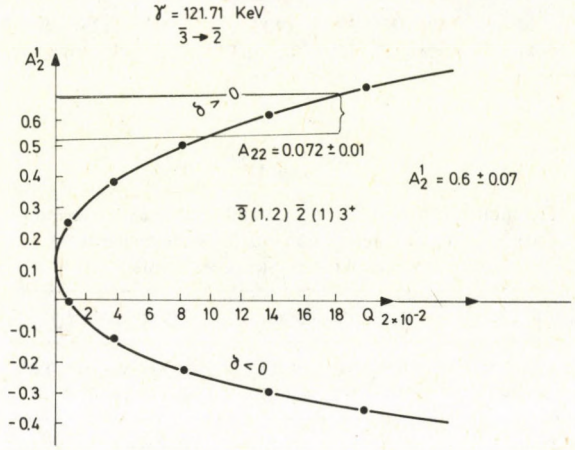

Fig. 4. Parametric plot of $A_2^{(1)}$, Q_2 against δ for $3^-(1, 2)2^-(1)_3^+$ cascade ($E_\gamma=121.71$ keV)

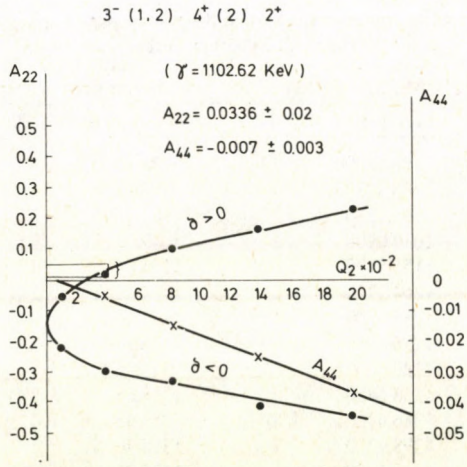

Fig. 5. Parametric plot of A_{22}, A_{44} against δ for $3^-(1, 2)\,4^+(2)2^+$ cascade ($E_\gamma=1102.62$ keV)

Table III

Directional angular correlation results

Gate energy [keV]	Display energy [keV]	Experimental coefficient	
		A_{22}	A_{44}
215.637	121.71	0.072 ± 0.01	0.001 ± 0.001
197.04	1102.62	0.0336 ± 0.02	-0.007 ± 0.003

Energy and I^π initial state	Energy and I^π final state	Mixing ratio δ	Multipolarity
1386.44 3^-	1264.73 2^-	$0.403 + 0.1$	$M1 + (13.9 \pm 4)\%\ E2$
1386.44 3^-	383.82 4^+	$0.2 + 0.014$	$E1 + (3.8 \pm 0.8)\%\ M2$

Table IV

The multipolarities of the 121.71 and 1102.62 keV transitions derived from the internal conversion measurements [9, 15] and theoretical conversion coefficients [16]

Display energy	Mixing ratio	Multipolarity
121.71	0.5 ± 0.15	$M1 + (20 \pm 5)\%\ E2$
1102.62	0.17 ± 0.015	$E1 + (2 \pm 0.2)\%\ M2$

Table V

The energy levels deduced in the present work including spin–parity assignments together with those reported by other authors

Present work		McAdams [13]		Keller [12]		Ludington [9]	
Level in keV	J^π	Level in keV	J^π	Level in keV	J^π	Level in keV	J^π
86.79	2^+	86.78800	2^+	86.80	2^+	86.788	2^+
283.82	4^+	283.82300	4^+	283.83	4^+	283.820	4^+
266.15	2^+	966.15200	2^+	966.15	2^+	966.200	2^+
1049.09	3^+	1049.0900	3^+	1049.08	3^+	1049.000	3^+
1155.87	(4^+)	1155.8700	$(4)^+$	1155.86	4^+	1155.800	4^+
1264.73	2^-	1264.7270	2^-	1264.73	2^-	1264.700	2^-
1285.58	1^-	1285.5800	1^-	—	—	—	—
1286.69	3^-	1286.6900	3^-	1286.70	3^-	1286.800	3^-
1288.80	5^+	1288.8000	5^+	—	—	1288.800	(5^+)
1358.69	2^-	1358.6480	2^-	1358.65	2^-	1358.700	2^-
1386.44	3^-	1386.4400	$(3)^-$	1386.45	4^-	1386.500	4^-
1398.93	3^-	1398.9300	3^-	1398.96	3^-	1399.000	3^-
1535.14	$(4)^-$	1535.1400	$(4)^-$	1535.21	4^-	1535.200	?

Table IV shows the multipolarities of the 121.71 and 1102.62 keV transitions derived from the internal conversion measurements [9, 15] and the theoretical conversion coefficients [16]. These results are compatible with the present angular correlation results.

Table V represents the energy levels deduced in the present work including spin–parity assignments together with those reported by other authors for comparison.

3. Discussion and conclusion

In this Section we integrate our results into a level scheme which is shown in Fig. 3. The main contribution of the present work is the investigation of the five new gamma transitions mentioned before and the establishment of 3^- spin–parity assignment for the 1386.44 keV level by $\gamma-\gamma$ directional correlation technique. In addition we have calculated the rotational–vibrational structure, using the results of the rotation–vibration model proposed by Faessler and Greiner [10, 17]. The expression for the eigenvalues of the Hamiltonian if properly symmetrized is

$$E_{IKn_2n_0}=(n_0+1/2)E_\beta+(2n_2+1/2K+1)E_\gamma+(I(I+1)-K^2)1/2\varepsilon\,,$$

$$I=\begin{cases}0, 2, 4 & \text{for } K\\ K, K+1 & \text{for } K\neq 0\end{cases} \qquad n_0\,, n_2=0, 1, 2, \ldots,$$

where

$$E_\beta=\hbar\left(\frac{C_0}{B}\right)^{1/2}, \qquad E_\gamma=\hbar\left(\frac{C_2}{B}\right)^{1/2}, \qquad \varepsilon=\frac{\hbar^2}{\varphi_0}=\frac{h^2}{3B\beta_0^2},$$

$$\varphi_0=3B\beta_0^2\,.$$

K is the projection of angular momentum along the symmetry axis, n_0, n_2 characterize the vibrational quantum numbers and ε is the moment of inertia.

The typical band structure of the deformed nucleus ^{160}Dy is shown in Fig. 6 together with our experimental results for comparison. The ground state band is given by $|\,1000\rangle$. The β-vibrational band is given by $|\,1001\rangle$ and lies at energy E_β above the ground state which is in ^{160}Dy about 1600 keV. The γ-vibrational band is described by $|\,1200\rangle$. This state is called a γ-vibration even though $n_2=0$. Indeed the energy of $|\,2200\rangle$ is $E_\gamma+\varepsilon$ above the ground state. Higher γ-bands $|\,1400\rangle$ are also shown in Fig. 6. This study indicates that the rotational–vibrational model can give the correct ordering of the low energy levels but still there are some ambiguities when we extrapolate to higher energies.

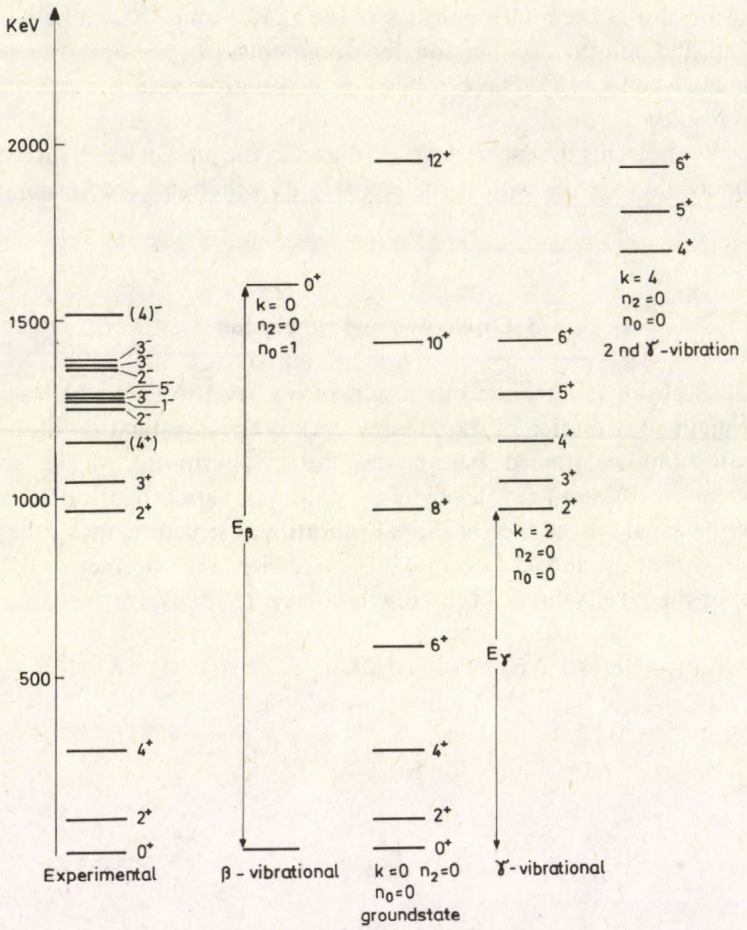

Fig. 6. Experimental energy levels of ^{160}Dy compared with the predictions of the rotational vibrational model

References

1. O. Nathan, Nucl. Phys., *4*, 125, 1957.
2. S. Ofer, Nucl. Phys., *5*, 331, 1958.
3. R. G. Arns, R. E. Sund and M. L. Wiedenbeck, Nucl. Phys., *11*, 411, 1969.
4. G. T. Ewan, R. L. Graham and J. S. Geiger, Nucl. Phys., *22*, 610, 1961.
5. W. Michaelis, Nucl. Phys., *44*, 78, 1963.
6. S. L. Gupta and N. K. Saha, Nucl. Phys., *70*, 203, 1965.
7. J. M. Jaklevic, E. C. Frenk and J. W. Mihelich, Nucl. Phys., *A99*, 83, 1967.

8. C. Gunter and F. Ryde, Nucl. Phys., *A122*, 401, 1968.
9. J. J. Ludington and M. L. Reidy, Nucl. Phys., *A119*, 398, 1968.
10. A. Faessler and W. Greiner, Z. Physik, *168*, 425, 1962; Z. Physik, *190*, 190, 1964;
A. Faessler, Nucl. Phys., *59*, 177, 1964;
A. Faessler and W. Greiner, Nucl. Phys., *80*, 417, 1965.
11. M. R. Radwan, Ph. D. Thesis, Faculty of Science, Ain Shams Univ., 1983.
12. G. E. Keller and E. F. Zganjar, Nucl. Phys., *A147*, 527, 1970.
13. O. H. McAdams, Z. Phys., *250*, 259, 1972.
14. M. L. Arns and M. L. Wiedenbeck, Phys. Rev., *111*, 1631, 1958.
15. C. M. Lederer and V. S. Shirtly, Table of Isotopes, J. Wiley, New York, 1978.
16. R. S. Hage and E. C. Seltzer, Nucl. Data, *4A*, 1, 1968.
17. J. M. Eisenber and W. Greiner, in Nuclear Theory, Vol. 1, North-Holland Publishing Company, Amsterdam, 1970.

Acta Physica Hungarica 60 (3—4), pp. 279—287 (1986)

SEMICLASSICAL IMPACT-PARAMETER EXPANSION OF DELTA-ELECTRON SPECTRUM

S. A. GERASIMOV

Department of Nuclear Physics, Institute of Physics
Rostov State University, Rostov-on-Don, 344090, USSR

(Received 24 January 1985)

The impact-parameter dependence of the secondary electron production in collisions of heavy charged particles with atoms and the energy distribution of delta-electrons are studied using a statistical model of an atom and the binary encounter approximation. As a result of this model the analytical expressions, describing inelastic scattering of heavy charged particles by a statistical atom have been derived.

1. Introduction

This paper deals with the so-called binary encounter approximation which is widely used for describing inelastic collisions of charged particles by atoms [1]. The classical binary encounter approximation is based on the assumption that the dominant process in atomic collisions is a direct interaction between an incident particle and an electron. An energy exchange arises in this process as a result of the elastic Coulomb interaction between an incident particle and a bound electron. In this consideration the binary encounter model is equivalent to the first Born approximation. In the Born approximation the assumption is that the interaction of the incident particle with the atom is weak and can be treated as a perturbation. Hydrogenic wave functions are usually used for describing the initial state of an atom. The binary encounter approximation treats the interaction between the incident particle and the bound electron exactly in the sense that the bound electrons are viewed as free particles with the defined velocity distribution function. The study of the inner-shell vacancy production is more simple and exact in both the first Born approximation and binary encounter model. It is connected with the fact that inner shells may be described exactly by the hydrogenic wave function, obtained for the Coulomb field. The screening effects are more significant for the states with large quantum numbers. Therefore, more real wave functions must be used for outer electrons in an atom. This procedure is the most difficult for the Born approximation. The initial state of an atom is defined by the electron speed distribution in the binary encounter approximation. Since the calculation of speed distribution does not depend on the description of the inelastic collision process the binary encounter approximation is the most simple and

universal. But a choice of orbitals for the calculation of the speed distribution by means of the Fourier transformation is more difficult for outer electrons in atoms with a large atomic number Z.

In this paper the Thomas–Fermi method is used for the study of the delta electron emission in collisions of heavy charged particles with atoms. Though the idea of this work is very simple it is first discussed in this article.

2. The calculation method

In the binary encounter approximation the energy distribution of secondary electrons ejected in collisions of heavy charged particles with atoms is given by

$$\frac{d\sigma}{dW} = \sum_i N_i \int_0^\infty \sigma_{\Delta E} f_i(v) dv \,, \tag{1}$$

where W is the energy of an ejected electron, E is the energy of an atomic electron, N_i is the number of atomic electrons in the i-th subshell of the target atom and $f_i(v)$ is the corresponding electron speed distribution. The electron speed distribution must be normalized to unity. The sum goes over all occupied states. $\sigma_{\Delta E}$ denotes the differential cross section for an elastic energy transfer ΔE between the projectile with the velocity v_1, the mass m_1, the kinetic energy T_1 and the target electrons with an initial velocity v, the mass m, kinetic energy T. In the well-known approximation [2] the distribution function $f_i(v)$ is defined by the module square of a wave function in the momentum representation.

For the Coulomb interaction between an incident particle and an atomic electron the appropriate expressions for $\sigma_{\Delta E}$ have been developed by Garcia [3] and Gerjuoy [4]. In the case with $m_1 \gg m$ these expressions can be written as follows:

$$\sigma_{\Delta E} = \sigma_1 = \frac{\pi e^4 m_1}{m T_1 \Delta E^3}\left(\Delta E + \frac{4}{3} T\right)$$

for

$$-E \leq \Delta E \leq 4\frac{m}{m_1} T_1 - 4\left(\frac{m}{m_1} T_1 T\right)^{1/2} \tag{2}$$

and

$$\sigma_{\Delta E} = \sigma_2 = \frac{\pi e^4 m_1}{m T_1 \Delta E^3} \frac{T}{6}\left\{\left(\frac{4mT_1}{m_1 T}\right)^{3/2} + \left[1 - \left(\frac{\Delta E}{T} + 1\right)^{1/2}\right]^3\right\}$$

for

$$4\frac{m}{m_1} T_1 - 4\left(\frac{m}{m_1} T_1 T\right)^{1/2} \leq \Delta E \leq 4\frac{m}{m_1} T_1 + 4\left(\frac{m}{m_1} T_1 T\right)^{1/2}.$$

In the statistical model of an atom it is assumed that the potential energy $-eU(r)$ of an electron varies slowly with the radial coordinate r and that at each point of the phase

space the system can be treated as a uniform gas of electrons with the density of state $1/(2\pi\hbar)^3$. It means that the differential cross section for the delta-electron emission can be written in the binary encounter approximation as

$$\frac{d\sigma}{dW} = \frac{1}{\pi^2\hbar^3}\iint \sigma_{\Delta E}(r, p)p^2 dp\, dV. \tag{3}$$

Formally, this expression follows from Eq. (1) for the system of electrons with the grand energy state density. In such an approach the number of electrons with energies between E and $E+dE$ and velocities between v and $v+dv$ coincides with the number of electrons in the corresponding phase volume element and is equal to

$$dN = \frac{1}{\pi^2\hbar^3} p^2 dp\, dV. \tag{4}$$

It is assumed that a relationship between the electron energy E and its radial coordinate r has been established in Eqs (2) and (3). In atoms with a large atomic number the wavelength of most electrons is much less than an atomic size. In this case the semiclassical approximation

$$E = \frac{p^2}{2m} - \frac{Ze^2}{r}\varphi(x) \tag{5}$$

is valid. Here, $\varphi(x)$ is the Thomas–Fermi screening function, $x = rZ^{1/3}/b$; $b = (3\pi/4)^{2/3}\hbar^2/2me^2$.

Suppose the kinetic energy of an incident particle is so large that a classical trajectory of the incident particle is a straight-line. This assumption is also valid for incident particles with low energies but at great impact parameters l. Let z be the axis of a fixed system of cylindrical coordinates with a radius vector equal to an impact parameter l. It is useful to choose the z-axis parallel to the rectilinear trajectory of the incident particle. Taking into account that $r^2 = z^2 + l^2$ the spatial volume element dV may be written

$$dV = 4\pi \frac{rdr}{(r^2 - l^2)^{1/2}} ldl. \tag{6}$$

Let us now compare the expression (3) for the delta-electron spectrum with the classical definition of the scattering probability density dP/dW [5]:

$$\frac{d\sigma}{dW} = 2\pi \int_0^\infty \frac{d}{dW} P(W, l) ldl. \tag{7}$$

Thus,

$$\frac{dP}{dW} = \frac{2}{\pi^2\hbar^3} \int_{I0}^{\infty}\int \sigma_{\Delta E}(r, p)p^2 dp \frac{rdr}{(r^2 - l^2)^{1/2}}. \tag{8}$$

To calculate the integral over p in Eq. (8) it is necessary to solve the system of inequalities in (2). Let us define the dimensionless variables given by

$$\kappa = b/(e^2 Z^{4/3}); \qquad \varepsilon = -E\kappa;$$

$$k^2 = \kappa p^2/2m; \qquad t = mT_1\kappa/m_1;$$

$$\eta = W\kappa; \quad \rho = lZ^{1/3}/b.$$

In these notations Eq. (5) can be written

$$k^2 + \varepsilon = \varphi(x)/x \tag{9}$$

and the system of conditions (2)

$$\frac{\varphi(x)}{x} + \eta \leq (2t^{1/2} - k)^2 \tag{10}$$

and

$$(2t^{1/2} - k)^2 \leq \frac{\varphi(x)}{x} + \eta \leq (2t^{1/2} + k)^2, \tag{11}$$

respectively.

Electrons are bound in an initial state, hence

$$\frac{\varphi(x)}{x} - k^2 \geq 0. \tag{12}$$

The joint solution of inequalities (10) and (12) is

$$\begin{cases} 0 \leq k \leq 2t^{1/2} - (\eta + \varphi(x)/x)^{1/2}, \\ 0 \leq k \leq (\varphi(x)/x)^{1/2}, \end{cases} \tag{13}$$

and corresponds to the region BCD in Fig. 1a, where x_1 is the solution of the equation

$$\frac{\varphi(x_1)}{x_1} = \frac{(4t - \eta)^2}{16t} \tag{14}$$

and x_0 is the solution of the equation

$$\frac{\varphi(x_0)}{x_0} = 4t - \eta. \tag{15}$$

The joint solution of inequalities (11) and (12) is

$$|(\varphi(x)/x + \eta)^{1/2} - 2t^{1/2}| \leq k \leq (\varphi(x)/x)^{1/2} \tag{16}$$

and corresponds to the region ABCE in Fig. 1a.

The system of conditions (13) has no solution at $4t < \eta$. In this case the condition (16) is

$$(\varphi(x)/x + \eta)^{1/2} - 2t^{1/2} \leq k \leq (\varphi(x)/x)^{1/2}. \tag{17}$$

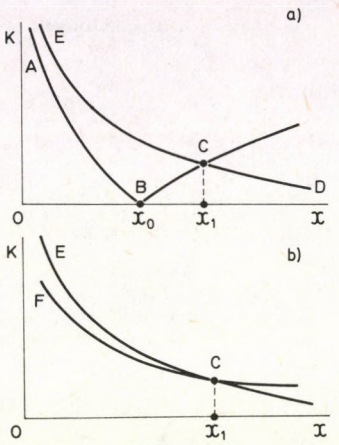

Fig. 1. Integration region in the k, x plane. Lines EC and BC are plots of relationships $k=(\varphi/x)^{1/2}$ and $k=2t^{1/2}-(\eta+\rho/x)^{1/2}$, respectively. Lines AB and FC are the relationship $k=(\eta+\varphi/x)^{1/2}-2t^{1/2}$

The region corresponding to the inequality (17) at $4t<\eta$ is shown in Fig. 1b by the curvilinear triangle FCE. Hence,

$$\int_0^\infty \sigma_{\Delta E} p^2\, dp = \int_{BCD} \sigma_1 p^2\, dp + \int_{ABCE} \sigma_2 p^2\, dp; \qquad 4t \geq \eta \tag{18}$$

and

$$\int_0^\infty \sigma_{\Delta E} p^2\, dp = \int_{FCE} \sigma_2 p^2\, dp; \qquad \text{if} \quad 4t<\eta\,. \tag{19}$$

Substituting for σ_1 and σ_2 from Eqs (2) and integrating over p one obtains

$$\frac{dP}{dW} = \frac{1}{\pi}\left(\frac{3\pi}{4}\right)^{5/3} \frac{Z_1^2}{Z^{7/3}} \frac{\hbar^2}{me^4} \frac{1}{t}\left\{\int_\rho^\infty \frac{\varphi^{3/2}dx}{3\eta^2[x(x^2-\rho^2)]^{1/2}} + \right.$$

$$+ \int_\rho^{x_1} \left[\frac{4t^{3/2}-2a(\varphi/x)^{3/2}+(\varphi/x+\eta)^{1/2}(\eta-2\varphi/x)}{12\eta^2} - \right.$$

$$\left.\left. - \frac{1}{16((\varphi/x+\eta)^{1/2}-t^{1/2})}\right] \frac{x\,dx}{(x^2-\rho^2)^{1/2}}\right\}, \tag{20}$$

where $a=1$ at $4t\geq\eta$ and $a=-1$ if $4t<\eta$. Integrals in Eq. (20) must be equal to zero at $4t<\eta$ and $\rho>x_1$, respectively.

The expression (20) is a general solution of the task. The electron production, corresponding to impact parameters l from l_1 to l_2, may be found from

$$\frac{d\sigma_{12}}{dW} = 2\pi \int_{l_1}^{l_2} \frac{dP}{dW}\, l\,dl\,. \tag{21}$$

3. Results and discussion

Let us introduce the notation

$$\frac{dP}{dW} = \left(\frac{3\pi}{4}\right)^{2/3} \frac{\hbar^2}{2me^4 Z^{4/3}} \frac{dP}{d\eta}, \tag{22}$$

thus at $\rho > x_1$ as well as at large energies of the projectile

$$t\eta^2 \frac{Z}{Z_1^2} \frac{dP}{d\eta} = \frac{1}{2} \int_{\rho}^{\infty} \frac{\varphi^{3/2} dx}{[x(x^2-\rho^2)]^{1/2}}. \tag{23}$$

Evidently, this expression is a scaling law and describes an asymptotic behaviour of the value dP/dW at large impact parameters. As an example of the results of calculation Figs 2 and 3 show an impact-parameter dependence of the delta-electron spectrum. The main result of this calculation is the following. The secondary electron production does not depend practically on the impact parameter at small ρ. The impact-parameter dependence of $dP/d\eta$ is identical to the scaling law (23) at large ρ. This is demonstrated in Fig. 2. Collisions with large impact parameters play a basic role at small energies of the incident particle and secondary electrons. This is connected with the fact that this range of energies corresponds to atomic electrons localized at great distances from the nucleus. The energy of outer electrons is very small, therefore its emission is more effective.

Unfortunately, there is no possibility to test these results of the calculation experimentally. Therefore, to test this method one can use the following procedure. Let us calculate the energy distribution of secondary electrons ejected in collision of heavy

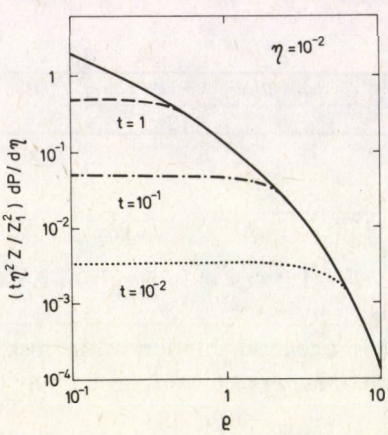

Fig. 2. Impact-parameter dependence of the secondary electron production for various projectile energies. The solid curve is the scaling law

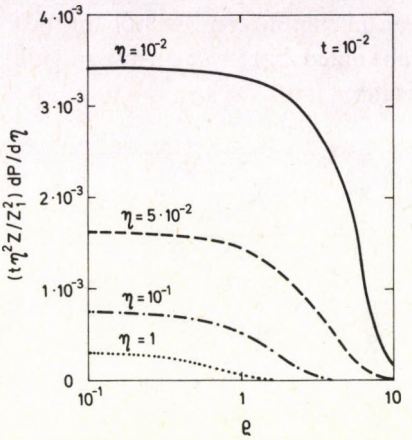

Fig. 3. Impact-parameter dependence of the secondary electron production for various delta-electron energies

charged particles using Eqs (7) and (19). By substituting Eq. (19) into Eq. (7) and interchanging the order of integration and taking account of [6]

$$\int_0^\infty \varphi^{3/2} x^{1/2}\, dx = 1\,, \tag{24}$$

one can obtain

$$\frac{d\sigma}{d\eta} = \left(\frac{3\pi}{4}\right)^{7/3} \frac{\hbar^4}{m^2 e^4} \frac{Z_1^2}{Z^{5/3}} \frac{1}{t} \left\{ \frac{1}{3\eta^2} + \right.$$

$$\left. + \int_0^{x_1} \left[\frac{4t^{3/2}x^2 - 2a\varphi^{3/2}x^{1/2} + (\varphi+\eta x)^{1/2}(\eta x - 2\varphi)x^{1/2}}{12\eta^2} - \right.\right.$$

$$\left.\left. - \frac{x^{5/2}}{16((\varphi+\eta x)^{1/2} - (tx)^{1/2})} \right] dx \right\}. \tag{25}$$

The integral in Eq. (25) has a very small value at large energies of the incident particle. The first term in Eq. (25) is the well-known Livingston–Bethe formula [7]. In the usual notations it is

$$\frac{d\sigma}{dW} = \frac{2\pi e^4}{m v_1^2} \frac{Z_1^2}{W^2} Z\,. \tag{26}$$

But it is known [8] that the expression (26) is valid in a very limited range of energies of the incident particle and secondary electrons. The validity range of Eq. (25) is more wide. Therefore, one can conclude that the expression (25) is the generalization of the Livingston–Bethe formula and the first term in Eq. (20) is the semiclassical impact-parameter expansion of Eq. (26).

Typical results of the differential cross section for the delta-electron emission are shown in Fig. 4. It should be noted that these correspond fully to known theoretical [8] and experimental [9] results.

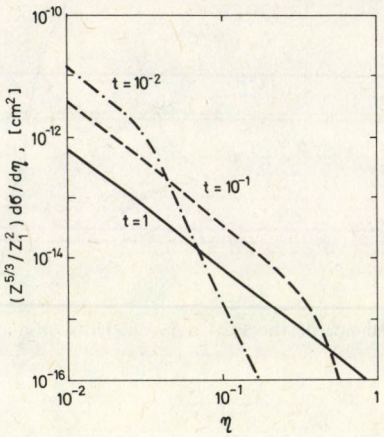

Fig. 4. Energy distribution of delta-electrons for various incident particle energies

4. Conclusion

This method of calculation is a high-energy formulation, in the sense that it is expected to be valid only for the secondary particle energies much larger than the maximum electron energy (or the minimum binding energy) for a given atom.

All results of this work were obtained for the Thomas–Fermi screening function. Any radially non-restricted model of an atom may be used for the calculation of dP/dW or $d\sigma/dW$ using Eqs (20) and (25), respectively.

There is a number of problems connected with a successful application of this method of calculation. One problem is the study of the secondary electron emission accompanying the collisions of channelled heavy charged particles moving in a crystal. The bremsstrahlung from secondary electrons ejected in collisions of heavy particles with atoms can be studied effectively using this model.

I wish to thank Prof. Yu. A. Vdovin and Dr. V. I. Ochkur for stimulating discussions that improved this manuscript.

References

1. J. D. Garcia, R. J. Fortner and T. M. Kavanagh, Rev. Mod. Phys., *45*, 111, 1973.
2. F. F. Komarov and M. M. Temkin, J. Phys., *B9*, L225, 1976.
3. J. D. Garcia, Phys. Rev., *A1*, 280, 1970.
4. E. Gerjuoy, Phys. Rev., *148*, 54, 1966.

5. J. S. Hansen, Phys. Rev., *A8*, 822, 1973.
6. P. Gombás, Die statistische Theorie des Atoms und ihre Anwendungen, Springer, Vienna, 1949.
7. L. Livingston and H. Bethe, Rev. Mod. Phys., *9*, 245, 1937.
8. L. D. Landau and E. M. Lifshitz, Kvantovaja Mehanika, Nauka, Moskva, 1974.
9. F. Bell, G. Trollmann and H. D. Betz, Phys. Lett., *A88*, 37, 1982.

Acta Physica Hungarica 60 (3—4), pp. 289—298 (1986)

DETERMINATION OF THE MEAN FREE PATH OF ELECTRONS IN SOLIDS FROM THE ELASTIC PEAK

III. THE EFFECTIVE BACKSCATTERING CROSS SECTION FOR 5–40 keV RANGE AND DIFFERENTIAL SCATTERING CROSS SECTIONS

G. GERGELY, M. MENYHÁRD, A. SULYOK*

Research Institute for Technical Physics of the Hungarian Academy of Sciences
1325 Budapest, Hungary

A. JABLONSKI and P. MROZEK**

Institute of Physical Chemistry of the Polish Academy of Sciences
01-224 Warsaw, Poland

(Received 25 January 1985)

In Parts I and II the inelastic mean free path of electrons has been determined from their elastic scattering measured by elastic peak electron spectroscopy. The simple theoretical model based on the Thomas–Fermi–Dirac (TFD) atomic potential has been extended to higher kinetic energies. The σ_{eff} effective and σ_T total elastic scattering cross sections have been calculated for $Z = 2$–50 atomic number and $E = 5$–40 keV kinetic energy range. The σ_{eff} values deduced from Riley's results are similar and agree within a factor of 2. The elastic differential cross sections determining also the angular distribution of elastic scattering are discussed for the TFD, screened Rutherford, Fink and Riley models. The application of elastic scattering is promising for scanning electron and Auger microscopy and for thin film in depth analysis using REELS and EPES. Some possibilities are briefly treated.

Introduction

In Part I of this work [1] a simplified method has been described for determining the inelastic mean free path (IMFP) by evaluating EPES experimental data [2] with Eqs (4–6) in [1]. The effective scattering cross sections have been tabulated in [1] for the $Z = 2$–50 atomic number and $E = 1$–3 keV kinetic energy range.

Very recently elastic scattering came in the focus of interest for scanning electron microscopy. A number of new works have been published in this field by Niedrig [3], Seiler [4], Reimer [5], Hoffmann et al [6], dealing also with the differential scattering cross sections $\frac{d\sigma(\Theta)}{d\Omega}$ and considering previously published tabulated data of Riley et al [7].

* Address: 1325 Budapest, P.O. Box 76, Hungary
** Address: 01-224 Warszawa, ul. Kasprzaka 44

As shown in [1] the probability of electron elastic scattering P_e is:

$$P_e = \lambda N_A \sigma_{\text{eff}}, \tag{1}$$

with

$$\sigma_{\text{eff}} = 2\pi \int_{\pi/2}^{\pi} \frac{d\sigma(\Theta)}{d\Omega} \frac{\sin \Theta}{1 - \sec \Theta} d\Theta \tag{2}$$

denoting by Θ the scattering angle and by N_A the density of atoms in the solid.

In this paper σ_{eff} calculations based on the Thomas–Fermi–Dirac potential model are extended to the $E = 5$–40 keV kinetic energy range useful for electron microscopy. $\frac{d\sigma(\Theta)}{d\Omega}$ has been calculated for angular corrections in EPES experimental work and electron microscopy applications. The total elastic scattering cross sections σ_T have been calculated with TFD model.

In this Part III the same notations are used as in Part I [1].

1. The effective backscattering cross sections for the $E = 5$–40 keV range

The σ_{eff} elastic backscattering cross sections have been calculated for the $Z = 2$–50 atomic number range using the Thomas–Fermi–Dirac (TFD) atomic potential model as described in [1]. Our extended σ_{eff} data versus Z are presented in Figs 1 and 2.

For comparing our σ_{eff} data with those deduced from Riley's work some results are recollected in Table I. In Riley's paper [7] tabulated $\frac{d\sigma(\Theta)}{d\Omega}$ results have been published for a number of elements and some selected E kinetic energy values. To determine λ by EPES, $\frac{d\sigma(\Theta)}{d\Omega}$ values are needed in the $\Theta = 90$–$180°$ range. The steps in Riley's Tables are $\Delta\Theta = 10°$ in this range.

In Table I σ_{eff} is given also for Ta and Au using Riley's data missing in [1] since the first Born approximation is valid below $Z < 50$ [8].

Comparing the σ_{eff} data of Table I with those in [1] calculated with the TFD etc. models, they agree within a factor 0.5–0.86 and they exhibit similar variations with Z and E.

2. Differential elastic scattering cross-sections

In the literature abundant data are available on the differential elastic cross-sections [5], [7], Fink [9], Ichimura [10]. Ichimura et al used the partial plane wave expansion method and for some elements they compared results with the screened Rutherford cross sections without indicating the screening factor. The various electron

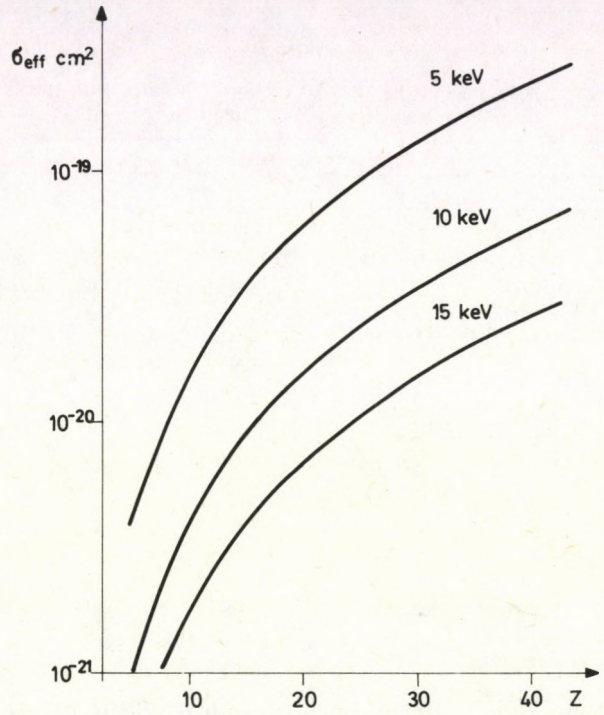

Fig. 1. The variation of σ_{eff} with atomic number Z in the 5–15 keV kinetic energy range

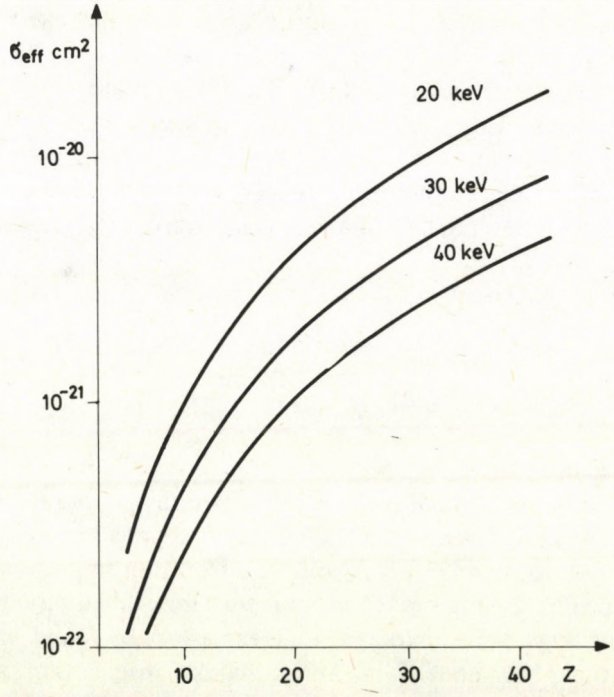

Fig. 2. The variation of σ_{eff} with atomic number Z in the 20–40 keV kinetic energy range

Table I

The effective elastic backscattering cross sections calculated with Riley's data: for some elements: σ_{eff} [10^{-18} cm^2]

Z	Kinetic energy of electrons in keV				
	1	2	4	8	16
6	0.1736	0.04118			
8	0.3188	0.07568	0.01788	0.004259	0.001024
13	0.9544	0.2177	0.05046	0.011886	0.002824
14	1.12305	0.2570			
26	3.7056	1.0034	0.2403	0.05483	0.012766
29	4.5523	1.2735	0.3104	0.07109	0.01643
42	7.0836	2.5299	0.6969	0.1705	0.03996
47	7.8817	2.9891			
73	11.341	5.1951			
79	11.1495	5.61959			

scattering models supply considerable differences in $\frac{d\sigma(\Theta)}{d\Omega}$ for very low angle scattering ($\Theta \cong 0$, forward scattering).

Some of our $\frac{d\sigma(\Theta)}{d\Omega}$ results calculated with the TFD model are presented in Table II for $Z = 8$ and 29, $E = 1$ and 2 keV kinetic energy. They are compared with the screened Rutherford cross sections (screening factor = 1) using the Wentzel formula cited by Niedrig [11]. In Table II comparison is made with the Mott factor R [5] denoting the ratio of cross section TFD/screened Rutherford.

To determine the IMFP by EPES, electron spectrometers are used. Experimental data have been reported using CMA [8] or retarding field analyser (RFA) [12–13]. The CMA is collecting electrons under $\Theta = 138°$ scattering angle with $\Delta\alpha = 7°$ opening whereas the retarding field analyser is integrating electrons scattered within $\alpha = 180° - \Theta$, $\alpha = 6$ to $52°$.

The distribution of electrons scattered at angle α $N_{en}(\alpha, Z)$ is determined by [1], [13], [16]

$$N_{en}(\alpha, Z) \sim \frac{d\sigma(\alpha, Z)}{d\Omega} \frac{\sin \alpha}{1 + \sec \alpha} \Delta\alpha . \tag{3}$$

$\Delta\alpha$ is the angular opening of the spectrometer.

In Figs 3–5 the normalized $N_{en}(\alpha, Z)$ distributions are plotted versus α for the TFD, Fink and Riley differential scattering cross sections and compared with the Lambertian distribution. $\alpha = 42°$ (CMA) and the integration limits $\alpha = 6°$ and $52°$ (RFA) [12–13] are marked in the Figures. They are needed for evaluating experimental data.

Comparing Figs 3–5 remarkable differences can be found among the three models. Using the TFD model (Fig. 5) the angular distribution of backscattered

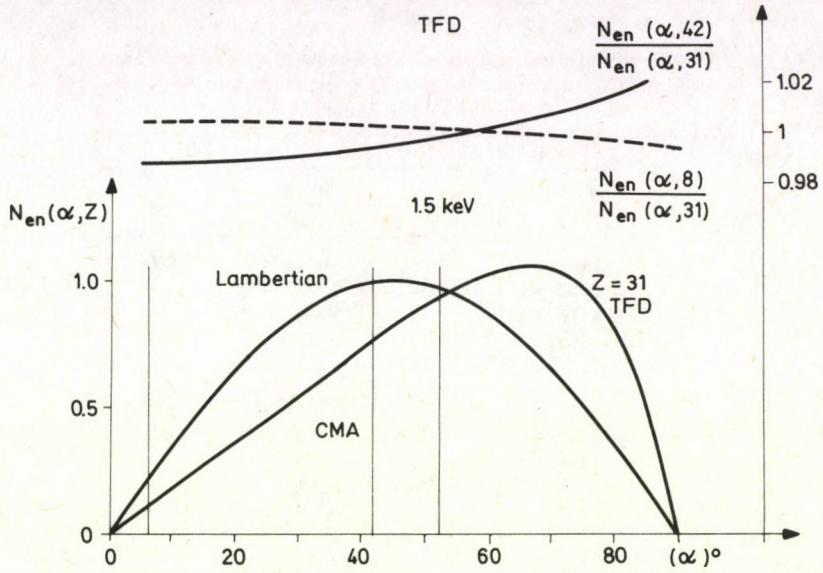

Fig. 3. The normalized angular dependence $N_{en}(\alpha, Z)$ of elastically scattered electrons, based on the TFD model. The upper curves present comparison of O and Mo resp. with Ga on enlarged scale. Kinetic energy 1.5 keV

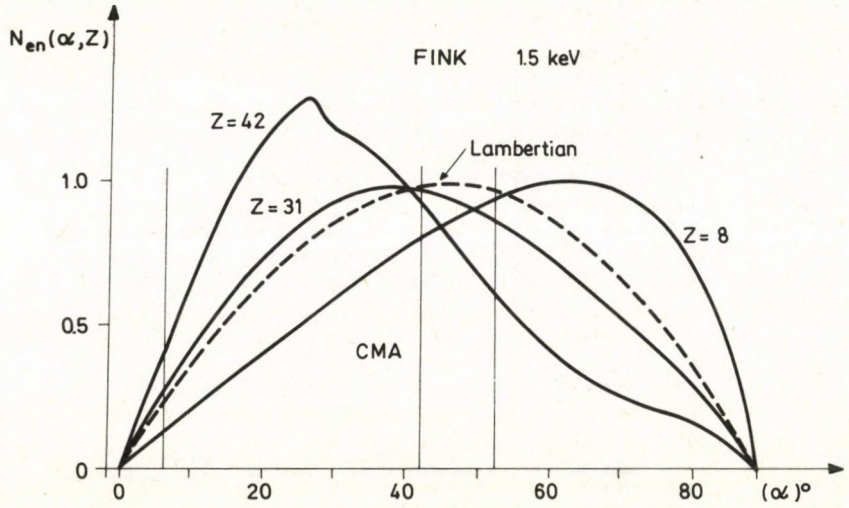

Fig. 4. The angular dependence of $N_{en}(\alpha, Z)$ for O, Ga and Mo based on Fink's data. Kinetic energy 1.5 keV

electrons hardly differs. On the upper part of Fig. 5 $N_{en}(\alpha, Z)$ are compared for $Z = 8, 31$ and 42, resp. In the backscattered angular range max. $\pm 2\%$ deviations occur.

In Fig. 5 $N_{en}(\alpha, 79)$ is presented for Au. The shift of the maximum toward low α has been mentioned in [12, 13], however, the extreme low value at $\alpha = 42°$ is

Table II

The differential elastic scattering cross sections in 10^{-16} cm^2/sr units for Al and Cu, calculated with the TFD model and for comparison the corresponding Mott factors ($X = 1$)

Angle Θ^0	Al 1 keV		Cu 1 keV	
	$\frac{d\sigma(\Theta)}{d\Omega}$	R	$\frac{d\sigma(\Theta)}{d\Omega}$	R
0	0.1664 +2	2.68	0.4942 +2	4.66
5	0.1047 +2	2.05	0.3203 +2	3.39
10	0.4129 +1	1.31	0.1342 +2	1.94
15	0.1666 +1	0.976	0.5763 +1	1.274
20	0.7707 +0	0.843	0.2817 +1	1.00
25	0.4033 +0	0.793	0.1543 +1	0.880
30	0.2320 +0	0.779	0.9205 +0	0.829
35	0.1434 +0	0.781	0.5858 +0	0.806
40	0.9380 −1	0.789	0.3919 +0	0.799
45	0.6420 −1	0.801	0.2730 +0	0.798
50	0.4557 −1	0.811	0.1968 +0	0.802
55	0.3342 −1	0.822	0.1461 +0	0.807
60	0.2519 −1	0.831	0.1112 +0	0.812
65	0.1946 −1	0.840	0.8660 −1	0.818
70	0.1535 −1	0.848	0.6882 −1	0.823
75	0.1235 −1	0.855	0.5569 −1	0.829
80	0.1011 −1	0.862	0.4582 −1	0.834
85	0.8408 −2	0.867	0.3829 −1	0.839
90	0.7096 −2	0.872	0.3244 −1	0.843
95	0.6071 −2	0.877	0.2785 −1	0.847
100	0.5260 −2	0.881	0.2420 −1	0.851
105	0.4610 −2	0.885	0.2127 −1	0.854
110	0.4086 −2	0.888	0.1890 −1	0.858
115	0.3659 −2	0.891	0.1696 −1	0.860
120	0.3310 −2	0.894	0.1537 −1	0.863
125	0.3022 −2	0.896	0.1406 −1	0.865
130	0.2785 −2	0.898	0.1298 −1	0.868
135	0.2589 −2	0.909	0.1208 −1	0.870
140	0.2427 −2	0.902	0.1134 −1	0.872
145	0.2294 −2	0.903	0.1072 −1	0.873
150	0.2185 −2	0.904	0.1022 −1	0.874
155	0.20975−2	0.905	0.9823 −2	0.875
160	0.2029 −2	0.906	0.9508 −2	0.876
165	0.1979 −2	0.907	0.9271 −2	0.877
170	0.1942 −2	0.907	0.9106 −1	0.877
175	0.1921 −2	0.907	0.9008 −2	0.878
180	0.1914 −2	0.907	0.8977 −2	0.878

Table II (cont.)

Angle Θ^0	Al 2 keV		Cu 2 keV	
	$\frac{d\sigma(\Theta)}{d\Omega}$	R	$\frac{d\sigma(\Theta)}{d\Omega}$	R
0	0.1664 +2	2.68	0.4942 +2	4.66
5	0.7242 +1	1.29	0.2269 +2	2.68
10	0.1923 +1	1.01	0.6585 +1	1.35
15	0.6465 +0	0.825	0.2393 +1	0.960
20	0.2735 +0	0.781	0.1074 +1	0.841
25	0.1353 +0	0.782	0.5546 +0	0.805
30	0.7463 −1	0.795	0.3154 +0	0.798
35	0.4459 −1	0.812	0.1928 +0	0.802
40	0.2835 −1	0.827	0.1247 +0	0.810
45	0.1896 −1	0.841	0.8444 −1	0.818
50	0.1321 −1	0.853	0.5946 −1	0.826
55	0.9537 −1	0.863	0.4329 −1	0.835
60	0.7096 −2	0.872	0.3244 −1	0.843
65	0.5422 −2	0.880	0.2493 −1	0.850
70	0.4240 −2	0.887	0.1960 −1	0.857
75	0.3385 −2	0.893	0.1572 −1	0.863
80	0.2754 −2	0.898	0.1283 −1	0.868
85	0.2278 −2	0.903	0.1065 −1	0.873
90	0.1914 −2	0.907	0.8977 −2	0.878
95	0.1631 −2	0.911	0.7670 −2	0.882
100	0.1408 −2	0.914	0.6638 −2	0.886
105	0.1231 −2	0.918	0.5814 −2	0.889
110	0.1088 −2	0.920	0.5150 −2	0.893
115	0.9722 −3	0.923	0.4610 −2	0.895
120	0.8778 −3	0.925	0.4168 −2	0.898
125	0.8002 −2	0.927	0.3805 −2	0.900
130	0.7363 −3	0.929	0.3505 −2	0.902
135	0.6836 −3	0.930	0.3258 −2	0.905
140	0.6401 −3	0.931	0.3053 −2	0.906
145	0.6044 −3	0.933	0.2885 −2	0.908
150	0.5753 −3	0.934	0.2748 −2	0.909
155	0.5520 −3	0.934	0.2638 −2	0.910
160	0.5337 −3	0.935	0.2552 −2	0.911
165	0.5195 −3	0.936	0.2487 −2	0.911
170	0.5104 −3	0.936	0.2442 −2	0.912
175	0.5046 −3	0.936	0.2416 −2	0.912
180	0.5029 −3	0.436	0.2407 −2	0.912

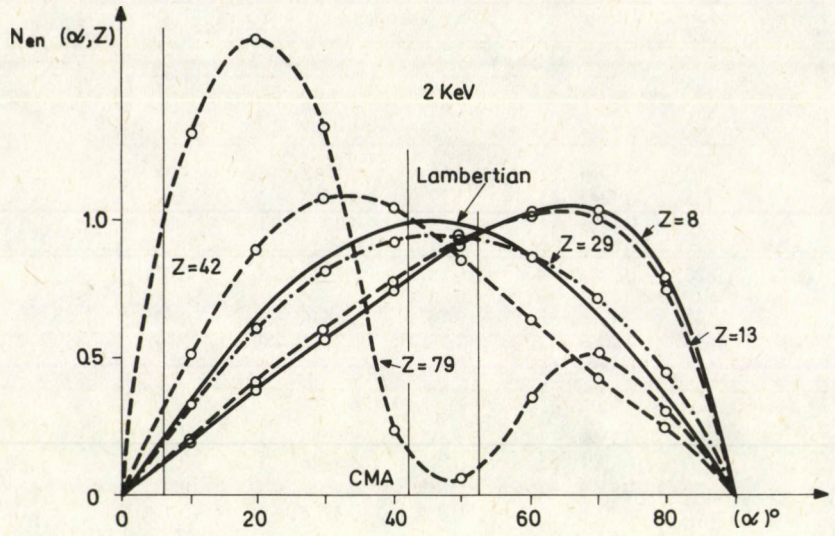

Fig. 5. The angular dependence of $N_{en}(\alpha, Z)$ based on Riley's data for O, Al, Cu and Au. Kinetic energy 2 keV

contradictory to experimental results [2, 8, 12, 13]. On the other hand, for low atomic numbers ($Z \leq 15$) the angular distributions are very similar for the TFD and Riley models.

For elastic peak electron spectroscopy the $\alpha = 0$–$90°$ angular range is used. The angular distribution of elastic scattering, however, is very important in Monte Carlo analysis of scattering processes (Shimizu et al [14], Fitting [15]). Very recently a Monte Carlo analysis for multiple elastic scattering has been elaborated using the TFD model [16] and supplying a more accurate approach for determining λ.

3. The total elastic scattering cross section

Integrating $d\sigma(\Theta)/d\Omega$ supplies the total elastic scattering cross sections σ_T, an important physical parameter needed also for Monte Carlo analysis [14–16]. In the recent literature several papers have been published containing σ_T data [5, 7, 17]. They are more or less different, like $d\sigma(\Theta)/d\Omega$, corresponding to the model used in calculations. σ_T has been calculated for selected elements and kinetic energies. In this work σ_T has been calculated for $Z = 2$–50 atomic number and $E = 1$–15 keV kinetic energy range using the Hartree–Fock, Thomas–Fermi and Thomas–Fermi–Dirac atomic potential models [1]. Some results are presented in Fig. 6 for C, O, Al, Ti, Ge, Cu, Mo, etc.

Regarding our recent results, σ_T calculated with the Hartree–Fock or Thomas–Fermi models are somewhat larger than those deduced by the TFD model. Our σ_T data

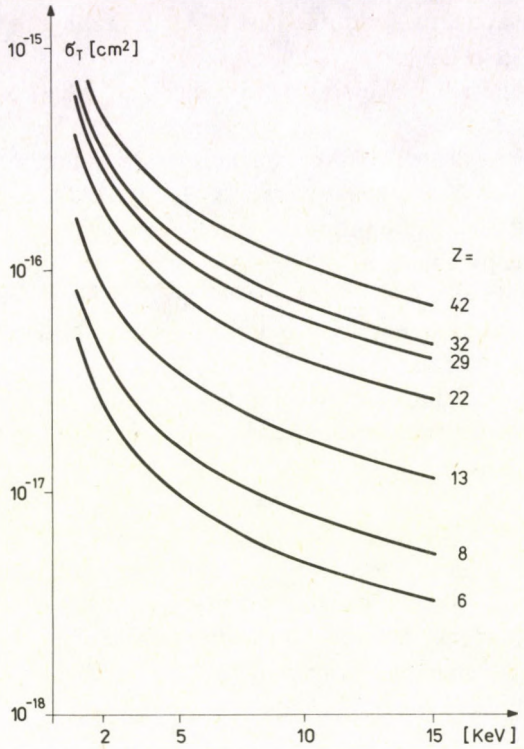

Fig. 6. The dependence of σ_T on the kinetic energy, based on the TFD model

are higher than Ichimura's or Riley's results. For low atomic numbers $Z \leq 13$ they are quite close. σ_T cross sections are approaching with increasing kinetic energy for all the models. Our σ_T results exhibit similar character for the total $Z = 2$–50 range like the corresponding σ_{eff} data presented in detail in [1].

4. Applications of elastic electron scattering in thin film studies

Niedrig [3] and Seiler [4] discussed applications of elastic peak electron spectroscopy to scanning electron microscopy (SEM) in their lectures presented at EUREM'84. Beside of many details of applications the image contrast can be improved considerably in this way. For this purpose the effective elastic scattering cross sections have been calculated by extending the kinetic energy range up to 40 keV as discussed in paragraph 1 of this paper. The angular distribution of elastic scattering is determined by the differential cross sections being very important also in SEM and treated in Section 2 of this paper. Conventional scanning electron microscopes are not supplied with an electron spectrometer. Scanning Auger microscopes are confined to

the $E \leq 2$–3 keV energy range. A double pass CMA operating up to 20 keV has been described by Varga et al [18].

Beside topographic surface studies, the depth profiling of thin films is very important and needed in electron microprobe analysis. Recently Pouchou [19] developed EPMA for in-depth profiling thin films by scanning the primary energy and analysing X-ray (or soft X-ray) emission peaks. By this method a wide range of film thickness can be analysed. The depth resolution is determined and limited by the total wide range of impinging electrons.

A much better depth resolution can be achieved by ion milling generally used in thin film in-depth profiling, its depth resolution, however, is determined and limited by ion beam effects and artifacts.

Presently the best depth resolution in thin film analysis is obtained by angular resolved X-ray photoelectron spectroscopy (ARXPS). The range of analysis is determined by the X-ray source (in practice using Mg or Al anodes) making 3–4 nm. Similar good depth resolution can be expected of elastic electron scattering. EPES can be used for non destructive depth profiling of thin films by scanning the primary energy. A two components system (e.g. oxide on a metal or semiconductor) can be studied in this way. As shown in [2] the information depth of EPES makes λ for a CMA type spectrometer. A similar possibility is offered by REELS (EELS in reflection mode) applying plasmon or core level loss peaks [20, 21].

References

1. A. Jablonski, P. Mrozek, G. Gergely, M. Menyhárd and A. Sulyok; Acta Phys. Hung., *57*, 131, 1985.
2. G. Gergely, Surf. Interface Anal., *3*, 201, 1981.
3. H. Niedrig, Proc. Electron Microscopy, EUREM '84 Budapest, Ed. MOTESZ, Budapest, p. 627, 1984.
4. H. Seiler, Proc. Electron Microscopy, EUREM '84, Budapest, Ed. MOTESZ, Budapest, p. 563, 1984.
5. L. Reimer and B. Lödding, Scanning, *6*, 128, 1984.
6. K. E. Hoffmann and H. Schmoranzer, in Electron Beam Interactions, SEM Inc. AMF I'Hare, p. 209, 1983.
7. M. E. Riley, C. J. MacCallum and F. Biggs, Atomic Data, *15*, 443, 1975.
8. G. Gergely, M. Menyhárd, A. Sulyok, A. Jablonski and P. Mrozek, Acta Phys. Hung., *57*, 139, 1985.
9. M. Fink et al., Atomic Data *1*, 385, 1970; *4*, 129, 1972; *14*, 39, 1974.
10. Y. Ichimura, M. Aratama and R. Shimizu, J. Appl. Phys., 2854, 1980.
11. H. Niedrig, Scanning Electron Microscopy, *I* 841, 1978.
12. R. Schmid, K. H. Gaukler and H. Seiler, Scanning Electron Microscopy, *II*, 501, 1983.
13. R. Schmid, Dissertation, Eberhard–Karls Universität zu Tübingen, 1982.
14. R. Shimizu and S. Ichimura, Surface Sci., *133*, 250, 1983.
15. H. J. Fitting and J. U. Friedmann, phys. stat. sol. (a), *69*, 349, 1983.
16. A. Jablonski, Surface Sci., *151*, 166, 1985.
17. S. Ichimura and R. Shimizu, Surface Sci., *112*, 386, 1981.
18. D. Varga, I. Kádár, I. Cserny, Gy. Mórik, V. Brabac, O. Dragoun, A. Kovalik and J. Adam, Nucl. Instrum. and Meth., *192*, 277, 1982.
19. J. L. Pouchou, J. Microsc. Spectrosc. Electronique, *9*, 99, 1984.
20. C. Jardin, Thèse, Université Claude Bernard de Lyon, 1981.
21. M. Menyhárd, A. Sulyok and G. Gergely, Proc. Electron Microscopy EUREM '84 Budapest, Ed. MOTESZ p. 459, 1984.

Acta Physica Hungarica 60 (3—4), pp. 299—303 (1986)

TECHNICAL CONSTRAINTS FOR THE GUT SCALE PARAMETER

L. DIÓSI and B. LUKÁCS

Central Research Institute for Physics
1525 Budapest, Hungary

BETTINA KESZTHELYI

Roland Eötvös University, 1088 Budapest, Hungary

and

G. PAÁL

Konkoly Observatory of the Hungarian Academy of Sciences
1525 Budapest, Hungary

(Received 12 February 1985)

The influence of the Grand Unification scale on the thermal history of the early Universe is discussed. Above $M \simeq 6.8 \cdot 10^{15}$ GeV the irreversibilities seem to be too strong to ignore them, and the usual calculations lose their validity. Therefore at such scale parameters the low upper bound yielded by observations for the monopole/entropy ratio is not neccessarily a counterevidence against the minimal SU(5) GUT.

To describe the very early Universe one needs a theory with definite predictions at energies much higher than the observed particle masses. This is the case in Grand Unified Theories (GUTs). Such theories contain a mass scale parameter M, much higher than the experimentally accessible energies, so it cannot be directly measured. If M is taken as a free parameter, it seems that any choice for it leads to some problem. If M is too low, the proton lifetime is too short (except for sophisticated models where it is absolutely stable [1]). At medium values the monopole problem appears: the massive monopoles created in the symmetry breaking phase transition tend to survive and to dominate the present Universe, leading to unacceptable dynamical consequences [2–5]. Finally, for too high M values the predictions of the present form of the theory cease to be definite [2].

Perhaps the most direct contradiction between theory and observation is represented by the monopole dominance. Various mechanisms have been suggested for avoiding this problem, as inflation [6–8], multiple phase transition [9], colors for monopoles [10], exponential suppression by a Boltzmann factor [11], etc. It has also been observed that one can at least choose among the above problems. Namely, extreme values of M may eliminate the monopole problem in some sense [2, 12], because the recent predictions for the surviving monopole number are not valid if

a) $M < 10^{10}$ GeV, when the annihilation rate is high enough, or if
b) $M > 3 \cdot 10^{17}$ GeV, when the monopole mass is above the Planck mass. Then the calculations would need a full and well elaborated quantum gravity theory, which is not at reach.

In Case b) there is no prediction for the surviving monopole number, so, according to the presumption of innocence, there is no evidence against GUT. Nevertheless, the critical value for M seems to be improbably high [2, 12].

Here we are going to show a lower value for M, above which the validity of the recent calculations is not well founded. Namely, the effects of some irreversible processes increase with M [13] so that for some higher values of M they are to be taken into account, but from a critical value $M = M_{\text{crit}} \simeq 10^{16}$ GeV there is no more guarantee whatsoever that the only technically accessible formalism for their calculation—the linear perturbation technique—still yields realistic results. In addition to this, calculations performed above M_{crit} lead to violation of the dominant energy condition [14] which may also be a signal that the model may have been used beyond the limits of its applicability. Since a more general proper inequilibrium treatment seems to be not at reach, so, from a technical viewpoint, we arrive at a limit above which the recent calculations are no more reliable. While such a value may still be too high compared to the extrapolations of low energy observations, it is definitely more conceivable than the quantum limit $M = 3 \cdot 10^{17}$ GeV, so this technical upper limit deserves some attention.

Assume that the matter is a charge-symmetric fluid (which seems to be true for the very early Universe), and that the linear transport laws are valid. Then, for a parabolic Robertson–Walker Universe, the evolution is governed by the equations [13]

$$\begin{aligned} \ddot{R} &= -\frac{4\pi}{3m_{\text{Pl}}^2}\left(\rho + 3p - 9\zeta\frac{\dot{R}}{R}\right)R\,, \\ \dot{R}^2 &= \frac{8\pi}{3m_{\text{Pl}}^2}\rho R^2\,, \\ p &= p(T)\,, \\ \zeta &= \zeta(T)\,, \\ \rho &= Tp_T - p\,, \end{aligned} \tag{1}$$

where m_{Pl} stands for the Planck mass, $1.22 \cdot 10^{19}$ GeV, p is the pressure, ρ is the energy density, ζ is the bulk viscosity coefficient, and the lower index denotes derivation; $\hbar = c = k_B = 1$. By eliminating the scale factor R of the Universe, hence one gets an equation for the thermal history as follows [13]:

$$p_{TT}\,T\dot{T} = -3\left\{Tp_T\frac{1}{m_{\text{Pl}}}\sqrt{\frac{8\pi}{3}(Tp_T - p)} - 8\pi\frac{\zeta}{m_{\text{Pl}}^2}(Tp_T - p)\right\}. \tag{2}$$

If the second term on the right hand side is not negligible, then the influence of the bulk viscosity is serious. If the second term dominates the first one, the temperature is increasing during expansion, and at the same time Eq. (1) shows that $\rho + P < 0$ (where $P = p - 3\zeta\dot{R}/R$ is the isotropic stress), so the dominant energy condition [14] is violated, too. An approximate balance of the two terms would lead to inflation [13], thus eliminating the monopole dominance [6].

Simple GUTs contain a single mass scale parameter, therefore the ratio of the two terms is a function of M alone at the phase transition temperature, but the correct evaluation of Eq. (2) is still technically impossible. Let us assume a radiation-dominated approximation [6] for p:

$$p(T) = \frac{\pi^2}{90} N T^4 , \tag{3}$$

where $N \simeq 160$ in minimal GUT. Assume, too, that the symmetry breaking phase transition is of first order. Then the transition temperature T_{tr}, the massive boson (leptoquark) mass m and the scale parameter M are in the same order of magnitude, the numerical factors depend on the actual model (for further discussions see e.g. [1] and [15]). As a model-independent estimation here we take

$$T_{tr} = m = M . \tag{4}$$

If T_{tr} and m are in the same order of magnitude, the bulk viscosity is substantial. Namely, in a gas of point particles a bulk viscosity appears [16] which is maximal at $T \sim m$. If the cross section is $\sigma \sim \alpha^2/T^2$, then, neglecting numerical factors of order of 1, depending on the details of the differential cross section, the maximal value of ζ is

$$\zeta \simeq m^3/\alpha^2 . \tag{5}$$

Then, accepting the approximate equalities (3–5), just after the phase transition Eq. (2) yields

$$(\dot{T})_{T_{tr}-0} \simeq -2\pi m_{Pl}^2 x^3 \left(\sqrt{\frac{N\pi}{45}} - \frac{3}{\alpha^2} x \right),$$

$$x = \frac{M}{m_{Pl}} . \tag{6}$$

So the critical value separating cooling and heating is $x = 5.5 \cdot 10^{-4}$, that is, $M = 6.8 \cdot 10^{15}$ GeV. Thus, when M is several times 10^{15} GeV, the irreversibilities are not negligible, the entropy is growing. Such an effect may lead to a low present monopole/proton ratio. Above $M = 6.8 \cdot 10^{15}$ GeV the linear approximation of momentum transfer leads to a reheated Universe going back to the symmetric phase.

Since the phase transition has obviously been finished, accepting the linear transport laws one could conclude that $M \lesssim 6.8 \cdot 10^{15}$ GeV. However, the applicability of the linear laws seems awkward at this M value. First, $M > 6.8 \cdot 10^{15}$ GeV would

violate the energy positivity. While energy positivity is a principle rather than an established law [14] there are no evidences that $\rho + P < 0$ violates fundamental laws, and such states can sometimes be produced by seemingly innocent transport laws (cf. Sol. VIII in [17]), on the other hand, $\rho + P < 0$ states are sufficiently exotic to be sceptical about them. Second, the actual form of the isotropic stress in Eq. (1) is a power expansion in the deformation velocity tensor, and at the critical point the second term of the expansion is already greater than the first one.

Thus one should check the validity of the linear laws. They belong to near-equilibrium thermodynamics. This latter formalism is not self-consistent if the changes (e.g. in momentum distribution) are not moderate between two subsequent collisions. This, following the idea in [18] leads to an order of magnitude unequality

$$\frac{(sR^3)^{\cdot}}{(sR^3)} \lesssim \frac{1}{\tau}. \tag{7}$$

Now, calculating the entropy density s from Eq. (3) and estimating the collision time as $\tau \sim (n\sigma)^{-1} \simeq (\alpha/\pi)^2 NT$, one obtains that the two sides of inequality (7) are equal at $M = 3.2 \cdot 10^{15}$ GeV [19], which is in the same order of magnitude as the critical value of M. Therefore the result is not decisive: it seems that if $M = 6.8 \cdot 10^{15}$ GeV, the actual state is not necessarily far from equilibrium, but it is not necessarily near either. In any case, at $M = 6.8 \cdot 10^{15}$ GeV the irreversibilities are strong and important in the system, thus their neglection invalidates the usual calculations.

Because of the strong simplifications this calculation is scarcely more than a dimensional analysis. As such, it can, however, be used to formulate the following conclusions. Having so far no proper nonperturbative treatment of the momentum transfer processes in a GUT continuum near to the phase transition, the upper limit for M, until which the recent calculations are reliable, is determined by the breakdown of the linear transport formalism. As far as this value can be estimated, it is in the same order of magnitude as the critical value $M = 6.8 \cdot 10^{15}$ GeV, where the linear laws lead to the breakdown of the energy positivity. With such a high scale parameter two alternative conclusions would be possible: if the linear laws are still approximately valid, the entropy growth drives an inflation eliminating the monopole dominance; if the linear laws are not valid, one cannot make definite predictions without manufacturing nonperturbative techniques for the nonequilibrium thermodynamics of the GUT continuum (which may be quite as complicated technically as quantum gravity).

This technical upper limit lies well below $M \simeq 3 \cdot 10^{17}$ GeV, where the unknown quantum corrections are expected to become large. Of course, the troubles between $6.8 \cdot 10^{15}$ GeV and $3 \cdot 10^{17}$ GeV arise from less august source than those above $3 \cdot 10^{17}$ GeV. Nevertheless, from a higher (and still unoccupied) viewpoint the difference is not absolute but of degree, and in both cases the problems are technical. Namely, in the final and well elaborated unification of gravity and field theories both problems would be somehow solved.

References

1. P. Langacker, Phys. Rep., *72*, 185, 1981.
2. J. Preskill, Phys. Rev. Lett., *43*, 1365, 1979.
3. Ya. B. Zel'dovich and M. Y. Khlopov, Phys. Lett., *79B*, 239, 1973.
4. T. W. Kibble, J. Phys. *A9*, 1387, 1976.
5. T. W. Kibble, in: Monopoles in Quantum Field Theories (eds. M. S. Craigie et al), World Scientific, Singapore, 1982, pp. 341–376.
6. A. Guth, Phys. Rev., *D23*, 347, 1981.
7. A. D. Linde, Phys. Lett., *108B*, 389, 1982.
8. A. Albrecht and P. J. Steinhardt, Phys. Rev. Lett., *48*, 1220, 1982.
9. P. Langacker and S–Y. Pi, Phys. Rev. Lett., *45*, 1, 1980.
10. A. D. Linde, Phys. Lett., *96B*, 293, 1980.
11. F. A. Bais and S. Rudaz, Nucl. Phys., *B170*, 507, 1980.
12. J. N. Fry and D. N. Schramm, Phys. Rev. Lett., *44*, 1361, 1980.
13. L. Diósi, Bettina Keszthelyi, B. Lukács and G. Paál, Acta Phys. Pol., *B15*, 909, 1984.
14. S. Hawking and G. F. R. Ellis, The Large Scale Structure of Space-Time, Cambridge Univ. Press, London 1973.
15. L. Diósi, Bettina Keszthelyi, B. Lukács and G. Paál, Astron. Nachr. *306*, 213, 1985.
16. J. M. Stewart, in: Cargèse Lectures in Physics VI (ed. E. Schatzman), Gordon and Breach, New York–London–Paris, 1973.
17. B. Lukács, Gen. Rel. Grav., *7*, 653, 1976.
18. L. P. Csernai and B. Lukács, Acta Phys. Pol., *B15*, 149, 1984.
19. For an alternative approach to compare the characteristic time of cooling to the collision time, which yields practically the same value for T, see e.g.: J. Ellis and G. Steigman, Phys. Lett., *89B*, 186, 1980.

Acta Physica Hungarica 60 (3—4), pp. 305—317 (1986)

NONLINEAR CORRECTIONS TO THE THERMODYNAMICS OF NORMAL FERMI LIQUID

I. H. KRZYŻANOWSKI and L. JACAK

Institute of Physics, Technical University of Wrocław
*Wrocław, Poland**

(Received 19 February 1985)

Thermal properties of the normal Fermi liquid are studied including nonlinear corrections to the Landau kinetic theory. It is established that the effective mass formula is temperature invariant. The expressions for the most important thermal quantities are obtained with accuracy up to T^3 order. The corrections obtained include the additional external parameters being essential to the nonlinear approach.

1. Introduction

The purpose of the present paper is to rediscuss the thermal properties of the normal Fermi liquid including nonlinear corrections to the Landau theory (cf. [1]–[4]). The nonlinear generalization of the Landau theory is based on some quasiparticle-effective-interaction extensions which are introduced in [5]. In this paper we have obtained formulae for such characteristics of the normal Fermi liquid as heat capacity, entropy, compressibility and pressure. New parameters analogous with Landau amplitudes, i.e. the derivatives of Landau's $f_{pp'}$ interaction function with respect to lengths of momentum vectors and the same for the additional interaction function $g_{pp'p''}$ (cf. [5]), enter all the obtained formulae.

Our results are equivalent in the lowest order with respect to temperature to the previous calculations performed originally by Landau in the linear approximation (cf. [1]–[2]). Heat capacity of the normal Fermi liquid was considered also by Richards (cf. [11]), in the framework of the linear theory. His results, analogous, however, with the respective ones from the present paper, were calculated in an inconsistent way due to exceeding the accuracy of the linear approach. Our predictions concerning the hydrodynamic sound velocity are, in the limit $T=0$, in a good agreement with the respective ones in the original theory (cf. [3]–[4]).

Let us emphasize that we do not consider an influence of collective excitations of the system on the thermal characteristics, even though it is well known that some

* Address: Instytut Fizyki, Politechnika Wrocławska, Wybrzeże Wyspiańskiego 27, 50–370 Wrocław, Poland

singular contributions are connected with the coupling of quasiparticles with the collective excitations. For the entropy of the system such a term is of the type $T^3 \ln T$. That problem was previously examined for the scattering of quasiparticles with a small energy and momentum transfer by Amit et al (cf. [6]–[8]), and recently for spin fluctuations by Pethick et al (cf. [9]–[10]).

All corrections obtained in the present paper are rather small in comparison with the non-analytic terms mentioned above which play the major role for the lowest temperatures. Nevertheless, it seems that the recent development of the experiment in the topic of normal He^3 (cf. [13]–[14]) needs inclusion of more precise, nonlinear analytical-type corrections to the thermal characteristics of this system.

2. Thermodynamics of the normal Fermi liquid

In this part of the paper we discuss the thermodynamics of the normal Fermi liquid in the framework of the nonlinear Landau theory proposed in [5].

Let us briefly recall the main assumptions of that approach. It is based on the Landau idea that the ground state and lowlying excited states of Fermi liquid exactly correspond with the respective states of Fermi gas, which makes an introduction of the distribution function of quasiparticles n_P possible (cf. [1]–[4]). For the ground state it is assumed that as for Fermi gas: $n_P^0 = 1 - \vartheta(\varepsilon_P - \mu_0)$, μ_0 is the chemical potential at $T=0$ and ε_P is the quasiparticle energy. The energy of the system is a functional with respect to $\delta n_P = n_P - n_P^0$ (cf. [5]):

$$\varepsilon E = \sum_P (\tilde{\varepsilon}_P - \mu_0)\delta n_P , \tag{1}$$

where

$$\tilde{\varepsilon}_P = \varepsilon_P^0 + \sum_{P'} f_{PP'}\delta n_{P'} + \sum_{P'P''} g_{PP'P''}\delta n_{P'}\delta n_{P''} \tag{2}$$

and

$$\varepsilon_P^0 = \mu_0 + v_F(|P| - P_F) + \alpha(|P| - P_F)^2 , \tag{3}$$

P_F is the Fermi momentum, $v_F = P_F/m^*$ is the Fermi velocity, m^* is the effective mass, α is an additional parameter introduced in order to include the nonlinear correction to ε_P^0, $f_{PP'}$ is the obvious Landau function. The function $g_{PP'P''}$ is the kernel of the introduced nonlinear term into the energy expansion. We have assumed that for short-range forces:

$$f_{PP'}(x, x') \sim \delta(x - x') , \quad g_{PP'P''}(x, x', x'') \sim \delta(x - x')\delta(x - x'') .$$

In order to be consistent with that accuracy, the effective interaction functions f and g do not depend only on the angles (i.e. on $\hat{P} \circ \hat{P}'$), but should be also the functions of magnitudes of the momentum vectors. Further via the Landau kinetic equation together with the gauge invariance, one can obtain the following formulae for the

effective mass m^* and α (cf. [5]):

$$m^* = m\left(1 + \frac{1}{3} F_1 \Big|_{|P|=|P'|=P_F}\right), \tag{4}$$

$$\alpha = \frac{1}{2}\left(\frac{1}{m} + \frac{P_F^2}{9m^{*2}} N_0 G_{110} \Big|_{|P|=|P'|=|P''|=P_F}\right), \tag{5}$$

where m is the bare mass of the particle, N_0 is the density of states on Fermi surface, F_1 is the spin symmetric part of the first Lengendre amplitude of $f_{PP'}$ multiplied by N_0 and

$$G_{110}|_{|P|=P'|=|P'''|=P_F} = -\frac{3m^*}{P_F N_0} \frac{\partial F_1}{\partial |P|}\Big|_{|P|=|P'|=P_F},$$

where indices of G correspond to a special choice of an angular representation for $g_{PP'P''}$ (for details cf. [5]).

Now we pay our attention to static thermal properties of the system described in the above manner. The quasiparticle distribution function n_P can be found from the maximum entropy principle. The entropy of the system can be written in the standard form (cf. [1]):

$$S = -\sum_P \{n_P \ln n_P + (1-n_P)\ln(1-n_P)\}. \tag{6}$$

Taking the additional conditions into account:

$$\delta E = \sum_P (\tilde{\varepsilon}_P - \mu_0)\delta n_P = 0 \qquad \text{and} \qquad \delta N = \sum_P \delta n_P = 0, \tag{7}$$

we obtain the well-known formula for the distribution function:

$$\tilde{n}_P^0 = \left(\exp\left(\frac{\tilde{\varepsilon}_P - \mu}{T}\right) + 1\right)^{-1}, \tag{8}$$

where μ is the chemical potential at temperature T. Note that Eq. (8) does not give the explicit form of $\tilde{n}_P^0$ because $\tilde{\varepsilon}_P$ also depends on $\tilde{n}_P^0$. The formula (8) describes the equilibrium distribution function for $T \neq 0$. In the kinetic equation, however, δn_P is a deviation of the quasiparticle distribution n_P from the ground state

$$n_P^0 = 1 - \vartheta(\varepsilon_P - \mu_0),$$

i.e.:

$$\delta n_P = n_P - n_P^0.$$

For a nonequilibrium state for $T \neq 0$ we can write:

$$\delta\tilde{n}_P = n_P - \tilde{n}_P^0 = \delta n_P + (n_P^0 \div \tilde{n}_P^0).$$

It is easy to notice that (cf. [15]):

$$\sum_P(\tilde{n}_P^0-n_P^0)=0\,,\qquad \sum_P P(\tilde{n}_P^0-n_P^0)=0$$

and

$$\sum_P J[\delta n_P]=0\,,\qquad \sum_P PJ[\delta n_P]=0\,, \tag{9}$$

where $J[\delta n_P]$ is the collision integral. Hence the temperature does not influence a derivation of the formulae for m^* and α performed in [5]. In the Landau-type theory the functions $f_{PP'}$ and $g_{PP'P''}$ are external parameters and we assume them to be independent of temperature. If we write now:

$$\tilde{\varepsilon}_P(T)=\varepsilon_P^0+\delta\varepsilon_P(T)\,, \tag{10}$$

where ε_P^0 is given by Eq. (3) (and is temperature independent) then $\delta\varepsilon_P(T)$ is defined by Eqs (2)–(3).

Let us emphasize that the small parameter of this theory:

$$\psi=\frac{\sum_P|\delta n_P|}{\sum_P n_P} \tag{11}$$

can be written as $\psi=6\ln 2\,\frac{m^*}{P_F^2}\,T+O(T^2)$. The expansion of the energy given by formula (2) includes the terms of order up to ψ^3. Thus, the assumed accuracy with respect to the temperature is T^3.

The average number of quasiparticles in the normal Fermi liquid is defined as:

$$\langle N\rangle=\sum_P n_P\,. \tag{12}$$

We will use the standard formula for the pressure:

$$P=-\frac{T}{V}\sum_P\ln(1-n_P)\,. \tag{13}$$

Note that in our approximation the Fermi liquid is treated as a Fermi gas of quasiparticles with assumed dispersion $\tilde{\varepsilon}_P$ (cf. [1]–[4], [11]).

Let us consider the problem of performing the integration with respect to momentum in formulae (6) and (12)–(13). They have the general form $\sum_P K[\tilde{n}_P^0]$, where K is the functional with respect to $\tilde{n}_P^0$. For this purpose we apply the procedure used by Richards (cf. [11]) which consists in a development of $K[\tilde{n}_P^0]$ into a power series with

respect to $\delta\varepsilon_P(T)$. We can write:

$$\sum_P K[\tilde{n}^0(\tilde{\varepsilon}_P)] = V\int_\lambda^{+\infty} d\varepsilon\rho(\varepsilon)\int\frac{d\Omega}{4\pi}\left\{K[\tilde{n}^0(\varepsilon)]+\right.$$

$$\left.+\left(\frac{\partial}{\partial\varepsilon}K[\tilde{n}^0(\varepsilon)]\right)\delta\varepsilon(\varepsilon)+\frac{1}{2}\left(\frac{\partial^2}{\partial\varepsilon^2}K[\tilde{n}^0(\varepsilon)]\right)\delta\varepsilon^2(\varepsilon)+\ldots\right\}, \tag{14}$$

where

$$\lambda=\varepsilon^0(P=0)$$

and

$$\rho(\varepsilon)=\frac{P^2}{\pi^2\hbar^3}\frac{d\,|P|}{d\varepsilon_P^0}.$$

Taking into account the definition of the entropy (cf. Eq. (6)) we have:

$$S=-V\int_\lambda^{+\infty} d\varepsilon\rho(\varepsilon)\left\{\tilde{n}^0(\varepsilon)\ln\tilde{n}^0(\varepsilon)+(1-\tilde{n}^0(\varepsilon))\ln(1-\tilde{n}^0(\varepsilon))-\right.$$

$$\left.-\frac{\varepsilon-\mu}{T}\tilde{n}^{0\prime}(\varepsilon)\delta\tilde{\varepsilon}(\varepsilon)-\frac{1}{2}\left(\frac{\varepsilon-\mu}{T}\tilde{n}^{0\prime\prime}(\varepsilon)+\frac{1}{T}\tilde{n}^{0\prime}(\varepsilon)\right)\delta\tilde{\varepsilon}^2(\varepsilon)+\ldots\right\}=$$

$$=\frac{V}{T}\int_\lambda^{+\infty} d\varepsilon\left\{\rho(\varepsilon)(\varepsilon-\mu)+R(\varepsilon)-\rho(\varepsilon)\delta\tilde{\varepsilon}(\varepsilon)-(\varepsilon-\mu)\frac{\partial}{\partial\varepsilon}(\rho(\varepsilon)\delta\tilde{\varepsilon}(\varepsilon))-\right.$$

$$\left.-\frac{1}{2}\frac{\partial}{\partial\varepsilon}(\rho(\varepsilon)\delta\tilde{\varepsilon}^2(\varepsilon))+\frac{1}{2}\frac{\partial^2}{\partial\varepsilon^2}((\varepsilon-\mu)\rho(\varepsilon)\delta\tilde{\varepsilon}^2(\varepsilon))+\ldots\right\}\tilde{n}^0(\varepsilon), \tag{15}$$

where

$$R(\varepsilon)=\int_\lambda^\varepsilon\rho(\varepsilon')d\varepsilon', \qquad \delta\tilde{\varepsilon}(\varepsilon)=\int\frac{d\Omega}{4\pi}\delta\varepsilon(\varepsilon).$$

The integral in the above equation (and similar in the present paper) can be calculated using the so-called Sommerfeld method (cf. [12]). This is plausible by virtue of inequality $\mu\gg T$. Thus we can write as follows:

$$\langle N\rangle=V\left\{R(\mu)+c_2T^2\rho'(\mu)+c_4T^4\rho'''(\mu)-\rho(\mu)\delta\tilde{\varepsilon}(\mu)-\right.$$

$$\left.-c_2T^2\frac{\partial^2}{\partial\varepsilon^2}(\rho(\varepsilon)\delta\tilde{\varepsilon}(\varepsilon))\,|_{\varepsilon=\mu}+\frac{1}{2}\frac{\partial}{\partial\varepsilon}(\rho(\varepsilon)\delta\tilde{\varepsilon}^2(\varepsilon))\,|_{\varepsilon=\mu}\right\}, \tag{16}$$

$$P=\left\{\int_\lambda^\mu R(\varepsilon)d\varepsilon+c_2T^2\rho(\mu)+c_4T^4\rho''(\mu)-\int_\lambda^\mu\rho(\varepsilon)\delta\tilde{\varepsilon}(\varepsilon)d\varepsilon-\right.$$

$$-c_2T^2\frac{\partial}{\partial\varepsilon}(\rho(\varepsilon)\delta\tilde{\varepsilon}(\varepsilon))\,|_{\varepsilon=\mu}+\frac{1}{2}\rho(\mu)\delta\tilde{\varepsilon}^2(\mu)\Big\}, \tag{17}$$

$$S=V\Big\{2c_2T\rho(\mu)+4c_4T^3\rho''(\mu)-2c_2T\frac{\partial}{\partial\varepsilon}(\rho(\varepsilon)\delta\tilde{\varepsilon}(\varepsilon))\,|_{\varepsilon=\mu}+$$

$$+c_2T\frac{\partial^2}{\partial\varepsilon^2}(\rho(\varepsilon)\delta\tilde{\varepsilon}^2(\varepsilon))\,|_{\varepsilon=\mu}\Big\}, \tag{18}$$

where c_2, c_4 are constants: $c_2=\frac{\pi^2}{6}$, $c_4=\frac{7\pi^4}{360}$ and

$$\rho'(\mu)=\frac{\partial}{\partial\varepsilon}\rho(\varepsilon)\,|_{\varepsilon=\mu}, \qquad \rho''(\mu)=\frac{\partial^2}{\partial\varepsilon^2}\rho(\varepsilon)\,|_{\varepsilon=\mu}, \quad \text{etc.}.$$

Let us further assume that the average number of the quasiparticles $\langle N\rangle$ is equal to that at the zeroth temperature:

$$\langle N(T)\rangle=\langle N(T=0)\rangle=VR(\mu_0).$$

Taking this assumption and Eq. (16) into account we can find the dependence of the chemical potential μ on temperature which has the form:

$$\mu-\mu_0=aT^2+O(T^4). \tag{19}$$

Note that we have omitted terms of higher order than T^3, which is consistent with the assumed accuracy. For the coefficient a we have the formula:

$$a=(1-z_0(\mu_0))^{-1}\left(y_2(\mu_0)-c_2\frac{\rho'(\mu_0)}{\rho(\mu_0)}\right), \tag{20}$$

where

$$\delta\tilde{\varepsilon}(\varepsilon)=y_2(\varepsilon)T^2, \qquad \frac{\partial}{\partial\mu}\delta\tilde{\varepsilon}(\varepsilon)=z_0(\varepsilon)+z_2(\varepsilon)T^2.$$

The temperature dependence of $\delta\tilde{\varepsilon}(\varepsilon)$, $\frac{\partial}{\partial\mu}\delta\tilde{\varepsilon}(\varepsilon)$ and the higher-order derivatives of $\delta\tilde{\varepsilon}$ follows from its definition (cf. Eq. (10)). Note that by virtue of the functional dependence of $\delta\tilde{\varepsilon}$ on δn_P in our system the equality:

$$\left(\frac{\partial}{\partial\mu}\delta\tilde{\varepsilon}(\varepsilon)\right)\Big|_{\varepsilon=\mu}=\frac{\partial}{\partial\mu}\delta\tilde{\varepsilon}(\mu)$$

(i.e. $z_0(\mu)=y_2'(\mu)$) may not be satisfied in general.

In order to calculate the thermal properties of our system first we should determine $\delta\tilde{\varepsilon}(\varepsilon)$ and its derivatives in terms of f and g amplitudes and microscopic parameters P_F, v_F, m. By direct calculation we obtain a system of the coupled equations for $\delta\tilde{\varepsilon}(\varepsilon)$, $\frac{\partial}{\partial\mu}\delta\tilde{\varepsilon}(\varepsilon)$, $\frac{\partial}{\partial T}\delta\tilde{\varepsilon}(\varepsilon)$, $\frac{\partial^2}{\partial\mu\partial T}\delta\tilde{\varepsilon}(\varepsilon)$ and $\frac{\partial^2}{\partial\mu^2}\delta\tilde{\varepsilon}(\varepsilon)$. The explicit forms

of the solutions of this system are presented in Appendix A. Note that only zeroth amplitudes enter those formulae, i.e.

$$F_0 \mid_{|P|=|P'|=P^F}, \qquad \left.\frac{\partial F_0}{\partial |P|}\right|_{|P|=|P'|=P^F}, \ldots$$

and

$$G_{000} \mid_{|P|=|P'|=|P''|=P^F}, \qquad \left.\frac{\partial G_{000}}{\partial |P|}\right|_{|P|=|P'|=|P''|=P^F}, \ldots .$$

By virtue of those results the coefficient a can be rewritten in the form:

$$a = c_2\left(F' - \frac{\rho'(\mu_0)}{\rho(\mu_0)}\right) \tag{21}$$

with F' defined in Appendix A (cf. Eq. (A8)).

Using Eqs (16)–(18) and (A1)–(A7) one can find the temperature dependences of derivatives of the entropy S, of the pressure P and of the average number of quasiparticles $\langle N\rangle$ with respect to temperature T, to the chemical potential μ and to the system volume V. The explicit forms thereof are presented in Appendix B. The derivatives mentioned above are calculated at the constant chemical potential μ. It is easy to change them into the representation with $\langle N\rangle = \text{const.}$ using the formula:

$$\left(\frac{\partial X}{\partial Y}\right)_{\langle N\rangle} = \left(\frac{\partial X}{\partial Y}\right)_{\mu} - \left(\frac{\partial X}{\partial Y}\right)_{Y}\left(\frac{\partial \langle N\rangle}{\partial Y}\right)_{\mu}\left(\frac{\partial \langle N\rangle}{\partial \mu}\right)_{Y}^{-1}. \tag{22}$$

Thus we obtain:

$$c_v = T\left(\frac{\partial S}{\partial T}\right)_{V,\langle N\rangle} = V\{2c_2\rho(\mu_0)T + (12c_4\rho''(\mu_0) -$$

$$-6c_2^2(\rho'(\mu_0))^2\rho^{-1}(\mu_0) - 6c_2^2\rho(\mu_0)F''_{12})T^3\}, \tag{23}$$

$$c_P = T\left(\frac{\partial S}{\partial T}\right)_{P,\langle N\rangle} = c_V + 4c_2^2\rho(\mu_0)R^{-1}(\mu_0)\times$$

$$\times K(\mu_0)L(\mu_0)M(\mu_0)VT^3, \tag{24}$$

$$\gamma = \frac{c_P}{c_V} = 1 + 2c_2R^{-1}(\mu_0)K(\mu_0)L(\mu_0)M(\mu_0)T^2, \tag{25}$$

$$\alpha = \frac{1}{V}\left(\frac{\partial V}{\partial T}\right)_{P,\langle N\rangle} = 2c_2\rho(\mu_0)R^{-1}(\mu_0)K(\mu_0)\times$$

$$\times M(\mu_0)T + O(T^3), \tag{26}$$

$$\kappa_T = -\frac{1}{V}\left(\frac{\partial V}{\partial P}\right)_{T,\langle N\rangle} = \rho(\mu_0)R^{-1}(\mu_0)K(\mu_0) +$$

$$+c_2 R^{-1}(\mu_0)K^2(\mu_0)\left\{(\mu_0)\left(\rho''(\mu_0)-\rho(\mu_0)F''_{12}-\right.\right.$$

$$-2\rho(\mu_0)F''_{11}+2\rho(\mu_0)F'^2-2\rho(\mu_0)F'-\frac{(\rho'(\mu_0))^2}{\rho(\mu_0)}-$$

$$\left.-2\rho^2(\mu_0)G'\right)+\rho^2(\mu_0)F'+(\rho'(\mu_0)-2\rho(\mu_0)F')\times$$

$$\times\int_{\lambda}^{\mu_0}\rho(\varepsilon)F'(\varepsilon)\,d\varepsilon+\rho(\mu_0)\int_{\lambda}^{\mu_0}\rho(\varepsilon)F''_{11}(\varepsilon)\,d\varepsilon+$$

$$\left.+2\rho^2(\mu_0)\int_{\lambda}^{\mu_0}\rho(\varepsilon)G'(\varepsilon)\,d\varepsilon\right\}T^2, \tag{27}$$

$$\beta=\frac{1}{P}\left(\frac{\partial P}{\partial T}\right)_{V,\langle N\rangle}=2c_2\left(\int_{\lambda}^{\mu_0}R(\varepsilon)\,d\varepsilon\right)^{-1}L(\mu_0)T+O(T^3), \tag{28}$$

where c_V, c_P are heat capacities at a constant volume and constant pressure, respectively, κ_T is the isothermal compressibility, α is the isobaric expansion coefficient and β is the isochoric coefficient of pressure. Amplitudes F, F', F''_{11}, F''_{12}, G, G' are defined in Appendix A. The K, L, M functions are defined in Appendix B (cf. Eqs (B11)–(B13)). Note that $O(T^3)$ corrections to α and β are not explicitly written owing to a very spacious form. Let us note that the term proportional to T^3 in heat capacity c_v is analogous with that obtained by Richards (cf. [11]). Note also that the leading term in the adiabatic compressibility $\kappa_s=\kappa_T\cdot\gamma$ agrees with the previous results given in paper [1] if we substitute F_0^s by the renormalized amplitude $(F-R^{-1}(\mu_0)\int_{\lambda}^{\mu_0}\rho(\varepsilon)F(\varepsilon)\,d\varepsilon)$. Hence, the previously established formula for a velocity of the hydrodynamic sound (cf. [1]–[4]) holds in our theory in the limit $T=0$, with the redefined above zeroth symmetric Landau amplitude $f_{pp'}$.

Let us underline that the additional terms in thermal characteristics of the normal Fermi liquid appearing due to nonlinear corrections allow us to consider temperature-dependent Landau parameters which is sufficient to fit the experimental data. In the linear theory case such an operation has not been possible; owing to the too small number of external parameters (usually one) it has been necessary to assume them to be temperature dependent in order to compare them with the experiment.

Appendix A

In this Appendix the expressions for $\delta\tilde{\varepsilon}$ and for its derivatives are presented in a form of power series with respect to temperature. Let us write with the demanded accuracy:

$$\delta\tilde{\varepsilon}(\varepsilon)=y_2(\varepsilon)T^2=\frac{c_2}{(1+F)}\left(F'(\varepsilon)+FF'(\varepsilon)-F'F(\varepsilon)+\frac{\rho'(\mu_0)}{\rho(\mu_0)}F(\varepsilon)\right)T^2. \tag{A1}$$

For the derivatives of $\delta\tilde{\varepsilon}$ we have:

$$\frac{\partial}{\partial\mu}\delta\tilde{\varepsilon}(\varepsilon)=z_0(\varepsilon)+z_2(\varepsilon)T^2,$$

$$\frac{\partial^2}{\partial\mu^2}\delta\tilde{\varepsilon}(\varepsilon)=w_0(\varepsilon)+O(T^2),$$

$$\frac{\partial}{\partial T}\delta\tilde{\varepsilon}(\varepsilon)=\lambda_1(\varepsilon)T+O(T^3),$$

$$\frac{\partial^2}{\partial\mu\partial T}\delta\tilde{\varepsilon}(\varepsilon)=\varphi_1(\varepsilon)T+O(T^3), \tag{A2}$$

where

$$z_0(\varepsilon)=(1+F)^{-1}F(\varepsilon), \tag{A3}$$

$$z_2(\varepsilon)=c_2\Big\{(1+F)^{-1}\Big(F''_{11}(\varepsilon)-2F'F'(\varepsilon)+\frac{\rho'(\mu_0)}{\rho(\mu_0)}F'(\varepsilon)+$$

$$+2\rho(\mu_0)G'(\varepsilon)\Big)+(1+F)^{-2}\Big(2F'^2F(\varepsilon)-F'F'(\varepsilon)-2F''_{11}F(\varepsilon)-$$

$$-F''_{12}F(\varepsilon)+\frac{\rho'(\mu_0)}{\rho(\mu_0)}(F'(\varepsilon)-2F'F(\varepsilon)\Big)+\frac{\rho''(\mu_0)}{\rho(\mu_0)}F(\varepsilon)+2\rho'(\mu_0)\times$$

$$\times G(\varepsilon)-2\rho(\mu_0)F'G(\varepsilon)-2\rho(\mu_0)G'F(\varepsilon)\Big)+(1+F)^{-3}\times$$

$$\times\Big(3F'^2F(\varepsilon)-\Big(\rho'(\mu_0)\rho(\mu_0)\Big)^2FF(\varepsilon)-4\frac{\rho'(\mu_0)}{\rho(\mu_0)}F'F(\varepsilon)-$$

$$-2\rho'(\mu_0)GF(\varepsilon)+2\rho(\mu_0)GF'F(\varepsilon)\Big)\Big\}, \tag{A4}$$

$$w_0(\varepsilon)=(1+F)^{-2}(F'(\varepsilon)+2\rho(\mu_0)G(\varepsilon))+(1+F)^{-3}\times$$

$$\times\Big(\frac{P'(\mu_0)}{\rho(\mu_0)}F(\varepsilon)-3F'F(\varepsilon)-2\rho(\mu_0)GF(\varepsilon)\Big), \tag{A5}$$

$$\lambda_1(\varepsilon)=2y_2(\varepsilon), \tag{A6}$$

$$\varphi_1(\varepsilon)=2z_2(\varepsilon)+4c_2F^2(\rho(\mu_0)F'-\rho'(\mu_0))\times$$

$$\times(G(\varepsilon)+FG(\varepsilon)-GF(\varepsilon)). \tag{A7}$$

In the above formulae we have introduced the following extra symbols:

$$F(\varepsilon,\varepsilon')=\rho(\mu_0)\int\frac{d\Omega'}{4\pi}f_{pp'}, \tag{A8}$$

which is the zeroth spin-symmetric Landau amplitude F_0^s,

$$F(\varepsilon)=F(\varepsilon,\mu_0), \qquad F'(\varepsilon)=\frac{\partial}{\partial\varepsilon}F(\varepsilon),$$

$$F''_{11}(\varepsilon)=\frac{\partial^2}{\partial\varepsilon^2}F(\varepsilon), \qquad F''_{12}(\varepsilon)=\frac{\partial^2}{\partial\varepsilon\partial\varepsilon'}F(\varepsilon,\varepsilon')|_{\varepsilon'=\mu_0},$$

$$F=F(\mu_0), \qquad F'=F'(\mu_0),$$

$$F''_{11}=F''_{11}(\mu_0), \qquad F''_{12}=F''_{12}(\mu_0)$$

and analogously for the $g_{PP'P''}$ function:

$$G(\varepsilon,\varepsilon',\varepsilon'')=\rho(\mu_0)\int\frac{d\Omega'}{4\pi}\int\frac{d\Omega''}{4\pi}g_{PP'P''}, \tag{A9}$$

which is the G_{000} amplitude defined in paper [5],

$$G(\varepsilon)=G(\varepsilon,\mu_0,\mu_0), \qquad G'(\varepsilon)=\frac{\partial}{\partial\varepsilon}G(\varepsilon),$$

$$G=G(\mu_0), \qquad G'=G'(\mu_0).$$

Taking the definition of ε_P^0 into account (cf. Eq. (3)) we have calculated the $R(\varepsilon)$ function and its derivatives at the point $\varepsilon=\mu_0$. They have the following forms:

$$R(\mu_0)=\frac{P_F^3-}{3\pi^2\hbar^3}, \qquad \int_{\lambda}^{\mu_0}R(\varepsilon)\,d\varepsilon=\frac{P_F^4\,V}{12\pi^2\hbar^3},$$

$$\rho(\mu_0)=\frac{P_F m^* V}{\pi^2\hbar^3}, \qquad \rho'(\mu_0)=\frac{2m^{*2}V}{P_F\pi^2\hbar^3}(1-\alpha m^*),$$

$$\rho''(\mu_0)=\frac{2m^{*3}V}{P_F^3\pi^2\hbar^3}(1-6\alpha m^*+6\alpha^2 m^{*2}),$$

$$\rho'''(\mu_0)=-\frac{24m^{*5}\alpha V}{P_F^5\pi^2\hbar^3}(1-5\alpha m^*+5\alpha^2 m^{*2}). \tag{A10}$$

Appendix B

In this Appendix we give the formulae for the derivatives of macroscopic parameters of the system:

$$\left(\frac{\partial S}{\partial T}\right)_{\mu,V}=V\left\{2c_2\rho(\mu_0)+\left(12c_4\rho''(\mu_0)-2c_2^2\frac{(\rho'(\mu_0))^2}{\rho(\mu_0)}-\right.\right.$$

$$-6c_2^2\rho(\mu_0)F''_{12}+4c_2^2(1+F)^{-1}(\rho(\mu_0)F'^2-2\rho'(\mu_0)F'-$$

$$-(\rho'(\mu_0))^2\rho^{-1}(\mu_0)F)\Big)T^2\Big\}, \tag{B1}$$

$$\left(\frac{\partial S}{\partial V}\right)_{T,\mu}=\left\{2c_2\rho(\mu_0)T+\left(4c_4\rho''(\mu_0)-2c_2^2\frac{(\rho'(\mu_0))^2}{\rho(\mu_0)}-2c_2^2\rho(\mu_0)F''_{12}\right)T^3\right\}, \tag{B2}$$

$$\left(\frac{\partial S}{\partial \mu}\right)_{T,V}=V\left\{2c_2(1+F)^{-1}(\rho'(\mu_0)-\rho(\mu_0)F')T+\right.$$

$$+4\Big[c_4\rho'''(\mu_0)-c_4(1+F)^{-1}(\rho'''(\mu_0)+3\rho''(\mu_0)F'+$$

$$+3\rho'(\mu_0)F''_{11}+\rho(\mu_0)F'''_{111})-c_2^2\frac{\rho'(\mu_0)\rho''(\mu_0)}{2\rho(\mu_0)}-\frac{1}{2}c_2^2\times$$

$$\times(1+F)^{-1}\Big(2\rho(\mu_0)F'''_{112}+2\rho^2(\mu_0)G''_{12}+2\rho'(\mu_0)F''_{12}-$$

$$-4\rho(\mu_0)F'F''_{12}-2\rho'F''_{11}-\frac{\rho'(\mu_0)\rho''(\mu_0)}{\rho(\mu_0)}F-$$

$$-3\frac{(\rho'(\mu_0))^2}{\rho(\mu_0)}F'\Big)-\frac{1}{2}c_2^2(1+F)^{-2}\Big(\rho'(\mu_0)F''_{12}+2\rho'(\mu_0)F''_{11}+$$

$$+\rho'(\mu_0)F'-4\rho'(\mu_0)F'^2+2\rho(\mu_0)F'^3+\frac{\rho'(\mu_0)\rho''(\mu_0)}{\rho(\mu_0)}F-$$

$$-\frac{(\rho'(\mu_0))^3}{(\rho(\mu_0))^2}F+\frac{(\rho(\mu_0))^2}{\rho(\mu_0)}F'+2\rho'(\mu_0)\rho(\mu_0)G'-$$

$$\left.-2\rho^2(\mu_0)G'F'-2\rho(\mu_0)F'F''_{11}-\rho(\mu_0)F'F''_{12}\Big)\Big]T^3\right\}, \tag{B3}$$

$$\left(\frac{\partial\langle N\rangle}{\partial V}\right)_{T,\mu}=R(\mu_0), \tag{B4}$$

$$\left(\frac{\partial\langle N\rangle}{\partial\mu}\right)_{T,V}=V(1+F)^{-1}\{\rho(\mu_0)+c_2(1+F)^{-1}(\rho''(\mu_0)-$$

$$-(\rho'(\mu_0))^2\rho^{-1}(\mu_0)-\rho(\mu_0)F''_{12}-2\rho(\mu_0)F''_{11}+2\rho(\mu_0)F^{12}-$$

$$-2\rho'(\mu_0)F'-2\rho^2(\mu_0)G')T^2\}, \tag{B5}$$

$$\left(\frac{\partial\langle N\rangle}{\partial T}\right)_{V,\mu}=V\left\{2c_2(1+F)^{-1}(\rho'(\mu_0)-\rho(\mu_0)F')T+\right.$$

$$+4\Big[c_4\rho'''(\mu_0)-c_4(1+F)^{-1}(\rho'''(\mu_0))F+3\rho''(\mu_0)F'+$$

$$+3\rho'(\mu_0)F''_{11}+\rho(\mu_0)F'''_{111})+c_2^2(1+F)^{-1}(\rho'(\mu_0)F''_{11}+$$

$$+2\rho(\mu_0)\rho'(\mu_0)F'G-\rho'^2(\mu_0)G+\frac{3(\rho'(\mu_0))^2}{2\rho(\mu_0)}F'-\rho(\mu_0)F'''_{112}+$$

$$+2\rho(\mu_0)F'F''_{12}-\rho'(\mu_0)F''_{12}-\rho(\mu_0)\rho'(\mu_0)G'-2\rho'(\mu_0)\rho(\mu_0)\times$$

$$\times GF'-2\rho^2(\mu_0)G''_{12})+\frac{1}{2}c_2^2(1+F)^{-2}\Big(6\rho(\mu_0)F'^3-$$

$$-\rho''(\mu_0)F'-\rho'(\mu_0)F''_{12}-2\rho'(\mu_0)F''_{11}+4\rho'(\mu_0)F'^2+$$

$$+\frac{(\rho'(\mu_0))^3}{(\rho(\mu_0))^2}F-2\frac{\rho'(\mu_0)\rho''(\mu_0)}{\rho(\mu_0)}F-\frac{(\rho'(\mu_0))^2}{\rho(\mu_0)}F'-$$

$$-\frac{\rho'(\mu_0)\rho''(\mu_0)}{(\mu_0)}+2\rho(\mu_0)F'F''_{11}+\rho(\mu_0)F'F''_{12}+2\rho^2(\mu_0)G'F'-$$

$$-2\rho(\mu_0)\rho'(\mu_0)G')-\frac{1}{2}c_2^2(1+F)^{-3}\rho'(\mu_0)F^{12}\Big]T^3\Big\}, \tag{B6}$$

$$P=\int_{\lambda}^{\mu_0}R(\varepsilon)\,d\varepsilon+c_2M(\mu_0)T^2, \tag{B7}$$

$$\left(\frac{\partial P}{\partial V}\right)_{T,\mu}=0, \tag{B8}$$

$$\left(\frac{\partial P}{\partial T}\right)_{V,\mu}=2c_2\Big[\rho(\mu_0)-\int_{\lambda}^{\mu_0}\rho(\varepsilon)F'(\varepsilon)\,d\varepsilon+(1+F)^{-1}\times$$

$$\times\left(F'-\frac{\rho'(\mu_0)}{\rho(\mu_0)}\int_{\lambda}^{\mu_0}\rho(\varepsilon)F(\varepsilon)\,d\varepsilon\right)\Big]T+O(T^3), \tag{B9}$$

$$\left(\frac{\partial P}{\partial\mu}\right)_{V,T}=\Big\{(1+F)^{-1}K^{-1}(\mu_0)+c_2\Big[-(1+F)^{-1}\times$$

$$\times\rho(\mu_0)F'-(1+F)^{-2}\Big(\rho''(\mu_0)-\rho(\mu_0)(F''_{12}+2F''_{11})+2\rho(\mu_0)\times$$

$$\times F'^2-2\rho'(\mu_0)F'-2\rho^2(\mu_0)G'-\frac{(\rho'(\mu_0))^2}{\rho(\mu_0)}\Big)\int_{\lambda}^{\mu_0}\rho(\varepsilon)F(\varepsilon)\,d\varepsilon+$$

$$+(1+F)^{-3}\left(\int_{\lambda}^{\mu_0}\rho(\varepsilon)F''_{11}(\varepsilon)\,d\varepsilon+2\rho(\mu_0)\int_{\lambda}^{\mu_0}\rho(\varepsilon)G'(\varepsilon)\,d\varepsilon+\right.$$

$$\left.+\left(\frac{\rho'(\mu_0)}{\rho(\mu_0)}-2F'\right)\int_{\lambda}^{\mu_0}\rho(\varepsilon)F'(\varepsilon)\,d\varepsilon\right)\Bigg]T^2\Bigg\}, \tag{B10}$$

$$K(\varepsilon)=\left(R(\varepsilon)(1+F)-\int_{\lambda}^{\varepsilon}\rho(\varepsilon')F(\varepsilon')\,d\varepsilon'\right)^{-1}, \tag{B11}$$

$$L(\varepsilon)=\rho(\varepsilon)+R(\varepsilon)F'-R(\varepsilon)\rho'(\varepsilon)\rho^{-1}(\varepsilon), \tag{B12}$$

$$M(\varepsilon)=L(\varepsilon)-\int_{\lambda}^{\varepsilon}\rho(\varepsilon')F'(\varepsilon')\,d\varepsilon'. \tag{B13}$$

References

1. L. D. Landau, Zh. Eksp. Teor. Fiz., *30*, 1058, 1956.
2. L. D. Landau, Zh. Eksp. Teor. Fiz., *32*, 59, 1957.
3. D. Pines and P. Noziéres, The Theory of Quantum Liquids, W. A. Benjamin, Inc., New York, 1966.
4. P. Noziéres, Theory of Interacting Fermi Systems, W. A. Benjamin, Inc., New York, 1963.
5. I. Krzyżanowski and L. Jacak, Acta Phys. Polon., *A65*, 241, 1984.
6. D. J. Amit, J. W. Kane and H. Wagner, Phys. Rev. Lett., *19*, 425, 1967.
7. D. J. Amit, J. W. Kane and H. Wayner, Phys. Rev., *175*, 313, 1968.
8. V. J. Emery, Phys. Rev., *170*, 205, 1968.
9. G. E. Brown and C. J. Pethick, J. Low Temp. Phys., *48*, 349, 1982.
10. V. K. Mishra, G. E. Brown and C. J. Pethick, J. Low Temp. Phys., *52*, 379, 1983.
11. P. M. Richards, Phys. Rev., *126*, 1909, 1962.
12. L. D. Landau, E. M. Lifshic, Statističeskaia fizika 1, Moskva, Nauka (1977), Ch. 5.
13. D. S. Greywall, Phys. Rev. B, *27*, 2747, 1983.
14. P. R. Roach, Y. Eckstein, M. W. Meisel and L. Anida-Jedrzejek, J. Low Temp. Phys., *52*, 433, 1983.
15. L. Jacak, Proceedings of LT-17 Conference, Karlsruhe (1984) (to be published).

Acta Physica Hungarica 60 (3—4), pp. 319—331 (1986)

MOLECULAR DYNAMICS OF DIHALOGERMANES

S. MOHAN*

Division of Applied Sciences
Anna University, Madras Institute of Technology, Chromepet
Madras 600 044, India

and

T. J. BHOOPATHY

Department of Physics Pachaiyappa's College
Madras 30, India

(Received 26 February 1985)

A complete vibrational analysis has been carried out for some XY_2Z_2 type molecules using a revised set of symmetry coordinates and a set of molecular constants, viz. kinetic constants, potential constants, compliance constants, vibrational mean amplitudes, Coriolis coupling constants, and centrifugal distortion constants have been reported in the present investigation for the first time. The values of the major potential constants evaluated in the present work are in good agreement with the literature values.

Introduction

Several investigations [1–10] have been carried out for this type of molecules in the recent years. But most of the works are based on the symmetry coordinates given by Davis et al [1]. According to him, the symmetry coordinates R_1 and R_2 of A_1 species correspond to symmetric X–Y and X–Z stretching combinations of the whole system. But the frequencies assigned for these molecules in the A_1 species, in earlier work correspond to individual X–Y [ν_S(XY)] and X–Z [ν_S(XZ)] stretchings. Hence the symmetry coordinates are modified in the present investigation, i.e. in this paper, for the A_1 vibration, it was found expedient to use a new set of symmetry coordinates in order to get F matrix elements easier to use. The above considerations have been applied to evaluate the force constants of dihalogermanes of the XY_2Z_2 type, which have not been studied completely so far. Using the present set of potential constants, the other molecular constants, viz. compliance constants, vibrational mean amplitudes, Coriolis coupling constants and centrifugal distortion constants have been evaluated and they are reported for these molecules for the first time.

* The author for correspondence

Theoretical considerations

The XY_2Z_2 type molecules belong to the symmetry C_{2v} and hence the vibrational modes are classified as $\Gamma = 4A_1 + A_2 + 2B_1 + 2B_2$. All the vibrations are Raman active. The only mode forbidden in the infrared is A_2 type. The structure and nomenclature of the parameters of the molecular type are shown in Fig. 1.

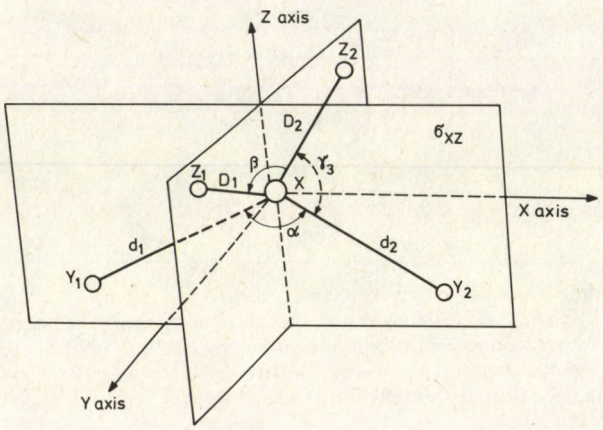

Fig. 1

The symmetry coordinates for A_2, B_1 and B_2 vibration types were the same as those obtained by Davis [1] and they are not given here. For the A_1 type, the following symmetry coordinates have been constructed:

$$A_1 \text{ type: } R_1 = \frac{1}{\sqrt{2}}(\Delta d_1 + \Delta d_2),$$

$$R_2 = \frac{1}{\sqrt{2}}(\Delta\beta - \Delta\alpha),$$

$$R_3 = \frac{1}{\sqrt{2}}(\Delta D_1 + \Delta D_2),$$

$$R_4 = \frac{1}{\sqrt{12}}[\Delta\gamma_1 + \Delta\gamma_2 + \Delta\gamma_3 + \Delta\gamma_4 - 2(\Delta\alpha + \Delta\beta)],$$

$$R' = \frac{1}{\sqrt{6}}[\Delta\alpha + \Delta\beta + \Delta\gamma_1 + \Delta\gamma_2 + \Delta\gamma_3 + \Delta\gamma_4] \equiv 0,$$

where Δd's change in X–Y bond distances; ΔD's change in X–Z bond distances; $\Delta\alpha$'s change in $Y_1\hat{X}Y_2$ interbond angles; $\Delta\beta$'s change in $Z_1\hat{X}Z_2$ interbond angles; $\Delta\gamma$'s change in $Y\hat{X}Z$ interbond angles.

The most general quadratic potential energy function has been considered and the F matrix elements have been obtained:

A_1 species:

$$F_{11}=f_d+f_{dd},$$

$$F_{22}=\frac{1}{2}(d^2f_\alpha+D^2f_\beta-2dDf_{\alpha\beta}),$$

$$F_{33}=f_D+f_{DD},$$

$$F_{44}=\frac{1}{3}[d^2f_\alpha+D^2f_\beta+2Ddf_{\alpha\beta}-6\sqrt{dD}(df_{d\gamma}+Df_{\beta\gamma})+Dd(f_\gamma+f_{\gamma\gamma}+f'_{\gamma\gamma}+f''_{\gamma\gamma})],$$

$$F_{12}=-df_{d\alpha}+Df_{d\beta},$$

$$F_{13}=2f_{dD},$$

$$F_{14}=\sqrt{2/3}\,[-df_{d\alpha}-Df_{d\beta}+\sqrt{dD}(f_{d\gamma}+f'_{d\gamma})],$$

$$F_{23}=-df_{D\alpha}+Df_{D\beta},$$

$$F_{24}=\frac{1}{\sqrt{6}}[d^2f_\alpha-D^2f_\beta-2\sqrt{dD}(df_{\alpha\gamma}-Df_{\beta\gamma})],$$

$$F_{34}=\sqrt{2/3}\,[-df_{D\alpha}-Df_{D\beta}+\sqrt{Dd}(f_{D\gamma}+f'_{D\gamma})].$$

A_2 species:

$$F_{55}=dD(f_\gamma-f_{\gamma\gamma}+f'_{\gamma\gamma}-f''_{\gamma\gamma}).$$

B_1 species:

$$F_{66}=f_d-f_{dd},$$

$$F_{77}=Dd(f_\gamma+f_{\gamma\gamma}-f'_{\gamma\gamma}-f''_{\gamma\gamma}),$$

$$F_{67}=-\sqrt{2Dd}(f_{d\gamma}-f'_{d\gamma}).$$

B_2 species:

$$F_{88}=f_D-f_{DD},$$

$$F_{99}=Dd(f_\gamma-f_{\gamma\gamma}-f'_{\gamma\gamma}+f''_{\gamma\gamma})$$

$$F_{89}=-\sqrt{2Dd}(f_{D\gamma}-f'_{D\gamma}),$$

The elements of the kinetic energy matrix G obtained, using Wilson's [11] expression are given below

A_1 type:

$$G_{11}=2C_\omega^2\mu_X+\mu_Y,$$

$$G_{22}=(2A-2C)^2\mu_X+\frac{1}{d^2}\mu_Y+(2B^2+2C^2)\mu_Z,$$

$$G_{33}=2C_\omega^2\mu_X+\mu_Z,$$

$$G_{44}=\left[\frac{E(D-d)}{dD}+F-G\right]^2\mu_X+2\left[\left(H-\frac{I}{d}\right)^2+\left(\frac{G}{2}-\frac{E}{2d}\right)^2\right]\mu_Y$$
$$+2\left[\left(\frac{I}{D}-J\right)^2+\left(\frac{E}{2D}-\frac{F}{2}\right)^2\right]\mu_Z,$$

$$G_{12}=(2A-2C)\sqrt{2}C_\omega\mu_X,$$

$$G_{13}=-2C_\omega^2\mu_X,$$

$$G_{14}=\left[\frac{E(D-d)}{dD}+F-G\right]\sqrt{2}C_\omega\mu_X+\sqrt{2}\left[\left(\frac{I}{d}-H\right)S_\omega-\left(\frac{G}{2}-\frac{E}{2d}\right)C_\omega\right]\mu_Y,$$

$$G_{23}=-(2A-2C)\sqrt{2}C_\omega\mu_X+[\sqrt{2}BS_\omega+\sqrt{2}CS_\omega]\mu_Z,$$

$$G_{24}=(2A-2C)\left[\frac{E(D-d)}{dD}+F-G\right]\mu_X$$
$$+\left[\sqrt{2}C\frac{\omega}{d}\left(H-\frac{I}{d}\right)-2A\left(\frac{G}{2}-\frac{E}{2d}\right)\right]\mu_Y$$
$$+\left[2B\left(\frac{I}{D}-J\right)+2C\left(\frac{E}{2D}-\frac{F}{2}\right)\right]\mu_Z,$$

$$G_{34}=-\sqrt{2}C_\omega\left[\frac{E(D-d)}{dD}+F-G\right]\mu_X$$
$$+\left[\sqrt{2}S_\omega\left(\frac{I}{D}-J\right)+\sqrt{2}C_\omega\left(\frac{E}{2D}-\frac{F}{2}\right)\right]\mu_Z.$$

A_2 type:

$$G_{55}=4K^2\mu_Y+4L^2\mu_Z.$$

B_1 type:

$$G_{66}=2S_\omega^2\mu_X+\mu_Y,$$

$$G_{77}=(2L-2KC_\gamma)^2\mu_X+\left[2K^2C_\gamma^2+\frac{2M^2}{d^2}\right]\mu_Y+2L^2\mu_Z,$$

$$G_{67}=(2L-2KC_\gamma)\sqrt{2}S_\omega\mu_X-\sqrt{2}\left[KC_\gamma S_\omega+\frac{MC_\omega}{d}\right]\mu_Y.$$

B_2 type:

$$G_{88}=2S_\omega^2\mu_X+\mu_Z,$$

$$G_{99}=(2LC_\gamma-2K)^2\mu_X+2K^2\mu_Y+\left[2L^2C_\gamma^2+\frac{M^2}{D^2}\right]\mu_Z,$$

$$G_{89}=-\sqrt{2}S_\omega(2LC_\gamma-2K)\mu_X-\sqrt{2}\left[LC_\gamma S_\omega+\frac{MC_\omega}{D}\right]\mu_Z,$$

where $A=\dfrac{S_\omega}{\sqrt{2}d}$, $H=\dfrac{2S_\omega}{\sqrt{12}}\left[\dfrac{C_\alpha+1}{dS_\alpha}\right]$,

$B=\dfrac{S_\omega(C_\beta+1)}{\sqrt{2}DS_\beta}$ $I=\dfrac{2S_\omega}{\sqrt{12}}\left[\dfrac{C_\gamma}{S_\gamma}\right]$,

$C=\dfrac{C_\omega(C_\beta-1)}{\sqrt{2}DS_\beta}$, $J=\dfrac{2S_\omega}{\sqrt{12}}\left[\dfrac{1+C_\beta}{DS_\beta}\right]$,

$E=\dfrac{4C_\omega}{\sqrt{12}}\left[\dfrac{1+C_\gamma}{S_\gamma}\right]$, $K=\dfrac{S_\omega}{dS_\gamma}$,

$F=\dfrac{4C_\omega}{\sqrt{12}}=\left[\dfrac{C_\beta-1}{DS_\beta}\right]$, $L=\dfrac{S_\omega}{DS_\gamma}$,

$G=\dfrac{4C_\omega}{\sqrt{12}}\left[\dfrac{C_\gamma-1}{dS_\alpha}\right]$, $M=\dfrac{C_\omega(C_\gamma+1)}{S_\gamma}$.

μ corresponds to the reciprocal mass of the respective atoms; $S_\omega=\sin\alpha/2$; $C_\omega=\cos\alpha/2$; $S_\gamma=\sin\gamma$; $C_\gamma=\cos\gamma$; $S_\beta=\sin\beta$ and, $C_\beta=\cos\beta$.

The secular equations involving symmetric potential energy constants have been solved using the method of kinetic constants. The study of kinetic constants provides the required number of additional data through the symmetry kinetic constants [12–15]. This method has been utilized to solve the vibrational problems of 4×4, and 2×2 orders of XY_2Z_2 type molecules.

The compliance constants are also determined for the molecules under investigation by the Decius method [16]. The mean square amplitude elements are obtained using Cyvin's relation [17], $\Sigma=L\Delta L'$, where L is the normal coordinate transformation matrix and hence the vibrational mean amplitudes for bonded and nonbonded distances at 298.16 K are evaluated.

The Coriolis vibration–rotation constants $\zeta^{\alpha}(\alpha = X, Y, Z)$ in this type of molecules arise from the couplings

$$A_1 \times A_2(\text{Z axis}); \quad A_1 \times B_1(\text{Y axis});$$

$$A_1 \times B_2(\text{X axis}); \quad A_2 \times B_1(\text{X axis});$$

$$A_2 \times B_2(\text{Y axis}) \quad \text{and} \quad B_1 \times B_2(\text{Z axis}).$$

The Coriolis matrix elements* $C_{ij}^{\alpha}(\alpha = X, Y, Z)$ are obtained by the vector method of Meal and Polo [18] and zeta matrix elements are evaluated from the relation $\zeta^{\alpha} = L^{-1}C^{\alpha}(L')^{-1}$ making use of the kinetic constants.

The centrifugal distortion constants are evaluated using Cyvin's reformulated theory [19]. The nonvanishing $T_{\alpha\beta,S}$ elements in terms of the symmetry coordinates are given below:

$$T_{XX,S_1} = \sqrt{8}dC_{\omega}^2,$$

$$T_{YY,S_1} = \sqrt{8}d,$$

$$T_{ZZ,S_1} = \sqrt{8}dS_{\omega}^2,$$

$$T_{XX,S_1} = 4C_{\omega}(dA + CD) + 4DBS_{\omega},$$

$$T_{YY,S_2} = 4C_{\omega}(dA + CD) - \sqrt{2}S_{\alpha},$$

$$T_{ZZ,S_2} = 4BDS_{\omega} - \sqrt{2}S_{\alpha},$$

$$T_{XX,S_3} = \sqrt{8}D,$$

$$T_{YY,S_3} = \sqrt{8}DC_{\omega}^2,$$

$$T_{ZZ,S_3} = \sqrt{8}DS_{\omega}^2,$$

$$T_{XX,S_4} = 4C_{\omega}\left[D\left(\frac{E}{2D} - \frac{F}{2}\right) - d\left(\frac{G}{2} - \frac{E}{2d}\right)\right] + 4S_{\omega}D\left(\frac{I}{D} - J\right),$$

$$T_{YY,S_4} = 4C_{\omega}\left[D\left(\frac{E}{2D} - \frac{F}{2}\right) - d\left(\frac{G}{2} - \frac{E}{2d}\right)\right] - 4S_{\omega}d\left(H - \frac{I}{d}\right),$$

$$T_{ZZ,S_4} = 4S_{\omega}\left[D\left(\frac{I}{D} - J\right) - d\left(H - \frac{I}{d}\right)\right],$$

$$T_{XY,S_5} = -\sqrt{8}LDS_{\omega},$$

$$T_{ZX,S_6} = \frac{dS_{\alpha}}{\sqrt{2}},$$

* C matrix elements are available from the authors on request.

$$T_{ZX,S_7} = -2C_\omega[KdC_\gamma + LD],$$

$$T_{YZ,S_8} = \frac{DS_\alpha}{\sqrt{2}},$$

$$T_{YZ,S_9} = -2C_\omega[Kd + LDC_\gamma].$$

Results and discussion

The structural parameters and vibrational frequencies for the molecules studied in this investigation are taken from [8,9] and they are presented here in Table I. The kinetic constants and potential constants of these molecules are given in Tables II and III, respectively. The molecular kinetic constants exhibit the following trends.

Table I

The molecular parameters and the vibrational frequencies [cm^{-1}] of dihalogermanes

Molecule	ν_1 X–Y str	ν_2 XY_2 bend	ν_3 X–Z str	ν_4 XZ_2 bend	ν_5 twist
GeH_2F_2	2154.5	860	720	270.4	664
GeH_2Cl_2	2132.0	840	404	163.0	648
GeH_2Br_2	2114.0	826	285	105.0	640
GeH_2I_2	2038.0	788	220	96.0	628

ν_6 X–Y antisym	ν_7 wagging	ν_8 X–Z antisym	ν_9 rocking	d [nm] (X–Y)	D [nm] (X–Z)
2174.4	596	720	813.5	0.15	0.17
2155.0	533	420	772.0	0.15	0.213
2144.0	496	311	739.0	0.15	0.23
2078.0	474	255	692.0	0.15	0.25

All the bond angles are tetrahedral angles.

With the increasing mass of the Z atom, the major stretching constant k_D increases while the stretching constant k_d (Ge–H) remains constant. On the other hand, the bending constants k_α, k_β, k_γ increase, with the increasing mass of the Z atom. The bond–angle interaction kinetic constants $k_{d\beta}$, $k_{D\alpha}$, $k_{D\gamma}$, $k'_{D\gamma}$ and angle–angle interaction kinetic constants $k_{\alpha\beta}$, $k_{\beta\gamma}$ are negative for all the cases studied here.

The following observations may be made from Table III:

1. The X–Y (Ge–H) stretching potential constants f_d almost constant in all the cases studied here.

Table II

Kinetic constants [10^{-26} kg]

Mol. Symbol	GeH_2F_2	GeH_2Cl_2	GeH_2Br_2	GeH_2I_2
k_d	0.1655	0.1656	0.1657	0.1658
k_D	2.5894	4.2417	7.7882	10.9561
k_α	0.0610	0.0735	0.0998	0.1364
k_β	0.8160	1.2923	2.3093	3.2494
k_γ	0.1286	0.1456	0.1994	0.2574
k_{dd}	0.0009	0.0010	0.0011	0.0012
k_{DD}	0.2138	0.6256	0.2550	4.3767
k_{dD}	0.0093	0.0135	0.0195	0.0228
$k_{d\alpha}$	0.0030	0.0048	0.0068	0.0082
$-k_{d\beta}$	0.0109	0.0154	0.2120	0.0239
$k_{d\gamma}$	0.0051	0.0060	0.0075	0.0082
$k_{d\gamma}$	−0.0007	0.0011	0.0029	0.0040
$-k_{D\alpha}$	0.0575	0.1673	0.5313	1.0269
$k_{D\beta}$	0.2070	0.5351	1.6602	3.0032
$-k_{D\gamma}$	0.0241	0.1013	0.3732	0.7326
$-k'_{D\gamma}$	0.0591	0.1473	0.4402	0.8082
$-k_{\alpha\beta}$	0.2185	0.4264	0.8111	1.2612
$k_{\alpha\gamma}$	0.0438	0.1116	0.2344	0.3806
$-k_{\beta\gamma}$	0.1659	0.2955	0.5489	0.8045
$k_{\gamma\gamma}$	0.0580	0.0881	0.1456	0.2076
$k'_{\gamma\gamma}$	−0.0372	0.0031	0.0639	0.1312
$k''_{\gamma\gamma}$	−0.0139	0.0218	0.0815	0.1476

2. The X–Z stretching potential constants f_D and bending force constants f_β, f_γ as well as most of the interaction constants decrease with the decreasing electronegativity of the substituent halogen atom.

3. The bond–bond interaction force constant f_{dd}, the bond angle interaction force constants $f_{d\beta}, f'_{d\gamma}, f_{D\alpha}, f'_{D\gamma}$ and angle–angle interaction force constants $f_{\alpha\beta}, f_{\beta\gamma}, f'_{\gamma\gamma}$ and $f''_{\gamma\gamma}$ are uniquely negative for all these cases studied here.

4. The fact that the force constant f_D is higher than f_d in GeH_2F_2 suggests that the Ge–F bond is much stronger than the Ge–H bond. The same trend for Ge–Cl bond is also noticed in GeH_2Cl_2 molecule. It may also be added that Ge–Br and Ge–I bond strengths are weaker than Ge–H bond in GeH_2Br_2 and GeH_2I_2 molecules, respectively.

5. Drake has already reported potential constants for some molecules of this type. But most of the interaction constants have been neglected by him. Here all the interaction constants are reported for the first time. The major stretching force constants f_d, f_D values agree quite well with earlier works [8, 9].

6. All the general quadratic potential constants for the molecules under study are available here for the first time.

The compliance constants for the molecules under study are given in Table IV. These constants are invariant to the choice of coordinate defining the force field and

Table III

Potential constants [10^2 Nm^{-1}]

Mol. Symbol	GeH_2F_2	GeH_2Cl_2	GeH_2Br_2	GeH_2I_2
f_d	2.7428	2.6915	2.6537	2.4797
	(2.7440)	(2.6900)	(2.6600)	(2.4830)
	(2.7620)	(2.6904)	(2.6750)	(2.5350)
f_D	4.4608	2.8876	2.2165	1.5122
	(4.8130)	(2.7310)	(2.1180)	(1.5230)
	(4.5860)	(2.7313)	(2.1760)	(1.5310)
f_α	0.2723	0.1919	0.2051	0.1896
f_β	0.4114	0.2135	0.1759	0.1729
f_γ	0.1572	0.1130	0.0954	0.0823
$-f_{dd}$	0.2147	0.0169	0.0271	0.0386
f_{DD}	0.0912	0.6243	0.3177	−0.0058
f_{dD}	0.0151	0.0098	0.0049	0.0022
$f_{d\alpha}$	0.0057	0.0030	0.0022	0.0016
$-f_{d\beta}$	0.0072	0.0032	0.0021	0.0016
$f_{d\gamma}$	0.0042	0.0028	0.0022	0.0019
$-f'_{d\gamma}$	0.0031	0.0021	0.0018	0.0015
$-f_{D\alpha}$	0.2142	0.3065	0.3488	0.2313
$f_{D\beta}$	0.2295	0.2552	0.2789	0.2168
$f_{D\gamma}$	0.0214	0.0027	−0.0044	−0.0165
$-f'_{D\gamma}$	0.0430	0.0261	0.0274	0.0339
$-f_{\alpha\beta}$	0.2830	0.1704	0.1634	0.1523
$f_{\alpha\gamma}$	0.0114	0.0105	0.0092	0.0124
$-f_{\beta\gamma}$	0.0430	0.0279	0.0215	0.0263
$f_{\gamma\gamma}$	0.0102	0.0044	0.0012	0.0041
$-f'_{\gamma\gamma}$	0.1026	0.0720	0.0595	0.0468
$-f''_{\gamma\gamma}$	0.0296	0.0210	0.0179	0.0153

Values in parentheses refer to literature values [8, 9].

they may be used as a measure of the bond strengths and interactions instead of potential constant as pointed out by Decius [16] and Jones [20]. It may also be noted that the compliance constants exhibit trends opposite to that of the force constants.

The vibrational mean square amplitude for the bonded and nonbonded distances evaluated at 298.16 K are presented in Table V. The values of mean amplitude for bonded and nonbonded distance deviations are given in Table VI. From the Table, it may be observed that these constants are independent of the bond order, and depend only on the mass of the atom. The Ge–H mean amplitude of vibration remains the same in all cases. Also, the mean amplitude of vibrations for Ge–F, Ge–Cl, Ge–Br and Ge–I bonds in these molecules increases as one goes from lower to the higher member of the halogen group. These values of the mean amplitudes are useful in defining the non-rigid model of the molecules, in the determination of the complete harmonic force field and also in verifying the mean amplitude of vibration obtained experimentally from electron diffraction investigations. Since electron diffraction data are not available a direct comparison is not made in the present investigation.

Table IV

Compliance constants [10^{-2} mN^{-1}]

Mol. Symbol	GeH_2F_2	GeH_2Cl_2	GeH_2Br_2	GeH_2I_2
n_d	0.3962	0.3716	0.3769	0.4034
n_D	0.2339	0.4165	0.6280	0.8826
n_α	1.0012	1.5898	1.8168	1.5123
n_β	0.2726	0.1924	0.2101	0.1456
n_γ	0.9313	0.8081	0.7936	0.7487
n_{dd}	0.0335	0.0024	0.0038	0.0063
n_{DD}	0.0031	−0.0274	0.0992	0.2214
$-n_{dD}$	0.0020	0.0021	0.0024	0.0020
$-n_{d\alpha}$	0.0029	0.0035	0.0035	0.0018
$n_{d\beta}$	0.0019	0.0011	0.0011	0.0009
$n_{d\gamma}$	0.0019	0.0018	0.0016	0.0013
$-n'_{d\gamma}$	0.0016	0.0009	0.0009	0.0011
$n_{D\alpha}$	0.0574	0.2193	0.3968	0.3042
$-n_{D\beta}$	0.0189	0.0324	0.0827	0.1323
$-n_{D\gamma}$	0.0048	0.0238	0.0415	0.0022
$-n'_{D\gamma}$	0.0217	0.0489	0.0675	0.0302
$n_{\alpha\beta}$	0.2576	0.2076	0.1924	0.1099
$-n_{\alpha\gamma}$	0.3037	0.3954	0.4264	0.3282
$-n_{\beta\gamma}$	0.1330	0.1009	0.1039	0.0683
$-n_{\gamma\gamma}$	0.4611	0.3492	0.3158	0.3379
$n'_{\gamma\gamma}$	0.3221	0.2668	0.2418	0.1839
$-n''_{\gamma\gamma}$	0.3654	0.2736	0.2466	0.2523

The Coriolis coupling constants evaluated in this work are reported in Table VII. The Coriolis coupling coefficients give a measure of the extension of the infrared band contours. The coupling coefficients between the degenerate modes are found to be very useful in the high resolution studies on the perpendicular bonding. The high values of constants $|\zeta^Z_{15}|$, ζ^Y_{26}, ζ^Y_{17}, $|\zeta^X_{48}|$, ζ^X_{29}, ζ^X_{57}, $|\zeta^Z_{69}|$ suggests the heavy mixing of the corresponding vibrational modes. Further the ζ-values are found to obey the following sum rules,

$$(\zeta^X_{18})^2+(\zeta^X_{28})^2+(\zeta^X_{38})^2+(\zeta^X_{48})^2=1\,,$$

$$(\zeta^X_{19})^2+(\zeta^X_{29})^2+(\zeta^X_{39})^2+(\zeta^X_{49})^2=1\,,$$

$$(\zeta^Y_{16})^2+(\zeta^Y_{26})^2+(\zeta^Y_{36})^2+(\zeta^Y_{46})^2=1\,,$$

$$(\zeta^Y_{17})^2+(\zeta^Y_{27})^2+(\zeta^Y_{37})^2+(\zeta^Y_{47})^2=1\,,$$

$$(\zeta^Z_{15})^2+(\zeta^Z_{25})^2+(\zeta^Z_{35})^2+(\zeta^Z_{45})^2=1\,.$$

The centrifugal distortion constants of these molecules are listed in Table VIII. The centrifugal distortion constants D_J, D_K, D_{JK} decrease with the decreasing electronegativity of the substituent halogen atom. These constants are found to be in the expected range.

Table V

Bonded and nonbonded mean square amplitudes of vibration [10′ (pm)²] at 298 · 16 K

Mol. Symbol	GeH_2F_2	GeH_2Cl_2	GeH_2Br_2	GeH_2I_2
$\sigma_d(x-y)$	7.8336	7.9103	7.9643	8.2396
$\sigma_D(x-z)$	1.6443	2.2288	2.3729	2.8895
σ_α	9.1711	10.7420	11.1493	10.3357
σ_β	1.1505	0.7523	0.7836	0.4822
σ_γ	6.7382	5.5914	5.3979	5.1127
σ_{dd}	0.0009	0.0070	0.0204	0.0432
$-\sigma_{DD}$	0.1162	0.2110	0.2468	0.2380
$-\sigma_{dD}$	0.0356	0.0376	0.0380	0.0375
$-\sigma_{d\alpha}$	0.0484	0.0529	0.0510	0.0429
$\sigma_{d\beta}$	0.0348	0.0227	0.0197	0.0169
$-\sigma_{d\gamma}$	0.0355	0.0246	0.0224	0.0221
$\sigma'_{d\gamma}$	0.0397	0.0333	0.0308	0.0278
$\sigma_{D\alpha}$	0.2141	0.9671	1.0653	0.7474
$-\sigma_{D\beta}$	0.1131	0.1643	0.2409	0.3179
$-\sigma_{D\gamma}$	0.1489	0.3844	0.4970	0.5189
$\sigma'_{D\gamma}$	0.1085	0.0765	0.2160	0.4347
$\sigma_{\alpha\beta}$	0.7799	0.6871	0.7820	0.4376
$-\sigma_{\alpha\gamma}$	2.3613	2.4583	2.4930	2.1427
$-\sigma_{\beta\gamma}$	0.4893	0.3683	0.4005	0.2404
$-\sigma_{\gamma\gamma}$	3.6670	2.9037	2.7156	2.7448
$\sigma'_{\gamma\gamma}$	2.0693	1.6236	1.4193	1.1028
$-\sigma''_{\gamma\gamma}$	2.4016	1.8095	1.5924	1.5007
σ_p(Y . . . Y)	26.8824	29.7925	30.6888	32.0768
σ_q(Z . . . Z)	6.1196	9.1338	11.1347	12.0341
σ_γ(Y . . . Z)	28.4211	33.0545	35.0892	37.7937

Table VI

Bonded and nonbonded mean amplitudes of vibration [10^2 (pm)] at 298.16 K

Mol. Symbol	GeH_2F_2	GeH_2Cl_2	GeH_2Br_2	GeH_2I_2
Bonded				
L_d (X−Y)	0.0885	0.0889	0.0892	0.0908
L_D (X−Z)	0.0405	0.0472	0.0487	0.0538
Nonbonded				
l_p (Y . . . Y)	0.1640	0.1726	0.1752	0.1791
l_q (Z . . . Z)	0.0782	0.0956	0.1055	0.1097
l_r (Y . . . Z)	0.1686	0.1818	0.1873	0.1944

Table VII

Coriolis coupling constants

Couplings	Elements	GeH_2F_2	GeH_2Cl_2	GeH_2Br_2	GeH_2I_2
$A_1 \times A_2$	$-\zeta^Z_{15}$	0.7969	0.8077	0.8110	0.8079
	ζ^Z_{25}	0.6032	0.5829	0.5817	0.5761
	$-\zeta^Z_{35}$	−0.0321	0.0890	0.0629	0.0162
	ζ^Z_{45}	0.0010	0.0022	−0.0102	0.0027
$A_1 \times B_1$	ζ^Y_{16}	0.0120	0.0521	0.0120	0.0473
	ζ^Y_{26}	0.9558	0.9465	0.9777	0.9940
	$-\zeta^Y_{36}$	0.1951	0.2901	0.1857	0.0793
	ζ^Y_{46}	0.2208	0.1428	0.0998	0.0777
	ζ^Y_{17}	0.9220	0.9627	0.9767	0.9826
	$-\zeta^Y_{27}$	−0.0031	0.0393	0.0294	0.0072
	$-\zeta^Y_{37}$	0.2557	0.1840	0.1631	0.1521
	$-\zeta^Y_{47}$	0.2897	0.1923	0.1338	0.1038
$A_1 \times B_2$	ζ^X_{18}	0.0477	0.0587	0.0725	0.0804
	ζ^X_{28}	0.2398	0.1217	0.0936	0.1232
	$-\zeta^X_{38}$	0.2299	0.3392	0.5028	0.6033
	$-\zeta^X_{48}$	0.9381	0.9186	0.8357	0.7605
	$-\zeta^X_{19}$	0.5757	0.5771	0.5768	0.5820
	ζ^X_{29}	0.7259	0.6955	0.7786	0.7999
	$-\zeta^X_{39}$	0.2555	0.2597	0.1298	0.0106
	ζ^X_{49}	0.2766	0.2310	0.2090	0.1885
$A_2 \times B_1$	$-\zeta^X_{56}$	0.5607	0.5681	0.5706	0.5714
	ζ^X_{57}	0.7412	0.7841	0.7989	0.8047
$A_2 \times B_2$	ζ^Y_{58}	0.0992	0.0537	0.0273	0.0170
	$-\zeta^Y_{59}$	0.0291	0.0133	0.0067	0.0041
$B_1 \times B_2$	$-\zeta^Z_{68}$	0.0675	0.0831	0.1024	0.1115
	$-\zeta^Z_{69}$	0.8113	0.8137	0.8128	0.8032
	ζ^Z_{78}	0.0621	0.0522	0.1462	0.1781
	$-\zeta^Z_{79}$	0.5513	0.5748	0.5960	0.6056

Table VIII

Centrifugal distortion constants [MHz]

Mol. Symbol	GeH_2F_2	GeH_2Cl_2	GeH_2Br_2	GeH_2I_2
D_J	0.0584	0.0184	0.0101	0.0055
D_K	0.0885	0.0242	0.0115	0.0058
$-D_{JK}$	0.1380	0.0414	0.0214	0.0113

Conclusion

A new attempt has been made to evaluate all the molecular constants of dihalogermanes of XY_2Z_2 type using a revised set of symmetry coordinates. The molecular constants evaluated by the new procedure seem to be reasonable and the systematic set of molecular constants is available in the present work. The vibrational mean amplitude, Coriolis coupling constants and centrifugal distortion constants of GeH_2X_2 (X = F, Cl, Br and I) molecules, are available here for the first time. There are, to the author's knowledge, no experimental data available for these molecules, for the comparison of values of the mean amplitude, Coriolis coupling constants, and centrifugal distortion constants.

Acknowledgement

The authors are thankful to Prof. S. Sathikh, Director of Madras Institute of Technology, for the facilities provided to carry out this work. One of the authors (TJB) is thankful to UGC for financial assistance.

References

1. A. Davis, F. F. Cleveland and A. G. Meister, J. Chem. Phys. *20*, 454, 1952.
2. C. E. Decker, A. G. Meister and F. F. Cleveland, J. Chem. Phys., *21*, 1781, 1953.
3. K. Venkateswarlu and P. T. Sambandam, Force Constants of Molecules of XY_2Z_2 Type, Akademische Verlagsgesellschaft m.b.H., Frankfurt am Main, 234, 1957.
4. J. S. Ziomele, J. R. Ferraro and D. F. Peppard, J. Mol. Spectr., *8*, 212, 1962.
5. T. Shimanouchi and Isaosuzuki, J. Mol. Spec., *8*, 221, 1962.
6. K. Venkateswarlu and V. Malathy Devi, Indian J. Pure Appl. Phys., *3*, 195, 1965.
7. D. H. Christensen and O. F. Nielsen, J. Mol. Spectr., *27*, 489, 1968.
8. J. E. Drake, C. Riddle and D. E. Rogers, J. Chem. Soc. A., 910, 1969.
9. J. E. Drake and C. Riddle, J. Chem. Soc. A, 2114, 1969.
10. R. Namasivayam and S. Viswanathan, Proc. Indian. Acad. of Sciences, *89*, 469, 1980.
11. E. B. Wilson, J. C. Decius and P. C. Cross, Molecular Vibration, McGraw-Hill, New York, 1955.
12. S. Mohan and K. G. Ravikumar, Acta Phys. Pol., *65A*, 557, 1984.
13. S. Mohan and S. Gunasekaran, Journal de Chimie Physique 255, 1984.
14. S. Mohan and S. Gunasekaran, Acta Phys. Pol., *66A*, 81, 1984.
15. K. G. Ravikumar, S. Mohan and A. Mukunthan, J. of Mol. Struct. Theochem, *110*, 389, 1984.
16. J. C. Decius, J. Chem. Phys., *38*, 241, 1963.
17. S. J. Cyvin, Molecular Vibrations and Mean Square Amplitudes, Elsevier Pub. Co., Amsterdam, 1968.
18. J. H. Meal and S. R. Polo, J. Chem. Phys., *24*, 1119, 1126, 1956.
19. S. J. Cyvin, B. N. Cyvin and G. Hagen, Z. für Naturforschg., *23A*, 1649, 1968.
20. L. H. Jones, Inorganic Vibrational Spectroscopy, Vol. I, Marcel Dekker Inc., New York, 1971.

Acta Physica Hungarica 60 (3—4), pp. 333—338 (1986)

ROTATIONAL LINE STRENGTHS IN A $^5\Pi$(int)–$^5\Pi$(int) TRANSITION

I. KOVÁCS

Department of Atomic Physics, Technical University
1521 Budapest, Hungary

(Received 15 May 1985)

A comparison has been given between the algebraic expressions of the line strengths of the branches and the results of the numerical diagonalization computer method applied to the $^5\Sigma$–$^5\Pi$(int) transition of the CrO molecule. Moreover, explicit algebraic expressions are obtained for the line strengths in the $^5\Pi$–$^5\Pi$ transitions where both $^5\Pi$ states may belong to the coupling case intermediate between Hund's cases (a) and (b).

1. Introduction

In the CrO molecule the (2, 0), (1, 0), (0, 0), (0, 1) and (0, 2) bands of the $A^5\Pi$–$X^5\Pi$ transition have been observed and analysed rotationally by Ninomiya [1] and Hocking et al [2]. In general, the theoretical investigations of intensities in electronic bands provide the experimental researchers with some guidance in case of an analysis of a new kind. In the case of the $^5\Pi$–$^5\Pi$ transition the intensity treatments carried out till now are restricted to the line strengths of the limiting case transitions, namely of the $^5\Pi(a)$–$^5\Pi(a)$, $^5\Pi(a)$–$^5\Pi(b)$ and $^5\Pi(b)$–$^5\Pi(b)$ transitions [3], [4], [5], [6]. Recently, a number of quintet transitions containing $^5\Pi$ states in the spectra of NdO [7] and CrO [8] molecules have been observed and analyzed. The detailed theoretical investigations of the Λ-type doublets of these $^5\Pi$ states show that the formulas valid not only for pure limiting cases but also in the neighbourhood of limiting cases [9] are not satisfactory in all cases for the interpretation of the observed values [7]. Therefore to interpret the Λ-type doublings observed on the $^5\Pi$ states of the NdO molecule, algebraic expressions have been produced for the quintet term formulae, for the transition matrix elements and for the Λ-type doublet formulae in the coupling case intermediate between Hund's cases (a) and (b), i.e. valid for any value of the coupling constant Y[10]. Applying these intermediate case formulas of the Λ-doublets to the $X^5\Pi$ state of the CrO molecule excellent agreement has been obtained between the observed and calculated values [11].

In the case of the $^5\Sigma$–$^5\Pi$ transition observed in the spectrum of the CrO molecule, however, not only the wavenumbers but also the intensities of the lines of the branches have been measured. Owing to this, no wonder that the intensity formulas given to the limiting case transitions, namely to the $^5\Sigma(b)$–$^5\Pi(a)$ transition fail [8].

Having the explicit form of the $^5\Pi$ transformation matrix elements valid for any value of the coupling constant algebraic expressions have been produced for the line strengths of the branches of the $^5\Sigma$–$^5\Pi$ transition where the $^5\Pi$ state may belong to the coupling case intermediate between Hund's cases (a) and (b) [12]. Using these formulas it has been possible to eliminate all discrepancies mentioned by Cheung et al [8] but, unfortunately, due to the small number and approximative character of the observed values (about $\pm 5\%$–$\pm 15\%$ error limit) the agreement between the observed and calculated values was only moderate [12]. In the same issue of the same periodical Sassenberg et al published a paper [13] in which they have reexamined the intensities observed previously, giving them with about 1% error limit and applying a numerical diagonalization computer method of the Hamiltonian matrices to the calculation of the line intensities. A detailed comparison of the observed and calculated intensities for $J = 20$ is given in the (I^{obs}) second and (I_S^{calc}) third column of Table I. The values given in Table I are not the line strengths themselves but the intensities measured in arbitrary units, which are, of course, proportional to these. The detailed theoretical investigations show that previous expectations [8], [13] were not fulfilled: the observed anomalies are not due to the perturbation of a $^5\Sigma$ term (the effect of this, if any, is smaller than 1% which is the uncertainties in the experimental intensities) but to the fact that the $^5\Pi$ term belongs to the intermediate case between Hund's cases (a) and (b). The agreement between the observed and calculated values can be regarded as fairly good, only this numerical computer method cannot be used by other workers and there is no substitute for the algebraic method if accurate numbers are wanted. Using the algebraic expressions of the line strengths given in the paper [12] for the new reexamined observed intensities we get the values in the fourth (I_K^{calc}) column of Table I. The root mean square of the deviations for the theoretical values given by Sassenberg et al [13] is 0.44 cm^{-1} and for the values of algebraic expressions given by us [12] it is 0.49 cm^{-1}. It is remarkable that the algebraic formulas contain only one single constant, Y, and give results almost as good as the much more complicated numerical computer method containing more than one single constant.

As can be seen thus the $X^5\Pi$ state of the CrO molecule ($Y'' = 120,56\ cm^{-1}$ [8]) belongs to the intermediate case already at $J = 20$. Because the value of the coupling constant Y' of the upper $^5\Pi$ state is nearly the same [2] it is obvious that the $A^5\Pi$–$X^5\Pi$ transition is a $^5\Pi$(int)–$^5\Pi$(int) transition already at the lower rotational quantum numbers. This is the reason for producing the algebraic expressions of the line strengths of a $^5\Pi$(int)–$^5\Pi$(int) transition. The aim of the present paper is to derive such formulae for the intensity distribution.

2. Intensity distribution for $^5\Pi'$(int)—$^5\Pi''$(int) transition

As is known, in case of the thermal equilibrium the intensity of the lines of emission bands can be given by the following expression [4]:

Table I

A comparison of the observed and calculated relative line intensities for the $A^5\Sigma - X^5\Pi$ (int) (0, 0) band for $J = 20$

Branches	I^{obs}	I_S^{calc}	I_K^{calc}	Branches	I^{obs}	I_S^{calc}	I_K^{calc}
P_1	2.6	2.4	2.4	${}^{N}P_{35}$	5.5	4.9	4.7
Q_1	5.0	5.1	5.4	${}^{O}Q_{35}$	7.5	7.5	7.4
R_1	3.0	2.8	3.0	${}^{P}R_{35}$	2.7	2.9	2.9
${}^{O}P_{12}$	5.5	5.3	4.9	${}^{T}Q_{41}$	2.8	2.5	2.3
${}^{P}Q_{12}$	10.7	10.4	10.0	${}^{R}P_{42}$	3.6	3.5	3.7
${}^{Q}R_{12}$	4.8	5.1	5.1	${}^{S}Q_{42}$	7.5	7.5	8.2
${}^{N}P_{13}$	4.5	4.5	4.2	${}^{T}R_{42}$	4.4	4.1	4.6
${}^{O}Q_{13}$	8.3	8.0	7.6	${}^{R}Q_{43}$	3.5	3.3	3.9
${}^{P}R_{13}$	3.5	3.5	3.5	${}^{S}R_{43}$	2.5	1.6	2.0
${}^{Q}P_{21}$	4.0	4.4	4.5	Q_4	1.4	1.4	1.5
${}^{R}Q_{21}$	10.0	10.0	10.4	${}^{O}P_{45}$	6.2	6.0	6.0
${}^{S}R_{21}$	5.8	5.6	6.0	${}^{P}Q_{45}$	11.0	9.4	9.8
Q_2	1.9	1.4	1.3	${}^{Q}R_{45}$	3.2	3.8	4.1
${}^{O}P_{23}$	3.0	2.0	1.8	${}^{T}Q_{52}$	3.0	2.3	2.5
${}^{P}Q_{23}$	3.5	3.6	3.5	${}^{R}P_{53}$	3.8	3.5	3.8
${}^{N}P_{24}$	4.8	4.8	4.6	${}^{S}Q_{53}$	7.0	7.1	7.9
${}^{O}Q_{24}$	8.0	8.0	7.8	${}^{T}R_{53}$	3.8	3.6	4.1
${}^{P}R_{24}$	3.0	3.3	3.3	${}^{Q}P_{54}$	4.8	5.0	5.6
${}^{R}P_{31}$	3.0	3.2	3.0	${}^{R}Q_{54}$	10.0	9.1	10.5
${}^{S}Q_{31}$	7.4	7.4	7.4	${}^{S}R_{54}$	4.8	4.2	4.9
${}^{T}R_{31}$	4.2	4.3	4.4	P_5	2.7	2.7	3.1
${}^{R}Q_{32}$	4.0	3.5	4.1	Q_5	4.9	4.4	5.2
Q_3	3.4	3.0	3.0				
${}^{O}P_{34}$	1.8	2.0	1.9	I_S (RMS) = 0.44 cm^{-1}			
${}^{P}Q_{34}$	4.0	3.5	3.3	I_K (RMS) = 0.49 cm^{-1}			

$$I_{J''N''}^{J'N'} = GS_{N'N''}^{J'J''} \exp\left(-\frac{hcF_{J'}}{kT}\right), \tag{1}$$

where G can be regarded as constant to a good approximation within a particular band and $S_{N'N''}^{J'J''}$ is the line strength. In the case of intermediate case transition the form of $S_{N'N''}^{J'J''}$ will be [4]

$$S_{N'N''}^{J'J''} = \left| \sum_{\Sigma=-S}^{+S} S_{\Lambda'+\Sigma,N'}^{J'} \sqrt{S_{J'',\Lambda''+\Sigma}^{J',\Lambda'+\Sigma}}\, S_{\Lambda''+\Sigma,N''}^{J''} \right|^2, \tag{2}$$

where $S_{J'',\Lambda''+\Sigma}^{J',\Lambda'+\Sigma}$ is the line strength where both the upper and lower electronic states may belong to Hund's case (a), i.e. the so-called Hönl–London factor and $S_{\Lambda'+\Sigma,N'}^{J'}$ and $S_{\Lambda''+\Sigma,N''}^{J''}$ are the transformation matrix elements for the ${}^5\Pi$ states given by [10]. These line strength formulae are listed in Table II in a quite condensed form where $\begin{pmatrix} i, N' \\ k, N'' \end{pmatrix}$ $= (1, J-2), (2, J-1), (3, J), (4, J+1), (5, J+2)$. The values of the numerical coefficients

$a_{ik}^{(s)}$ will be given in matrix form

$$\mathbf{a}^{(s)}=\begin{pmatrix} a_{11}^{(s)} & \cdot & \cdot & \cdot & a_{15}^{(s)} \\ \cdot & & & & \cdot \\ \cdot & & & & \cdot \\ \cdot & & & & \cdot \\ a_{51}^{(s)} & \cdot & \cdot & \cdot & a_{55}^{(s)} \end{pmatrix}, \tag{3a}$$

where $s=1, 2, 3, 4, 5, 6$. The explicit form of these will be

$$\mathbf{a}^{(1)}=\begin{pmatrix} 1 & 1 & 3 & 1 & 1 \\ 1 & 1 & 3 & 1 & 1 \\ 3 & 3 & 1 & 3 & 3 \\ 1 & 1 & 3 & 1 & 1 \\ 1 & 1 & 3 & 1 & 1 \end{pmatrix}; \quad \mathbf{a}^{(2)}=\begin{pmatrix} 1 & 2 & 1 & 2 & 1 \\ 2 & 4 & 2 & 4 & 2 \\ 1 & 2 & 3 & 2 & 1 \\ 2 & 4 & 2 & 4 & 2 \\ 1 & 2 & 1 & 2 & 1 \end{pmatrix};$$

$$\mathbf{a}^{(3)}=\begin{pmatrix} 1 & 1 & 1 & 1 & -1 \\ 1 & 1 & 1 & 1 & -1 \\ 1 & 1 & 3 & 1 & -1 \\ 1 & 1 & 1 & 1 & -1 \\ -1 & -1 & -1 & -1 & 1 \end{pmatrix}; \quad \mathbf{a}^{(4)}=\begin{pmatrix} 3 & 3 & -1 & 3 & 3 \\ 3 & 3 & -1 & 3 & 3 \\ -1 & -1 & 1 & -1 & -1 \\ 3 & 3 & -1 & 3 & 3 \\ 3 & 3 & -1 & 3 & 3 \end{pmatrix}; \tag{3b}$$

$$\mathbf{a}^{(5)}=\begin{pmatrix} 1 & 2 & -1 & 2 & 1 \\ 2 & 4 & -2 & 4 & 2 \\ -1 & -2 & 3 & -2 & -1 \\ 2 & 4 & -2 & 4 & 2 \\ 1 & 2 & -1 & 2 & 1 \end{pmatrix}; \quad \mathbf{a}^{(6)}=\begin{pmatrix} 1 & -1 & 1 & -1 & -1 \\ -1 & 1 & -1 & 1 & 1 \\ 1 & -1 & 3 & -1 & -1 \\ -1 & 1 & -1 & 1 & 1 \\ -1 & 1 & -1 & 1 & 1 \end{pmatrix}.$$

Furthermore*

$$\begin{aligned} &A_5^1(J)=u^{\pm}(J)\mp 4\tau(J); && B_5^1(J)=u^{\mp}(J)\mp 2\tau(J) \\ &A_4^2(J)=Y-8\pm u^{\pm}(J)+2\tau(J); && B_4^2(J)=Y+4\mp u^{\mp}(J)-4\tau(J) \\ &A_3(J)=Y-6+3\tau(J); && B_3(J)=Y+2-3\tau(J) \end{aligned} \tag{4}$$

* To save space, the upper signs belong to the upper subscripts and the lower signs to the lower subscripts.

where

$$\tau(J)=\frac{4J(J+1)}{(Y-2)^2+4J(J+1)};$$

$$u^{\pm}(J)=\sqrt{(Y-2+\tau(J))^2+4J(J+1)}\pm(Y-2+\tau(J)) \tag{5}$$

and

$$C_N(J)=2(J-1)(J+2)[f_N(J)]^2L_N(J)+M_N[f_N(J)]^2[g_N(J)]^2+$$
$$+2J(J+1)[g_N(J)]^2N_N(J), \tag{6}$$

where

$$f_{J\mp2}(J)=\mp[Y-4+4(\tau)]u^{\mp}(J)+2J(J+1)-\frac{2}{3}\tau(J)[Y+4-4\tau(J)],$$

$$g_{J\mp2}(J)=\mp[Y-4\tau(J)]u^{\pm}(J)-2[J(J+1)+2]-\frac{4}{3}\tau(J)[Y-8+8\tau(J)],$$

$$f_{J\mp1}(J)=\mp[Y-2\tau(J)]u^{\mp}(J)-\frac{4}{3}\tau(J)[Y+4-4\tau(J)], \tag{7}$$

$$g_{J\mp1}(J)=\mp[Y-4+2\tau(J)]u^{\pm}(J)-\frac{2}{3}\tau(J)[Y-8+2\tau(J)]-8,$$

$$f_J(J)=B_3(J)[Y-6\tau(J)]-2J(J+1),$$
$$g_J(J)=A_3(J)[Y-4+6\tau(J)]-2(J-2)(J+3)$$

and

$$L_N(J)=\frac{3}{M_N}\{[A_i(J)]^2+b_i(J-2)(J+3)\},$$
$$N_N(J)=\frac{3}{M_N}\{[B_i(J)]^2+b_iJ(J+1)\}, \tag{8}$$

where

$$(N,i)=(J-2,1),\ (J-1,2),\ (J,3),\ (J+1,4),\ (J+2,5),$$
$$M_{J-2}=M_{J-1}=M_{J+1}=M_{J+2}=3;\qquad M_J=1; \tag{9}$$
$$b_1=b_3=b_5=1;\qquad b_2=b_4=4.$$

In the expressions A_i, B_i, f_N, g_N, C_N, τ, $u^{\pm}$ related to the upper state denoted by one prime ($^5\Pi'$) for the line strengths of P and R branches, $J-1$ and $J+1$ are to be substituted for the J value, respectively. Substituting successively all values of i, k and N', N'' we get the line strengths of all the possible 75 branches. In Table II both $^5\Pi$ terms were assumed to be normal. In the case of inverted terms for the transition $^5\Pi'_i$(int)–$^5\Pi''_n$(int) the first indices 1, 2, ..., 5 in the denotation of the branches should be replaced by the indices 5, 4, ..., 1. For $^5\Pi'_n$(int)–$^5\Pi''_i$(int) this applies to the second indices and, finally, for $^5\Pi'_i$(int)–$^5\Pi''_i$(int) this applies to both indices.

Table II

Line strengths for $^5\Pi$ (int)–$^5\Pi$ (int) transitions

Branches	Line strengths
$^5\Pi'$–$^5\Pi''$	$^5\Pi'$ (int)–$^5\Pi''$ (int)
$P_{ik}(J)$	$\frac{a_{ik}^{(1)}(J-1)(J+1)}{JC'_{N'}(J-1)C''_{N''}(J)}\{2(J-2)(J+2)[a_{ik}^{(2)}(J-3)(J+3)+a_{ik}^{(3)}A'_i(J-1)A''_k(J)]f'_{N'}(J-1)f''_{N''}(J)+$ $+a_{ik}^{(4)}f'_{N'}(J-1)f''_{N''}(J)g'_{N'}(J-1)g''_{N''}(J)+2J^2[a_{ik}^{(5)}(J-1)(J+1)+a_{ik}^{(6)}B'_i(J-1)B''_k(J)]g'_{N'}(J-1)g''_{N''}(J)\}^2$
$Q_{ik}(J)$	$\frac{a_{ik}^{(1)}(2J+1)}{J(J+1)C'_{N'}(J)C''_{N''}(J)}\{2(J-1)(J+2)[3a_{ik}^{(2)}(J-2)(J+3)+2a_{ik}^{(3)}A'_i(J)A''_k(J)]f'_{N'}(J)f''_{N''}(J)+$ $+a_{ik}^{(4)}f'_{N'}(J)f''_{N''}(J)g'_{N'}(J)g''_{N''}(J)-2J^2(J+1)^2a_{ik}^{(5)}g'_{N'}(J)g''_{N''}(J)\}^2$
$R_{ik}(J)$	$\frac{a_{ik}^{(1)}J(J+2)}{(J+1)C'_{N'}(J+1)C''_{N''}(J)}\{2(J-1)(J+3)[a_{ik}^{(2)}(J-2)(J+4)+a_{ik}^{(3)}A'_i(J+1)A''_k(J)]f'_{N'}(J+1)f''_{N''}(J)+$ $+a_{ik}^{(4)}f'_{N'}(J+1)f''_{N''}(J)g'_{N'}(J+1)g''_{N''}(J)+2(J+1)^2[a_{ik}^{(5)}J(J+2)+a_{ik}^{(6)}B'_i(J+1)B''_k(J)]g'_{N'}(J+1)g''_{N''}(J)\}^2$

The substitution of $Y'=Y''\to\infty$ yields the simple formulas of the $^5\Pi(a)$–$^5\Pi(a)$ transition and $Y'=Y''=0$ the formulas of the $^5\Pi(b)$–$^5\Pi(b)$ transition [3], [4]. Finally, if one $Y\to\infty$ and the other is equal to zero we obtain the formulas of the $^5\Pi(a)$–$^5\Pi(b)$ transition given in [6].

The theoretical formulas contain only two constants, the coupling constant Y' of the upper state and the coupling constant Y'' of the lower state.

References

1. M. Ninomiya, J. Phys. Soc. Japan, *10*, 829, 1955.
2. W. H. Hocking, A. J. Merer, D. J. Milton, W. E. Jones and G. Krishnamurty, Can. J. Phys., *58*, 516, 1980.
3. D. Premaswarup, Ind. J. Phys., *27*, 415, 578, 1953.
4. I. Kovács, Rotational Structure in the Spectra of Diatomic Molecules, Akadémiai Kiadó, Budapest and Adam Hilger Ltd, London, 1969.
5. E. E. Whiting, I. A. Peterson, I. Kovács and R. W. Nicholls, J. Mol. Spectr., *47*, 91, 1973.
6. I. Kovács and M. I. M. El Agrab, Acta Phys. Hung., *43*, 185, 1977.
7. L. A. Kaledin, E. A. Shenyavskaya and I. Kovács, Acta Phys. Hung., *54*, 189, 1983.
8. A. S.-C. Cheung, W. Zyrnicki and A. J. Merer, J. Mol. Spectr., *104*, 315, 1984.
9. I. Kovács and I. Péczeli, J. Mol. Spectr., *88*, 264, 1981.
10. I. Kovács, J. Mol. Spectr., *98*, 41, 1983.
11. I. Kovács and J. Antal, Acta Phys. Hung., *56*, 255, 1984.
12. I. Kovács and J. Antal, Can. J. Phys., *62*, 1603, 1984.
13. V. Sassenberg, A.S.-C. Cheung and A. J. Merer, Can. J. Phys., *62*, 1610, 1984.

Acta Physica Hungarica 60 (3—4), pp. 339—346 (1986)

SHORT COMMUNICATION

THE LORENTZ TIME TRANSFORMATIONS INCOMPATIBLE WITH EINSTEIN'S AND LORENTZ'S THEORIES AND EXPERIMENTS

JÓZEF WILCZYŃSKI*

Wrocław, Poland

(Received in revised form 10 August 1984)

Let us take two internal reference frames S and S'; frame S' is assumed to be moving with speed v relative to frame S. Note that frame S is preferred and frame S' is moving in the Lorentz-type theory (L – tT), but in Einstein's special theory of relativity (STR) the former is "stationary" and the latter is "moving". The relativistic effects are absent in frame S for both theories, but they exist or are to exist in frame S' as long as frame S' is moving relative to frame S in L – tT and as long as frame S' is taken (treated) to be "moving" relative to "stationary" frame S in STR. Such kinematical states of motion of the two frames are kept in our considerations. Let us remind of the fact that *in STR* the relativistic effects exist or arise in the "moving" frame only when they are considered or observed or compared or measured from or/and in the "stationary" frame. Our considerations within the framework of STR will be made as if we are in frame S. In a given region of space there can be only one preferred frame and infinitely many "stationary" frames but only one of them can coincide with this preferred frame.

In frames S and S' there exist coordinate systems, respectively, $S(O, x, t)$ and $S'(O', x', t')$; $O(O')$ is the origin of system, $x(x')$ is the coordinate parallel to speed v, and $t(t')$ is the time. The Lorentz transformations for a one-dimensional space, in STR and L – tT, are

$$x' = \gamma (x - vt), \tag{1a}$$

$$t' = \gamma (t - vx/c^2), \tag{1b}$$

$$x = \gamma (x' + vt'), \tag{2a}$$

$$t = \gamma (t' + vx'/c^2), \tag{2b}$$

* Mailing address: Skr. p. 2057, Wrocław 1, Poland

where $\gamma = 1/(1-v^2/c^2)^{1/2}$. The above formulas reduce to

$$x' = -\gamma vt. \tag{3a}$$

$$t' = \gamma t, \tag{3b}$$

$$x = \gamma vt', \tag{4a}$$

$$t = \gamma t', \tag{4b}$$

when the origins coincide at the moment $t = t' = 0$. What do formulas (3a) and (3b) tell us? In frame S, after time $t = t_1$, the origin O' will be at the distance $x_1 = vt_1$ from the origin O. Whereas in frame S', according to (3a), the distance between O and O' is $x' = -\gamma vt_1 = -\gamma x_1$. This means that $|x'_1| > |x_1|$. It ought to be just so if there exists length contraction in frame S': the distance between O and O' is the same for both frames but it must have a greater value in the moving ("moving") frame S' than in the preferred ("stationary") frame S if identical measures are used to scale the coordinates in both systems. But the case is the same with times. In formulas (1b) and (3b) we have also the length of time (but not the time units) as that in formulas (1a) and (3a): to time t in S corresponds time t' in S'. Here, similarly, we have in (3b): $t'_1 = \gamma t_1$, and $t'_1 > t_1$ if identical clocks are used in both frames. Analogously to the explanation of formula (3a), it follows from formula (3b) that the time flows faster in S' than in S! We think another explanation cannot exist when one relies on formulas (3a) and (3b).

The time length, when measured with the help of clocks, is connected with the clock rate, that is, with the frequency of "ticks" ν or period $T = 1/\nu$. The greater the frequency the faster goes the clock (the faster "moves the hand on the clock face") and the faster flows the time, and vice versa. Following the above we receive from formula (3b) that the clock frequency is greater in S' than in S! But what do the relativists tell us and what do the experiments give?

In the light of existing experiments the relativists assume as a fact free of discussion that the frequency of the "moving" clock undergoes relativistic decrease. It is the so-called quadratic (transverse) Doppler effect defined as

$$\nu' = \nu/\gamma. \tag{5}$$

This effect is always to be negative in STR, that is to say $\nu' < \nu$; thus flowing the time t' in frame S' is slower than flowing the time t in frame S. We have therefore the divergence between what gives formula (3b) and what give experiments confirming formula (5). The conclusion, the time relations in formulas (1b–4b) are contradictory to experiments.

In reality, however, almost in all the existing experiments the sign of the relativistic change of the frequency of the atomic clocks is not consistent with the prediction of STR. Only the experiments in which the "stationary" frame is at rest on the Earth's surface confirm formula (5); we have here, e.g. the experiments with moving emitting ions [1], and when the absorber is in the centre of a rotating disk in the rotor

experiments [2]. But in the temperature-dependent experiments [3, 4] we have the transition from the negative to the positive (or vice versa) quadratic Doppler effect *in the same experiment* when the temperature either of the absorber or of the emitter is changing! In the rotor experiments (if to explain within the framework of STR) the positive effects ($\nu' > \nu$) are received when the absorber is further from the disk centre than the emitter placed in the centre [5, 6]. Instead, when emitter E and absorber A both are at the opposite edges of a rotor, the effect is null [7, 8], although the *relative* speed between E and A is then doubled. Let us remember, in STR, the "stationary" frame must be the frame in which the comparison (observation, measurement) of the frequency of the clock resting in another "moving" frame (usually with the help of the photons or gamma rays coming from that other frame or emitted by a source at rest in that other frame) with the frequency of the clock resting in this frame takes place. This means that the frame attached to the absorber and the absorber itself *must* be "stationary" ones (!) in the rotor experiments; the process of comparison takes place inside the absorber through absorption of gamma rays.

Note that the formulas derived (or taken), in STR and L – tT, for the experiments basing on the Mössbauer effect differ from each other. In both derivations the speeds related to the laboratory are taken. In STR the relativistic change of frequency must be a function of the *relative* speed $v = v_E - v_A$ between emitter and absorber, where v_A and v_E are the absorber's and emitter's speeds, respectively, relative to the laboratory; we have assumed that both v_A and $v_E \ll c$, then the relativistic velocity addition formula gives $v = v_E - v_A$. But in L – tT, each relativistic effect is related only and exclusively to the preferred frame, that is, is a function only and exclusively of the absolute speed between moving and preferred frames. In the theory of preferred frame all the relativistic effects are *absolute* ones but not relative (as in STR) and can have the positive as well as negative or even null sign; these effects as physical ones do not depend on the relative speeds between the moving frames. Besides, the preferred frame cannot move relative to any other frame (in a given region of space). Thus we have that the relativistic frequency change is proportional to the *square of the relative speed* v in STR and to the *difference of the squares of the speeds* v_A *and* v_E in L – tT, and

$$D^{\pm}_{\mathrm{Lor}} = \left| \frac{v_A^2 - v_E^2}{2c^2} \right| > \frac{(v_A - v_E)^2}{2c^2} = \frac{v^2}{2c^2} = D_{\mathrm{Ein}}, \tag{6}$$

where terms $D^{\pm}_{\mathrm{Lor}}$ and D_{Ein} are equal to the relative frequency difference $(v_E - v_A)/v_A$, respectively, in both theories. In the rotor experiments the investigators make use of both left and right hand side terms of inequality (6). Of course, this is of no importance if either $v_A = 0$ or $v_E = 0$ is taken in these experiments. But the left hand side term in (6) follows also from the general theory of relativity (GTR) when the pseudogravitational field is introduced. However, the results in the temperature-dependent experiments are proportional to the *difference of the squares* of the speeds related to the laboratory (!) and cannot be explained by GTR [20].

Thus one cannot state which side of inequality (6) finds its confirmation in the results received in the existing rotor experiments. It would be possible if either the emitter or the absorber were half way to the edge instead of in the centre (see Fig. 1). In Fig. 1 terms $D^{\pm}_{\mathrm{Lor}}$ and D_{Ein} from (6) are shown graphically. The maximum absolute difference between these terms, $\Delta D^{\pm} = D^{\pm}_{\mathrm{Lor}} - D_{\mathrm{Ein}}$, is when the emitter is half way to the edge and the absorber at the edge (D^{+}_{Lor} and ΔD^{+}) or vice versa (D^{-}_{Lor} and $|\Delta D^{-}|$). Thus, these experiments could confirm either L – tT and GTR or STR, this time also with the help of the *value* of this effect. We claim that these experiments modified in this way will deny STR.

Both the signs of the relativistic effect and the dependence on the difference of the squares of the speeds in the temperature-dependent experiments, the positive effect when the absorber is at the edge of a rotor, and the lack of this effect when the emitter and the absorber are at the opposite edges of a rotor, all these three groups of experiments do not confirm STR but suggest that a preferred frame exists. Such a frame, in these experiments, seems to be attached to the Earth's surface (in the first

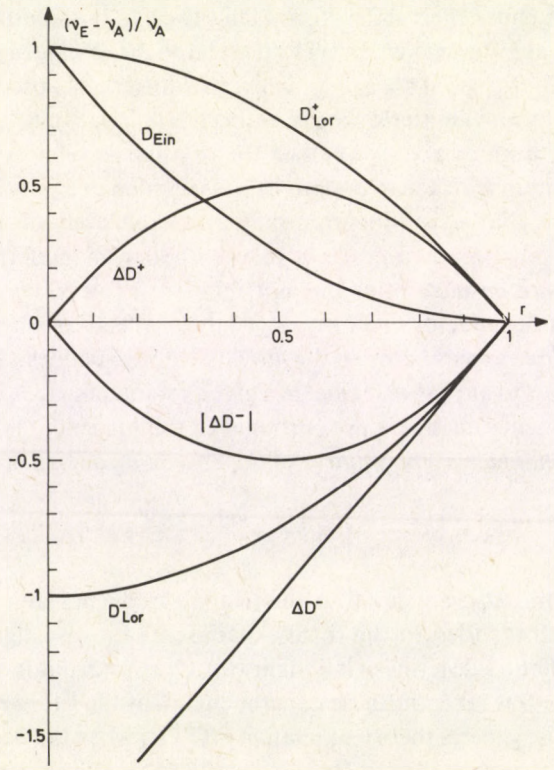

Fig. 1. Graphical representation of inequality (6).
$\Delta D^{+} = D^{+}_{\mathrm{Lor}} - D_{\mathrm{Ein}}$; $\Delta D^{-} = D^{-}_{\mathrm{Lor}} - D_{\mathrm{Ein}}$; $|\Delta D^{-}| = D^{-}_{\mathrm{Lor}} + D_{\mathrm{Ein}}$.
Emitter for D^{+} (absorber for D^{-}) at distance $r=1$ and absorber (emitter) changes its position from $r=0$ to $r=1$

approximation at least). But in such a situation one can put a question whether the Lorentz transformations are useful in the theory of preferred frame, especially for the transformations between two moving frames? The Lorentz transformations could be correct between the preferred and the moving frames but for the consequence of formula (3b). Besides, these transformations give the two-way symmetry (necessary in STR!), but in the theory of preferred frame there can exist only the one-way symmetry. (One cannot accept that the preferred frame moves relative to the moving frame, and that in this preferred frame there exists a relativistic effect). Concluding, the Lorentz transformations cannot be carried out in the theory of preferred frame especially when two frames are taken as moving relative to this preferred frame.

The t and t' in formulas (1b), (2b), (3b), and (4b) cannot be the periods of clocks if they denote the length of time in terms vt and vt' in formulas (1a), (2a), (3a), and (4a). In formulas (1b–4b) there are terms vx/c^2 or vx'/c^2. These terms are to be connected [9, 10] with the assumption that the light velocity is isotropic in *every* inertial reference frame. But in the theory of preferred frame (of Lorentz-type) the one-way light velocity is isotropic only in one frame, in the preferred frame.

The isotropy of light velocity in every inertial reference frame must exist in STR, it is the Einstein second postulate. But is this postulate true? Let us consider Einstein's train-embankment thought experiment [11] but complemented. When the lightning strikes simultaneously at points A and B in the "stationary" embankment S (or at A'

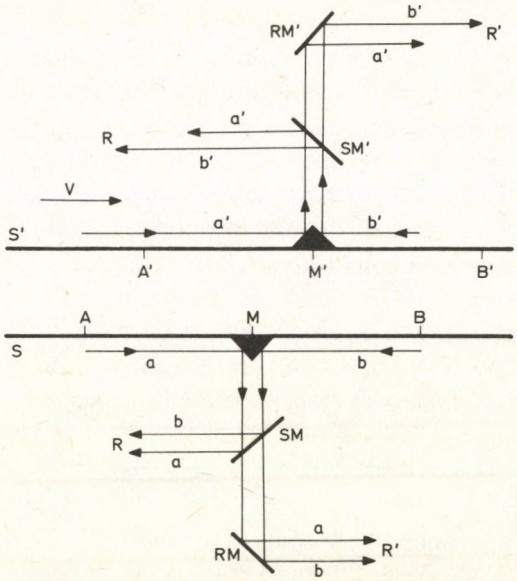

Fig. 2. Flashes a and b coming from A and B, and flashes a' and b' coming from A' and B' (coinciding with A and B, respectively, at a moment of striking), ought to reflect perpendicularly relative to speed v from mirrors, respectively, SM, RM, SM' and RM' at suitable orientations of the mirrors

and B' in the "moving" trains S'), the points $M(AM = BM)$ in S and $M'(A'M' = B'M')$ in S' coincide. The flashes coming to $M(M')$ reflect perpendicularly to speed v of S' and fall on the semi-transparent mirror $SM(SM')$ at rest in S(in S'); note that using such a mirror has been proposed by Einstein himself [11]. One part of each flash reflects *again perpendicularly* relative to speed v and can be observed (registered) by the rows of observers in S (R-observers) as well as in S' (R'-observers). The second part transits through $SM(SM')$, reflects *also perpendicularly* relative to speed v from mirror $RM(RM')$ at rest in S (in S'), and can be observed by the (same) rows of observers at rest in S (R-observers) as well as in S' (R'-observers). In STR, the R-observers must say that the simultaneity exists in M and therefore cannot exist in M'!, and the R'-observers (for which frame S' becomes the "stationary" frame!) must say that the simultaneity exists in M' and therefore cannot exist in M!; the simultaneity ought to be observed at M by R and at M' by R'. But what follows from our thought experiment in Fig. 2? If there exists the simultaneity at M (as in Fig. 2) of the flashes coming from A and B or from A' and B', it will be observed *in S as well as in S'*!. Then the simultaneity *cannot* exist in M' (as it is in Fig. 2), but this absence of simultaneity must be observed *also in S' as well as in S*!. The conclusion is that the simultaneity, if any, can exist *only in one frame* in a given region of space; this frame is called the preferred frame. It follows from Fig. 2 that the R'-observers cannot say that the flashes have come simultaneously to M' in the train (as a "stationary" for them) if the R-observers say that they have observed the simultaneity at M, and vice versa. But, if the embankment and the train were moving relative to any preferred frame (that is, in which the light velocity is isotropic), the two groups of observers should see the simultaneity neither at M nor at M'.

To claim that the light velocity is isotropic in every inertial reference frame (the gravitational field is excluded here), according to STR, is a logical and physical nonsense. Then one would assume that: 1) each inertial reference frame, even *imaginary* one!, should have its own ether, 2) the source, in the act of emission of a single photon or gamma ray observed then in every frame, should emit an infinitely great number of the "twin" rays to "serve" all possible (natural, artificial, imaginary) frames, 3) the "twin" rays should have different initial velocities relative to their own source, 4) each of these "twins" enters and propagates only in this frame in which its velocity will be isotropic, and 5) such a "twin" ought to be visible only in the "stationary" frame.

In the light of the above and based on the relativistic time dilation of a moving clock confirmed in experiments, the experiments considered herein suggest the formula

$$t = t'_1/(1 - V_1^2/c^2)^{1/2} = t'_2/(1 - V_2^2/c^2)^{1/2} = t'_i/(1 - V_i^2/c^2)^{1/2} \tag{7}$$

for the length of time instead of formulas (1b) and (2b); t is the time length in the preferred frame, and subscripts 1, 2 and i at the absolute speed V and time t' refer to different moving frames–clocks. Note that we have in (7) only the one-way symmetry between: S'_1 and S, S'_2 and S, S'_1 and S'_2, and so on. And just so it ought to be in the theory of preferred frame.

A separate question is, to what the preferred frame is attached. This "what" must be *material* since the photons are material and if the photons need any ether (or physical space or whatever to "transport" photon energies or for photons to have the same observed velocities in vacuum, that is, in space without medium). Keeping the above in mind, would each frame, *even imaginary one*, have its own *material* ether? No, it can be but only in a, say, religion-like theory. The theories (except STR) being held in esteem assume usually that the Earth is moving relative to such an ether. But why is not the Earth to possess its own ether the density of which is predominant relative to the density of the ethers belonging to the other celestial bodies, in the space inside the Earth and surrounding its surface? This predominance, in the case of the Earth, diminishes with the distance from the surface. The ether can be a "shadow" of gravitational field, if not this field itself, with the same properties [12]. Then the "stationary" frame in STR attached to the Earth's surface will at the same time be the preferred frame in L − tT; then the two theories predict the same results. But these results should be different (divergent) if the laboratory (with the "stationary" frame-clock resting in it) is moving relative to (or on) the Earth's surface, or when the emitter and the absorber are moving relative to the Earth's surface. On assuming such an ether to exist one must admit that not all *necessary* experiments have been performed to confirm or refute STR and its postulates.

Is it possible to distinguish experimentally between GTR and L − tT when using the rotors? Is it possible to state experimentally whether the laboratory is moving or not relative to an ether? The rotor experiments (with a single disk) that have been performed till now, and even if the emitter (absorber) were half way to the edge, cannot distinguish between GTR and L − tT. Some physicists (see, e.g., [13]) claim that the absolute motion of the Earth cannot be tested with the help of rotor experiments. But the two distinctions can be realized with the help of the second variant of Dos Santos' proposal [14]: two rotors, one over the other, with the coinciding axes. Here, the pseudogravitational field cannot exist along the direction of radiation being perpendicular to the planes of disks rotating in parallel (one with absorber and the other with emitter). The speeds of the disks ought to be equal, various and different, in the same and opposite directions. Then, if the left hand side of (6) is confirmed, what we expect, the equivalence principle of GTR will have to be rejected. Here, also the objection [13] concerning a single rotor cannot be valid, and the Earth's speed V relative to an ether can be found. Then $V_A = V + v_A$ and $V_E = V + v_E$, and

$$\frac{V_A^2 - V_E^2}{2c^2} = \frac{v_A^2 - v_E^2}{2c^2} + \frac{2V(v_A - v_E)}{2c^2}, \tag{8}$$

where V_A and V_E are the speeds, respectively, of the absorber and emitter relative to the preferred frame relative to which the Earth's laboratory is to be moving. We predict the confirmation of (8) but with $V=0$ (that is to say as in the temperature-dependent experiments and according to our model of ether). But somebody can say that Dos Santos' proposal has been refuted [15, 16]. However, as we have shown [17], the proofs

of these papers on the one hand are not performed within the framework of STR, and, on the other, even in using the same methods of derivation it is easy to show that the angle φ [16] (and θ_{abs} [15]) of the emitted signal, measured in the laboratory frame, cannot be equal to 270°! for any value of $v_E \neq 0$ if the experimental facts (showers of cosmic rays, headlight radiation in synchrotrons, annihilations in flight, Marinov's "wired photocells on a rotating disk" experiment [18]) are taken into account. Note that based on these experiments, if the signal subtends an angle $\varphi'' = 270°$, measured in emitter's frame, with the direction of emitter's speed v_E *but when* $v_E = 0$ (that is, when the emitter's and the laboratory's frames are identical), this angle must be unchanged in the emitter's frame for any value of v_E, but it is angle φ that must depend on the value of v_E; then even the authors' proofs cannot give null results. Marinov's objection [19] does not refer [17] to the second variant of Dos Santos' proposal.

References

1. H. I. Mandelberg and L. Witten, J. Opt. Soc. Am., *52*, 529, 1962.
2. K. C. Turner and H. A. Hill, Phys. Rev., *134*B, 252, 1964.
3. R. V. Pound and G. A. Rebka, Phys. Rev. Lett., *4*, 274, 1960.
4. A. J. F. Boyle, D. St. P. Bunbury, C. Edwards, and H. E. Hall, Proc. Phys. Soc., *76*, 165, 1960.
5. D. C. Champeney, G. R. Isaak and A. M. Khan, Proc. Phys. Soc., *85*, 583, 1965.
6. D. C. Champeney, G. R. Isaak and A. M. Khan, Nature, *198*, 1186, 1963.
7. D. C. Champeney and P. B. Moon, Proc. Phys. Soc., *77*, 350, 1961.
8. D. C. Champeney, G. R. Isaak and A. M. Khan, Phys. Lett., *7*, 241, 1963.
9. J. Palacios, Nuovo Cimento, *43*B, 413, 1966.
10. B. L. Rawat, Indian J. Theor. Phys., *28*, 161, 1980.
11. A. Einstein, Über die spezielle und die allgemeine Relativitätstheorie, Fried. Vieweg und Sohn, Braunschweig, 1920, §§9, 8, 7.
12. J. Wilczyński, Acta Phys. Hung., *54*, 361, 1983.
13. S. Marinov, Found. Phys., *8*, 637, 1978.
14. A. N. Dos Santos, Nuovo Cimento, *32*B, 519, 1976.
15. W. A. Rodriguez and V. Buonomano, Nuovo Cimento, *34*B, 240, 1976.
16. D. G. Ashworth and P. A. Davies, Nuovo Cimento, *36*B, 1, 1976.
17. J. Wilczyński, "Defence of Dos Santos' Proposal", unpublished.
18. S. Marinov, Eppur si muove, C. B. D. S., Bruxelles, 1977, p. 174.
19. S. Marinov, Found. Phys., *7*, 947, 1977.
20. C. W. Sherwin, Phys. Rev., *120*, 17, 1960.

NOTES TO CONTRIBUTORS

I. PAPERS will be considered for publication in Acta Physica Hungarica only if they have not previously been published or submitted for publication elsewhere. They may be written in English, French, German or Russian.

Papers should be submitted to

Prof. I. Kovács, Editor
Department of Atomic Physics, Technical University
1521 Budapest, Budafoki út 8, Hungary

Papers may be either articles with abstracts or short communications. Both should be as concise as possible, articles in general not exceeding 25 typed pages, short communications 8 typed pages.

II. MANUSCRIPTS

1. Papers should be submitted in three copies.
2. The text of papers must be of high stylistic standard, requiring minor corrections only.
3. Manuscripts should be typed in double spacing on good quality paper, with generous margins.
4. The name of the author(s) and of the institutes where the work was carried out should appear on the first page of the manuscript.
5. Particular care should be taken with mathematical expressions. The following should be clearly distinguished, e.g. by underlining in different colours: special founts (italics, script, bold type, Greek, Gothic, etc.); capital and small letters; subscripts and superscripts, e.g. x^2, x_3; small *l* and l; zero and capital O; in expressions written by hand: *e* and *l*, *n* and *u*, *v* and v, etc.

A List of Symbols on a separate sheet should be attached to each paper.

6. References should be numbered serially and listed at the end of the paper in the following form: J. Ise and W. D. Fretter, Phys. Rev., *76*, 933, 1949.

For books, please give the initials and family name of the author(s), title, name of publisher, place and year of publication, e.g.: J. C. Slater, Quantum Theory of Atomic Structures, I. McGraw-Hill Book Company, Inc., New York, 1960.

References should be given in the text in the following forms: Heisenberg [5] or [5].

7. Captions to illustrations should be listed on a separate sheet, not inserted in the text.
8. In papers submitted to Acta Physica all measures should be expressed in SI units.

III. ILLUSTRATIONS AND TABLES

1. Each paper should be accompanied by three sets of illustrations, one of which must be ready for the blockmaker. The other sets attached to the copies of the manuscript may be rough drawings in pencil or photocopies.
2. Illustrations must not be inserted in the text.
3. All illustrations should be identified in blue pencil by the author's name, abbreviated title of the paper and figure number.
4. Tables should be typed on separate pages and have captions describing their content. Clear wording of column heads is advisable. Tables should be numbered in Roman numerals (I, II, III, etc.).

IV. RETURN OF MATERIAL

Owing to high postage costs, the Editorial Office cannot undertake to return *all* material not accepted for any reason for publication. Of papers to be revised (for not being in conformity with the above Notes or other reasons) only *one* copy will be returned. Material rejected for lack of space or on account of the Referees' opinion will not be returned to authors outside Europe.

Periodicals of the Hungarian Academy of Sciences are obtainable at the following addresses:

AUSTRALIA
C.B.D. LIBRARY AND SUBSCRIPTION SERVICE
Box 4886, G.P.O., *Sydney N.S.W. 2001*
COSMOS BOOKSHOP, 145 Ackland Street
St. Kilda (Melbourne), Victoria 3182

AUSTRIA
GLOBUS, Höchstädtplatz 3, *1206 Wien XX*

BELGIUM
OFFICE INTERNATIONAL DE LIBRAIRIE
30 Avenue Marnix, *1050 Bruxelles*
LIBRAIRIE DU MONDE ENTIER
162 rue du Midi, *1000 Bruxelles*

BULGARIA
HEMUS, Bulvar Ruszki 6, *Sofia*

CANADA
PANNONIA BOOKS, P.O. Box 1017
Postal Station "B", *Toronto, Ontario M5T 2T8*

CHINA
CNPICOR, Periodical Department, P.O. Box 50
Peking

CZECHOSLOVAKIA
MAD'ARSKÁ KULTURA, Národní třida 22
115 66 Praha
PNS DOVOZ TISKU, Vinohradská 46, *Praha 2*
PNS DOVOZ TLAČE, *Bratislava 2*

DENMARK
EJNAR MUNKSGAARD, Norregade 6
1165 Copenhagen K

FEDERAL REPUBLIC OF GERMANY
KUNST UND WISSEN ERICH BIEBER
Postfach 46, *7000 Stuttgart 1*

FINLAND
AKATEEMINEN KIRJAKAUPPA, P.O. Box 128 *SF- 00101 Helsinki 10*

FRANCE
DAWSON-FRANCE S. A., B. P. 40, *91121 Palaiseau*
EUROPÉRIODIQUES S. A., 31 Avenue de Versailles, *78170 La Celle St. Cloud*
OFFICE INTERNATIONAL DE DOCUMENTATION ET LIBRAIRIE, 48 rue Gay-Lussac
75240 Paris Cedex 05

GERMAN DEMOCRATIC REPUBLIC
HAUS DER UNGARISCHEN KULTUR
Karl Liebknecht-Straße 9, *DDR-102 Berlin*
DEUTSCHE POST ZEITUNGSVERTRIEBSAMT Straße der Pariser Kommüne 3–4, *DDR-104 Berlin*

GREAT BRITAIN
BLACKWELL'S PERIODICALS DIVISION
Hythe Bridge Street, *Oxford OX1 2ET*
BUMPUS, HALDANE AND MAXWELL LTD.
Cowper Works, *Olney, Bucks MK46 4BN*
COLLET'S HOLDINGS LTD., Denington Estate *Wellingborough, Northants NN8 2QT*
WM. DAWSON AND SONS LTD., Cannon House *Folkstone, Kent CT19 5EE*
H. K. LEWIS AND CO., 136 Gower Street
London WC1E 6BS

GREECE
KOSTARAKIS BROTHERS INTERNATIONAL BOOKSELLERS, 2 Hippokratous Street, *Athens-143*

HOLLAND
MEULENHOFF-BRUNA B. V., Beulingstraat 2, *Amsterdam*
MARTINUS NIJHOFF B.V.
Lange Voorhout 9–11, *Den Haag*
SWETS SUBSCRIPTION SERVICE
347b Heereweg, *Lisse*

INDIA
ALLIED PUBLISHING PRIVATE LTD., 13/14
Asaf Ali Road, *New Delhi 110001*
150 B-6 Mount Road, *Madras 600002*
INTERNATIONAL BOOK HOUSE PVT. LTD.
Madame Cama Road, *Bombay 400039*
THE STATE TRADING CORPORATION OF INDIA LTD., Books Import Division, Chandralok 36 Janpath, *New Delhi 110001*

ITALY
INTERSCIENTIA, Via Mazzé 28, *10149 Torino*
LIBRERIA COMMISSIONARIA SANSONI, Via Lamarmora 45, *50121 Firenze*
SANTO VANASIA, Via M. Macchi 58
20124 Milano
D. E. A., Via Lima 28, *00198 Roma*

JAPAN
KINOKUNIYA BOOK-STORE CO. LTD.
17-7 Shinjuku 3 chome, Shinjuku-ku, *Tokyo 160-91*
MARUZEN COMPANY LTD., Book Department, P.O. Box 5050 Tokyo International, *Tokyo 100-31*
NAUKA LTD. IMPORT DEPARTMENT
2-30-19 Minami Ikebukuro, Toshima-ku, *Tokyo 171*

KOREA
CHULPANMUL, *Phenjan*

NORWAY
TANUM-TIDSKRIFT-SENTRALEN A.S., Karl Johansgatan 41–43, *1000 Oslo*

POLAND
WĘGIERSKI INSTYTUT KULTURY, Marszalkowska 80, *00-517 Warszawa*
CKP-I W, ul. Towarowa 28, *00-958 Warszawa*

ROUMANIA
D. E. P., *Bucuresti*
ILEXIM, Calea Grivitei 64–66, *Bucuresti*

SOVIET UNION
SOJUZPECHAT — IMPORT, *Moscow*
and the post offices in each town
MEZHDUNARODNAYA KNIGA, *Moscow G-200*

SPAIN
DIAZ DE SANTOS, Lagasca 95, *Madrid 6*

SWEDEN
GUMPERTS UNIVERSITETSBOKHANDEL AB
Box 346, *401 25 Göteborg 1*

SWITZERLAND
KARGER LIBRI AG, Petersgraben 31, *4011 Basel*

USA
EBSCO SUBSCRIPTION SERVICES
P.O. Box 1943, *Birmingham, Alabama 35201*
F. W. FAXON COMPANY, INC.
15 Southwest Park, *Westwood Mass. 02090*
READ-MORE PUBLICATIONS, INC.
140 Cedar Street, *New York, N.Y. 10006*

YUGOSLAVIA
JUGOSLOVENSKA KNJIGA, Terazije 27, *Beograd*
FORUM, Vojvode Mišića 1, *21000 Novi Sad*

Index: 26.022